Transactions of the ASME®

Journal of Fluids Engineering

Published Quarterly by The American Society of Mechanical Engineers

VOLUME 116 • NUMBER 1 • MARCH 1994

(Contents continued on page 4)

FLUIDS ENGINEERING DIVISION
Technical Editor
DEMETRI P. TELIONIS (1995)
Executive Secretary
PAT WHITE (1995)
Calendar Editor
M. F. ACKERSON

Associate Technical Editors
R. E. A. ARNDT (1995)
O. BAYSAL (1994)
M. GHARIB (1995)
A. F. GHONIEM (1995)
H. HASHIMOTO (1996)
J. A. C. HUMPHREY (1996)
O. C. JONES (1995)
J. H. KIM (1996)
G. KARNIADAKIS (1995)
R. W. METCALFE (1995)
L. NELIK (1995)
W.-F. NG (1996)
R. L. PANTON (1994)
M. W. REEKS (1994)
W. S. SARIC (1995)
D. E. STOCK (1996)
S. P. VANKA (1996)

BOARD ON COMMUNICATIONS
Chairman and Vice-President
R. D. ROCKE

Members-at-Large
T. BARLOW, T. DEAR, L. KEER,
J. KITTO, W. MORGAN, E. M. PATTON,
S. PATULSKI, R. E. REDER, R. SHAH,
A. VAN DER SLUYS, F. M. WHITE,
J. WHITEHEAD

OFFICERS OF THE ASME
President, **J. H. FERNANDES**
Exec. Dir.
D. L. BELDEN
Treasurer,
R. A. BENNETT

PUBLISHING STAFF
Mng. Dir., Publ.,
CHARLES W. BEARDSLEY
Managing Editor,
CORNELIA MONAHAN
Production Asstistant, **MARISOL ANDINO**

Transactions of the ASME, Journal of Fluids Engineering (ISSN 0098-2202) is published quarterly (Mar., June, Sept., Dec.) for $130.00 per year by The American Society of Mechanical Engineers, 345 East 47th Street, New York, NY 10017. Second class postage paid at New York, NY and additional mailing offices. POSTMASTER: Send address changes to Transactions of the ASME, Journal of Fluids Engineering, c/o THE AMERICAN SOCIETY OF MECHANICAL ENGINEERS, 22 Law Drive, Box 2300, Fairfield, NJ 07007-2300.
CHANGES OF ADDRESS must be received at Society headquarters seven weeks before they are to be effective. Please send old label and new address.
PRICES: To members, $40.00, annually: to nonmembers, $130.00. Add $24.00 for postage to countries outside the United States and Canada.

STATEMENT from By-Laws. The Society shall not be responsible for statements or opinions advanced in papers or . . . printed in its publications (B7.1, Par. 3).
COPYRIGHT © 1994 by The American Society of Mechanical Engineers. Authorization to photocopy material for internal or personal use under circumstances not falling within the fair use provisions of the Copyright Act is granted by ASME to libraries and other users registered with the Copyright Clearance Center (CCC) Transactional Reporting Service provided that the base fee of $3.00 per article is paid directly to CCC, 27 Congress St., Salem, MA 01970. Request for special permission or bulk copying should be addressed to Reprints/Permission Department.

INDEXED by Applied Mechanics Reviews and Engineering Information, Inc.
Canadian Goods & Services Tax Registration #126148048

Downloaded 03 Jun 2010 to 171.66.16.158. Redistribution subject to ASME license or copyright; see http://www.asme.org/terms/Terms_Use.cfm

Contents (continued)

Technical Briefs

Announcements and Special Notices

Journal of
Fluids
Engineering

Editorial

Every year in the March issue, we publish a report on the operation of the Journal. This report provides information on matters like our efforts to make our papers more accessible to fluids engineers, reduce reviewing time, as well as our special activities, like the publication of special articles, the establishment of the JFE Data Bank, publishing in color and others. We also include standard information on the four issues of the previous volume, namely, the list of reviewers and an index of papers listed under certain technical categories.

The Editorial Board of the Journal has had many discussions over the past years on what this Journal could do to improve the process of technology transfer. For the time being, the Editor urges authors strongly and in specific terms to include in their conclusions information that could be appreciated by practicing fluids engineers. This is an issue of current concern (see also the series of editorials on U.S. Competitiveness that appeared in our Technical Forum) and we are eager to participate more actively in the process of technology transfer after the Division defines the Journal's role.

An informal investigation indicated that only a few papers presented at the Division meetings are submitted to the Journal. To some extent, this may be due to the impression shared by some authors that papers included in symposium proceedings cannot be submitted for Journal publication. In fact, ASME does not consider proceedings papers archival and such papers are accepted by all ASME transactions for publication. We do not actively solicit conference papers but it appears that we could serve our readership better if the most significant papers from our meetings were eventually published in the Journal.

In the past year, we experienced again an increase in the number of submitted papers. This trend started about five years ago and the increase since then has been monotonic. The number of papers received has nearly tripled in this period. For a few years now, we were able to secure more pages for the Journal for a total increase of about 60 percent. Unfortunately, in the past two years, no further increase was possible. Due to the global recession, many libraries have discontinued their subscription to a large number of technical journals. The JFE does cover its expenses of publication but the ASME Publications Committee decided to follow a uniform, conservative approach and did not approve any increase in allotted pages for any of the ASME Transactions. This situation has increased our backlog and as a result lengthened the acceptance-to-publication time.

In the past year we were able to decrease the time between submission and the editorial decision on publication to an average of ten months. This figure may not seem encouraging but one should bear in mind that it includes the time required for revisions, which unfortunately for many authors is six or more months. More disturbing to individual authors are delays on the first return of reviews and editorial advice. These are usually due to individuals who accept the responsibility to review a paper, but fail to respond, even after many telephone or e-mail prompts. Authors should understand that if two of the three reviewers do not respond after a few months, the Editorial Board is at an impasse. We usually turn to new reviewers to whom we explain the situation but we cannot expect from them a response sooner than the traditional two to three weeks usually allowed for a review.

In the past year we established a data bank for data that accompany selected JFE papers. Today, modern equipment can generate massive numbers of experimental data. Since only a small set of such data can be presented in the few figures of a paper, it was decided to provide to the Journal readership selected files of data electronically. Data are reviewed and archived and once deposited to the JFE Data Bank, they are considered an integral part of a JFE paper and should be appropriately referenced if employed or manipulated by other authors. Papers accompanied by data are identified by a subtitle. Readers can log on to the JFE Data Bank, examine and if they desire, download files. Directions appear in the last few pages of each issue.

The JFE Data Bank initiative appears to have been received enthusiastically by the JFE readers. In the month of April 1993 alone, immediately after the appearance of the March issue, over 1,500 individuals logged on to the JFE Data Bank and about half of them downloaded data. The March 1993 issue contained two review articles, which were accompanied by data and should have been very useful to the readers. This rate has been reduced since but at any month, a few hundred readers log on to the JFE Data Bank.

Our readers must have noticed that the December issue appeared in color. This is an option now available. Unfortunately, there is a charge to the authors, but thanks to the efforts of our publisher, Mr. James Sheridan and our copy editor, Ms. Cornelia Monahan, this was reduced to a fraction of what other technical journals charge for color. Depending on how many papers accompanied by color figures can be grouped in one issue, a color page could cost between \$300 and \$800 to the authors.

Finally we should acknowledge the valuable contribution of seven of our associate editors whose tenure has expired. They are (i) Dr. Nicholas A. Cumpsty in the area of fluid application and systems, (ii) Dr. Thomas T. Huang, in the area of fluid measurements, (iii) Dr. Ramesh K. Agarwal, (iv) Mr. Dennis M. Bushnell, (v) Dr. Ho, Chih-Ming, in the area of fluid mechanics, (vi) Dr. Andrea Prosperetti, in the area of multiphase flow, and (vii) Dr. Saad A. Ragab, technical editor's office. We sincerely appreciate their hard work. We should also acknowledge the contributions of our reviewers. The names of the individuals who helped us out this year are listed in the last pages of this issue.

Individuals have been nominated to serve three-year terms as associate editors. These and the areas they will be working on are: Professor Hiroyuki Hashimoto (Tohoku University, Japan), Professor Wing-Fai Ng (Virginia Polytechnic Institute and State University)—fluid application and systems; Dr. Jong H. Kim (Electric Power Research Institute, Palo Alto, CA)—multiphase flow; Professor David E. Stock (Washington State University)—fluid measurement; and Professor S. Pratap Vanka (University of Illinois)—computational fluid dynamics. Professor Joseph A. C. Humphrey was reappointed for a second three year term and will work in the area of fluid mechanics.

The Technical Editor

Journal of Fluids Engineering
Technical Forum

Questions in Fluid Mechanics:

Reynolds Number Effects in Wall-Bounded Flows

by Mohamed Gad-el-Hak[1] and Promode R. Bandyopadhyay[2]

For wall-bounded flows, what are the Reynolds number effects on the mean and statistical turbulence quantities and on the organized motion?

The Reynolds numbers encountered in many practical situations are orders of magnitude higher than those studied computationally or experimentally. For this reason, our knowledge of high-Reynolds number flows is limited and a complete understanding is yet to emerge. Free shear flows are nearly inviscid at sufficiently high Reynolds number, and by implication are Reynolds number-independent. However, the situation is more complicated in wall-bounded flows, where no matter how large the Reynolds number is, there is always a finite region near the surface where viscosity effects are important. The key question is then what are the Reynolds number effects in wall-bounded flows on the mean and statistical turbulence quantities and on the organized turbulent motions?

The Direct Numerical Simulation (DNS) of turbulent boundary layers have so far been carried out up to a Re_θ of 1410 (Spalart, 1986). Since the computational resource required varies as the cube of the Reynolds number, it would not be possible to simulate very high-Reynolds number turbulent shear flows any time soon (Karniadakis and Orszag, 1993). This has created a resurgence of interest in turbulence modeling particularly for high-Reynolds number flows. Understanding of turbulence and modeling will continue to play vital roles in the computation of high-Reynolds number practical flows using the Reynolds-averaged Navier-Stokes equations. Apart from turbulence modeling, the knowledge of Reynolds number effects is useful to flow control, a field of obvious practical utility. For economic reasons, typical control devices are initially developed and tested at rather low speeds. Extrapolation to field conditions is not always straightforward though, and it often fails.

One of the earliest studies of the Reynolds number effects in turbulent boundary layers was due to Coles (1962). When measurements of mean velocity profiles were expressed in inner layer form based on *directly measured* local skin-friction values, a logarithmic region was found to exist even at a Re_θ of 50×10^3. The wall-layer variables appear to describe the mean flow in the inner layer universally in flat plates, pipes and channels at all Reynolds numbers. On the other hand, in a boundary layer, the behavior of the outer layer, when expressed in terms of the wall layer variables by the strength of the wake component ΔU^+, which is the maximum deviation of the mean velocity profile from the log law, appeared to reach an asymptotic value for $Re_\theta > 6 \times 10^3$. Above this limit, the inner and outer layer mean flows are then expected to reach an asymptotic state which the turbulence quantities are also hypothesized to follow. This is, however, not the case since the wake component starts decreasing, albeit slowly, at about $Re_\theta > 15 \times 10^3$. This raises the question, does the mean flow ever achieve true self-preservation? There is some new evidence that in boundary layers even the mean flows normalized with inner variables show Reynolds number dependence all the way down to the edge of the viscons sublayer (George et al., 1992).

The situation is murkier for higher-order turbulence statistics. Measurements in pipes (Morrison et al., 1971), channels (Wei and Willmarth, 1989) and boundary layers (Andreopoulos et al., 1984; Erm et al., 1985) show that the turbulence quantities do not scale with wall-layer variables even in the inner layer. Therefore, the question arises, can we apply mean-flow scales to turbulence?

Furthermore, the outer-layer-device drag reduction experiments of Anders (1990) show that for $Re_\theta > 6 \times 10^3$, the maximum skin-friction reduction and the recovery length (the latter with some exception) do not remain constant but decrease with increasing Reynolds number. The loss of performance at higher Reynolds numbers is puzzling and Anders attributed this to a significant change in the turbulence structure. In this background, a relevant question is: does the turbulence structure change above this Reynolds number limit?

Consider another puzzling high-Reynolds-number behavior. Clauser (1954) had experimentally shown that in a turbulent boundary layer at a given low Reynolds number, disturbances survive much longer in the outer layer ($y/\delta > 0.2$) than in the inner layer. He demonstrated this by placing a circular rod in the outer and inner layers. In viscous drag reduction techniques where a device drag penalty is involved, as with the use of an outer-layer-device, a recovery length of $O[100\delta]$ is desirable to achieve a net gain. To date, such recovery lengths have been achieved only at low Reynolds numbers as mentioned earlier. One normally expects the recovery length to be far less if the disturbances are applied near the wall, and the length to reduce even more as Re_θ is increased. However, published data (Klebanoff and Diehl, 1952; Bandyopadhyay, 1991) show that, in fact, at higher Reynolds numbers, an opposite trend sometimes takes place. This unexpected result raises the question, what is the Reynolds number effect on post-transition memory?

More details could be found in a forthcoming article by Gad-el-Hak and Bandyopadhyay (1994).

References

Anders, J. B., 1990, "Boundary Layer Manipulators at High Reynolds Numbers," *Structure of Turbulence and Drag Reduction*, A. Gyr, ed., Springer-Verlag, Berlin, pp. 475–482.

---

[1] University of Notre Dame, Notre Dame, IN 46556-5637.

[2] Naval Undersea Warfare Center, Newport, Rhode Island, 02841-5047.

Andreopoulos, J., Durst, F., Zaric, Z., and Jovanovic, J., 1984, "Influence of Reynolds Number on Characteristics of Turbulent Wall Boundary Layers," *Experiments in Fluids*, Vol. 2, pp. 7-16.

Bandyopadhyay, P. R., 1991, "Comments on Reynolds Number Effects in Wall-Bounded Shear Layers," AIAA Paper No. 91-0231, New York.

Clauser, F., 1954, "Turbulent Boundary Layers in Adverse Pressure Gradient," *Journal of the Aeronautical Sciences*, Vol. 21, pp. 91-108.

Coles, D. E., 1962, "The Turbulent Boundary Layer in a Compressible Fluid," Rand Corporation Report No. R-403-PR, Santa Monica, CA.

Erm, L. P., Smits, A. J., and Joubert, P. N., 1987, "Low Reynolds Number Turbulent Boundary Layers on a Smooth Flat Surface in a Zero Pressure Gradient," *Fifth Symposium on Turbulent Shear Flows*, F. Durst et al., eds., Springer-Verlag, Berlin, pp. 2.13-2.18.

Gad-el-Hak, M., and Bandyopadhyay, P. R., 1994, "Reynolds Number Effects in Wall-Bounded Flows," *Applied Mechanics Reviews*, to appear.

George, W. K., Castillo, L., and Knecht, P., 1992, "The Zero-Pressure Gradient Turbulent Boundary Layer Revisited," *Thirteenth Symposium on Turbulence*, X. B. Reed, ed., Univ. Missouri at Rolla, April 21-23.

Karniadakis, G. Em., and Orszag, S. A., 1993, "Nodes, Modes and Flow Codes," *Physics Today*, Vol. 46, No. 3, pp. 34-42.

Klebanoff, P. S., and Diehl, Z. W., 1952, "Some Features of Artificially Thickened Fully Developed Turbulent Boundary Layers With Zero Pressure Gradient," NACA Report No. 1110, Washington, D.C.

Morrison, W. R. B., Bullock, K. J., and Kronauer, R. E., 1971, "Experimental Evidence of Waves in the Sublayer," *Journal of Fluid Mechanics*, Vol. 47, pp. 639-656.

Spalart, P. R., 1986, "Direct Simulation of a Turbulent Boundary Layer up to $Re_\theta = 1410$," NASA Technical Memorandum No. TM-89407, Washington, D.C.

Wei, T., and Willmarth, W. W., 1989, "Reynolds-Number Effects on the Structure of a Turbulent Channel Flow," *Journal of Fluid Mechanics*, Vol. 204, pp. 57-95.

Andreopoulos, J., Durst, F., Zaric, Z., and Jovanovic, J., 1984, "Influence of Reynolds Number on Characteristics of Turbulent Wall Boundary Layers," *Experiments in Fluids*, Vol. 2, pp. 7-16.

Bandyopadhyay, P. R., 1991, "Comments on Reynolds Number Effects in Wall-Bounded Shear Layers," AIAA Paper No. 91-0231, New York.

Clauser, F., 1954, "Turbulent Boundary Layers in Adverse Pressure Gradient," *Journal of the Aeronautical Sciences*, Vol. 21, pp. 91-108.

Coles, D. E., 1962, "The Turbulent Boundary Layer in a Compressible Fluid," Rand Corporation Report No. R-403-PR, Santa Monica, CA.

Erm, L. P., Smits, A. J., and Joubert, P. N., 1987, "Low Reynolds Number Turbulent Boundary Layers on a Smooth Flat Surface in a Zero Pressure Gradient," *Fifth Symposium on Turbulent Shear Flows*, F. Durst et al., eds., Springer-Verlag, Berlin, pp. 2.13-2.18.

Gad-el-Hak, M., and Bandyopadhyay, P. R., 1994, "Reynolds Number Effects in Wall-Bounded Flows," *Applied Mechanics Reviews*, to appear.

George, W. K., Castillo, L., and Knecht, P., 1992, "The Zero-Pressure Gradient Turbulent Boundary Layer Revisited," *Thirteenth Symposium on Turbulence*, X. B. Reed, ed., Univ. Missouri at Rolla, April 21-23.

Karniadakis, G. Em., and Orszag, S. A., 1993, "Nodes, Modes and Flow Codes," *Physics Today*, Vol. 46, No. 3, pp. 34-42.

Klebanoff, P. S., and Diehl, Z. W., 1952, "Some Features of Artificially Thickened Fully Developed Turbulent Boundary Layers With Zero Pressure Gradient," NACA Report No. 1110, Washington, D.C.

Morrison, W. R. B., Bullock, K. J., and Kronauer, R. E., 1971, "Experimental Evidence of Waves in the Sublayer," *Journal of Fluid Mechanics*, Vol. 47, pp. 639-656.

Spalart, P. R., 1986, "Direct Simulation of a Turbulent Boundary Layer up to $Re_\theta = 1410$," NASA Technical Memorandum No. TM-89407, Washington, D.C.

Wei, T., and Willmarth, W. W., 1989, "Reynolds-Number Effects on the Structure of a Turbulent Channel Flow," *Journal of Fluid Mechanics*, Vol. 204, pp. 57-95.

U.S. Technological Competitiveness: A Fluids Engineers' Viewpoint

Column #6—Epilogue

by J. L. Dussourd[1]

A Report on the Panel Events at the '93 WAM in New Orleans and Definition of a Course of Action.

Fluids engineers were not the only ones at the '93 WAM to identify technology transfer as a major bottleneck stifling the working effectiveness of their peers. It was also identified as such by at least three other working groups who had scheduled discussions on this very same topic. As such, our panel echoed the general sentiment throughout the engineering community that there are inherent road blocks out there which frustrate a fuller utilization of our technologies to hone a more highly competitive edge into our industrial products.

Several perceived factors responsible for this state of affairs were introduced in this column in earlier issues of the *Journal of Fluids Engineering*. The authors/panelists conceived of a number of solutions having the potential of lubricating the critical transfers from the work places where the technologies are being generated to the work places where they are being used. At this '93 panel these solutions were to be critically examined by a core of responders selected for their maturity and experience and by an audience who would speak for the broad membership. Although time was short and the '93 attendance was less impressive than at the 1991 panel, the discussions were exceptionally lively and they reflected divergences of opinions, particularly between those at the far ends of the transfer chain.

The three central themes introduced by the panelists were as follows.

1. An effective person-to-person relationship between those engaged in exchanging technologies. This can typically be initiated by a member of academia working to establish a productive and mutually beneficial rapport with a counterpart in industry, by helping him solve his more difficult problems. Compensations for these services take the form of grant support by his company to the university where they are used to support research programs, which may or may not be related to the particular consulting problem at hand. Through such interactions, industry receives infusions from technical specialists from universities and the university benefits from exposure to real life problems and from industrially financed support to supplement its dwindling government sources.
2. A scheme for the ASME to take an active role in promoting such relationships on a national scale. By so doing, the ASME is greatly extending its main charter responsibility, i.e., that of disseminating technology. It can do this by assuming now the role of a broker or matchmaker between those who have it and those who need it. In this capacity, the ASME would develop data banks of the technologies that are available and match them against corresponding data banks of technologies that are advertised as being wanted. Under ASME guidance, consortia and consulting relationships are brought into being at regional as well as at national levels. Monetary compensations are paid by those who benefit from the transfer for the time and effort expended, supplemented perhaps by government matching funds. All these would be used for research or for further technology developments. Once such a consortium is established, the ASME withdraws, allowing the new partnership to self-expand.
3. From the realization that much of the world technologies can now be found offshore as well as in the US and that these sources are essentially untapped, it can be concluded that if US industry availed itself of them, its competitiveness would be greatly increased at little cost to itself. Thus the problem is how to best mine these sources to bring them as quickly as possible onto the computer screens of those in need of the technologies. Clearly this could best be done with federal participation for the searches, translations and the conversions into digestible forms.

The great majority of responders on the panel echoed the need for vastly increased transfer means. It was recognized that existing agencies, such as the various Institutes for Air Conditioning and Refrigeration, Gas Research, Electric Power Research, Industrial Research, the various government laboratories commercialization efforts, the various university industrial liaison programs, the on and off-campus sponsored conferences, the industrial technical councils and extension centers, the many new Technology Centers, while they perform admirably, do not come close to meeting all the needs that have been publicly admitted or that are known to be latent in occluded states. Many of the above-mentioned associations serve their affiliated industries only and do not perform the broad function of meeting the random needs as they arise.

There were voices of opposition, mainly from the academic sector. To help industry solve its problems is seen as a distraction at the more research oriented institutions, diluting the established scientific activities. The notion was also expressed

---

[1] President, Fluids Engineering Associates, 14 Cleveland Road West, RD 2, Princeton, NJ 08540.

There were voices of opposition, mainly from the academic sector. To help industry solve its problems is seen as a distraction at the more research oriented institutions, diluting the established scientific activities. The notion was also expressed that because there are already so many agencies dedicated to that purpose, academia must remain one that is free to carry out research for its own sake in a setting that is fully independent, free of confidentiality entanglements and strong in its conviction that its research work remains at the core as a driving force for progress. Industry's need for help was seen as a problem of industry, endemic to its culture, to its preoccupation with secretiveness and to its inability or unwillingness to think long term and adopt advanced technologies.

These sentiments express the magnitude of the gap between these cultures, each claiming a modus vivendi which is unique to themselves and which cannot be changed. They are at the root cause for the state of gridlock referred to in earlier columns, inhibiting a more effective flow of information between the cultures. The ASME has in the past assumed a passive role in bridging this gap. It has provided a forum for publicizing the technologies, supplied current interest and archival repositories to store them, library services to disseminate them, computerized searching means to retrieve them. The Federal Government has done likewise through its many laboratories and its technological indices. These are *passive* roles, however, which assume that information once it is made available will be aggressively dug out by those who need it. These assumptions now appear to be unrealistic. A more active role is needed on the part of the ASME to help the process along, opening doors that are closed, easing the assimilation problems by multiplying the opportunities for mutually beneficial interactions.

Such a new role assumed by the ASME would meet all three basic themes expressed earlier in this column. Only basic or emerging technologies of the type now available from library shelves would be involved with minimum vulnerability to issues of confidentiality. Offshore, as well as onshore sources, would be tapped equally. The key elements rest with the willingness on the part of the technology producers to get themselves involved and with the willingness on the part of the users to dedicate time and skills to master the technologies and put them into daily use.

The challenge of such an effort is not to be underestimated. It cuts into many existing "sacred cows" and safe refuges. It forces the various sectors of our technological world to work together in ways that have mostly been forgotten. As a follow up to the ideas advanced by the authors and panelists, a model for action will be defined and formally submitted to the leadership of the Fluids Engineering Division, as an opportunity to lead an endeavor that hopefully would then catch on across the breadth of the ASME. Some other engineering societies such as the AIChE already have similar action programs in effect. Their experience will be invaluable in developing our own.

Perspective: Numerical Simulations of Wakes and Blade-Vortex Interaction

Dean T. Mook
N. Waldo Harrison Professor.
Fellow ASME

Bonian Dong[1]

Department of Engineering Science
and Mechanics,
Virginia Polytechnic Institute
and State University,
Blacksburg, VA 24061

A method for simulating incompressible flows past airfoils and their wakes is described. Vorticity panels are used to represent the body, and vortex blobs (vortex points with their singularities removed) are used to represent the wake. The procedure can be applied to the simulation of completely attached flow past an oscillating airfoil. The rate at which vorticity is shed from the trailing edge of the airfoil into the wake is determined by simultaneously requiring the pressure along the upper and lower surface streamlines to approach the same value at the trailing edge and the circulation around both the airfoil and its wake to remain constant. The motion of the airfoil is discretized, and a vortex is shed from the trailing edge at each time step. The vortices are convected at the local velocity of fluid particles, a procedure that renders the pressure continuous in an inviscid fluid. When the vortices in the wake begin to separate they are split into more vortices, and when they begin to collect they are combined. The numerical simulation reveals that the wake, which is originally smooth, eventually coils, or wraps, around itself, primarily under the influence of the velocity it induces on itself, and forms regions of relatively concentrated vorticity. Although discrete vortices are used to represent the wake, the spatial density of the vortices is so high that the computed velocity profiles across a typical region of concentrated vorticity are quite smooth. Although the computed wake evolves in an entirely inviscid model of the flowfield, these profiles appear to have a viscous core. The computed spacing between the regions of concentrated vorticity in the wake and the circulations around them are in good agreement with the experimental results. As an application, a simulation of the interaction between vorticity in the oncoming stream and a stationary airfoil is also discussed.

1 Introduction

The numerical simulation of unsteady vorticity-dominated flow is a long-standing interest of many researchers. In this paper we consider one small aspect of the total problem: the numerical simulation of the wake generated by a moving airfoil. The recent extensive reviews and discussions of vortex methods and modelling of vorticity-dominated flowfields by Leonard (1980), McCroskey (1982), Aref (1983), Aref and Kambe (1988), Spalart (1988), and Sarpkaya (1989) provide the background for the present discussion. No attempt is made to paraphrase or elaborate on them. The present discussion is focused on some recent developments and comparisons between numerical and experimental results; it is part review, part perspective, and part presentation of new results. A similar discussion of an analytical approach with some historical perspectives can be found in the recent article by McCune and Tavares (1993).

The panel method described here employs a continuous distribution of vorticity on the surface of the airfoil. The advantage is that continuous surface velocity, pressure, etc. are obtained directly from the solution. Versions of the method have been used to model steady flows by Raj and Gray (1978) and unsteady flows by Kim and Mook (1986).

In unsteady attached flows past airfoils a thin layer of concentrated vorticity (simulated as a vortex sheet) forms at the trailing edge. It rolls up and stretches, forming regions of concentrated vorticity that spread and distort as they convect downstream. McCroskey (1982) gave a review of the work on the unsteady aerodynamics of oscillating airfoils, such as those pitching and/or plunging. In certain ranges of the amplitude and frequency of the oscillation, the flow on the surface of the airfoil stays attached. Some experiments have been conducted, focusing on the flow near the trailing edge. Ohashi and Ishikawa (1972) and Ho and Chen (1980, 1981) experimentally studied the Kutta condition using a plunging airfoil. Poling and Telionis (1986) were able to explore the neighborhood of the trailing edge of a pitching airfoil in greater detail by using an ensemble-averaging scheme. Park et al. (1988) also conducted an experiment on the near wake of a pitching airfoil

---

[1] Present address: Assistant Professor, Department of Mechanical and Production Engineering, National University of Singapore, Singapore.

Contributed by the Fluids Engineering Division for publication in the JOURNAL OF FLUIDS ENGINEERING. Manuscript received by the Fluids Engineering Division October 31, 1991; revised manuscript received October 7, 1993. Associate Technical Editor: D. P. Telionis.

and detected the trailing-edge stall and found that its occurrence is related to the reduced frequency of the pitching. Liu et al. (1990) studied the unsteady flow near the trailing edge of a fixed-airfoil by disturbing the oncoming stream.

The far wake has also been investigated. In an experimental and numerical study, Mathioulakis et al. (1985) concluded that the flowfield is controlled almost entirely by the inviscid self-interaction of vorticity. This conclusion is further substantiated by the experimental and numerical work of Wilder et al. (1990). Mook et al. (1987, 1989) numerically simulated the wake of an oscillating airfoil by using discrete vortices and obtained a large-scale structure that is very similar to the one observed by Bratt (1950) through flow visualization. Koochesfahani's experiment (1989) showed that the wake structure can be controlled by the frequency, amplitude, and the shape of the oscillation waveform. Booth (1987) measured the velocity behind a pitching airfoil in a wind tunnel and numerically integrated the measurements to obtain the circulations around the regions of concentrated vorticity. The numerical results of Mook and Dong (1990) obtained by using discrete vortices agree very well with Booth's experimental results.

Wakes are often approximated by a system of discrete point vortices (called vortex points here) or vortex blobs. The use of vortex points to simulate continuous vortex sheets apparently was first proposed by Rosenhead (1931). The flowfield induced by a vortex point is singular so that some special treatment, such as setting a cutoff criterion, is necessary. The vortex-blob method also deletes the singularity (Spalart, 1988); it is used in simulations presented here and discussed below.

In order to model closely coupled aerodynamic interference, especially the situation in which one airfoil is near or in the wake of another, an accurate simulation of the wake is needed. Mook et al. (1987) developed an innovation that captures some details of the wake by adding more discrete vortices to the wake and then redistributing the circulations among them. The innovation is described below and used in most of the simulations presented here. The present numerical results are in good agreement with the experiments.

As an application of the numerically simulated wake, blade-vortex interaction (BVI), which happens in the flowfields of helicopter blades and is a primary source of unsteady loads and noise, is briefly discussed in this review. When a rotor advances, the blades encounter the vortex filaments generated by the preceding blades. Generally, BVI is a complicated three-dimensional unsteady phenomenon, but it is sometimes considered as the combination of the following two limit cases (Srinivasan, 1985): one in which the vortex filament is parallel to the span of the blade, and one in which the vortex filament is perpendicular to the span. The former is often idealized as a two-dimensional problem and, as such, it is discussed here.

The two-dimensional BVI has been experimentally investigated by Poling et al. (1988), Booth and Yu (1986), Booth (1986, 1987), and Straus et al. (1990). In all these experiments, which were conducted in both wind and water tunnels, similar apparati were used: a stationary airfoil was placed in or near the wake generated by a pitching airfoil upstream. The flowfield and loads on the stationary airfoil were measured.

In the early numerical simulations of BVI, a single vortex point was released far upstream and allowed to pass through the neighborhood of an airfoil. This situation has been treated by employing the Euler equations for compressible flows and the Navier-Stokes equations for incompressible flows (Srinivasan, 1985; Srinivasan et al., 1984, 1986; Damodaran and Caughey, 1988; Wu et al., 1985; Hsu and Wu, 1986). Conformal mapping and vortex methods have also been used to simulate BVI for incompressible inviscid flows (Huang and Chow, 1982; Chow and Huang, 1983; Wu et al., 1985; Hsu and Wu, 1986, 1988; Poling et al., 1987, 1988; Dong, 1987). The major shortcoming of this single-vortex model is that in an actual situation vorticity is not confined to a point; instead it is distributed over a finite area. Consequently, the single-vortex model appears to be reasonable only when the dimension of the vorticity-bearing area is small compared to its distance from the airfoil. Improved models have been developed by using more than just one vortex to simulate the finite vorticity-bearing area (Panaras, 1987; Lee and Smith, 1987; Poling et al., 1988; Renzoni and Mayle, 1991).

In the present discussion of BVI, first the interaction of a vortex point with an airfoil is investigated. The inviscid simulation closely matches some solutions of the Navier-Stokes equations for attached turbulent flow and of the Euler equations for inviscid transonic flow. Then a simulation of the experiment of Booth (1987) is discussed, in which a stationary airfoil is placed in the wake of a pitching airfoil. A numerical solution is described that accounts for the aerodynamic interference between the two airfoils and for the interactions among all wakes and all blades. The discrete vortices simulating the wake of the pitching airfoil are neither uniform nor arranged in a simple pattern, but arranged in a manner consistent with the wake of the pitching airfoil. Renzoni and Mayle (1991) also attempted to do this, but they did not split the vortex points. The predicted aerodynamic loads on the stationary airfoil are similar to other numerical solutions, but differ from Booth's measurement (1987). An explanation for the difference is given. In the authors' paper on BVI (Dong and Mook, 1991), the numerical simulation of the experiments by Straus et al. (1990), which are similar to Booth's, is found to be in good agreement with the observations.

2 Description of the Numerical Models of the Flowfield

There are several good models for attached unsteady flows past airfoils. Here the concentration is on a recent development based on panels of continuously varying vorticity. One appealing characteristic of this approach is that the unknown is a primitive variable, the velocity of the fluid particles next to the surface. With no post-processing, the solution provides a continuous estimate of the velocity next to the surface of the airfoil. With very little post-processing, the solution also provides a continuous pressure distribution over the surface.

Any model of unsteady flow past an airfoil must predict both the rate at which vorticity is shed from the trailing edge into the wake and the way in which the shed vorticity is transported downstream. These features of the model are described in this section. First the basic concepts and the governing equations are discussed. Then some simplifications, a panel method coupled with vortex dynamics, and the Kutta condition at the trailing edge are introduced. The flowfield is considered two-dimensional in all that follows. Mracek and Mook (1988) developed a three-dimensional version of the present panel method.

2.1 Basic Concepts. The continuity equation for incompressible flows is

$$\mathrm{Div}\mathbf{V}=0 \tag{1}$$

where **V** is the velocity vector, and vorticity is defined by

$$\boldsymbol{\Omega}=\mathrm{Curl}\mathbf{V} \tag{2}$$

Equations (1) and (2) can be inverted to give **V** as a function of **Ω** (see, e.g., the general discussion of Sommerfeld, 1964, Section IV. 20, more recent discussions by Wu and Thompson, 1973, and Wu and Sankar, 1980)

$$\mathbf{V}(\mathbf{r},\,t)=\frac{1}{2\pi}\int_S\frac{\boldsymbol{\Omega}(\mathbf{r}_0,\,t)\times(\mathbf{r}-\mathbf{r}_0)}{|\mathbf{r}-\mathbf{r}_0|^2}\,dS(\mathbf{r}_0)+\mathbf{V}_\infty \tag{3}$$

where S is the entire region of interest, $\mathbf{r}_0$ is the position of the area element dS, $\mathbf{r}$ is the position where the velocity is being evaluated, t is the time, $\mathbf{V}_\infty$ is the uniform velocity of the freestream, and × denotes a cross product of vectors.

Six important characteristics of the velocity field **V** given by Eqs. (1)–(3) are worth mentioning:

1. The disturbance velocity [the first term of the right-hand side of Eq. (3)] is a version of the Biot-Savart law.
2. The region S includes the flowfield as well as the interiors of the objects in the flowfield, and the vorticity in those interiors is twice the angular velocity of these objects. (More details are given in Section 2.3.)
3. The vorticity, $\boldsymbol{\Omega}$, may be zero in large subregions of S and the velocity, **V**, is irrotational in these regions.
4. Vorticity anywhere in S creates velocity everywhere in S.
5. The disturbance velocity decays as the reciprocal of the distance from the vorticity-bearing subregions.
6. Equation (3) is a purely kinematic relationship; in deriving it, one does not need to make any assumptions regarding the velocity field other than **V** is continuous, and Div**V** = 0. Consequently, Eq. (3) is valid for "viscous" as well as "inviscid" models of flows.

In the model of attached unsteady flow past an airfoil, one postulates a priori that all the vorticity is in the following three subregions: a thin layer of fluid adjoining the surface of the airfoil, the wake (a free shear layer emanating from the trailing edge), and the interior of the airfoil itself. Thus, instead of having to integrate over the entire flowfield, one only needs to integrate over three relatively small subregions.

By using the vorticity-transport equation and the no-slip condition on the surfaces of the solid bodies, Wu and Sankar (1980) also obtained the following equation expressing the temporal conservation of "total vorticity" (i.e., circulation)

$$\frac{d}{dt}\int_S \boldsymbol{\Omega}\, dS=0 \qquad (4)$$

where the integral is carried out over the same region as the integral in Eq. (3). Equation (4) is also valid for viscous as well as inviscid models of flows.

2.2 Boundary Layer Adjoining the Surface of the Airfoil. It is assumed that the flow in the layer adjoining the surface of the airfoil is accurately predicted by the boundary-layer theory, a theory that provides an asymptotic approximation for high Reynolds numbers to the solution of the Navier-Stokes equations. However, in some cases of strong blade-vortex interaction, the boundary-layer approximation could break down locally when vorticity in the stream passes very close to the surface of the blade. In boundary-layer theory, the pressure predicted by the outer (irrotational) flow on the surface of the airfoil appears as the driving (forcing) term in the governing equations and the tangential component of the velocity given by the outer flow at the surface of the airfoil appears in the boundary (matching) condition. Thus, according to this theory, the outer flow must be known before the flow in the boundary layer can be obtained. But it is also true that, if the flow (specifically the vorticity) is known in the boundary layer and wake and if the motion of the airfoil is known, the corresponding outer flow can be computed by means of Eq. (3). The flow created by the vorticity disturbs the oncoming freestream in such a way that the no-penetration and no-slip conditions are satisfied by the resulting velocity field.

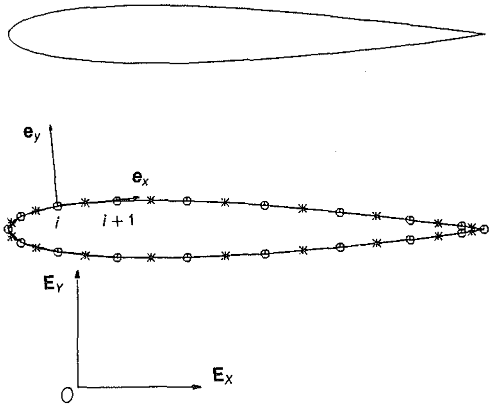

Fig. 1 Airfoil and the coordinate systems: (*a*) before discretization; (*b*) after discretization. ○ represents a node point (where two panels join) and * is a control point (where the no-penetration condition is imposed). The spacing is nonuniform; smaller panels are used near the leading and trailing edges. ($\mathbf{e}_x$, $\mathbf{e}_y$) are base vectors in the local frame, and ($\mathbf{E}_X$, $\mathbf{E}_Y$) are those in the global frame.

In the vorticity-panel approach, one first integrates Eq. (3) across the thickness of the boundary layer, using the boundary-layer approximation for the vorticity, and then lets the boundary-layer thickness approach zero. The contribution of the boundary layer in Eq. (3) is

$$\mathbf{V}_b(\mathbf{r},t)=\frac{1}{2\pi}\int_{S_b}\frac{\boldsymbol{\Omega}(\mathbf{r}_0,t)\times(\mathbf{r}-\mathbf{r}_0)}{|\mathbf{r}-\mathbf{r}_0|^2}\,dS_b(\mathbf{r}_0) \qquad (5a)$$

$$=-\frac{1}{2\pi}\,\mathbf{e}_z\times\oint_C\frac{\gamma[l(\mathbf{r}_0),t](\mathbf{r}-\mathbf{r}_0)}{|\mathbf{r}-\mathbf{r}_0|^2}\,dl(\mathbf{r}_0) \qquad (5b)$$

where $\mathbf{V}_b$ is the velocity induced by the vorticity in the boundary layer, S_b is the region of the boundary layer, $\mathbf{e}_z$ is a unit vector perpendicular to the flowfield chosen so as to form a right-hand system with the base vectors in the plane of the flow, the line integral is carried out along the contour of the airfoil C, l is the distance along C measured from the lower trailing edge, and

$$\gamma(l,t)\mathbf{e}_z=\lim_{\substack{\mathrm{Re}\to\infty\\ \delta\to 0}}\left[-\int_0^{\delta(l)}\boldsymbol{\Omega}(l,n,t)\,dn\right] \qquad (6a)$$

$$\gamma(l,t)=\lim_{\substack{\mathrm{Re}\to\infty\\ \delta\to 0}}\left[\int_0^{\delta(l)}\frac{\partial u}{\partial n}\,dn\right]=u(l,0^+,t)-u(l,0,t)=\Delta u(l,t) \qquad (6b)$$

where Re is the Reynolds number, δ the thickness of the boundary layer, n is the coordinate in the outward-pointing normal direction on the contour of the airfoil C, Δu is the velocity of the fluid relative to the surface of the airfoil and is positive in the direction of increasing l, $u(l, 0^+, t)$ is the velocity at the outer edge of the boundary layer, and $u(l, 0, t)$ is the velocity of the fluid in contact with the surface.

Hence, the thin boundary layer is approximated as a bound vortex sheet of strength $-\gamma$ on the surface of the airfoil. If the no-slip condition is imposed on the surface, γ is the tangential component of the velocity of the fluid at the edge of the boundary layer relative to the nearest point in the surface. The normal component of the relative velocity is zero if the no-penetration condition is satisfied.

The line integral in Eq. (5) is evaluated first by dividing the contour of the airfoil into a number of short straight elements (see Fig. 1) and then by approximating γ as a linear function of position along each element. The values of γ in adjoining elements are equal at the common point where the two are connected, the so-called node.

The calculation of the velocity induced by the vorticity on the individual elements is facilitated by introducing a local coordinate system. The origin of the local frame of reference for element i is placed at node i, the local x-axis runs along the element, and the local y-axis points outward from the airfoil into the flowfield (see Fig. 1). For a typical element i, the transformations between the two frames are

$$\begin{Bmatrix} x \\ y \end{Bmatrix}=\begin{bmatrix} d_1 & d_2 \\ -d_2 & d_1 \end{bmatrix}\begin{Bmatrix} X-X_i \\ Y-Y_i \end{Bmatrix} \qquad (7a)$$

$$\begin{Bmatrix} \mathbf{e}_x \\ \mathbf{e}_y \end{Bmatrix} = \begin{bmatrix} d_1 & d_2 \\ -d_2 & d_1 \end{bmatrix} \begin{Bmatrix} \mathbf{E}_X \\ \mathbf{E}_Y \end{Bmatrix} \tag{7b}$$

where (x, y) are coordinates in the local frame which has the base vectors $(\mathbf{e}_x, \mathbf{e}_y)$ and (X, Y) are the corresponding coordinates in the global frame which has the base vectors $(\mathbf{E}_X, \mathbf{E}_Y)$, (X_i, Y_i) are the global coordinates of the node that serves as the origin of the local frame, and

$$d_1 = (X_{i+1} - X_i)/\Delta l_i$$

$$d_2 = (Y_{i+1} - Y_i)/\Delta l_i \tag{8}$$

where

$$\Delta l_i = \sqrt{(X_{i+1} - X_i)^2 + (Y_{i+1} - Y_i)^2} \tag{9}$$

is the length of element i.

The two linear basis functions

$$f_1(\xi) = 1 - \frac{\xi}{\Delta l_i} \tag{10a}$$

and

$$f_2(\xi) = \frac{\xi}{\Delta l_i} \tag{10b}$$

are used to describe γ on each element:

$$\gamma_i(\xi, t) = G_i(t) f_1(\xi) + G_{i+1}(t) f_2(\xi) \tag{11}$$

where $0 \le \xi \le \Delta l_i$, G_i and G_{i+1} are the values of γ at nodes i and $i + 1$, and Δl_i is given by Eq. (9).

From Eqs. (5), (10), and (11), it follows that, in the local frame, the components of the velocity induced by the vorticity on a single element are given by

$$\mathbf{V}_{bi}(x, y, t) = \frac{1}{2\pi} \int_0^{\Delta l_i} \frac{\gamma_i(\xi, t)[y\mathbf{e}_x - (x-\xi)\mathbf{e}_y]}{(x-\xi)^2 + y^2} d\xi$$

$$= G_i[v_{1xi}\mathbf{e}_x + v_{1yi}\mathbf{e}_y] + G_{i+1}[v_{2xi}\mathbf{e}_x + v_{2yi}\mathbf{e}_y] \tag{12}$$

where

$$v_{1xi} = \frac{1}{2\pi\Delta l_i}[\Delta l_i - x)\Delta\theta - 0.5y \ln R]$$

$$v_{1yi} = \frac{1}{2\pi\Delta l_i}[y\Delta\theta - \Delta l_i + 0.5(\Delta l_i - x) \ln R]$$

$$v_{2xi} = \frac{1}{2\pi\Delta l_i}(x\Delta\theta + 0.5y \ln R)$$

$$v_{2yi} = \frac{1}{2\pi\Delta l_i}(\Delta l_i - y\Delta\theta + 0.5x \ln R) \tag{13}$$

where

$$\Delta\theta = \tan^{-1}\left(\frac{x}{y}\right) - \tan^{-1}\left(\frac{x - \Delta l_i}{y}\right) \tag{14}$$

and

$$R = \frac{(x - \Delta l_i)^2 + y^2}{x^2 + y^2} \tag{15}$$

Using the inverse transformation of Eq. (7) one can obtain the velocity induced by element i in terms of components in the global frame:

$$\mathbf{V}_{bi}(X, Y, t) = G_i[V_{1Xi}\mathbf{E}_X + V_{1Yi}\mathbf{E}_Y] + G_{i+1}[V_{2Xi}\mathbf{E}_X + V_{2Yi}\mathbf{E}_Y] \tag{16}$$

where

$$\begin{Bmatrix} V_{kXi} \\ V_{kYi} \end{Bmatrix} = \begin{bmatrix} d_1 & -d_2 \\ d_2 & d_1 \end{bmatrix} \begin{Bmatrix} v_{kxi} \\ v_{kyi} \end{Bmatrix} \tag{17}$$

for $k = 1$ and 2.

2.3 Contribution to the Flowfield From the Rotation of Airfoils. As discussed in the articles of Wu and Thompson (1973) and Wu and Sankar (1980), the motion of the airfoil also makes a contribution to the flowfield:

$$\mathbf{V}_a(\mathbf{r}, t) = \frac{1}{2\pi} \oint_C \frac{(\mathbf{r} - \mathbf{r}_0)[\mathbf{v}_l(\mathbf{r}_0) \cdot \mathbf{n}(\mathbf{r}_0)] - [\mathbf{v}_l(\mathbf{r}_0) \times \mathbf{n}(\mathbf{r}_0)] \times (\mathbf{r} - \mathbf{r}_0)}{|\mathbf{r} - \mathbf{r}_0|} dl(\mathbf{r}_0) \tag{18}$$

where $\mathbf{V}_a$ is the velocity induced by the motion of the airfoil, $\mathbf{n}$ is the unit outward-pointing vector normal to the contour of the airfoil C, $\mathbf{v}_l$ is the velocity of the airfoil at $\mathbf{r}_0$. Equation (18) can also be written as

$$\mathbf{V}_a(\mathbf{r}, t) = \frac{1}{2\pi} \boldsymbol{\Omega} \times \int_{S_a} \frac{\mathbf{r} - \mathbf{r}_0}{|\mathbf{r} - \mathbf{r}_0|^2} dS_a(\mathbf{r}_0) \tag{19}$$

where S_a is the interior of the airfoil, and

$$\boldsymbol{\Omega} = 2\omega_a \tag{20}$$

where ω_a is the angular velocity of the airfoil.

It follows from Eq. (20) that the rotation of the airfoil only makes a contribution to $\mathbf{V}_a$ when $\omega_a \neq 0$, which explains why the region S in Eq. (3) includes the flowfield as well as the interiors of any objects in the flowfield. Here S includes the flowfield, S_f, and the interior of the rotating airfoil, S_a, i.e.,

$$S = S_f + S_a \tag{21}$$

To expedite the numerical calculations, Eq. (18) is used instead of Eq. (19).

2.4 Condition at the Trailing Edge and Vorticity-Shedding Rate. The Euler equation can be applied on the flow side (as opposed to the airfoil side) of the bound vortex sheet that imitates the boundary layer, where viscous effects are ignorable, and written in terms of the relative velocity γ. The equation takes the following form

$$\frac{\partial\gamma}{\partial t} + \gamma\frac{\partial\gamma}{\partial l} + [\mathbf{a}_a + \omega_a \times \mathbf{r} + \omega_a \times (\omega_a \times \mathbf{r})] \cdot \mathbf{e}_l = -\frac{1}{\rho}\frac{\partial p}{\partial l} \tag{22}$$

where $\mathbf{r}$ is the position vector relative to the origin of the moving coordinate system fixed on the airfoil, $\mathbf{e}_l$ is the unit vector tangent to the contour pointing in the direction of increasing l, p is the pressure, ρ is the density of the fluid, $\mathbf{a}_a$ is the acceleration of the origin of the moving coordinate system, and

$$\omega_a = \dot{\theta}\mathbf{e}_z$$

$$\omega_a = \ddot{\theta}\mathbf{e}_z \tag{23}$$

are the angular velocity and acceleration of the airfoil, respectively, where θ is the angle of rotation which is positive in the counterclockwise direction.

Integrating Eq. (22) in the clockwise direction from the lower to the upper trailing edge and then equating the pressures on the upper and lower surfaces (no pressure discontinuity) at the trailing edge lead to

$$\frac{\gamma_L^2 - \gamma_U^2}{2} = \frac{d}{dt}\left[\oint_C \gamma(l, t)dl - 2\dot{\theta}S_a\right] = \frac{d\Gamma}{dt} \tag{24}$$

where the subscripts U and L denote quantities on the upper and lower surfaces at the trailing edge, respectively, $\oint_C \gamma dl$ is the relative circulation (i.e., circulation computed with the relative velocities) in the clockwise direction around the airfoil, S_a is the cross-section area of the airfoil and

$$\Gamma = \oint_C \gamma(l, t)dl - 2\dot{\theta} S_a \tag{25}$$

is the absolute circulation around the airfoil in the clockwise direction.

When the flow is unsteady, $d\Gamma/dt$ is not zero and the relative velocities on the upper and lower surfaces must be different. This difference is a manifestation of the vortex sheet (wake) that must form there in an unsteady flow.

It follows from Eq. (4) that

$$\frac{d}{dt}(\Gamma + \Gamma_w) = \frac{d\Gamma}{dt} + \frac{d\Gamma_w}{dt} = 0 \tag{26}$$

where Γ_w is the circulation around the wake, and

$$\Gamma + \Gamma_w = \text{constant} \tag{27}$$

is the total circulation around the flowfield.

Then it follows from Eqs. (24) and (26) that

$$\frac{d\Gamma_w}{dt} = -\frac{d\Gamma}{dt} = \frac{\gamma_U^2 - \gamma_L^2}{2} \tag{28}$$

where $d\Gamma_w/dt$ is often called the vorticity-shedding rate. Vorticity is shed from the airfoil and added to the wake as described by Eq. (28).

To determine the vorticity-shedding rate, an understanding of the flowfield in the immediate neighborhood of the trailing edge is necessary so that γ_U and γ_L can be determined. For unsteady flows, Giesing (1969) analyzed the kinematic characteristics around the trailing edge by the conformal-mapping method. Based on the assumption that the mean velocity at the trailing edge is finite and nonzero, he showed that the vortex sheet was shed parallel to the upper or lower surface of the trailing edge depending on the direction of the shed vorticity. Maskell (1971) came to the same conclusion later. But Basu and Hancock (1978) pointed out that the Giesing/Maskell model cannot reach the steady case as $d\Gamma/dt$ in Eq. (28) goes to zero because the stagnation streamline bisects the trailing-edge angle in the steady case. They argued without proof that, as $d\Gamma/dt \rightarrow 0$, the curvature of the streamline emanating from the trailing edge tends to infinity.

The flow in the trailing-edge region has also been investigated experimentally. Studies by Poling and Telionis (1986, 1987) and the thesis of Poling (1985) contain extensive reviews of earlier work. In their experiment, Poling and Telionis released dyes of different colors into the upper-surface and lower-surface boundary layers on a NACA 0012 airfoil oscillating in pitch around the quarter-chord point. For reduced frequencies in the range considered here, they observed that during most of the downstroke, the shear layer emanating from the trailing edge had the color of the lower-surface boundary layer while a pool of the color of the upper-surface boundary layer formed on the upper surface at the trailing edge. The observations support the Giesing/Maskell model of trailing-edge flow. More recently, Liu et al. (1990) studied the flow in the trailing-edge region. In this experiment, they placed a rotating ellipse downstream from and below the trailing edge of a fixed NACA 0012 airfoil. They observed the unsteady flow near the trailing edge of the fixed airfoil, and also concluded that the model described above is realistic.

In the present discussion, the simulation of the flowfield in the region of the trailing edge is based on the Giesing/Maskell model. As illustrated in Fig. 2, the flow at the trailing edge has the following characteristics:

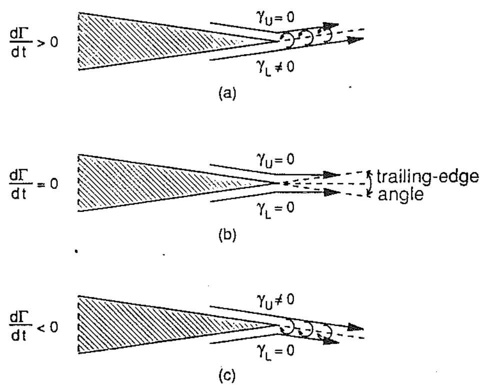

Fig. 2 Physical model of the trailing-edge flow used in the numerical simulation: (*a*) clockwise circulation (Γ) around the airfoil is increasing; (*b*) the flow is steady; (*c*) clockwise circulation is decreasing. The direction of the vorticity being shed is indicated on the trailing-edge streamline. γ_U and γ_L refer to the relative velocities on the upper and lower surfaces at the trailing edge. The trailing edge streamline lies either on or within the trailing-edge angle.

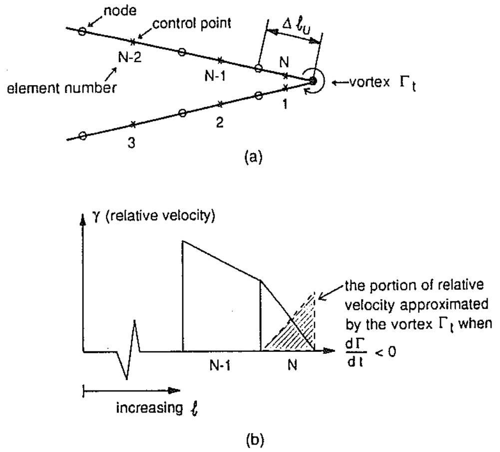

Fig. 3 Numerical model of the trailing edge: (*a*) a vortex point of circulation Γ_t is placed exactly on the trailing edge; (*b*) the piecewise linear continuous velocity distribution. For the case shown, $d\Gamma/dt < 0$ (Γ is the clockwise circulation around the foil), $\Gamma_t = (1/2)\,\gamma_U \Delta l_U$.

1. When $d\Gamma/dt > 0$, $\gamma_L \neq 0$ and $\gamma_U = 0$; the streamline (for the velocity field relative to the moving airfoil) along the lower surface of the airfoil leaves the airfoil smoothly (i.e., tangent to the lower surface), and its counterpart along the upper surface has a sharp corner at the trailing edge (i.e., the relative velocity along the upper surface is zero at the trailing edge).
2. When $d\Gamma/dt = 0$, $\gamma_L = \gamma_U = 0$; the stagnation streamline bisects the trailing-edge angle.
3. When $d\Gamma/dt < 0$, $\gamma_L = 0$ and $\gamma_U \neq 0$; the flow relative to the airfoil comes smoothly off the upper surface and contains a stagnation point on the lower surface at the trailing edge.

In the numerical model discussed here, the values of the relative velocity on both the upper and lower surfaces of the trailing edge (γ_U and γ_L) are not directly calculated. Instead, a vortex point of circulation Γ_t is placed at the trailing edge to approximately represent the nonzero, linearly distributed relative velocity given by Eq. (11) on either the upper or the lower surface at the trailing edge (refer to Fig. 3). The relationship between Γ_t and the relative velocities is given by

$$\Gamma_t = \int_0^{\Delta l_U} \gamma_U f_2(\xi) d\xi = \frac{\gamma_U \Delta l_U}{2} \quad \gamma_L = 0, \quad \text{for} \quad \Gamma_t > 0 \tag{29a}$$

$$\Gamma_t = \int_0^{\Delta l_L} \gamma_L f_1(\xi) d\xi = \frac{\gamma_L \Delta l_L}{2} \quad \gamma_U = 0, \quad \text{for} \quad \Gamma_t < 0 \tag{29b}$$

where Δl_U and Δl_L are the panel lengths on the upper and lower surfaces at the trailing edge, respectively. From Eq. (29) γ_U and γ_L can be calculated if Γ_t is known.

It follows from Eqs. (28) and (29) that the vorticity shed into the wake during the time interval Δt is given by

$$\Delta\Gamma_W = \frac{2\Gamma_t^2}{\Delta l_U^2}\,\Delta t \quad \text{for} \quad \Gamma_t > 0 \tag{30a}$$

$$\Delta\Gamma_W = -\frac{2\Gamma_t^2}{\Delta l_L^2}\,\Delta t \quad \text{for} \quad \Gamma_t < 0 \tag{30b}$$

Hsu and Wu (1986, 1988) developed an alternative to the above model of the trailing-edge flowfield. After applying the momentum equation to a small control volume at the trailing edge, they concluded that the trailing-edge flow does not have to be tangent to one of the surfaces. However, in arriving at their conclusion, they did not impose Eq. (28). When Eq. (28) is imposed, the Giesing/Maskell model and the Hsu/Wu model agree.

For the potential flow past infinitesimally thin boundary layers, it is noted that, if the trailing-edge streamline is above the trailing-edge wedge, the speed along the lower-surface streamline is infinite at the trailing edge and there is still a stagnation point on the upper-surface streamline.

When the reduced frequency and amplitude are sufficiently high it appears that the vorticity being shed from the trailing edge is strong enough to create a stagnation point on the surface, slightly away from the trailing edge. And, in fact, Ohashi and Ishikawa (1972) observed such a flowfield experimentally. Such a flowfield can also develop at the instant following an impulsive start. The simulation discussed here also predicts a stagnation point close to, but not at, the trailing edge both for the instant after an impulsive start and during cyclic motion when the reduced frequency is greater than five.

Doing their experiment in air, Ohashi and Ishikawa (1972) placed thin paper containing a solution of Nessler reagent on one side of the trailing edge and released ammonia gas into the boundary layer on the other side. The reagent changed color during the motion, indicating that it came in contact with the ammonia and suggesting that the flow turned the corner instead of coming off the surface smoothly. However, the reduced frequency and the amplitude had to exceed certain limits before this happened. For amplitudes and frequencies below the limits, the observations of Ohashi and Ishikawa also appear consistent with the Giesing-Maskell model.

2.5 Discretization of Wakes. Ideally, the wake should be modelled as a continuous vortex sheet emanating from the trailing edge with the circulation being added according to Eq. (28). However, the sheet wraps around and rolls up while stretching. In fact, it seems that a discontinuity in the curvature appears. This is a process that is difficult to simulate with a continuous sheet (Rosenhead, 1931). Actually, the evolution of vortex sheets is accompanied by the problem of instability. Krasny (1986, 1988a,b) studied the stability of vortex sheets and their simulations. Extensive work on this subject has also been presented in the articles by Meiron et al. (1982), Moore (1979, 1984), Pozrikidis and Higdon (1985), Caflisch (1988), Aref et al. (1988), and many others.

An alternative to the continuous vortex sheet as a model of the wake is the system of vortex points or vortex blobs. At every time step, a vortex blob of circulation $\Delta\Gamma_W$ given by Eq. (30) is shed into the wake. Then the circulation around the wake, Γ_W, is the sum of the circulations around the individual vortices

$$\Gamma_W = \sum_{k=1}^{M} \Gamma_k \tag{31}$$

where M is the number of vortices in the discretized wake, and Γ_k is the circulation of vortex k.

The use of a system of vortex points to represent a continuous vortex sheet was first proposed by Rosenhead (1931), though the concept of a vortex point was introduced much earlier by Helmholtz (1858). The system of vortex points is not without a major problem of its own: eventually two vortex points are convected close to each other, and then, as a result of the singularity in the expression for the velocity field generated by a vortex point, at the next time step they are convected very far apart.

One of the methods to correct this irregular, seemingly chaotic behavior involves the concept of vortex blobs (see, e.g., Chorin and Bernard, 1973; Leonard, 1980; and Spalart, 1988). The vortex blob distributes the vorticity of a vortex point over a small, but finite, circular core by means of a so-called core function and thereby eliminates singularities. For the numerical results presented here, the following core function is used

$$F(d) = \frac{d^2}{1+d^2} \tag{32a}$$

where

$$d = \frac{|\mathbf{r}-\mathbf{r}_k|}{\sigma} \tag{32b}$$

where σ is the small radius of the vortex blob, $\mathbf{r}$ represents the point in the flowfield where the velocity is being calculated, and $\mathbf{r}_k$ represents the point where the vortex is located. With the core function described in Eq. (32), the contribution of the wake in Eq. (3) is approximated by

$$\mathbf{V}_W(\mathbf{r},t) = -\frac{1}{2\pi}\,\mathbf{e}_z \times \sum_{k=1}^{M} \Gamma_k F(d)\frac{\mathbf{r}-\mathbf{r}_k}{|\mathbf{r}-\mathbf{r}_k|^2}$$

$$= -\frac{1}{2\pi}\,\mathbf{e}_z \times \sum_{k=1}^{M} \Gamma_k \frac{\mathbf{r}-\mathbf{r}_k}{|\mathbf{r}-\mathbf{r}_k|^2+\sigma^2} \tag{33}$$

where $\mathbf{V}_W$ is the velocity induced by the wake and clockwise is taken as the positive direction of Γ_k. Vortex blobs cannot induce velocity on themselves.

However, this approach is not entirely satisfactory. Vortex blobs collect in some regions and separate in others [refer to part (*a*) of Fig. 6]; the result can be a very uneven spatial distribution and, consequently, a very poor representation of the wake. The numerical phenomenon corresponds to the physical stretching and coiling of the actual vortex sheet. The vortex-blob simulation of the continuous vortex sheet can only be improved by splitting the vortices as they begin to separate (see, e.g., Mook et al., 1987, 1989). Splitting is discussed below.

The wake is viewed as a thin free shear layer in an inviscid fluid. Associated with each element of its length are mean values of thickness (averages over the elemental lengths) and circulation (averages over the cross-section areas associated with the elemental lengths). For each element of the wake in a barotropic, two-dimensional, inviscid flow

$$\frac{D}{Dt}(\Omega\delta A) = \frac{D}{Dt}(\delta\Gamma) = 0 \tag{34}$$

and, when the flow is incompressible, it follows that

$$\frac{D}{Dt}(\delta A) = 0 \quad \text{and} \quad \frac{D\Omega}{Dt} = 0 \tag{35}$$

where $(D/Dt)(\;)$ is the substantial derivative, δA is the cross-sectional area of the element of the wake, Ω is the mean value of the vorticity associated with that element, and $\delta\Gamma$ is the circulation around that element.

When a system of discrete vortices is used to imitate the wake, each vortex point (or vortex blob) approximates one of the elemental lengths of the free shear layer, and the value of the circulation around an individual point or blob is the $\delta\Gamma$ of the corresponding elemental length. In other words, each circulation in the system of discrete points or blobs represents

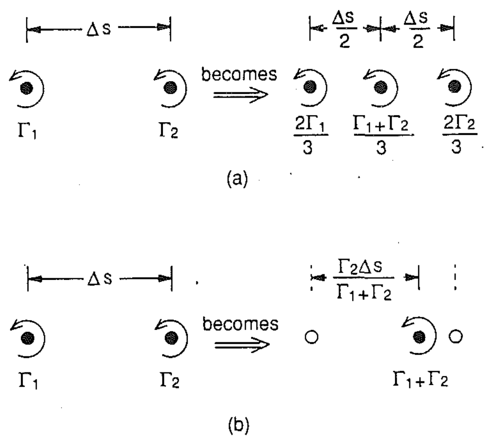

Fig. 4 Splitting and combining schemes: (*a*) the original two vortices with circulations Γ_1 and Γ_2 separated by the distance Δs, which is greater than a critical length for splitting, are divided into three vortices as indicated; (*b*) the original two vortices with circulations Γ_1 and Γ_2 separated by the distance Δs, which is less than a critical length for combining, are merged into a single vortex as indicated.

an elemental length of the free shear layer that imitates the actual wake.

When the vortex sheet stretches, its thickness decreases while its length increases [in such a way that $(D/Dt)\ (\delta A) = 0$] and $\delta\Gamma$ remains constant. In the system of discrete blobs, stretching is manifested when two sequentially shed blobs increasingly separate as they convect. If the elemental lengths are to remain approximately uniform as the wake stretches, then more elements will be needed to represent the stretched portion of the free shear layer. The addition of more elemental lengths corresponds to the addition of more discrete vortices to the system.

As illustrated in part (*a*) of Fig. 4, whenever two successively shed blobs are convected apart by a distance greater than a specified critical length, they are split into three. The new vortex has the circulation equal to one third of the sum of the circulations of the original two and is placed at the midpoint between them. The circulations around the original two vortices are reduced to two thirds of their original values. The above procedure is repeated at each time step until no two sequencial blobs are farther apart than the critical distance.

When two blobs are convected very close, they are combined. The new blob has circulation equal to the sum of the circulations of the original two and is placed at the centroid of the original two (Spalart, 1988) as shown in part (*b*) of Fig. 4. Blobs having circulations of different signs are not combined because the denominator in the formula given in Fig. 4 can be very small.

Sarpkaya and Schoaff (1979) proposed a scheme in which the vortex points are repositioned in order to achieve uniform spacing and the circulations are redistributed in order to maintain (approximately) the spatial distribution. However, because no more vortices are added (i.e., there is no splitting), this approach does not adequately account for stretching.

Pozrikidis and Higdon (1985) simulated the evolution of thick shear layers of uniform vorticity. They expressed the velocity field generated by the vortex layer as a line integral, which they evaluated numerically. The computed velocity field was used to determine the displacements of so-called marker points on the boundary of the vorticity-bearing region. Then the velocity field was recomputed, etc. Some of their results show the shear layers forming regions similar to the vortical structures obtained in the present simulation. However, in their results the regions resembling the vortical structures have uniform vorticity instead of a spatial variation such as the results presented here contain.

2.6 Aerodynamic Loads. For the 2-D problem considered here, the pressure distribution on the surface on the airfoil can be obtained by integrating Eq. (22) from the lower trailing edge

$$p(l)-p_t=-\rho\left\{\frac{d}{dt}\int_0^l \gamma dl+\frac{\gamma(l)^2-\gamma_L^2}{2}+\int_0^l[\mathbf{a}_a+\omega_a\times\mathbf{r}+\omega_a\times(\omega_a\times\mathbf{r})]\cdot\mathbf{e}_l dl\right\} \tag{36}$$

where p_t is the pressure at the trailing edge. It is not necessary to know p_t in the calculation of the aerodynamic loads because p_t is only a function of time and the aerodynamic loads are obtained by integrating the pressure around the closed contour of the airfoil. When the airfoil is stationary, $\mathbf{a}_a$, ω_a and ω_a in Eq. (36) are zero.

2.7 Equations for the Unknowns and Numerical Procedures. If the contour of the airfoil C is approximated by N panels, then there are $N + 1$ nodes, with the lower trailing edge being numbered 1 and the upper trailing edge being numbered $N + 1$. The element size is nonuniform in the present scheme, the elements near the leading and trailing edges being smaller than those in the mid-chord region. The approximation of the very last portion of γ by a vortex point becomes more accurate as the panels adjoining the trailing edge become smaller. The number of elements in Fig. 1 is 18, but all the results presented here were computed with 36 or more.

Comparisons of results obtained with a single vortex at the trailing edge and those obtained with a continuous distribution of vorticity over the element at the trailing edge agree to two places for 36 elements. The agreement can be expected to improve when the number of elements is increased. The comparisons were made for an impulsive start; in this case, the vorticity being shed from the trailing edge always has the same sign. In other cases, such as an airfoil oscillating in pitch or plunge, the vorticity being shed can change sign. As discussed above, vorticity with different signs is shed from different surfaces. Thus, for the oscillating airfoils, one must guess at the beginning of each time step from which surface the vorticity will be shed and then at the end of the time step check if the assumption is true. If the assumption is not true, the guess must be changed and the calculation must be repeated. The use of a discrete vortex at the trailing edge can simplify the procedure by eliminating the need to guess and speed the calculations.

Because the vorticity over either the first or the last element is concentrated in a vortex point of circulation Γ_t at the trailing edge [refer to Eq. (29)], G_1 and G_{N+1} are both zero. In other words, the vortex point of circulation Γ_t at the trailing edge accounts for the fact that either γ_U or γ_L is nonzero, depending on the sign of $d\Gamma/dt$. The values of the relative surface velocity at each node, except the two at the trailing edge, G_i, and the circulation around the vortex at the trailing edge, Γ_t, are together N unknowns.

With Eq. (11), the relative circulation around the airfoil appearing in Eq. (24) is approximated as

$$\oint_C \gamma dl=\frac{1}{2}\sum_{i=1}^{N}(G_i+G_{i+1})\Delta l_i+\Gamma_t \tag{37}$$

where N is the number of elements on the contour of the airfoil, Δl_i is given by Eq. (9) and $G_1 = G_{N+1} = 0$.

It follows from Eq. (5) that the velocity induced by the bound vortex sheet on the surface of the airfoil at point $\mathbf{r}$ at time t is approximated as

$$\mathbf{V}_b(\mathbf{r},t)=\sum_{i=1}^{N}\mathbf{V}_{bi}(\mathbf{r},t)-\frac{1}{2\pi}\mathbf{e}_z\times\frac{\Gamma_t(t)(\mathbf{r}-\mathbf{r}_t)}{|\mathbf{r}-\mathbf{r}_t|^2} \tag{38}$$

where $\mathbf{V}_{bi}$ is given by Eq. (16) with $G_1 = G_{N+1} = 0$, and $\mathbf{r}_t$ is the position vector of the trailing edge.

The total velocity is

$$\mathbf{V} = \mathbf{V}_b + \mathbf{V}_a + \mathbf{V}_W + \mathbf{V}_\infty \tag{39}$$

where $\mathbf{V}_b$, $\mathbf{V}_a$, $\mathbf{V}_W$ are given by Eqs. (38), (18), and (33), respectively, and $\mathbf{V}_\infty$ is the velocity of the freestream.

It follows from Eqs. (27), (25), (37), and (31) that

$$\frac{1}{2}\sum_{i=1}^{i=N} (G_i + G_{i+1})\Delta l_i + \Gamma_t - 2\dot{\theta} S_a + \sum_{k=1}^{M} \Gamma_k = \text{constant} \tag{40}$$

This equation is the principle of total-vorticity conservation in the flowfield, and is linear in the G_i and Γ_t.

The no-penetration condition on the surface of the airfoil is

$$(\mathbf{V} - \mathbf{v}_l)\cdot\mathbf{n} = 0 \tag{41}$$

where $\mathbf{V}$ is given by Eq. (3) or Eq. (39), $\mathbf{v}_l$ is the velocity of the surface of the airfoil, and $\mathbf{n}$ is a vector normal to the contour of the airfoil.

Equation (41) is applied at the control point of each element (in the present model, control points are the midpoints of the elements as shown in Figs. 1 and 3). Then the number of linear equations for the G_i and Γ_t that result from applying Eq. (41) is N. With Eq. (40) which is the constraint on the circulation around both the airfoil and its wake, there is a total of $N + 1$ linear equations for N unknowns. Consequently, an optimal solution is obtained by minimizing the sum of the squares of the errors at the control points subject to the equality constraint [Eq. (40)] imposed on the circulation.

If there are more than one airfoil in the flow, Eq. (41) should be applied on the surface of each airfoil, and the left-hand side of Eq. (40) should be the circulation around the entire flowfield.

At every time t_k, a vortex blob with circulation $\Gamma_k = \Delta\Gamma_W$ is released from the trailing edge into the wake. The vortex blobs already in the wake are convected at the velocity of the local fluid particles while their circulations remain unchanged. The procedure produces a continuous pressure field in an inviscid fluid; thus, the wake is modelled as a region of inviscid, rotational flow. During the time interval Δt, the displacement of a vortex blob is given by

$$\Delta\mathbf{r} = \mathbf{V}\Delta t \tag{42}$$

The numerical procedure can be summarized as follows:

1. The initial flow is specified. As examples, the flow may be steady for some specified angle of attack, or the fluid may be at rest, or the flow may start from a previously calculated unsteady condition.
2. The time is advanced one step.
3. The wake is convected and the splitting/combining procedure is implemented.
4. The position and velocity of the airfoil are computed from the prescribed motion.
5. The values of γ at the nodes, the G_i (except for $i = 1$ and $N + 1$), and Γ_t are computed from the constrained-optimization scheme.
6. If desired, pressure and loads are computed.
7. The computation is returned to step 2.

To check the convergence of this method as the number of elements on the contour of the airfoil and the size of the time-step are varied, an impulsively started flow around a NACA 0012 airfoil at 10 deg angle of attack is tested by calculating the velocities at the trailing edge and the circulation around the wake at time $t = 1$. For such a case, the relative velocity at the upper trailing edge, γ_U, is zero while the relative velocity at the lower trailing edge, γ_L, is nonzero.

Table 1 The velocity at the trailing edge as a function of the time step, Δt, and the number of elements, N

Δt	$N = 36$	$N = 72$	$N = 108$	$N = 144$
0.02	−0.4736			
0.01	−0.4762	−0.4801		
0.005	−0.4788	−0.4824	−0.4840	
0.0025	−0.4796	−0.4840	−0.4856	−0.4864
0.00125	−0.4800	−0.4846	−0.4865	−0.4876
0.000625	−0.4802	−0.4849	−0.4869	−0.4881

Table 2 The circulation around the wake a function of the time step, Δt, and the number of elements, N

Δt	$N = 36$	$N = 72$	$N = 108$	$N = 144$
0.02	−0.4819			
0.01	−0.4735	−0.4727		
0.005	−0.4678	−0.4660	−0.4753	
0.0025	−0.4653	−0.4620	−0.4711	−0.4764
0.00125	−0.4641	−0.4601	−0.4686	−0.4736
0.000625	−0.4635	−0.4592	−0.4674	−0.4722

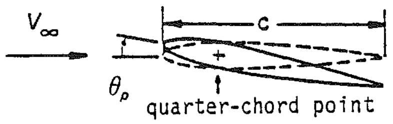

Fig. 5 Airfoil pitching about its quarter-chord point

In Table 1, the values of the relative velocity at the trailing edge, γ_L, at time $t = 1$ are listed for different sizes of the time step, Δt, and different numbers of elements, N.

In Table 2, the values of the circulation around the wake, Γ_W, at time $t = 1$ are listed for different sizes of the time step, Δt, and different numbers of elements, N.

The blank boxes in Table 1 and Table 2 indicate that the size of the time-step is too large to use with the corresponding number of elements. The smaller the elements are (the larger N is), the smaller the time step must be to obtain reasonable results. As Δt decreases by being cut in half, γ_L and Γ_W have only slight changes. And for the same time step, the results obtained by using different numbers of elements are close. The method gives reasonably convergent solutions as the number of the elements increases and the size of the time step decreases.

The unsteady solution is nearly equal to the steady-state solution after the wing has traveled 60 chords following an impulsive start. The numerical value for the steady-state lift is about eight to ten percent higher than the experimental value for a Reynolds number of 10^6.

3 Examples

In this section, some examples of numerical simulations of wakes and blade-vortex interaction are presented. In all calculations unless otherwise stated, NACA 0012 airfoils are used, and all variables have been nondimensionalized by the freestream speed, V_∞, and the chord length, C, of the airfoil.

3.1 Wakes of Airfoils. An airfoil pitching around its fixed quarter-chord point is represented in Fig. 5. The pitch angle, θ_p (degrees), is positive in the clockwise direction and given by

$$\theta_p = -10 \text{ deg } \cos(2kt) \tag{43}$$

where $k = \omega C/2V_\infty$ is the reduced frequency and ω is the dimensional frequency. Initially, the flow around the airfoil is steady. As soon as the pitching starts, the motion becomes unsteady and the airfoil starts to shed vorticity from the trailing edge.

First the reduced frequency is chosen as $k = 2.77$, so that the present results can be compared with some experimental results. In Fig. 6, the wake after one and one quarter cycles of pitching is shown. Each dot in the wake region gives the

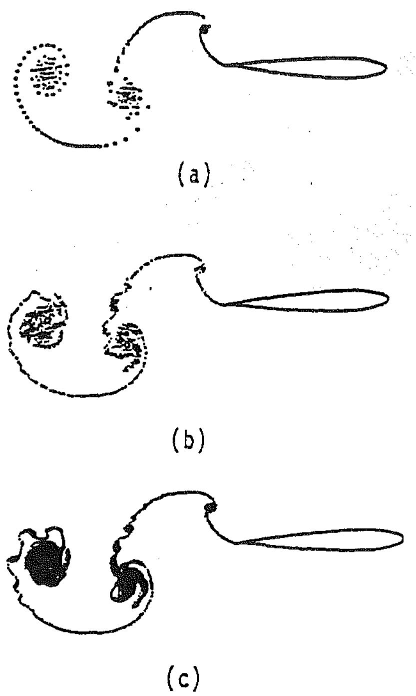

Fig. 6 Computed wakes of a pitching airfoil: the pitch angle is given by Eq. (43) with $k = 2.77$. After one and one quarter cycles (250 time steps), the airfoil is rotating counter-clockwise. Each point shows the location of a vortex blob: (*a*) without splitting, 250 vortex blobs, (*b*) with splitting and combining, 512 vortex blobs, and (*c*) with splitting for a smaller critical length, 3818 vortex blobs.

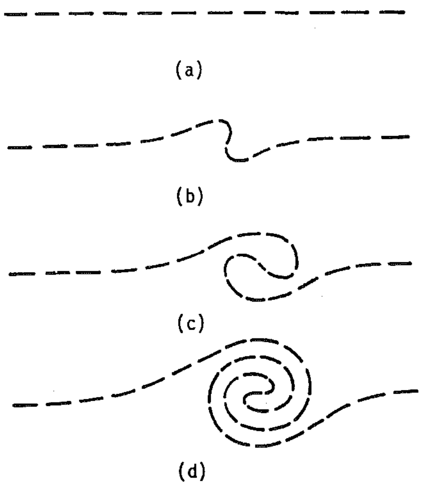

Fig. 7 Physical mechanism for coiling of the free shear layer under the influence of the velocity it induces on itself: (*a*) undisturbed layer of clockwise vorticity; (*b*) the layer after the introduction of a small disturbance; (*c*) and (*d*) the subsequent coiling.

location of a vortex blob. In part (*a*) of Fig. 6 the splitting and combining procedures are not used, and there are 250 vortex blobs in the wake after 250 time steps. In part (*b*) of Fig. 6, the splitting and combining procedures are used for the same time step used in part (*a*). The blobs are split (by using a critical length related to the shortest panel on the airfoil) and combined at each time step, and there are 512 blobs in the wake after 250 time steps. In part (*c*) of Fig. 6, a smaller critical length for splitting is used, and there are 3818 blobs. Comparing the three wakes, one sees that the large-scale structures of the wake are about the same, but the splitting procedure provides more details. These results clearly show a strong trend to converge, which is typical of all cases treated by the method described here.

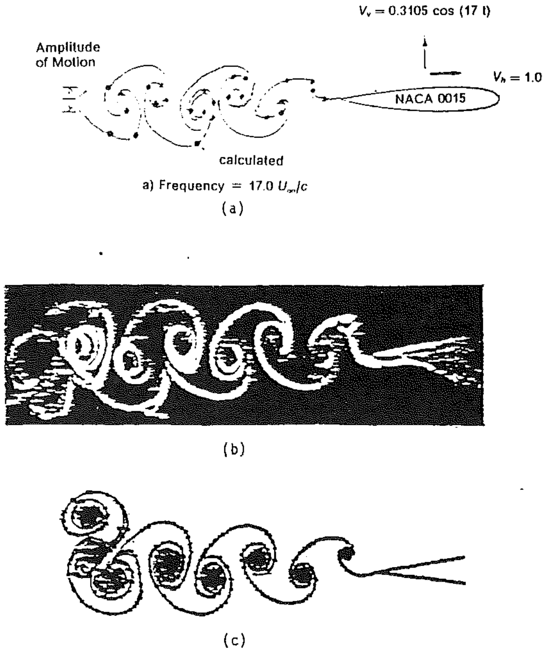

Fig. 8 Wakes of a plunging airfoil: (*a*) the numerical result calculated by Giesing (1968) where V_v and V_h are, respectively, the vertical and horizontal velocity components, (*b*) the flow visualization obtained by Bratt (1950), and (*c*) the numerical result obtained by the present method.

The dark regions in parts (*b*) and (*c*) of Fig. 6, which contain many vortices, are called regions of concentrated vorticity in this paper. The points in parts (*b*) and (*c*) of Fig. 6 are not connected; however, they are so densely packed that the representation of the wake appears to be continuous.

The physical mechanism causing the regions of concentrated vorticity to form is illustrated in Fig. 7. In part (*a*) an undisturbed sheet of clockwise vorticity is represented. In part (*b*) a small disturbance is introduced. The elements of the sheet above their original position are accelerated to the right under the influence of the velocity field induced by the elements of the sheet below their original position. Conversely, the elements below their original position are accelerated to the left. The effect is to stretch the sheet (requiring the addition of more vortices to maintain the spatial resolution when the sheet is represented by a system of discrete vortices) initially and then to coil, or to wrap, the sheet which eventually causes the vorticity to collect. The direction of wrapping agrees with the direction of the vorticity. In parts (*c*) and (*d*) of Fig. 7, the sheet is represented at subsequent times. During the stretching/coiling process, vorticity is drawn into the region where the disturbance was introduced from the portions of the sheet on both sides; consequently, regions of rather concentrated vorticity form. The strength along the sheet connecting two successively shed regions of concentrated vorticity is very small, practically zero. The regions of densely packed vorticity yield smooth velocity fields, as shown later in another example.

The importance of splitting discrete vortices is further illustrated in the case where the airfoil oscillates in plunge: the vertical displacement, y, is given by

$$y = A \sin \Omega t \tag{44}$$

where A is the amplitude of oscillation, $\Omega = \omega C/V_\infty$ is the reduced frequency and ω is the dimensional frequency. In part (*a*) of Fig. 8, which is taken from Giesing's paper (1968), the solution was computed by a source-panel method, where $A = 0.3105$ chord and $\Omega = 17$. The dots represent the positions of the vortices shed previously at the trailing edge, and the line connecting the vortices was faired in by Giesing. The sequence in which the vortices were shed, some prior knowledge of the

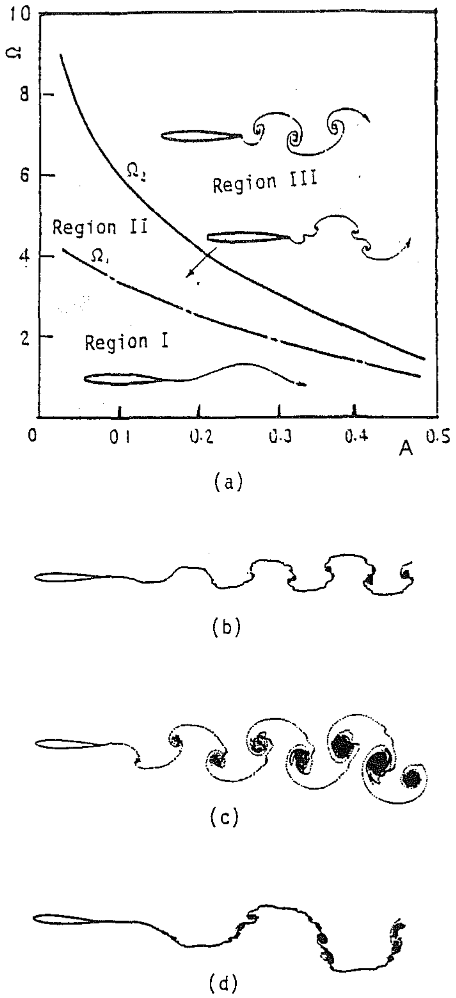

Fig. 9 *Wake structures of a plunging airfoil: (a) the three regions observed by Ohashi and Ishikawa (1972) in the frequency-amplitude space where the wakes have distinct structures. The numerical results are shown in (b), (c), and (d). (b) $A = 0.014$, $\Omega = 5$; (c) $A = 0.05$, $\Omega = 5$; (d) $A = 0.05$, $\Omega = 2.5$.*

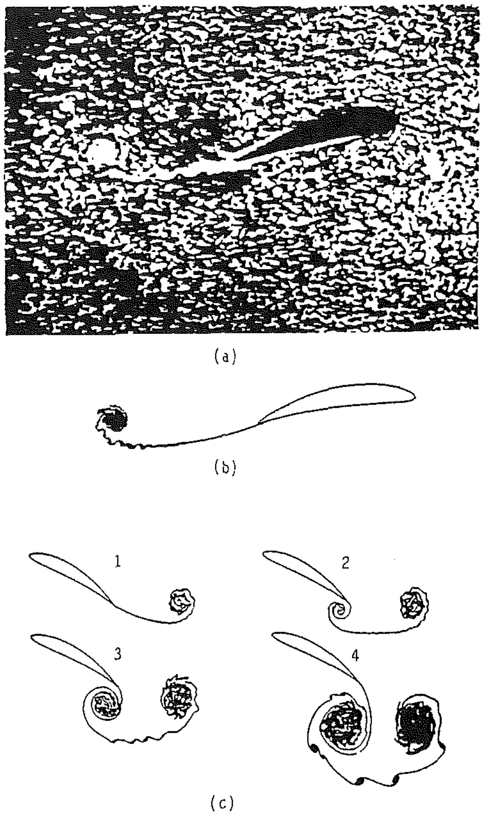

Fig. 10 Wakes behind an impulsively started airfoil: (*a*) visualization from the film loop (Wu and Thompson, 1973); (*b*) numerical result; (*c*) a time sequence of computed wakes behind an airfoil experiencing an impulsive start followed by an impulsive stop.

wake, and clearly some imagination were needed to draw the line. Similar results were obtained by Katz and Weihs (1978, 1981). The wrapping/stretching mechanism is clearly evident and so is the need to add more vortices in order to preserve the spatial resolution. In part (*b*) of Fig. 8, the flow visualization obtained by Bratt (1950) is shown. Bratt introduced smoke into the airstream ahead of the leading edge. Part (*b*) of Fig. 8 served as a guide in the construction of part (*a*) of Fig. 8. In part (*c*), the wake computed by implementing the splitting scheme is shown. The large-scale structures of the wake seem to be accurately predicted by the numerical results. Using vortex blobs, Krasny (1991) simulated some wakes. He prescribed initial locations and distributions of circulations for some vortex sheets and then computed their evolution. He compared his results qualitatively with the observations of Couder and Basdevant (1986) and found good agreement.

Ohashi and Ishikawa (1972) also studied the wakes behind plunging airfoils. They heated the air that passed over the upper surface of an NACA 65-010 airfoil. The resulting sharp gradient in the density of the air downstream from the trailing edge was observed by means of a Schlieren apparatus. They observed three regions in the frequency-amplitude domain where the wakes have distinct structures. These regions are given in part (*a*) of Fig. 9. The numerically calculated wakes are shown in parts (*b*), (*c*), and (*d*). In part (*b*), the amplitude of plunge ($A = 0.014$ chord) is small and the frequency ($\Omega = 5$) is high; the structure of the wake is similar to the one shown in Region I of part (*a*). In part (*c*), the amplitude of plunge ($A = 0.05$ chord) is larger and the frequency ($\Omega = 5$) is the same; the structure of the wake is similar to the one in Region III of part (*a*). In part (*d*) the amplitude of plunge ($A = 0.05$ chord) is the same as that in the previous case but the frequency ($\Omega = 2.5$) is smaller; the structure of the wake is similar to the one in Region II of part (*a*). The calculated results follow the same trend as the observations, but the calculated boundaries between the regions are neither clear nor in the same approximate locations as the observed boundaries. The different airfoils used in the experiment and the numerical calculation (*NACA 0012 airfoil is used in the numerical solution*) is one of the reasons causing this discrepancy. It is also not known how much influence the buoyant forces caused by heating have on the wake geometry.

In Fig. 10, the wakes behind an impulsively started airfoil are shown. In part (*a*), one frame from a well-known film loop (see the last reference) shown to beginning classes in fluid mechanics is given. The experiment was performed by placing powder on the surface of a fairly thin sheet of water flowing across a smooth, nearly level, plane surface. The results given in part (*b*) were obtained by considering the flow past a cambered Karman-Trefftz airfoil. In both cases, the airfoil has travelled about one chord. There is qualitative agreement. Shown in part (*c*) is a sequence of computed results for a different airfoil that experiences an impulsive start followed by an impulsive stop. Two counter-rotating regions of concentrated vorticity are clearly evident. These two regions are migrating downward. The space between these two large-scale regions of concentrated vorticity is nearly devoid of vorticity because the vorticity is being drawn toward the centers of each region, and the connecting vortex sheet is being stretched and weakened.

Now we consider again the case of a pitching airfoil (the

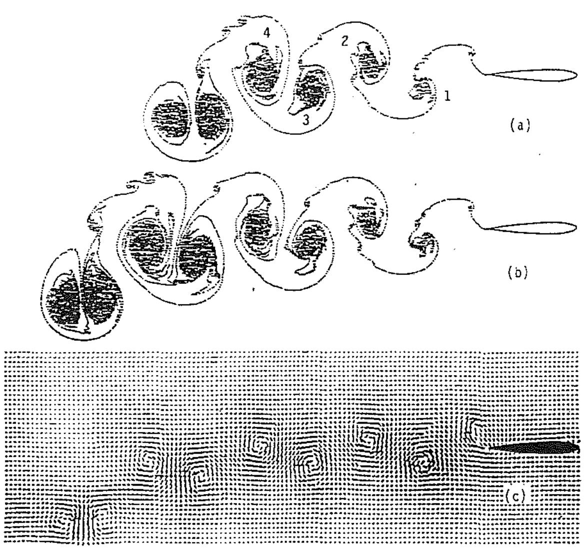

Fig. 11 Computed wakes of a pitching airfoil: the same case as in Fig. 6. (*a*) After three and one quarter cycles; (*b*) after four and one quarter cycles; (*c*) the disturbance-velocity field corresponding to the wake in (*b*) above. Frequency and amplitude of the motion agree with those in the experiment represented in Fig. 12.

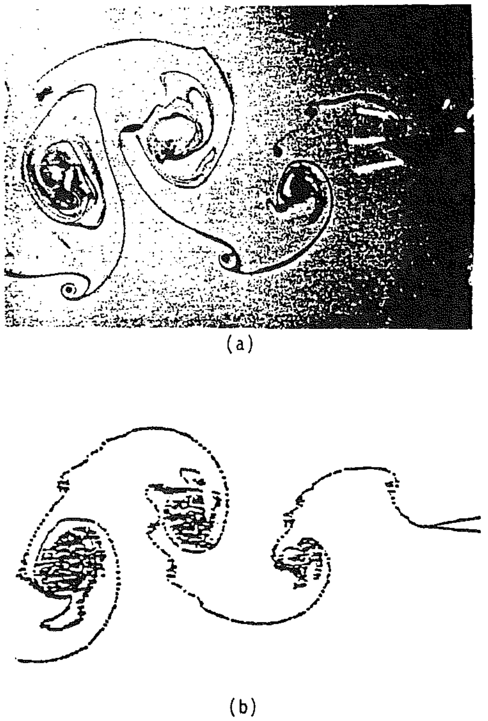

Fig. 12 Comparison between experimental and simulated wakes: pitching frequency and amplitude agree with those in Figs. 6 and 11. (*a*) Photograph of the wake behind a pitching airfoil in a water tunnel (Wilder et al., 1990); (*b*) the same as in part (*b*) of Fig. 11.

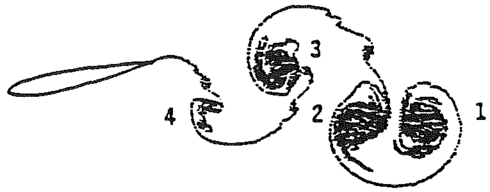

Fig. 13 Computed wake behind a pitching airfoil: the pitch angle is given by Eq. (43) with $k = \pi$, and the amplitude and frequency agree with those in the experiment of Booth (1987)

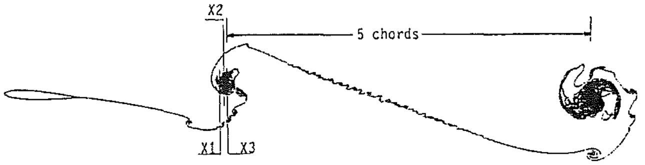

Fig. 14 Computed wake behind a pitching airfoil the pitch angle is given by Eq. (45). The numerical result agrees with the observation in the experiment by Booth (1987).

same case shown in Fig. 6), where the pitch angle is given by Eq. (43) and $k = 2.77$. During each cycle two regions of concentrated vorticity are created. In parts (*a*) and (*b*) of Fig. 11 the wakes are shown after three and one quarter cycles and four and one quarter cycles, respectively. A comparison of parts (*a*) and (*b*) shows that after three and one quarter cycles the structure of the wake has nearly reached a steady state in the area from the trailing edge to approximately 2.75 chords downstream. The circulations around regions of concentrated vorticity 1 and 3 are negative (counterclockwise) while those around regions 2 and 4 are positive. The disturbance flowfield corresponding to part (*b*), obtained by subtracting the free-stream velocity from the total velocity field, is shown in part (*c*). Vorticity is obvious in the regions where the vortices are densely packed and there is practically no evidence of vorticity outside these regions. The centers of the regions of concentrated vorticity can be approximately located, and the horizontal spacing between two regions of the same sign of circulation (i.e., between 1 and 3 and between 2 and 4) is approximately 1.25 chords.

Part (*a*) of Fig. 12 is a photograph by Wilder et al. (1990) of flow past a pitching airfoil in a water tunnel for the same reduced frequency and amplitude as in Fig. 11. Part (*b*) of Fig. 12 is the same as part (*b*) of Fig. 11 and is put here for comparison. Comparing part (*a*) with part (*b*) of Fig. 12, one sees that the numerical method simulates the wake structure very well, even in some of the finer details. The distance between the centers of vortical structures of the same sign measured by Wilder et al. is 1.2 to 1.4 chords, very close to the numerical result (about 1.25 chords). Although a dyed streakline between the regions of concentrated vorticity is evident, no experimental evidence of vorticity along the streakline was found (that is, abrupt changes in velocity were not perceptible), which is consistent with the numerical simulation. The vortex layer has been stretched and in the process rendered thin; consequently, the velocity generated by this portion of the wake is quite weak. It should be noticed that, for both experimental and numerical results, there are some small spirals on the weak vortex layers connecting two adjacent big regions of concentrated vorticity. According to the numerical tests of Krasny (1986), the computer round-off caused those spirals, and they could be diminished by higher-precision arithmetic. Here the splitting scheme might also be responsible for causing the spirals and the agreement with the flow visualization might be fortuitous. On the other hand, one cannot exclude the possibility that the numerical model accurately catches some true characteristics of the flowfield.

Next the pitch angle is given by Eq. (43) and $k = \pi$ in order to simulate an experiment by Booth (1987), who used a pitching airfoil to generate wakes. In Fig. 13, the wake with four regions of concentrated vorticity, is shown after two and one quarter cycles; regions 1 and 2 were generated during the first cycle and 3 and 4 were generated during the second. The circulations around regions of concentrated vorticity 1, 2, 3 and 4 are, respectively, $\Gamma_1 = 1.042$, $\Gamma_2 = -0.929$, $\Gamma_3 = 1.059$, and $\Gamma_4 = -1.106$. We note that $\Gamma_1 + \Gamma_2 = 0.113$, $\Gamma_3 + \Gamma_4 = -0.047$, and one can see that the vorticity distribution of the second

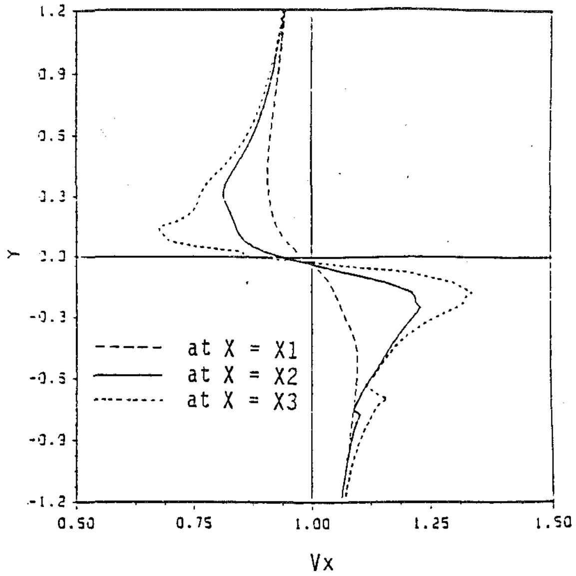

Fig. 15 Computed profiles of the horizontal velocity component at the three stations indicated in Fig. 14: As a result of the high density of vortices in the wake, the profiles are smooth. The profiles are computed by an inviscid model of the flowfield but exhibit what is often thought to be a viscous core.

cycle is more nearly symmetric than that of the first cycle. It is expected that, if the calculation were continued, the wake would continue to become more nearly symmetric. Booth measured the velocity behind an airfoil and numerically integrated his measurements to obtain the circulations around regions of concentrated vorticity. His results for the circulations, which are nondimensionalized here, are 1.12 and -0.992. The numerical predictions are in good agreement with Booth's observations.

Corresponding to another of Booth's experiments (1987), the pitch angle for one cycle of the motion is given by the following

$$\theta_p = \begin{cases} -10^\circ \cos(\pi t) & 0.0 \le t \le 1.05 \\ -25.1607^\circ \left(\dfrac{t}{T} - 0.6026\right) & 1.05 < t \le 5.0 \end{cases} \tag{45}$$

where the period $T = 5.0$. In Fig. 14, the computed wakes are shown after one and a half cycles. The purpose of choosing θ_p as defined in Eq. (45) is to create relatively isolated regions of concentrated vorticity. They are generated by the rapid sinusoidal variation of θ_p from -10 to 10 deg in the first 20 percent of the cycle. The vorticity that is generated when θ_p linearly returns to -10 deg during the remainder of the cycle is much weaker, and the corresponding portion of the wake does not roll up much. The vorticity generated during the first 20 percent of the cycle is negative (counterclockwise). As indicated in the figure, the centers of the regions of concentrated vorticity are about 5 chord lengths apart; this result agrees quite well with Booth's experimental results.

In Fig. 15, the horizontal components of the total (computed) velocity are plotted as functions of vertical position for the three different locations shown in Fig. 14. Because of the high density of blobs in the regions of concentrated vorticity, the computed velocity is smooth. The numerical simulation shows a rather concentrated vortical flow. The value of the nondimensional circulation for a path around the region of concentrated vorticity is 0.712 for the numerical solution and 0.707 for Booth's experimental results (when a freestream speed of 15 ft/sec is used). Again, the agreement is quite good.

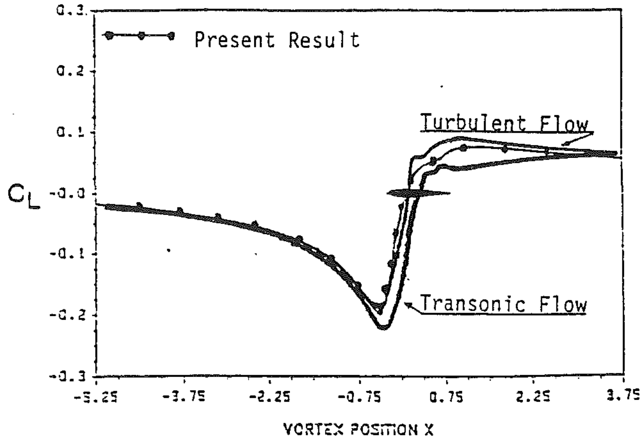

Fig. 16 Lift coefficient for the interaction between a vortex point and an airfoil: The present numerical result, the result of turbulent flow was computed by Hsu and Wu (1986), and the result of transonic flow was computed by Srinivasan et al. (1986).

3.2 Blade-Vortex Interaction. First the interaction of an airfoil with a single passing vortex point (called simply a vortex in this discussion) is investigated. Then the interaction between a stationary airfoil and the wake generated by a pitching airfoil is simulated.

The quarter-chord point of the airfoil is chosen as the origin of the coordinate system, and the angle of attack is zero. At the beginning, the flow is steady. Then a single vortex with strength $\Gamma_v = 0.2$ is introduced at the position $x_v = -5.25$ and $y_v = -0.26$ (five chords upstream from and slightly below the origin) and convected downstream at the local particle velocity. The flow becomes unsteady. The variation of the lift coefficient C_L $(=L/(1/2)\rho V_\infty^2 C^2)$ with the position of the vortex is shown in Fig. 16. When the vortex is far from the airfoil, a small negative lift acts on the airfoil. As the vortex approaches the airfoil, the lift becomes more negative and reaches its maximum negative value just before the vortex reaches the leading edge. As the vortex passes under the airfoil, the lift increases, changing from negative to positive. After the vortex passes the trailing edge, the lift decreases gradually toward zero. As shown in Fig. 16, the present solution is in very good agreement with the attached turbulent-boundary-layer solution obtained by Hsu and Wu (1986) (marked Turbulent Flow in the figure) and with the solution of the Euler equations for transonic flow obtained by Srinivasan et al. (1986) (marked Transonic Flow).

There have been several attempts to improve the model of blade-vortex interaction by having the oncoming stream contain a system of vortices. It appears that Hardin and Lamkin (1984) were the first to consider a spatial distribution of vorticity rather than a single vortex in the oncoming stream. Poling et al. (1987) extended the single-vortex model by sequentially releasing a series of vortex points from a fixed location upstream. Panaras (1987) modeled a finite, vorticity-bearing region by releasing a cloud of vortex points upstream from an airfoil. The initial deployment of the points was prescribed, and all had the same prescribed circulation. Lee and Smith (1987) also released a cloud of vortex points upstream. Poling et al. (1988) also considered the interaction between a cloud of vortex points and an airfoil. They chose a distribution of circulations in the initial arrangement that produced a velocity field similar to their experimental observations (also similar to the profile in Fig. 15). Renzoni and Mayle (1991) used a vortex cluster of vortex points resulting from a pitching flat plate, but they did not split the vortex points. Both Panaras (1987) and Poling et al. (1988) considered flow past a Joukowski airfoil, both used conformal mapping to obtain their results, Poling et al. imposed the general unsteady Kutta condition, but Panaras did not. Lee and Smith used a source-panel method

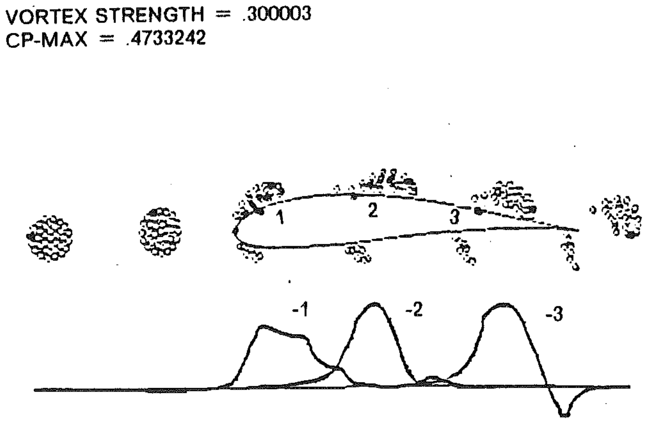

Fig. 17 Blade-vortex interaction computed by Panaras (1987) at six different times: The curves at the bottom show the pressure at points 1, 2, and 3 on the airfoil surface as functions of time.

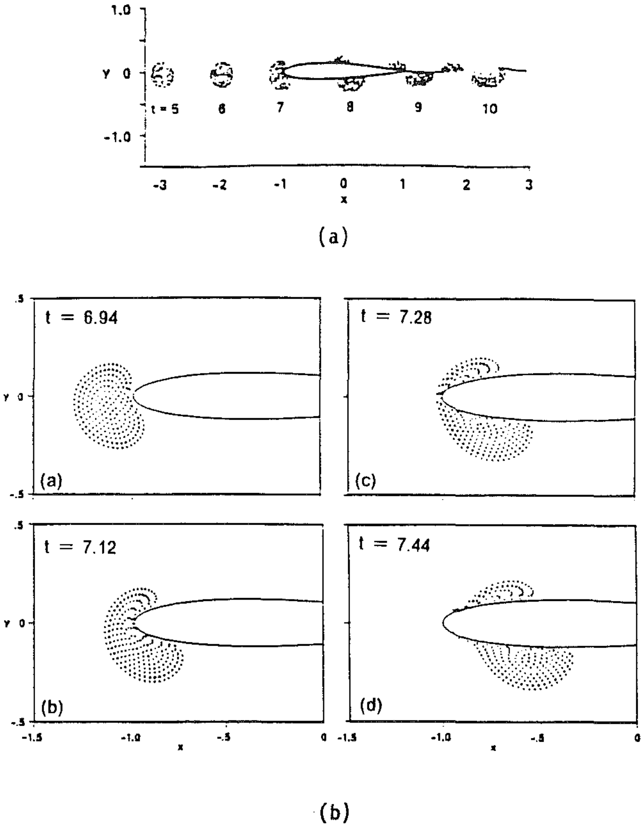

Fig. 18 Blade-vortex interaction computed by Lee and Smith (1987): (*a*) cloud of vortex points at six different times; (*b*) details of the interaction near the leading edge while the cloud is being split

(instead of the vorticity-panel method described here) and imposed the general unsteady Kutta condition at the trailing edge.

The example of blade-vortex interaction computed by Panaras (1987) is given in Fig. 17. The solid dots are vortex points; the hollow dots are simply markers to help visualize the motion. The cloud of vortex points is shown at six different times. The cloud is split by the airfoil, and the portion going along the upper surface arrives at the trailing edge a little before the portion moving along the lower surface. The plots under the airfoil give the pressures at three locations on the upper surface as functions of time.

Some results from another example of blade-vortex interaction computed by Lee and Smith (1987) are given in Fig. 18.

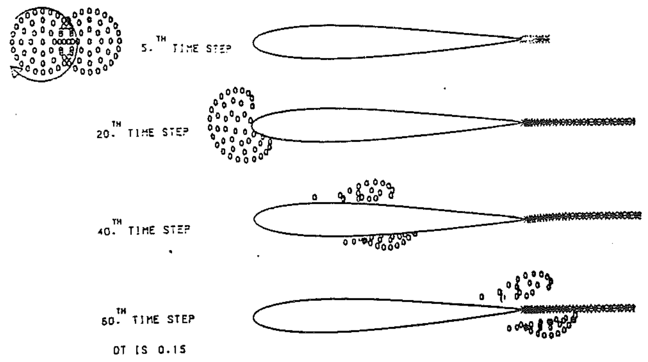

Fig. 19 Blade-vortex interaction computed by Poling et al. (1988) at four different times

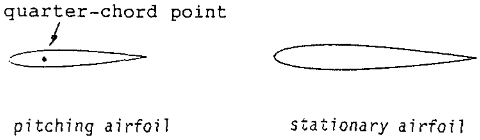

Fig. 20 Setup for blade-vortex interaction

In part (*a*), the cloud of vortex points is shown at six different times. The cloud is divided by the airfoil, and the portion moving along the lower surface arrives at the trailing edge ahead of the portion moving along the upper surface. More details are shown in part (*b*).

Some results from the blade-vortex interaction computed by Poling et al. (1988) are shown in Fig. 19. Again the cluster of vortex points is divided by the airfoil. The wake generated at the trailing edge of the airfoil is also shown. In the cases shown in Figs. 18 and 19, it appears that vorticity moving along the lower surface arrives at the trailing-edge slightly ahead of the vorticity moving along the upper surface, in contrast with Panaras's results. The airfoils and the initial distributions of circulations are different.

The vortex-panel/core-splitting method can also be used to achieve a partial numerical simulation of the BVI experiment conducted by Booth (1986, 1987). In the experiment, the wake generated by a pitching airfoil of chord length 0.75 interacts with a stationary airfoil of unit chord downstream. As shown in Fig. 20, the quarter-chord point of the pitching airfoil is at (0.0, 0.0), and the quarter-chord point of the stationary one is at (1.5625, −0.094), i.e., the horizontal distance from the leading edge of the stationary airfoil to the trailing edge of the pitching airfoil is 0.75 when both airfoils are at zero angle of pitch. The case where the angle of attack of the stationary airfoil is zero is considered here. The pitch angle of the oscillating airfoil is given by Eq. (45), which generates a relatively isolated region of concentrated vorticity of circulation 0.534 nondimensionalized by the velocity of the freestream and the length of the stationary airfoil.

In Fig. 21, the two airfoils with their wakes and the pressure distribution on the stationary one are shown at different times. In part (*a*) of Fig. 22, the history of the lift coefficient C_L is shown. At the beginning, there is positive (upward) lift acting on the stationary airfoil because the pitching airfoil upstream is at a negative angle of attack and deflects the oncoming stream upward. For this steady state, the airfoils and the calculated pressure distribution on the stationary one are shown in part (*a*) of Fig. 21. The lift reaches its maximum value at $t = 1.37$ just before the strong concentrated vorticity generated in the first 20 percent of the cycle reaches the leading edge of the stationary airfoil as shown in part (*b*) of Fig. 21, where the wake of the pitching airfoil is plotted with and without the stationary airfoil present. In part (*c*) of Fig. 21, the wakes and

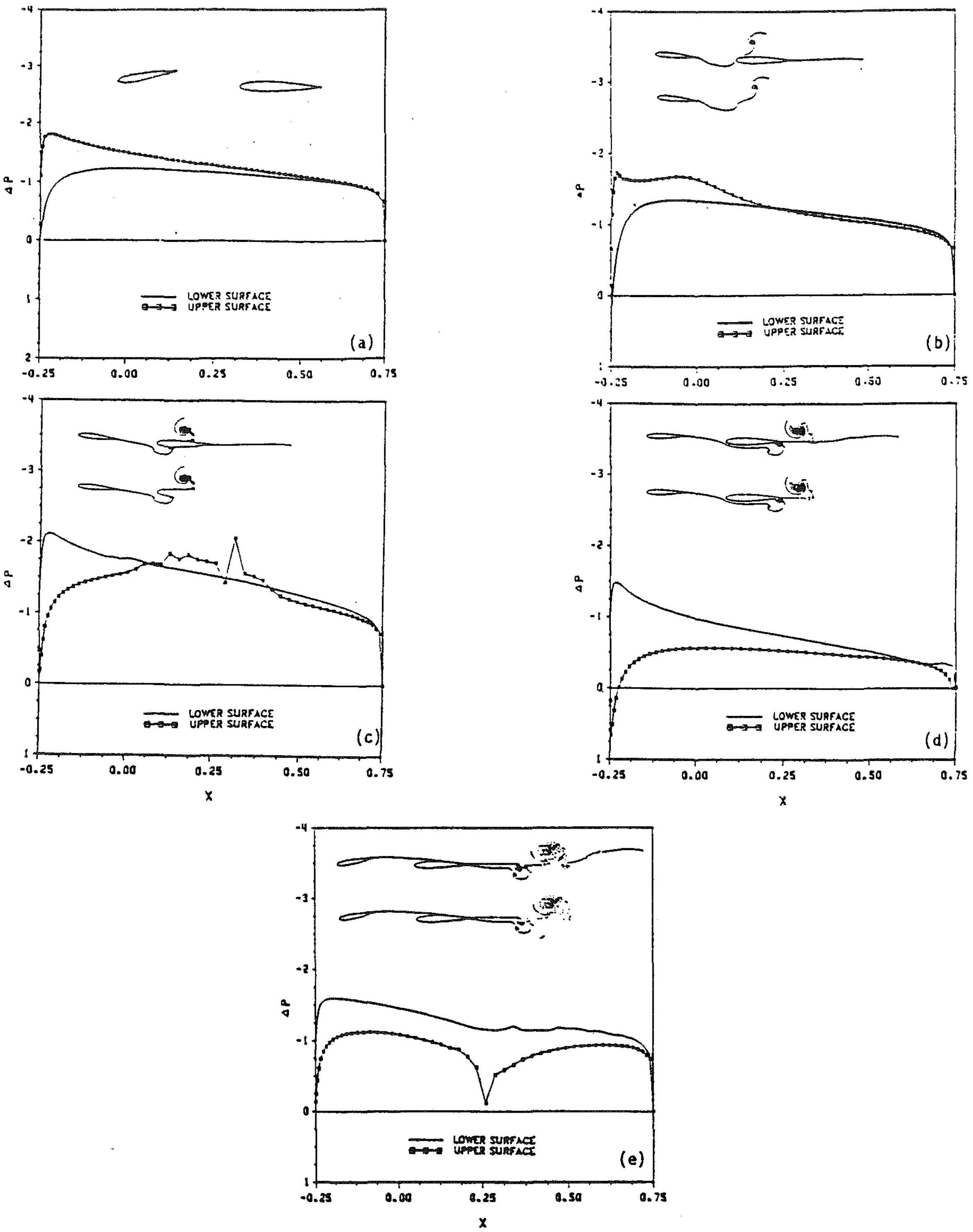

Fig. 21 Pressure distributions on the stationary airfoil during blade-vortex interaction: the pitch angle is given by Eq. (45). (*a*) Steady state before the motion starts; (*b*) at time $t = 1.37$; (*c*) at time $t = 2$; (*d*) at time $t = 3$; (*e*) at time $t = 4.5$. The inserts show both the airfoils and their wakes in the upper view, and only the pitching airfoil and its wake in the lower view. The wake can be seen enveloping the stationary airfoil.

the pressure distribution are shown at $t = 2$. From the view of the wake without the stationary airfoil present, one can see that the vortex sheet generated by the pitching airfoil is enveloping the stationary airfoil and is stretching. The more this vortex sheet is stretched, the weaker its strength is. The pressure distribution on the upper surface is very rough in the region close to the strong vorticity.

For the unsteady problem evaluating the pressure through Eq. (36) involves the relative surface velocity γ and both its spatial and temporal derivatives. When the wake is close to the surface, the gradient of the surface velocity can be very large. Maskew (1980) suggested that additional subpanels be put on the surface to capture the resolution of the velocity, but no subpanels are added in the present model. As a result,

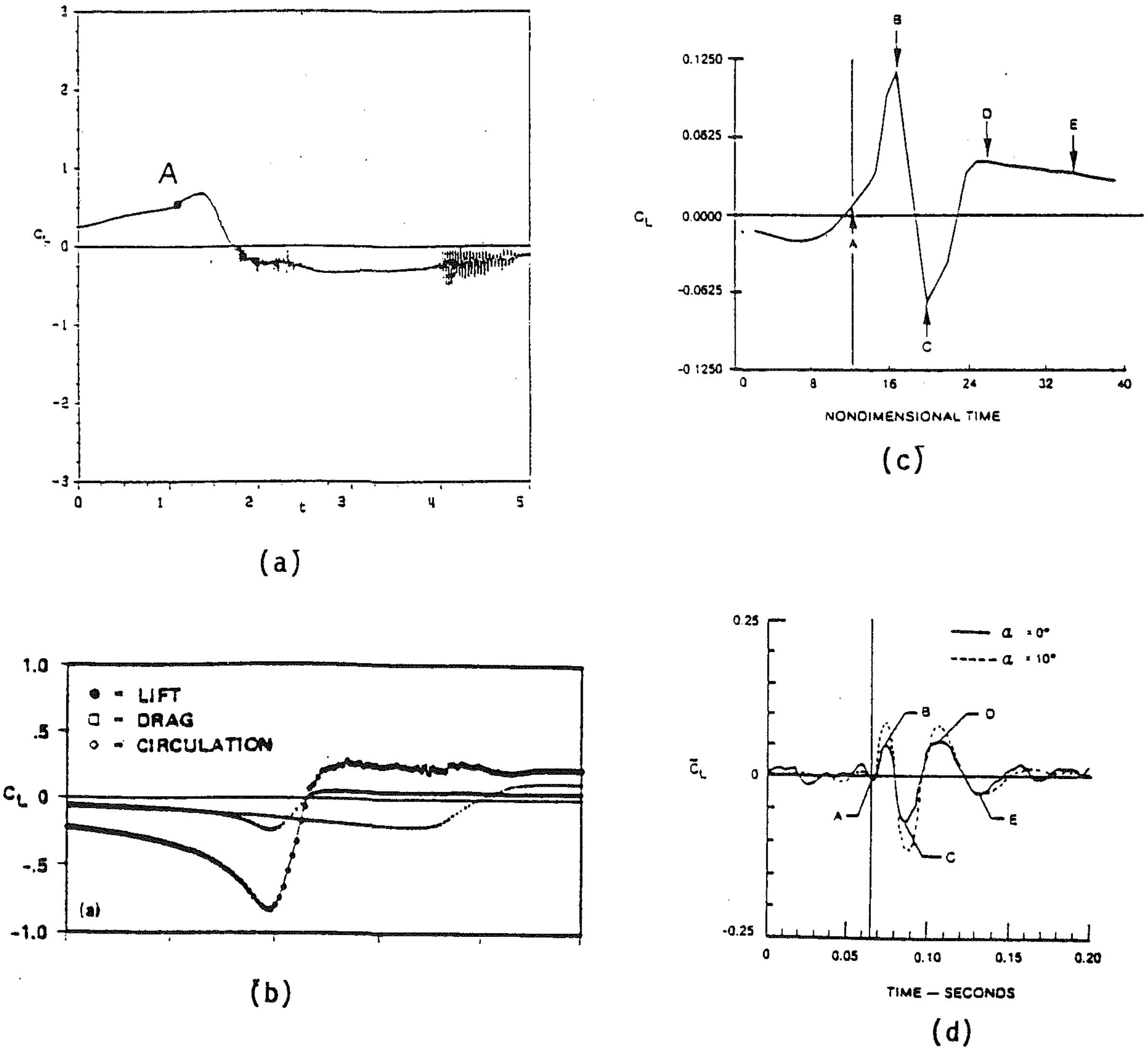

Fig. 22 Lift coefficient as a function of time: (*a*) computed by the method described here; (*b*) computed by Lee and Smith (1987); (*c*) computed by Poling et al. (1987); (*d*) measured by Booth (1986)

the pressure distribution is rough; this roughness moves towards the trailing edge as the concentrated vorticity convects. In part (*d*) of Fig. 21, the pressure and the wakes are shown at time $t = 3$. The pressure distribution is very smooth. The very weak vortex sheet (as the result of stretching) covers almost the entire airfoil except a small portion near the lower trailing edge. In part (*e*) of Fig. 21, the pressure and the wakes are shown at time $t = 4.5$. The sharp rise in the pressure on the upper surface is caused by the (weak) clockwise vorticity in the wake coming very close to the surface.

In Fig. 22, the history of the lift coefficient is shown for several different studies. The plot of C_L in part (*a*) was obtained by the numerical scheme discussed here for the same conditions used to make Fig. 21. In part (*b*), a sample of the result computed by Lee and Smith (1987) is shown; in part (*c*), the result computed by Poling et al. (1987) is given; and in part (*d*), the experimental result of Booth (1986) is presented. The results in parts (*b*) and (*c*) were computed by releasing a cloud of vortices upstream. The one in part (*a*) is the numerical simulation of Booth's experiment in part (*d*), the one in part (*c*) was computed with the conditions chosen in such a way to imitate the experiment in part (*d*).

In the case (computed by Lee and Smith) shown in part (*b*) of Fig. 22, the direction of the vorticity is opposite to that in the other cases shown in parts (*a*), (*c*), and (*d*) of Fig. 22. When the sign is changed the result of Lee and Smith is similar to the result obtained by the vorticity-panel method shown in part (*a*). The jagged regions of the curve in part (*a*) of Fig. 22 correspond to the times when the wake actually brushes along the surface of the stationary airfoil. Apparently, the re-distribution of panels nearly eliminated this feature from the results of Lee and Smith. The mean-value curve (i.e., the curve faired through the jagged regions) for the present vorticity-panel results converged rapidly as the number of panels was increased and the time step is decreased, which is typical of all vorticity-panel results. Point *A* in part (*a*) of Fig. 22, corresponds to the end of the sinusoidal portion of the cycle defined by Eq. (45).

The result of Poling et al. (1987) shown in part (*c*) of Fig. 22 has the best qualitative agreement with the experimental result of Booth. Booth gives only the increment in lift in part (*d*) of Fig. 22; the lift created by the initial negative angle of attack of the forward airfoil has been subtracted.

The difference between Booth's experiment and the numerical simulations is most likely due to the separation caused by the strong interaction. Separation can occur when strong vorticity is close to the airfoil in some experiments. Telionis and co-workers (1990) have observed a significant separation bubble that moves along the surface with the passing region of concentrated vorticity. In Booth's experiment, the Reynolds number was first given as 85,300 (Booth, 1986) based on the flow speed 20 ft/s. But later he found that the mean flow speed was about 15 ft/s when the flow reached the stationary airfoil (Booth, 1987). Then the Reynolds number should be 63,975. At this Reynolds number, the boundary layer was likely laminar when the separation occurred. The calculation of BVI for viscous flow by Hsu and Wu (1986) showed that when separation occurs the lift differs considerably from that corresponding to attached flow. The numerical results presented here are based on the assumption that the flow is always attached.

4 Summary

A vorticity-panel method coupled with vortex dynamics has been reviewed. The method predicts the rate at which vorticity is shed into the wake generated by unsteady flow over an airfoil and the subsequent development of the wake. The numerical solutions are in good agreement with the experimental results and support the argument that the evolution of the wake within a certain distance behind the trailing edge is almost entirely controlled by an inviscid mechanism.

The boundary layer adjoining the surface of the airfoil is simulated by a vortex sheet, and the wake that adjoins the trailing edge is simulated by a system of vortex blobs (a vortex blob is in essence a classical vortex point with the singularity removed). By requiring the pressures along the upper and lower surfaces of the airfoil to approach the same value at the trailing edge and the total vorticity to be conserved, one can predict the rate at which the vorticity is shed at the trailing edge into the wake.

As the discrete vortices in the wake begin to separate they are split in such a way that maintains the total circulation exactly and the spatial distribution approximately. The computations clearly reveal a coiling or wrapping process that, qualitatively at least, is in good agreement with flow visualizations done in both water and wind tunnels. Vorticity in the wake is drawn into relatively isolated regions called regions of concentrated vorticity. The velocity distributions through such regions appear to have a viscous core, but the flowfield is developed entirely by an inviscid model. The process resembles diffusion, but happens much too rapidly to be explained by viscous effects.

Numerical experiments show that the results obtained from the method described here tend to converge as the time step decreases and the number of the elements on the surface of the airfoil increases. Moreover, the general unsteady algorithm produces the correct steady-state solution when it is applied to an airfoil that translates at constant velocity following an impulsive start.

An inviscid panel method coupled with vortex dynamics for numerically simulating the flowfield has potential as a model of blade-vortex interactions.

The present perspective of unsteady, incompressible, attached flow over airfoils is by no means exhaustive; it does provide several points where one can begin a more thorough study.

Acknowledgment

The authors were supported by the Air Force Office of Scientific Research under Grant No. AFOSR-90-0032 and gratefully acknowledge this support.

References

Aref, H., 1983, "Integrable, Chaotic and Turbulent Vortex Motion in Two-Dimensional Flows," *Annual Review of Fluid Mechanics*, Vol. 15, pp. 345–389.

Aref, H., Kadtke, J. B., and Zawadzki, I., 1988, "Point Vortex Dynamics: Recent Results and Open Problems," *The Japan Society of Fluid Mechanics*, Vol. 3, pp. 63–74.

Aref, H., and Kambe, T., 1988, "Report on the IUTAM Symposium: Fundamental Aspects of Vortex Motion," *Journal of Fluid Mechanics*, Vol. 190, pp. 571–595.

Basu, B. C., and Hancock, G. J., 1978, "The Unsteady Motion of a Two-Dimensional Airfoil in Incompressible Inviscid Flow," *Journal of Fluid Mechanics*, Vol. 87, pp. 159–178.

Booth, E. R., Jr., 1986, "Surface Pressure Measurement During Low Speed Two-Dimensional Blade-Vortex Interaction," AIAA Paper No. 86-1856.

Booth, E. R., Jr., 1987, "Measurement of Velocity and Vorticity Fields in the Wake of an Airfoil in Periodic Pitching Motion," NASA TP-2780 and "Experimental Observations of Two Dimensional Blade-Vortex Interaction," AIAA Paper No. 87-2745.

Booth, E. R., Jr., and Yu, J. C., 1986, "New Technique for Experimental Generation of Two-Dimensional Blade-Vortex Interaction at Low Reynolds Number," NASA TP-2551 and "Two-Dimensional Blade-Vortex Flow Visualization Investigation," *AIAA Journal*, Vol. 24, pp. 1467–1473; also NASA TP-2551.

Bratt, J. B., 1950, "Flow Patterns in the Wake of an Oscillating Airfoil," Aeronautical Research Council Reports and Memoranda No. 2773.

Caflisch, R. E., 1988, "Nonlinear Analysis for the Evolution of Vortex Sheets," *Fluid Dynamics Research*, Vol. 3, pp. 75–77.

Chorin, A. J., and Bernard, P. S., 1973, "Discretization of a Vortex Sheet, with an Example of Roll Up," *Journal of Computational Physics*, Vol. 13, pp. 423–428.

Chow, C.-Y., and Huang, M.-K., 1983, "Unsteady Flow About a Joukowski Airfoil in the Presence of Moving Vortices," AIAA Paper No. 83-0129.

Couder, Y., and Basdevant, C., "Experimental and Numerical Study of Vortex Couples in Two-Dimensional Flows," *Journal of Fluid Mechanics*, Vol. 173, pp. 225–251.

Damodaran, M., and Caughey, D. A., 1988, "Finite-Volume Calculation of Inviscid Transonic Airfoil-Vortex Interaction," *AIAA Journal*, Vol. 26, pp. 1346–1353.

Dong, B., 1987, "Numerical Simulation of Two-Dimensional Lifting Flow," Master Thesis, Department of Engineering Science and Mechanics, Virginia Polytechnic Institute and State University, Blacksburg, Virginia.

Giesing, J. P., 1968, "Nonlinear Two-Dimensional Unsteady Potential Flow with Lift," *Journal of Aircraft*, Vol. 5, pp. 135–143.

Giesing, J. P., 1969, "Vorticity and Kutta Condition for Unsteady Multienergy Flows," ASME *Journal of Applied Mechanics*, Vol. 36, pp. 608–613.

Hardin, J. C., and Lamkin, S. L., 1984, "Aeroacoustic Interaction of a Distributed Vortex with a Lifting Joukowski Airfoil," AIAA Paper No. 84-2237.

Helmholtz, H., von, 1858, "On Integrals of the Hydrodynamic Equations Which Express Vortex Motion," Translation by P. G. Tait, 1867, *Philosophical Magazine*, Vol. 4, pp. 485–512.

Ho, C. M., and Chen, S. H., 1980, "Unsteady Wake of a Plunging Airfoil," AIAA Paper No. 80-1446.

Ho, C. M., and Chen, S. H., 1981, "Unsteady Kutta Condition of a Plunging Airfoil," *Unsteady Turbulent Shear Flows*, R. Michel et al., eds., Springer, Berlin, pp. 197–206.

Hsu, T. M., and Wu, J. C., 1986, "Theoretical and Numerical Studies of a Vortex-Airfoil Interaction Problem," AIAA Paper No. 86-1094.

Hsu, T.-M., and Wu, J. C., 1988, "Vortex Flow Model for the Blade-Vortex Interaction Problem," *AIAA Journal*, Vol. 26, pp. 621–623.

Huang, M.-K., and Chow, C.-Y., 1982, "Tapping of a Free Vortex by Joukowski Airfoil," *AIAA Journal*, Vol. 20, pp. 292–298.

Katz, J., and Weihs, D., 1978, "Behavior of Vortex Wakes from Oscillating Airfoils," *AIAA Journal*, Vol. 15, pp. 861–863.

Katz, J., and Weihs, D., 1981, "Wake Rollup and the Kutta Condition for Airfoils Oscillating at High Frequency," *AIAA Journal*, Vol. 19, pp. 1604–1606.

Kim, M. J., and Mook, D. T., 1986, "Application of Continuous Vorticity Panels to General Unsteady Two-Dimensional Lifting Flows," *Journal of Aircraft*, Vol. 23, pp. 464–471.

Koochesfahani, M. M., 1989, "Vortical Patterns in the Wake of an Oscillating Airfoil," *AIAA Journal*, Vol. 27, pp. 1200–1205.

Krasny, R., 1986, "A Study of Singularity Formation in a Vortex Sheet by the Point-Vortex Approximation," *Journal of Fluid Mechanics*, Vol. 167, pp. 65–93.

Krasny, R., 1988a, "Desingularization of Periodic Vortex Sheet Roll-Up," *Journal of Computational Physics*, Vol. 65, pp. 292–313.

Krasny, R., 1988b, "Numerical Simulation of Vortex Sheet Evolution," *Fluid Dynamics Research*, Vol. 3, pp. 93–97.

Krasny, R., 1991, "Vortex Sheet Computations: Roll-Up, Wakes, Separation," *Lectures in Applied Mathematics*, Vol. 28, pp. 385–402.

Lee, D. J., and Smith, C. A., 1987, "Distortion of the Vortex Core During Blade/Vortex Interaction," AIAA Paper No. 87-1243.

Leonard, A., 1980, "REVIEW Vortex Methods for Flow Simulation," *Journal of Computational Physics*, Vol. 37, pp. 289–335.

Liu, X. L., Wo, A., and Covert, E. E., 1990, "Unsteady Streamlines Near the Trailing Edge of a NACA 0012 Airfoil at Reynolds Number of 125,000," *AIAA Journal*, Vol. 28, pp. 169–170.

Maskell, E. C., 1971, "On the Kutta-Joukowski Condition in Two-Dimensional Unsteady Flow," unpublished note, Royal Aircraft Establishment, Farnborough, England.

Maskew, B., 1980, "Calculation of Two-Dimensional Vortex-Surface Interference Using Panel Methods," NASA Contractor Report 159334, N81-13020.

Mathioulakis, D. S., Kim, M. J., Telionis, D. P., and Mook, D. T., 1985, "On the Wake of a Pitching Airfoil," AIAA Paper No. 85-1621.

McCune, J. E., and Tavares, T. S., 1993, "Unsteady Wing Theory—The Karman/Sears Legacy," ASME JOURNAL OF FLUIDS ENGINEERING, Vol. 115, No. 4.

McCroskey, W. J., 1982, "Unsteady Airfoils," *Annual Review of Fluid Mechanics*, Vol. 14, pp. 285–311.

Meiron, D. I., Baker, G. R., and Orszag, S. A., 1982, "Analytical Structure of Vortex-Sheet Dynamics, Part 1. Kelvin-Helmholtz Instability," *Journal of Fluid Mechanics*, Vol. 114, pp. 283–298.

Mook, D. T., and Dong, B., 1990, "Application of Vortex Dynamics to Simulations of the Wakes of Airfoils," *Proceedings of the International Symposium on Nonsteady Fluid Dynamics*, FED-Vol. 92, Toronto, Canada, June 4–7, pp. 435–448.

Mook, D. T., Roy, S., Choksi, G., and Alexander, D. M., 1987, "On the Numerical Simulation of the Unsteady Wake Behind an Airfoil," AIAA Paper No. 87-0190.

Mook, D. T., Roy, S., Choksi, G., and Dong, B., 1989, "Numerical Simulation of the Unsteady Wake Behind an Airfoil," *Journal of Aircraft*, Vol. 26, pp. 509–514.

Moore, D. W., 1979, "The Spontaneous Appearance of a Singularity in the Shape of an Evolving Vortex Sheet," *Proceedings of the Royal Society of London*, Vol. A365, pp. 105–119.

Moore, D. W., 1984, "Numerical and Analytical Aspects of Helmholtz Instability, in: Theoretical and Applied Mechanics," *Proceedings of the XVI IUTAM Conference*, eds. Niordson and Olhoff, North Holland, Amsterdam, pp. 629–633.

Mracek, C. P., and Mook, D. T., 1988, "Numerical Simulation of Three-Dimensional Lifting Flows by a Vortex Panel Method," AIAA Paper No. 88-4335-CP.

Ohashi, H., and Ishikawa, N., 1972, "Visualization Study of Flow Near the Trailing Edge of an Oscillating Airfoil," *Bulletin of the Japan Society of Mechanical Engineers*, Vol. 15, pp. 840–847.

Panaras, A. G., 1987, "Numerical Modeling of the Vortex/Airfoil Interaction," *AIAA Journal*, Vol. 25, pp. 5–11.

Park, S. O., Kim, J. S., and Lee, B. I., 1988, "Hot-wire Measurements of Near Wakes Behind an Oscillating Airfoil," AIAA Paper No. 88-3715.

Poling, D. R., 1985, "Airfoil Response to Periodic Disturbances—The Unsteady Kutta Condition," Ph.D. dissertation, Department of Engineering Science and Mechanics, Virginia Polytechnic Institute and State University, Blacksburg, Virginia.

Poling, D. R., Dadone, L., and Telionis, D. P., 1987, "Blade-Vortex Interaction," AIAA Paper No. 87-0497.

Poling, D. R., and Telionis, D. P., 1986, "The Response of Airfoils to Periodic Disturbances—The Unsteady Kutta Condition," *AIAA Journal*, Vol. 24, pp. 193–199.

Poling, D. R., and Telionis, D. P., 1987, "The Trailing Edge of a Pitching Airfoil at High Reduced Frequencies," ASME JOURNAL OF FLUIDS ENGINEERING, Vol. 109, pp. 410–414.

Poling, D. R., Wilder, M. C., and Telionis, D. P., 1988, "Two-Dimensional Interaction of Vortices with a Blade," AIAA Paper No. 88-0044.

Pozrikidis, C., and Higdon, J. J. L., 1985, "Nonlinear Kelvin-Helmholtz Instability of a Finite Vortex Layer," *Journal of Fluid Mechanics*, Vol. 157, pp. 225–263.

Raj, P., and Gray, R. B., 1978, "Computation of Two-Dimensional Potential Flow Using Elementary Vortex Distributions," *Journal of Aircraft*, Vol. 15, pp. 698–700.

Renzoni, P., and Mayle, R. E., 1991, "Incremental Force and Moment Coefficients for a Parallel Blade-Vortex Interaction," *AIAA Journal*, Vol. 29, pp. 6–13.

Rosenhead, L., 1931, "The Formation of Vortices from a Surface of Discontinuity," *Proceedings of the Royal Society of London*, Vol. A134, pp. 170–192.

Sarpkaya, T., 1989, "Computational Methods with Vortices—The 1988 Freeman Scholar Lecture," ASME JOURNAL OF FLUIDS ENGINEERING, Vol. 111, pp. 5–52.

Sarpkaya, T., and Schoaff, R. L., 1979, "Inviscid Model of Two-Dimensional Vortex Shedding by a Circular Cylinder," *AIAA Journal*, Vol. 17, pp. 1193–1200.

Sommerfeld, A., 1964, *Mechanics of Deformable Bodies*, Academic Press, New York.

Spalart, P. R., 1988, "Vortex Methods for Separated Flows," NASA Technical Memorandum 100068, N88-26342.

Srinivasan, G. R., 1985, "Computations of Two-Dimensional Airfoil-Vortex Interactions," NASA Contractor Report 3885.

Srinivasan, G. R., McCroskey, W. J., and Baeder, J. D., 1986, "Aerodynamics of Two-Dimensional Blade-Vortex Interaction," *AIAA Journal*, Vol. 24, pp. 1569–1576.

Srinivasan, G. R., McCroskey, W. J., and Kutler, P., 1984, "Numerical Simulation of the Interaction of a Vortex with Stationary Airfoil in Transonic Flow," AIAA Paper No. 84-0254.

Straus, J., Renzoni, P., and Mayle, R. E., 1990, "Airfoil Pressure Measurements During a Blade Vortex Interaction and a Comparison with Theory," *AIAA Journal*, Vol. 28, pp. 222–228.

Telionis, D. P., 1990, Private Communications.

Wilder, M. C., Mathioulakis, D. S., Poling, D. R., Dong, B., Mook, D. T., and Telionis, D. P., 1990, "On the Wake of a Pitching Airfoil," submitted for publication.

Wu, J. C., and Sankar, N. L., 1980, "Aerodynamic Force and Moment in Steady and Time-Dependent Viscous Flows," AIAA Paper No. 80-0011.

Wu, J. C., Sankar, N. L., and Hsu, T. M., 1985, "Unsteady Aerodynamics of an Airfoil Encountering a Passing Vortex," AIAA Paper No. 85-0203.

Wu, J. C., and Thompson, J. F., 1973, "Numerical Solutions of Time-Dependent Incompressible Navier-Stokes Equations Using an Integro-Differential Formulation," *Computer & Fluids*, Vol. 1, pp. 197–215.

"Generation of Circulation and Lift for an Airfoil," Film Loop SFM10, a production of National Committee for Fluid Mechanics Films, with the support of the National Science Foundation, produced by Education Development Center, Inc., distributed by Encyclopedia Britannica Educational Corp. Experiments done under the direction of L. Prandtl. Film edited by A. H. Shapiro and R. Bergman.

Comparison of the Triple-Deck Theory, Interactive Boundary Layer Method, and Navier-Stokes Computation for Marginal Separation

Chao-Tsung Hsiao
Research Assistant.

Laura L. Pauley
Assistant Professor.
Mem. ASME

Mechanical Engineering Department,
Pennsylvania State University,
University Park, PA

The steady two-dimensional marginal separation of an incompressible boundary layer flow within a channel was solved independently by three different methods: the triple-deck method of marginal separation, the interactive boundary layer method, and the full Navier-Stokes computation. From comparison of the results between these three methods, the accuracy and appropriateness of each method was determined. The critical condition beyond which the steady marginal separation solution of triple-deck method does not exist was related to a physical phenomenon in which the separation bubble becomes unsteady. Factors such as Reynolds number and pressure gradient distribution which might influence the accuracy of the marginal separation solution were also investigated.

1 Introduction

For a high Reynolds number flow over a thin airfoil, a region of separated flow can appear within the adverse pressure gradient laminar boundary layer near the leading edge. The separated flow will form a steady closed separation bubble if the adverse pressure gradient is relatively weak. It is important in many practical situations to predict the inception and the structure of the separation bubble since the development of boundary layer separation may lead to dynamic stall. It is well-known that both analytical (Brown and Stewartson, 1969) and numerical methods (Werle and Davis, 1972) encounter a Goldstein-type singularity at the separation point when the boundary layer equations are solved with a prescribed pressure gradient. Although such difficulties can be avoided by solving the full Navier-Stokes equations (Briley, 1971), computational requirements often prohibit its use as a powerful design tool.

Since the boundary layer assumptions are still valid when studying thin separation bubbles, many numerical schemes have been developed to avoid the singularity by modifying the classical boundary layer computation to include the pressure gradient as part of the solution. The typical triple-deck method (Stewartson, 1974; Smith, 1982) and the interactive boundary layer (IBL) method (Kwon and Pletcher, 1979; Veldman, 1981) both suggest that the adjustment of the pressure gradient by the displacement thickness can avoid the singularity. Still, several iterations between the inviscid flow and the boundary layer computation are required to obtain compatible solutions and may reduce the computational speed. We, therefore, seek a more efficient technique to predict such thin small bubbles.

Stewartson et al. (1982) applied the triple-deck theory to solve the laminar marginal separation flow, i.e., the situation where the skin friction just vanishes but immediately recovers. For marginal separation the triple-deck scalings were different than those used in the typical triple-deck analysis. Considering the local solution of the Navier-Stokes equations as $\mathrm{Re} \rightarrow \infty$, the wall skin friction was expressed in terms of the local pressure gradient, the velocity profile at the marginal separation, and a constant Γ resulting from an integration in the solution procedure. In the study, they determined that Γ is related to a parameter which will slightly increase the pressure gradient beyond marginal separation. The greatest benefit of this analytical method is that there is no iteration needed in order to obtain the skin friction.

After the Stewartson et al. study, the triple-deck method for marginal separation has been applied to study the quasi-two-dimensional (Brown, 1985), three-dimensional (Duck, 1989) and unsteady three-dimensional (Duck, 1990) boundary layer flow. However, all these works are qualitative.

The present work implements the triple-deck method based on the Stewartson et al. (1982) study to investigate a small separation bubble of a steady incompressible laminar flow. Previous studies all considered a triple-deck analysis of marginal separation for infinite Reynolds number. However, in practice we would like to study marginal separation at a finite Reynolds number. Therefore, the primary objective of the present work is to investigate the appropriateness of the triple-deck method of marginal separation in practical problems. To achieve this objective three different methods: the triple-deck

---

Contributed by the Fluids Engineering Division for publication in the Journal of Fluids Engineering. Manuscript received by the Fluids Engineering Division October 7, 1992; revised manuscript received October 7, 1993. Associate Technical Editor: S. Ragab.

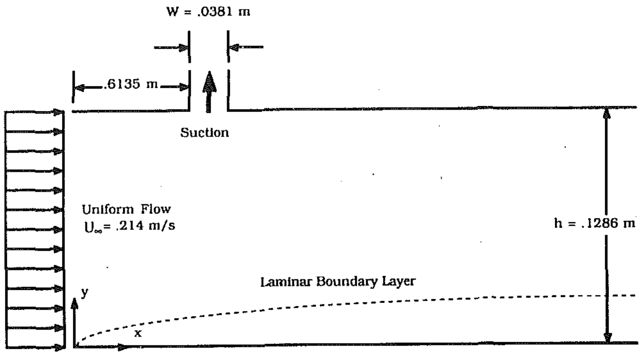

Fig. 1 Geometry for computing laminar boundary layer separation bubbles

method of marginal separation, the IBL method, and the full Navier-Stokes computation are applied to solve the same flow field independently at different Reynolds numbers. It was found that the full Navier-Stokes computation did not yield a stable solution of laminar flow at a high Reynolds number although the IBL method and the triple-deck method still performed well. Therefore, comparison between the IBL method and the Navier-Stokes computation is performed only at a low Reynolds number to demonstrate the accuracy of the IBL method in practical problems. Comparison is performed between the triple-deck method of marginal separation and IBL method for all Reynolds numbers to demonstrate the theoretical accuracy of the triple-deck method.

The comparison between the IBL method and the full Navier-Stokes computation was first made by Briley and McDonald (1975). Although they showed the results between these two methods to be in good agreement, the required displacement thickness for the IBL computation was not evaluated from the global viscous-inviscid interaction. Instead, the displacement thickness from the Navier-Stokes computation was applied to the IBL computation. The IBL method therefore relied on the Navier-Stokes computation result and was not computed independently. When Cebeci and Stewartson (1983) applied the IBL method to solve Howarth's flow independently, they did not obtain a favorable comparison with the results of Briley (1971). Discrepancy between the results was attributed to the upper boundary condition specified by Briley. Cebeci and Stewartson suggested that the upper boundary of Briley was too close to boundary layer edge for a finite Reynolds number and the free stream velocity should be disturbed by the viscous-inviscid interaction. This hypothesis was never verified by modifying the free-stream boundary condition of the Navier-Stokes computation and showing favorable comparison between the results of the two methods. Since the free stream boundary condition applied to the Navier-Stokes computation will influence the calculation of the displacement thickness, the second objective of the present work is to find the boundary condition which in effect describes an external flow. In this way the IBL method and the full Navier-Stokes computation can be compared at the same flow conditions.

For easy comparison of the results from the three different methods, a very simple water channel geometry consisting of a test wall and a control wall is considered (see Fig. 1). A laminar boundary layer develops on the test wall in the presence of an adverse pressure gradient produced by a suction port on the control wall. By adjusting the suction strength S one can create marginal separation conditions.

2 The Methods of Solution

In the present study three different methods are used to solve the same flow field independently. The classical boundary layer calculation with a prescribed pressure gradient is first applied to determine the conditions of marginal separation. The triple-deck method then is used to calculate the skin friction in the neighborhood of the separation. The composite solution of skin friction will be made from the solution of the classical boundary layer calculation and the triple-deck method. Second, the IBL method is used in the region where the interaction between boundary layer and inviscid flow is believed to be important. Finally, the computation of the Navier-Stokes equations is used as a third method to verify the solution of skin friction near the separation point.

Nomenclature

$a_1, a_2, a_3 \ldots$ = coefficients of streamwise velocity expansion at $X=0$
$\hat{A}$ = integral constant related to skin friction
c = average exit velocity
C_f = skin friction coefficient
C_p = pressure coefficient
L^* = characteristic length (m)
L_p^* = pressure gradient length (m)
p = pressure
P_0, P_1, P_2 = terms of pressure gradient expansion
Re = Reynolds number
S = suction strength
t = time
u = streamwise velocity
U, V = scaled velocity
U_0, U_1, U_2 = terms of streamwise velocity expansion
U^* = dimensional streamwise velocity (m/s)
v = normal velocity
V_0, V_1, V_2 = terms of normal velocity expansion
W = width of suction port
x = streamwise distance from leading edge
x_b, x_e = start and end point of interaction region
x_1, x_2 = start and end point of suction port
x_s = marginal separation point
X = streamwise distance from separation point
$\hat{X}$ = rescaled X
y = normal distance from wall
Y = scaled normal distance from wall
Γ = deviation from marginal separation condition
δ_1 = displacement thickness
δ^* = dimensional displacement thickness (m)
μ = integral constant
ν^* = kinematic viscosity (m^2/s)
τ = reduced skin friction
τ_b = reduced skin friction obtained from boundary layer equations
τ_i = reduced skin friction obtained from triple-deck with interaction
τ_n = reduced skin friction obtained from triple-deck without interaction
ω = over-relaxation parameter
λ = decaying factor

Subscripts

Blasius = Blasius solution
c = critical condition
e = condition at the edge of boundary layer
m = condition at marginal separation
max = maximum value
top = condition at control wall
∞ = condition at inlet

Superscript

n = iteration number

The Reynolds number used in present study is defined as

$$\mathrm{Re}_L = \frac{U_\infty^* L^*}{\nu^*} \tag{1}$$

where L^* is the characteristic length which is equal to the streamwise start location of the suction port. All variables are nondimensionalized by the quantities which appear in the Reynolds number. Dimensional variables are noted by a starred superscript while the superscript is absent from all nondimensional quantities.

Since comparison between the methods is performed using the skin friction, we define the reduced skin friction τ and the skin friction coefficient as

$$\tau = \frac{1}{\mathrm{Re}_L^{1/2}} \left.\frac{\partial u}{\partial y}\right|_{y=0}, \quad C_f = \frac{2\tau}{\mathrm{Re}_L^{1/2}}. \tag{2}$$

2.1 Triple-Deck Method

Classical Boundary Layer Calculation. Before applying the triple-deck method of marginal separation, the classical boundary layer calculation with a prescribed pressure gradient is first used to determine the conditions of marginal separation. Such a pressure gradient is determined by the inviscid flow

$$-\frac{dp}{dx} = u_e \frac{du_e}{dx}. \tag{3}$$

From the potential flow analysis, the inviscid surface velocity u_e for the present geometry is given by (see Pauley et al., 1988)

$$u_e(x) = \left(1 - \frac{S}{2}\right) + \frac{S}{(x_2 - x_1)\pi} \ln \left\{ \frac{\cosh\left[\frac{(x-x_2)\pi}{2}\right]}{\cosh\left[\frac{(x-x_1)\pi}{2}\right]} \right\}, \tag{4}$$

where x_1 and x_2 are the start and end location of the suction port, respectively, and S is the suction strength defined as the fraction of the through-flow which is removed through the suction port. After transforming the boundary layer equations in terms of Levy-Lee variables, the Keller Box scheme (1978) is applied to solve the governing equations.

Noninteracting Flow Analysis. To apply the asymptotic theory, the coordinate within the boundary layer is defined as $x = x_s + X$ and $y = \mathrm{Re}_L^{-1/2} Y$, where x_s is the marginal separation point obtained from a classical boundary layer calculation with a prescribed pressure gradient. Also, the velocities are rescaled as $u(x, y) = U(X, Y)$ and $v(x, y) = \mathrm{Re}_L^{-1/2} V(X, Y)$.

Without including interaction effects, the velocities and pressure gradient are expanded as

$$\begin{aligned} U(X, Y) = {} & U_0(Y) + U_1(Y)X + U_2(Y)X^2 - \mu U_0'(y)X \\ & + \mu V_0''(Y)X^2 + 1/2\mu^2 U_0''(Y)X^2 + \cdots \end{aligned} \tag{5a}$$

$$\begin{aligned} V(X, Y) = {} & V_0(Y) + V_1(Y)X + \mu U_0(Y) \\ & - 2\mu V_0'(Y)X - \mu^2 U_0'(Y)X + \cdots \end{aligned} \tag{5b}$$

$$\frac{dp(X)}{dX} = P_0 + P_1 X + P_2 X^2 + P_3 X^3 + \cdots \tag{5c}$$

where μ is an integral constant to be determined from the no-slip condition. $U_0(Y)$ is the velocity profile at the marginal separation point which can be expanded as a power series in Y. Other coefficients in Eqs. (5*a*) and (5*b*) can also be expanded as a power series in Y. Following Goldstein (1948), through substituting these expansions into the boundary layer equations and equating terms of the same order, the velocity profile at the marginal separation point can be determined as

$$U_0(Y) = \frac{1}{2} a_2 Y^2 + \frac{1}{6!} a_6 Y^6 + \frac{1}{8!} a_8 Y^8 + O(Y^{10}). \tag{6}$$

where

$$a_2 = P_0 \quad a_6 = 2P_0 P_1 \tag{7}$$

Also the reduced skin friction near the separation without interaction can be obtained as a series expansion in X.

$$\tau_n = -\mu a_2 X - \frac{a_6}{2a_2} \mu X^2 + \cdots \tag{8}$$

When only $O(X)$ is retained and the no-slip condition is applied to Eq. (5*a*), the reduced skin friction at the wall becomes

$$\tau_n = -\frac{1}{3}\left(\frac{a_8}{a_2}\right)^{1/2} X. \tag{9}$$

It can be shown that τ_n is consistent with τ_b, the reduced skin friction obtained from the classical boundary layer calculation at marginal separation, as $X \to 0_\pm$. This implies a_8 can be determined using the upstream boundary layer parameters a_2 and τ_b.

Interacting Flow Analysis. A significant interaction between the inviscid flow and the boundary layer arises near the separation region. As in Stewartson et al. (1982), the appropriate streamwise scale for the interaction region centered at $X=0$ is $X = O(\mathrm{Re}^{-1/5})$. In the normal direction the flow is divided into three decks: $Y = O(1)$ for the main deck, $Y = O(\mathrm{Re}^{3/10})$ for the upper deck, and $Y = O(\mathrm{Re}^{-1/20})$ for the lower deck. Following the work of Stewartson et al., the method of matched asymptotics is used between the lower deck and main deck and between the main deck and upper deck. A rescaled nonlinear integral equation which describes the skin friction in the neighborhood of the separation region is obtained as

$$\hat{A}^2(\hat{X}) = \hat{X}^2 - \Gamma + \int_{\hat{x}}^{\infty} \frac{\hat{A}''(\hat{X}_1)\,d\hat{X}_1}{(\hat{X}_1 - \hat{X})^{1/2}}. \tag{10}$$

where $\hat{A}$ and $\hat{X}$ are the rescaled variables of A and X. The arbitrary constant Γ represents the departure of the disturbance parameter from marginal separation. The reduced skin friction with interaction is given as

$$\tau_i = \alpha \hat{A}(\hat{X}). \tag{11}$$

where

$$\alpha = \left(\frac{4q^2}{27}\right)^{1/5} \frac{a_8^{3/10}}{a_2^{13/10}}, \quad q = \frac{(-1/4)!\, a_2^{1/2} U_0^2(\infty)}{2^{3/2}(1/4)!\,\mathrm{Re}^{1/2}} \tag{12}$$

Composite Solution of Skin Friction. For practical application and easy comparison with the results of the IBL, a composite solution is constructed using the solutions of the triple-deck method and the classical boundary calculation at marginal separation. The composite solution of skin friction τ is obtained by

$$\tau = \tau_b + (\tau_i - \tau_n) \tag{13}$$

where τ_b is obtained from classical boundary layer calculation while τ_n and τ_i are obtained from Eqs. (9) and (11), respectively.

2.2 Interactive Boundary Layer Method. In the classical boundary layer calculation the pressure gradient is prescribed a priori but in the IBL method the pressure gradient reflects the displacement effect of the viscous flow in the interaction region. Therefore, the actual inviscid surface velocity including the displacement thickness effect is given as

$$u_{e,\mathrm{INV}}(x) = u_e(x) + \frac{1}{\pi}\int_{-\infty}^{\infty} \frac{d(u_e(\tilde{x})\delta_1)}{d\tilde{x}} \frac{d\tilde{x}}{(x-\tilde{x})}. \tag{14}$$

where δ_1 is the nondimensional displacement thickness and $u_e(x)$ is calculated from Eq. (4). In the present study the "semi-inverse method" is applied, i.e., the boundary layer is calculated inversely but the inviscid flow is calculated directly (Veldman, 1981).

The numerical procedure of the IBL method starts from the classical boundary layer calculation. The inverse mode is first applied at the streamwise location x_b which is chosen where the displacement effect is believed to be negligible. The same condition is considered when choosing the end point x_e for the inverse calculation. The classical boundary calculation is performed only once and the solution of the velocity profile is retained at x_b to serve as the initial boundary condition for the inverse calculation. The Mechul function scheme (Cebeci and Keller, 1973) is applied for the inverse calculation.

An initial prescribed δ_1 is needed to start the inverse calculation. In the present study the Blasius solution is used as the initial guess. The FLARE (Reyhner and Flugge-Lotz, 1968) approximation, in which the momentum term $u\partial u/\partial x$ is neglected wherever $u<0$, is applied when the inverse calculation is carried through the separation region. From the inverse calculation the inviscid surface velocity $u_{e,BL}$ can be determined.

Subsequently, Eq. (14) is used to evaluate the $u_{e,\mathrm{INV}}$ directly with the same δ_1 prescribed for the inverse calculation. In order to evaluate the Hilbert integral of Eq. (14), the limited region, $x_b \leq x \leq x_e$, is used.

An iterative cycle is completed when the displacement thickness is updated by the successive over-relaxation (SOR) formula,

$$\delta_1^{n+1}=(1-\omega)\delta_1^n+\omega\left[\delta_1^n\left(\frac{u_{e,BL}}{u_{e,\mathrm{INV}}}\right)\right] \tag{15}$$

where ω is the relaxation parameter. $\omega=1.5$ is used in the present study to accelerate the convergence. The convergence criterion of the global iterative process is taken as

$$\max|\delta_1^{n+1}(x)-\delta_1^n(x)|<10^{-4}. \tag{16}$$

2.3 Navier-Stokes Computation. In the present study the incompressible unsteady Navier-Stokes equations are solved by a fractional-step method developed by Kim and Moin (1985). Although the steady-state solution is of interest in the current study, the time-dependent approach has been solved for three reasons. First, the effect of free stream oscillations on a separated flow can be studied using the present method without any modification. Second, for high Reynolds number flow the convergence rate of a steady-state iterative procedure and a time-dependent approach are similar. Finally, physical instability associated with eventual turbulent transition is easier to distinguish in the time-dependent approach.

The second-order-implicit Crank-Nicolson method is used for the viscous terms while the pressure and the convective terms are evaluated through the use of the second-order-explicit Adams-Bashforth method. All spatial derivatives are approximated by second-order central differencing on a staggered grid. This leads to second order accuracy both in time and space.

In the current study a rectangular computational domain is used. At the inlet of the computational domain, the velocity profiles are specified by the Blasius boundary layer solution. The no-slip boundary condition $u=0$ and nontranspiration condition $v=0$ are used on the lower wall. On the upper wall the no-stress boundary condition $\partial u/\partial y=0$ is applied for the streamwise boundary condition. For the transverse boundary condition, except in the suction port region, several transverse velocity distributions will be tested in order to eliminate the internal flow effect. The convective equation $\partial u_i/\partial t+c\partial u_i/\partial x=0$ which was recommended by Pauley et al. (1988) for unsteady boundary layer flow is applied to exit boundary condition in the present study. The average exit velocity is used for the convective velocity c.

The computational domain is set so that the separation solution is independent of inlet and outlet boundary effect. The height of the channel is set such that the boundary layer never occupies more than 10% of the height of the channel to reduce the internal flow effect. All computations contain 256 evenly spaced grid nodes in the streamwise direction and 128 stretched grid nodes in the normal direction. Half of the grid points are clustered in the boundary layer on the test wall. The grid-dependence of the solution was tested by doubling the number of points in the streamwise or normal directions; for both cases the changes in the velocity were less than 0.5 percent.

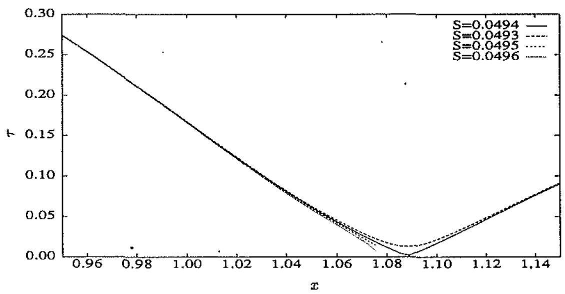

Fig. 2 The solution τ of classical boundary layer calculation for various suction strengths near $S=S_m$ for $W=0.0621$

3 Results and Discussion

3.1 Marginal Separation. By adjusting the suction strength S, one could determine the marginal separation conditions from the classical boundary layer calculation. However, due to numerical resolution it was difficult to find an exact value of the suction strength which caused the skin friction to vanish to zero at one point and then recover immediately. Therefore, the marginal separation condition was defined when $S=S_m$ while the classical boundary layer calculation began to predict separation as $S=S_m+\epsilon$. The ϵ was chosen to be an appropriately small positive value so that $\epsilon \ll \mathrm{Re}_L^{-2/5}$. The marginal separation point was then defined as the point at which the skin friction had the minimum value as $S=S_m$. Figure 2 shows that the reduced skin friction τ_b decreases to a minimum point then recovers immediately at the marginal separation condition as $S=S_m$ but leads to a singularity when $S>S_m$.

After the marginal separation conditions were determined, the coefficients a_2 and a_6 of the series expansion of the marginal separation profile then were obtained by fitting the curve of the pressure gradient near the marginal separation point. a_8 was chosen so that Eq. (9) accurately matched the slope of τ_b as $X\rightarrow 0_\pm$.

3.2 Comparison Between IBL Method and Triple-Deck Method. In Stewartson et al. (1982), it was found that no solution of $\hat{A}$ existed for Eq. (10) when Γ was larger than a critical value Γ_c and there were two or even four solutions when $0\leq\Gamma\leq\Gamma_c$. Further investigation of these nonunique solutions was made by Brown and Stewartson (1983). However, only the upper branch solution is consistent with the physical phenomenon that the minimum skin friction decreases monotonically when the adverse pressure gradient is increased. Therefore, all composite solutions of skin friction from the triple-deck method were carried out using the upper branch solutions.

All computations of the IBL and the triple-deck methods were carried out for $\mathrm{Re}_L=1.21\times10^5$, 1.84×10^6, 1.84×10^8. Two different suction port widths, $W=0.0621$ and 0.621, were tested with the same suction port start location. Figure 3 shows the comparison of reduced skin friction from the IBL and the composite solutions at the marginal separation conditions for different Re_L and $W=0.0621$. It is noted that although the classical boundary layer calculation predicts marginal separation, the elliptic nature of the flow described by the triple-deck and IBL methods delays separation. To produce a separated flow the adverse pressure gradient must be increased beyond the marginal separation conditions. This comparison also shows that a higher Re_L leads to a more favorable comparison between the triple-deck and IBL results. However, the Reynolds number range which results in a favorable compar-

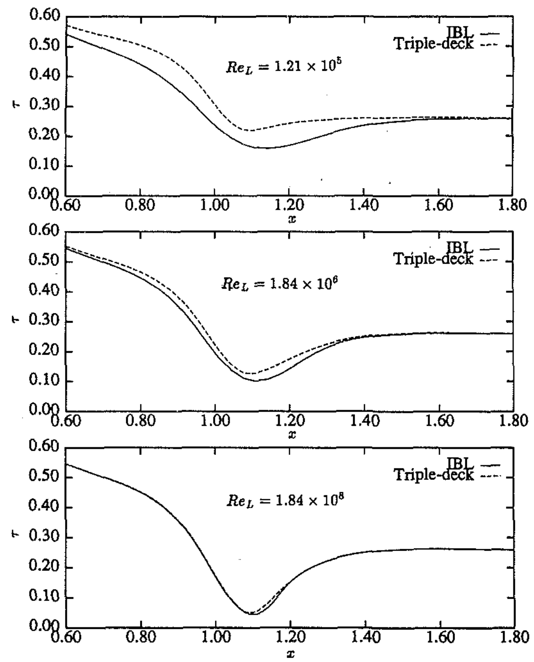

Fig. 3 Comparison of τ from the IBL method and the triple-deck method at marginal condition for three different Re_L and $W = 0.0621$

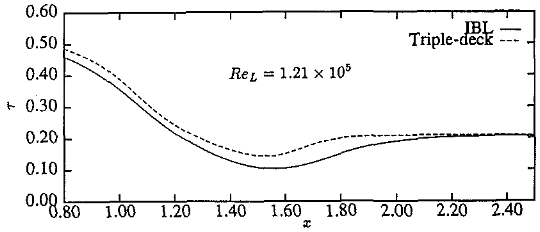

Fig. 4 Comparison of τ from the IBL method and the triple-deck method at marginal condition for $Re_L = 1.21 \times 10^5$ and $W = 0.621$

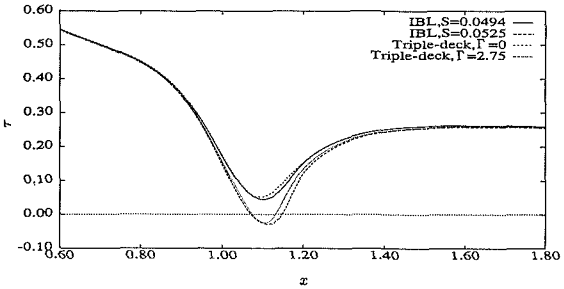

Fig. 5 Comparison of τ from the IBL method and the triple-deck method for $S = S_m$ and $S = S_c$ at $Re_L = 1.8405 \times 10^8$ and $W = 0.0621$

ison between the triple-deck and IBL methods is far above the conditions which produce a laminar boundary layer flow in the present geometry.

The influence of suction port width can be noted by comparing Figs. 3(*a*) and 4 where Fig. 4 shows the results obtained at $W = 0.621$. It is seen that the wider suction port also leads to a more favorable comparison when computations were carried at the same Re_L. Since the narrow suction port creates a more severe pressure gradient, it is concluded that a more gradual pressure gradient improves the solution of the triple-deck method. In fact, from Eqs. (8) and (9) one also can justify this conclusion. Equation (9) was obtained when higher order terms in Eq. (8) were neglected. This implies that

Table 1 Summary of S_c and Reynolds numbers for different cases

$W = 0.0621$			$W = 0.621$		
Re_L	Re_{L_p}	S_c	Re_L	Re_{L_p}	S_c
1.21×10^5	8.37×10^3	0.094	1.21×10^5	1.95×10^4	0.100
1.84×10^6	1.29×10^5	0.065	1.84×10^6	2.98×10^5	0.080
1.84×10^8	1.29×10^7	0.053	1.84×10^8	2.98×10^7	0.069

$$a_2 \gg \frac{a_6}{2a_2} X \tag{17}$$

must be satisfied in order to obtain an accurate solution. Equation (17) can be rewritten as

$$P_0 \gg P_1 X. \tag{18}$$

Since $X \sim O(\mathrm{Re}^{-1/5})$, in order to satisfy Eq. (18) the Reynolds number must be sufficiently large or the slope of the pressure gradient must be gradual near the marginal separation point.

However, if an appropriate characteristic length is chosen, then a criterion only dependent on Reynolds number will be obtained. In order to describe the strength of the pressure gradient, the characteristic length is defined as

$$\frac{L_p^*}{L^*} = \frac{\Delta p}{(dp/dx)_{\max}} \tag{19}$$

where Δp is the pressure difference across the suction port, $(dp/dx)_{\max}$ is the maximum slope determined from Eqs. (3) and (4) at the marginal separation condition $S = S_m$. When the Reynolds number is based on the pressure gradient length, it is seen that the discrepancy between the IBL method and the triple-deck method decreases as the Reynolds number increases. Obviously, Re_{L_p} is more appropriate to provide an accuracy criterion for the triple-deck method. The values of Re_{L_p} for the different cases tested are listed in Table 1.

Another noteworthy feature is the comparison of the critical condition. Stewartson et al. (1982) commented that the solutions of the fundamental equation of marginal separation cease to exist when $\Gamma \geq \Gamma_c$, where $\Gamma_c \approx 2.75$. For the IBL calculation, a convergent solution was also unable to be obtained when the suction strength was larger than a critical value. Figure 5 compares the solutions of skin friction between these two methods at the marginal and critical condition. The comparison shows that the solutions agree very well when the Reynolds number is sufficiently large. This critical condition will be further compared with the solutions of the Navier-Stokes computation and related to a physical phenomenon. The results of critical suction strength S_c for different Reynolds numbers and suction port widths are summarized in Table 1.

3.3 Comparison Between IBL Method and Navier-Stokes Computation.

The comparison between the IBL method and the full Navier-Stokes computation was only conducted for $\mathrm{Re}_L = 1.21 \times 10^5$ to verify the IBL results in practical problems. Since the effect of withdrawing flow from the suction port is to reduce the transition Reynolds number, the computational results showed that a stable laminar flow solution could be obtained only at the lowest Reynolds number examined in the present study.

When comparing these two methods, a difficulty was encountered in specifying the upper wall boundary condition for the Navier-Stokes computation. This difficulty is similar to that discussed in Cebeci and Stewartson (1983) in which the IBL method was compared to the Navier-Stokes computation of Briley (1971). In Briley's study the upper boundary condition at $y = y_e$ was specified by the potential flow. The viscous-inviscid interaction can be constrained by positioning the edge of the computational domain too close to the outer edge of the boundary layer. Apparently, the upper boundary condition

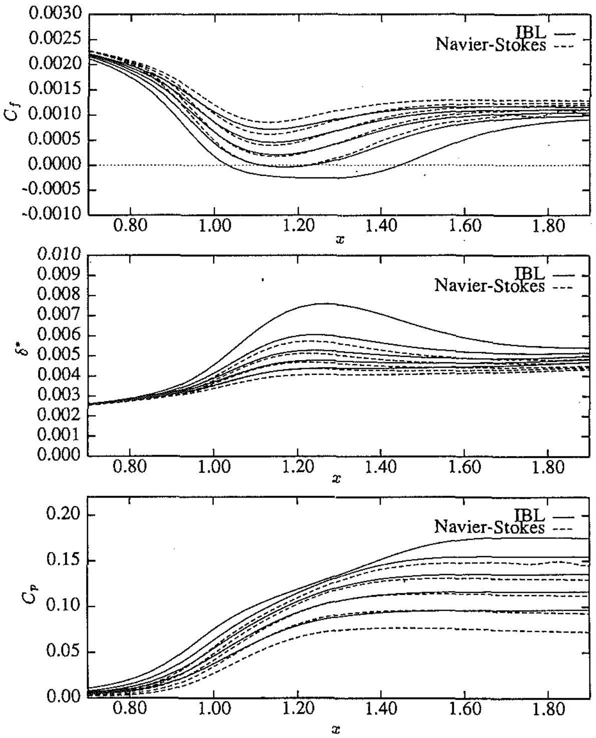

Fig. 6 Comparison of C_f, δ^*, C_p from IBL method and Navier-Stokes computations with nontranspiration wall for various S ($S=0.0494$, 0.060, 0.070, 0.080, 0.090) and $W=0.0621$

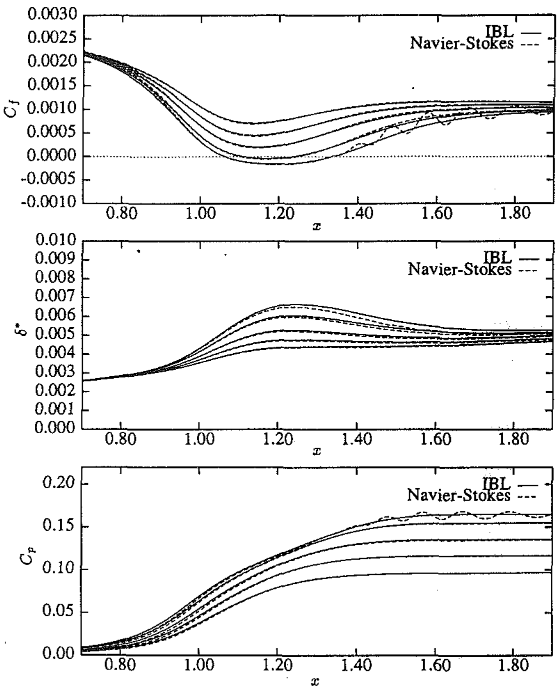

Fig. 7 Comparison of C_f, δ^*, C_p from IBL method and Navier-Stokes computations with transpiration wall for various S ($S=0.0494$, 0.060, 0.070, 0.080, 0.085) and $W=0.0621$

caused the external flow condition of Briley to be different than that of Cebeci and Stewartson and resulted in a different flow field solution.

In the present study, the viscous-inviscid interaction was not constrained severely since the upper boundary was set much farther away from the outer edge of the boundary layer. However, a discrepancy between the IBL method and Navier-Stokes computation was still observed when the nontranspiration upper wall was applied to the Navier-Stokes computation. This discrepancy was caused by the internal flow effect, i.e., the flow velocity was accelerated due to the boundary layer displacement thickness, since the IBL method applied here actually solved an external flow. The discrepancy between the results of these two methods due to the internal flow effect is demonstrated in Fig. 6. It is seen that the dimensional displacement thickness δ^* and the pressure coefficient C_p of the Navier-Stokes computation is smaller than those of the IBL method. Obviously, the nontranspiration wall had confined the boundary layer development and accelerated the flow velocity so that separation was delayed as the suction strength was increased. In order to obtain the same free-stream velocity, which was applied to the IBL calculation, the internal flow effect must be eliminated. A normal velocity distribution was applied along the upper wall, except in the suction port region, to eliminate the internal flow effect. Since the normal velocity was not applied in the suction port, a wide suction port will influence the accuracy of the results. Thus, only the narrow suction port was considered here.

Since the internal flow effect is attributed to the boundary layer development and the significant inviscid-viscous interaction due to the separation bubble, the normal velocity distribution must reflect these two effects. However, the inviscid-viscous interaction due to the separation bubble will decay far away from the boundary layer edge. Therefore, the normal velocity of the upper wall was specified by

$$v_{\text{top}} = v_{\text{Blasius}} + \lambda(v_e - v_{\text{Blasius}}) \tag{20}$$

where v_{Blasius} obtained from Blasius solution reflects the boundary layer development on a flat plate while $\lambda(v_e - v_{\text{Blasius}})$ reflects the induced transpiration velocity due to the separation bubble. Since v_e is the normal velocity which was measured at the boundary layer edge, Eq. (20) was updated at every time step in the Navier-Stokes computation. λ is the decaying factor which can be determined from a potential flow analysis which considers the flow outside the boundary layer to be inviscid. The inviscid flow over a hump due to the increased displacement thickness of the separation bubble was determined by selecting the appropriate streamline produced by the inviscid flow over a cylinder in a free stream. The upper wall deflection streamline generated by the inviscid hump flow produced a decaying factor of about 0.5. Figure 7 shows that the results of the IBL method and the Navier-Stokes computation are in very good agreement when Eq. (20) with $\lambda=0.5$ was applied to the Navier-Stokes computation. Even when the oscillations of the skin friction curve occur, the mean skin friction distribution still matches the solution of the IBL computation.

Comparison of the critical condition between the IBL method and the Navier-Stokes computation was conducted in order to establish the physical significance of the critical suction strength found in Section 3.2. In the Navier-Stokes computation the boundary layer became unstable near the reattachment point when separation occurred at high suction strength and the instantaneous skin friction curve formed oscillations near the reattachment point. The oscillations propagated downstream as "waves" and passed through the computational domain. Following Pauley et al. (1990), the separation bubble was classified as steady when the oscillations of the skin friction curve did not pass through zero skin friction condition. For the Navier-Stokes computation the oscillations of the skin friction curve passed through the zero line at the critical value of $S_c \approx 0.09$. This situation was related to the onset of vortex shedding at which the separation bubble becomes unsteady in Pauley et al. From Table 1, the critical value at which the IBL method was unable to converge is $S_c \approx 0.094$. From the favorable comparison of S_c obtained using the Navier-Stokes and IBL methods, it is concluded that the critical value of Γ corresponds to the onset of vortex shedding.

4 Conclusions

The present study compared the results of the triple-deck method of marginal separation and the IBL method to demonstrate the accuracy of the triple-deck method for marginal separation. This comparison showed that the Re_L range where the triple-deck method can accurately predict the marginal separation is above the laminar boundary layer flow conditions for the present geometry. However, the Reynolds number based on the pressure gradient length gives a more appropriate criterion to describe the accuracy of the triple-deck method of marginal separation. A geometry which can generate a sufficiently gradual adverse pressure gradient may be sought to improve the prediction of the triple-deck method for marginal separation at Reynolds numbers which produce laminar flow.

The Navier-Stokes computation was carried out at a laminar Reynolds number to verify the accuracy of the IBL method in practical problems. The comparison between these two methods indicates that the internal flow effect in the present geometry alters the marginal separation solution. Once the internal flow effect was eliminated, a good agreement of solutions between these two methods was obtained.

From these two different comparisons the critical value of Γ involved in the fundamental equation of marginal separation is related to the critical value of suction strength beyond which the separation bubble becomes unsteady.

Among these three methods studied, the IBL method is the most suitable method for solving a flow with a small separation bubble since it accurately determines the boundary layer separation solution at low Reynolds number and requires less programming efforts and CPU time than the Navier-Stokes computation.

References

Briley, W. R., 1971, "A Numerical Study of Laminar Separation Bubbles using the Navier-Stokes Equations," *Journal of Fluid Mechanics*, Vol. 47, pp. 713–736.

Briley, W. R., and McDonald, H., 1975, "Numerical Prediction of Incompressible Separation Bubbles," *Journal of Fluid Mechanics*, Vol. 69, pp. 631–656.

Brown, S. N., and Stewartson, K., 1969, "Laminar Separation," *Annual Review of Fluid Mechanics*, Vol. 1, pp. 45–72.

Brown, S. N., and Stewartson, K., 1983, "On an Integral Equation of Marginal Separation," *SIAM Journal of Applied Mathematics*, Vol. 43, pp. 1119–1126.

Brown, S. N., 1985, "Marginal Separation of a Three-Dimensional Boundary Layer on a Line of Symmetry," *Journal of Fluid Mechanics*, Vol. 159, pp. 95–111.

Cebeci, T., and Keller, H. B., 1973, "Laminar Boundary Layers with Assigned Wall Shear," *Lecture Notes in Physics*, Springer-Verlag, Vol. 19, pp. 79–85.

Cebeci, T., and Stewartson, K., 1983, "On the Calculation of Separation Bubbles," *Journal of Fluid Mechanics*, Vol. 133, pp. 287–296.

Duck, P. W., 1989, "Three-Dimensional Marginal Separation," *Journal of Fluid Mechanics*, Vol. 202, pp. 559–575.

Duck, P. W., 1990, "Unsteady Three-Dimensional Marginal Separation, Including Breakdown," *Journal of Fluid Mechanics*, Vol. 220, pp. 85–98.

Goldstein, S., 1948, "On Laminar Boundary-Layer Flow near a Position of Separation," *The Quarterly Journal of Mechanics and Applied Mathematics*, Vol. 1, pp. 43–69.

Keller, H. B., 1978, "Numerical Methods in Boundary-Layer Theory," *Annual Review of Fluid Mechanics*, Vol. 10, pp. 417–433.

Kim, J., and Moin, P., 1985, "Application of a Fractional-Step Method to Incompressible Navier-Stokes Equations," *Journal of Computational Physics*, Vol. 59, pp. 308–323.

Kwon, O. K., and Pletcher, R. H., 1979, "Prediction of Incompressible Separated Boundary-Layers Including Viscous-Inviscid Interaction," ASME JOURNAL OF FLUIDS ENGINEERING, Vol. 101, pp. 466–472.

Pauley, L. L., Moin, P., and Reynolds, W. C., 1988, "A Numerical Study of Unsteady Laminar Boundary Layer Separation," Report TF-34, Department of Mechanical Engineering, Stanford University.

Pauley, L. L., Moin, P., and Reynolds, W. C., 1990, "The Structure of Two-Dimensional Separation," *Journal of Fluid Mechanics*, Vol. 220, pp. 397–411.

Reyhner, T. A., and Flugge-Lotz, I., 1968, "The Interaction of a Shock Wave with a Laminar Boundary Layer," *International Journal of Nonlinear Mechanics*, Vol. 3, pp. 173–199.

Smith, F. T., 1982, "On the High Reynolds Number Theory of Laminar Flows," *IMA Journal of Applied Mathematics*, Vol. 28, pp. 207–281.

Stewartson, K., 1974, "Multistructured Boundary Layers on Flat Plates and Related Bodies," *Advances in Applied Mechanics*, Vol. 14, pp. 145–239.

Stewartson, K., Smith, F. T., and Kaups, K., 1982, "Marginal Separation," *Studies in Applied Mathematics*, Vol. 67, pp. 45–61.

Veldman, A. E. P., 1981, "New, Quasi-Simultaneous Method to Calculate Interacting Boundary Layers," *AIAA Journal*, Vol. 19, pp. 79–85.

Werle, M. J., and Davis, R. T., 1972, "Incompressible Laminar Boundary Layers on a Parabola at Angle of Attack: A Study of the Separation Point," ASME *Journal of Applied Mechanics*, Vol. 12, pp. 7–12.

Yang, Jing-Tang
Professor.
Mem. ASME

Tsai, Bor-Bin
Graduate Student.

Tsai, Go-Long
Graduate Student.

Department of Power Mechanical
Engineering,
National Tsing Hua University,
Hsinchu, Taiwan 30043

Separated-Reattaching Flow Over a Backstep With Uniform Normal Mass Bleed

(Data Bank Contribution)*

The effect of normal mass bleed into the separated-reattaching flow behind a backward-facing step has been experimentally investigated. Results of LDA measurements showed that normal mass bleed suppressed the reverse horizontal velocity, the reverse flow rate, turbulence intensity, and Reynolds shear stress within the whole recirculating zone. An analysis of the distributions of vertical velocity and turbulence intensity indicates that the interaction between the injected fluid and the main stream began at 0.4 step height and became significant after 0.8 step height behind the backstep.

1 Introduction

The air stream over a backward-facing step produces a separated flow containing a recirculation zone and a shear layer. Such a flow pattern is intimately related to the performance of various devices such as diffusers, airfoils, and combustors. Although there have been many investigations of the flow field behind a backward-facing step, the detailed mechanism of mixing in such a flow, especially within the recirculation zone, was not thoroughly explored. The reattachment length and distribution of mean velocity and turbulent properties of such flows without mass addition have been the primary focus of previous research. Five factors influencing the reattachment length were summarized by Eaton and Johnston (1981). Varying the upstream flow Isomoto and Honami (1989) discovered that a significant parameter governing the reattachment length is the turbulence intensity in the boundary layer at the separation point. The maximum turbulence intensity in the boundary layer was found to be inversely proportional to the reattachment length. The reverse flow rate in the recirculation zone was compared with the flow rate of the redeveloping boundary layer by Etheridge and Kemp (1978), who estimated that one sixth of the fluid present in the shear layer was rolled into the recirculation zone. Kim et al. (1980) measured the vertical distribution of mean static pressure at a fixed horizontal position and found that the pressure was greatest in the mainstream, moderate in the recirculation zone, and smallest in the shear layer, quite different from the nearly invariant pressure distribution of the flow over a flat plate.

Richardson (1984) used wall injection to simulate fuel vapor addition in a sudden-expansion combustor; he reported that wall injection enhanced the turbulence intensity of the recirculating flow. de Groot (1985) used laser Doppler anemometry to probe the complex turbulent flow over a two-dimensional backward-facing step, finding that the maximum shear stress at each axial location increased due to side-wall injection, and that the reattachment length was insensitive to the injection velocity. In addition, side-wall injection smoothed the distribution of turbulence intensity and Reynolds shear stress in the recirculation zone and reduced the reverse velocity. The effects of wall injection on the behavior of mass and momentum transport across a shear layer associated with a separated flow are worthy of further investigation. For the attached flow case Schetz and Nerney (1977) and Schetz and Collier (1984) indicated that the velocity fluctuation level and turbulence intensity in the turbulent boundary layer increased with increasing rate of injection at the wall.

To study the interaction between simulated fuel vapor and a recirculating flow for the purpose of improving our physical understanding of combustor flows and of verifying existing turbulence models, we took as our objective the examination of the turbulence features in the recirculation zone and the shear layer of a backward facing step with normal mass injection from the wall downstream of the step.

2 Experimental Design

2.1 Test Rig. A schematic diagram of the wind tunnel and instrumentation appears in Fig. 1. Experiments were conducted in an open-circuit wind tunnel powered by a 75 kW Roots blower with a speed controller. The blower provided a maximum flow rate of 50 m^3/min with a maximum static pressure of 70 kPa.

---

*Data have been deposited to the JFE Data Bank. To access the file for this paper, see instructions on p. 193 of this issue.

Contributed by the Fluids Engineering Division for publication in the JOURNAL OF FLUIDS ENGINEERING. Manuscript received by the Fluids Engineering Division August 10, 1992; revised manuscript received November 10, 1993. Associate Technical Editor: D. M. Bushnell.

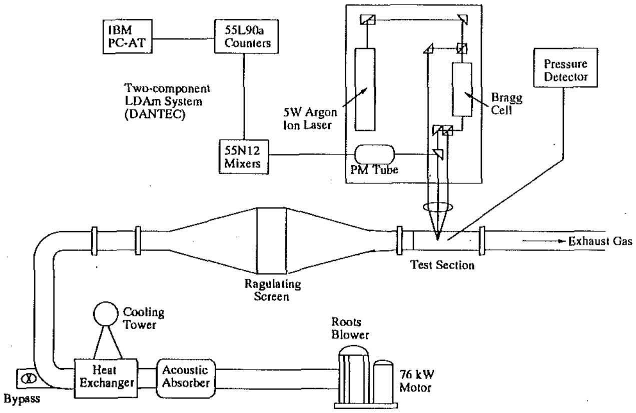

Fig. 1 A schematic diagram of experimental apparatus

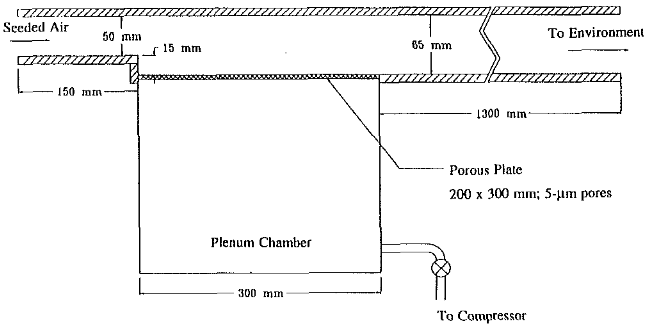

Fig. 2 Configuration and dimensions of test section

The dimensions of the test section were 5×20 cm^2. The step height was chosen to be 1.5 cm, corresponding to an aspect ratio 13.3 to ensure two-dimensional flow conditions (Ellzey and Berbee, 1988). The configuration and dimensions of the test section are shown in Fig. 2. The base of the Plexiglass test section consisted of a porous stainless steel plate 20×30 cm^2 with 5-μm pores. The air injected from the base plate into the test section was supplied by a 1.5 kW compressor. The pressure differences across the plate for various test conditions were in the range $4.8 \sim 6.4$ kPa, whereas the maximum pressure drop in the recirculation zone was 0.1 kPa. Since the variation of the pressure difference across the porous plate within the test section was two-orders of magnitude higher than the variation of the static pressure in the flow, the normal bleed rates over the whole plate varied only 3 percent and thus assumed to be uniform. The flow structures were investigated quantitatively via the measurement of velocities and pressures.

2.2 Instrumentation. The velocities were measured with a three-beam, 2-component backward-scattering LDA, which was connected to a computer-controlled traversing system for two-dimensional movement. The resolution of the traverse system was 0.03 mm. The instruments were mounted on an optical bench that was placed on a traverse table for major movement.

The laser beam from an argon-ion laser (5 W), with radiation mainly at wavelengths 514.5 and 488 nm, was split into two beams. One beam passed through a Bragg cell to produce a 40-MHz frequency shift and was then split again, through a color-selective beam splitter, into two beams, one of wavelength 514.5 and the other 488 nm. The resulting two beams and the original beam passed through a beam translator, a beam expander and a convergent lens of focal length 310 mm. The two axes of the blue beam of the optical probe were 0.128 and 1.625 mm, whereas those of the green beam were 0.135 and 1.713 mm. The backward-scattering Doppler signals were detected by two photomultipliers and processed by a coincidence filter and two counter processors. A beam-waist adjuster was used to improve signal strength. The seeding particles were generated and heated before being introduced into the air stream at the divergent section upstream of the screens in the wind tunnel. The particles, with a diameter of the order of 1 μm, were made of 25 percent glycerin resolvent and a water solvent.

The static pressures near the base were measured with a tube, outer diameter 1.5 mm and L-shaped, having eight 0.1 mm holes drilled around its end; the tube passed through the side wall of the Plexiglass test section. The probe used in the experiment was verified (Yang and Tsai, 1993) to be suitable for pressure measurement in the flow field. The measuring points were located at intervals of 1.0 H along the horizontal direction. The measured data were transmitted through a differential pressure gage and analyzed by a waveform analyzer. Measurements of pressure fluctuation were made by a piezoelectric transducer, a charge amplifier and noise filter.

2.3 Experimental Conditions. The principal parameters of the experiments were the stream velocity ahead of the step ($U_0 = 20 \sim 60$ m/s) and the normal bleed rate of air ($Q = 0 \sim 540$ liter/min). The corresponding Reynolds numbers based on the upstream velocity and the step height, U_0H/ν, were $(1.91 \sim 5.74) \times 10^4$. Injection velocities of the air bleed were 0, 0.05 m/s, 0.10 m/s, and 0.15 m/s. Turbulence intensity of the flow upstream of the step was 0.8 percent. The boundary layer just upstream of the step was turbulent, having a maximum turbulence intensity around 6 percent. The thickness of the boundary layer before the step was 0.6 H at $U_0 = 20$ m/s.

Westphal and Johnson (1984) reported that a similar flow structure could be attained if the spatial coordinate was normalized by the reattachment length. We chose the length of the recirculating zone, X_r, as the reference of normalization, and defined it as the distance from the step to the location at which the mean horizontal velocity at 0.05 H above the wall was zero. The LDA measurements were conducted across the 14 cross sections at 0, 0.2, 0.3, 0.4, 0.5, 0.6, 0.7, 0.8, 0.9, 1.0, 1.1, 1.3, 1.5 and 2.0 X_r away from the backstep. Velocity data were conducted at every 0.05 H in the range $Y/H = -0.9 \sim +1.0$ with the lowest location 0.05 H above the wall. The measurement period for each data point was controlled to be less than 1 minute.

2.4 Data Accuracy. 2048 measurements were normally made at each measuring point. The corresponding maximum uncertainties were 3.2 percent for mean axial velocity, 4.9 percent for mean normal velocity and 4.9 percent for turbulence intensity at the 95 percent confidence level. The corresponding maximum uncertainty for Reynolds shear stress was 13 percent. As the definition of the Reynolds shear stress is $-\overline{u'v'}$, it is estimated that a 5 percent error of the root mean square quantities $(\overline{u'^2})^{1/2}$ and $(\overline{v'^2})^{1/2}$ causes about 13 percent uncertainty of the Reynolds shear stress.

The signal processing was conducted with two burst-period counters which used eight fringe crossings to determine the period of the signal. The counters then applied a 5/8 comparison and a three-level validation circuit to minimize erroneous periodic readings. The coincidence interval between the counters was of the order of nanoseconds to ensure the validity of the readings. The frequency offset of the Bragg cells was large compared with the frequency shift from the flow velocity. The cycle period of the data acquisition system was small compared with the measurement period in the recirculating zone. This allowed multiple readings on the same seeding particle, and the influence of the sampling bias is thus significantly reduced. Furthermore, a two-dimensional weighting model proposed by Johnson et al. (1984) was applied to the analysis of the raw data and showed fairly good agreement with our results. More than 2000 data points were taken for each pres-

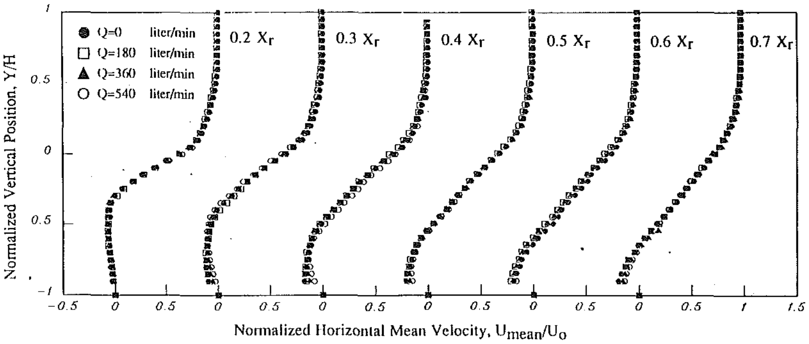

Fig. 3(*a*) Effects of the normal injection rate on mean horizontal velocity profiles at $U_0=20$ m/s; cross sections of $X/X_r=0.2$, 0.3, 0.4, 0.5, 0.6 and 0.7. (Uncertainty in mean horizontal velocity is less than ±3.2 percent.)

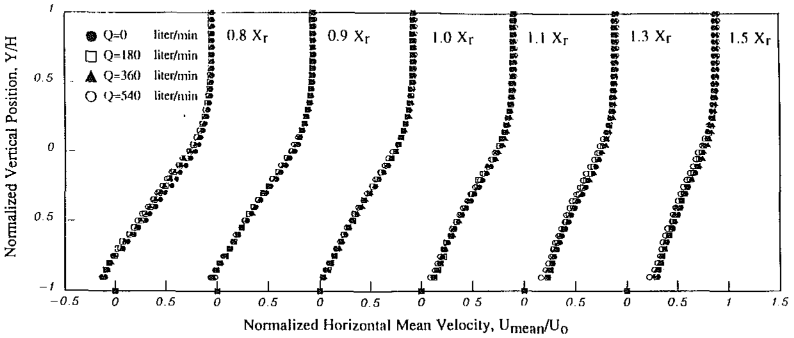

Fig. 3(*b*) Effects of the normal injection rate on mean horizontal velocity profiles at $U_0=20$ m/s; cross sections of $X/X_r=0.8$, 0.9, 1.0, 1.1, 1.3 and 1.5. (Uncertainty in mean horizontal velocity is less than ±3.2 percent.)

sure measurement; the sampling period was 500 μs. The uncertainty of the pressure data was estimated to be less than 5 percent.

3 Results and Discussion

3.1 Mean Horizontal Velocity. A comparison between the mean horizontal velocity profiles with and without various normal mass bleed rates at $U_0=20$ m/s is shown in Figs. 3(*a*) and 3(*b*). Curves for injection rates of 0, 0.5, 0.10, 0.15 m/s are almost coincident at $0.2\,X_r$. After $0.3\,X_r$, the mean velocity is reduced near the wall as the injection rate is increased. This trend agrees with that of Schetz and Collier Jr. (1984), Cebeci and Mosinskis (1971), and de Groot (1985). As the horizontal momentum is conserved, the mixing between the injected mass and the recirculating fluid near the wall creates an increase of mass, and thus results in a smaller horizontal velocity. The affected area is, however, restricted to 0.3 H above the wall ($Y/H=-0.7$) as a result of the velocity of the injected fluid being significantly less than that in recirculation zone. This behavior differs from that in the redeveloping region, in which the greater rate of injection generates a smaller horizontal velocity within the boundary layer but a higher velocity outside the boundary layer.

Streamlines of the flow field with and without normal mass addition are sketched in Figs. 4(*a*)-4(*b*), respectively. The stream function is defined as

$$d\Psi=\frac{\partial\Psi}{\partial x}\,dx+\frac{\partial\Psi}{\partial y}\,dy \tag{1}$$

The mass flow rate, equals to the difference between the two stream functions, is calculated from the following equations.

$$\int_1^2 d\Psi=-\int_{x1}^{x2}\overline{V}dx+\int_{y1}^{y2}\overline{U}dy \tag{2}$$

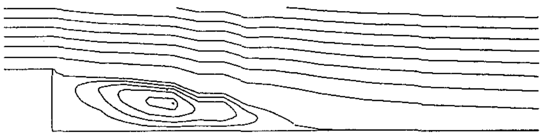

Fig. 4 (*a*) $V_s=0$

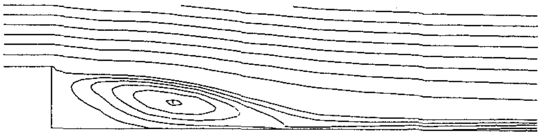

Fig. 4(*b*) $V_s=0.10$ m/s. (Uncertainty in mean horizontal velocity is less than ±3.2 percent.)

Fig. 4 Streamlines of the flowfield when the upstream velocity is 20 m/s

$$\int_1^2 d\Psi=-V_s(x_2-x_1)+\sum_1^2\overline{U}dy \tag{3}$$

Normal injection induces partial mass bleed from the recirculating zone into the redeveloping boundary layer downstream.

The effect of normal mass bleed on maximum reverse velocity at various cross sections in the recirculating zone at $U_0=20$ m/s is depicted in Fig. 5. The mass bleed rate reduces the maximum reverse velocities at each cross section. The greatest reverse velocity occurs at $0.6\,X_r$, with values in the range $0.16U_0\sim0.22U_0$. Divergence of maximum reverse velocities for various mass bleed rates are prominent in the rear part of the recirculating zone, but not significant in the leading part.

The dimensionless local reverse flow rate is defined as

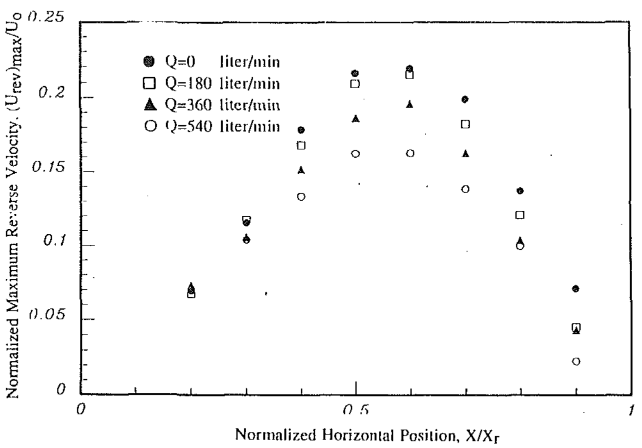

Fig. 5 Effect of normal injection on maximum reverse velocity at $U_0 = 20$ m/s. (Uncertainty in mean horizontal velocity is less than ±3.2 percent.)

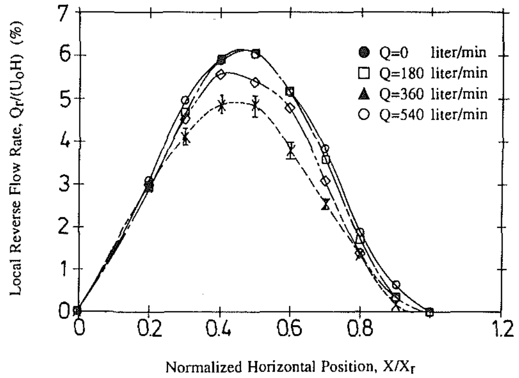

Fig. 6 Dimensionless reverse flow rate of each section along the horizontal direction at $U_0 = 20$ m/s. (Uncertainty in dimensionless reverse flow rate is less than ±3.2 percent.)

$$Q_r/U_0H = -\int_{-H}^{y^*} udy/U_0H \tag{4}$$

in which y^* corresponds to the point of zero horizontal velocity with negative horizontal velocity between $y = -H$ and y^*. The distributions of the reverse flow rates (Q_r/U_0H) along the normalized horizontal distance (Fig. 6) show that the maximum reverse flow rates are located between $0.4 \sim 0.5\,X_r$. The reverse flow rate decreases as the wall injection velocity increases. Differences in reverse flow rates for various mass injection rates are small in the leading part, but prominent in the rear part of the recirculating zone. Hence less mass is rolled up from the main stream into the recirculating zone when the fluid is normally injected.

3.2 Static Pressure on the Wall. Horizontal variations of the static pressure coefficient along the wall for various injection rates at $U_0 = 20$ m/s are depicted in Fig. 7. The border of the recirculating zone, separately denoted by arrows, is located where the highest pressure gradients are. Static pressure increases significantly in the front part of the recirculating zone as the injection rate increases. The vertical pressure difference across the shear layer is therefore subdued and the bending downward of the shear layer is prolonged. As a result, the length of recirculating zone increases with increasing rate of injection. Deviations among the distributions of the dimensionless static wall pressure, which correspond to different injection rates, gradually diminish after the recirculating zone.

A similar trend for $U_0 = 60$ m/s is indicated in Fig. 8. The lengths of the recirculating zone are 6.57 H, 6.6 H, 6.67 H, and 6.7 H for the injection rates 0, 180, 360, and 540 liter/min, respectively. The value of the smallest pressure coefficient without mass bleed at $U_0 = 60$ m/s is almost the same as that of 20 m/s. Deviations of both pressure coefficients and length of the recirculating zone are smaller than those for 20 m/s. The length of the recirculating zone for $U_0 = 60$ m/s is also smaller than for 20 m/s.

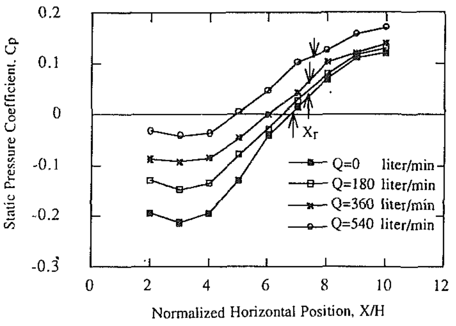

Fig. 7 Horizontal variation of wall static pressure coefficient with various injection rates at $U_0 = 20$ m/s. (Uncertainty in mean pressure is less than ±5 percent.)

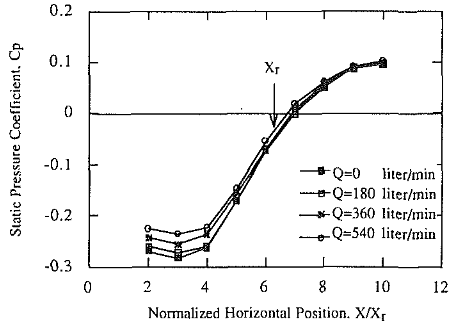

Fig. 8 Horizontal variations of wall static pressure coefficient with various injection rates at $U_0 = 60$ m/s. (Uncertainty in mean pressure is less than ±5 percent.)

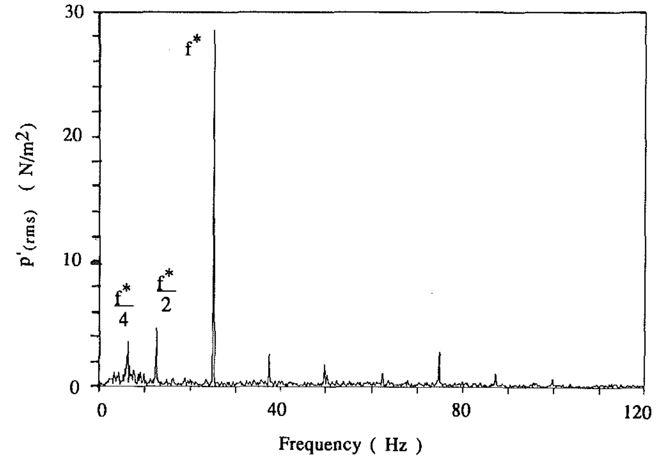

Fig. 9 Wall pressure spectrum of flow at $U_0 = 20$ m/s, $X/X_r = 1.0$

The vortex shedding frequency is analyzed through the measurements of pressure fluctuations. A typical spectrum of the wall pressure fluctuation near the end of the recirculating zone at $U_0 = 20$ m/s appears in Fig. 9. The frequency of the vortex train, denoted by a symbol f^*, is linearly proportional to the upstream flow velocity no matter how much mass is injected (Fig. 10). The dimensionless Strouhal number has a value of 0.0134. The frequencies of $1/2f^*$ and $1/4f^*$ may come from the pairing of eddies. However, alteration of the injection rate creates no obvious variation in the spectra.

The relationship between the length of the recirculating zone, the injection rate, and the upstream flow velocity is shown in Fig. 11. The length of the recirculating zone increases as the injection rate increases. According to the wall pressure distribution in Fig. 7, normal injection raises the static pressure in the recirculating zone. The pressure difference across the shear layer is greatly enhanced with increased stream velocity. That, in turn, decreases the length of the recirculating zone. The influence of the normal injection rate is inversely proportional to the inlet flow velocity. The length of the recirculating zone between normal mass bleed rates 0 and 540 liter/min increases 0.5 H at $U_0 = 20$ m/s, but only 0.1 H at $U_0 = 60$ m/s.

3.3 Turbulent Features. The definition of turbulence intensity is two dimensional and expressed as follows:

$$\text{Turbulence intensity} = \left(\frac{\overline{u'^2} + \overline{v'^2}}{2} \right)^{1/2} \qquad (5)$$

The influence of mass bleed through the porous wall on turbulence intensity is more remarkable than its effect on the mean horizontal velocity, as depicted in Figs. 12(*a*) and 12(*b*). The turbulence intensity near the porous plate is significantly dampened when the amount of mass bleed increases. This trend is similar to that found by de Groot (1989), but different from that by Schetz and Nerney (1977) and Schetz and Collier, Jr. (1984). The reduction of the turbulence intensity is obvious at $X/X_r = 0.2$ and 0.3, which are near the step. The four curves corresponding to the injection velocities of 0, 0.05, 0.10, 0.15 m/s converge at $Y/H = -0.3$, where the vertical velocity changes from positive to negative. The reduction of the tur-

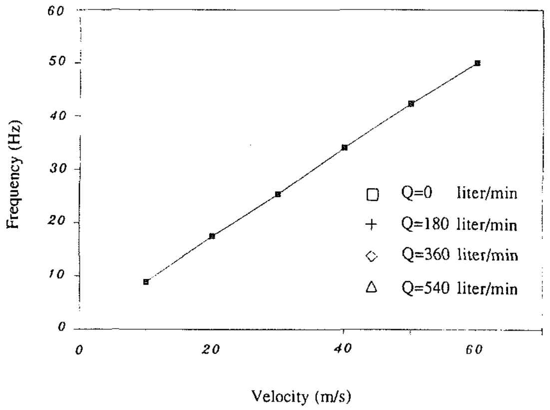

Fig. 10 Variation of the fluctuating frequency in the recirculating zone with various inlet velocities and mass bleed

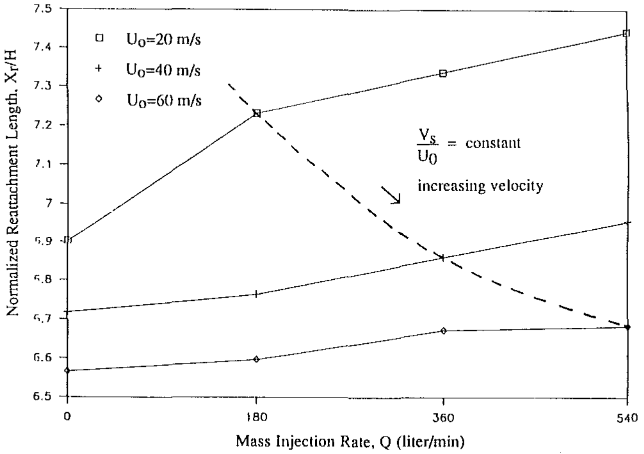

Fig. 11 Effect of normal injection on reattachment length at various upstream velocities. (Uncertainty in reattachment length is less than ±1.4 percent.)

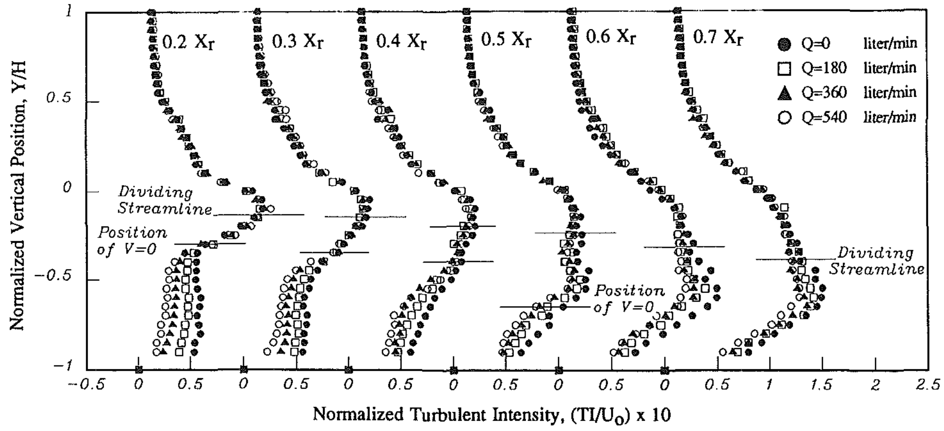

Fig. 12(*a*) Effects of the normal injection rate on turbulence intensity profiles at $U_0 = 20$ m/s; cross sections of $X/X_r = 0.2$, 0.3, 0.4, 0.5, 0.6, and 0.7. (Uncertainty in turbulence intensity is less than ±4.9 percent.)

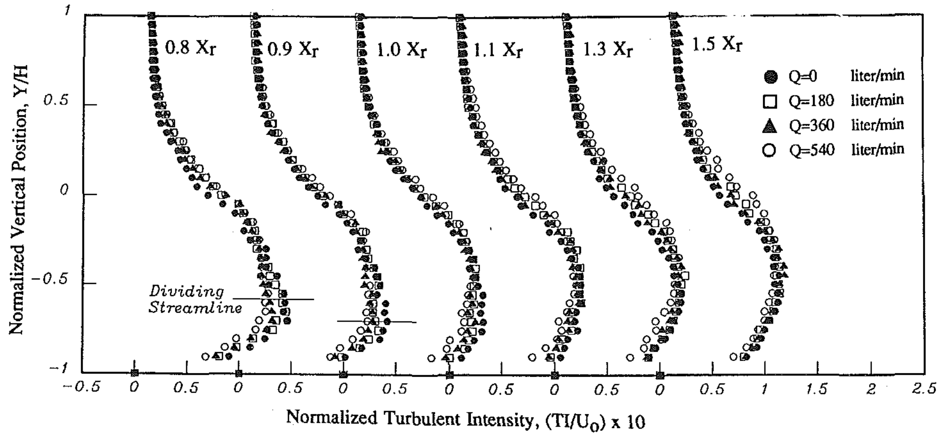

Fig. 12(*b*) Effects of the normal injection rate on turbulence intensity profiles at $U_0 = 20$ m/s; cross sections of $X/X_r = 0.8$, 0.9, 1.0, 1.1, 1.3, and 1.5. (Uncertainty in turbulence intensity is less than ±4.9 percent.)

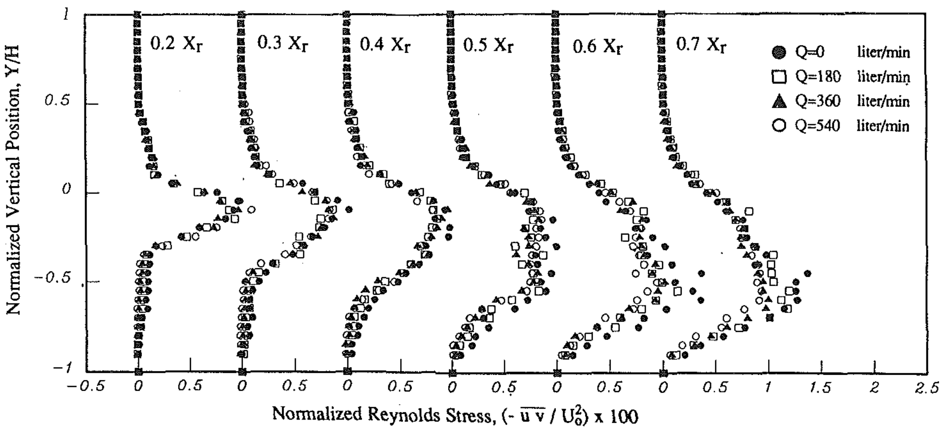

Fig. 13(*a*) Effect of normal injection rate on profiles of Reynolds shear stress at $U_0 = 20$ m/s; cross sections of $X/X_r = 0.2$, 0.3, 0.4, 0.5, 0.6, and 0.7. (Uncertainty in Reynolds shear stress is less than ±13 percent.)

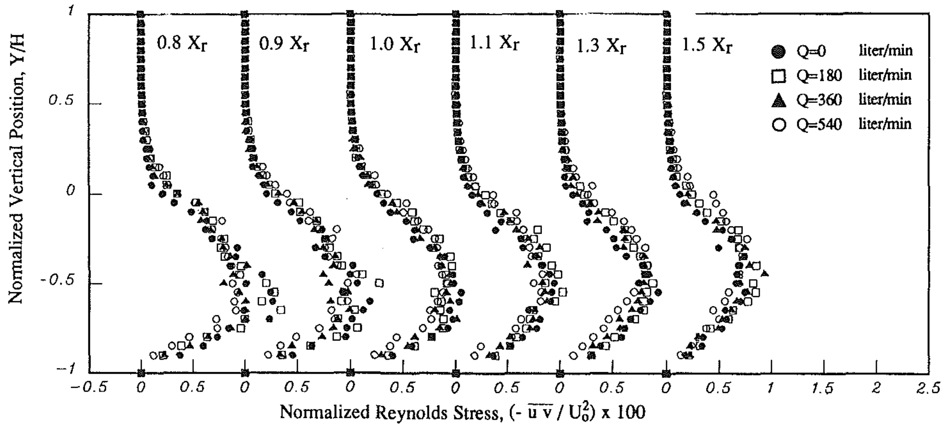

Fig. 13(*b*) Effect of normal injection rate on profiles of Reynolds shear stress at $U_0 = 20$ m/s; cross sections of $X/X_r = 0.8$, 0.9, 1.0, 1.1, 1.3, and 1.5. (Uncertainty in Reynolds shear stress is less than ±13 percent.)

bulence intensity is limited in the region $V > 0$. The differences among the four curves near the porous wall remain large for the profiles $X/X_r = 0.4$ and 0.5. The convergent positions move upward to the dividing streamlines of the step, which indicates that the injected fluid, with a smaller turbulence intensity, penetrates into the upper side of the recirculating zone.

The effects of mass bleed on the distribution of Reynolds shear stress at $U_0 = 20$ m/s is depicted in Figs. 13(*a*) and 13(*b*). Near the wall region ($Y/H = -0.8 \sim 0.9$) at $X/X_r = 0.2$, although the velocity fluctuations may vary 100 percent for different conditions, no obvious change in Reynolds shear stress was observed because of the negligible velocity gradient in that region. The effect of mass bleed on Reynolds shear stress becomes significant in the region of $Y/H = -0.8 \sim -0.45$ and it decreases as the rate of mass bleed increases. The maximum gradients of Reynolds shear stress are located on both boundaries of the shear layer; for example, at $Y/H = -0.45$ and $Y/H = 0.1$ on the cross section of 0.2 X_r. The shear layer certainly retains high level of shear stress as well as a large velocity gradient and velocity fluctuation level. As shown in the figure, the distribution of Reynolds shear stress in the shear layer region is diffuse and no clear trend is observed. The Reynolds shear stress in the shear layer is expected to be unaffected as the velocity and velocity fluctuation in this region are unaffected by wall injection. Generally, the region near the wall in the front of the recirculation zone is more affected than that in the rear. The flow near the wall of the recirculation zone has a negative dU/dY and is expected to display a negative Reynolds shear stress. However, data cannot be collected very near the wall because of instrument limitations. The flow field, therefore, displays no negative Reynolds stress except for a few points near the wall in the front part of the recirculation zone.

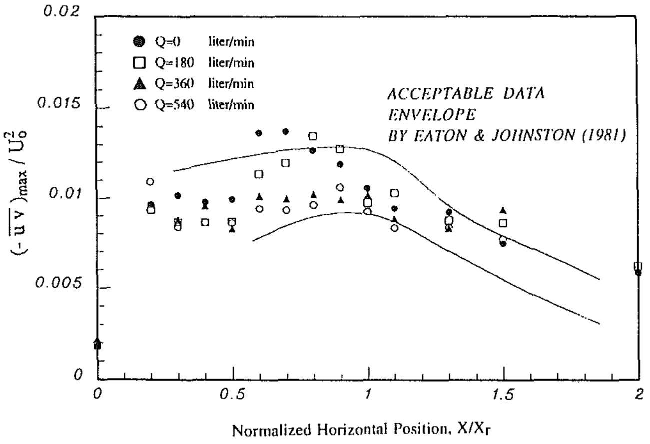

Fig. 14 Effect of normal injection rate on maximum Reynolds shear stress of each cross section. (Uncertainty in Reynolds shear stress is less than ±13 percent.)

The effect of normal mass bleed rate on the maximum Reynolds shear stress along the axial direction at $U_0 = 20$ m/s is shown in Fig. 14. The previous data on the maximum Reynolds shear stress summarized by Eaton and Johnson (1981) are also indicated in the figure. All corresponding data from this work fall within the envelope, except for those at $X_r = 0.6$, 0.7 for $Q = 0$ and $X_r = 0.8$ for $Q = 180$ liter/min. The results of the cases $Q = 0$ and 180 liter/min reveal that the peak values occur at locations in front of those previously indicated by Eaton and Johnson. The distributions of the maximum Reynolds shear stresses are smoother for the cases of $Q = 360$ and 540 liter/min than for those with no normal mass bleed. The maximum Reynolds shear stresses are generally dampened due to normal injection. The effects of the injection rate on the profiles of turbulence intensity and Reynolds number at $U_0 = 40$ and 60 m/s were less significant, but qualitatively similar to those at 20 m/s.

4 Conclusions

Normal injection significantly affects the flow features of the recirculation zone behind a backstep. The horizontal velocity near the wall in the recirculation zone decreases with increasing rate of mass bleed. Both the maximum reverse velocities and reverse flow rates along the axial position in the recirculation zone decrease when the normal bleed is introduced. Reductions of the reverse velocities by various rates of mass bleed are evident at the rear of the recirculation zone, but ambiguous at the front. Normal mass bleed also induces greater recovery of pressure in the redevelopment region and reduces the pressure difference across the shear layer.

Concerning turbulent features, mass bleed through the wall effectively suppresses the velocity fluctuations, the turbulence intensity and the Reynolds shear stress within the whole recirculation zone. The fluctuations in the region of the re-developing boundary layer are however enhanced. Maximum attenuation of turbulence intensity occurs at the cross section near the backstep. The results for the vertical velocities and the turbulent intensities at various normal bleed rates indicate that the interaction of the injected fluid with the shear layer of the recirculation zone begins at 0.4 X_r and becomes appreciable after 0.8 X_r. The results also reveal that the peak values of Reynolds shear stress are located in front of those previously indicated by Eaton and Johnson (1981). The distributions of the maximum Reynolds shear stresses were smoother for the cases of larger bleed rates than for no normal mass bleed.

JFE Data Bank Contribution

The data presented in the figures of this paper have been edited and deposited in the JFE Data Bank for the use of any of the readers. The data included mean and r.m.s. fluctuation of horizontal velocity, mean and r.m.s. fluctuation of vertical velocity, reverse velocity and reverse flow rate in the recirculating zone, wall static pressure coefficient, wall pressure spectrum, reattachment length, turbulence intensity and Reynolds shear stress. The files also include instructions on the data format. To access the file of this paper, see instruction on p. 193 of this issue.

Acknowledgment

We thank the National Science Council of the Republic of China for support under Contract No. NSC81-0401-E-007-06, and Mr. Mour, Shyuh-Gang and Mr. Hsin-Min Law for assistance in setting up the experiments.

References

de Groot, W. A., 1985, "Laser Doppler Diagnostics of the Flow behind a Backward Facing Step," Ph.D. thesis, Georgia Institute of Technology.

de Groot, W. A., Walterick, R. E., and Jagoda, J. I., 1989, "Combined LDA and Rayleigh Measurements in a Complex Turbulent Mixing Flow," *AIAA Journal*, Vol. 27, pp. 108–110.

Eaton, J. K., and Johnston, J. P., 1981, "A Review of Research on Subsonic Turbulent Flow Reattachment," *AIAA Journal*, Vol. 19, pp. 1093–1100.

Ellzey, J. L., and Berbee, J. G., 1988, "Aspect Ratio and Reynolds Number Effects on the Flow behind a Rearward-Facing Step," AIAA Paper, AIAA-88-0612.

Etheridge, D. W., and Kemp, P. H., 1978, "Measurement of Turbulent Flow Downstream of a Rearward-facing Step," *Journal of Fluid Mechanics*, Vol. 86, pp. 545–566.

Isomoto, K., and Honami, S., 1989, "The Effect of Inlet Turbulence Intensity on the Reattachment Process over a Backward-Facing Step," ASME JOURNAL OF FLUIDS ENGINEERING, Vol. 111, pp. 87–92.

Johnson, D. A., Modarress, D., and Owen, F. K., 1984, "An Experimental Verification of Laser-Velocimeter Sampling Bias and Its Correction," ASME JOURNAL OF FLUIDS ENGINEERING, Vol. 106, pp. 5–12.

Kim, J., Kline, S. J., and Johnston, J. P., 1980, "Investigation of a Reattaching Turbulent Shear Layer: Flow Over a Backward-Facing Step," ASME JOURNAL OF FLUIDS ENGINEERING, Vol. 102, pp. 302–308.

Richardson, J., 1984, "Analysis of Sudden Expansion Flow in a Two-Dimensional Duct With and Without Side-Wall Injection," Ph.D. thesis, Georgia Institute of Technology.

Schetz, J. A., and Collier Jr., F. S., 1984, "Injection into a Turbulent Boundary Layer through Different Porous Surfaces," *AIAA Journal*, Vol. 22, pp. 839–841.

Schetz, J. A., and Nerney, B., 1977, "Turbulent Boundary Layer with Injection and Surface Roughness," *AIAA Journal*, Vol. 15, pp. 1288–1293.

Westphal, R. V., and Johnston, J. P., 1984, "Effect of Initial Condition on Turbulent Reattachment Downstream of a Backward-Facing Step," *AIAA Journal*, Vol. 22, pp. 1727–1732.

Yang, J. T., and Tsai, G. L., 1993, "Near-Wake Flow of a V-gutter with Slit Bleed," ASME JOURNAL OF FLUIDS ENGINEERING, Vol. 115, pp. 13–20.

Cavity Flow Predictions Based on the Euler Equations

Manish Deshpande

Jinzhang Feng

Charles L. Merkle

Propulsion Engineering Research Center,
Department of Mechanical Engineering,
The Pennsylvania State University,
University Park, PA 16802

An Euler solver based on artificial-compressibility and pseudo-time stepping is developed for the analysis of partial sheet cavitation in two-dimensional cascades and on isolated airfoils. The computational domain is adapted to the evolution of the cavity surface and the boundary conditions are implemented on the cavity interface. This approach enables the cavitation pressure condition to be incorporated directly without requiring the specification of the cavity length or the location of the inception point. Numerical solutions are presented for a number of two-dimensional cavity flow problems, including both leading edge cavitation and the more difficult mid-chord cavitation condition. Validation is accomplished by comparing with experimental measurements and nonlinear panel solutions from potential flow theory. The demonstrated success of the Euler cavitation procedure implies that it can be incorporated in existing incompressible CFD codes to provide engineering predictions of cavitation. In addition, the flexibility of the Euler formulation may allow extension to more complex problems such as viscous flows, time-dependent flows and three-dimensional flows.

Introduction

The literature of the past several decades contains numerous models and analyses of sheet cavitation for flows over simple bodies such as airfoils. Some representative papers that describe a portion of this include Tulin (1953), Wu (1972), Geurst (1959), Hsu (1975), Tulin and Hsu (1980), Schultz and Kueny (1986), and Uhlman (1987). The classical approach to cavitation analysis is to treat the liquid/cavity interface as a constant pressure surface and to describe the flowfield by the velocity potential equations. The resulting cavity predictions are generally in reasonable agreement with experiment, although the application of potential methods to more complex configurations is difficult. The objective of the present paper is to incorporate cavitation models analogous to those that have been used in potential flow analyses into Euler equation solvers to provide a method for incorporating cavitation modeling in modern CFD codes. A further reason for using the Euler equations is to provide a foundation for developing more complex and physically complete cavitation models.

In the velocity potential approaches, the earlier workers used conformal mapping to determine the flow field (Geurst, 1959; Hsu, 1975; Tulin and Hsu, 1980), while more recently workers have used surface singularity distribution methods (Uhlman, 1987). Some of these cavitation analyses have been based on linear theories in which the constant pressure condition is enforced on the airfoil surface (Tulin, 1953; Geurst, 1959), while others have used nonlinear theories in which the pressure condition is applied on the cavity surface (Tulin and Hsu, 1980; Uhlman, 1987).

The traditional approach that is selected with velocity potential methods is the indirect, rather than the direct, cavitation problem. That is to say, the constant pressure condition is typically implemented by starting from a prescribed cavity length and allowing the level of the cavitation pressure to be determined as a part of the solution. Thus, after the flowfield has been obtained for a known cavity length, the level of the pressure in the cavitation region is deduced. In principle, a number of such inverse calculations for different cavity lengths can be used to obtain a particular cavitation pressure, but this iterative approach is seldom used. Researchers instead have preferred to conduct parametric studies as a function of cavity length. Although a bit more difficult, it is possible to formulate velocity potential methods so that the cavitation pressure can be specified and the cavity length determined, but the authors are unaware of any application of this procedure.

In general, all velocity potential models require some sort of closure condition at the trailing edge of the cavitation bubble. This closure condition frequently takes the form of a singularity or an afterbody shape that guides the flow back to the solid surface in a smooth fashion (Uhlman, 1987; Buist and Raven, 1990). This approximation to the local physics at reattachment allows reasonable comparison with experiment.

In the present paper we use numerical solutions of the Euler equations to replace the velocity potential methods. The solution of the Euler equations is more CPU-intensive than that of the singularity distribution methods that are used in the potential formulation, but there are a number of types of application for which the Euler methods appear to have an advantage. For example, potential flow methods become difficult to apply in complex geometries when multiple bodies are present, and they fail entirely in the presence of rotational effects such as those that arise from nonuniform inflows. These limitations are more easily overcome when using the Euler

---

Contributed by the Fluids Engineering Division for publication in the JOURNAL OF FLUIDS ENGINEERING. Manuscript received by the Fluids Engineering Division August 21, 1992; revised manuscript received June 8, 1993. Associate Technical Editor: R. H. Panton.

equations. Another drawback of potential flow methods is that the indirect cavitation analysis effectively restricts the cavitation models to two-dimensional steady flows. Extensions to three-dimensional or unsteady flows will most likely require direct solution methods based on cavitation pressure. These are more easily incorporated in Euler analyses. There is also the promise that the application of the Euler equations to cavitation modeling may enable improved physics to be incorporated into the cavitation model (although in this initial application, the cavitation model chosen is philosophically the same as those used for the potential flow theories). For example, the combination of cavitation models with the Euler equations serves as a precursor to incorporating similar models in the full Navier-Stokes equations allowing more realistic treatments of the cavitation inception point and the cavitation closure condition. Finally, an Euler based cavitation model also provides a method for including cavitation in inducer and pump-flow CFD codes that are currently being developed for design purposes (McConnaughey et al., 1992).

Although the cavity model chosen for use with the Euler equations in the present paper is analogous to those used in previous velocity potential studies, the method of application is somewhat different. For the Euler equations, the prediction of a constant pressure region on the cavity surface is most readily accomplished directly rather than indirectly. The pressure is specified on the cavity surface and the length is determined by the computation. The Euler equations are solved by an explicit multi-step method (Merkle and Tsai, 1986), that does not require an *a priori* knowledge of the location of the cavity. The cavity inception point as well as the cavity profile are determined by enforcing both the constant cavitation pressure and the zero normal velocity condition on the cavity surface. To avoid numerical difficulties, an after-body like that used in the potential flow models, is added in the closure region where the flow behavior is not well understood.

Both linear and nonlinear cavity models are attempted but it is shown that the linear model is not well-founded for the Euler equations because of a lack of physical boundary conditions. This shortcoming is circumvented in the nonlinear application of the theory, and the results are in good agreement with experiment and with velocity potential models, as is shown below. In the nonlinear method, an iterative procedure is used to update the cavity surface and the computational domain is re-gridded accordingly over the body/cavity surface. The cavity conditions are always applied directly on the latest cavity surface.

Besides comparing the predictions of the Euler-equation-based cavitation model with experiment and with the predictions of a similar potential-flow method, parametric studies of the effects of angle of attack on single airfoils are presented along with predictions for airfoils in cascade with different cascade spacing and for different cavitation pressure levels. The present analysis is limited to two-dimensional steady flows.

Governing Equations and Computational Procedure

The steady-state two-dimensional incompressible Euler equations in vector form are

$$\nabla\cdot\mathbf{V}=0 \qquad \textit{Continuity}$$

$$(\mathbf{V}\cdot\nabla)\mathbf{V}=-\nabla p \qquad \textit{Momentum}$$

where the density has been absorbed in the pressure. When written in a strongly conservative form in generalized coordinates using the unsteady artificial compressibility formulation the above equations become

$$\Gamma\frac{\partial Q}{\partial \tau}+\frac{\partial E}{\partial \xi}+\frac{\partial F}{\partial \eta}=0 \tag{1}$$

where

$$\Gamma=\begin{pmatrix}1/\beta & 0 & 0\\ 0 & 1 & 0\\ 0 & 0 & 1\end{pmatrix}$$

and

$$Q=\begin{pmatrix}p\\ u\\ v\end{pmatrix},\quad E=\begin{pmatrix}U\\ uU+y_\eta p\\ vU-x_\eta p\end{pmatrix},\quad F=\begin{pmatrix}V\\ uV-y_\xi p\\ vV+x_\xi p\end{pmatrix}$$

Here β is the artificial compressibility parameter and U and V are the contravariant velocities in the ξ and η directions respectively

$$U=uy_\eta-vx_\eta$$

$$V=vx_\xi-uy_\xi$$

The time derivatives and the artificial compressibility term in Eq. (1) are added for computational purposes to enable a time marching scheme to advance the flow variables in the system. The resulting unsteady Euler system is solved numerically by an explicit time-marching procedure. When the solution converges, the time derivatives approach zero and the steady state Euler solution corresponding to the specified boundary conditions is recovered. The artificial compressibility term has no physical meaning but its coefficient β is chosen to scale the eigenvalues of the system to the same order of magnitude so that efficient convergence rate can be achieved. In general curvilinear coordinates, β is defined by:

$$\beta=\frac{(U+V)^2}{(x_\xi^2+x_\eta^2+y_\xi^2+y_\eta^2)} \tag{2}$$

Nomenclature

c = chord length
C_p = non-dimensional pressure
$\mathbf{E}$ = ξ flux vector
$\mathbf{F}$ = η flux vector
$\mathbf{h}$ = cascade spacing
$\mathbf{L}$ = selection matrix
$\mathbf{M}$ = inverse of modal matrix
$\mathbf{n}$ = Pseudo-time step
$\mathbf{p}$ = local static pressure
p_0 = total pressure
p_∞ = static pressure at far-field
p_c = cavitation pressure
$\mathbf{Q}$ = vector of primary dependent variables
$\mathbf{u}$ = x-direction velocity component
u_∞ = velocity at inlet
$\mathbf{U}$ = ξ-direction contravariant velocity
$\mathbf{v}$ = y-direction velocity component
$\mathbf{V}$ = η-direction contravariant velocity
x, y = Cartesian coordinates
α = angle of attack
$\alpha_1, \alpha_2, \alpha_3$ = Runge-Kutta constants
β = artificial compressibility factor
Γ = modified identity matrix
ξ, η = transformed coordinates
ρ = fluid density
σ = cavitation number
τ = Pseudo time variable
Ω = boundary condition vector

Subscripts

ξ, η = differentiation with respect to transformed coordinates

A four-step Runge-Kutta explicit scheme is used to advance the solution in pseudo-time, given as

$$Q^* = Q^n - \alpha_1 \Delta\tau \left(\frac{\partial E}{\partial \xi} + \frac{\partial F}{\partial \eta}\right)^n$$

$$Q^{**} = Q^n - \alpha_2 \Delta\tau \left(\frac{\partial E}{\partial \xi} + \frac{\partial F}{\partial \eta}\right)^*$$

$$Q^{***} = Q^n - \alpha_3 \Delta\tau \left(\frac{\partial E}{\partial \xi} + \frac{\partial F}{\partial \eta}\right)^{**}$$

$$Q^{n+1} = Q^n - \Delta\tau \left(\frac{\partial E}{\partial \xi} + \frac{\partial F}{\partial \eta}\right)^{***} \qquad (3)$$

Here the constants α_1 through α_3 are set to the sequence 1/4, 1/3, and 1/2, respectively. All spatial derivatives are central-differenced and local time stepping is used to achieve better convergence rates. A fourth order artificial viscosity (Kwak et al., 1986) of the form

$$D = \frac{\partial^4 Q}{\partial \xi^4} + \frac{\partial^4 Q}{\partial \eta^4} \qquad (4)$$

is added to prevent odd-even splitting in the numerical solution.

With the addition of the artificial time derivative, the governing Euler equations become hyperbolic thereby enabling the use of the Method of Characteristics (MOC) to formulate the boundary conditions in a manner analogous to compressible flow. The mathematical theory of the MOC states that only the information that propagates into the computational domain from the boundary should be specified at the boundary, whereas the information that propagates towards the boundary from within the computational domain must be determined from a subset of the governing equations inside the domain. This equation subset is determined from MOC theory.

The MOC type of boundary can be formulated as (Merkle and Tsai, 1986):

$$\left(\frac{\partial \Omega}{\partial Q} + LM^{-1}\right)\Delta Q^{n+1} = -\Delta t LM^{-1}\left(\frac{\partial E}{\partial \xi} + \frac{\partial F}{\partial \eta}\right)^n \qquad (5)$$

Here the equation(s)

$$\Omega = 0 \qquad (6)$$

represent(s) the specified boundary condition(s): The diagonal selection matrix, L, which contains ones corresponding to the characteristics propagating toward the boundary and zeros for those coming into the domain, selects the appropriate subset of equations after they have been premultiplied by the eigenmatrix, M, of the system.

Applying the method of characteristics to the above flow problems indicates that the inflow shall be determined by two boundary conditions plus one characteristic equation. For the present solutions we specify the total pressure and the inflow angle. At outflow only one boundary condition is needed. Hence, the static pressure along with two characteristic equations form the outflow boundary equations. On the noncavitating portion of the airfoil surface zero normal velocity is specified augmented by two characteristic equations. Boundary conditions on the cavitating interface are given in the next section.

Cavitation Model

The procedure for determining the shape and location of the cavity interface is analogous to that used for potential flow analyses. The interface location is determined by over-specifying the boundary relations on it. The set of over-specified boundary conditions includes those that are normally prescribed on an inviscid solid surface plus the additional specification of the cavity pressure on the interface. With these boundary relations specified, the interface location is determined as a part of the marching process.

In keeping with the potential flow models, both a "linear" and a "nonlinear" procedure may be used to enforce the cavity conditions. These terms are used in a manner analogous to that used in airfoil theory. ("Linear" airfoil theory enforces the boundary conditions on the chord line, while "nonlinear" theory enforces the boundary conditions on the surface of the surface of the airfoil.) For the "linear" cavitation case, the cavity conditions are transferred to the corresponding airfoil surface so that the computational domain is independent of the cavity size and shape. For the nonlinear procedure, cavity conditions are applied directly on the cavity interface. As a consequence, the boundary of the computational domain evolves with the cavity in the nonlinear case, and regridding is required when the cavity surface is updated.

For both the linear and nonlinear theories the cavitation computations are started from a converged noncavitating solution for the flow over the geometry of interest. The cavitation model is then incorporated into the numerical analysis by checking the pressure distribution on the airfoil against the specified cavitation pressure. If the pressure at any point on the airfoil surface drops below the vapor pressure, that point is switched from a "solid wall" point to a "cavity" point. One or more time steps are then taken with the cavitation pressure specified as the surface boundary condition at these cavitating points. This boundary conditions allows the normal velocity at the surface to deviate from zero.

After identifying the cavitating points and updating the velocity, a first cavity profile is defined by integrating the streamline starting from the first cavitating point to the last one. The upstream-most cavitating point fixes the location of the cavitation inception point. The resulting cavitation interface is established by ensuring that the cavity profile is non-negative at each grid point. Negative cavity thicknesses correspond to the cavity interface moving inside the airfoil surface. Points with negative cavity thickness are treated as noncavitating points in the next time step. This check on cavity thickness is the primary technique that allows the cavity length to contract if necessary as the iteration proceeds.

If the cavity ends with a finite thickness (this is the normal condition), the cavity is closed by adding an afterbody (Tulin and Hsu, 1980; Buist and Raven, 1990). The afterbody shape chosen here is a cubic profile that merges smoothly with the cavity interface and approaches the body surface tangentially. The standard surface boundary condition (zero normal velocity) is applied on the afterbody. For all cases presented herein, the afterbody length was empirically fixed as three times the height at the end of the cavity. Comparison with data indicates that this gives reasonable results.

Linear Cavitation Theory

The linear cavitation approximation is analogous to the classical linear theories that are widely used for airfoils under small angles of attack. The cavitating region is identified from the pressure distribution on the airfoil surface as discussed above. The pressure at the interface is fixed at the vapor pressure and the liquid-vapor interface conditions are transferred to the relevant part of the body surface. The zero normal velocity condition is then relaxed and replaced by a combination of mass injection and mass removal at such a rate that the desired interface location becomes a streamline. Although this linear cavity approximation has been widely used for velocity potential methods, it introduces some difficulties into the Euler analysis as is discussed below.

The difficulties arising in the linear Euler analysis are associated with the boundary conditions on the cavitating portion of the airfoil surface. In the linear approximation, the cavity interface position requires that fluid be injected through some parts of the airfoil surface (to accommodate growth of the cavity) while it is removed through other parts (to accommodate thinning of the cavity). These regions of inflow and outflow require corresponding inflow and outflow boundary conditions. In an Euler solution based on artificial compressibility, the number of boundary conditions to be specified equals the number of inward-running characteristics at the boundary.

The removal of fluid, which corresponds to an outflow boundary, creates no difficulties because there is one in-running characteristic and one obvious physical boundary condition, the cavity pressure. This boundary condition is augmented by two characteristic equations corresponding to the out-running characteristic lines. These three conditions represent a complete set of boundary relations, and the necessary outflow velocity is obtained from the computational solution.

By contrast, the injection portion of the cavity surface corresponds to an inflow boundary for which there are two out-running characteristics. The inflow portion of the cavity therefore requires an extra boundary condition in addition to the cavity pressure. This additional boundary condition is difficult to extract from the fluid dynamics, and an arbitrary numerical condition must be provided. One approach we have tested is to specify the total pressure of the inflow as equal to that corresponding to upstream conditions. Although this appears to be a plausible choice, it causes some problems in obtaining solutions that are qualitatively realistic. A second approach, and one that was used for the solutions reported in this paper is to treat this inflow region as an outflow boundary with one boundary condition and two differential relations from the equations of motion. This approach provided reasonable solutions so long as the linearized cavity was reasonably small. This arbitrariness vanishes in the nonlinear procedure as is noted below.

In addition to problems with boundary conditions for the linear problem, the translation of the boundary condition to the airfoil surface makes it difficult to apply an afterbody to close the cavity, and all linear calculations were made without a closure condition. As a result, the strong curvature in the termination region of the cavity introduces a singularity into the linear representation. This local singularity is difficult to accommodate in an Euler solution. Additional effort to circumvent this difficulty was not made because it disappears in the nonlinear formulation. Further, our primary emphasis was on the nonlinear method and the linear method was used only as a means to obtain the nonlinear solution.

Nonlinear Cavitation Theory

In the nonlinear theory the cavity boundary conditions are applied directly on the cavity surface so the controversy of "inflow" and "outflow" is removed. The two boundary conditions that are used for defining the cavity interface shape are that the flow be tangent to the currently assumed cavity shape (replacing the inflow/outflow condition for the linear case), and that the pressure on the interface be equal to the cavitation pressure.

The nonlinear approach is a sequence of linear solutions performed over the most recently updated cavity surface, coupled with modifications of the computational domain to incorporate the current cavity shape. In the limit of convergence the flow satisfies the constant pressure condition and is tangent to the cavity surface. As before, the cavity location is identified from the pressure distribution on the airfoil surface and the constant pressure condition is used to replace the zero normal velocity condition for cavitating points. The finite normal velocities on the current cavity surface are then obtained from the linear solution as described above. These velocities are subsequently used to update the cavity surface by tracing the streamline emanating from the cavity inception point.

Once an initial cavity geometry has been established, the grid is again updated to include the change in the boundary due to the cavity. The computation on this new grid at the next time step follows a linear cavitation pattern. The noncavitating points on the body surface are treated in standard fashion, while those points on the cavitation interface are treated as constant pressure points, with mass injection or removal specified on the interface to adjust the flow to the cavity pressure. The cavity interface shape is then updated by again tracing the streamline emanating from the initial cavitating point. As the iterative procedure marches forward, the cavity surface evolves and the solution approaches a converged one with both the tangency and the pressure conditions being satisfied. Because each intermediate surface shape is an improved approximation to the converged cavity shape, the strength of the mass injection and removal goes to zero as the calculation proceeds. Thus, at convergence, there are no remaining grid points with mass injection or removal. Consequently, the boundary condition at convergence is the cavity surface, and the combination of two characteristics and one boundary condition on the surface is mathematically and physically correct.

Numerical experiments have demonstrated that this method of enforcing the pressure on the cavity surface during the iteration is more effective than using the predicted interface shape for an "impermeable wall" calculation. For the calculations presented here, grid updating was accomplished every five to twenty time steps.

Results

Representative Euler predictions for leading edge cavitation, mid-chord cavitation and cavity length are given below and compared with experiment. In addition, comparison of cavitation in a cascade of airfoils is compared with a panel method solution, and parametric studies of the effect of cascade spacing, angle of attack and cavitation pressure are presented. The Euler calculations are computed on stretched grids of 262×91 nodes. Convergence to steady-state required nominally 5000 time-steps for all cases. The presence of cavitation slowed down the convergence by 10–20 percent.

Leading Edge Cavitation Prediction

The first step in the validation of the cavitation model is to compare with the measurements of Shen and Dimotakis (1989) for a NACA66(MOD) + $a = 0.8$ airfoil. The airfoil geometry and the near-field details of the C-grid used for the computations are shown in Fig. 1. The experiments were conducted with the airfoil centered in a water tunnel whose walls were five chord lengths apart. The presence of the walls was simulated in the computations by placing an inviscid boundary at that location. This outer boundry condition implies that tunnel wall boundary layer effects have been omitted. Calculations show that wall blockage effects have a noticeable impact on the airfoil pressure distribution as is noted below, but the omission of tunnel wall boundary layers should not affect this distribution materially.

To set the stage for the cavitation predictions, we first compare the pressure distribution on the noncavitating (fully-wetted) hydrofoil with the experimental measurements. Representative comparisons for an angle of attack of one degree and chord Reynolds number of 3×10^6 are given on Fig. 2. As can be seen, the predicted pressure distribution is in relatively good agreement with the measurements. (Note that all the pressure taps were placed on the suction side.) Corresponding computations for an isolated airfoil (which were also verified by panel method potential flow solutions) demonstrated the importance of the tunnel walls on the surface pressure distribution, even at this relatively small blockage ratio.

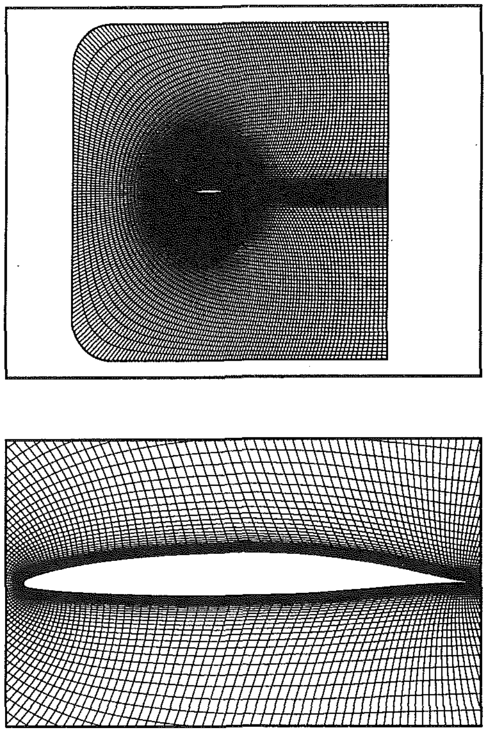

Fig. 1 Details of airfoil geometry and C-grid used in CFD computations for cavitating flow over NACA66(MOD) + $a = 0.8$ airfoil. Grid size is 262 × 91.

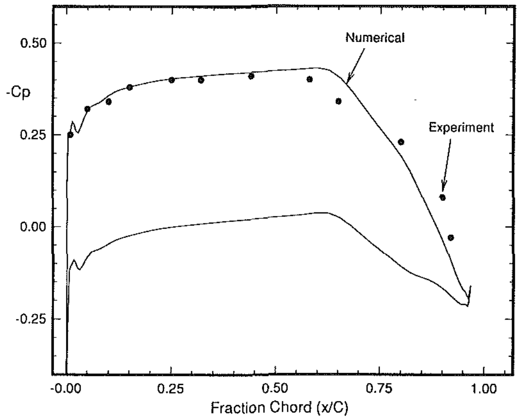

Fig. 2 Pressure distribution on a NACA66(MOD) + $a = 0.8$ hydrofoil for noncavitating flow. Comparison between Euler computations and experimental measurements from Shen and Dimotakis at one degree angle of attack.

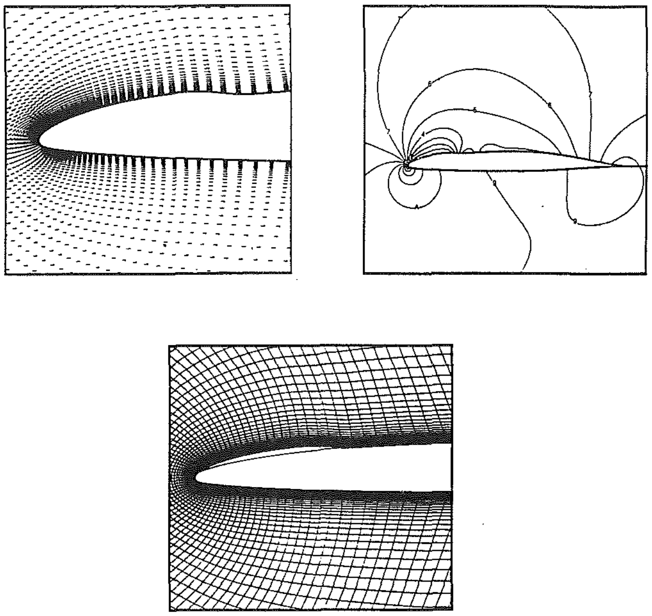

Fig. 3 Near-field details of converged solution over NACA66(MOD) + $a = 0.8$ hydrofoil from nonlinear Euler computations

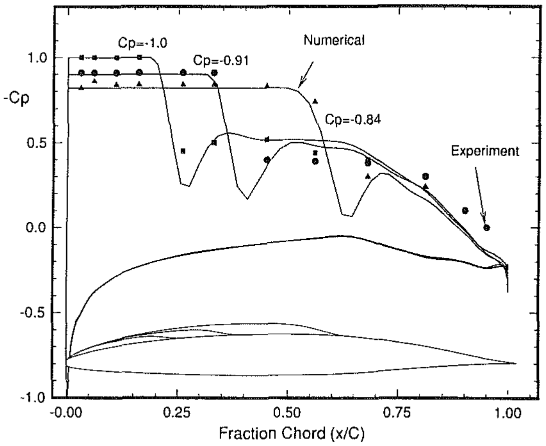

Fig. 4 Pressure distribution and cavity profiles on a NACA66(MOD) + $a = 0.8$ hydrofoil for cavitating flow. Comparison between nonlinear Euler computations and experimental measurements from Shen and Dimotakis at four degrees angle of attack.

Overall, this comparison (as well as numerous others not presented here) demonstrates that our Euler calculation (in the absence of cavitation) gives satisfactory agreement with experimental measurements and with potential flow theory. Consequently, we next turn to predictions of cavitation on this same airfoil.

Measurements for a Reynolds number of 1.2×10^6, but an angle of attack of four degrees, show a significant cavitation region on the suction side of the airfoil for most tunnel pressure conditions. A series of cavitation calculations for the four degree angle of attack case were performed on a 262×91 grid similar to that shown in Fig. 1. Details of the computed flowfield for one such case corresponding to a nondimensional cavitation pressure of $\sigma = (p_c - p_\infty)/1/2\rho u_\infty^2 = 1.0$ are presented in Fig. 3. The final grid of the flow domain is shown in Fig. 3(*a*) which also shows the cavitation which also shows the cavitation region. The deformed grid around the cavitation bubble appears clearly in the figure. Details of the solution showing the pressure contours and velocity vector fields around the cavity are presented in Figs. 3(*b*) and 3(*c*).

Detailed predictions of cavitation on this airfoil are compared with experimental measurements in Fig. 4. Both the airfoil pressure distribution and the computed cavity profiles are shown in the figure. Four cases, the noncavitating condition, and three cavitating conditions at different pressure levels (cavitation numbers, $\sigma = 1.0$, 0.9 and 0.84), were carried out and compared with experiment. For the cavitating conditions the pressure levels in the cavity were taken from the experiment. Cavity lengths greater than about $l/c = 0.75$ were not computed, since, as discussed by Shen and Dimotakis (1989), the cavity becomes unsteady and oscillates for long cavities.

The comparisons in the figure show the predicted cavity lengths are in good agreement with the measurements for all three cavitation conditions. The favorable comparison of the pressure distribution over the remainder of the airfoil suggests that the shape of the cavity is also well predicted. A further characteristic of the predictions is the presence of a steep pressure rise following the cavity termination region. This local

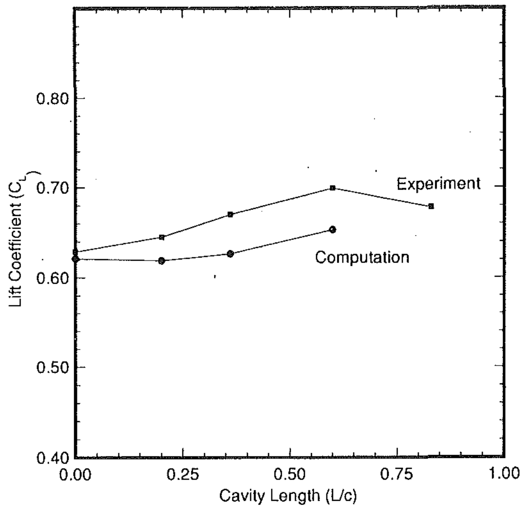

Fig. 5 Lift coefficient on a cavitating NACA66(MOD) + $a = 0.8$ hydrofoil. Comparison between nonlinear Euler computations and experimental measurements from Shen and Dimotakis at four degrees angle of attack.

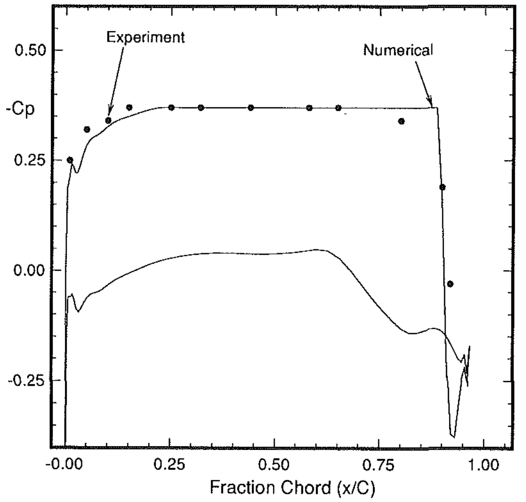

Fig. 6 Mid-chord cavitation: Comparison of pressure distribution between nonlinear Euler computations and experimental measurements of Shen and Dimotakis for NACA66(MOD) + $a = 0.8$ airfoil at one degreee angle of attack.

minimum in the C_p distribution and the ensuing pressure rise is neither confirmed nor denied by the experimental data because no pressure taps were located in this region. However, it is generally expected that such a minimum will be observed (Shen and Dimotakis, 1989). Overall, these results indicate that the model provides a reasonably accurate prediction of the cavitation region for these experimental conditions.

Figure 5 shows the calculated lift coefficient as a function of the cavity length for the above airfoil at four degrees angle of attack. The calculated coefficients agree quite well with the experimental measurements, although the computations slightly under-predict the increase in the measured lift in the presence of cavitation. Both the experiments and the predictions, however, show that the lift increases with increasing cavity length, as expected.

Mid-chord Cavitation Prediction

Existing cavitation models usually pre-specify a cavity inception point, such as the leading edge or the minimum pressure location in the noncavitating solution. With a marine propeller operating at its design point, the shape of the pressure loading on the blade section generally resembles a rooftop with the minimum pressure, and hence the cavitation location, occurring around mid-chord. The absence of a distinct minumum pressure location makes it difficult to specify a cavitation inception point accurately. Mid-chord cavitation is therefore difficult to predict in codes based on potential theory.

In the Euler analysis, such a pre-specification of the cavity inception point is not needed and the prediciton of mid-chord cavitation becomes straightforward. Mid-chord cavitation is, in fact, predicted rather well by our model as is demonstrated by comparison with the measurements of Shen and Dimotakis (1989).

Shen and Dimotakis (1989) generated mid-chord cavitation on the NACA66(MOD) + $a = 0.8$ foil, by testing the airfoil at one degree angle of attack and a Reynolds number based on chord length of 3×10^6. The noncavitating pressure distribution for this case, shown in Fig. 2, has been discussed above. The comparison between predictions and experiments for the mid-chord cavitation condition are given on Fig. 6. The predictions show quite good agreement with the experiments both with respect to the location of the cavity inception point, and with respect to the length of the cavity. In addition, the pressure distribution over the remainder of the airfoil is in good agreement with the experiments, again suggesting that the shape of the mid-chord cavity is well predicted. The expected stagnation pressure at the termination of the mid-chord cavity is also apparent in the calculate pressure distribution even though it cannot be clearly resolved in the experiment because of the finite number of pressure taps and the resulting uncertainty in the location of the cavity termination point. This capability for predicting mid-chord cavitation represents an important advantage of the Euler analysis over potential flow analyses.

Cavity Length Predictions

Each of the above cavitation predictions (Figs. 3-6) include comparisons of both the cavity length and the airfoil pressure distribution with the data of Shen and Dimotakis (1989). There exist few other cavitation measurements that characterize the pressure distribution over the entire airfoil. A limited number of cavity length measurements have, however, been reported. In the present section, we compare cavity length predictions with the data of Shen and Peterson (1978) and Dong (1983).

Dong (1983) reported experimental measurements of the cavity length on a NACA16009 hydrofoil for two incidence angles $\alpha = 3.6$ deg and 4.6 deg. The relationship between the cavitation number (σ) and the cavity length as a fraction of chord (l/c) is presented in the form of curves of α/σ versus l/c. We compare our computational predictions with these measurements on Fig. 7. The computations agree quite well with the experiments when the cavitation length is less than about 40 percent chord. For cavities longer than this, the predictions underestimate the length by a larger and larger amount. Part of this discrepancy may be due to unsteadiness in the closure region of these larger cavitation bubbles. The general trends of the experimental behavior are, however, well predicted by the Euler analysis.

Shen and Peterson's experiments were performed on a pitching Joukowski airfoil to study the effects of airfoil motion on cavitation inception. Although their emphasis is on pitching airfoils, they also reported cavity length measurements at zero reduced frequency for two angles of attack. The zero frequency measurements were reported at a cavitation number $\sigma = 1.13$ for angle of attack of 3.8 and 4.3 degrees. These two cavity length measurements are compared with computational predictions from the present method in Table 1. The measured cavity lengths for these two angles of attack are approximately 25 percent and 40 percent chord respectively. The predictions agree with these measured cavity lengths to within about 10 percent in both cases. At both angles of attack the cavity lengths are under-predicted, indicating that the predicted trend of cavity length with angle of attack is in good agreement with the

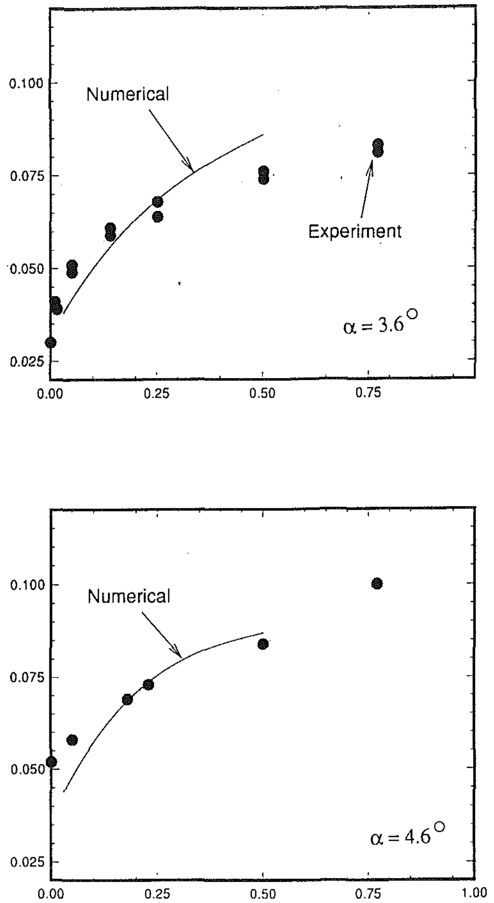

Fig. 7 Cavity length prediction: Comparison with experimental measurements from Dong at 3.6 and 4.6 degrees angle of attack.

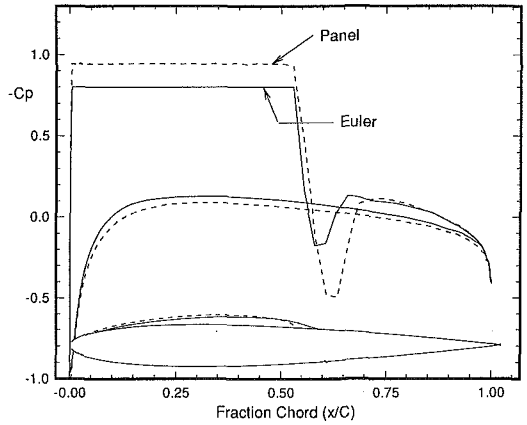

Fig. 8 Comparison of pressure distribution/cavity geometry between nonlinear Euler analysis and potential flow for an NACA0012 cascade at five degrees angle of attack. The cascade spacing is 4 chord lengths.

experiments. Taken together, the predicted cavity length comparisons with the data of Shen and Dimotakis (1989), Dong (1983), and Shen and Peterson (1978) give reasonable confidence in the ability of the Euler formulation to provide acceptable engineering predictions of cavitating flow fields.

Cascade Computations

Having presented validation comparisons of the Euler cavitation model against several sets of experimental data, we turn now to looking at parametric predictions of the Euler model. Our first parametric study is of the size and shape of cavitation bubbles in a cascade. Because few measurements of cavitating flow in cascades have been reported, we compare the Euler cavitation predictions for this geometry with similar results based on the velocity potential equations. For these comparisons, a two-dimensional potential flow code was used. This code is based on a panel method that involves the representation of the potential function as a distribution of uniform sources and piece-wise linear vortices (Feng and Lee, 1990; Lee et al., 1991). The code has been extensively validated against a large variety of analytical solutions and experimental measurements in noncavitating flows and was extended to include both linear and nonlinear cavitation prediction capabilities for single airfoils and cascades as part of the present work.

Table 1 Comparison of cavity length predictions with Shen and Peterson (1978)

α	Experiment	Computations
3.8°	0.25	0.22
4.6°	0.39	0.355

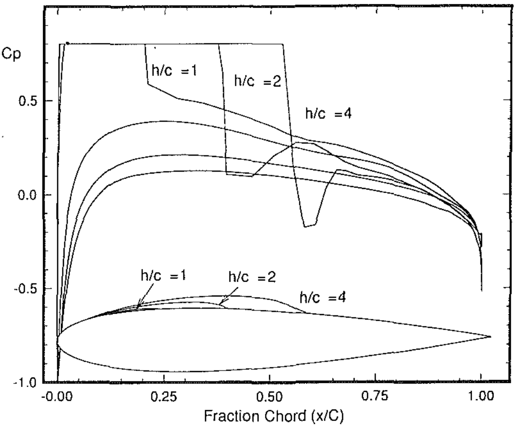

Fig. 9 Parametric study of the effect of cascade spacing using Euler analysis. NACA0012 cascade at cascade spacings = 1, 2, and 4 chord lengths; angle of attack = 5 deg $Cp = 1.0$.

Figure 8 presents predictions from these two cavitation models for a cascade with a spacing of 4 chord lengths. The figure shows the agreement between the results of the panel and Euler codes is, in general, quite good. The two pressure distributions and the resulting cavity profile shapes are quite similar to each other. The pressure rise around the airfoil leading edge is milder for the cascade than for an isolated airfoil resulting in a thinner cavitation bubble. Compared with an isolated airfoil case, the cavity length is about the same, but the maximum cavity thickness is some 40 percent less due to the cascade effect.

For the panel method calculations the airfoil was represented by about 100 panels. Panel refinement showed this resolution was sufficient to obtain a panel-independent solution. The panel method, however, requires substantially less CPU time than the Euler code (which was similarly demonstrated to provide a grid-independent solution on the 262×91 grid) as is typically the case between Euler and panel codes. The strength of the Euler method is in its ability to solve the direct problem, that is, requiring no presumptions about the cavity location, as well as in applying it to problems where velocity potential methods fail (as for example, in rotational flows) or experience difficulties (as for example, in mid-chord cavitation calculations).

To study the effect of cascade spacing on the cavitation performance, calculations were performed on the NACA0012 airfoil for three cascade spacings ranging from 1 to 4, each at 5 degrees of incidence. The predicted cavity profiles and pressure distributions are presented in Fig. 9. The pressure peak

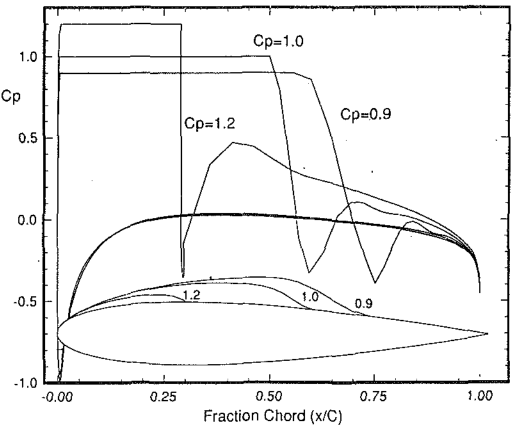

Fig. 10 Parametric study of the effect of cavitation pressure using Euler analysis. NACA0012 isolated airfoil at five degrees angle of attack. $Cp = 0.9$, 1.0, and 1.2.

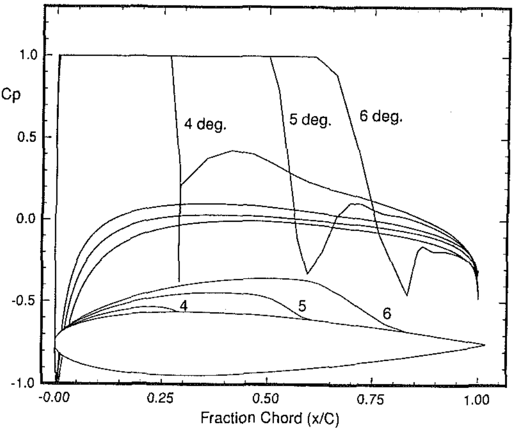

Fig. 11 Parametric study of the effect of angle and of attack using Euler analysis. NACA0012 isolated airfoil angle of attack = 4, 5, and 6 degs, $Cp = 1.0$.

near the leading edge is further suppressed as the cascade spacing is decreased, so that both the cavity length and the cavity thickness are reduced. These results clearly show that both the cavity thickness and the cavity length are strongly affected by cascade spacing.

Effect of Cavitation Pressure and Angle of Attack

The effects of varying cavitation pressure and angle of attack for an isolated airfoil were studied for a NACA0012 airfoil. The grid used in these computations is again similar to the grid shown in Fig. 1. The farfield boundary in the isolated airfoil cases was fixed at four times the chord length. Numerical calculations are conducted for the single airfoil at three cavitation pressure levels and under three different angles of attack. The results are presented in Fig. 10 and 11 which include the pressure coefficients and the final converged cavity geometries for each case. The results indicate, as expected, that the cavity grows with decreasing cavitation pressure and with increasing angle of attack. Cavity lengths ranging from 30 percent to 70 percent chord are predicted for cavitation numbers 0.9, 1.0 and 1.2 (Fig. 10). Increasing the angle of attack from 4 to 6 degrees likewise increases the cavitation length from 30 percent to 70 percent (Fig. 11).

Conclusions

Cavitation is a widely existing hydrodynamic phenomenon, that remains a persistent problem in hydraulic machinery design. The numerical model developed in this paper is analogous to the existing potential flow models, and presents good potential to incorporate cavitation modeling in existing turbomachinery CFD codes. This makes the modeling of cavitation in complex geometries, rotational flows or three-dimensional flows more feasible.

The numerical approach uses an artificial-compressibility procedure and pseudo-time stepping to solve the Euler equations with a finite difference scheme. It requires no presumptions of either the cavity length or the location of the cavity inception point. Although we have demonstrated that the linear formulation where the cavitation boundary condition is translated to the body surface may lead to difficulty, this difficulty vanishes for the full nonlinear problem in which the cavitation condition is satisfied on the cavity interface. The nonliner calculation does, however, require re-gridding of the computational domain as the calculation converges. In the converged limit, the nonlinear problem satisfies both the cavity pressure condition and the velocity condition on the cavity interface.

Numerical solutions have been obtained for a number of two-dimensional cavity flow problems, both for single airfoils and cascades. Comparisons with experimental measurements are presented for isolated airfoils for both pressure distribution and cavity length. The results of computations show good agreement with experimental measurements from several experiments. Since experimental measurements of cavitation in cascades were not available, comparisons are presented with panel code solutions based on velocity potential theory for this geometry. These comparisons are also in good general agreement.

In addition to leading edge cavitation predictions, the Euler code also provides the capability for accurate predictions of mid-chord cavitation. This calculation is relatively difficulty to predict with potential flow codes because of the absence of a distinct cavitation inception point at which to begin the bubble.

In summary, the Euler cavitation model provides good engineering predictions of cavitation on airfoils and in cascades. Further extensions from the current two-dimensional steady-state analysis to three-dimensional and/or unsteady analyses should be relatively straightforward for the Euler formulation. In addition, this approach presents good potential for improved physical analysis of cavitation, including the effects of viscous forces which may lead to improved understanding of cavity formation.

Acknowledgments

This work was supported by the Propulsion Engineering Research Center, Pennsylvania State University under NASA USERC Grant NAGW-1356 and using the computational resources provided by the Numerical Aerodynamic Simulation (NAS) program at NASA Ames.

References

Buist, J., and Raven, H. C., 1990, "A Consistently Linearized Approach for the Calculation of Partial Sheet Cavitation," *Cavitation and Multiphase Flow Forum*, ASME, FED, Vol. 98.

Dong, S. T., 1983, "A Theoretical Solution to Partially Cavitating Flow Past a Hydrofoil with Thickness," The Ship Building of China, No. 80, Jan.

Feng, J., and Lee, Y-T., 1990, "Flow Calculation for Linear Cascades," ASME 1990 Winter Annual meeting, Nov., Dallas, TX.

Geurst, J. A., 1959, "Linearized Theory for Partially Cavitating Hydrofoils," *International Shipbuilding Progress*, Vol. 6, No. 60, Aug.

Hsu, C. C., 1975, "Some Remarks on the Progress of Cavity Flow Studies," ASME JOURNAL OF FLUIDS ENGINEERING, Vol. 97, No. 4.

Kwak, D., Chang, J. L. C., Shanks, S. P., and Chakravarthy, S. R., 1986, "A Three-Dimensional Navier-Stokes Flow Solver Using Primitive Variables," *AIAA Journal*, Vol. 24.

Lee, Y-T., Feng, J., and Merkle, C. L., 1991, "Unsteady Rotor Dynamics," 1991 IGTI, Gas Turbine Conference, June, Orlando, FL.

McConnaughey, P., Garcia, R., and Eastland, A., 1992, "Activities of the NASA Marshall Space Flight Center (MSFC) Pump Stage Technology Team," AIAA Paper 92-3222, 28th Joint Propulsion Conference, Nashville, TN.

Merkle, C. L., and Tsai, Y-L. P., 1986, "Application of Runge-Kutta Schemes to Incompressible Flows," AIAA Paper 86-0553, AIAA 24th Aerospace Sciences Meeting, Jan., Reno, NV.

Schultz, J. L., and Kueny, J. L., 1986, "Partial Cavitation on Pump Blades," Proceedings, *Fluid Dynamics and Space Symposium*, VKI, Rhode-Saint-Genese, June.

Shen, Y. T., and Dimotakis, P. E., 1989, "The Influence of Surface Cavitation on Hydrodynamic Forces," *Proc. 22nd ATTC*, St. Johns, 1989.

Shen, Y. T., and Peterson, F. B., 1978, "Unsteady Cavitation on an Oscillation Hydrofoil," *Proc. 12th Symposium on Naval Hydrodynamics*, Washington, D. C., pp. 362-384.

Tulin, M. P., 1953, "Steady Two-Dimensional Cavity Flows about Slender Bodies," David Taylor Model Basin Rep. 834.

Tulin, M. P., and Hsu, C. C., 1980, "New Applications of Cavity Flow Theory," *Proceedings, 13th Symposium on Naval Hydrodynamics*, Tokyo.

Uhlman, J. S., 1987 "The Surface Singularity Method Applied to Partially Cavitating Hydrofoils," *Journal of Ship Research*, Vol. 31, No. 2, June.

Wu, T. Y., 1972, "Cavity and Wake Flows," *Annual Review of Fluid Mechanics*, Vol. 4.

Origin and Decay of Longitudinal Vortices in Developing Flow in a Curved Rectangular Duct

(Data Bank Contribution*)

Wu J. Kim[1]
Postdoctural Fellow.

Virendra C. Patel
Professor.
Fellow ASME

Iowa Institute of Hydraulic Research &
Department of Mechanical Engineering,
The University of Iowa,
Iowa City, IA 52242

Developing turbulent flow in a 90 deg curved duct of rectangular cross-section, and an aspect ratio of 6, was investigated. Mean-velocity and Reynolds-stress components were measured using a five-hole pressure probe and two-sensor hot-wire probes, respectively, in the boundary layers on the duct walls to document the pressure-driven secondary motion and the formation of a longitudinal vortex near the corner on the convex wall. Special attention was paid to the three-dimensionality of the flow exiting the two-dimensional contraction of the wind tunnel in order to provide proper inlet boundary conditions for future computational work. The mean velocities and wall shear stresses were measured at seven sections and turbulence measurement were made at four sections. The data provide insights into the development of three-dimensional turbulent boundary layers under the influence of strong streamwise curvature, both convex or concave, and attendant pressure gradients, and clearly elucidate the mechanism by which strong pressure-driven secondary motion results in a longitudinal vortex.

Introduction

Computational fluid dynamics (CFD) codes have come to occupy an important place among methods of analysis and design of fluids engineering systems and products. The validation of such codes for turbulent flows relies on comparisons with carefully conducted experiments which highlight some particular fluid flow phenomenon or influence, the central uncertainty being the fidelity of the turbulence closure model employed in the code. Among the factors that have defied accurate representation in CFD codes are the influence of streamwise surface and/or streamline curvature, and the development and decay of secondary motion, by either the Reynolds stresses or cross-stream pressure gradients associated with curvature. Many experiments have been carried out to understand the basic mechanisms involved, and some of the data have been considered refined enough for use in CFD code validation. This paper describes the results of an experiment designed to elucidate the development of secondary motion and vortices in turbulent boundary layers on the walls of a curved rectangular duct.

Curved ducts of varying lengths and aspect ratios have been employed in the past to study the streamwise curvature effects and secondary motions. A review of the literature indicates basically two types of experiments. In one, developing flow in curved ducts of "large" aspect ratio has been measured to study the effect of convex or concave curvature on a nominally two-dimensional turbulent boundary layer. In some cases, attempts were made to remove the attendant pressure gradients and isolate the effects of curvature, while in others, the pressure gradient effects were not documented and were generally ignored. In some others, two dimensionality was either not documented or the channel aspect ratio was not large enough to guarantee two dimensionality. Among experiments of this type are those of Smits et al. (1979), Gillis and Johnston (1983), Hoffmann et al. (1985), and Muck et al. (1985). These studies in two-dimensional boundary layers indicate that convex curvature has a stabilizing influence (reduces turbulent transport) whereas concave curvature has a destabilizing effect (increases the turbulence). The differences between the two are not equal and opposite, however, and no turbulence model has yet succeeded in representing the effect of curvature with precision.

The second type of experiments have been conducted mostly in ducts of square cross section, with short or long straight sections upstream of the curved portion, to study the evolution of the secondary motion in developing and fully developed flows. Representative experiments of this type are those of Humphrey et al. (1981), Chang et al. (1983), and Iacovides et

---

*Data have been deposited to the JFE Data Bank. To access the file for this paper, see instructions on p. 193 of this issue.

[1] Present address: KRISO, Daejon, Korea 305-606.

Contributed by the Fluids Engineering Division and presented at the Symposium on Data for Validation of CFD Codes, ASME Fluids Engineering Meeting, June 20-24, 1993, Washington, D.C., of THE AMERICAN SOCIETY OF MECHANICAL ENGINEERS. Manuscript received by the Fluids Engineering Division June 15, 1992; revised manuscript received May 13, 1993. Associate Technical Editor: Ho, Chih-Ming.

al. (1990). Measurements in fully developed flow in a square duct clearly reveal that the secondary motion arises from curvature-induced pressure gradients which drive low-momentum fluid from the outer (concave) wall on to the inner (convex) wall. Strong and prolonged curvature leads to the formation of longitudinal vortices on the convex wall. The principal difference between developing (boundary layer) and fully developed flow is that, in the former, the secondary motion is weaker and confined to the boundary layers. The effects of surface curvature on turbulence are obviously present in these flows as well but they are generally masked by those of the secondary motion. Also, the stress-driven secondary motion that is present in any straight upstream segment of the duct, interacts with the much stronger pressure-driven secondary motion in the curved section, resulting in a flow that is influenced by many factors. Because of these complexities, square-duct experiments have been used in CFD code validation to test not only the numerical capabilities but also to investigate the performance of turbulence models.

Developing boundary-layer flow in curved rectangular ducts has not been studied to the same level of detail as that in a square duct. Some preliminary measurements were made in such a flow by Patel (1968) during the course of a study on curvature effects in nominally two-dimensional turbulent boundary layers. Mean velocity distributions measured at several spanwise stations in the boundary layers developing in a curved rectangular duct of aspect ratio six revealed not only Goertler type vortices on the concave wall but also much stronger longitudinal vortices on the convex wall some distance from the duct corners. These latter vortices are induced by the curvature-driven secondary motion. It was concluded that these vortices had to be reduced in order to realize two dimensionality of the flow along the duct centerplane. The authors are not aware of any other experiments in rectangular ducts of similar dimensions in spite of the fact they offer the opportunity to isolate and study, in a single simple geometry, two important flow features mentioned above, namely, the effects of streamwise curvature on the turbulence in a nearly two-dimensional flow, and vortex formation from a pressure-driven secondary flow. The latter feature is related to the so-called crossflow or open type of separation of a three-dimensional boundary layer. The present experiment is concerned with turbulent boundary layers developing in a curved rectangular duct. A computational study was conducted in parallel (Kim, 1991) to guide the experiments. As a result, special attention was paid to the three-dimensionality of the flow on the flat walls downstream of the wind tunnel contraction to properly document the flow conditions ahead of the curved section. The data from this experiment have been compared, by Kim (1991) and Sotiropoulos and Patel (1992), with two different numerical methods. Therefore, the authors are well aware of the need to present the experiment results in a form that is convenient for testing and validating computational methods.

The experimental facilities are described, along with the instrumentation and measurement procedures. Measurement uncertainties were determined by the method of Kline and McClintock (1953). The quantities measured include the distributions of surface pressure and shear stress, the three components of the mean velocity vector, and all but one component of the Reynolds stress tensor.

Experimental Apparatus

The experiments were conducted in the curved-wall wind tunnel shown in Fig. 1. This open-circuit, suction-type wind tunnel has a 90 deg bend. A 0.25 in (6.35 mm) honeycomb and three 16-mesh screens are installed at the entrance, and these are followed by a two-dimensional lateral contraction with an area ratio of 6. The 5-ft (1.52 m) long straight upstream section provides a well-developed, flat-plate type turbulent boundary layer before the start of the curved section. The 17-ft (5.18 m) long downstream section enables the study of flow recovery following the curvature and attendant pressure gradients. The bend has an inner radius of 24 in (61.0 cm) and an outer radius of 32 in (81.3 cm). The tunnel cross section is rectangular, with a width of 8 in (20.3 cm) and a height of 48 in (121.9 cm). Thus, the duct aspect ratio is 6. In the design of the tunnel, the dimensions were determined after careful consideration of previous work on curvature effects on turbulent boundary layers, and the need to isolate the effects of curvature in the flow along the tunnel mid-section from those of secondary motion and vortex formation at the corners. The resulting configuration is versatile insofar as these effects can be studied either in isolation or together. The present experiments exploit both capabilities.

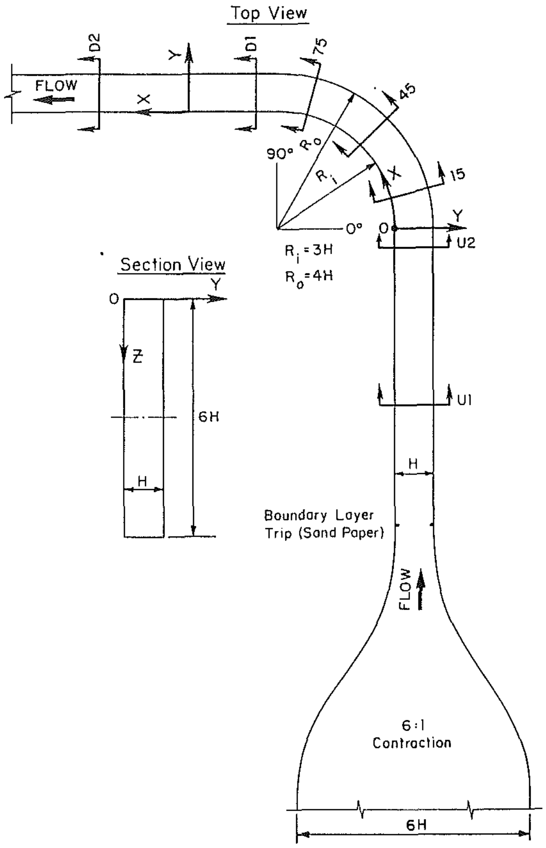

Fig. 1 Curved-wall wind tunnel; coordinates and location of measurement stations

The boundary layers on all walls of the test section were tripped by a one-inch (25.4 mm) wide, #80 sandpaper, just downstream (12.7 mm) of the contraction. The air speed was controlled by adjusting the fan speed and monitoring the pressure difference along the contraction. A Pitot tube located in the freestream at the station marked U1 in Fig. 1 was used to calibrate the tunnel and establish the relation between the contraction pressure drop and the velocity in the tunnel. The wind-tunnel reference pressure had a maximum variation of 0.6 percent during a normal measurement time. A HP-1000 minicomputer was used to control the experiments and collect the data, and an Apollo workstation was used for post-processing and plotting. A computer-controlled, two-axis, probe-traversing unit was installed for rapid and accurate positioning of pressure and hot-wire probes. The traverse had two stepping motors which drive Unislide gears with an accuracy of 1/4000 in. The traversing unit was mounted on the top of the tunnel, and could be manually moved from one section to another along the tunnel.

Table 1 Pressure distribution along the tunnel symmetry plane*

Upstream (straight)				90 degree bend				Downstream (straight)			
Inside		Outside		Convex		Concave		Inside		Outside	
X	Cp	X	Cp	X	Cp	X	Cp	X	Cp	X	Cp
-7.09	0.169	-7.09	0.185	0.13	-0.062	0.06	0.241	4.78	-0.089	4.71	0.189
-6.34	0.141	-6.34	0.149	0.25	-0.105	0.12	0.249	4.88	-0.070	4.82	0.153
-5.59	0.117	-5.59	0.125	0.38	-0.145	0.21	0.265	5.00	-0.046	4.95	0.129
-4.84	0.106	-4.84	0.110	0.50	-0.189	0.31	0.274	5.13	-0.034	5.07	0.117
-4.09	0.094	-4.09	0.102	0.63	-0.229	0.40	0.285	5.25	-0.018	5.20	0.098
-3.34	0.086	-3.34	0.094	0.75	-0.253	0.49	0.297	5.38	-0.006	5.32	0.078
-2.59	0.082	-2.59	0.090	0.88	-0.265	0.59	0.304	5.50	-0.006	5.45	0.066
-1.84	0.074	-1.84	0.094	1.00	-0.277	0.68	0.312	5.63	-0.006	5.57	0.046
-1.22	0.082	-1.22	0.106	1.38	-0.221	0.78	0.301	5.75	-0.010	5.70	0.026
-1.13	0.078	-1.12	0.102	1.75	-0.209	0.87	0.309	5.88	-0.010	5.82	0.010
-1.00	0.074	-0.99	0.110	2.13	-0.265	0.96	0.312	5.97	-0.010	5.95	-0.002
-0.88	0.074	-0.87	0.102	2.50	-0.269	1.06	0.305	6.59	-0.006	6.57	-0.010
-0.75	0.078	-0.74	0.114	2.88	-0.249	1.15	0.312	7.34	-0.022	7.32	-0.018
-0.63	0.078	-0.62	0.121	3.25	-0.241	1.24	0.312	8.09	-0.038	8.07	-0.034
-0.50	0.070	-0.49	0.133	3.63	-0.261	1.34	0.301	8.84	-0.050	8.82	-0.042
-0.38	0.066	-0.37	0.145	4.00	-0.241	1.43	0.309	9.59	-0.058	9.57	-0.062
-0.25	0.050	-0.24	0.169	4.13	-0.229	1.53	0.285	10.34	-0.070	10.32	-0.062
-0.13	0.034	-0.12	0.201	4.25	-0.201	1.71	0.289	11.09	-0.078	11.07	-0.074
-0.03	0.002	-0.03	0.217	4.38	-0.173	1.81	0.309	11.84	-0.082	11.82	-0.078
				4.50	-0.153	1.90	0.309	12.59	-0.089	12.57	-0.058
				4.59	-0.129	1.99	0.309	13.34	-0.129	13.32	-0.097
				4.66	-0.109	2.09	0.309	14.09	-0.105	14.07	-0.100
						2.18	0.310	14.84	-0.109	14.82	-0.101
						2.28	0.312	15.59	-0.113	15.57	-0.112
						2.37	0.305	16.34	-0.113	16.32	-0.125
						2.46	0.301	17.09	-0.121	17.07	-0.113
						2.56	0.301	17.84	-0.093	17.82	-0.118
						2.65	0.301	18.59	-0.117	18.57	-0.125
						2.74	0.285	19.34	-0.129	19.32	-0.145
						2.84	0.297	20.09	-0.145	20.07	-0.137
						2.93	0.281	20.84	-0.149	20.82	-0.141
						3.03	0.293	21.59	-0.157	21.57	-0.150
						3.12	0.285	22.34	-0.161	22.32	-0.157
						3.31	0.293	23.09	-0.173	23.07	-0.165
						3.40	0.301	23.84	-0.169	23.82	-0.172
						3.49	0.297	24.59	-0.185	24.57	-0.181
						3.59	0.301	25.34	-0.189	25.32	-0.193
						3.68	0.301	26.09	-0.193	26.07	-0.193
						3.78	0.297	26.87	-0.197	26.82	-0.193
						3.87	0.297				
						3.96	0.285				
						4.06	0.285				
						4.15	0.281				
						4.24	0.281				
						4.34	0.249				
						4.43	0.257				
						4.53	0.205				
						4.62	0.193				

* X denotes the distance from the start of bend along the inside convex wall, divided by H.
$C_p = (P-P_0)/\frac{1}{2}\rho U_0^2$, where P_0 represents pressure at the inside wall at X=0.

Uniformity of the mean-velocity distribution at station U1, located 2 ft (61.0 cm) downstream of the turbulence stimulator, was ascertained by traversing a Pitot tube. The velocity was uniform outside the boundary layers, with a deviation from the mean less than 1.0 percent. As will be discussed more fully later, the two-dimensional contraction introduced secondary motion in the boundary layers on top and bottom flat walls of the tunnel. However, the boundary layers on the wider, vertical walls were two dimensional over the middle 32 in (81.3 cm).

Figure 1 also shows the coordinates employed in the presentation of experimental results; X is the longitudinal distance along the inside wall, Y is the outward distance from the inside wall, and Z is the distance measured downward from the top inside corner. The origin of the coordinate system is located at the start of the bend at the top inside corner. The mean and fluctuating velocity components in the (X, Y, Z) directions are (U, V, W) and (u, v, w), respectively. Thus, U represents the longitudinal component whose direction follows the duct curvature, while V and W are the transverse components. The reference station U1 is at $X = -4.5\ H$, upstream of the bend, H being the duct width. Station U2 is at $X = -0.5\ H$, just inside the influence of the pressure gradients induced by the duct curvature. The following three stations are located at 15, 45, and 75 degrees along the bend, and are so designated. Two downstream stations, D1 and D2 which are 0.5 H, 4.5 H downstream of the bend, respectively, were selected to study the recovery of the flow following the curvature. In the following discussion, all velocity components are nondimensionalized by the freestream velocity (16 m/s) at station U1.

Mean-Flow Measurements

The mean-velocity field was measured with a five-hole pressure probe. Using this probe, it was possible to measure the three components of mean velocity at any location in the tunnel without yawing and pitching the probe. The overall diameter of the probe was 0.13 in (3.30 mm) and it had five 0.023 in (0.584 mm) holes: one on the flat surface facing upstream and four equally spaced on 45 deg facets. All pressure measurements were made with a Validyne pressure transducer (±0.125 psi range) which was calibrated against a micromanometer, having a resolution of 0.001 in (0.0254 mm) of alcohol. The pressure measurements were accurate to within 2 percent of the freestream dynamic pressure.

The five-hole pressure probe was calibrated in the freestream at station U1 against a standard Pitot tube, following Treaster and Yocum (1979). A specially designed probe-holder base enabled the probe to be yawed and pitched in desired positions, in the range ±35 deg, in 5 deg intervals. For each pressure measurement, a sampling rate of 200 samples/second and a measuring period of 3 seconds was used by suitably programming the A/D converter of the computer. Thus, the mean pressure was obtained by averaging 600 samples. The pressures measured by the probe were converted to the calibration coefficients defined in Treaster and Yocum, and the calibration charts were used, with fourth-order polynomials for interpolation, to calculate the yaw and pitch angles, velocity magnitude, and static pressure. The velocity components were then calculated. Errors from the approximation of the calibration chart were estimated to be 1 deg in flow angle when the yaw and pitch angles were less than 25 deg. Most of the measurements were found to be within this range. The overall uncertainty in the mean-velocity measurements was estimated to be 1.5 percent in the streamwise component (U) and 3 percent in the transverse components (V and W) of the reference velocity.

Measurement of Wall Pressure and Wall Shear Stress

The pressure distribution on the tunnel walls was measured by pressure taps. Along the centerline of the side walls of the wind tunnel, 80 taps were placed on the inside wall and 106 taps were placed on the outside wall. The location of these taps and the measured pressures are given in Table 1 and plotted in Fig. 4. Additional pressure taps were provided in the spanwise direction at several streamwise sections but these were used mainly to check the flow symmetry about the tunnel centerplane.

The wall shear stress was determined by employing two different types of pressure probes at the same location. A total-head tube with inner and outer diameters of 0.047 and 0.065 in (1.19 and 1.65 mm), respectively, was used in the manner of a Preston tube. However, the static pressure at the same point was obtained from a separate static-pressure probe. The difference between the readings of the two probes was used, along with the Preston-tube calibration of Patel (1965), to obtain the wall friction coefficient. This method of determining the static pressure (instead of using wall taps) enabled wall-friction measurements to be made rapidly and at closely-spaced positions. However, it should be pointed out that, due to the relative insensitivity of the probes to yaw, this method gives the magnitude of the wall shear but not its direction. This limitation should be kept in mind in future use of these data.

Turbulence Measurements

A constant-temperature hot-wire system was employed to measure the fluctuating velocity components. At the beginning of this study, it was thought that a triple-sensor probe could be used to obtain all the necessary information in a single set of experiments. However, more detailed consideration of the flow to be measured soon led to the conclusion that commercially available triple-sensor probes were much too large to properly resolve the near-wall flow. Therefore, a miniature two-sensor (X-wire) probe, whose overall size is less than 2 mm (DISA 55P61), was employed. The probe had a 1.25-mm long, 5-mm diameter platinum-plated tungsten wires, giving a

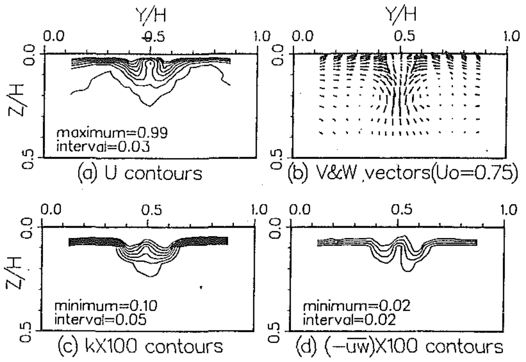

(a) U contours (b) V&W vectors(Uo=0.75)

(c) kX100 contours (d) $(-\overline{uw})$X100 contours

Fig. 2 Top-wall boundary layer at station U1

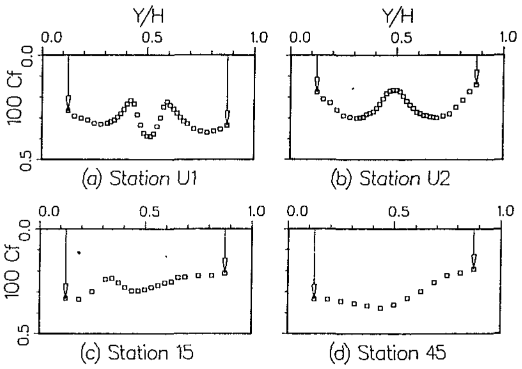

(a) Station U1 (b) Station U2

(c) Station 15 (d) Station 45

Fig. 3 Measured friction coefficients on the top wall

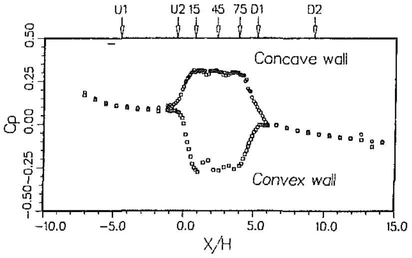

Fig. 4 Pressure distribution along the curved walls in the symmetry plane

length-diameter ratio of 250. It was used in two orientations, with the sensors in the XY plane, and then in the XZ plane, to obtain all except one $(-\overline{vw})$ component of the Reynolds stress tensor. Each sensor was connected to a DISA 55P10 Constant Temperature Anemometer bridge operating with an overheat ratio of 1.5. The probe was speed-calibrated to obtain the calibration constants before and after each experiment. This was intended to monitor the drift in the calibration due to variations in ambient temperature or deposits accumulating on the sensors. Since the wind tunnel is of the open-circuit type, temperature increases inside the tunnel were usually quite small (less than 2°C during a one or two hour period). However, the temperature was monitored and corrections were made in the calibration.

The modified King's law was used to relate the anemometer voltage E to the effective cooling velocity U_e:

$$\frac{\mathrm{E}^2}{T_w - T_a} = A + B(U_e)^n \tag{1}$$

where T_w is the constant wire temperature, T_a is the ambient temperature, A and B are calibration constants, and $n = 0.5$. The instantaneous effective cooling velocity was converted to instantaneous in-plane velocity in the laboratory frame using the cosine law and a constant directional sensitivity coefficient, $k = 0.2$, with cooling by the out-of-plane velocity component ignored. The main source of error comes from the out-of-plane velocity cooling. The overall uncertainty in the measured Reynolds stresses was estimated as 5 percent in $\overline{u^2}$ and 10 percent in other stresses.

The data-acquisition procedure was similar to that used for the five-hole pressure probe. Voltages from the hot-wire sensors and the tunnel temperature were sampled simultaneously for 5 seconds with a sampling rate of 200 Hz, and processed to determine the instantaneous velocity components and then the Reynolds stresses. Although the hot-wire measurements also yielded the mean-velocity components, the measurements with the pressure probe are considered more reliable. Therefore, only the pressure-probe data are presented for the mean velocities.

Influence of Wind-Tunnel Contraction

From the measurements at station U1 it became apparent quite early that the flow on the flat top (and bottom) wall was influenced by the two-dimensional contraction of the wind tunnel. Figure 2 shows selected data. It is clear that a pair of vortices exists inside the top-wall boundary layer, rendering it highly three dimensional. As observed by Mokhtari and Bradshaw (1983), these vortices are induced by the lateral pressure gradients that exist on the top wall of the wind-tunnel contraction. These gradients deflect the slow-moving boundary-layer fluid toward the vertical centerplane more strongly than the inviscid fluid outside the boundary layer, inducing a pressure-driven secondary motion. The secondary flows collide at the vertical centerplane of the top wall, forming a pair of vortices with the common flow between them away from the wall. However, in the present case, the roll-up process was not sufficiently advanced to form vortices with identifiable cores of velocity defect.

The data in Fig. 2 indicate that the secondary flow magnitude reaches almost 5 percent of the freestream velocity, while the longitudinal velocity contours indicate that the boundary layer thickness at the center of the top wall is almost three times that near the corners. This extraordinarily thick boundary layer leads to the large vertical component of velocity near the center. The contours of turbulent kinetic energy and the Reynolds shear-stress $-\overline{uw}$, which is principally responsible for the transport of X-momentum in the vertical direction, normal to the top wall, indicate that the flow is approximately symmetric about the vertical centerplane. A more careful study of the secondary motion and the various contours indicates that there may be yet another pair of counter-rotating vortices forming under the primary pair. These secondary vortices produce a flow towards the wall in the centerplane and lead to increased axial velocity, turbulent kinetic energy, and Reynolds stress very close to the wall.

The downstream persistence of the top-wall vortices observed in Fig. 2 can be clearly seen from the friction coefficients measured at stations U1, U2, 15, and 45, which are shown in Fig. 3. First of all, the higher friction coefficient near the centerplane at U1 is indicative of a local flow divergence associated with the counter-rotating secondary vortices mentioned above. By station U2, these secondary vortices have disappeared and the friction distribution is that associated with only the primary pair, the low friction at the centerplane being due to the flow convergence induced by the primary pair of vortices. There exists some asymmetry due to the fact that some radially inward pressure gradient exists at station U2 (see Fig. 4). This asymmetry is obvious at station 15, where the curvature related radial pressure gradient drives low-momentum fluid in the top wall boundary layer from the inside to the outside corner. The effect of the thickened boundary layer (due to the vortices) is still in evidence at station 15 in the dip

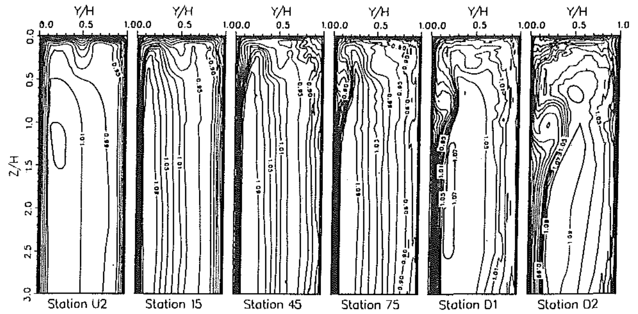

Fig. 5(*a*) Contours of longitudinal velocity (U = 1.09, 1.07, 1.05, 1.03, 1.01, 0.99, 0.95, 0.9, 0.85, 0.8, 0.75, 0.7, 0.65)

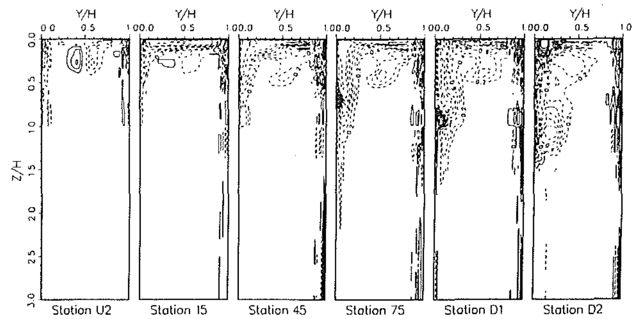

Fig. 5(*b*) Contours of longitudinal vorticity (Ω_x = 0.2, 0.4, 0.6, 0.9, 1.2, 1.5, 2.0, 3.0, 5.0, 7.0, 10.0)

Fig. 5 Measured mean velocity field

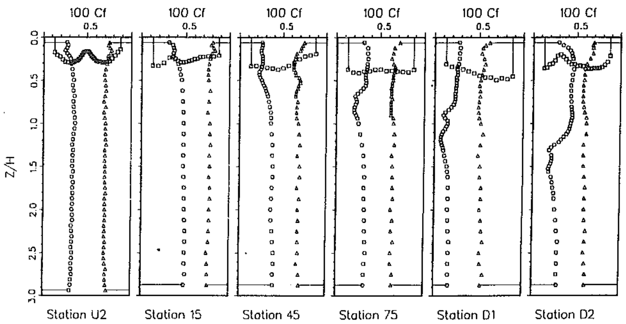

Fig. 6 Wall shear stress distributions

in the friction coefficient. By station 45, however, there is little evidence of the contraction-induced vortices.

Measurements similar to those shown in Fig. 2 were made along the vertical side walls of the duct at station U1. These revealed that the boundary layers on the two walls were essentially two dimensional except for a short region close to the corners. The boundary layer thickness at midspan of the vertical walls was $0.08H$ ($\mathrm{Re}_\delta = 18{,}000$), and wall friction coefficient ($C_f = 2\tau_w/\rho U_0^2$) was 0.0038. While these two integral parameters are usually sufficient to prescribe the initial conditions (under the assumption of a flat-plate boundary layer) for the calculation of the subsequent flow, the observed contraction-induced vortical flow should be taken into account to properly model the flow in the corners. The measured data can be used to construct realistic inlet condition for such computations.

Results and Discussion

The experiment was conducted with the freestream velocity U_0, outside the boundary layers at the reference section U1 (Fig. 1), of 16 m/s. In the presentation of results, this is used as the reference velocity. With these values, the duct Reynolds number, $U_0H/\nu = 224{,}000$ and the corresponding Dean number $(U_0R_h/\nu)[R_h/(R_i + 0.5H)]^{0.5} = 95{,}000$, where the hydraulic radius $R_h = 0.857\ H$ and the inner radius of the duct $R_i = 3.0\ H$. However, it should be noted that these are not particularly meaningful for the developing boundary layers that are of interest in the present situation. Instead, it is the state of the boundary layer in the upstream section, at station U1, say, that determines the effects of surface curvatures and pressure gradients that are imposed on the boundary layers as they negotiate the curve and recover from it. At this station, the boundary layers on the vertical walls have essentially the same characteristics as they have developed in identical circumstances. Measurements indicated that, at the center of these walls, the momentum-thickness Reynolds number, $R_\theta = U_0\theta/\nu$, was 1650. The boundary layers on these walls were found to be essentially two-dimensional in regions out of the immediate influence of the corners. However, as described above, the boundary layers on the top and bottom walls are not two dimensional. Measurements were made in the upper half of the duct cross section, the symmetry of flow in the upper and lower halves of the duct being assumed following some preliminary measurements.

Mean Pressure and Velocity Fields. The pressure distribution ($C_p = 2(p - p_0)/\rho U_0^2$) along the channel walls in the plane of symmetry, given in Table 1, is presented in Fig. 4, where p_0 represents pressure at (0, 0, $3H$) and U_0 is the freestream velocity at U1. The pressure gradients induced by the curvature are clearly seen. On the convex side, the boundary layer is subjected to a favorable pressure gradient starting upstream of the bend, and this is followed by an adverse gradient around the bend exit. The boundary layer on the concave side is subjected to pressure gradients of similar magnitude but opposite signs.

The mean-velocity field measured by the pressure probe is shown in Fig. 5. The longitudinal vorticity shown in Fig. 5(*b*) was obtained by numerical differentiation of the measured secondary velocity components and non-dimensionalized by the freestream velocity at U1 and the duct width H. The top-wall vortices are clearly seen, particularly in the vorticity plots, at station U2 and they are still in evidence at station 15. Thereafter, they are smeared out by the curvature-driven secondary motion, which is directed from the outer to the inner corner. The experiments indicate that, near the center of the duct, the boundary layers remain relatively thin and there exists an inviscid region in which the velocity gradient is small. Near the top wall, however, the boundary layer on the convex wall thickens as it is fed by fluid coming down from the top-wall boundary layer, and by station 75, there appears a longitudinal vortex with its core approximately at $Y/H = 0.08$ and $Z/H = 0.7$. Vortical flow now begins to fill the top of the channel. The vortex on the convex wall grows in size and is pushed away from the top. The vortex persists even after the end of curvature. At station D2, the core of the vortex, identified by low axial velocity and high longitudinal vorticity, is located around $Y/H = 0.17$ and $Z/H = 1.0$. Previous studies of the flow in curved ducts of square section, mentioned in the Introduction, indicated two vortices forming near the convex wall, colliding at the centerline, and lifting from the wall. In the present case, however, the longitudinal vortex develops without interference from a similar vortex in the other half of the duct.

The wall shear stresses are shown in Fig. 6. A circle, a triangle and a square denote the values on the convex, concave and top walls, respectively. As expected from the longitudinal velocity contours of Fig. 5(*a*), flow symmetry about the vertical centerplane is observed until station U2, where the radial pressure gradient begins. In general, near the duct center, the friction coefficient on the convex wall first increases due to the favorable longitudinal pressure gradient and then decreases due to the adverse pressure gradient near the exit. The opposite is found on the concave side. The top-wall vortices are seen at station U2 through the dip in the friction distribution. The

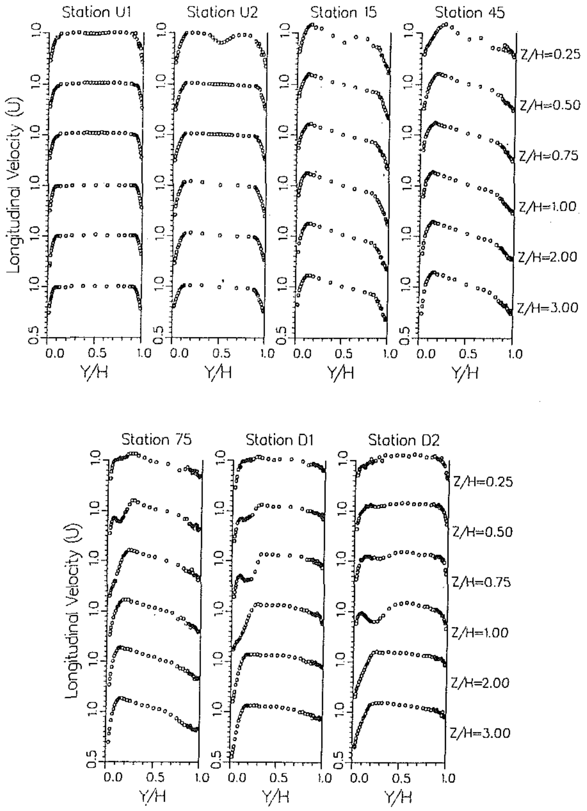

Fig. 7 Longitudinal velocity (U) profiles

data also show similar dips on both vertical walls near the corners. Unfortunately, the resolution of the velocity measurements was not sufficient to identify these with corner vortices. As the flow progresses downstream, the most prominent feature of the measurements is a significant drop in the friction coefficient on the convex wall. This begins around station 45, where the minimum is located at $Z/H = 0.45$, and moves downward to about $Z/H = 1.5$ at station D2. At the last three stations, this minimum in friction is preceded by another local minimum, and the entire spanwise distribution acquires a characteristic shape. This shape of the friction distribution is associated with the flow convergence and divergence induced by the longitudinal vortex. Yet another interesting feature of the measured friction coefficients is found on the top wall near the junction with the convex wall at station D2. The pronounced trough in the local friction distribution suggests the development of yet another vortex which arises from the strong inflow towards the convex wall. The corner vortex rotates in a sense opposite to that of the vortex on the convex wall described above.

Figure 7 shows the profiles of the longitudinal velocity component (U) across the duct, from the inner to the outer wall, at six positions: $Z/H = 0.25$, 0.50, 0.75, 1.00, 2.00, and 3.00, the last being the symmetry plane of the duct. These results represent only a small sample of the total database. The corresponding distributions of the transverse components (V and W) are not shown. The velocity profiles at stations U1 and U2 show flat-plate type boundary layers on the vertical walls except at $Z/H = 0.25$, which is under the influence of the secondary flow on top wall. The longitudinal velocity outside the boundary layers at station 45 decreases from the inner to the outer wall, as required by inviscid-fluid theory. Further downstream, at stations D1, much fuller longitudinal velocity profiles are observed in the outer-wall boundary layer in the two-dimensional flow region near the duct center. This is consistent with the effect of concave curvature, which acts to increase turbulent mixing, and leads to increased velocity close to the wall and larger friction. This effect persists on the straight wall, even after removal of the curvature. The longitudinal vortex on the convex wall is seen through the profiles of U at $Z/H = 0.50$ and 0.75 at station D1, and at $Z/H = 0.75$ and 1.00 at station D2, which depict the two peaks commonly observed in vortical flows.

Reynolds-Stress Distributions. The effect of surface curvature on the boundary layers on the convex and concave walls in the two-dimensional flow near the plane of symmetry of the duct, and the growing three-dimensionality associated with the vortex on the convex wall were already evident from the mean-velocity field. These two effects combine to produce a quite complex distribution of the Reynolds stresses. The hot-wire measurements were made at four streamwise stations and included all except one ($-\overline{vw}$) component of the Reynolds stress tensor. Figure 8 shows the turbulent kinetic energy (k) and the five Reynolds stresses. At each station, profiles are shown at six sections ($Z/H = 0.25$-3.00) across the duct.

Figure 8 shows that, at the reference station U1, there are thin, two-dimensional boundary layers on the inner and outer walls and a large inviscid core. The vortex pair on the top wall is not seen at $Z/H = 0.25$. Within the boundary layers in the central portion of the duct ($Z/H = 0.75$-3.00, say), the kinetic energy and the primary Reynolds shear stress $-\overline{uv}$ behave as expected, with peak values near the wall. The shearing stress $-\overline{uw}$ is small, there being no transport of momentum in the Z-direction if the flow is two-dimensional, the structure parameter ($a_1 = -\overline{uv}/k$) attains a value of about 0.3, which is generally accepted for fully turbulent flows, and the normal stresses are anisotropic in the same way as in thin two-dimensional boundary layers, i.e., $\overline{uu} > \overline{ww} > \overline{vv}$. The standard flat-plate turbulent boundary layer behavior over much of station U1 and the details of the flow near the top provided in a previous section are sufficient to specify proper inlet conditions for a CFD code applied to calculate the subsequent development of the flow through the duct.

Comparison of the profiles of k and $-\overline{uv}$ at stations U2 and 45 near the symmetry plane show the direct effects of surface curvature. At U2, the profiles near the two walls are quite similar, but at 45, they develop marked differences. Both k and $-\overline{uv}$ are suppressed near the convex wall and greatly amplified near the concave wall. For example, at station 45, $Z/H = 3.00$, the peak value of k near the concave wall is almost three times that near the convex wall, and there is a similar difference in the shear stress. It is again confirmed that production of the turbulence energy is enhanced by the concave curvature, while it is suppressed by convex curvature. However, as discussed in Richmond and Patel (1991), most commonly used two-equation turbulence models fail to predict this asymmetric behavior of turbulence production in curved wall boundary layers. The measurements of k and the individual Reynolds stresses at the last station, D1, which is just downstream of the bend in the duct, continue to indicate the curvature effects described above in the boundary layer near the duct center ($Z/H = 2.00$-3.00, say).

Although the evolution of the longitudinal vortex on the convex wall near the top of the duct is evident from the turbulence profiles at station D1 in the region $Z/H = 0.50$-1.00, the global features of the vortex are more conveniently visualized from the contour plots shown in Fig. 9. It is clear that the two shear stresses change sign in the region where the longitudinal velocity contours are most distorted, indicating a more vigorous transport of momentum and energy by the vortex. A high level of turbulent kinetic energy is also observed near $Z/H = 0.825$, because the boundary layer fluid near the convex wall is lifted outward by the vortical flow. The distributions shown in Fig. 9 are typical of a longitudinal vortex inside a boundary layer.

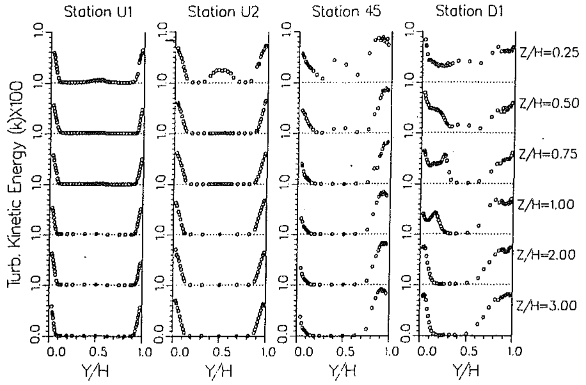

Fig. 8(*a*) Turbulent kinetic energy (*k*)

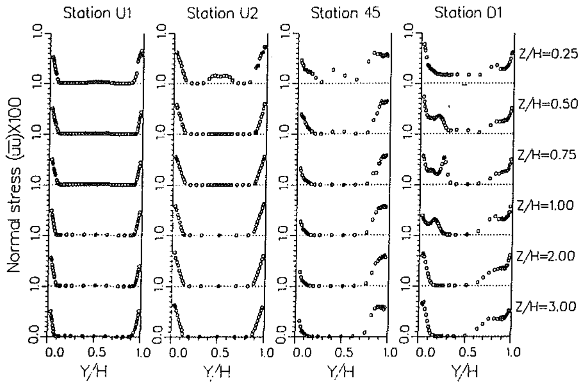

Fig. 8(*b*) Normal stress $(\overline{u^2})$

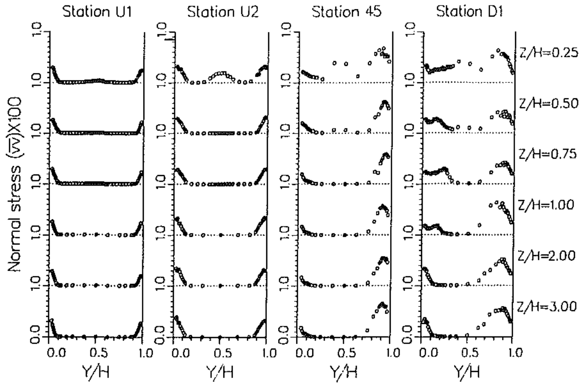

Fig. 8(*c*) Normal stress $(\overline{v^2})$

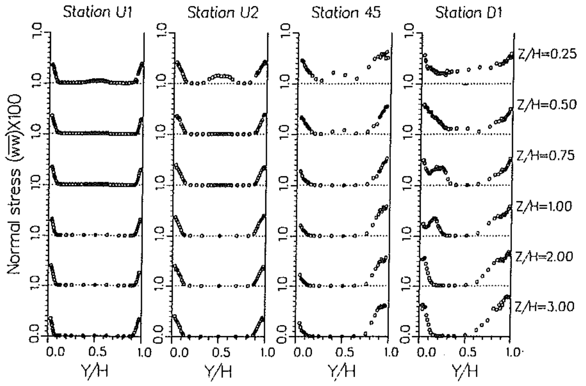

Fig. 8(*d*) Normal stress $(\overline{w^2})$

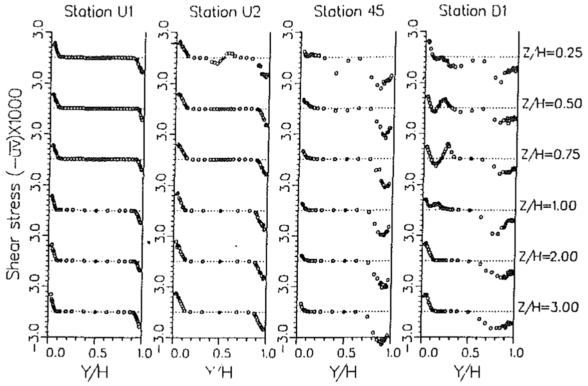

Fig. 8(*e*) Shear stress $(-\overline{uv})$

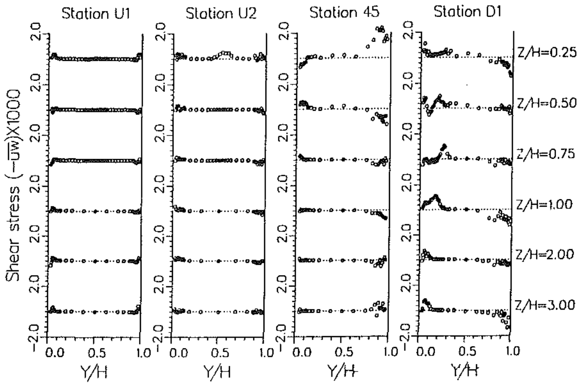

Fig. 8(*f*) Shear stress $(-\overline{uw})$

Fig. 8 Reynolds stress profiles

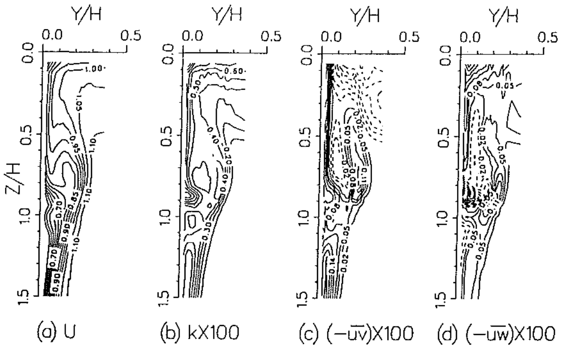

(a) U (b) kX100 (c) (−uv)X100 (d) (−uw)X100

Fig. 9 Vortex on the convex wall at station D1

Concluding Remarks

Measurements in developing turbulent boundary-layer flow in a 90 deg curved duct of rectangular cross section with an aspect ratio of six were presented and discussed. Despite the relatively simple geometry this flow offers two challenges to physical and computational modeling. First, there is an extensive region of nominally two-dimensional boundary layers subjected to strong streamwise curvatures and related pressure gradients, and second, the data document the development of the pressure-driven secondary motion in the corner region which eventually leads to the formation of a longitudinal vortex on the convex wall. The duct aspect ratio was such that these two features develop more or less independently, without interaction. Together, these features of a complex turbulent flow present a formidable challenge to any CFD code that claims a high level of generality. Calculations carried out by the authors (Kim, 1991; Sotiropoulos and Patel, 1992) suggest that prediction of the details of such a flow require methods that solve the Reynolds-averaged Navier-Stokes equations with an advanced turbulence model capable of resolving the joint effects of curvature and pressure gradients.

The data were obtained in such detail, with respect to the location of measurement points, that they can be used to test or validate computational methods and turbulence models. In particular, special care was given to documenting the flow at an upstream section so that realistic upstream boundary conditions could be provided for computational studies.

Data Bank Contribution

Data from this experiment have been deposited in the JFE Data Bank. A fuller account of the data is given in the paper "An Experimental Study of Boundary Layer Flow in a Curved Rectangular Duct," presented by the authors at the 1993 Fluids Engineering Conference, FED-Vol. 146, *Data for Validation of CFD Codes* (D. Goldstein, D. Hughes, R. Johnson and D. Lankford, eds.) pp. 13-28. Annotated text of the conference paper is included in the Data Bank to guide interpretation and use of the data.

Acknowledgments

This study was sponsored by the Office of Naval Research under Grant N00014-89-J-1342 in support of the DARPA Subtech Program, and Grant N00014-91-J-1204. Partial support was also derived from a grant from the Tennessee Valley Authority on the Autoventilating Hydroturbine Project.

References

Chang, S. M., Humphrey, J. A. C., Johnson, R. W., and Launder, B. E., 1983, "Turbulent Momentum and Heat Transfer in Flow Through a 180-Degree Bend of Square Cross Section," *Proceedings of 4th Symposium on Turbulent Shear Flows*, Karlsruhe, Germany.

Gillis, J. C., and Johnston, J. P., 1983, "Turbulent Boundary Layer Flow and Structure on a Convex Wall and its Redevelopment on a Flat Wall," *Journal of Fluid Mechanics*, Vol. 135, pp. 123-153.

Hoffmann, P. H., Muck, K. C., and Bradshaw, P., 1985, "The Effect of Concave Surface Curvature on Turbulent Boundary Layers," *Journal of Fluid Mechanics*, Vol. 161, pp. 371-403.

Humphrey, J. A. C., Whitelaw, J. H., and Yee, G., 1981, "Turbulent Flow in a Square Duct With Strong Curvature," *Journal of Fluid Mechanics*, Vol. 103, pp. 443-463.

Iacovides, H., Launder, B. E., Loizou, P. A., and Zhao, H. H., 1990, "Turbulent Boundary Layer Development Around a Square-Sectioned U-Bend: Measurements and Computation," ASME JOURNAL OF FLUIDS ENGINEERING, Vol. 112, pp. 409-415.

Kim, W. J., 1991, "An Experimental and Computational Study of Longitudinal Vortices in Turbulent Boundary Layers," Ph.D. thesis, Mechanical Engineering, University of Iowa.

Kline, S. J., and McClintock, F. A., 1953, "Describing Uncertainties in Single Sample Experiments," *Mechanical Engineering*, Vol. 75, pp. 3-8.

Mokhtari, S., and Bradshaw, P., 1983, "Longitudinal Vortices in Wind Tunnel Wall Boundary Layer," *Aeronautical Journal*, Vol. 87, pp. 233-236.

Muck, K. C., Hoffmann, P. H., and Bradshaw, P., 1985, "The Effect of Convex Surface Curvature on Turbulent Boundary Layers," *Journal of Fluid Mechanics*, Vol. 161, pp. 347-369.

Patel, V. C., 1965, "Calibration of the Preston Tube and Limitations on Its Use in Pressure Gradient," *Journal of Fluid Mechanics*, Vol. 23, pp. 185-208.

Patel, V. C., 1968, "Measurements of Secondary Flow in the Boundary Layer of a 180 Degree Curved Channel," Aeronautical Research Council, U.K., ARC CP No. 1043.

Richmond, M. C., and Patel, V. C., 1991, "Convex and Concave Surface Curvature Effects in Wall-Bounded Turbulent Flows," *AIAA Journal*, Vol. 29, pp. 895-902 (see also AIAA paper 87-1301).

Smits, A. J., Young, S. T. B., and Bradshaw, P., 1979, "The Effect of Short Regions of High Surface Curvature on Turbulent Boundary Layers," *Journal of Fluid Mechanics*, Vol. 94, pp. 209-242.

Sotiropoulos, F., and Patel, V. C., 1992, "Flow in Curved Ducts of Varying Cross-Section," Institute of Hydraulic Research, University of Iowa, IIHR Report No. 358.

Treaster, A. L., and Yocum, A. M., 1979, "The Calibration and Application of Five-Hole Probes," *ISA Transaction*, Vol. 18, pp. 23-34.

Fluid Flow Behavior in the Curved Annular Sector Duct

G. Yang

M. A. Ebadian*
Fellow ASME

Department of Mechanical Engineering,
Florida International University,
Miami, FL 33199

A numerical analysis of the axial and secondary flow behavior in a curved annular sector duct is presented in the paper. The flow is considered to be fully developed laminar flow with constant physical properties. Five parameters have been identified as major variables in controlling the flow behavior. The study indicates that with a moderate Dean number and when the sector angle is smaller than $\pi/2$, only two vortices will appear in the cross section of the curved annular sector duct. When the sector angle is larger than $\pi/2$, the vortex structure can be very complex, and is often determined by other parameters, especially by the angle between the annular sector duct centerline and the curvature radius direction. The friction coefficient of the curved annular sector duct is affected mainly by the radius ratio, curvature, and axial pressure gradient. The radius ratio of the inner/outer walls can affect the vortex structure only when the radius ratio is very small. When the radius ratio is larger than 0.6, the friction coefficient is only slightly higher than that of a straight annular sector duct. Nevertheless, for the small radius ratio duct, the friction coefficient can be tripled, as compared with a straight annular sector duct. Although the holding pipe curvature and the axial pressure gradient cannot significantly change the vortex structure of the secondary flow, they can however, remarkably increase the friction coefficient by increasing the velocity gradient near the solid boundary.

Introduction

Curved annular sector ducts are commonly applied in the design of multi-channel compact heat exchangers, evaporators, and condensers being used in the food, pharmaceutical and chemical industries. For these applications, several annular sector ducts are combined side by side to form a circular holding pipe, which is bent in the shape of a coil. Much research has been conducted on the straight annular sector duct. Sparrow et al. (1964) analytically obtained the axial velocity distribution and the friction factor for fully developed laminar flow through an annular sector duct. Niida (1980) studied the same problem analytically and expressed his solution in terms of an equivalent diameter. However, to the authors' knowledge, few information is available in the open literature for laminar flow in a curved annular sector duct.

In a curved duct, the centrifugal force on the order of w^2/R acts on the fluid particles, forcing them to flow outward from the center of the curvature. Due to the nonuniform axial velocity distribution in the cross section, secondary flow is generated by the unbalanced centrifugal force and the pressure gradient. The secondary flow in the curved duct enhances the flow resistance, which results in a large pressure drop along the curved duct when compared to a straight duct. Numerous studies have been conducted on curved ducts. The early stages of study on curved duct flow relied heavily on experimental tests. Dean (1927) was the first to achieve significant progress in theoretical study of the curved duct. In recent years, Truesdell and Adler (1970), Akiyama and Cheng (1971), Austin and Seader (1973), Collins and Dennis (1975), Dennis and Ng (1982), and Berger et al. (1983) have numerically solved the fully developed axial and secondary flow in a curved duct with a circular cross section. Cheng and Akiyama (1970), Mori, et al. (1971), Joseph et al. (1975), Cheng et al. (1976), Ghia and Sokhey (1977), Mille et al. (1985), and Kumar et al. (1989) have studied fully developed flow in the curved duct with a rectangular cross section. Thomas and Walters (1965), Takami and Sudou (1984), and Topakoglu and Ebadian (1985, 1987) have studied fully developed laminar flow in a curved duct with an elliptical cross section. Ghia et al. (1987) studied the curved ducts of square and polar sector cross sections by multigrid technique. They pointed out that there exists significant difference between the flow patterns of the square and annular duct. However, only limited cases of the annular sector duct (small Ω and constant, $\alpha = \pi/2$, correspond in this paper) have been discussed in their paper. These previous studies indicate that the secondary flow pattern strongly depends on the cross section configuration of the curved duct. There are two major differences between the curved annular sector duct and the curved duct studied previously. First, the curved annular sector duct has both convex and concave boundaries, while other curved ducts have convex boundaries only. Second, in the majority of cases, the symmetry line of the annular sector does not coincide with the direction of the centrifugal force. This study demonstrates that these two differences can profoundly change the secondary flow pattern in the curved annular sector duct.

---

* The author to whom all correspondence should be addressed.

Contributed by the Fluids Engineering Division for publication in the JOURNAL OF FLUIDS ENGINEERING. Manuscript received by the Fluids Engineering Division July 6, 1992; revised manuscript received August 17, 1993. Associate Technical Editor: O. Baysal.

The Governing Equations

Two geometry parameters are needed to determine the geometry of a straight annular sector duct: the sector angle and the radius ratio of the inner and outer walls. However, for a curved annular sector duct, the relative location of the sector duct to the curvature direction of the holding pipe also becomes a critical parameter. Figure 1 illustrates the definition of a curved annular sector duct, where R_i and R_o indicate the radius of the inner and outer walls, respectively; α is the relative location of the curved annular sector to the symmetry centerline; Ω represents the angle of the annular sector; and κ and s are the curvature and the centerline of the holding pipe, respectively.

To make the governing equation more general, the following dimensionless parameters are introduced:

$$r=\frac{r^*}{R_o},\ s=\frac{s^*}{R_o},\ u=\frac{u^*R_o}{\nu},\ v=\frac{v^*R_o}{\nu},$$

$$w=\frac{w^*R_o}{\nu},\ p=p^*/(\rho\nu^2/R_o^2),\ \epsilon=\kappa R_o,\ r^\#=R_i/R_o \tag{1}$$

$$d_h=D_h/(2\ R_o),\ D_h=\begin{cases}\dfrac{2\Omega(R_o^2-R_i^2)}{2(R_o-R_i)+\Omega(R_o+R_i)} & \Omega<2\pi\\[2ex] (2R_o-R_i) & \Omega=2\pi\end{cases},$$

$$\mathrm{De}=\frac{dp^*}{ds^*}\bullet\frac{R_o^3}{\nu^{*2}\rho}\ (\kappa\bullet R_o)^{1/2}=\frac{dp}{ds}\,\epsilon^{1/2},$$

where the variables with superscript (*) indicate dimensional variables. Subscripts i and o, indicate the inner and outer walls, respectively. ν, ρ, and p represent the kinematic viscosity density and pressure of the fluid. D_h and d_h indicate the dimensional and nondimensional hydraulic diameters, and De represents the Dean number. The governing equations in a toroidal pipe can then be written as:

$$\frac{1}{r}\frac{\partial u}{\partial\theta}+\frac{1}{r}\frac{\partial(rv)}{\partial r}=Q \tag{2}$$

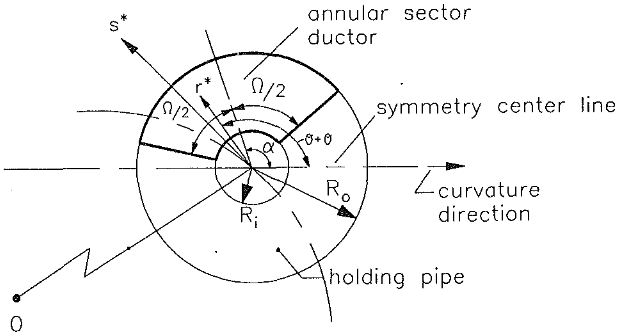

Fig. 1 Definition of the curved annular sector duct and the coordinate system

$$\frac{1}{r}\frac{\partial(uu)}{\partial\theta}+\frac{1}{r}\frac{\partial(rvu)}{\partial r}=-\frac{1}{r}\frac{\partial p}{\partial\theta}+\frac{\partial^2u}{\partial r^2}+\frac{1}{r}\frac{\partial u}{\partial r}+\frac{1}{r^2}\frac{\partial^2u}{\partial\theta^2}+uQ-\frac{vu}{r}$$
$$+w^2\omega\epsilon\sin(\theta+\theta_o)+\omega\epsilon\cos(\theta+\theta_o)\beta$$
$$-\left(\frac{1}{r^2}\frac{\partial^2u}{\partial\theta^2}+\frac{u}{r^2}+\frac{1}{r}\frac{\partial^2v}{\partial r\partial\theta}-\frac{1}{r^2}\frac{\partial v}{\partial\theta}\right) \tag{3}$$

$$\frac{1}{r}\frac{\partial(uv)}{\partial\theta}+\frac{1}{r}\frac{\partial(rvv)}{\partial r}=-\frac{\partial p}{\partial r}+\frac{1}{r^2}\frac{\partial^2v}{\partial\theta^2}+\frac{1}{r}\frac{\partial v}{\partial r}+\frac{\partial^2v}{\partial r^2}+vQ+\frac{u^2}{r}$$
$$-w^2\omega\epsilon\cos(\theta+\theta_o)+\omega\epsilon\sin(\theta+\theta_o)\beta-\left[\frac{1}{r}\frac{\partial v}{\partial r}+\frac{\partial^2v}{\partial r^2}+\frac{1}{r^2}\frac{\partial^2(ru)}{\partial\theta\partial r}\right] \tag{4}$$

$$\frac{1}{r}\frac{\partial(uw)}{\partial\theta}+\frac{1}{r}\frac{\partial(rvw)}{\partial r}=-\omega\frac{\mathrm{De}}{\sqrt{\epsilon}}+\frac{1}{r^2}\frac{\partial^2w}{\partial\theta^2}+\frac{\partial^2w}{\partial r^2}+\frac{1}{r}\frac{\partial w}{\partial r}+2wQ$$
$$+\frac{1}{r}\frac{\partial}{\partial\theta}[w\epsilon\omega\sin(\theta+\theta_o)]-\frac{1}{r}\frac{\partial}{\partial r}[w\epsilon r\omega\cos(\theta+\theta_o)], \tag{5}$$

where the angle θ_o is applied to consider the relative location of the annular sector duct.

Nomenclature

A_E, A_N, A_P, A_S, A_W = coefficients, Eq. (14)
$\mathbf{a}_\theta$, $\mathbf{a}_r$, $\mathbf{a}_s$ = unit vectors in the θ, r, and s directions
b = function, Eq. (15)
De = Dean number, Eq. (1)
D_h = hydraulic diameter [m]
d_h = dimensionless hydraulic diameter
f = friction coefficient
p = dimensionless pressure
p^* = pressure [Pa]
Q = function, Eq. (7)
R_i = inner radius [m]
R_o = outer radius [m]
Re = Reynolds number, $D_h w_b/\nu$
r, r^* = dimensional and dimensionless radial direction coordinate
$r^\#$ = radius ratio, R_i/R_o
S = source term, Eq. (13)
s = axial coordinate
s^* = dimensional axial coordinate
u, v, w = dimensionless velocity components $(u^*, v^*, w)/(\nu/R_o)$
u^*, v^*, w^* = velocity components in the θ, r, and s directions [m s^{-1}]
$u^\#$, $v^\#$ = predicted velocities, Eq. (15)
w_b = dimensionless average axial velocity
w_b^* = dimensional average axial velocity [m s^{-1}]
α = angle, Fig. 1
β = function, Eq. (8)
Γ = coefficient, Eq. (14)
ϵ = dimensionless curvature
θ = angle, Fig. 1
θ_o = angle, Eq. (6)
κ = curvature [m^{-1}]
μ = viscosity
ν = kinematic viscosity [m^2 s^{-1}]
ρ = density [kg m^{-3}]
ϕ = general variable, Eq. (16)
Ω = annular sector angle, Fig. 1
ω = function, Eq. (9)

Subscripts

c = curved
i = inner
o = outer
s = straight

Superscript

* = dimensional

$$\theta_o=\left(\alpha-\frac{\pi}{2}\right) \tag{6}$$

$$Q=\epsilon\omega[-u\,\sin(\theta+\theta_o)+v\,\cos(\theta+\theta_o)] \tag{7}$$

$$\beta=\frac{1}{r}\frac{\partial v}{\partial\theta}-\frac{u}{r}-\frac{\partial u}{\partial r} \tag{8}$$

$$\omega=\frac{1}{1-\epsilon r\cos(\theta+\theta_o)}. \tag{9}$$

The boundary condition for Eqs. (2) to (5) is a non-slip condition for all solid walls. The friction factor, f, of the duct can be found by:

$$f\mathrm{Re}=2d_h^2\mathrm{De}/(w_b\epsilon^{1/2}), \tag{10}$$

where the Reynolds number is defined by:

$$\mathrm{Re}=\frac{D_h w_b^*}{\mu}=2w_b d_h, \tag{11}$$

and the bulk axial velocity, w_b can be calculated by:

$$w_b=\frac{2}{\Omega(1-r^{\#2})}\int_o^{\Omega}\int_{r^{\#}}^{1} wRdRd\theta \tag{12}$$

Numerical Analysis

The governing equations, Eqs. (2) to (5), are nonlinear partial differential equations, which can be expressed in the following general form:

$$\frac{1}{r}\frac{\partial(u\phi)}{\partial\theta}+\frac{1}{r}\frac{\partial(rv\phi)}{\partial r}=\Gamma\left(\frac{\partial^2\phi}{\partial r^2}+\frac{1}{r}\frac{\partial\phi}{\partial r}+\frac{1}{r^2}\frac{\partial^2\phi}{\partial\theta^2}\right)+S. \tag{13}$$

For the general dependent variables, $\phi = 1$, u, v, and w, Eq. (13) refers to the continuity and momentum equations. Γ and S are general diffusivity and source terms, respectively. The SIMPLE algorithm is used as the starting point (Patankar, 1980). Due to the existence of source term, Q, in Eq. (2), the A_E, A_W, A_S, A_N, and b in the pressure correction equation have been changed to balance this source term:

$$\begin{aligned}
A_E&=d_e\left[\Delta r+\frac{\epsilon\omega}{2}\,r\Delta\theta\Delta r\,\sin(\theta+\theta_o)\right]\\
A_W&=d_w\left[\Delta r+\frac{\epsilon\omega}{2}\,r\Delta\theta\Delta r\,\sin(\theta+\theta_o)\right]\\
A_S&=d_s\left[r_s\Delta\theta-\frac{\epsilon\omega}{2}\,r\Delta\theta\Delta r\,\cos(\theta+\theta_o)\right]\\
A_S&=d_n\left[r_n\Delta\theta-\frac{\epsilon\omega}{2}\,r\Delta\theta\Delta r\,\cos(\theta+\theta_o)\right]
\end{aligned} \tag{14}$$

$$\begin{aligned}
b=&-[(v_n^{\#}r_n-v_s^{\#}r_s)\Delta\theta+(u_e^{\#}-u_w^{\#})\Delta r]\\
&+\epsilon\omega[-u_p^{\#}\sin(\theta+\theta_o)+v_p^{\#}\cos(\theta+\theta_o)]r\Delta\theta\Delta r.
\end{aligned} \tag{15}$$

The $u^{\#}$ and $v^{\#}$ indicate the calculated value before the pressure correction. During the numerical calculation, the following controlling parameters were specified: radius ratio, $r^{\#}$, the dimensionless curvature, ϵ, and the axial pressure gradient $(-dp/ds)$. The iteration procedure will be stopped when the convergence criterion is satisfied for all nodes:

$$\frac{\|\phi_{ij}^{k+1}-\phi_{ij}^{k}\|}{\|\phi_{i,j}^{k+1}\|}\le 10^{-5}, \tag{16}$$

where ϕ refers to u, v, w, and p'. Subscripts, i and j, represent the θ and r coordinates, respectively, and superscript, k, represents the kth iteration. Under-relaxation factors have been applied to obtain a convergent solution. Generally speaking, the greater the Dean number, the smaller the relaxation factor. The under-relaxation factors ranging from 0.1 to 0.8 have been used according to different computation cases. After obtaining the convergent velocities, u, v, and w, Eq. (10) is applied to calculate the friction factor.

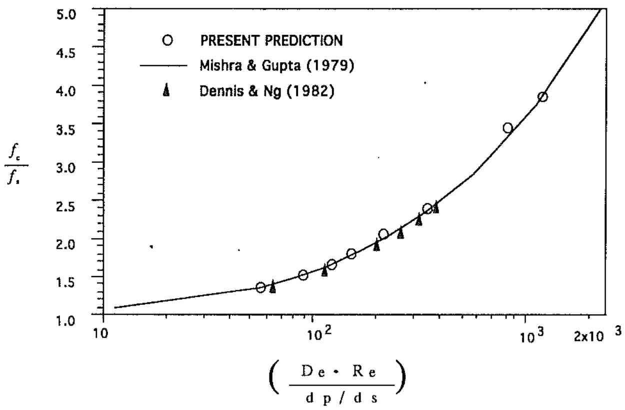

Fig. 2 Comparison of the dimensionless friction coefficient

To assess the accuracy of the governing equations and the validity of the associated computer program, the predicted results have been compared with bench mark results from Sparrow et al. (1964) for the case of the straight annular sector duct. In this case, the dimensionless curvature, ϵ, has been set to equal zero. The present prediction agrees very well with the results of Sparrow et al. (1964), and the maximum deviation between these two results is less than 1 percent.

By setting Ω = 360 deg and $r^{\#} = 0$, the annular sector duct reduces to a circular duct. To further verify the accuracy of the computer code, the predicted results for the curved circular duct have been compared with the other experimental and numerical predictions. Mishra and Gupta (1979) experimentally studied coiled duct flow, and the test data can be presented by one equation in the laminar flow region for the circular duct.

$$\frac{f_c}{f_s}=1+0.033\left[\log_{10}\left(\frac{\mathrm{DeRe}}{dp/ds}\right)\right]^4. \tag{17}$$

Figure 2 shows the comparison of the current work and the predicted results by Dennis and Ng (1982) and Mishra and Gupta (1979). This figure reveals that the present numerical results agree well with the results of the other research. Figure 3 shows the comparison of the axial velocity distributions in an annular sector duct between the present investigation and Ghia et al. (1987). In this calculation, parameter of $\Omega = \pi/6$, $\alpha = \pi$, $r^{\#} = 0.5$, $\epsilon = 0.1$ have been applied. Figure 3(a) shows the axial velocity distribution along the tangential direction, where $r = (r_o + r_i)/2$. In this figure, lines indicate the prediction results by Ghia et al. (1987) while the symbols are the prediction by this study. Figure 3(b) shows the comparison along the radial direction, where $\theta = \alpha = \pi$. Inspection of this figure indicates that an acceptable agreement can be found.

Numerical experiments have also been conducted to determine adequate grid distribution for the present study. First, the overall performance has been examined for three distinct radius ratios and α angles: $r^{\#} = 0.9$, $\alpha = 0$; $r^{\#} = 0.5$, $\alpha = \pi$; and $r^{\#} = 0.1$, $\alpha = \pi/2$. Uniformed grids of 15 × 15, 20 × 20, 30 × 30, 60 × 60 (the grid number in the tangential direction x the grid number in the radius direction) have been applied. For the $r^{\#} = 0.9$ duct, an additional grid distribution of 80 × 20 is also tested due to the considerable difference in length in the tangential and radius directions. During the calculation, parameters, $\epsilon = 0.2$ and $-dp/ds = 50{,}000$, are used. The major results are listed in Table 2. These data indicate that a grid size 30 × 30 is adequate for the majority of cases. Even for the case of $r^{\#} = 0.9$, the deviation of the friction coefficient between the results of grid size, 30 × 30, and that of the finer grid is less than 1 percent. Therefore, the major results that are illustrated in these figures are based on a grid size of 30 × 30.

Results and Discussion

As mentioned earlier, the five major parameters controlling the flow behavior of an annular sector duct are: the sector angle, the relative location of the duct to the curvature direction, the duct radius ratio, the dimensional curvature, and the axial pressure gradient. The general behavior of the axial and secondary velocity distributions in an annular sector duct will be discussed in this section first. The effect of each major parameter on the flow behavior will then be discussed in sequence.

Figure 4 shows the typical flow patterns in the annular sector duct with a π degree sector angle. $\epsilon = 0.2$, $-dp/ds = 50{,}000$, and $r^{\#} = 0.5$ have been used to calculate these figures. When $\alpha = 0$, Fig. 4(*a*) indicates that the centrifugal force direction is from left to right, which coincides with the symmetrical centerline of the annular sector duct. Due to the flow symmetry, only half-axial and secondary flows are presented in this figure. The top half of Fig. 4(*a*) represents the axial velocity distribution, while the bottom half represents a vector plot for the secondary flow. Since high axial velocity is near the core region, between the inner and outer wall, a northeast direction flow in the cross section is generated by centrifugal force, as seen in this figure. For mass conservation, the downward (southeast direction) flow is generated near the inner and outer walls by the pressure gradient. As a result, two vortices are created in each half-domain. The vortex near the outer wall is much stronger than the one near the inner wall. This figure also shows that the high axial velocity contours are pushed toward the outer wall, which creates a large velocity gradient along the outer wall region. Figure 4(*b*) shows the axial and secondary flows in a π degree annular sector duct when $\alpha = \pi$. As in Fig. 4(*a*), only half-domains for axial and secondary flows are plotted in this figure due to the symmetry of the flows. Centrifugal force drives the fluid flowing along the middle of the duct, and two backward flows are generated in the opposite direction near the solid walls. As a result, the high axial velocity region is pushed toward the straight surface in the right hand side, which creates two separate and symmetrical velocity peaks in the cross section. Unlike the case in Fig. 4(*a*), however, three vortices are detected in each half-domain in Fig. 4(*b*). Two of them are near the inner wall and one is near

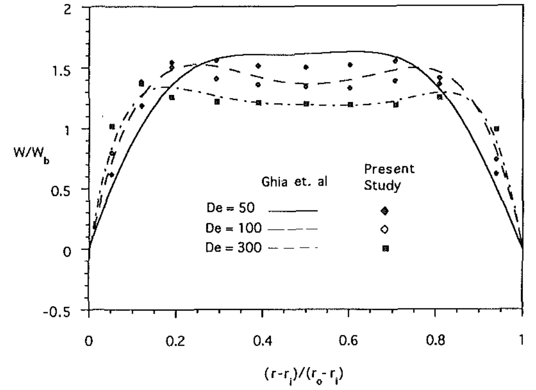

b) radial direction.

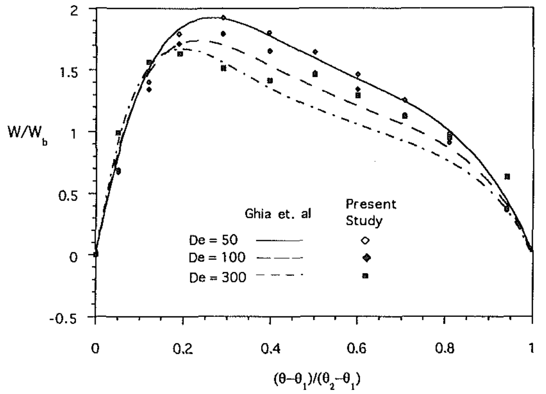

b) tangential direction.

Fig. 3 Comparison of the axial velocity distribution

Table 1 Comparison of the present results with Sparrow et al. (1964)

$r^{\#} = \frac{R_i}{R_o}$	fRe Present Study	fRe Sparrow et al. (1964)	Deviation
0.1	15.76	15.61	0.95
0.3	16.98	16.86	0.77
0.5	18.84	18.76	0.43
0.7	20.87	20.84	0.14
0.9	22.92	23.00	0.35

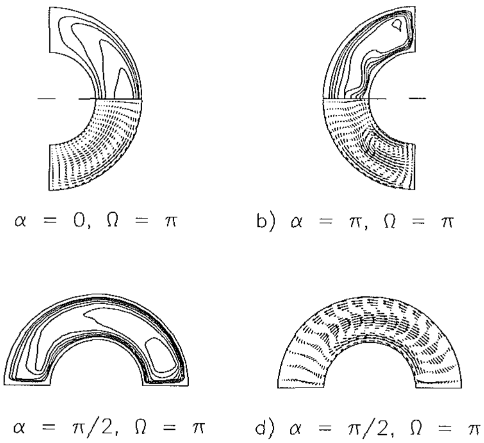

a) $\alpha = 0$, $\Omega = \pi$ b) $\alpha = \pi$, $\Omega = \pi$

c) $\alpha = \pi/2$, $\Omega = \pi$ (axial velocity) d) $\alpha = \pi/2$, $\Omega = \pi$ (secondary flow)

Fig. 4 General flow behavior in the curved annular sector duct ($r^{\#} = 0.5$, $-dp/ds = 50{,}000$, $\epsilon = 0.2$)

Table 2 Independent test for fully developed flow

$l \times m$	$dp/ds = -50{,}000$, $\epsilon = 0.2$, $\Omega = \pi$, $\alpha = \pi$, $r^{\#} = 0.5$		$dp/ds = -50{,}000$, $\epsilon = 0.2$ $\Omega = \pi$, $\alpha = 0$, $r^{\#} = 0.9$		$dp/ds = -50{,}000$, $\epsilon = 0.2$, $\Omega = \pi$, $\alpha = \frac{\pi}{2}$, $r^{\#} = 0.1$	
	fRe	Re	fRe	Re	fRe	Re
15×15	26.13	598.3	6.45	25.06	347.3	41.48
20×20	26.30	594.2	6.42	25.23	337.6	42.67
30×30	26.47	590.4	6.38	25.40	337.6	42.67
60×60	26.47	590.4	6.33	25.58	337.6	42.67
80×20			6.34	25.53		

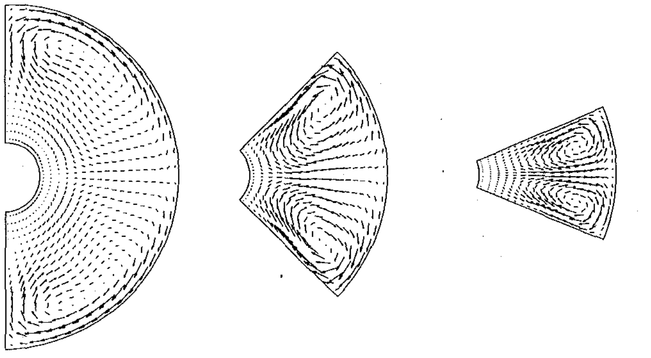

a) $\Omega = \pi$ b) $\Omega = \pi/2$ c) $\Omega = \pi/4$

Fig. 5 Effect of the sector angle on the secondary flow pattern ($r^{\#} = 0.2$, $-dp/ds = 50{,}000$, $\epsilon = 0.2$, $\alpha = 0$)

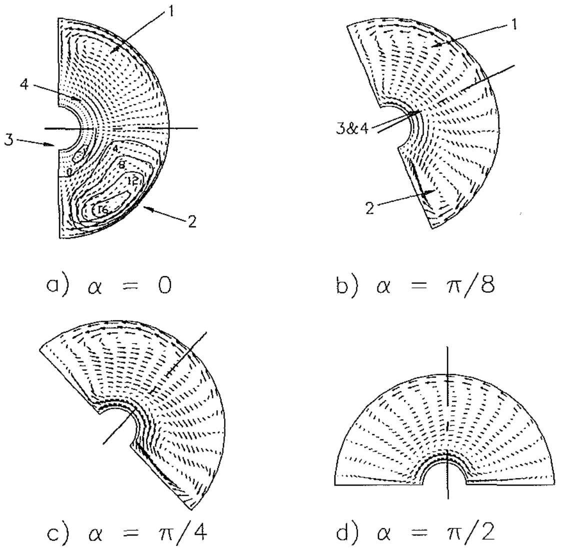

a) $\alpha = 0$ b) $\alpha = \pi/8$

c) $\alpha = \pi/4$ d) $\alpha = \pi/2$

Fig. 6 Effect of angle, α, on the secondary flow pattern ($-dp/ds = 50{,}000$, $r^{\#} = 0.2$, $\epsilon = 0.2$, $\Omega = \pi$)

Table 3 Friction coefficient changes with the α angle

α	0	$\frac{\pi}{8}$	$\frac{\pi}{4}$	$\frac{\pi}{2}$
fRe	37.6	37.7	38.3	39.3

the outer wall. Figures 4(*c*) and 4(*d*) illustrate the axial velocity and vector in the cross section plots for the case of the annular sector duct when $\alpha = \pi/2$ and $\Omega = \pi$. Figure 4(*c*) shows that the high axial velocity contours are pushed to the right hand side by centrifugal force. Figure 4(*d*) illustrates that only two vortices are generated in the entire domain of the curved annular sector duct.

Figure 5 demonstrates the effect of sector angle, Ω, on the vector plot of the secondary flow. In the computation, $r^{\#} = 0.2$, $-dp/ds = 50{,}000$, $\epsilon = 0.2$, and $\alpha = 0$ have been applied. As seen in the figure, four vortices exist in the $\Omega = \pi$ duct. As the Ω angle is reduced to $\pi/2$, the number of vortices reduces to two. Upon further reduction of sector angle, Ω, the number of vortices still remain at two. When $\Omega = \pi$ (Fig. 5(*a*)), the left-hand side wall is perpendicular to the direction of the curvature. A secondary flow can be easily generated starting from these straight side walls, which results in two vortices in each half-domain of the cross section. When the Ω angle becomes small, the side wall is almost parallel to the curvature direction, as seen in Figs. 5(*b*) and 5(*c*). In these cases, the high axial velocity near the symmetrical centerline region will generate a stronger centrifugal force along the center instead of being generated near the side wall region. As a result, only one vortex will be created in each half-domain.

Figure 4 shows that the axial and secondary flow patterns in a curved annular sector duct can be dramatically affected with different α angles, which is due mainly in response to the interaction of the irregular boundary and centrifugal force. The ducts represented in Fig. 4 are three very special cases of $\alpha = 0$, $\pi/2$, and π. In fact, the flow patterns in the duct with other α angles are different from these three special cases. However, one might express the flow pattern in some combination of these three typical flow patterns. Figure 6 reveals the effect of angle, α, on the secondary flow pattern for a curved annular sector duct when $\Omega = \pi$. The other controlling parameters in this figure are: $r^{\#} = 0.2$, $-dp/ds = 50{,}000$, and $\epsilon = 0.2$. Figure 6(*a*) shows the typical symmetrical flow for an $\alpha = 0$ duct. As was discussed earlier, two vortices exist in each half-domain. In order to clearly explain this phenomena, these vortices are labeled by numbers, 1 to 4. In fact, the vortices near the outer wall is much stronger than that near the inner wall, which can be easily found by examining the stream function in the bottom half-domain. As α rotates from 0 to $\pi/8$, vortex number 1 is pushed toward the bottom half of the domain, and vortex number 2 is pushed toward the bottom corner. Vortex numbers 3 and 4 are combined into one vortex near the inner wall. As α rotates from $\pi/8$ to $\pi/4$, vortex number 1 is pushed even deeper along the outer wall, and vortex number 2 in the bottom corner is pushed toward the inner wall. As α rotates further, to $\pi/2$, the two vortices near the inner wall are eventually combined, and a two-vortex flow pattern is created. The change in the flow pattern between these ducts results in a change in the friction coefficient. Table 3 gives a comparison of the friction coefficient as a function of the α angle. This table indicates that the friction coefficient increases as α increases. The value of the friction coefficients for the $\alpha = \pi/8$ and $\alpha = \pi/4$, angle ducts lay between that of the $\alpha = 0$ and $\alpha = \pi/2$ ducts.

Figure 5 indicates that when the Ω angle is reduced from π to $\pi/2$, the number of vortices reduces from four to two. Figure 6 shows the effect of α angle on the secondary flow. The parameters used during the calculations are $\Omega = \pi$, $-dp/ds = 50{,}000$, $\epsilon = 0.2$, and $r^{\#} = 0.2$. When $\alpha = 0$, symmetrical vortices are found in the duct. As α increases, the flow still remains to the two vortex pattern. However,the vortex originally in the top half domain moves toward the outer wall, and the other vortex moves toward the inner wall. When $\alpha = \pi/2$, one vortex is located near the outer wall and the other one is located near the inner wall. Figure 6 indicates that the vortex structure of the secondary flow is strongly dependent on the Ω angle. Although it is not shown here, the larger the Ω angle, the more complex the secondary flow pattern will be. Therefore, we will hereinafter concentrate our discussion on the flow behavior of a curved annular sector duct when $\Omega = \pi$. It is impossible, however, and also unnecessary, to discuss all of the possibilities of α angle. Therefore, only three typical ducts ($\alpha = 0$, $\pi/2$, and π) have been studied.

Figure 7 illustrates that the axial and secondary flow patterns are changed profoundly with the radius ratio for these ducts with an $\alpha = \pi$ angle. The controlling parameters used in these calculations are $\alpha = \pi$, $-dp/ds = 50{,}000$, $\epsilon = 0.2$, and $\Omega = \pi$. Figure 7(*a*) shows that three vortices exist in the half-domain of the duct when $r^{\#} = 0.5$, two near the inner wall and one near the outer wall, which are labeled as vortex numbers 1 to 3. When $r^{\#}$ is reduced from 0.5 to 0.2, vortex number 1 becomes stronger than before. Vortex 2 is pushed towards the region near the straight boundary between the inner and outer walls, and dramatically reduces its intensity. It is worthwhile to note that a right-to-left direction high velocity flow near the centerline is generated by the vortex. This flow is in the opposite direction to the centrifugal force direction. Brought on by this secondary flow stream, the low axial velocity fluid penetrates into the high axial velocity contour along the centerline, Fig. 7(*b*). When $r^{\#}$ is further reduced from 0.2 to 0.1, vortex number 2 vanishes, and only two vortices exist in each half-domain, as seen in Fig. 7(*c*). When $r^{\#} = 0$, the annular sector duct becomes a semicircular duct. Figure 7(*d*) shows that only one vortex exists in each half-domain. This figure also illustrates that the high axial velocity contours are pushed toward the right side boundary, and create a larger velocity gradient along this boundary.

Table 4 compares the changes in the friction coefficient with the radius ratio variation for the curved annular sector duct when $\Omega = \pi$. The results of the friction coefficient of the straight annular duct are listed in this table. In this table, subscripts, *c* and *s* represent the curved and straight ducts, respectively. It can also be seen that the fRe increases as $r^{\#}$ is increased for the straight annular sector duct. For example, when $r^{\#}$ is increased from 0.1 to 0.9, the fRe increases almost 47 percent. However, for the curved annular sector duct, fRe increases as $r^{\#}$ is decreased, which is due to the higher velocity gradient near the solid boundary created by the secondary flow. The smaller the $r^{\#}$, the stronger the secondary flow, and ultimately the higher the fRe will be. It is interesting to see that when $r^{\#} = 0.9$, the fRe of the curved annular sector duct is smaller than that of a straight annular duct. This phenomenon has been found by Larrain and Bonilla (1970) for a curved duct with a circular cross section for a very small Dean number. In fact, due to the large boundary/cross section area ratio, the Reynolds number of the $r^{\#} = 0.9$ duct is less than 0.2 percent of the Reynolds number in the $r^{\#} = 0$ duct. This represents a very small Dean number flow, if one uses the definition of the Dean number defined by Larrain and Bonilla (1970), De = Re $\epsilon^{1/2}$. Table 4 also indicates that for the curved duct, the fRe increases significantly only when $r^{\#}$ is smaller than 0.6. The large $r^{\#}$ duct indicates a longer, narrower cross section duct. It is difficult to generate a considerable secondary flow in this kind of duct. This table also shows the effect of the α angle on the fRe. For a large radius ratio, the $\alpha = 0$ duct has the highest fRe value. When $r^{\#}$ is smaller than 0.6, the $\alpha = \pi/2$ duct has the higher fRe value among the three ducts. In this table, the $\alpha = \pi$ duct has the lowest fRe value among the three ducts. This is true only when the Dean number is small. Generally speaking, the secondary flow in an $\alpha = \pi$ duct is more complex and is usually stronger than in the duct with other α angles. Keeping in mind that $-dp/ds$ is defined on the centerline of the holding pipe, the duct with the $\alpha = \pi$ angle has the smallest surface area, while the duct with the $\alpha = 0$ angle has the largest surface area among all possible annular sector ducts for a fixed length of the centerline, *ds*. This is why the duct with the $\alpha = 0$ angle has a larger fRe value when the secondary flow is weak.

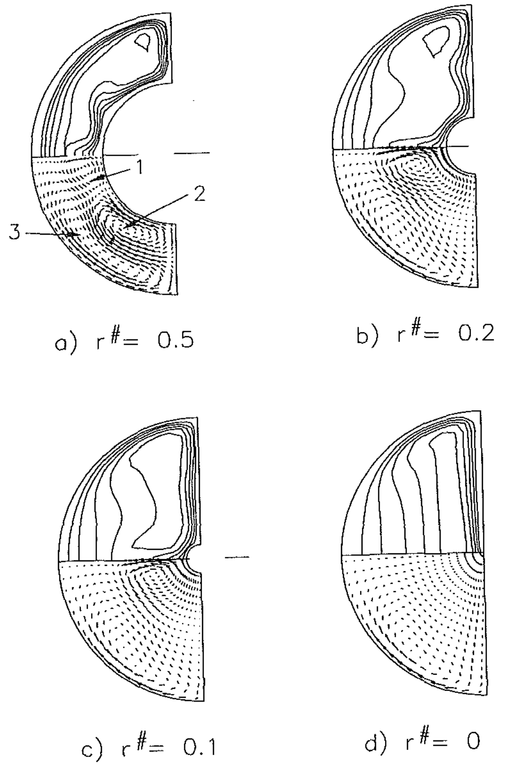

a) $r^{\#} = 0.5$ b) $r^{\#} = 0.2$

c) $r^{\#} = 0.1$ d) $r^{\#} = 0$

Fig. 7 Effect of $r^{\#}$ on the flow behavior of the curved annular sector duct ($-dp/ds = 50{,}000$, $\epsilon = 0.2$, $\Omega = \pi$, $\alpha = \pi$)

For the study of a curved duct with a circular cross section, usually only one parameter, the Dean number, which reflects both the axial pressure gradient and the dimensionless curvature, is used. For a curved annular sector duct, however, retaining the same Dean number usually cannot guarantee that the two ducts produce the same axial and secondary flow patterns. For example, in Table 5, the two cases have the same Dean number with different $-dp/ds$ and ϵ combinations. The results indicate that the fRe values in these two cases can have an almost 14 percent difference. Therefore, the effect of the

Table 4 Effect of the radius ratio $\epsilon = 0.2$ $-dp/ds = 50{,}000$

$r^{\#}$	$(f\mathrm{Re})_s$	$\alpha = 0$		$\alpha = \frac{\pi}{2}$		$\alpha = \pi$	
		$(f\mathrm{Re})_c$	$(f\mathrm{Re})_c/(f\mathrm{Re})_s$	$(f\mathrm{Re})_c$	$(f\mathrm{Re})_c/(f\mathrm{Re})_s$	$(f\mathrm{Re})_c$	$(f\mathrm{Re})_c/(f\mathrm{Re})_s$
0.9	23.0	22.9	0.996	22.7	0.987	22.7	0.987
0.8	21.9	22.1	1.01	21.7	0.991	21.5	0.982
0.7	20.8	21.7	1.04	22.7	1.09	21.2	1.02
0.6	19.8	23.2	1.17	23.8	1.20	22.3	1.13
0.5	18.8	26.6	1.41	27.9	1.49	26.3	1.40
0.3	16.9	33.9	2.01	34.0	2.01	31.42	1.86
0.1	15.6	37.6	2.41	39.7	2.54	35.3	2.26
0.0	15.7	39.5	2.52	41.9	2.67	37.6	2.39

Table 5 Effect of the dimensionless curvature

ϵ	$-dp/ds$	De	Re	fRe
0.05	50,000	11,180	843	25.45
0.5	15,811	11,180	327	22.45

axial pressure gradient and the dimensionless curvature on the flow behavior will be studied separately.

Since the Dean number is proportional to the axial pressure gradient, $-dp/ds$, it can be expected that $-dp/ds$ will significantly affect the flow pattern of a curved annular sector duct. Figure 8 shows the axial and secondary flow patterns in the annular sector ducts when $\alpha = 0$ and $\alpha = \pi$, $\epsilon = 0.2$, $\Omega = \pi$ and $r^{\#} = 0.4$. At a small pressure gradient, $-dp/ds =$ 2,000, Fig. 8(*a*) shows that for the $\alpha = 0$ duct, the axial velocity gradient near the solid walls does not significantly increase as compared with the straight annular sector duct. However, as $-dp/ds$ increases from 2,000 to 200,000, Fig. 8(*b*) shows that the axial velocity gradient near the outer wall dramatically increases, which indicates a considerable increase in the friction coefficient. However, Fig. 8(*c*) and Fig. 8(*d*) reveal totally different axial velocity flow patterns. At a low pressure gradient, the axial velocity contour is in a crescent shape, while for the large pressure gradient, the high axial velocity contours are separated from the centerline, and for a large pressure gradient, are isolated near the straight boundary on the right-hand side. Increasing the axial pressure gradient significantly increases the axial velocity gradient along the solid boundaries, as seen in Fig. 8(*d*). Considering the secondary flow, Fig. 8(*c*) shows that in the case of a low axial pressure gradient flow, two vortices exist in each half-domain, while the one near the outer wall dominates the secondary flow. For the case of a high axial pressure gradient, three vortices are observed in each half-domain, while the vortex near the inner wall makes a significant contribution to the axial velocity distribution.

Table 6 shows the effect of the friction coefficient as a function of the axial pressure gradient. For a small axial pressure gradient value and the $\alpha = 0$ angle, the straight annular sector duct has a higher fRe value than the other ducts listed in this table. When $\alpha = \pi$, the annular sector duct has the smallest fRe, while for the $\alpha = \pi/2$ duct the fRe value for the annular sector duct appears in between the $\alpha = 0$ and $\alpha = \pi/2$ duct. As the axial pressure gradient increases due to the strong secondary flow, the fRe value for the $\alpha = \pi$ duct rapidly surpasses that of the $\alpha = 0$ duct. For example, at

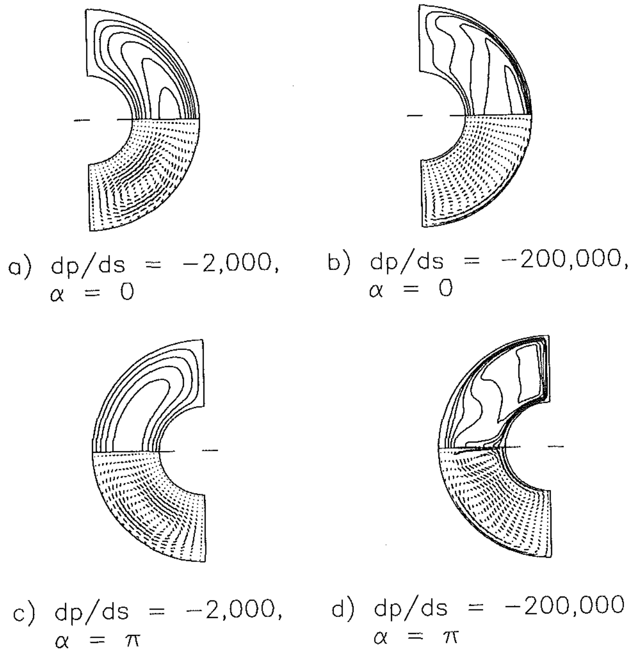
a) dp/ds = −2,000, α = 0
b) dp/ds = −200,000, α = 0
c) dp/ds = −2,000, α = π
d) dp/ds = −200,000 α = π

Fig. 8 Effect of the axial pressure gradient on the flow behavior of the curved annular sector duct ($\epsilon = 0.2$, $r^{\#} = 0.4$, $\Omega = \pi$)

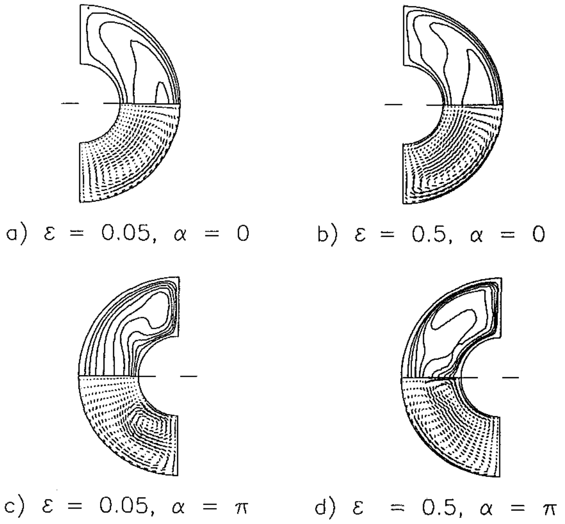
a) ε = 0.05, α = 0
b) ε = 0.5, α = 0
c) ε = 0.05, α = π
d) ε = 0.5, α = π

Fig. 9 Effect of the curvature ratio on the flow behavior of the curved annular sector duct ($-dp/ds = 50{,}000$, $r^{\#} = 0.4$, $\Omega = \pi$)

Table 6 Effect of the axial pressure gradient $r^{\#} = 0.4$ $\epsilon = 0.2$ $(f\text{Re})_s = 18.8$

$-dp/ds$	$\alpha = 0$		$\alpha = \frac{\pi}{2}$		$\alpha = \pi$	
	$(f\text{Re})_c$	$(f\text{Re})_c/(f\text{Re})_s$	$(f\text{Re})_c$	$(f\text{Re})_c/(f\text{Re})_s$	$(f\text{Re})_c$	$(f\text{Re})_c/(f\text{Re})_s$
1,000	20.6	1.10	17.80	0.947	16.80	0.89
5,000	20.8	1.11	18.70	0.990	17.90	0.95
10,000	21.4	1.14	20.90	1.110	20.20	1.070
50,000	28.2	1.50	30.60	1.630	31.60	1.680
100,000	33.2	1.76	36.20	1.930	38.40	2.040
500,000	51.8	2.76	58.00	3.090	64.40	3.430

Table 7 Effect of the dimensionless curvature $r^{\#} = 0.5$ $-dp/ds = 20{,}000$ $(f\text{Re})_s = 18.8$

ϵ	$\alpha = 0$		$\alpha = \frac{\pi}{2}$		$\alpha = \pi$	
	$(f\text{Re})_c$	$(f\text{Re})_c/(f\text{Re})_s$	$(f\text{Re})_c$	$(f\text{Re})_c/(f\text{Re})_s$	$(f\text{Re})_c$	$(f\text{Re})_c/(f\text{Re})_s$
0.7	26.60	1.42	31.30	1.66	32.30	1.72
0.5	25.20	1.34	27.40	1.46	27.80	1.48
0.3	23.40	1.24	23.80	1.27	24.30	1.29
0.2	22.40	1.19	22.50	1.20	22.40	1.19
0.1	20.60	1.10	20.40	1.09	20.40	1.09
0.01	19.00	1.01	18.80	1.00	18.90	1.01

$-dp/ds = 500{,}000$ with an $f\mathrm{Re}$ value of the $\alpha = \pi$ duct is about 24 percent higher than that for the $\alpha = 0$ duct.

Figure 9 shows the effect of the dimensionless curvature on the axial and secondary flows for $\alpha = 0$ and π ducts. The controlling parameters during the calculation are: $-dp/ds = 50{,}000$, $\Omega = \pi$, and $r^{\#} = 0.4$. Figures 9(*a*) and 9(*b*) indicate that even when the curvature increases 10 times, from 0.05 to 0.5, no significant change is found in the axial and secondary flow patterns for the $\alpha = 0$ duct. However, Figs. 9(*c*) and 9(*d*) reveal a considerable difference in the flow patterns for the $\alpha = \pi$ duct with different curvatures. When $\epsilon = 0.05$, only two vortices are observed in the half-domain, while three vortices can be found when the curvature reaches 0.5. Table 7 shows the effect of curvature on the friction coefficient for fully developed flow. This table indicates that when curvature, ϵ, is smaller than 0.2, the $f\mathrm{Re}$ value for the three ducts is almost the same. However, as the curvature increases, the $f\mathrm{Re}$ value for the $\alpha = \pi$ duct rapidly surpasses that of the other two ducts. Finally, at $\epsilon = 0.7$, the $f\mathrm{Re}$ value for the $\alpha = \pi$ duct is almost 21 percent higher than for the $\alpha = 0$ duct.

Concluding Remarks

In this paper, the flow behavior in the fully developed curved annular sector duct is investigated and discussed. Five parameters have been identified as the major controlling variables: the sector angle, Ω; the angle between the duct symmetrical centerline and the curvature direction, α; the radius ratio of the inner/outer walls, $r^{\#}$; the holding pipe curvature, ϵ; and the axial pressure gradient, $-dp/ds$. The sector angle, Ω, can significantly affect secondary flow behavior. For a small Ω angle, only two vortices are observed in the case of a moderate Dean number. When $\Omega = \pi$, the vortex structures can be very complex, which may depend on other parameters, especially the α angle. For example, when $\alpha = 0$, four vortices are observed in the $\Omega = \pi$ duct. As α increases, the vortex number reduces to three, and then to two, when $\alpha = \pi/2$. Upon a further increase of α, the vortex number increases again, and eventually the vortex number reaches six, as $\alpha = \pi$. The radius ratio variation does not significantly affect the vortex structure, except in the small radius ratio region. However, the friction coefficient of the annular sector duct is considerably affected by the $r^{\#}$ ratio. When $r^{\#}$ is larger than 0.6, the friction coefficients of the curved annular sector duct are not remarkably different from the straight annular sector duct. However, with a small $r^{\#}$ ratio, the friction coefficient of a curved annular sector duct can be tripled as compared to the straight duct. For a moderate range of Dean numbers, increasing the pipe curvature and the axial velocity does not change the flow vortex structure. However, increasing ϵ and $-dp/ds$ can significantly increase the velocity gradient near the wall region, which results in an enhancement of the friction coefficient in the curved annular sector duct.

Acknowledgment

The results presented in this paper were obtained in the course of research sponsored by the National Science Foundation under grant no. CTS-9017732.

References

Akiyama, M., and Cheng, K. C., 1971, "Boundary Vorticity Method for Laminar Forced Convection Heat Transfer in Curved Pipe," *International Journal of Heat and Mass Transfer*, Vol. 14, p. 1659.

Austin, L. R., and Seader, J. D., 1973, "Fully Developed Viscous Flow in Coiled Circular Pipes," *American Institute of Chemical Engineering Journal*, Vol. 19, p. 85.

Berger, S. A., Talbot, L., and Yao, L. S., 1983, "Flow in Curved Pipes," *Annual Review of Fluid Mechanics*, Vol. 15, pp. 461–512.

Cheng, K. C., and Akiyama, M., 1970, "Laminar Forced Convection Heat Transfer in Curved Rectangular Channels," *International Journal of Heat and Mass Transfer*, Vol. 13, pp. 471–490.

Cheng, K. C., Lin, R. C., and Ou, J. W., 1976, "Fully Developed Laminar Flow in Curved Rectangular Channels," ASME JOURNAL OF FLUIDS ENGINEERING, Vol. 98, pp. 41–48.

Collins, W. M., and Dennis, S. C. R., 1975, "The Steady Motion of a Viscous Fluid in a Curved Tube," *Quarterly Journal of Mechanics and Applied Mathematics*, Vol. 28, p. 133.

Dean, W. R., 1927, "Note on the Motion of Fluid in a Curved Pipe," *Philosophy Magazine*, Vol. 4, pp. 208–223.

Dennis, S. C. R., and Ng, M., 1982, "Dual Solutions for Steady Laminar Flow Through a Curved Tube," *Journal of Mechanics and Applied Mathematics*, Vol. 35, pp. 305–324.

Ghia, K. N., Ghia, U., and Shin, C. T., 1987, "Study of Fully Developed Incompressible Flow in Curved Ducts Using a Multi-Grid Technique, " ASME JOURNAL OF FLUIDS ENGINEERING, Vol. 109, pp. 226–236.

Ghia, K. N., and Sokhey, J. S., 1977, "Laminar Incompressible Viscous Flow in Curved Ducts of Rectangular Cross Section," ASME JOURNAL OF FLUIDS ENGINEERING, Vol. 99, pp. 640–648.

Joseph, B., Smith, E. P., and Adler, R. J., 1975, "Numerical Treatment of Laminar Flow in Helically Coiled Tubes of Square Cross Section," *American Institute of Chemical Engineers*, Vol. 21, pp. 965–974.

Kumar, V. R., Rankin, G. W., and Szidhar, K., 1989, "Fully Developed Flow of Power Low Fluid in Curved Ducts with Heat Transfer," *Numerical Heat Transfer*, Part A, Vol. 16, pp. 101–118.

Larrain, J., and Bonilla, C., 1970, "Theoretical Analysis of Pressure Drop in the Laminar Flow of Fluid in a Coiled Pipe," *Transactions of Society Rheology*, Vol. 14, p. 135.

Mille, P., Vehrenkamp, R., and Schulz-Dubois, E. O., 1985, "The Development and Structure of Primary and Secondary Flow in a Curved Square Duct," *Journal of Fluid Mechanics*, Vol. 151, pp. 219–241.

Mishra, P., and Gupta, S. N., 1979, "Momentum Transfer in Curved Pipes," *Industrial Engineering and Chemical Process Design and Development*, Vol. 18, No. 1, pp. 130–137.

Mori, Y., Uchida, Y., and Ukon, T., 1971, "Forced Convective Heat Transfer in a Curved Channel with a Square Cross Section," *International Journal of Heat and Mass Transfer*, Vol. 14, pp. 1787–1805.

Niida, T., 1980, "Analytical Solution for the Velocity Distribution in Laminar Flow in the Annular-Sector Duct," *International Chemical Engineering*, Vol. 20, pp. 258–265.

Patankar, S. V., 1980, *Numerical Heat Transfer and Fluid Flow*, Hemisphere, Washington, D.C.

Sparrow, E. M., Chen, T. S., and Johnsson, V. K., 1964, "Laminar Flow and Pressure Drop in Internally Finned Annular Ducts," *International Journal of Heat and Mass Transfer*, Vol. 7, pp. 583–585.

Takami, T., and Sudou, K., 1984, "Flow Through a Curved Pipe with Elliptic Cross Sections," *Bulletin of Japanese Society of Mechanical Engineers*, Vol. 27, No. 228, pp. 1176–1181.

Thomas, R. M., and Walters, K., 1965, "On the Flow of an Elastico-Viscous Liquid in a Curved Pipe of Elliptic Cross Section Under a Pressure Gradient," *Journal of Fluid Mechanics*, Vol. 21, No. 1, pp. 173–182.

Topakoglu, H. C., and Ebadian, M. A., 1985, "On the Steady Laminar Flow of an Incompressible Viscous Fluid in a Curved Pipe of Elliptical Cross Section," *Journal of Fluid Mechanics*, Vol. 158, pp. 329–340.

Topakoglu, H. C., and Ebadian, M. A., 1987, "Viscous Laminar Flow in a Curved Pipe of Elliptical Cross Section," *Journal of Fluid Mechanics*, Vol. 184, pp. 571–580.

Truesdell, L. C., and Adler, R. J., 1970, "Numerical Treatment of Fully Developed Laminar Flow in Helically Coiled Tubes," *American Institute of Chemical Engineers*, Vol. 16, p. 1010.

The Stability of Pipe Entrance Flows Subjected to Axisymmetric Disturbances

D. F. da Silva

E. A. Moss

School of Mechanical Engineering,
University of the Witwatersrand,
Johannesburg,
WITS 2050 South Africa

This paper reexamines an important unresolved problem in fluid mechanics—the discrepancy between measurements and predictions of stability in pipe entrance flows. Whereas measured critical Reynolds numbers are relatively insensitive to velocity profile shape in the streamwise direction, the theoretical results indicate a rapid increase, both as the equilibrium profile is approached, and toward the inlet. The current work uses the displacement thickness based Reynolds number as a rational basis on which to compare new stability predictions obtained by means of the Q-Z algorithm, with existing theoretical results. Although the present data are shown to be the only that are consistent with the classical parallel boundary layer limit towards the inlet, they still deviate increasingly with axial distance from the only available experimental results. By examining pipe inlet stability data in relation to boundary layer measurements and predictions, the work effectively questions the commonly held belief that streamwise variations of flow alone are responsible for these deviations, suggesting that the finite amplitude nature of the applied disturbances is the most likely cause.

1 Introduction

This study is concerned with the unresolved issue of pipe entrance flow stability. Analyses of fully developed pipe Poiseuille flows have demonstrated that they are stable (both in a temporal and a spatial sense) to infinitesimal axisymmetric and nonaxisymmetric disturbances (Sexl, 1927; Corcos and Sellars, 1959; Gill, 1965; Lessen et al., 1968; Davey and Drazin, 1969; Burridge, 1970; Garg and Rouleau, 1972). Experimentally these calculations have been shown to accurate for axisymmetric disturbances by Leite (1959). Of the studies involving nonaxisymmetric disturbances, experiments (for example Fox et al., 1968) indicate spatial instability—in contradiction with the analysis—but attributed by Garg and Rouleau (1972) to the finite amplitude nature of the experimentally superimposed disturbances, rather than to flaws in the analysis. Patera and Orszag (1981) established that finite amplitude equilibria do not exist with respect to finite amplitude axisymmetric disturbances, thus indicating that fully developed pipe flows are stable to all axisymmetric disturbances. Although in a later paper Orszag and Patera (1983) showed that certain aspects of transition in such flows may be explained by a secondary instability, no definitive answers yet exist to this problem.

Aside from the possible local instability of Hagen Poiseuille flows to finite amplitude disturbances, experimentally observed turbulence in such systems may be attributed to the growth of small disturbances in the boundary layer associated with the hydrodynamic development region of a circular tube, leading to transition and the downstream transport of turbulent structures. Extensive analytical investigations of pipe entrance flow stability have been performed by Tatsumi (1952), Huang and Chen (1974a, b), Gupta and Garg (1981), and Garg (1981), some of which are shown for comparison purposes in Fig. 1. Even though these studies succeeded in ascertaining regions of instability within the laminar entrance region it may be seen that they differ considerably not only from one another, but also from the experimental results of Sarpkaya (1975), the axisymmetric portion of which is shown.

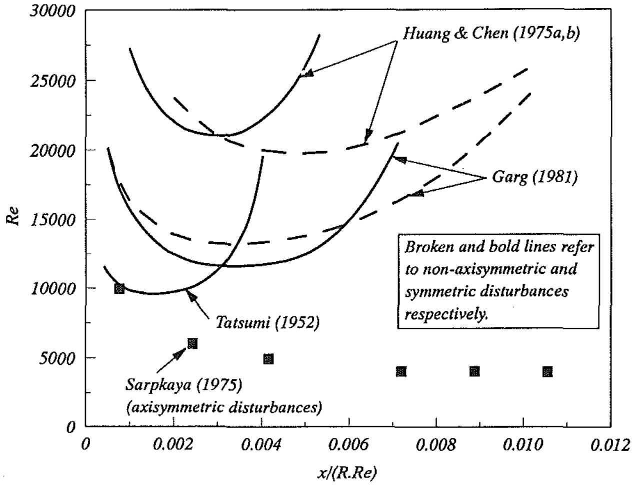

Fig. 1 Comparison of previous results: axial variation of critical Reynolds number

---

Contributed by the Fluids Engineering Division for publication in the JOURNAL OF FLUIDS ENGINEERING. Manuscript received by the Fluids Engineering Division June 16, 1992; revised manuscript received February 3, 1993. Associate Technical Editor: A. Prosperetti.

Of the above analyses, Tatsumi used *almost similar* velocity profiles in conjunction with a boundary layer type asymptotic solution of the Sexl equation. These early results are generally considered to be unreliable (see for example Chen and Sparrow, 1967). Huang and Chen (1974a, b) utilized the Sparrow et al., (1963) base flow model to investigate *temporal* stability, while Gupta and Garg (1981) and Garg (1981) used the Hornbeck (1963) base flow model to analyze the *spatial* stability problem. Nevertheless it is well established that the neutral curve does not depend on whether the disturbances grow or decay in time or in space: the alternatives degenerate to the same analytical problem (Gaster, 1962 and 1965). Gupta and Garg established that stability calculations are strongly sensitive to velocity profile data and ascribed deviations between their results and those of Haung and Chen to differences in the base flow models used. Since the Hornbeck model of developing flow in a pipe entrance has been shown (Schmidt and Zeldin, 1969; Shah, 1978) to be more precise than the Sparrow model, Garg's results are customarily considered to be the most accurate; however this opinion has never been particularly well justified in the literature.

It is commonly believed that deviations between experiment and analysis may be attributed to the latter ignoring the streamwise variations inherent to such flows. Nonetheless, prior to embarking on a non-parallel analysis which would probably use the parallel flow analysis as its leading approximation, a definitive solution to the parallel problem is required.

Arising from the above, the objectives of this study were (i) to establish an acceptable means of assessing the relative accuracies of the various analyses, and (ii) if Garg's results were found to be lacking in accuracy, to establish a better set of parallel flow results for the pipe entrance flow problem, as a leading approximation to a future non-parallel flow analysis.

2 Comparison Between Analytical Results

While it is generally accepted that pipe flows are boundary-layer like in the vicinity of the inlet, this appears not to have been quantified in the literature. Since the stability behavior of zero pressure gradient, parallel flow boundary layer results is well-established, it seemed logical to examine the asymptotic trends of the various entrance stability analyses towards the inlet as this boundary layer limit is approached.

Therefore the existing theoretical results of Tatsumi (1952), Huang and Chen (1974b), and Garg (1981) were compared (Fig. 2) in a framework of Re_{δ^*} versus $\bar{x}$ [$\bar{x}=x/(R.\mathrm{Re})$; $\mathrm{Re}=U_0R/\nu$; $\mathrm{Re}_{\delta^*}=U_0\delta^*/\nu$; δ^* = displacement thickness; R = pipe radius; U_0 = pipe cross-sectional mean velocity]. This was implemented simply by multiplying the critical Reynolds numbers of the existing results by the dimensionless displacement thicknesses δ^*/R computed using the method of Mohanty and Asthana (1978).

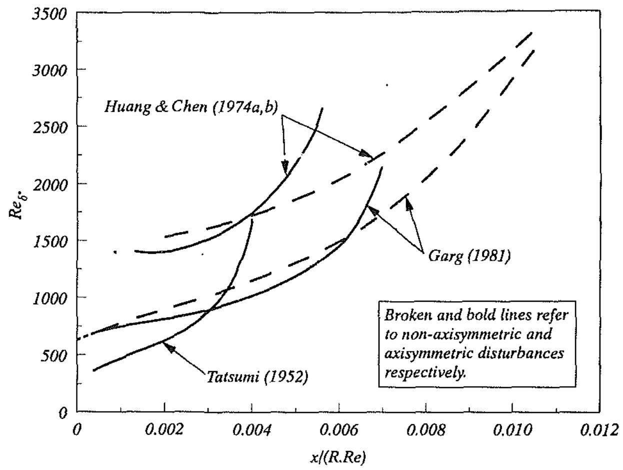

Fig. 2 Comparison of previous results: axial variation of critical Reynolds number based on displacement thickness

As $\bar{x}\to 0$ and the pressure gradient parameter $\Lambda=(\delta^2/\nu)dU_c/dx\to 0$ (U_c is centerline velocity and δ the boundary layer thickness), the results would be expected to approach the well-accepted *parallel* boundary layer stability limit of $\mathrm{Re}_{\delta^*}=520$ (given for example by Jordinson's (1970) study in the absence of a pressure gradient). It is seen that while Garg analysis is closest to fulfilling this requirement, the limit toward which his results approach is about 25 percent too high, motivating the further part of this study whose purpose was to develop a more accurate solution to the pipe entrance stability problem. From the outset it was decided to confine the current work to axisymmetric disturbances, for the reason that Garg (1981) found the flow to be more unstable to this mode of disturbance than to the nonaxisymmetric disturbance with an angular wavenumber of unity.

3 Analysis

The approach involved the development of an appropriate base flow system, and a solution to the Sexl equation, both of which are briefly outlined below.

The *entrance* of a steady pipe flow is characterized by that

Nomenclature

c = phase velocity
$\bar{c}$ = dimensionless phase velocity [c/U_0]
Re = Reynolds number based on radius [U_0R/ν]
Re_{δ^*} = Reynolds number based on displacement thickness [$U_0\delta^*/\nu$]
r = radial coordinate
$\bar{r}$ = dimensionless radial coordinate [r/R]
R = pipe radius
t = time
u = base flow axial velocity
$\bar{u}$ = dimensionless base flow axial velocity [u/U_0]
v = base flow radial velocity
$\bar{v}$ = dimensionless base flow radial velocity [$v\mathrm{Re}/U_0$]
$\bar{t}$ = dimensionless time [$\nu t/R^2$]
U_0 = pipe cross-sectional mean velocity
U_c = pipe centerline velocity
x = axial coordinate (distance from pipe inlet)
$\bar{x}$ = dimensionless axial coordinate [$x/(R.\mathrm{Re})$]
α = wavenumber
$\bar{\alpha}$ = dimensionless wavenumber [αR]
α^* = dimensionless wavenumber [$\alpha\delta^*$]
δ = boundary layer thickness
δ^* = displacement thickness
ζ = vorticity
$\bar{\zeta}$ = dimensionless vorticity [$\zeta R/U_0$]
θ = angular coordinate
Λ = pressure gradient parameter [$(\delta^2/\nu)dU_0/dx$]
$\bar{\lambda}$ = dimensionless wavelength [$2\pi/\bar{\alpha}$]
ν = fluid kinematic viscosity
ϕ = dimensionless amplitude function
ψ = stream function
$\bar{\psi}$ = dimensionless stream function [$\psi/(U_0R^2)$]
ψ' = dimensionless perturbation of stream function
$\bar{\omega}$ = dimensionless critical frequency [$\alpha^*\bar{c}$]

region over which velocity profiles change from a top-hat shape at the inlet to effectively parabolic (the so-called Hagen-Poiseuille shape) far downstream. A large number of investigators have attempted to analyze this class of flow (for example, Langhaar, 1942; Hornbeck, 1963; Campbell and Slattery, 1963; Sparrow et al., 1964; Mohanty and Asthana, 1978; Kanda, 1988). Van Dyke (1970) classified different methods in the literature into four categories: (i) numerical finite differences (ii) linearization of the inertia terms (iii) integral methods, and (iv) series expansions. A modified vorticity-stream approach was chosen for the present work.

The vorticity-stream ($\zeta - \psi$) form of the two-dimensional, incompressible, axisymmetric Navier Stokes equations were non-dimensionalized according to $\bar{r} = r/R$; $\bar{x} = x/(R.\mathrm{Re})$; $\bar{t} = (\nu t)/R^2$; $\bar{u} = u/U_0$; $\bar{v} = (v\mathrm{Re})/U_0$; $\bar{\psi} = \psi/(U_0 R^2)$ and $\bar{\zeta} = (\zeta R)/U_0$, where ζ is the vorticity and the other symbols have their usual meaning. Provided $\mathrm{Re} > > 1$ the equations reduce to the following:

$$\frac{\partial\bar{\zeta}}{\partial\bar{t}} + \frac{\partial(\bar{\zeta}\bar{v})}{\partial\bar{r}} + \frac{\partial(\bar{\zeta}\bar{u})}{\partial x} = \frac{\partial^2\bar{\zeta}}{\partial\bar{r}^2} + \frac{1}{\bar{r}}\frac{\partial\bar{\zeta}}{\partial\bar{r}} - \frac{\bar{\zeta}}{\bar{r}^2} \qquad (1)$$

with

$$\bar{u} = (1/2\pi\bar{r})\partial\bar{\psi}/\partial\bar{r};\ \bar{v} = -(1/2\pi\bar{r})\partial\bar{\psi}/\partial\bar{x};$$
$$-\bar{\zeta} = [\partial^2\bar{\psi}/\partial\bar{r}^2 - (1/\bar{r})\partial\bar{\psi}/\partial\bar{r}]/(2\pi)$$

The above equations do not contain Reynolds number and thus the truncation error known as implicit artificial viscosity (Roache, 1972a) will not affect the results. The first upwind differencing scheme was used to solve the equations[1] (Roache, 1972b). Dynamic instabilities were avoided by restricting the magnitude of the time increment, while static instabilities were not encountered. Pivotal increments were initially determined merely from centerline velocity convergence requirements.

The results of the current model (in the steady limit) were compared on the basis of centerline variations (U_c/U_0) with the experimental data of Nikuradse (published by Prandtl and Tietjens, 1931) and the analytical data of Hornbeck (1963), and were found to differ by less than 1 percent at any axial position.

A solution to the parallel flow stability problem is sought: thus the linear stability is required of an axisymmetric flow in cylindrical co-ordinates $(\bar{x},\bar{r},\theta)$ for a base flow having the velocity components $[\bar{u},(\bar{r}),0,0)]$ which is perturbed by an axisymmetric disturbance with the mathematically convenient form $\psi'(\bar{x},\bar{r},\bar{t}) = \phi(\bar{r} \exp[i\bar{\alpha}(\overline{xct})]$. For the temporal stability problem under consideration ϕ is a complex amplitude function given by $\phi(\bar{r}) = \phi_r + i\phi_i$ and the dimensionless celerity of disturbance propagation (phase velocity) is defined by $\bar{c} \equiv c/U_0 = \bar{c}_r + i\bar{c}_i$ where $\bar{c}_r$ is the velocity of wave propagation in the base flow direction and $\bar{c}_i$ determines the degree of damping (negative) or amplification (positive). The dimensionless wavenumber $\bar{\alpha}(\equiv \alpha R)$ is real and related to the dimensionless wavelength by $\bar{\lambda} = 2\pi/\bar{\alpha}$.

Implementation of the above into the incompressible form of the Navier Stokes equation in cylindrical coordinates and linearization leads to the Sexl (1927) equation given by

$$\frac{1}{(i\alpha\,\mathrm{Re})}(L - \bar{\alpha}^2)^2\phi = (\bar{u} - \bar{c})(L - \bar{\alpha}^2)\phi - \bar{r}(\bar{u}_{\bar{r}}\bar{r})_{\bar{r}}\phi \qquad (2)$$

where

$$\bar{u}_{\bar{r}} \equiv d\bar{u}/d\bar{r} \text{ and } L \equiv d^2/d\bar{r}^2 - (1/\bar{r})d/d\bar{r}.$$

The Sexl equation differs from the Orr-Sommerfeld equation in that the origin ($\bar{r} = 0$) is a regular singular point. A singular eigenvalue problem results, requiring that $\phi/\bar{r}$ and $\phi_{\bar{r}}/\bar{r}$ be bounded as $\bar{r} \rightarrow 0$. At the rigid boundary $(\bar{r} = 1)\phi = \phi_{\bar{r}} = 0$. Therefore the problem of stability has been reduced to a characteristic value (eigenvalue) problem of the form $\mathfrak{F}(\bar{\alpha},\bar{c},\mathrm{Re}) = 0$, the solution of which entails the determination of the complex celerity $\bar{c}$ (the eigenvalue), for various values of Re and $\bar{\alpha}$. Consequently the locus $\bar{c}_i = 0$ may be obtained, defining the curve of neutral stability for a particular velocity profile. The critical Reynolds number of stability is the point on the curve where the Reynolds number has its smallest value.

Of the procedures available for the solution of differential eigenvalue problems (expansions in orthogonal functions, initial value methods and finite differences) the method of finite differences was selected. The technique, briefly outlined below, is more fully described in da Silva and Moss (1988).

The Sexl equation was discretized using central difference approximations. Together with the appropriate boundary conditions a system of equations of the form $([A] + \bar{c}[B])\phi = 0$ was obtained. The complex matrices A and B are pentadiagonal and tridiagonal respectively. For given values of $\bar{\alpha}$ and Re this is a generalized eigenvalue problem for the celerity $\bar{c}$, with the eigenvalue relation given by the characteristic determinant $\det([A] + \bar{c}[B]) = 0$. The problem was solved using a generalization of the *Q–R* algorithm known as the *Q–Z* algorithm. This technique, developed by Moler and Stewart (1973), was selected because of its efficiency in computing the eigenvalues and corresponding eigenfunctions for problems in which matrix B is singular.

In order to improve the accuracy of the current system and yet circumvent undesirable truncation errors given by standard finite difference enhancement methods (Collatz, 1965; Hughes, 1972), the hydrodynamic stability equation was transformed according to $y = \sinh(Cr)/\sinh(C)$, effectively stretching the radial co-ordinate (the variable C being essentially a grading parameter) and giving a distribution of points that is dense near the wall where the flow variables change rapidly: this is particularly important in the vicinity of the inlet where the boundary layer is thin. A number of numerical experiments were performed utilizing both the transformed and unrefined procedures. The transformed procedure required about 1/4 of the number of mesh points of the untransformed one to achieve results of comparable accuracy, leading to savings in computing time of a factor of about 4^3. As indicated earlier the convergence of the flow model was initially established using mesh densities which ensured centerline velocity convergence. However it was found that this did not necessarily guarantee adequate stability results. Thus the base flow model and stability calculations were *linked*. In other words, the base flow model was recalculated using successively smaller pivotal increments. At each stage linear stability calculations were repeated and checked for convergence. Eventually convergence (within specified limits) was established, yielding a final stability map and optimized base flow results.[2] The predictions are shown in Table 1.

4 Results and Discussion

The current stability predictions ($\mathrm{Re}_\delta{}^*$ and Re) and those of Garg (1981) are shown in Figs. 3 and 4, together with the experimental results of Sarpkaya (1975). It is seen (Fig. 3) that the present results may be extrapolated closely to the *predicted* boundary layer value ($\mathrm{Re}_\delta{}^* = 520$) of Jordinson (1970) for zero pressure gradient ($\Lambda = 0$) and neglecting nonparallel effects; in contrast the results of Garg (1981) apparently tend towards a limiting value which is about 25 percent too high. Those of

---

[1] This entails the use of centered space differences for the first and second derivative diffusion terms thus allowing information to be diffused in all directions; however advection terms are approximated by using the first upwind scheme which allows the effect of advection to be felt only in the flow direction. While this method has been criticized by Roberts and Weiss (1966) among others, it has been found to produce results with good absolute accuracy (Wirz and Smoldern, 1978; Roache, 1972b)-attributed to the fact that the scheme is physically correct since it possesses the transportive property.

[2] Calculations on an IBM mainframe computer (3081K processor) required about 10 000 000 cpu seconds of machine time.

Table 1 Flow and stability data for the current investigation

$\bar{x}$ $\times 10^4$	Re	δ^*/R	$\bar{\alpha}$	$\bar{c}=\bar{c}_r$	$\bar{\omega}$	U_c/U_0	$\mathrm{Re}_\delta{}^*$
2.0	23454	0.02240	12.79	0.41762	0.11967	1.0455	525.465
3.0	19745	0.02700	10.28	0.42210	0.11717	1.0559	533.188
4.0	17802	0.03080	8.75	0.42422	0.11439	1.0645	548.331
5.0	16552	0.03408	7.70	0.42555	0.11164	1.0721	563.929
7.0	14938	0.03958	6.40	0.42846	0.10854	1.0851	591.251
10.0	13549	0.04626	5.21	0.43222	0.10417	1.1012	626.799
13.0	12679	0.05180	4.46	0.43579	0.10066	1.1150	656.654
17.0	11910	0.05802	3.80	0.44076	0.09717	1.1309	690.934
20.0	11525	0.06212	3.42	0.44411	0.09434	1.1415	715.861
30.0	10874	0.07330	2.61	0.45599	0.08723	1.1719	796.985
40.0	10992	0.08224	2.08	0.46629	0.07976	1.1972	903.909
50.0	12182	0.08972	1.65	0.47202	0.06988	1.2202	1092.944
60.0	13930	0.09622	1.31	0.47933	0.06042	1.2400	1340.356
70.0	18138	0.10194	0.94	0.48464	0.04644	1.2582	1849.121
80.0	38400	0.10718	0.44	0.48350	0.02280	1.2750	4222.995

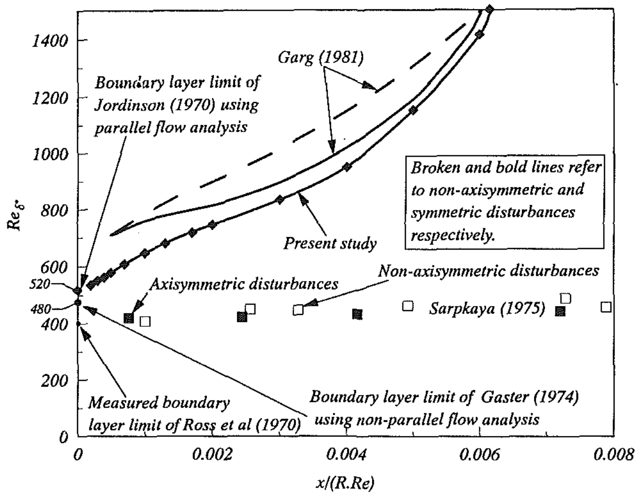

Fig. 3 Axial variation of critical Reynolds number based on displacement thickness, incorporating the results of the present study and limiting boundary layer values

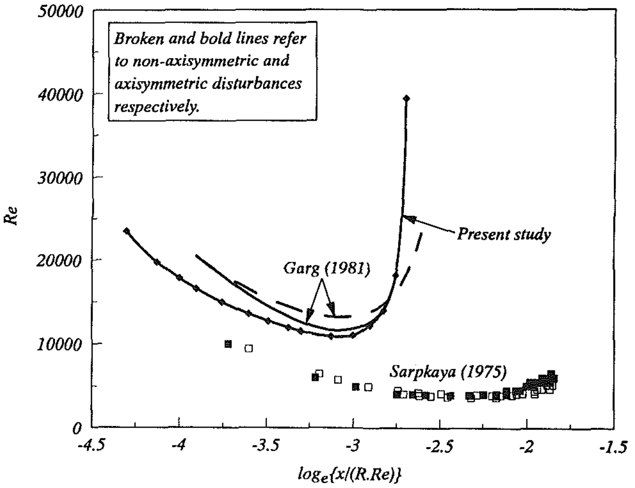

Fig. 4 Axial variation of critical Reynolds number

Sarpkaya tend within experimental error bounds towards the *measured* boundary layer limit (Schubauer and Skramstad, 1947; Ross et al., 1970) for $\Lambda = 0$ given by $\mathrm{Re}_\delta{}^* \simeq 400$.

Until recently discrepancies between the above well-documented measured and predicted *boundary layer* values were thought to arise from nonparallel effects. The further analyses of various researchers (for example, Barry and Ross, 1970; Ling and Reynolds, 1973; Gaster, 1974) only partly accounted for the differences. The favorable agreement of others (Saric and Nayfeh, 1975; Bouthier, 1972 and 1973; Bridges and Morris, 1987) with the value of $\mathrm{Re}_\delta{}^* = 400$ has been more recently dismissed convincingly by Fasel and Konzelman (1990) as "fortuitous." In fact Gaster's analysis, although predicting a critical Reynolds number of about 480, a significant deviation from the experimental value of about 400, is thought to be the most sound: therefore it is likely that the differences in the main are due to (reproducible) phenomena other than nonparallel effects.

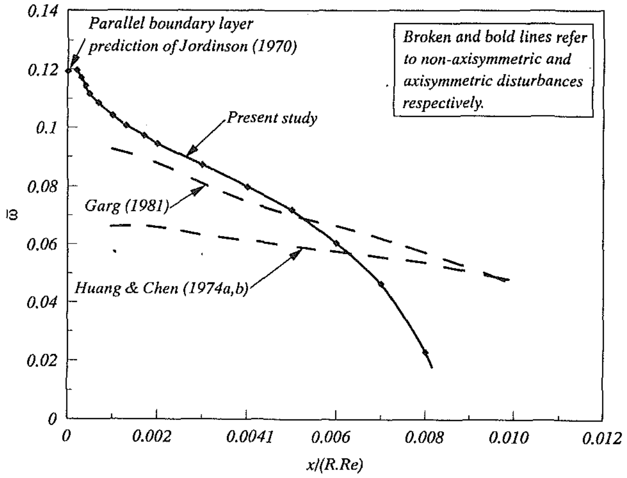

Fig. 5 Axial variation of critical frequency

In the context of pipe entrance flows, it would seem likely that nonparallel effects diminish away from the inlet, as the boundary layer curvature reduces: however this remains to be proven. Nevertheless, if this statement is true, the observed deviations between analysis and experimentation, *increasing* rather than *decreasing* with axial distance, may be attributable to differences between the theoretical and physical disturbances superimposed on the base flow. However this argument raises the question as to why physical disturbances which are of sufficiently correct form (relative to the mathematical formulation) to give stability limits which differ only by about 25 percent from the parallel stability predictions as $\bar{x} \rightarrow 0$, should deviate so grossly away from the inlet.

Variations of critical frequency $\bar{\omega}$ with $\bar{x}$ in Fig. 5 shows that the present analysis tends quite closely toward the boundary layer limit of 0.1193 (Jordinson, 1970). The papers of Garg (1981) and Huang and Chen (1974) presented comprehensive variations of $\bar{\omega}$ and $\bar{\alpha}$ only for the nonaxisymmetric case and $\bar{\omega}$ is shown for comparison purposes here. On the basis of the neutral stability curves presented by these authors it may be inferred that the axisymmetric and nonaxisymmetric cases approach one another with diminishing values of $\bar{x}$, rendering the comparison reasonable in the limit $\bar{x} \rightarrow 0$. Of the analyses, once again the data of the present work is seen to approach closest to the boundary layer limit.

5 Conclusion

(i) It is likely that the major cause of discrepancy between various analyses investigating the stability of pipe entrance flows may be ascribed to the varying accuracies with which base flow velocity, first derivative and second derivative data are calculated.

(ii) Representation of present and previous results scaled with respect to displacement thickness consolidates the data and provides a valid means of evaluating the correctness of their tendencies in the boundary layer limit. Arising from this the current scheme is adjudged more accurate than previous ones because it more closely approaches the accepted asymptotic limits of $\mathrm{Re}_\delta{}^* = 520$ and $\bar{\omega} = 0.1193$ at the pipe inlet. This may be ascribed to the fact that it uses an accurate eigenvalue solver coupled with the base flow solver using successive mesh refinement.

(iii) Subject to the assumption that the theoretical variations of δ^* are applicable to Sarpkaya's (1975) experimentation, his results conform fairly closely to the measured boundary layer limit, i.e., $\mathrm{Re}_{\delta^*} \rightarrow \simeq 400$ as $\bar{x} \rightarrow 0$.

(iv) Parallel flow predictions of critical Reynolds number based on displacement thickness exceed measurements by a minimum of about 30 percent toward the inlet, increasing rapidly downstream. The non-parallel boundary layer computation of Gaster (1974), asymptotically valid at the pipe inlet, overpredicts measurements by about 20 percent. It seems likely, therefore, that nonparallel effects contribute only about 10 percent to the discrepancy between measurement and parallel flow predictions for the boundary layer case and by inference, at the pipe inlet. Therefore, this would be the maximum contribution of the nonparallel effect, for the reason that streamwise rates of variation diminish away from the pipe inlet. Consequently, this work effectively questions the commonly held belief that an analysis embodying streamwise variations would resolve the theoretical/experimental disagreement. In fact it seems that the finite amplitude nature of the applied disturbances, and possible bypass mechanisms, may be central.

In view of the fact that Sarpkaya (1975) applied the same precautions (quality of the applied disturbances) throughout his experimentation, it is possible that the growing deviation with $\bar{x}$ may be attributed to an increasing sensitivity of the stability results to the nature of the disturbances as the flow becomes less boundary layer like, further downstream. More experimental work is required to resolve such issues.

Acknowledgments

The authors wish to thank the reviewers for useful comments and interpretations which they placed on the work.

References

Barry, M. D. J., and Ross, M. A. S., 1970, "The Flat Plate Boundary Layer Part 2. The Effect of Increasing Thickness on Stability," *Journal of Fluid Mechanics*, Vol. 43, pp. 813-818.

Bouthier, M., 1972, "Stabilite Lineaire des Ecoulements Presque Paralleles," *Journal Mecanique*, Vol. 11, pp. 599-621.

Bouthier, M., 1973, "Stabilite Lineaire des Ecoulements Presque Paralleles Partie II. La Couche Limite de Blasius," *Journal Mecanique*, Vol. 12, pp. 75-95.

Bridges, T. J., and Morris, P. J., 1987, "Boundary Layer Stability Calculations," *The Physics of Fluids*, Vol. 30, pp. 3351-3358.

Burridge, D. M., 1970, "The Stability of Poiseuille Flow to Non-axisymmetric Disturbances," *Geophysical Fluid Dynamics Institute*, Florida State University, Technical Report n34.

Campbell, W. D., and Slattery, N., 1963, "Flow in the Entrance of a Tube," ASME *Journal of Basic Engineering*, Vol. 85, pp. 41-46.

Chen, T. S., and Sparrow, E. M., 1967, "Stability of the Developing Laminar Flow in a Parallel-Plate Channel," *Journal of Fluid Mechanics*, Vol. 30, pp. 209-224.

Collatz, L., 1966, *The Numerical Treatment of Differential Equations*, Springer-Verlag, Berlin.

Corcos, G. M., and Sellars, J. R., 1959, "On the Stability of Fully Developed Flow in a Pipe," *Journal of Fluid Mechanics*, Vol. 5, pp. 97-112.

da Silva, D. F., and Moss, E. A., 1988, "The Stability of Plane Poiseuille Flow to Small Disturbances," *Symposium on Computational Fluid Dynamics*, CSIR, Pretoria, Vol. 5.2, pp. 1-8.

Davey, A., and Drazin, P. G., 1969, "The Stability of Poiseuille Flow in a Pipe, *Journal of Fluid Mechanics*, Vol. 36, pp. 209-218.

Fasel, H., and Konzelmann, U., 1990, "Non-parallel Stability of a Flat-Plate Boundary Layer using the Complete Navier-Stokes Equations," *Journal of Fluid Mechanics*, Vol. 221, pp. 311-347.

Fox, J. A., Lessen, M., and Bhat, W. V., 1968, *Experimental Investigation of the Stability of Hagen-Poiseuille Flow," The Physics of Fluids*, Vol. 11, pp. 1-4.

Garg, V. K., and Rouleau, W. T., 1972, "Linear Spatial Stability of Pipe Poiseuille Flow," *Journal of Fluid Mechanics*, Vol. 54, Part 1, pp. 113-127.

Garg, V. K., 1981, "Stability of Developing Flow in a Pipe: Non-axisymmetric Disturbances," *Journal of Fluid Mechanics*, Vol. 110, pp. 209-216.

Gaster, M., 1962, "A Note on the Relation Between Temporally-Increasing and Spatially-Increasing Disturbances in Hydrodynamics Stability, *Journal of Fluid Mechanics*, Vol. 14, pp. 222-224.

Gaster, M., 1965, "On the Generation of Spatially Growing Waves in a Boundary Layer," *Journal of Fluid Mechanics*, Vol. 22, pp. 433-441.

Gaster, M., 1974, "On the Effects of Boundary Layer Growth on Flow Stability," *Journal of Fluid Mechanics*, Vol. 66, pp. 465-480.

Gill, A. E., 1965, "On the Behavior of Small Disturbances to Poiseuille Flow in a Circular Pipe," *Journal of Fluid Mechanics*, Vol. 21, pp. 145-172.

Gupta, S. C., and Garg, V. K., 1981, "Effect of Velocity Distribution on the Stability of Developing Flow in a Pipe," *The Physics of Fluids*, Vol. 24, pp. 576-578.

Hornbeck, R. W., 1963, "Laminar Flow in the Entrance Region of a Pipe," *Applied Scientific Research*, Vol. 13, Section A, pp. 224-232.

Huang, L. M., and Chen, T. S., 1974a, "Stability of the Developing Pipe Flow," *The Physics of Fluids*, Vol. 17, pp. 245-247.

Huang, L. M., and Chen, T. S., 1974b, "Stability of the Developing Pipe Flow Subjected to Non-axisymmetric Disturbances," *Journal of Fluid Mechanics*, Vol. 63, pp. 183-193.

Huges, T. H., 1972, "Variable Mesh Numerical Method for Solving the Orr-Sommerfeld Equation," *The Physics of Fluids*, Vol. 15, pp. 725-728.

Jordinson, R., "The Flat Plate Boundary Layer Part 1. Numerical Integration of the Orr-Sommerfeld Equation," *Journal of Fluid Mechanics*, Vol. 53, Part 4, pp. 801-811.

Kanda, H., 1988, "Numerical Study of the Entrance Flow and its Transition in a Circular Pipe," The Institute of Space and Astronautical Science, Japan Report No. 626.

Langhaar, H. L., 1942, "Steady Flow in the Transition Region of a Straight Duct," ASME *Journal of Applied Mechanics*, Vol. 9, pp. A55-A58.

Leite, R. J., 1959, "An Experimental Investigation of the Stability of Poiseuille Flow," *Journal of Fluid Mechanics*, Vol. 4, pp. 81-96.

Lessen, M., Sadler, S. G., and Liu, T. Y., 1968, "Stability of Pipe Poiseuille Flow," *The Physics of Fluids*, Vol. 11, pp. 1404-1409.

Ling, C. H., and Reynolds, W. C., 1973, "Non-parallel Flow Corrections for the Stability of Shear Flows," *Journal of Fluid Mechanics*, Vol. 59, pp. 571-591.

Mohanty, A. K., and Asthana, S. B. L., 1978, "Laminar Flow in the Entrance Region of a Smooth Pipe," *Journal of Fluid Mechanics*, Vol. 90, pp. 433-447.

Moler, C. B., and Stewart, G. W., 1973, "An Algorithm for Generalized Matrix Eigenvalue Problems," *Society for Industrial and Applied Mathematics Journal of Numerical Analysis*, Vol. 110, No. 2, pp. 241-256.

Orszag, S. A., and Patera, A. T., 1983, "Secondary Stability of Wall-Bounded Shear Flows," *Journal of Fluid Mechanics*, Vol. 128, pp. 347-385.

Patera, A. T., and Orszag, S. A., 1981, "Finite Amplitude Stability of Axisymmetric Pipe Flow," *Journal of Fluid Mechanics*, Vol. 112, pp. 467-474.

Prandtl, L., and Tietjens, O. G., 1931, *Applied Hydro- and Aeromechanics*, Dover Publications, New York.

Roache, P. J., 1972a, "On Artificial Viscosity," *Journal of Computational Physics*, Vol. 10, pp. 169-184.

Roache, P. J., 1972b, *Computational Fluid Dynamics*, Hermosa Publishers, Alburquerque.

Roberts, K. V., and Weiss, N. O., 1966, "Convective Difference Schemes," *Mathematics of Computation*, Vol. 20, No. 94, pp. 272-299.

Ross, J. A., Barnes, F. H., Burns, J. G., and Ross, M. A. S., 1970, "The Flat Plate Boundary Layer Part 3. Comparison of Theory with Experiment," *Journal of Fluid Mechanics*, Vol. 43, pp. 819-832.

Saric, W. S., and Nayfeh, A. H., 1975, "Non-parallel Stability of Boundary Layer Flows," *The Physics of Fluids*, Vol. 18, pp. 945-950.

Sarpkaya, T., 1975, "A Note on the Stability of Developing Laminar Pipe Flow Subjected to Axisymmetric and Non-axisymmetric Disturbances," *Journal of Fluid Mechanics*, Vol. 68, Part 2, pp. 345-351.

Schmidt, F. W., and Zeldin, B., 1969, "Laminar Flows in the Inlet Sections of Tubes and Ducts," *American Institute of Chemical Engineering Journal*, Vol. 15, pp. 612-614.

Schubauer, G. G., and Skramstad, H. K., 1947, "Laminar Boundary Layer Oscillations and Transition on a Flat Plate," *Journal of Aeronautical Sciences*, Vol. 14, pp. 69-78.

Sexl, T., 1927 "Zum Stabilitatsproblem der Poiseuille-Stromung, *Annalen der Physik*, (Deutsche Physikalische Gesellschaft) Leipzig, Vol. 83, pp. 835-848.

Shah, R. K., 1976, "A Correlation for Laminar Hydrodynamic Entry Length Solutions for Circular and Non-circular Ducts," ASME JOURNAL OF FLUIDS ENGINEERING, Vol. 100, pp. 177-179.

Sparrow, E. M., Lin, S. H., and Lundgren, T. S., 1964, "Effect of Upstream Flow Processes on Hydrodynamic Development in a Pipe," *The Physics of Fluids*, Vol. 7, pp. 338-342.

Tatsumi, T., 1952, "Stability of the Laminar Inlet-Flow Prior to the Formation of Poiseuille Regime I & II," *Journal of the Physical Society of Japan*, Vol. 7, No. 5, pp. 489-502.

Van Dyke, M., 1970, "Energy Flow in a Channel," *Journal of Fluid Mechanics*, Vol. 44, Part 4, pp. 813-823.

Wirz, H. J., and Smolderen S., 1978, *Numerical Methods in Fluid Dynamics*, McGraw-Hill Book Co., London.

Steady Laminar Fluid Flow Through Variable Constrictions in Vascular Tube

T. S. Lee
Mechanical and Production
Engineering Department,
National University of Singapore,
Singapore 0511

Steady laminar flow fields in the neighborhoods of two consecutive constrictions in a vascular tube were studied for approaching Reynolds number Re in the range of 5 to 200. The upstream stenosis was set at a dimensionless diameter constriction c_1 of 0.5 while the downstream stenoses were allowed to vary from $c_2 = 0.2$ to 0.6. The proximity of the constrictions was determined by the spacing ratio of $S/D = 1$, 2, 3, and ∞. When $c_2 > c_1$, a recirculation zone filled the valley between the two constrictions with little changes to the separation and reattachment points as Re was further increased. For $c_2 < c_1$ and when Re was increased, the recirculating eddy formed downstream of the first constriction tended to spread beyond the region of the second constriction. This resulted in negative wall vorticity peak occurring in the region of the second constriction for smaller S/D at high Re.

Introduction

The possibility that hemodynamic factors may participate in the genesis and proliferation of atherosclerosis has fostered increased study of flow through constrictions during the past decade (Deshpande et al., 1976; Ahmed and Giddens, 1981; Back et al., 1986). One of the recent research interest concerns the relationship between the location of vascular disease and the magnitude of wall shear stress. There are two contradictory views: that the mass transfer rate is small in a low wall shear stress zone (Caro et al., 1971), where the flow stagnates, and conversely, that the endothelial cell might be damaged in a high wall shear stress zone (Fry, 1968). It seems worthwhile from the fluid dynamics point of view, therefore, to develop reliable numerical methods of identifying regions of very high shear and normal stresses in the flow (haemolysis), regions of very low or very high shear stress at walls (atheromatous lesions), and the extent of separated or reversed flow regions (thrombosis).

For single constriction flow, research investigations are numerous. Numerical studies of flow and pressure fields with various single constriction profiles and inflow conditions at different Re ranges were investigated by Lee and Fung (1970, 1971), Young and Tsai (1973), Oberkampt and Goh (1974), Bentz and Evans (1975), Deshpande et al. (1976), Mueller (1978), Wille (1980), and O'Brien and Ehrlich (1985). Velocity measurements in the neighborhood of constrictions in rigid tubes were investigated by Ahmed and Giddens (1981). Flow visualization of streamlines in steady flow through constrictions was obtained by Siouffi et al. (1984). Measurements and prediction of flow through a replica segment of a mildly atherosclerotic coronary artery were done by Back et al. (1986).

The influence of the upstream constriction on the flow field near the downstream constriction of various diameter constriction ratios was considered by few researchers. In experimental work, one of the main reasons is due to the difficulties in manufacturing accurately the double constrictions required for these types of studies. One such attempt was by Dreumel and Kuiken (1989). Sharp-edge constrictions in rigid perspex tubes was used. The constrictions are of trapezoidal shapes. As a result, the point of separation is fixed at the sharp edges of the trapezoidal constrictions irrespective of the Re. These approximations to the vascular constriction problems are not satisfactory nor realistic. Thus, no attempt was made to compare the present results with the results obtained by Dreumel and Kuiken. In the present work, a vascular tube with double stenoses of realistic bell shaped Gaussian normal distribution profiles was studied. Multiple constrictions in diseased vascular tube occurs because of the formation of the primary constriction results in downstream circulation flow. The downstream circulation in time will accumulate particles and formed a secondary constriction. The dynamics of the flow describing separation, reattachment, and the formation of recirculation eddy for the above multi-constrictions flow are studied through the streamline, velocity and vorticity fields in the present investigations.

Problem Formulation

Constant fluid properties are assumed and the flow is considered axisymmetric and laminar. The dimensionless governing equations representing the fluid flow through the constrictions (Fig. 1) in their unsteady form are:

$$\frac{\partial \zeta^*}{\partial t^*} + \frac{\partial (v_r^* \zeta^*)}{\partial r^*} + \frac{\partial (v_z^* \zeta^*)}{\partial z^*} = \frac{1}{\mathrm{Re}} \left(\frac{\partial^2 \zeta^*}{\partial r^{*2}} + \frac{\partial^2 \zeta^*}{\partial z^{*2}} + \frac{1}{r^*} \frac{\partial \zeta^*}{\partial r^*} - \frac{\zeta^*}{r^{*2}} \right) \quad (1)$$

Contributed by the Fluids Engineering Division for publication in the JOURNAL OF FLUIDS ENGINEERING. Manuscript received by the Fluids Engineering Division June 16, 1992; revised manuscript received May 24, 1993. Associate Technical Editor: N. A. Cumpsty.

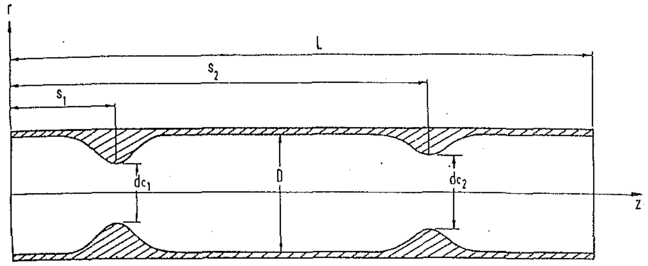

Fig. 1 Model of stenoses with different degree of constrictions

and the vorticity-stream function equation

$$\zeta^* = \frac{1}{r^*}\left(\frac{\partial^2\psi^*}{\partial r^{*2}} + \frac{\partial^2\psi^*}{\partial z^{*2}} - \frac{1}{r^*}\frac{\partial\psi^*}{\partial r^*}\right) \tag{2}$$

The velocities are given by

$$v_r^* = \frac{1}{r^*}\frac{\partial\psi^*}{\partial z^*}; \quad v_z^* = -\frac{1}{r^*}\frac{\partial\psi^*}{\partial r^*} \tag{3}$$

where the dimensionless variables are defined as: $r^* = r/a_0$; $z^* = z/a_0$; $v_r^* = v_r/v_\infty$; $v_z^* = v_z/v_\infty$; $\psi^* = \psi/(v_\infty a_0^2)$; $\zeta^* = \zeta/(v_\infty/a_0)$; $t^* = t/(a_0/v_\infty)$ and $\mathrm{Re} = v_\infty a_0/\nu$.

For expressions subsequent to Eq. (3), * is dropped for simplicity.

In dimensionless form, the geometry of the constrictions is described by the following bell-shaped Gaussian distribution profile

$$f(z) = 1 - c_i \exp(-c_s(z - s_i)^2) \tag{4}$$

where

c_i = constriction ratio $(D - dc_i)/D$

c_s = a shape constant

s_i = dimensionless distance of constriction from inlet plane

For the variable double constrictions considered here (Fig. 1), $c_1 = 0.5$ for the first constriction and c_2 has values from 0.2 to 0.6 for the second constrictions; the shape factor $c_s = 0.4$; the distance $s_i = s_1$ for $z_1 < z < z_2$; the distance $s_i = s_2$ for $z_3 < z < z_4$ and $c_i = 0$ elsewhere. z_1, z_2 are the upper and lower limits of the first constriction; z_3, z_4 are the upper and lower limits of the second constriction. s_1, s_2 are the distance of the first and second constriction from the inlet plane, respectively. The spacing between the two constrictions is given by $S = (s_2 - s_1)$ and $s_1 = 2.0$ in this study. When the dimensionless spacing ratio $S/D = \infty$, this is equivalent to a single constriction tube with $c_1 = 0.5$, $c_s = 0.4$, $s_i = s_1$ for $z_1 < z < z_2$ and $c_i = 0$ elsewhere.

For the present study, the incoming flow is assumed to be Poiseuillean and outflow is assumed unrestrictive. Non-slip boundary condition is assumed for the tube wall. The flow is assumed symmetric about its axis, i.e.,

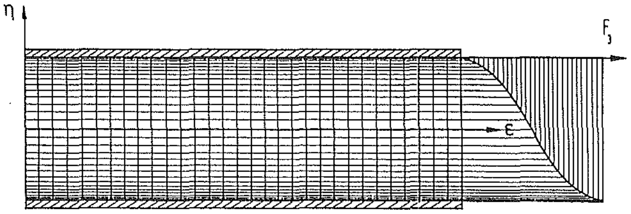

Fig. 2 The computational space with variable mesh system

At the inlet

$$v_r = 0; \quad v_z = (1 - r^2) \tag{5}$$

At the outlet

$$\frac{\partial^2\zeta}{\partial z^2} = 0; \quad \frac{\partial^2\psi}{\partial z^2} = 0 \tag{6}$$

Along the tube axis

$$v_r = 0; \quad \frac{\partial v_z}{\partial r} = 0 \tag{7}$$

Along the tube wall

$$v_r = v_z = 0 \tag{8}$$

The boundary stream function values follow closely from that of the velocity boundary conditions described above. $\psi = 0$ is arbitrarily chosen along the axis of the tube. The boundary values of vorticity and velocities follow that of the stream function boundary values.

The wall-vorticity distributions are of considerable interest to researchers as it is related to the wall shearing stress per unit area through

$$\tau_{\mathrm{wall}} = (\rho\nu v_\infty/a_0)\zeta_w \tag{9}$$

where ν is the kinematic viscosity of the fluid, a_0 is the radius of the unconstricted tube, ζ_w is the dimensionless wall vorticity value.

Numerical Solution

The tube with the bell-shaped constrictions are mapped into a rectangular solution domain (Fig. 2):

$$\epsilon = F_1(z) = z$$
$$\eta = F_2(r, z) = r/f(z) \tag{10}$$

Expressing the partial derivatives in the new coordinates, the governing equations and boundary conditions can all be expressed in the ϵ-η system.

The domain in the ϵ-η coordinate system as defined by Eq. (10) is a rectangular region (Back et al., 1977). In order to obtain better resolution of the solution near the wall regions

Nomenclature

(r, z) = coordinates in the original cylindrical coordinate system

a_0 = radius of the tube having a constant cross section ($a_0 = D/2$)

c_1 = upstream constriction, $c_1 = (D - dc_1)/D$

c_2 = downstream constriction, $c_2 = (D - dc_2)/D$

D = diameter of the tube having a constant cross section

d_c = opening of the constriction

L = length of the tube

s_1, s_2 = distance of first and second constrictions from inlet plane

S = spacing between constrictions, $S = (s_2 - s_1)$

v_r = radial (r-direction) velocity component

v_z = axial (z-direction) velocity component

v_∞ = centerline axial velocity at inlet

z_1, z_2 = limits of first constriction [Eq. (4)]

z_3, z_4 = limits of second constriction [Eq. (4)]

(η, ϵ) = coordinate variables in the transformed coordinates system

ψ = stream function

ζ = vorticity

t = time

Re = approaching Reynolds number, $\mathrm{Re} = v_\infty a_0/\nu$

p = pressure

ρ = density

ν = kinematic viscosity

ω = relaxation factor in the SOR method

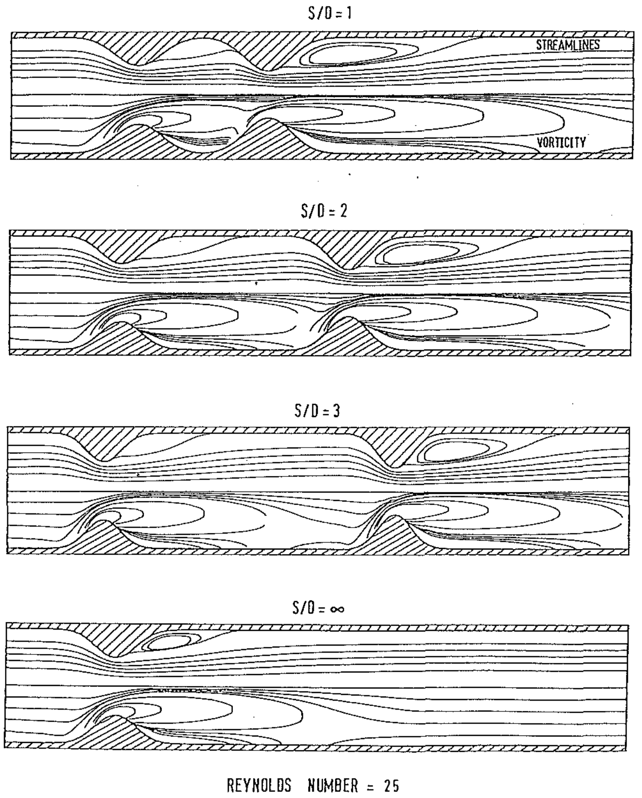

Fig. 3 Typical streamlines and vorticity contours $c_1 = 0.5$, $c_2 = 0.6$, Re = 25

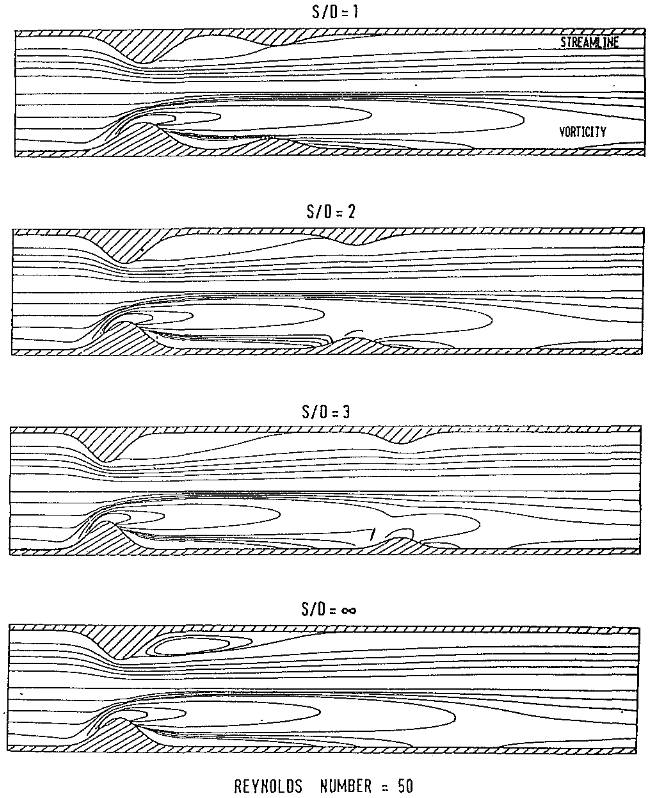

Fig. 4 Typical streamlines and vorticity contours $c_1 = 0.5$, $c_2 = 0.2$, Re = 50

while preserving the second order accuracy of the finite difference scheme, the rectangular solution domain is overlaid with the non-uniform mesh as shown in Fig. 2 and given by

$$F_3 = \frac{2}{\pi}\sin^{-1}((\eta + 0.5)^{1/2}) \qquad (11)$$

At the node points of the domain defined by Eq. (11), the finite-difference solution to the governing Eq. (1) and boundary equations in the ϵ-η coordinates, are obtained through an Alternating Direction Implicit (ADI) procedure proposed by Samarskii and Andreev (1963) with a weighted time-step factor $\sigma = 0.5$. Successive over-relaxation (SOR) with a relaxation parameter of $\omega = 1.1$ was used to solve the vorticity-stream function Eq. (2). All spatial derivatives are approximated by second-order-accurate central differences. The convective terms in Eq. (1) are approximated by second-order upwind differencing method. Three-point backward and forward difference formulae are used for derivatives at the boundaries.

Monotonic convergence towards a grid-independent value is found for all the solutions obtained here. An estimation of the grid-independent values can be made by applying the Richardson extrapolation. Assuming second-order behavior, the "exact" values of the solution field are obtained from $\Phi = \Phi_h + [\Phi_h - \Phi_{2h}]/3$. Since the convergence errors were kept below 0.001 percent in the present solutions, the results of the above extrapolation are assumed to have errors an order of magnitude lower than the finest grid solution. The mesh size used for the solutions illustrated here is 21×151. Other solutions with grid refinement of 41×301 were also investigated to ensure that the solutions obtained were mesh independent for the range of parameters considered here. The location of the downstream boundary was studied for $L/d_c = 12$, 14 and 16 to ensure that there is no influence on the upstream solution fields due to the outflow boundary location. Studies show that $L/d_c = 12$ is sufficient for the present solutions.

The steady-state solution of Eqs. (1)-(3) is said to have been reached when a difference of 0.001 percent of referenced values of ψ and ζ is detected. This has proven satisfactory. The stream-function contours, the velocity fields and the vorticity contours are noted to be steady after the above criteria are satisfied. A check on the mass flux balance was also made for all of the solutions obtained here. The maximum mass flux difference with respect to the inlet mass-flux for any of the test section results obtained is only of the order of 0.001 percent. All the computations here were made on the IBM 3081 mainframe computer with a typical CPU time of about 300 sec per solution run.

Results and Discussions

For a given Re, typical streamlines and vorticity fields at different proximity (S/D) of the constrictions in the present study are shown in Fig. 3 for $c_2 > c_1$ at Re = 25 and in Fig. 4 for $c_2 < c_1$ at Re = 50. Studies of the numerous similar flow fields for $c_1 = 0.5$ with $c_2 > c_1$ show that, a recirculation zone usually fills the valley between the two constrictions for small S/D ratios, with little changes to the separation and reattachment points as Re is increased. A separation streamline divides the flow into two parts: a recirculating flow field between the two constrictions and the main flow field near the center of the vascular tube with relatively straight and parallel streamlines. Streamlines and vorticity fields in similar studies for $c_1 = 0.5$ and $c_2 < c_1$ show that as Re increases, the recirculating eddy between the two constrictions spread beyond the second constriction, merging with the eddy that formed behind the second constriction.

Figure 5 shows the separation and reattachment points for (a) $c_1 = 0.5$ and $c_2 = 0.6$ and (b) $c_1 = 0.5$ and $c_2 = 0.6$ with various S/D and Re. With increasing Re, the point of separation of the eddy is seen to move slightly upstream from the constriction surface; and the point of reattachment of the recirculating flow moves downstream. In the double constric-

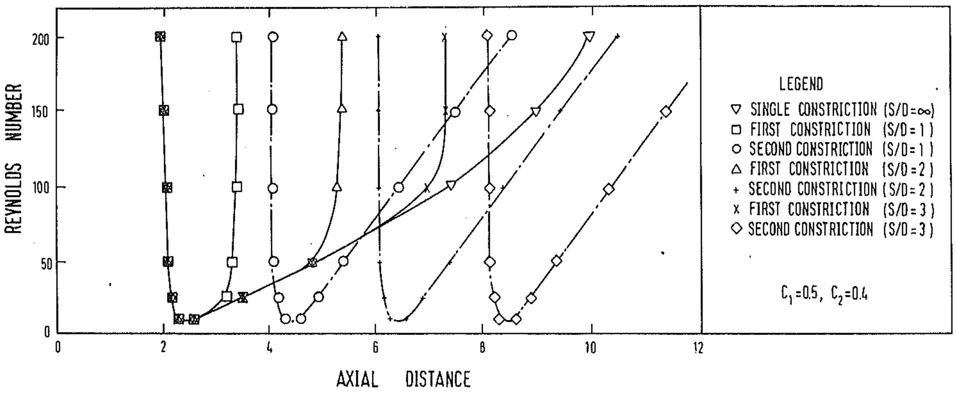

Fig. 5(*a*)

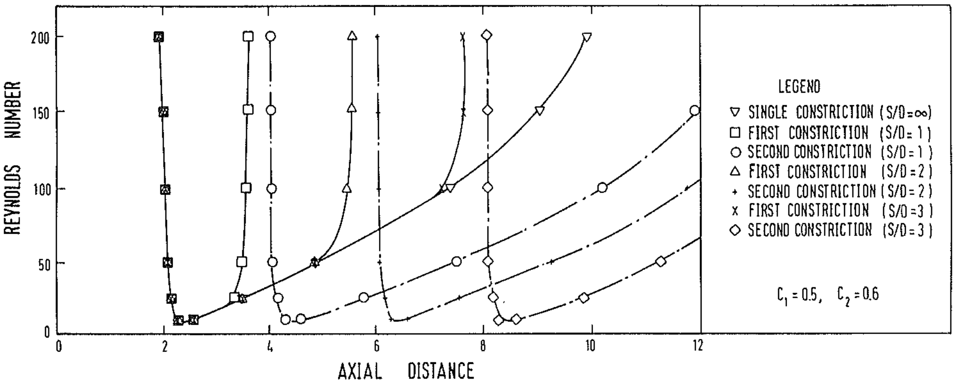

Fig. 5(*b*)

Fig. 5 Separation and reattachment of flow (*a*) $c_1 = 0.5$, $c_2 = 0.5$; (*b*) $c_1 = 0.5$, $c_2 = 0.6$

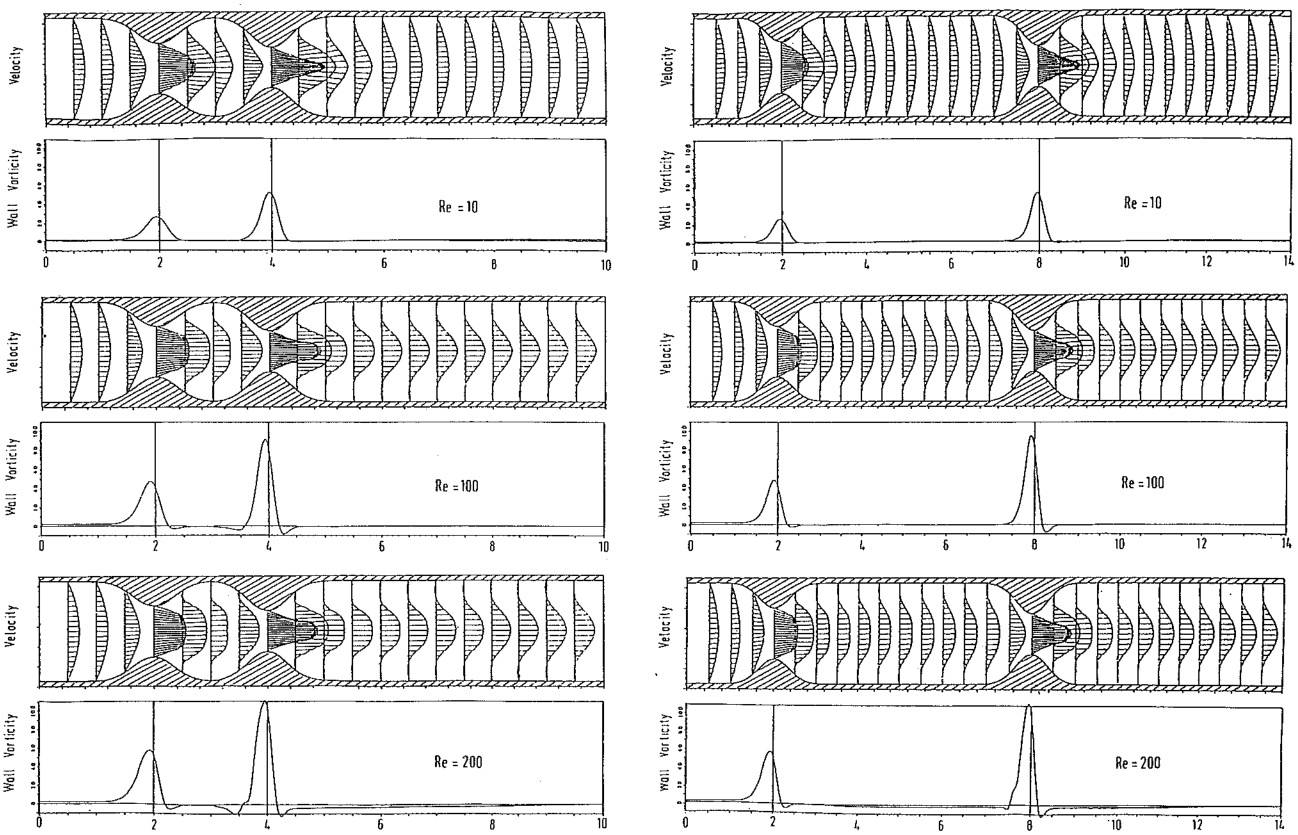

Fig. 6(*a*)

Fig. 6(*b*)

Fig. 6 Velocity profiles and wall vorticity distributions $c_1 = 0.5$, $c_2 = 0.6$: (*a*) $S/D = 1$; (*b*) $S/D = 3$

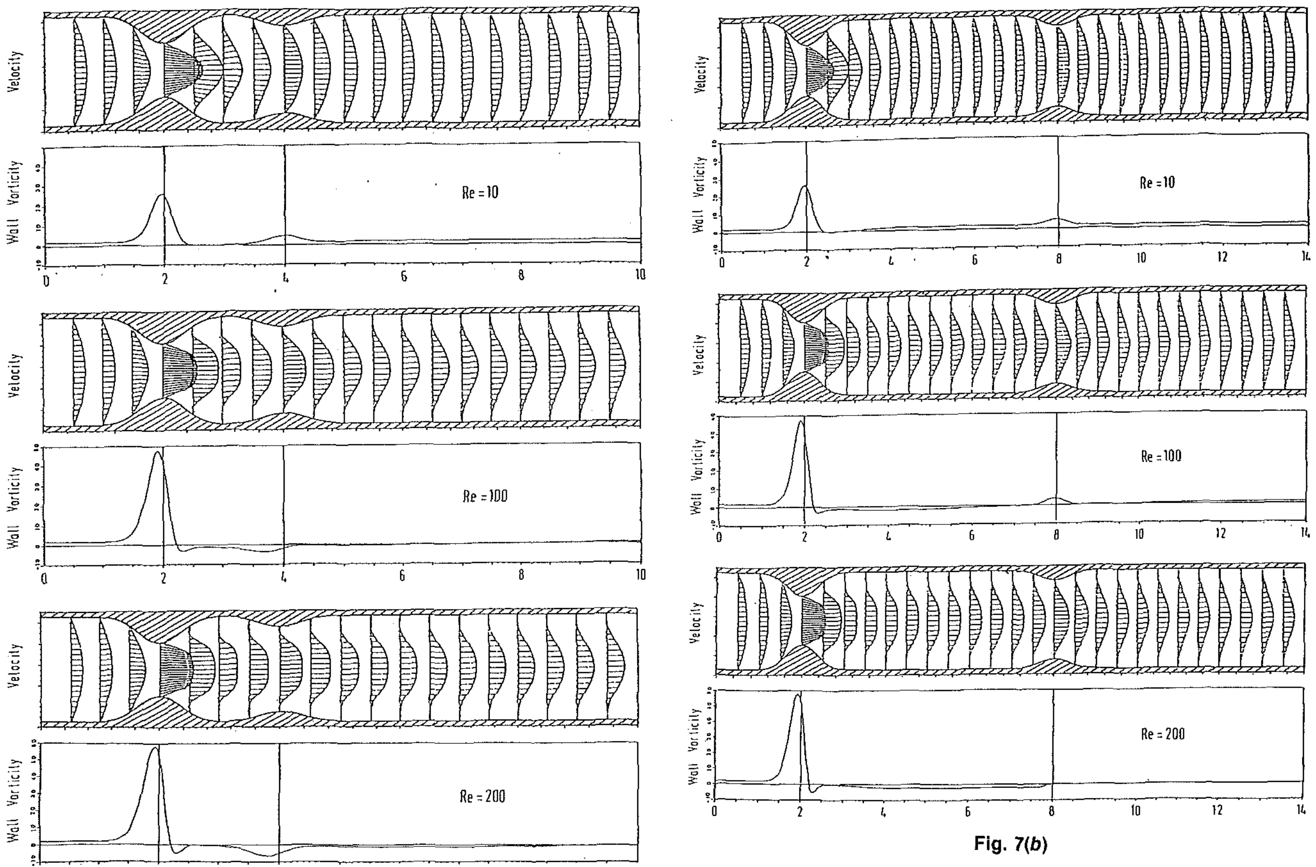

Fig. 7(a)

Fig. 7(b)

Fig. 7 Velocity profiles and wall vorticity distributions $c_1 = 0.5$, $c_2 = 0.2$: (a) $S/D = 1$; (b) $S/D = 3$

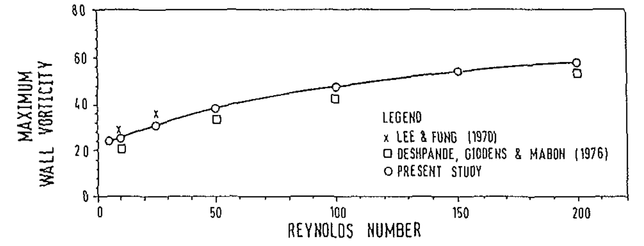

Fig. 8 Comparison of wall vorticity values $c_1 = 0.5$, $c_2 = 0.0$ (or $S/D = \infty$)

tion tube for $c_1 = 0.5$ and $c_2 = 0.6$, flow separation starts at Re≅5 downstream of the second constriction. With $c_1 = 0.5$ and $c_2 = 0.2$, flow separation starts at Re≅10 downstream of the first constriction and at Re≅50 behind the second constriction. For $c_1 = 0.5$ and $c_2 \cong 0.0$ or $S/D \rightarrow \infty$, the flow separation starts at Re≅10 and approaches the characteristics of the single constriction flow.

The velocity vectors in Fig. 6 and Fig. 7 for $S/D = 1$ and $S/D = 3$ for Re = 10, 100, 200 show that as fluid flows into the converging section, the parabolic velocity vector profiles point towards the tube axis. Elongation of the velocity vectors is observed indicating an accelerated flow through the constriction. Beyond the narrowest constriction, the velocity vectors point away from the tube axis with a corresponding decelerated flow. The formation of the weak recirculation region is indicated by the small reverse velocity vectors near the wall. For Fig. 8 with $c_2 = 0.6$, the velocity profiles at both constrictions are distinctly dissimilar due to the higher second constriction ratio. While the velocity profile at the first constriction is parabolic at low Re, the velocity profile at the second constriction is nearly triangular indicating a sharp velocity gradient. For Fig. 7, with Re = 200 at $S/D = 1$, it is observed that the negative velocity vectors near the wall extend over the second constriction, indicating the merging of the recirculation behind the first constriction with that of the second constriction.

The wall-vorticity values are shown in Fig. 6 and Fig. 7. The magnitude of the wall vorticity values increase rapidly when the flow approaches the constriction and reaching a peak value near the maximum constricted area. At higher Re, the peak wall vorticity value was found slightly upstream of the maximum constricted area. At a location downstream of this peak value, the wall vorticity decreases rapidly and reverses to negative values when separation begins at the wall of the tube. For the first constriction, it is observed that the peak wall vorticity value increases with increasing Re. For $c_1 = 0.5$ and $c_2 = 0.2$ with increasing Re, the merging of the recirculating eddy from the first constriction with the eddy formed behind the second constriction resulted in a negative wall vorticity peak occurring at the second constriction. However, for $c_1 = 0.5$ with $c_2 = 0.6$, the maximum wall vorticity at the second constriction ($\zeta_{\max,2}$) in the present investigation is found to be nearly twice that of the first constriction ($\zeta_{\max,1}$). It was also observed that the rate of increase of $\zeta_{\max,1}$ for the first constriction with Re was higher than for $\zeta_{\max,2}$ of the second constriction.

Attempts were made to compare experimental results with the present double constrictions work. However, no suitable experimental results were available in the literature. The present study with $c_2 = 0.0$ or $S/D \rightarrow \infty$ is similar to the study of a single constriction flow in the vascular tube. Hence, for the purpose of comparison and verification of results, computer solutions were obtained for $c_1 = 0.5$, $c_2 = 0.0$ and compared with Lee and Fung (1970) results of Re = 5 to 25. Another similar study was performed by Deshpande et al. (1976). The comparative results are all presented in Fig. 8. Lee and Fung assumed that the outflow was Poiseuille (i.e., $v_z = f(r)$; $v_z = 0$). In order to maintain a fixed physical domain for their investigation Deshpande et al. (1976) assumed at the outlet of the solution domain, the condition of $(\partial v_z/\partial z) = (\partial v_r/\partial z) = 0$ applied. The present study assumes an unrestrictive flow at the outlet and allows the flow profile to develop on its own. Numerical investigations showed that the results obtained for the present study falls between the two different methods used by Lee and Fung (1970) and Deshpande et al. (1976), respectively. The present method of specifying the boundary conditions for the flow, which allows the flow to develop by itself, is believed to perform better. The proposed method of handling the boundary conditions allows one to select a fixed solution domain and to extend the computation into higher Reynolds number flow regime without numerical instability.

Conclusion

The effects of fluid flow passes through two adjacent constrictions (c_1, c_2) are numerically studied. Effects on flow streamlines, velocity, vorticity, separation—reattachment points, and wall vorticity distribution are investigated. For $c_1 = 0.5$ with $c_2 > c_1$ and small constriction spacings, recirculation tends to fill the valley region between the two constrictions with little changes to the separation and reattachment points as Re is increased. For $c_1 = 0.5$ with $c_2 < c_1$ with small spacing ratios, the recirculating eddy between the two constrictions tends to merge with the eddy formed downstream of the second constriction when Re is increased. This produces negative wall vorticity peak near the second constriction. For $c_1 = 0.5$ and $c_2 = 0.6$, the maximum wall vorticity at the second constriction is nearly twice that of the first constriction. However, the rate of increase of the maximum wall vorticity with respect to Re is higher for the first constriction than it is for the second constriction. If no merging or interaction of the recirculation eddies occurred, the maximum wall vorticity near each constriction would increase with Re and S/D.

Acknowledgments

The author gratefully acknowledges the financial support of a National University of Singapore Research Grant No. 890633.

References

Ahmad, S. A., and Giddens, D. P., 1981, "Velocity Measurements in Steady Flow through Axisymmetric Constrictions at Moderate Reynolds Numbers," *Journal of Biomechanics*, Vol. 16, pp. 505-516.

Back, L. H., Radbill, J. R., and Cho, Y. I., 1986, "Measurement and Prediction of Flow Through a Replica Segment of a Mildly Atherosclerotic Coronary Artery of Man," *Journal of Biomechanics*, Vol. 19, No. 1, pp. 1-17.

Back, L. H., Radbill, J. R., and Crawford, D. W., 1977, "Analysis of Pulsatile, Viscous Blood Flow through Diseased Coronary Arteries of Man," *Journal of Biomechanics*, Vol. 10, pp. 339-353.

Bentz, J. C., and Evans, N. A., 1975, "Hemodynamic Flow in the Region of a Simulated Stenosis," ASME Paper No. 75-WA/BA10-10, The American Society of Mechanical Engineers, Winter Annual Meeting, Houston, Nov. 30-Dec. 4, 1975.

Caro, C. G., Fitz-Gerald, J. M., and Schroter, R. C., 1971, "Atheroma and Arterial Wall Shear Observation, Correlation and Proposal of a Shear Dependent Mass Transfer Mechanism for Atherogenesis," *Proceedings of the Royal Society of Medicine*, London, Series B, Vol. 177, pp. 109-159.

Deshpande, M. D., Giddens, D. P., and Mabon, R. F., 1976, "Steady Laminar Flow Through Modelled Vascular Stenoses," *Journal of Biomechanics*, Vol. 9, pp. 165-174.

Dreumel, S. C., and Kuiken, G. D. C., 1989, "Steady Flow Through a Double Converging-Diverging Tube Model for Mild Coronary Stenoses," ASME *Journal of Biomechanical Engineering*, Vol. 111, pp. 212-221.

Fry, D. L., 1968, "Acute Vascular Endothelial Changes Associated with Increased Blood Velocity Gradients," *Journal of Circulatory Research*, Vol. 22, pp. 167-197.

Fukushima, T., Azuma, T., and Matsuzawa, T., 1982, "Numerical Analysis of Blood Flow in the Vertebral Artery," ASME *Journal of Biomechanical Engineering*, Vol. 104, pp. 143-147.

Lee, J. S., and Fung, Y. F., 1970, "Flow in Locally Constricted Tubes at Low Reynolds Numbers," ASME *Journal of Applied Mechanics*, Vol. 37, pp. 9-16.

Lee, J. S., and Fung, Y. F., 1971, "Flow in Non-Uniform Small Blood Vessels," *Journal of Microvascular Research*, Vol. 3, pp. 272-287.

Mueller, T. J., 1978, "Application of Numerical Methods to Physiological Flows," Chapter 2, *Numerical Methods in Fluid Dynamics*, H. J. Wirz and J. J. Smolderen, eds., McGraw-Hill, pp. 89-154.

Oberkampf, W. L., and Goh, S. C., 1974, "Numerical Solution of Incompressible Viscous Flow in Irregular Tubes," *Proceedings of the International Conference on Computational Methods for Non-Linear Mechanics*, University of Texas, Austin, pp. 569-579.

O'Brien, V., and Ehrlich, L. W., 1985, "Simple Pulsatile Flow in a Artery with a Constriction," *Journal of Biomechanics*, Vol. 18, No. 2, pp. 117-127.

Samarskii, A. A., and Andreev, V. B., 1963, "On High Accuracy Difference Scheme for an Elliptic Equation with Serveralspace Variables," *USSR Computational Mathematical Physics*, Vol. 3, pp. 1373-1382.

Siouffi, M., Pelissier, R., Farahifar, D., and Rieu, R., 1984, "The Effects of Unsteadiness on the Flow Through Stenoses and Bifurcations," *Journal of Biomechanics*, Vol. 17, No. 5, pp. 299-315.

Wille, S. O., 1980, "Pressure and Flow in Arterial Stenoses Simulated in Mathematical Models," *Applied Mathematical Modelling*, Vol. 4, pp. 483-488.

Young, D. F., and Tsai, F. Y., 1973, "Flow Characteristics in Models of Arterial Stenoses—I. Steady Flow," *Journal of Biomechanics*, Vol. 6, pp. 395-410.

Uriel C. Goldberg
Member Technical Staff,
Rockwell International Science Center,
Thousand Oaks, CA 91360
Mem. ASME

Toward a Pointwise Turbulence Model for Wall-Bounded and Free Shear Flows

A modified version of the Baldwin-Barth k-$\mathcal{R}$ two-equation turbulence model is proposed, in which the near-wall function f_μ is based on the ratio of the large eddy and the Kolmogorov time scales. This results in a model applicable to both wall-bounded and free shear flows which, nevertheless, does not require explicit knowledge of local distance to walls, rendering it useful within both structured and unstructured computational frameworks for flow predictions involving complex geometries. The new model's predictive capability is demonstrated through a number of flow cases.

Introduction

The modeling of turbulence in near-wall regions usually involves distance to wall as an explicit parameter in the formulation. When dealing with complex flows involving multiple surfaces, the notion of wall distance becomes difficult to define properly and is often cumbersome to implement. It is, therefore, desirable to develop a model which, while applicable all the way to solid surfaces, does not involve wall distance explicitly. Such a model is described in this paper, based on the concept of large- to small eddy time scale ratio. The present approach utilizes this scale ratio as a basic parameter to construct the near-wall function f_μ which extends the validity of the k-$\mathcal{R}$ two-equation turbulence model (Baldwin and Barth, 1990) to near-wall regions, where damping and molecular viscosity effects are important. Consequently, the resulting model does not require explicit knowledge of distance to walls, making it a potentially useful tool in conjunction with both traditional structured grids and the increasingly popular unstructured grids for numerical computation of wall-bounded and free shear flows involving complex geometries.

A pointwise k-ϵ model was introduced by Launder and Sharma (1974). That model includes terms which involve $\partial\sqrt{k}/\partial y$ and $\partial^2 U/\partial y^2$, making it numerically "stiff" in near-wall regions. This demands careful choice of initial profiles for U, k, and ϵ, to avoid severe computational transients. The k-$\mathcal{R}$ model has a major advantage over this k-ϵ model: since $\mathcal{R} \equiv k^2/\epsilon$ naturally vanishes at solid surfaces, there is no need for extra terms in the $\mathcal{R}$ equation, unlike the situation with the ϵ equation. This renders the k-$\mathcal{R}$ model much more robust and permits simple flow-field initialization.

The performance of the new model is demonstrated through comparison with experimental data of several well documented flow cases. All the examples were initialized with freestream conditions and with constants for k and $\mathcal{R}$.

Model Formulation

The starting point of the present work is the k-$\mathcal{R}$ model of Baldwin and Barth (1990) which consists of the solution to the following two coupled partial differential equations: Turbulence kinetic energy (k) equation

$$\frac{D(\rho k)}{Dt} = \nabla \bullet [(\mu + \mu_t/\sigma_k)\nabla k] + P - \frac{(\rho k)^2}{\rho\mathcal{R}}, \qquad (1)$$

eddy viscosity ($\mathcal{R}$) equation

$$\frac{D\mathcal{R}}{Dt} = (\nu + \nu_t/\sigma_\epsilon)\nabla^2\mathcal{R} + (2 - C_{\epsilon 1})\frac{\mathcal{R}}{\rho k}P - (2 - C_{\epsilon 2})k - \frac{1}{\sigma_\epsilon}\nabla\nu_t \bullet \nabla\mathcal{R} \qquad (2)$$

where the turbulence production term is given in terms of the Boussinesq concept

$$P = \left[\mu_t\left(\frac{\partial U_i}{\partial x_j} + \frac{\partial U_j}{\partial x_i} - \frac{2}{3}\frac{\partial U_k}{\partial x_k}\delta_{ij}\right) - \frac{2}{3}\rho k\delta_{ij}\right]\frac{\partial U_i}{\partial x_j}. \qquad (3)$$

Here k is the turbulence kinetic energy; $\mathcal{R} \equiv k^2/\epsilon$ is the undamped eddy viscosity; ρ is the density; U_i are the cartesian mean velocity components; μ and ν are the molecular and kinematic viscosities, respectively; μ_t and ν_t are the corresponding eddy viscosities; x_i are the cartesian coordinates; and t is time. The model constants are those of the standard k-ϵ model,

$$\sigma_k = 1.0, \quad \sigma_\epsilon = 1.30, \quad C_{\epsilon 1} = 1.44, \quad C_{\epsilon 2} = 1.92.$$

The eddy viscosity is then given by

$$\nu_t = C_\mu f_\mu \mathcal{R} \qquad (4)$$

where $\nu_t \equiv \mu_t/\rho$, and $C_\mu = 0.09$.

The role of the function f_μ is to extend the validity of the model to near-wall regions, where anisotropy and molecular effects are significant. The ratio of the energy containing (large eddy) and the dissipative (small eddy, or Kolmogorov) time scales is used as the basic parameter to define the near-wall function. This ratio is given by $\mathcal{J} = (k/\epsilon)/(\nu/\epsilon)^{1/2} = k/\sqrt{\nu\epsilon} = (\mathcal{R}/\nu)^{1/2} \equiv R_T^{1/2}$. R_T is commonly called the "tur-

---

Contributed by the Fluids Engineering Division for publication in the JOURNAL OF FLUIDS ENGINEERING. Manuscript received by the Fluids Engineering Division October 7, 1992; revised manuscript received August 16, 1993. Associate Technical Editor: G. Karniadakis.

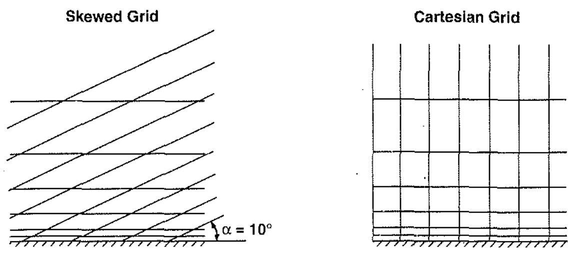

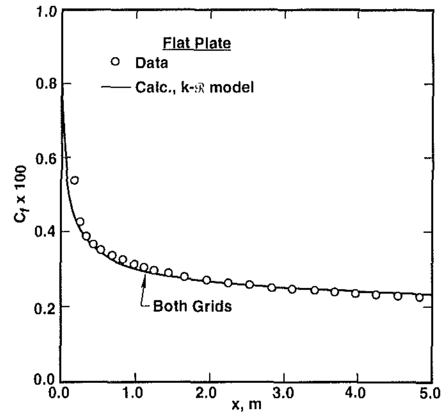

Fig. 1(*a*) Flat plate flow: skin friction distribution

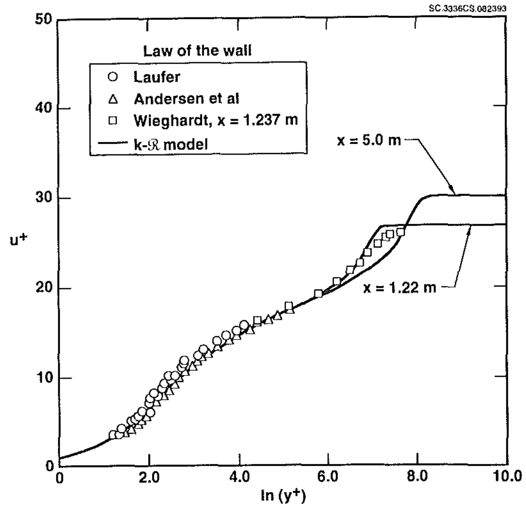

Fig. 1(*b*) Flat plate flow: comparison of velocity profile with law-of-the-wall

bulence Reynolds number.'' A promising choice for f_μ belongs to the family of functions given by

$$f_\mu=\frac{1-e^{-A_\mu R_T^n}}{1-e^{-A_\epsilon R_T^n}}. \tag{5}$$

In the current work the following values were used: $A_\mu = 2.5 \times 10^{-6}$, $A_\epsilon = C_\mu^{3/4}/2\kappa$ ($\kappa = 0.41$), and $n = 2$. This choice enables good prediction of the law-of-the-wall and of near-wall energy budget for flat plate flow at zero pressure gradient, as shown in the next section. (Launder and Sharma (1974) used the near-wall function $f_\mu = \exp\{-3.4/(1 + R_T/50)^2\}$.)

Equations (1) and (2) are subject to the following boundary conditions:

(i) Solid Walls

$$k=0,\ \mathcal{R}=0, \tag{6}$$

(ii) symmetry surface

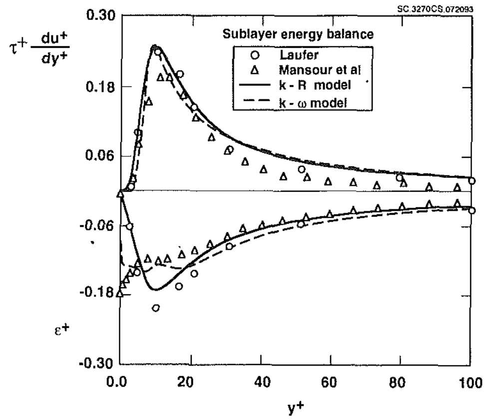

Fig. 1(*c*) Flat plate flow: near-wall production and dissipation profiles

$$\frac{\partial k}{\partial y}=0, \quad \frac{\partial \mathcal{R}}{\partial y}=0 \tag{7}$$

where y is the normal-to-surface direction,

(iii) freestream (and initial) conditions

$$k/U_{\rm ref}^2=10^{-6}, \quad \mathcal{R}/\nu_{\rm ref}\ll 1. \tag{8}$$

In the examples, a value of $\mathcal{R}/\nu_{\rm ref} = \mathcal{O}(10^{-5})$ was used. The new two-equation k-$\mathcal{R}$ model, Eqs. (1)-(8), is completely pointwise.

The near-wall relation between $\mathcal{R}$ and k is also of interest. Neglecting the material derivative term and taking into account the fact that $\nu_t \ll \nu$ at the immediate vicinity of walls, Eq. (1) assumes the approximate form

$$\mu\frac{\partial^2 k}{\partial y^2}+P-\rho\frac{k^2}{\mathcal{R}}=0. \tag{9}$$

The near-wall production term reduces to

$$P=\mu_t(\partial U/\partial y)^2=C_\mu(A_\mu/A_\epsilon)\rho\mathcal{R}(\partial U/\partial y)^2 \tag{10}$$

when Eqs. (4) and (5) are used, the latter in its near-wall limit. Also, the streamwise momentum equation reduces to

$$\partial U/\partial y=u_\tau^2/\nu, \quad u_\tau\equiv\sqrt{(\tau/\rho)_{\rm wall}}. \tag{11}$$

Combining Eqs. (9)-(11) and switching from $\mathcal{R}$ to R_T then yields

$$C_\mu(A_\mu/A_\epsilon)u_\tau^4R_T^2+\nu^2\frac{\partial^2 k}{\partial y^2}R_T-k^2=0. \tag{12}$$

Since R_T vanishes at walls, and assuming that $\partial^2k/\partial y^2$ remains finite there, the first term in Eq. (12) may be neglected relative to the second term, whence

$$R_T\approx\frac{k^2}{\nu^2\partial^2k/\partial y^2}, \quad y\to 0. \tag{13}$$

Thus, if $k \sim y^2$ then $R_T \sim y^4$ as $y \to 0$, consistent with the corresponding asymptotic behavior of k^2/ϵ.

Examples

The pointwise k-$\mathcal{R}$ turbulence model was included in the USA Reynolds-averaged Navier-Stokes structured grid flow solver, which is a highly (up to 3rd order) accurate solver based on a TVD formulation for the convection terms within a finite volume framework (Chakravarthy et al., 1988). The model was also incorporated into Wilcox's (1993) SUBLAYER flow solver. Four flow cases are reported here.

Case 1. This is the case of subsonic flow over an adiabatic flat plate with zero pressure gradient, considered a standard case for calibration and testing of turbulence models. Figure 1(*a*) shows comparison between calculation and data (Wieghardt and Tillmann, 1951) of skin friction along the plate. The

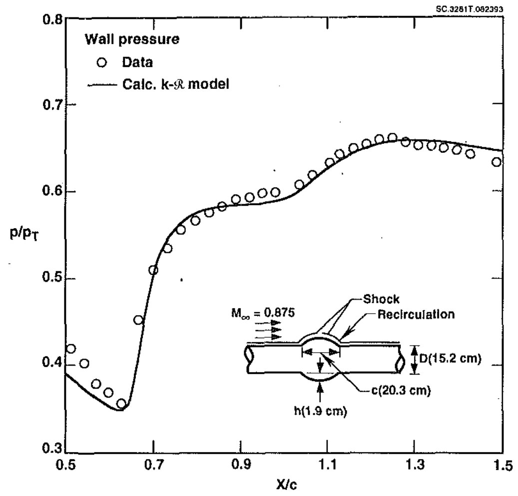

Fig. 2(*a*) **Transonic bump flow: wall pressure distribution**

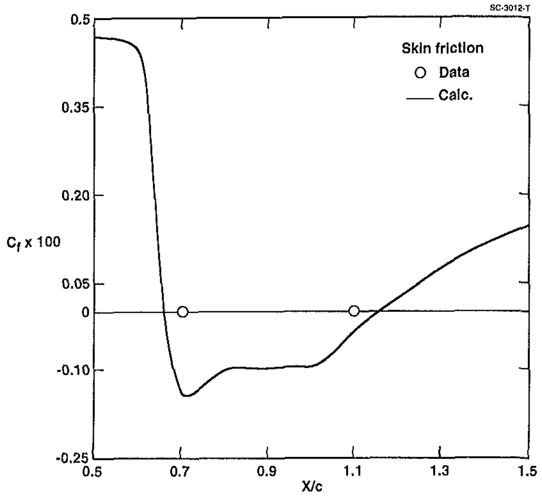

Fig. 2(*b*) **Transonic bump flow: skin friction distribution**

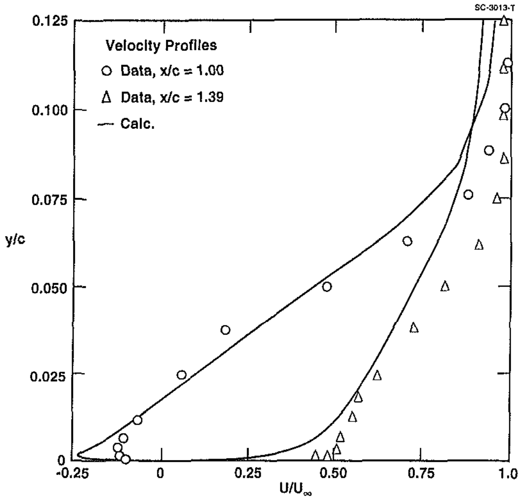

Fig. 2(*c*) **Transonic bump flow: velocity profiles**

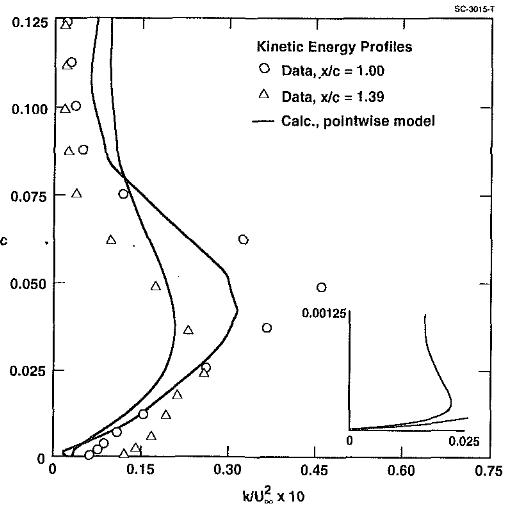

Fig. 2(*d*) **Transonic bump flow: turbulence kinetic energy profiles**

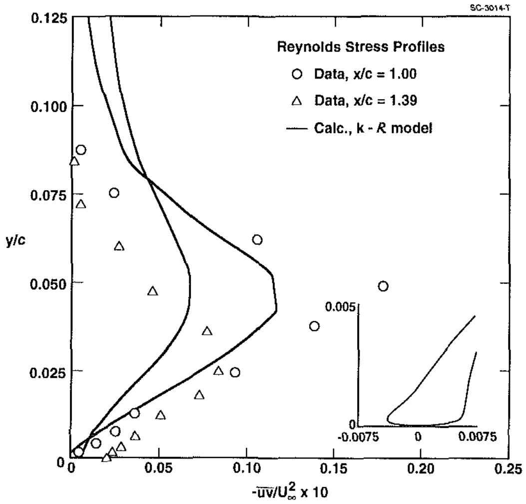

Fig. 2(*e*) **Transonic bump flow: Reynolds stress profiles**

computations were done on two grids: a cartesian and a highly skewed one, both with the same mesh density. The results demonstrate the immunity of the pointwise model to grid skewness. Figure 1(*b*) compares two near-wall velocity profiles, at $x = 1.22$ and 5.0 m, with law-of-the-wall measurements by Laufer (1952), Andersen et al. (1972), and Wieghardt (Coles and Hirst, 1969). A 110 × 50 grid size was used, with at least 14 cells inside the viscous sublayer ($y^+ \leq 11$). The first point off the wall was at $y^+ = 0.1$. Residuals were reduced by five orders of magnitude by the time the solution was converged. A 110 × 100 grid was also used, yielding the same results.

A near-wall computation was also performed using Wilcox's (1993) SUBLAYER code. Figure 1(*c*) compares near-wall energy balance with experimental data of Laufer (1952) and with DNS results of Mansour et al. (1988). The figure includes prediction by Wilcox's k-ω model (Wilcox, 1993) used with its near-wall functions.

Case 2. This is the transonic flow over an axisymmetric bump of Bachalo and Johnson (1979). Here a normal shock, impinging on the bump, causes flow detachment from the surface with subsequent reattachment further downstream on the cylindrical surface. A sketch of the geometry with main flow features is included in Fig. 2(*a*). In Figs. 2 x is the axial coordinate, with origin at the bump leading edge; and y is the radial coordinate, with origin at the axis of symmetry. Figs. 2(*a*), 2(*b*) present comparisons between predictions and data of surface pressure (p_w) and skin friction (C_f) distributions. All lengths are scaled by the bump cord, c, and pressure is scaled by the upstream total pressure, p_T. The extent of flow separation is seen by the region of negative skin friction in Fig. 2(*b*). Figs. 2(*c*), 2(*d*), and 2(*e*) compare predictions with data of velocity, turbulence kinetic energy, and Reynolds stresses, respectively, at two streamwise locations. A 101 × 50 grid size was employed, with at least three cells inside the

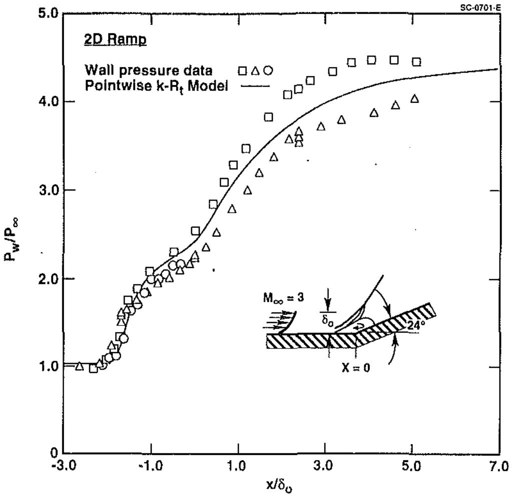

Fig. 3(*a*) **Supersonic ramp flow: wall pressure distribution**

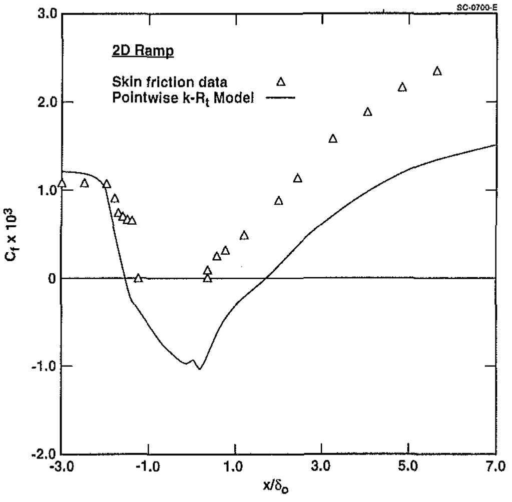

Fig. 3(*b*) **Supersonic ramp flow: skin friction distribution**

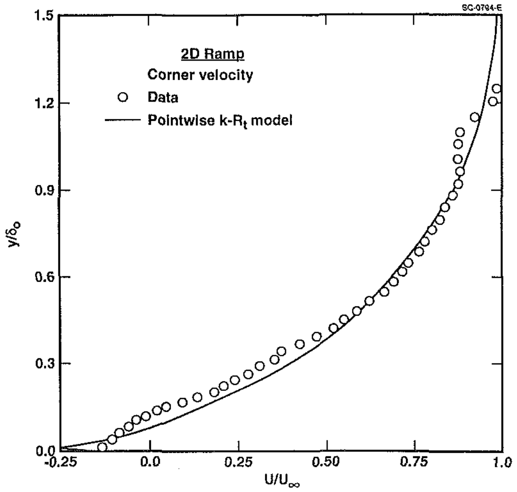

Fig. 3(*c*) **Supersonic ramp flow: corner velocity profile**

viscous sublayer. By the time the solution was converged, there was a four orders of magnitude reduction in residuals.

Case 3. This is the supersonic two-dimensional flow over a 24 deg ramp of Settles et al. (1979), with additional data by Dolling and Murphy (1983), and by Selig et al. (1989). An oblique shock, impinging on the boundary layer ahead of the ramp corner (due to upstream influence), induces flow detachment, with subsequent reattachment onto the ramp surface. Figures 3 show predictions and data comparisons of surface pressure, skin friction, and corner velocity profile. A sketch, showing the geometry and some flow features, is included in Fig. 3(*a*). The origin of the (x, y) cartesian coordinate system is located at the ramp corner, with directions along and normal to the upstream flat plate, respectively. These coordinates are scaled by the boundary layer thickness upstream of the shock, δ_0. Wall pressure (p_w) is scaled by the upstream inflow pressure (p_∞). The extent of flow separation is seen in the skin friction plot, Fig. 3(*b*), in the region where $C_f < 0$. A 125 × 50 grid size was used, with at least four cells within the viscous sublayer. Again, a four orders of magnitude reduction in residuals was achieved by the time of solution convergence.

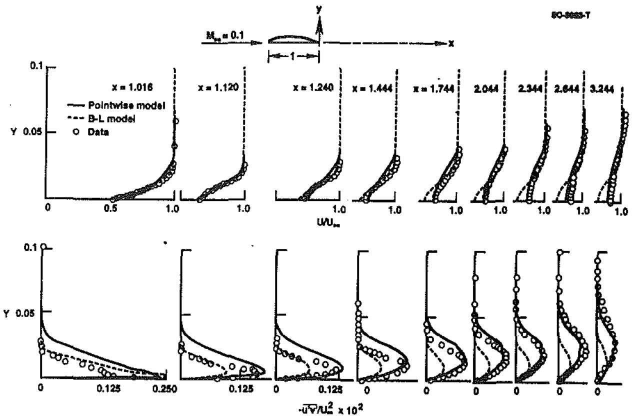

Fig. 4 Thin airfoil wake flow: velocity and Reynolds stress profiles

Case 4. This is a subsonic two-dimensional flow over a thin symmetric wing, with experimental data by Pot (1979) taken in the wake region. This case is particularly illuminating since the model is expected to detect automatically the switch from wall-bounded to wake flow and build the eddy viscosity field accordingly. A 104 × 75 "*C*" grid was used, with two cells inside the viscous sublayer over the wing. Figure 4 shows a sketch of the geometry, indicates the coordinate system and compares data of wake velocity and Reynolds stress profiles with predictions by the current model as well as by the Baldwin-Lomax algebraic turbulence model. Six orders of magnitude reduction in residuals was obtained when the solution converged.

Conclusions

This work demonstrated the feasibility of utilizing a pointwise k-$\mathcal{R}$ model for predicting wall-bounded and free shear turbulent flows at the level of detail usually needed for engineering analysis and design purposes. Since the model does not require explicit knowledge of distance to solid surfaces, it is most suitable for use with Navier-Stokes solvers which incorporate unstructured computational grid frameworks. As shown in the examples, the model is naturally applicable to traditional structured grids, in which case reduced effort in constructing multi-block grids is attainable thanks to the model's pointwise attributes.

References

Andersen, P. S., Kays, W. M., and Moffat, R. J., 1972, "The Turbulent Boundary Layer on a Porous Plate: An Experimental Study of the Fluid Mechanics for Adverse Free-Stream Pressure Gradients," Report No. HMT-15, Dept. Mech. Eng., Stanford University, CA.

Bachalo, W. D., and Johnson, D. A., 1979, "An Investigation of Transonic

Turbulent Boundary Layer Separation Generated on an Axisymmetric Flow Model," AIAA Paper 79-1479.

Baldwin, B. S., and Barth, T. J., 1990, "A One-Equation Turbulence Transport Model for High Reynolds Number Wall-Bounded Flows," NASA TM 102847.

Chakravarthy, S. R., Szema, K.-Y., and Haney, J. W., 1988, "Unified 'Nose-to-Tail' Computational Method for Hypersonic Vehicle Applications," AIAA Paper 88-2564.

Coles, D. E., and Hirst, E. A., 1969, "Computation of Turbulent Boundary Layers—1968 AFOSR-IFP-Stanford Conference," Vol. II, Stanford University, CA.

Dolling, D. S., and Murphy, M. T., 1983, "Unsteadiness of the Separation Shock Wave Structure in a Supersonic Compression Ramp Flowfield," *AIAA Journal*, Vol. 21, No. 12, pp. 1628–1634.

Laufer, J., 1952, "The Structure of Turbulence in Fully Developed Pipe Flow," NACA TM 1174.

Launder, B. E., and Sharma, B. I., 1974, "Application of the Energy-Dissipation Model of Turbulence to the Calculation of Flow Near a Spinning Disc," letters in *Heat and Mass Transfer*, Vol. 1, pp. 131–138.

Mansour, N. N., Kim, J., and Moin, P., 1988, "Reynolds Stress and Dissipation Rate Budgets in Turbulent Channel Flow," *Journal of Fluid Mechanics*, Vol. 194, pp. 15–44.

Pot, P. J., 1979, "Measurements in a 2-D Wake and in a 2-D Wake Merging Into a Boundary Layer. Data Report," NLR TR 79063 IL, Holland.

Selig, M. S., Andreopoulos, J., Muck, K. C., Dussauge, J. P., and Smits, A. J., 1989, "Turbulence Structure in a Shock Wave/Boundary Layer Interaction," *AIAA Journal*, Vol. 27, No. 7, pp. 862–869.

Settles, G. S., Fitzpatrick, T. J., and Bogdonoff, S. M., 1979, "Detailed Study of Attached and Separated Compression Corner Flowfields in High Reynolds Number Supersonic Flow," *AIAA Journal*, Vol. 17, No. 6, pp. 579–585.

Wieghardt, K., and Tillmann, W., 1951, "On the Turbulent Friction Layer for Rising Pressure," NACA TM 1314.

Wilcox, D. C., 1993, *Turbulence Modeling for CFD*, DCW Industries, Inc., La Cañada, CA.

D. G. Dommermuth
Research Scientist,
Naval Hydrodynamics Division,
Science Applications
International Corporation,
10260 Campus Point Drive, MS 34,
San Diego, CA 92121

Efficient Simulation of Short and Long-Wave Interactions With Applications to Capillary Waves

A perturbation expansion and a multigrid technique are developed for simulating the fully-nonlinear unsteady-interaction of short waves riding on long gravity waves. Both numerical techniques are capable of simulating wave slopes near breaking and wavelength ratios greater than thirty, but the multigrid technique converges more rapidly and it is more efficient. The results of numerical simulations agree qualitatively with experimental measurements of ripple formation on the front face of a gravity-capillary wave.

Introduction

The study of short waves riding on long waves is currently an active research area because of remote sensing applications. Knowledge of short and long-wave interactions is also required to understand how wind energy is transferred to water waves. When the orbital velocity of the long waves is comparable to the phase velocity of the short waves, a standard theoretical approach neglects the energy transfer from the short waves to the long waves so that the long wave can be prescribed in advance (see Longuet-Higgins, 1987).

In this paper, two numerical algorithms are developed for simulating the unsteady interactions of short waves with long waves. A useful feature of both numerical procedures is the output of the entire three-dimensional subsurface velocity field. Some possible applications of this feature include the study of wave scattering by turbulence (Phillips, 1959) and the formation of Langmuir circulations (Craik and Leibovich, 1976). In both cases a Helmholtz decomposition of the vortical and wavy portions of the flow is useful for modeling different flow regimes (see, for example, Dommermuth, 1992a). Two numerical techniques (a perturbation expansion and a multigrid technique) are proposed for efficiently solving the three-dimensional elliptic equations that are present in Helmholtz decompositions and other formulations of nonlinear free-surface flows.

The numerical methods are used to study parasitic capillary waves, which were first studied experimentally by Cox (1958) and theoretically by Longuet-Higgins (1963). Weak viscous effects are included based on the boundary-layer analysis of Lundgren (1989), and comparisons are made to the experiments of Ruvinsky et al. (1991).

Mathematical Formulation

The kinematic and dynamic free-surface boundary conditions including weak viscous effects are as follows:

$$\frac{\partial \eta}{\partial t}+\eta_x\phi_x+\eta_y\phi_y-\frac{2}{\mathrm{R_e}}(\eta_{xx}+\eta_{yy})=\phi_z+O\left(\frac{\epsilon^2}{\mathrm{R_e}},\ \mathrm{R_e}^{-3/2}\right)$$

$$\frac{d\phi}{dt}+\frac{1}{2}(\phi_x^2+\phi_y^2-\phi_z^2)+(\eta_x\phi_x+\eta_y\phi_y)\phi_z+\frac{1}{\mathrm{F_r^2}}\eta$$
$$-\frac{2}{\mathrm{R_e}}(\phi_{xx}+\phi_{yy})=-P_a-\frac{1}{\mathrm{W_e}}\nabla\cdot\mathbf{n}+O\left(\frac{\epsilon^2}{\mathrm{R_e}},\ \mathrm{R_e}^{-3/2}\right),\qquad (1)$$

where η and ϕ are the free-surface elevation and the velocity potential, $\mathrm{R_e}$, $\mathrm{F_r}$, and $\mathrm{W_e}$ are, respectively, the Reynolds, Froude, and Weber numbers, and $\mathbf{n}$ is the unit outward pointing normal. (The definitions of the nondimensional parameters are provided in the next section, which is focused on a specific type of flow.) P_a is the atmospheric pressure, and the wave steepness is denoted by ϵ. Equations (1) are satisfied on the exact position of the free surface. Note that Lundgren's (1989) analysis includes higher-order viscous terms and allows weak shear stresses such as wind forcing. For the present analysis, however, the lowest-order viscous effects are sufficient.

Laplace's equation is satisfied in the interior of the fluid. Based on Freeman et al.'s (1972) transformation, let $\hat{z}=F(x,y,z,t)=(z+D)/(\eta+D)$ account for the mapping of the free surface onto a flat plane, where D is the depth, and let $k=G(\hat{z})$ account for grid stretching. These mappings lead to the following expression for Laplace's equation:

$$\phi_{xx}+\phi_{yy}+(F_x^2+F_y^2+F_z^2)G_{\hat{z}}^2\phi_{kk}+2F_yG_{\hat{z}}\phi_{yk}+2F_xG_{\hat{z}}\phi_{xk}$$
$$-((F_{xx}+F_{yy})G_{\hat{z}}+(F_x^2+F_y^2+F_z^2)G_{\hat{z}\hat{z}})\phi_k=0.\qquad (2)$$

The first numerical solution that is considered for solving the preceding elliptic equation is a perturbation expansion. Let $\phi^m(x,y,k,t)$ denote the m-th iterant solution to the velocity potential, then the following arrangement of terms provides an efficient algorithm for solving Laplace's equation with Dirichlet free-surface boundary conditions:

Contributed by the Fluids Engineering Division for publication in the JOURNAL OF FLUIDS ENGINEERING. Manuscript received by the Fluids Engineering Division August 31, 1992; revised manuscript received May 6, 1993. Associate Technical Editor: O. Baysal.

$$\phi_{xx}^{m+1}+\phi_{yy}^{m+1}+\frac{G_{\hat{z}}^2}{D^2}\,\phi_{kk}^{m+1}+\frac{G_{\hat{z}\hat{z}}}{D^2}\,\phi_{k}^{m+1}=$$
$$-\left(F_x^2+F_y^2+F_z^2-\frac{1}{D^2}\right)G_{\hat{z}}^2\phi_{kk}^m-2F_yG_{\hat{z}}\phi_{yk}^m-2F_xG_{\hat{z}}\phi_{xk}^m$$
$$-\left((F_{xx}+F_{yy})G_{\hat{z}}+\left(F_x^2+F_y^2+F_z^2-\frac{1}{D^2}\right)G_{\hat{z}\hat{z}}\right)\phi_k^m, \qquad (3)$$

where the terms on the left side of the equation are $O(1)$ and the terms on the right side are $O(\epsilon)$. This ordering of terms occurs because ϕ, $G(\hat{z})$, and D are $O(1)$ quantities, and the x- and y-derivatives of $F(x,y,z,t)$ are $O(\epsilon)$ for $\eta/D=O(\epsilon)$. Since F_z-1/D is $O(\epsilon)$, the dominant behavior of F_z can be extracted by adding appropriate terms to the left and right-hand sides of Eq. (2) as in Eq. (3).

Laplace's equation is discretized using fourth-order finite differences in Eq. (3). A Fast Fourier transform with respect to x and y leads to a set of one-dimensional Poisson equations that are solved using banded LU-decomposition. The source term on the right-hand side of the equation is updated, and the solution scheme repeats itself. Generally, for moderate nonlinearity ($\epsilon \leq 0.3$) only two to four iterations are required because a good approximation to the potential is available during each stage of the fourth-order Runge-Kutta time-stepping procedure. An 8th-order smoothing scheme is used to inhibit the formation of sawtooth instabilities. Details of a similar numerical algorithm are provided by Dommermuth (1992a).

The second numerical algorithm is a preconditioned multigrid solution technique. The preconditioning stage is used to reduce the complexity of the multigrid algorithm. Multigrid is used to solve a second-order accurate problem which is used as a guess to the fourth-order solution. Let $\mathcal{L}_2$ and $\mathcal{L}_4$ respectively denote second-order and fourth-order accurate approximations to the elliptic operator in Eq. (2), and let $\phi^m=\psi^m+\Phi^m$, where ψ^m is a second-order preconditioner and Φ^m is the fourth-order solution to the Dirichlet problem. Then the iterative solution to Laplace's equation proceeds as follows:

$$\mathcal{L}_2\psi^m=-\mathcal{L}_4\Phi^m, \qquad (4)$$

where initially Φ^0 is equal to its value at a previous time step and the solution for ψ^0 is obtained using a V-cycle multigrid algorithm. Then Φ^1 is set equal to ϕ^0, where $\phi^0=\psi^0+\Phi^0$, and the solution scheme repeats itself until the fourth-order solution (Φ^m) has converged. A line Gauss-Seidel algorithm is used as a smoother, and the time-stepping procedure is the same as the perturbation scheme. Details of a similar multigrid procedure for solving the second-order solution to ψ^m are provided in Dommermuth and Yue (1990).

On a Cray Y-MP 8/8128 the perturbation scheme requires 1.8 CPU seconds (using a single processor) per iteration to solve a two-dimensional boundary-value problem with 256^2 unknowns. The multigrid scheme requires 0.9 CPU seconds per iteration to solve the same problem. However, as discussed in the next section the convergence of the multigrid scheme is much more rapid than the perturbation scheme, so that the overall efficiency of multigrid scheme is also much greater than the perturbation scheme for a given level of accuracy. Moreover, recent vectorization efforts have increased the speed of the multigrid code by a factor of ten.

Numerical Simulations

The convergence of the elliptic solvers is tested using the following Dirichlet boundary-value problem:

$$\eta=a\cos(k_1x)\cdot\quad \phi^s=\frac{\cosh(k_1(\eta+D))}{k_1\cosh(k_1(a+D))}\sin(k_1x)+\frac{\cosh(k_2(\eta+D))}{k_2\cosh(k_2(a+D))}\sin(k_2x), \qquad (5)$$

where η is the free-surface elevation, ϕ^s is the value of the potential on the free-surface (i.e., the surface potential), $a=0.1$ is the amplitude of the free-surface disturbance, $k_1=2\pi$ represents a long wave, $k_2=16\pi$, 32π, and 64π represents short waves, and $D=1$ is the depth. The boundary condition on the bottom is no flux. The preceding Dirichlet problem is solved using the perturbation and multigrid techniques and then the vertical velocity on the free surface (w^s) is calculated to test the accuracy and the convergence of the numerical algorithms.

Table 1 illustrates the convergence of the numerical algorithms as a function of the number of grid points and iterations. The expected fourth-order spatial accuracy is achieved for multigrid scheme as the grid resolution and the number of iterations increase. (The results of the multigrid scheme indicate that 16, 32, and 64 points per short wave, respectively, provide 3, 4 1/2, and 6 digits of accuracy.) However, the convergence of the perturbation scheme is not rapid enough to realize the fourth-order accuracy because the reduction in error at each stage of the iterative process is only proportional to the wave steepness. (For the perturbation scheme $\mathcal{E} \propto \epsilon^{N_m}$, where $\mathcal{E}$ is the error, ϵ is the wave steepness, and N_m is the number of iterations.) The perturbation scheme is also less efficient than the multigrid scheme because of the poorer convergence. For example, as shown in Table 1, the multigrid scheme converges in less than four iterations, whereas oftentimes the perturbation scheme has not converged even after sixteen iterations.

For both numerical schemes the number of operations per iteration (N_m) is roughly proportional to the number of unknowns, but the multigrid scheme requires fewer iterations than the perturbation scheme to achieve the same level of accuracy. The perturbation scheme requires at least $N_m=\log_2(k_2/k_1)$ iterations so that the higher harmonics of the long wave can interact with the short wave, whereas the convergence of the multigrid scheme is not sensitive to either the wave steepness or the ratio of the long wave to the short wave. The assumptions that are used in the perturbation expansion are much less stringent than either the Schrodinger or Zakaharov theories, but none of these theories is capable of simulating the two-way exchange of energy between short and long waves. The only viable alternative for the simulation of a directional wave spectrum with a broad band and strong nonlinearity is a direct numerical solution such as multigrid.

Nomenclature

$\mathrm{R_e}$ = Reynolds number
$\mathrm{F_r}$ = Froude number
$\mathrm{W_e}$ = Webber number
ρ = density
σ = surface tension
g = gravity
ν = kinematic viscosity
(x,y,z) = Cartesian coordinates
$\hat{z}$ = mapped z-coordinate
F,G, and H = Mapping functions
t = time
T = gravity-wave period
ϕ = potential field
η = free-surface elevation
ϵ = wave steepness
$\mathcal{E}$ = relative error
E = energy
λ = gravity wavelength
λ_r = ripple wavelength
θ_r = ripple steepness
$\mathbf{n}$ = unit normal on free surface
P_a = atmospheric pressure
D = depth
$(\ )^m$ = denotes iteration number
$\mathcal{L}$ = elliptic operator

As an illustration of the multigrid technique's effectiveness, consider the formation of ripples on the front face of a gravity-capillary wave. Let the characteristic length and velocity be denoted by $L_c = \lambda$ and $U_c = \sqrt{g\lambda}$, where λ is the length of the gravity-capillary wave and g is gravity. Then the Froude, Weber, and Reynolds numbers are $\mathrm{F_r} = 1$, $\mathrm{W_e} = \rho g \lambda^2/\sigma$, *and* $R_e = g^{1/2}\lambda^{3/2}/\nu$, where ρ is the fluid density, σ is the surface tension, and ν is the kinematic viscosity. The two-dimensional numerical simulation is initialized using an exact solution for a gravity wave (see Schwartz, 1974 and Dommermuth and Yue, 1987), and the parasitic capillaries are generated from rest due to a parametric resonance. This is a stringent test of the multigrid technique's effectiveness because a very high harmonic of the gravity wave is responsible for forcing the ripples at the crest.

Table 1 Stokes wave convergence test

Perturbation scheme				Multigrid scheme			
k_2	N_m	N_x	$\mathcal{E}$	k_2	N_m	N_x	$\mathcal{E}$
16π	4	128	4.6×10^{-1}	16π	4	128	1.4×10^{-3}
		256	9.6×10^{-1}			256	6.5×10^{-5}
		512	2.0×10^{0}			512	2.6×10^{-6}
	8	128	1.9×10^{-2}		8	128	1.4×10^{-3}
		256	3.1×10^{-2}			256	6.5×10^{-5}
		512	5.6×10^{-2}			512	2.6×10^{-6}
	16	128	1.8×10^{-3}		16	128	1.4×10^{-3}
		256	2.0×10^{-4}			256	6.5×10^{-5}
		512	1.9×10^{-4}			512	2.6×10^{-6}
32π	4	128	4.8×10^{-1}	32π	4	128	2.2×10^{-2}
		256	1.0×10^{0}			256	1.5×10^{-3}
		512	2.1×10^{0}			512	6.5×10^{-5}
	8	128	2.4×10^{-2}		8	128	2.2×10^{-2}
		256	3.2×10^{-2}			256	1.5×10^{-3}
		512	5.9×10^{-2}			512	6.5×10^{-5}
	16	128	2.4×10^{-2}		16	128	2.2×10^{-2}
		256	1.9×10^{-3}			256	1.5×10^{-3}
		512	1.9×10^{-4}			512	6.5×10^{-5}
64π	4	128	4.9×10^{-1}	64π	4	128	1.6×10^{-1}
		256	1.0×10^{0}			256	2.2×10^{-2}
		512	2.1×10^{0}			512	1.6×10^{-2}
	8	128	1.5×10^{-1}		8	128	1.6×10^{-1}
		256	3.3×10^{-2}			256	2.2×10^{-2}
		512	6.0×10^{-2}			512	1.5×10^{-3}
	16	128	1.5×10^{-1}		16	128	1.6×10^{-1}
		256	2.5×10^{-2}			256	2.2×10^{-2}
		512	2.0×10^{-3}			512	1.5×10^{-3}

k_2 is the wavenumber of the short wave. N_m is the number of iterations used to solve Laplace's equation, and N_x is the number of equally spaced grid points along the x- and z-axes. $\mathcal{E} = |\tilde{w}^s - w^s|_{\max}/|w^s|_{\max}$ is the maximum relative error in the vertical velocity on the free surface. The initial estimate is $\phi^0 = 0$. The multigrid scheme uses $N_\upsilon = 1$ V-cycles and $N_g = 4$ Gauss-Seidel sweeps during each stage of the preconditioning.

Table 2 Data for numerical simulations of ripples

	Run 1	Run 2	Run 3	Run 4	Run 5	Run 6	Run 7
λ(cm)	5	5	5	5	10	10	10
H/λ	.058	.062	.066	.070	.09	.09	.09
$\mathrm{F_r}$	1	1	1	1	1	1	1
$\mathrm{W_e}$	331	331	331	331	1,330	1,330	1,330
$\mathrm{R_e}$	35,000	35,000	35,000	35,000	99,000	99,000	99,000
L	1	1	1	1	1	1	1
D	1	1	1	1	1	1	1
N_t	400	400	400	400	1600	800	400
N_p	8	8	8	8	3	3	3
N_x	128	128	128	128	512	256	128
N_z	33	33	33	33	65	65	65
N_m	4	4	4	4	4	4	4
N_υ	1	1	1	1	1	1	1
N_g	6	6	6	6	4	4	4

λ is the length of the gravity-capillary wave in centimeters, and H/λ is the ratio of the wave height to the wave length. $\mathrm{F_r}$, $\mathrm{W_e}$, and $\mathrm{R_e}$ are, respectively, the Froude, Weber, and Reynolds numbers. L and D are, respectively, the length and depth of the computational domain. N_t is the number of time steps per gravity wave period, where $T \approx \sqrt{2\pi}\mathrm{F_r}$ is the dimensionless wave period. N_p is the number of wave periods that are simulated. N_x and N_z are the number of grid points along the x- and z-axes. N_m is the number of iterations used to perform the preconditioning. N_υ is the number of V-cycles used in the multigrid algorithm, and N_g is the number of Gauss-Seidel iterations.

An atmospheric forcing term is used to adjust the transition from a pure gravity wave to a gravity-capillary wave as follows:

$$P_a = -\frac{1}{\mathrm{W_e}} \nabla \cdot \mathbf{n} \exp\left(\frac{-t^2}{\delta^2}\right), \tag{6}$$

where $\delta = T$ is the adjustment time and T is the nondimensional wave period of the gravity wave. This adjustment procedure inhibits the generation of spurious high-frequency standing waves. Details of similar adjustment procedures are provided in Dommermuth (1992a and 1992b). As shown in the appendix, the grid is stretched near the free surface to resolve the exponential attenuation of the capillary waves. Table 2 provides other details of the numerical simulations.

Figures 1 and 2 illustrate the formation of ripples on 5 cm and 10 cm gravity-capillary waves. Based on the analysis of Longuet-Higgins (1963), the wave length of the ripples (λ_r) is determined by the condition that the phase velocity of the ripples is equal to the phase velocity of the gravity wave (c_o) plus the local water-particle velocity of the gravity wave (u_o). In our present notation, this relationship gives $\lambda_r = 2\pi/(\mathrm{W_e}(c_o + u_o)^2)$. The maximum wave length of the ripple occurs near the crest of the gravity wave where $c_o + u_o$ is a minimum. This formula gives $\lambda_r = 0.21$ and 0.069 at the crests of, respectively, the 5 cm and 10 cm waves, which agrees with the plots in Figs. 1 and 2. The initial steepness of the 5 cm wave ($\epsilon = \pi H = .22$, where H is the wave height) is less than the 10 cm wave ($\epsilon = .28$), *but the maximum steepness of the ripples* (θ_r) is greater for the 5 cm wave ($\theta_r \approx .24$) than it is for the 10 cm wave ($\theta_r \approx .06$). The explanation is that the harmonic of

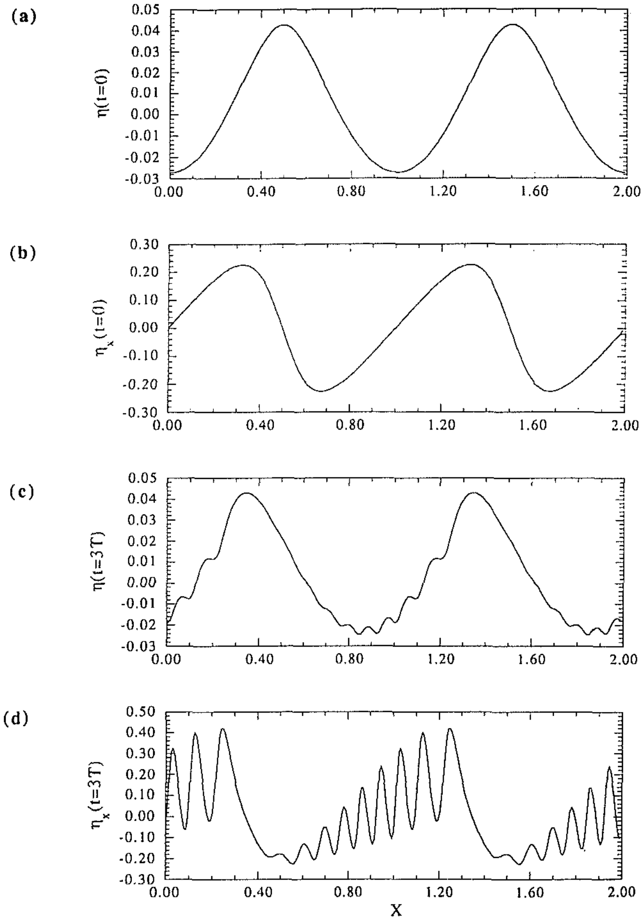

Fig. 1 Formation of ripples on a 5 cm gravity-capillary wave. Part (*a*) and (*b*) plot the initial free-surface elevation and slope. Parts (*c*) and (*d*) plot the same quantities after three gravity wave periods have elapsed. The *x*-axis has been periodically extended. Details of this simulation are provided in Run 4 of Table 2.

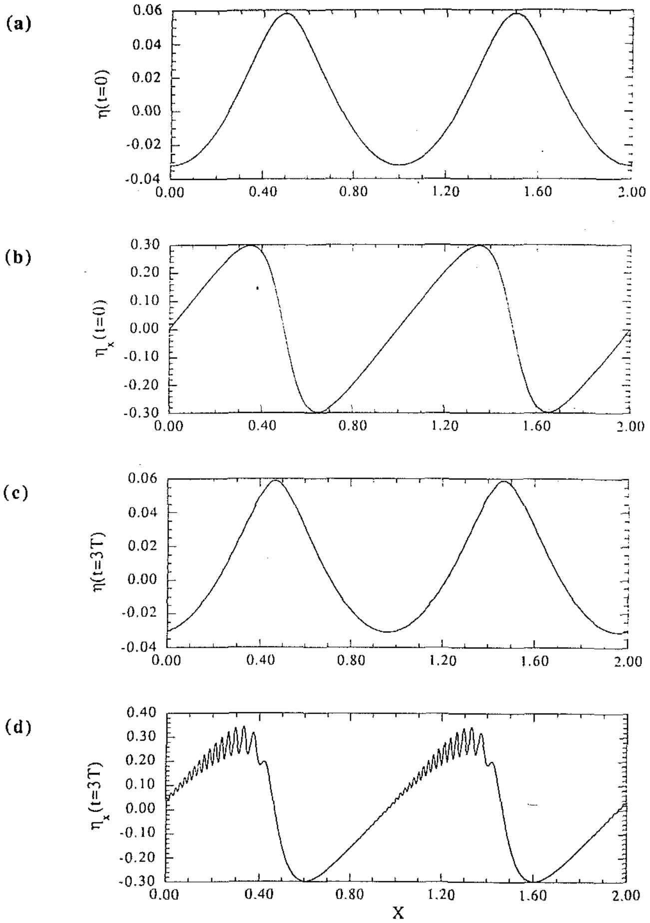

Fig. 2 Formation of ripples on a 10 cm gravity-capillary wave. See the preceding caption. Details of this simulation are provided in Run 5 of Table 2.

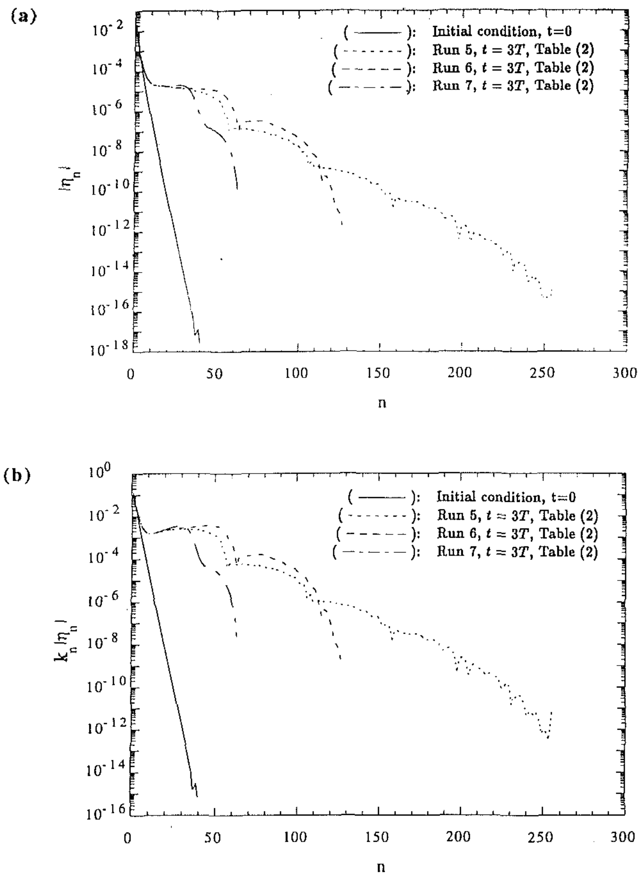

Fig. 3 Amplitude and slope spectra of a 10 cm gravity-capillary wave: a convergence study. Parts (*a*) and (*b*) are, respectively, the amplitude and slope spectra.

the gravity wave that forces the ripples on the 5 cm wave is greater than the forcing harmonic of the 10 cm wave. The steepness of the ripples actually exceeds the steepness of the 5 cm gravity wave.

In Fig. 3 the convergence of the multigrid scheme is illustrated using the 10 cm wave. Three numerical simulations with different resolutions are used to study the formation of the ripples. For these plots η_n are the Fourier coefficients of the free-surface elevation, where

$$\eta=\sum_{n=-N_x/2}^{N_x/2}\eta_n\exp(ik_nx) \qquad (7)$$

and $k_n=2\pi n$ is the wavenumber. The initial slopes of the spectra are very steep, but the subsequent formation of the ripples leads to much broader spectra. The slope spectrum becomes so broad that it even has some local minimums and maximums. We also observe that the spectra of the ripples converge as the grid resolution increases, especially at the lowest wavenumbers.

Figure 4 plots time histories of the amplitude of the gravity-capillary wave and the maximum steepness of the ripples. As is evident in Fig. 4(*a*) the attenuation of the gravity-capillary waves increases as the ripples form. The ripples form soon after the atmospheric forcing term (see Eq. 6)) has diminished to 40 percent of its initial value at time $t\approx T$, where recall T is the nondimensional wave period of the initial gravity wave. Figure 4(*b*) shows that upon reaching a maximum near time $t\approx 3T$, the ripples also steadily attenuate, but superimposed on top of this attenuation is an oscillation whose period ($3T\leq T_r\leq 4T$) depends on the steepness of the ripples. A similar periodic behavior has also been observed in the numerical simulations of Ferguson et al. (1978) who use a model equation to study various aspects of ripple formation. Aside from Ferguson et al.'s model equation, previous theories have not accounted for this nonlinear recurrence. Moreover, comparing Figs. 4(*a*) and 4(*b*) shows that a range of ripple steepnesses exists as a function of the instantaneous amplitude of the gravity-capillary wave. Consequently, laboratory and field measurements of ripples will be sensitive to the initial steepness of the gravity-capillary wave and the elapsed time since the ripples formed. For a free surface that is contaminated with surfactants the measurements are even more complex as is evident in the experiments of Hsu et al. (1983).

Figure 5 compares the results of numerical simulations and quasi-stationary theory to experimental measurements. The theory and experiments are due to Ruvinsky et al. (1991). Although the quasi-stationary theory models viscous attenuation, it does not account for the effects of the initial conditions, nor does it model nonlinear recurrence. A few of the experimental points and a portion of theoretical curve in Fig. 5 lie within the envelop of possible solutions that is calculated using the present numerical scheme. Since the experiments did not account for the exchange of the energy from the ripples to the gravity-capillary wave, better agreement is not expected, and future measurements will have to rigorously account for the effects of nonlinearity.

Figure 6 plots the total dissipation of energy by viscosity as a function of time. The dissipation of energy to leading order is

$$\dot{E}=\frac{2}{\mathrm{R_e}}\int_{S_o}(\phi_x\phi_{xz}+\phi_y\phi_{yz}+\phi_z\phi_{zz})+O\left(\frac{\epsilon^3}{\mathrm{R_e}}\right), \qquad (8)$$

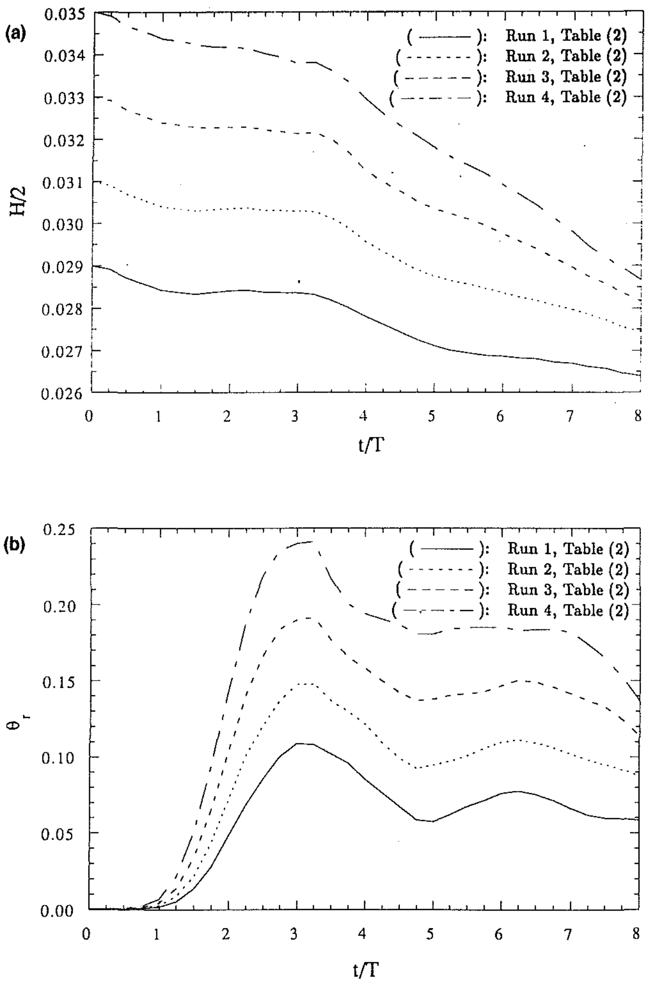

Fig. 4 Attentuation of the amplitude of gravity-capillary wave and the maximum steepness of the ripples. Part (*a*) is the amplitude of the gravity-capillary wave and Part (*b*) is the maximum steepness of the ripple near the crest of the gravity-capillary wave.

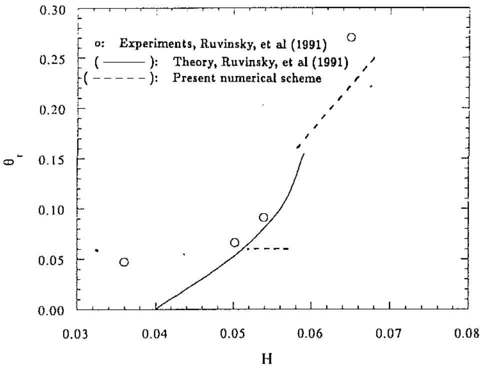

Fig. 5 Maximum ripple steepness: a comparison between experimental measurements and numerical simulations. The envelope that is formed by the dashed lines is calculated using the extreme values in Fig. 4.

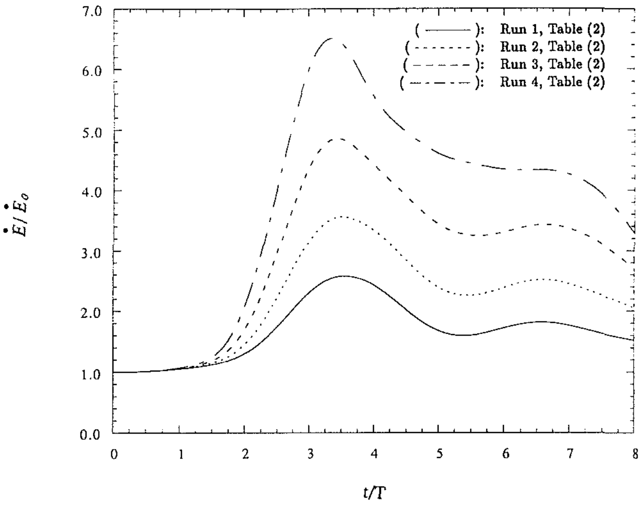

Fig. 6 Increased total energy dissipation due to the formation of parasitic capillary waves. The curves are normalized by the dissipation of energy for a pure gravity wave.

where S_o is the projection of the free surface onto the xy-plane.

As the ripples form near time $t = T$ in Fig. 6, the total dissipation of energy increases. This illustrates that a gravity-capillary wave with ripples riding on top decays more rapidly than a gravity-capillary wave without ripples. This effect agrees with the analysis of Lamb (1932), who shows that short waves decay more rapidly than longer waves. The gravity-capillary wave pumps energy into the ripples, where it dissipates more rapidly because the ripples are shorter than the original gravity-capillary wave. Depending on the steepness of the ripples, Fig. 6 also illustrates that the formation of the ripples is almost seven times more effective in damping the gravity waves than the direct action of viscosity. This agrees with the results of Longuet-Higgins (1962), who argues that a factor of ten could be expected for 6 cm gravity waves. Figure 6, together with Fig. 4, also shows that two gravity waves with same amplitude may attenuate at different rates depending on the initial conditions.

Conclusions

Although the perturbation scheme is the natural extension to the Zakaharov formalism (see, for example, Dommermuth and Yue, 1987), the convergence of the scheme is not rapid enough to simulate short wave to long wave ratios greater than ten. Consequently, the perturbation scheme relative to the preconditioned multigrid scheme is more suitable for narrower wave spectrums with moderate nonlinearity. The results of numerical simulations using the multigrid scheme agree qualitatively with laboratory measurements of ripples riding on the front face of gravity-capillary waves. At present, nonlinear effects that have not been accounted for in the experiments preclude better comparisons. A possible extension to the multigrid scheme includes using finite-difference methods with higher resolution such as compact schemes (see Lele, 1990) to simulate very broad wave spectra.

Acknowledgments

This research is financially supported by the Fluid Dynamics Program at the Office of Naval Research. The numerical simulations have been performed on the CRAY Y-MP 8/8128 at the Primary Oceanographic Prediction System (POPS).

References

Cox, C. S., 1958, "Measurements of Slopes of High-Frequency Wind Waves," *Journal of Marine Research*, Vol. 16, pp. 199–225.

Craik, A. D. D., and Leibovich, S., 1976, "A Rational Model for Langmuir Circulations," *Journal of Fluid Mechanics*, Vol. 73, pp. 401–426.

Dommermuth, D. G., and Yue, D. K. P., 1987, "A High-Order Spectral Method for the Study of Nonlinear Gravity Waves," *Journal of Fluid Mechanics*, Vol. 184, pp. 267–288.

Dommermuth, D. G., and Yue, D. K. P., 1990, "A Numerical Study of Three-Dimensional Viscous Interactions of Vortices with a Free Surface," *Proceedings of the 18th Symp. on Naval Hydro.*, National Academy of Sciences, Washington, D. C., pp. 727–788.

Dommermuth, D. G., 1992a, "The Laminar Interactions of a Pair of Vortex Tubes with a Free Surface," To appear in the *Journal of Fluid Mechanics*.

Dommermuth, D. G., 1992b, "The Initialization of Vortical Free-Surface Flows," Submitted for publication.

Ferguson, W., Saffman, P., and Yuen, H., 1978, "A Model Equation to Study the Effects of Nonlinearity, Surface Tension, and Viscosity in Water Waves," *Studies in Applied Mathematics*, Vol. 58, pp. 165-185.

Freeman, N. G., Hale, A. M., and Danard, M. B., 1972, "A Modified Sigma Equation Approach to the Numerical Modeling of Great Lakes' Hydrodynamics," *Journal of Geophysical Research*, Vol. 77, pp. 1050-1060.

Hsu, C. T., Lake, B. M., and Rungaldier, H., 1983, "An Experimental Investigation of the Response of Short Waves to Long Waves," TRW, Space and Technology Group, Report No. 41037-6004-UT-00.

Lele, S. K., 1990, "Compact Finite Difference Schemes with Spectral-Like Resolution," Center for Turbulence Research, Stanford University, Report No. 107.

Lamb, H., 1932, *Hydrodynamics*, Dover, New York.

Longuet-Higgins, M. S., 1963, "The Generation of Capillary Waves by Steep Gravity Waves," *Journal of Fluid Mechanics*, Vol. 16, pp. 138-159.

Longuet-Higgins, M. S., 1987, "The Propagation of Short Surface Waves on Longer Gravity Waves," *Journal of Fluid Mechanics*, Vol. 177, pp. 293-306.

Lundgren, T. S., 1989, "A Free-Surface Vortex Method with Weak Viscous Effects," *Mathematical Aspects of Vortex Dynamics*, R. E. Caflisch, ed., SIAM, pp. 68-79.

Phillips, O. M., 1959, "The Scattering of Gravity Waves by Turbulence," *Journal of Fluid Mechanics*, Vol. 5, pp. 177-192.

Ruvinsky, K. D., Feldstein, F. I., and Freidman, G. I., 1991, "Numerical Simulation of the Quasi-Stationary Stage of Ripple Excitation by Steep Gravity-Capillary Waves," *Journal of Fluid Mechanics*, Vol. 230, pp. 339-353.

Schwartz, L. W., 1974, "Computer Extension and Analytic Continuation of Stokes' Expansion for Gravity Waves," *Journal of Fluid Mechanics*, Vol. 62, pp. 553-578.

APPENDIX

Grid Stretching

The grid spacing along the $\hat{z}$-axis is stretched to resolve the exponential attenuation of the short capillary waves. The positions of the grid points are denoted by $\hat{z}_k$ for $1 \le k \le N_z$. The grid spacing is prescribed in terms of a Hermitian polynomial:

$$\hat{z}_k = \sum_{i=0}^{6} a_i \left(\frac{k-1}{N_z - 1} \right)^i \quad 1 \le k \le N_z, \tag{9}$$

where the coefficients a_i of the Hermitian polynomial $H(k)$ are assigned as follows:

$$H(1) = 1$$

$$H(N_z) = 0$$

$$H_k(1) = \frac{-\Delta x}{D}$$

$$H_{kk}(1) = 0$$

$$H_{kk}(N_z) = 0$$

$$H_{kkk}(1) = 0$$

$$H_{kkkk}(1) = 0,$$

where Δx is the uniform grid spacing along the x-axis. This mapping allows fewer grid points to be used near the bottom of the computational domain where the effects of the capillary waves are very small.

The Prediction of Velocity and Temperature Profiles in Gravity Currents for Use in Chilled Water Storage Tanks[1]

J. T. Nakos
Advanced Nuclear Power Technology
Department 6471,
Sandia National Laboratories,
Albuquerque, NM 87185-0741

It has been demonstrated that one way of producing thin thermoclines (temperature gradients) in a chilled water storage tank is by introducing the water horizontally in the form of a gravity current. A gravity current is a fluid intrusion into a body of stagnant fluid at a different density. The incoming fluid is introduced at the bottom of the body of fluid if it is more dense; it is introduced at the top if it is less dense. In the application considered here, chilled water is to be stored in an efficient manner under the original body of warmer water. Vertical profiles of velocity and temperature in transient, two-dimensional, laminar, thermally driven, constant inflow gravity currents are studied. This provides a basis for understanding the initial stages of the formation of a thermocline in a chilled water storage tank. Two laminar flow formulations were developed to predict velocity and temperature profiles in the inertia-buoyancy regime. One formulation uses a strictly numerical approach, while the other uses a singular perturbation method to analyze the flow. Experimental temperature profiles are compared with the results from both formulations, and show good agreement.

Introduction

The efficient storage of chilled water requires that a thin thermocline or large temperature gradient be established and maintained in the storage vessel. To generate a thin thermocline little mixing should occur between the incoming chilled water and the stagnant warmer water originally in the tank. The more dense chilled water will stay near the bottom of the tank if it is introduced in the proper manner (Yoo et al., 1986). One way to accomplish this is by introducing the water in the form of a gravity current because it is almost free of turbulence and therefore minimal mixing will occur (Britter and Simpson, 1978 and Simpson and Britter, 1979).

Gravity currents have a distinctive head region at the front and a relatively smooth laminar region behind the head. A sketch of a typical gravity current is shown in Fig. 1. Behind the head, the gravity current may be modelled using two regions: the "main body" near the floor and the "mixed region" above the main body (Nakos, 1987). The main body of the gravity current is driven by the buoyancy force, which generates a pressure gradient in the horizontal direction and is retarded by viscous and inertia forces. The mixed region is pulled along by the main body as a result of the viscous forces, and is retarded by inertia and shear at the top. There is little buoyancy force in most of the mixed region, due to the small temperature difference with the stagnant tank water.

Early in the flow the gravity current is controlled mainly by inertia and buoyancy forces, producing what is called the inertia-buoyancy (I-B) regime. Subsequently, the viscous force dominates inertia, and the flow is governed by viscous and buoyancy forces, resulting in the viscous-buoyancy (V-B) regime. Gravity currents are inherently transient in nature, evolving from the constant velocity I-B regime to the slowly decreasing velocity of the V-B regime. The V-B regime was modelled by Nakos (1987), and by Nakos and Wildin (1988). Only the I-B regime will be studied here.

Major features of the I-B regime temperature profiles are an almost constant temperature region from just above the floor to an elevation roughly equal to the top of the inlet diffuser opening and a region of rapidly increasing temperature above the top of the inlet. Major features of the I-B velocity profiles include a pointed "nose" with large gradients near the floor and above the top of the inlet diffuser opening.

There have been few known analytical or numerical studies on the prediction of temperature profiles in gravity currents except Nakos (1987) and Nakos and Wildin (1988). Most of the work on gravity currents has been done on saline currents, rather than ones with a temperature induced buoyancy force. In an extensive experimental study of gravity currents with heat transfer, Chobotov et al. (1986), presented temperature profiles in addition to velocity data and other gravity current characteristics. The application considered by Chobotov, et al., was that of gaseous ceiling gravity currents that occur in

---

[1] This work was supported by the United States Department of Energy under Contract DE-AC04-76DP0079.

Contributed by the Fluids Engineering Division for publication in the JOURNAL OF FLUIDS ENGINEERING. Manuscript received by the Fluids Engineering Division August 6, 1992; revised manuscript received March 30, 1993. Associate Technical Editor: J. A. C. Humphrey.

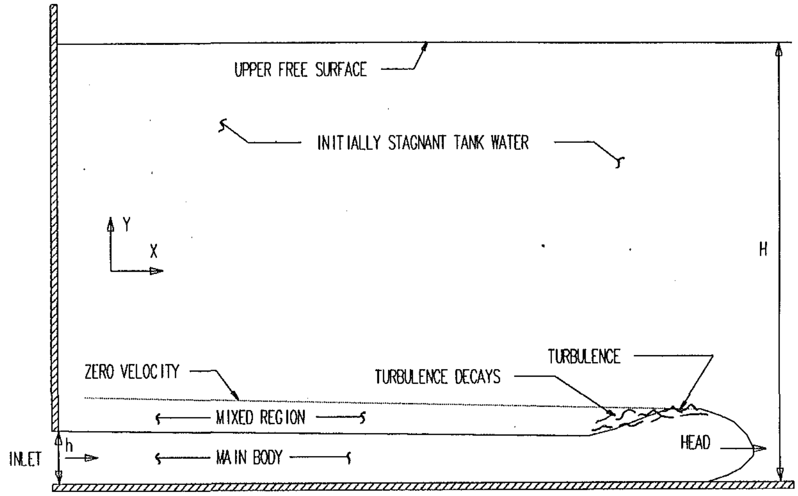

Fig. 1 Schematic of gravity current

a hallway fire. Vertical profiles of temperature and velocity were assumed, and an analysis was performed mainly to determine current characteristics in the direction of the flow. Comparison with assumed profiles and actual ones was not shown.

Nakos (1987), and Nakos and Wildin (1988), analyzed laminar gravity currents with a thermally induced buoyancy force and showed that they could be modelled with good agreement with experimental data. In Nakos (1987), two methods in the I-B regime and one in the V-B regime were introduced. In Nakos and Wildin (1988), the focus was on I-B and V-B regime comparisons. This work develops the work in the I-B regime by analyzing the two formulations originally introduced in Nakos (1987). Those two methods will be called the "numerical" and "perturbation" formulations.

This paper analyzes the first pass of a gravity current on a horizontal floor. The first pass refers to the flow of the gravity current before it reaches the end wall of the tank. Turbulence and the effects in the head are ignored because one of the objectives of this study was to develop a relatively simple model that could predict the basic shape of the thermocline, without excessive complexity. The region in which the gravity current flows is assumed to be of infinite length. With this formulation, the velocity of the head and initial stages of the flow cannot be accurately predicted. However, this does not preclude prediction of the velocity and temperature profiles behind the head. The results from the two formulations are compared with experimental data.

The following sections discuss the analytical and numerical methods used to solve for the temperature and velocity profiles. The results of the numerical predictions and several conclusions are contained in the remaining sections.

Analysis

Inertia-Buoyancy Regime: Numerical Formulation. Neglecting turbulence and the details of the head, the non-dimensional governing equations of a laminar, incompressible, transient, two-dimensional gravity current in Cartesian coordinates using an Eulerian frame of reference can be developed. The y-momentum equation does not appear explicitly for reasons stated below. Additional assumptions used in the derivation of these equations are the following:

1) Density variations are ignored except in body force term in the y-momentum equation.

2) Assume constant specific heat, thermal conductivity and viscosity and assume free surface pressure is constant.

3) Assume small vertical velocity as compared to the horizontal velocity, resulting in a hydrostatic pressure variation in the vertical direction.

4) Second partial derivatives in the horizontal direction

Nomenclature

a_i = thermal diffusivity, inlet value $(k/c_p\rho_i)$
c_p, k = specific heat, thermal conductivity, inlet values
g, g_r = gravitational acceleration, reduced gravitational acceleration, $g_r = g\Delta\rho/\rho$
h, H = inlet diffuser opening height, total water depth
L_x, L_y = characteristic lengths, $L_x = L_y = (q^2/g_r)^{1/3}$
p, q = pressure, inlet volume flow rate per unit width
SUMLT, SUMRT = integral approximation at left and right sides of node
t, t_c = nondimensional time, $t = t'/t_c$, characteristic time $t_c = L_x/U$
T', T = dimensional and nondimensional temperature, $T = (T_s - T')/(T_s - T_i)$
$T_x, T_y, T_t, T_{xx}, T_{yy}$ = partial derivative with respect to x, y, and t, second partial derivatives
T_i, T_s = dimensional inlet and (initial) stagnant tank temperature
TOLD, TNEW = temperature at time t, and at time $t + \Delta t$
u', u = dimensional and nondimensional horizontal velocities, $u = u'/U$
$u_x, u_y, u_t, u_{xx}, u_{yy}$ = partial derivative with respect to x, y, and t, second partial derivatives
U, V = horizontal and vertical characteristic velocities, $U = V = (qg_r)^{1/3}$
UINLT = non-dimensional inlet velocity at $x = 0$ (uniform in middle, rounded at corners)
UOLD, UNEW = horizontal velocity at time t, and $t + \Delta t$

behind the head were assumed to be negligible (and confirmed by numerical experiments).

In the I-B regime, the characteristic y-length and horizontal velocity are defined as follows (Nakos, 1987):

$$L_y=\left(\frac{q^2}{g_r}\right)^{1/3},\quad U=(g_rL_y)^{1/2}=(qg_r)^{1/3}. \tag{1}$$

The expression for L_y is an estimate of the current thickness obtained by Didden and Maxworthy, 1982, by equating the overall buoyancy and inertia forces. The value of U came from a similar force balance in which the overall buoyancy and inertia forces were equated. Because there is no obvious x-length scale in the inertia-buoyancy regime, L_x was set equal to L_y. Also, to simplify the continuity equation, V was set equal to U. The nondimensional I-B regime equations are the following:

continuity:

$$u_x+v_y=0 \tag{2}$$

x-momentum:

$$u_t+uu_x+vu_y=-\frac{\partial}{\partial x}\int_y^H \Delta\rho dy+\frac{1}{\mathrm{Re}}u_{yy} \tag{3}$$

and energy:

$$T_t+uT_x+vT_y=\frac{1}{\mathrm{PrRe}}T_{yy} \tag{4}$$

If one assumes the vertical velocity is an order of magnitude smaller than the horizontal velocity, an order of magnitude analysis performed on the y-momentum equation shows all terms except the pressure gradient and the buoyancy force (body force) are negligible and the hydrostatic pressure variation results. The integral term in Eq. (3) is the result of integrating the hydrostatic pressure variation with respect to y and then taking the derivative of that term with respect to x. The pressure gradient with respect to x is then obtained, is non-dimensionalized and then substituted into the x-momentum equation.

Inertia-Buoyancy Regime: Perturbation Formulation. The viscous term in the x-momentum Eq. (3) is multiplied by (1/Re) which is of order 10^{-2} in the flows considered here. As a result, the viscous term in the x-momentum equation is small as compared with the inertia and buoyancy terms, hence the name "inertia-buoyancy" regime. However, total neglect of the viscous term in the momentum equation would result in a reduction of the order of the equation. As a result of that reduction of order, only one boundary condition in the y-direction could be satisfied. This is called a "singularity" and may be dealt with by performing a singular perturbation analysis. Such an analysis was performed as an alternative solution, and is presented next. The perturbation formulation allows one to better grasp the "physics" of the I-B regime, provides an alternate method by which an analysis of a gravity current can be made, and may also have applications elsewhere, for example wall jets.

A physical model was first developed to better understand the "physics" of the perturbation analysis. Figure 2 shows how the flow in the I-B regime may be separated into three parts: the "core," "floor," and "interface" regions. The core and floor regions constitute the main body in Fig. 1, while the interface region is equivalent to the mixed region. The core region is in the middle of the flow and is governed by inertia and buoyancy forces. The floor region is located near the floor and is similar to a boundary layer in that viscous forces are present, in addition to the buoyancy and inertia forces. The interface region is also controlled by viscous, inertia and buoyancy forces, but the buoyancy forces are smaller than in the core and floor regions.

In the singular perturbation analysis, scalings are used to transform the momentum and energy equations in the floor and interface regions. Those scalings eliminate multiplication by the parameter 1/Re in the viscous and conduction terms. Three sets of equations are generated, one set for each of the three regions, therefore, nine equations have to be solved. The resulting solutions for each region are combined to form a single solution called a "composite expansion" which is valid over the entire I-B regime (see Van Dyke, 1975). The core region solution is referred to as the "outer" solution and the floor and interface solutions are referred to as the "inner" solutions. Only the "zeroth" (lowest) order perturbation equations and solutions will be presented here, as a result, the solution is only accurate to about $O(10^{-1})$. In view of the assumptions and approximations made in the analysis (i.e., small vertical velocity, turbulence neglected), adding more terms into the solution was not appropriate for the application being considered.

Scalings were found to be necessary only in the vertical coordinate and vertical velocity in the floor and interface regions (see Nakos, 1987). The scaled variables are:

$$Y_f=\frac{y}{\epsilon^{1/2}},\quad Y_i=\frac{(H-y)}{\epsilon^{1/2}},\quad V_f=\frac{v}{\epsilon^{1/2}},\quad V_i=\frac{v}{\epsilon^{1/2}} \tag{5}$$

where ϵ = 1/Re. Here the subscript "i" refers to the "interface" region, not the "inlet." Note that this scaling is the same

Nomenclature (cont.)

v', v = dimensional and nondimensional vertical velocity, $v = v'/U$
v_x, v_y = partial derivative with respect to x and y
VOLD, VNEW = vertical velocity at time t, and $t + \Delta t$
x, y = nondimensional horizontal and vertical coordinates, $x = x'/L_y$, $y = y'/L_y$
$\Delta x, \Delta y, \Delta t$ = increments of space and time
ν_i = kinematic viscosity, inlet value
ρ_s, ρ_i = stagnant water density and inlet water density
$\Delta\rho'$ = dimensional density difference, = $(\rho' - \rho_s)$
$\Delta\rho$ = nondimensional density difference, = $(\rho' - \rho_s)/(\rho_i - \rho_s)$
ϵ = 1/Re = singular perturbation scaling parameter

Fr = inlet Froude number, = $q/(g_rh^3)^{1/2}$
Pr = inlet Prandtl number, = ν_i/a_i
Re = inlet Reynolds number, = q/ν_i

Subscripts

i, s = inlet value and value in stagnant water far in front of head
x, y, t = horizontal and vertical length dimensions and time
B, T = "bottom" and "top" of node in upwind differencing, see Roache (1982)
LT, RT = "left" and "right" sides of node in upwind differencing (different from L and R)
L, R = "left and "right" sides of node in upwind differencing (different from LT and RT)
c, f, i = core, floor, and interface regions in perturbation formulation

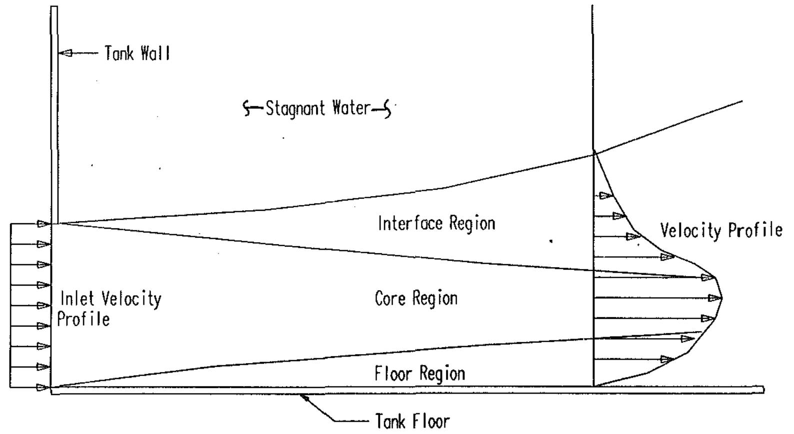

Fig. 2 Perturbation solution schematic

as the one for viscous flow over a flat plate (a boundary layer, see Van Dyke, 1975). With these scalings, the zeroth-order core and floor region equations become the following (the superscript 0 refers to the "zeroth-order" solution):

Core region:

continuity:

$$\frac{\partial u_c^0}{\partial x}+\frac{\partial v_c^0}{\partial y}=0, \tag{6}$$

x-momentum:

$$\frac{\partial u_c^0}{\partial t}+u_c^0\frac{\partial u_c^0}{\partial x}+v_c^0\frac{\partial u_c^0}{\partial y}=-\frac{\partial}{\partial x}\int_y^H \Delta\rho_c^0\,dy, \tag{7}$$

and energy:

$$\frac{\partial T_c^0}{\partial t}+u_c^0\frac{\partial T_c^0}{\partial x}+v_c^0\frac{\partial T_c^0}{\partial y}=0, \tag{8}$$

Floor region:

continuity:

$$\frac{\partial u_f^0}{\partial x}+\frac{\partial V_f^0}{\partial Y_f}=0, \tag{9}$$

x-momentum:

$$\frac{\partial u_f^0}{\partial t}+u_f^0\frac{\partial u_f^0}{\partial x}+V_f^0\frac{\partial u_f^0}{\partial Y_f}=-\frac{\partial}{\partial x}\int_y^H \Delta\rho_f^0\,dy+\frac{\partial^2 u_f^0}{\partial Y_f^2}, \tag{10}$$

and energy:

$$\frac{\partial T_f^0}{\partial t}+u_f^0\frac{\partial T_f^0}{\partial x}+V_f^0\frac{\partial T_f^0}{\partial Y_f}=\frac{1}{\Pr}\frac{\partial^2 T_f^2}{\partial Y_f^2}, \tag{11}$$

Equations in the interface region are almost exactly the same as those in the floor region (they differ only by signs in the terms that contain ∂Y_i because $\partial Y_i = -\partial y$), and so are not reproduced here.

To obtain a solution valid over the entire flow, a composite solution is required. To accomplish that, the method of additive composition was used (see Van Dyke, 1975). The composite is determined in three steps: first form an intermediate composite between the core and floor regions, second form a similar intermediate composite between the core and interface regions, and finally form a single composite from the two intermediate composites. Using temperature as an example, form the first intermediate composite as follows:

Core-floor composite:

$$T_{cf}=T_c+T_f-(T_c)_f, \tag{12}$$

where the term $(T_c)_f$ is called the "inner expansion of the outer solution." In actuality, this term is the "common part" (CP), or that part common to both the core and floor region solutions. It is subtracted out of the intermediate composite so that it is not counted twice. Similarly, the other intermediate composite is the following:

Core-interface composite:

$$T_{ci}=T_c+T_i-(T_c)_i, \tag{13}$$

where $(T_c)_i$ is similar to $(T_c)_f$. Finally, the overall composite is formed in the same manner with the common part to be determined: (CP = common part)

$$T=T_{cf}+T_{ci}-\mathrm{CP}=T_c+T_f-(T_c)_f+T_c+T_i-(T_c)_i-\mathrm{CP}. \tag{14}$$

By inspection, it can be seen that the part common to both intermediate solutions is T_c, therefore CP = T_c. As a result, the final composite expansion is the following:

$$T=T_c+T_f+T_i-(T_c)_f-(T_c)_i. \tag{15}$$

Equation (15) was used for all three variables: T, u, and v. Results are shown in the figures.

It was not possible to extend all three solutions (core, floor and interface) over the entire height of the tank due to differences in the boundary conditions at $x = 0$. The floor and core solutions extend from the floor to the top of the inlet ($0 \le y$ and $Y_f \le 1$), while the interface solution extends over the entire height ($0 \le Y_i \le H$). As a result, when the composite expansion was formed, the part of the solution from the floor to the top of the inlet ($0 \le y \le 1$) consisted of parts from all three regions, whereas the solution above the top of the inlet consisted only of the interface region solution.

Boundary and Initial Conditions. The boundary and initial conditions used for the numerical formulation were:

$$\begin{aligned}
&t=0: && u=v=T=0, && \\
&t>0; && x=0,\ H>y>h: && u=0,\ \partial T/\partial x=0 \\
& && x=0,\ 0<y<h: && u=\mathrm{UINLT},\ T=\text{uniform}, \\
& && x=\infty,\ \text{all } y: && u=T=0, \\
& && y=0: && u=v=0,\ \partial T/\partial y=0, \\
& && y=H: && u=0,\ \partial T/\partial y=0.
\end{aligned} \tag{16}$$

UINLT is the nondimensional inlet velocity boundary condition and was approximated by a profile flat in the middle and rounded at the corners. This shape was generated from physical considerations (Nakos, 1987 and Nakos and Wildin, 1988). The inlet diffuser in the experimental apparatus was not long enough to generate a parabolic profile, so the slightly rounded profile was used as a compromise.

The non-dimensional inlet temperature boundary condition was assumed to be uniform. The non-dimensional temperature was defined as $(T_s - T')/(T_s - T_i)$, where T_s was the initial stagnant water temperature and T_i was the temperature in the inlet piping upstream of the diffuser. Because some of the warmer water was in the inlet diffuser and there was some heat gain in the piping between where T_i was measured and the diffuser, the temperature T' at the inlet never reached the coldest possible value (T_i). As a result, the nondimensional temperature T never reached the maximum (1.00), but only about 0.86, which coincidentally was the same (inlet boundary condition) for all experiments.

The condition at $x = \infty$ states that there was no motion in front of the gravity current. The conditions at $y = H$ were not actually used. Since no motion was detected above about 4 cm from the floor, a numerical upper limit was set at 4 cm rather than at the actual free surface at about 30 cm from the floor. This saved considerable computer time. The conditions used at the numerical upper limit were the same as those at $y = H$ stated in Eq. (16).

Boundary conditions in the three regions of the perturbation formulation are shown below. The zeroth-order superscripts are dropped for convenience.

For the core region, $0 \leq y \leq h$:

$$\begin{array}{lll} t=0: & u_c=v_c=T_c=0, & \\ t>0; & x=0, \text{ all } y: & u_c=\text{uniform},\ T_c=\text{uniform}, \\ & y=0: & v_c=0,\ \partial T_c/\partial y=0, \\ & y=h: & \partial u_c/\partial y=0. \end{array} \tag{17}$$

For the floor region, $0 \leq Y_f \leq h$:

$$\begin{array}{lll} t=0: & u_f=v_f=T_f=0 & \\ t>0; & x=0, \text{ all } Y_f: & u_f=\text{uniform},\ T_f=\text{uniform}, \\ & Y_f=0, \text{ all } x: & u_f=v_f=0,\ \partial T_f/\partial Y_f=0, \\ & Y_f=\infty, \text{ all } x: & u_f(x,\infty,t)=u_c(x,0,t), \\ & & T_f(x,\infty,t)=T_c(x,0,t). \\ & & V_f(x,\infty,t)=\epsilon^{1/2}(v_c(x,0,t)). \end{array} \tag{18}$$

For the interface region, $0 \leq Y_i \leq H$:

$$\begin{array}{lll} t=0: & u_c=v_c=T_c=0, & \\ t>0; & x=0,\ 0\leq Y_i\leq h: & u_i=\text{uniform},\ T_i=\text{uniform}, \\ & x=0,\ h\leq Y_i\leq H: & u_i=0,\ \partial T/\partial x=0, \\ & Y_i=0, \text{ all } x: & u_i=T_i=0, \\ & Y_i=\infty, \text{ all } x: & u_i(x,\infty,t)=u_c(x,h,t), \\ & & T_i(x,\infty,t)=T_c(x,h,t), \\ & & V_i(x,\infty,t)=\epsilon^{1/2}(v_c(x,h,t)). \end{array} \tag{19}$$

The inlet velocity profiles in all three regions were "uniform," different than in the numerical formulation. This was required so that all three inlet flow rates were the same and that correct matching between regions could be accomplished. Note also that a pressure boundary condition is absent. This due to the fact that, to zeroth order, the pressure is the same between all three regions.

Numerical Analysis. Explicit finite difference methods were used to solve all of the equations. A forward difference operator was used to approximate the time derivatives. Centered space differencing was used in the second order derivatives. First upwind differencing was used in the nonlinear advection terms in the momentum and energy equations (Roache, 1982). A centered difference operator was used in the pressure gradient term. A backward difference was used in both terms in the continuity equation. The above differencing methods were used throughout the flows except in the core region in the perturbation formulation. In that case the only differences were that a second upwind difference scheme was used for the advection terms and a centered difference was used for $\partial u/\partial x$.

Overall energy balances were calculated as a comparison between the energy input into the tank and the amount of energy actually in the tank. The differences were less than one percent in the numerical formulation. In the perturbation formulation the balances were not good because of poor composite expansions near the very front of the current.

The momentum equation has to be solved to obtain "u" before the continuity equation can be solved to obtain "y". This is because new values of horizontal velocity u are used with old boundary values of vertical velocity to calculate new values of vertical velocity. Typical finite difference equations from the numerical formulation are shown below. The energy equation is:

$$\begin{aligned} \mathrm{TNEW}(i,j) &= \mathrm{TOLD}(i,j) - (\Delta t/\Delta x)\,(u_R T_{RT} - u_L T_{LT}) \\ &\quad - (\Delta t/\Delta y)\,(v_T T_T - v_B T_B) + (\Delta t/\Delta y^2/\mathrm{RePr})(\mathrm{TOLD}(i,j+1) \\ &\quad + \mathrm{TOLD}(i,j-1) - 2*\mathrm{TOLD}(i,j)). \end{aligned} \tag{20}$$

The momentum equation is:

$$\begin{aligned} \mathrm{UNEW}(i,j) &= \mathrm{UOLD}(i,j) - (\Delta t/\Delta x)\,(u_R u_{RT} - u_L u_{LT}) \\ &\quad - (\Delta t/\Delta y)\,(v_T u_T - v_B u_B) - (\Delta t\Delta y/\Delta x)(\mathrm{SUMRT} - \mathrm{SUMLT}) \\ &\quad + (\Delta t/\Delta y^2/\mathrm{Re})(\mathrm{UOLD}(i,j+1) + \mathrm{UOLD}(i,j-1) \\ &\quad - 2*\mathrm{UOLD}(i,j)). \end{aligned} \tag{21}$$

where SUMRT and SUMLT are difference representations of the integral term in the momentum equation, (3). The continuity equation is:

$$\begin{aligned} \mathrm{VNEW}(i,j) &= \mathrm{VNEW}(i,j-1) - (\Delta y/\Delta x)(\mathrm{UNEW}(i,j) \\ &\quad - \mathrm{UNEW}(i-1,j). \end{aligned} \tag{22}$$

The time-stepping procedure used was as follows: the "old" values were updated by substituting the "new" values after the new values were calculated in Eqs. (20)–(22). A new time increment was calculated at each step using the new values of velocity and temperature and a stability criterion. The time was then incremented and the process repeated.

Several values of Δx and Δy were used to check for convergence in both the numerical and perturbation formulations. Maximum velocity, maximum temperature and floor temperature were checked for convergence. Because most of the terms in the difference approximations were first order accurate, convergence was first order. Due to this slow convergence, a large grid was finally used, namely, 161 × 121. The final values of x and y used were about 0.20 and 0.033, respectively. Using the final values, the maximum velocity and maximum temperatures had converged to less than about 5 percent of their estimated "exact" values. On the other hand, the floor temperature had converged to only about 25 percent of its final value. Because the computer runs were already very long, no further increases in grid size were made.

Results and Discussion

Experimental results were obtained from a plexiglass tank 45 cm wide, 45 cm high and 240 cm long. The upper water level was about 30 cm high. The inlet diffuser spanned the entire 45 cm width of the bottom of the tank and was held constant at 1 cm. Cold water was introduced through the diffuser and travelled the length of the floor. Figure 1 shows a sketch of the setup and gravity current. The inlet is shown, but the upstream diffuser is not. The initial tank water temperature averaged about 25–30°C and the inlet chilled water temperature about 5°C, resulting in a temperature difference of about 20–25°C. A stationary array of 17 thermocouples mounted vertically about every 0.25 cm measured the water temperature as the gravity current passed. Velocity measure-

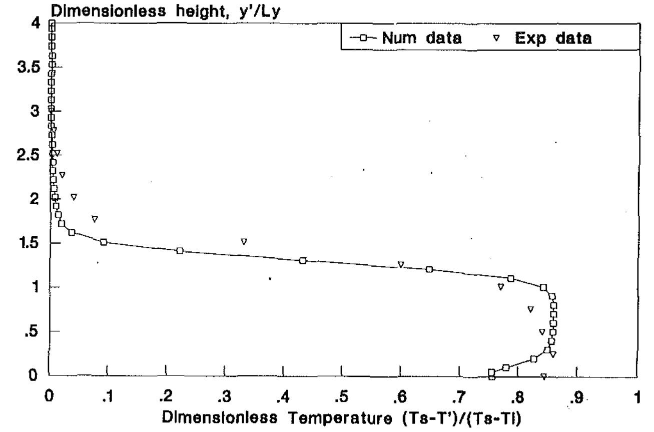

Fig. 3 Experimental-numerical temperature comparison, Re = 102, Fr = 0.99, Pr = 11.0, x = 10.1 t = 32.9, Ly = 0.99 cm, Ts = 24.9C, Ti = 5.0C

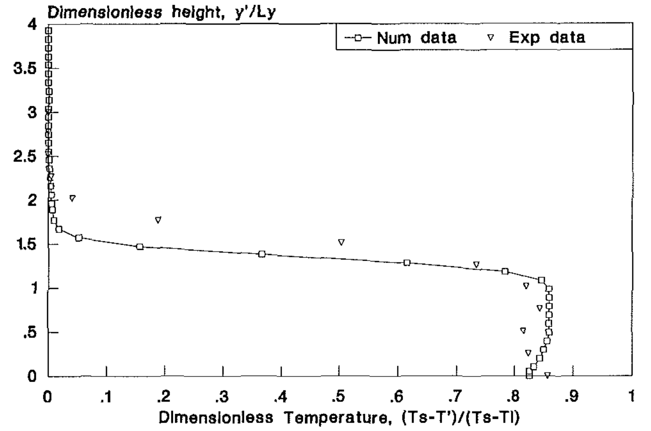

Fig. 4 Experimental-numerical temperature comparison, Re = 133, Fr = 1.03, Pr = 11.1, x = 9.8, t = 40.9, Ly = 1.02 cm, Ts = 29.1C, Ti = 4.7C

ments were made at the same horizontal location, but the results were to inaccurate to present (see Yoo, 1986). As a result, only vertical profiles of temperature were obtained. Inlet Froude numbers for the tests were 0.99 and 1.03, inlet Reynolds numbers were 102 and 133 and inlet Prandtl numbers were 11.0 and 11.1, respectively. The very low Reynolds numbers were due to the very low flow rates used. The experimental data were generated by Yoo (1986) and Nakos (1987). More details on the test apparatus can be found in Yoo (1986).

Comparison of experimental data and predicted temperatures for the numerical formulation are shown in Figs. 3 and 4 for two tests. These figures are generally representative of experimental data in the I-B regime. Large non-dimensional temperatures correspond to the coldest temperature, so that the warmest water was above the floor and the coldest was close to the bottom. The figures show plots of nondimensional temperature vs. nondimensional height above the floor at nondimensional time 32.9 (20.8 s) or 40.9 (20.7 s) after the initiation of the flow. These times were used for two reasons. First, the I-B regime lasted only about 24 seconds. After about 24 seconds, the flow transitioned to the V-B regime. Second, the flow was not well developed at earlier times. Measurements taken at t = 16.4 (12.4 seconds) were very erratic, indicating the flow had not yet recovered from the turbulence that resulted from the initial water put into the tank.

Several characteristics are evident in the experimental results in Figs. 3 and 4. First, there is a region between heights of about 1.0 and 2.0 in which there is a large temperature gradient, i.e., the nondimensional temperature drops very fast. This high gradient region is a very desirable characteristic in thermocline formation. Second, there is a relatively flat region of temperature between the heights 0–1.0. The junction of the high gradient region and the flat portion occurs at about 1.0, corresponding to the inlet diffuser height (1.0 cm) and the gravity current thickness. The gravity current "thickness" is equal to the diffuser opening height in the I-B regime, as shown in Yoo (1986).

As can be seen, overall agreement between experimental and numerical data in the I-B regime is generally good. The discrepancies that occur between heights 1.0 to 2.0 are due to several factors. First, in the experiments, some upwelling (turbulence) of cold fluid that occurred early in the flow settled downward due to its greater density. This was not modelled, and caused the measured temperature gradient to be less. Second, any other turbulence, mixing or entrainment were not accounted for in the model and tended to cause a less steep gradient region. A third possibility for the discrepancies could be due to flow perturbations caused by the thermocouple string.

The discrepancies between heights 0–0.25 are believed to be caused by turbulence in the head and gravitational instabilities. The gravitational instabilities were caused by heat transfer from the floor warming fluid near the floor. This warming caused pockets of warmer, less dense water to be present at the floor under colder, more dense fluid. This situation was unstable and caused the colder water to drop and the warmer water to rise, which resulted in replenishment of colder water near the floor. As a result, the water just above the floor was colder (higher nondimensional temperature) than that predicted by the purely laminar model. Gravitational instabilities were also described by Chobotov et al. (1986), and Simpson and Britter (1979).

An adiabatic boundary condition was used in the predictions, as can be seen in the figures at the floor ($\partial T/\partial y$ = 0). This was not an accurate assumption because there was always some heat conduction from the floor into the water. However, making quantitative assumptions about the heat transfer could not be easily justified, and so as a compromise the adiabatic condition was used.

Figures 5 and 6 show predictions of horizontal velocity from the numerical and perturbation formulations for increasing times at x = 5. Qualitative agreement between the predicted results of the two solution techniques is good. However, as can be seen, the maximum velocities in the perturbation solution are less than those in the numerical formulation for all times. One would expect that the velocities from the perturbation results would be less because only the zeroth order part of the solution is presented. However, the amounts of the differences range from 16 to 21 percent, more than might be expected. One would expect that the perturbation solution would be on the order of $\epsilon^{1/2}$, about 10 percent less than the numerical solution.

The maxima of all of the profiles occur between heights 0.5 and 1.0. The vertical location of the maximum rose with time, due to shear at the floor. The maxima are smaller with time due to the increasing viscous force as the current length increases.

Although it is difficult to see from Figs. 5 and 6, matching of the parts of the perturbation solution at height 1.0 occurs smoothly. As discussed earlier, the solution below y = 1 consists of parts from all three regions (core, floor and interface), but the solution above y = 1 is only from the interface region. Matching conditions require that there be continuity of velocity but not necessarily of slope or gradient. The profile at t = 12.6 shows very good continuity of slope, but the one at t = 32.9 shows a slight discontinuity at height 1.0, although it is difficult to see from Fig. 6. Because the I-B regime lasts only t = 34.8 (24 s) for this case, one might expect that the perturbation solution would begin to break down (i.e., slope discontinuity) at t = 32.9, and that is the case.

Figure 7 shows predicted temperature from the two formulations at t = 32.9 and x = 5. Because the perturbation

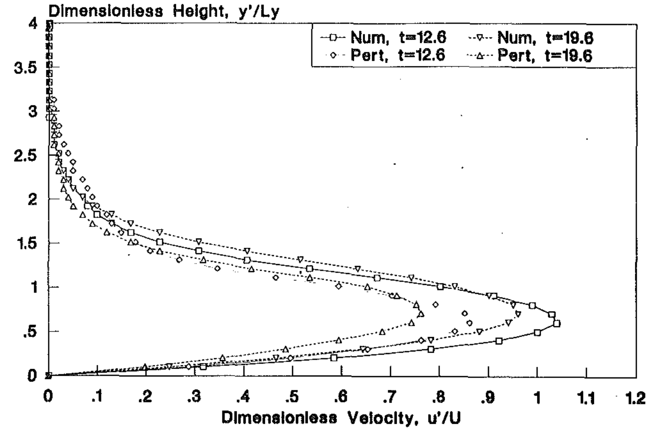

Fig. 5 Horizontal velocity for increasing time numerical and perturbation predictions, $x=5$, Re = 102, Fr = 0.99, Pr = 11.0, $Ly=0.99$ cm, $U=1.56$ cm/s

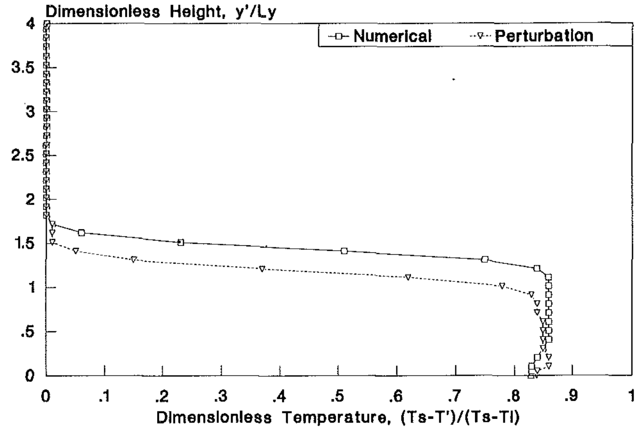

Fig. 7 Temperature predictions from numerical and perturbation formulations, $x=5$, Re = 102, Fr = 0.99, Pr = 11.0, $t=32.9$, $Ly=0.99$ cm, $Ts=24.9$C, $Tl=5.0$C

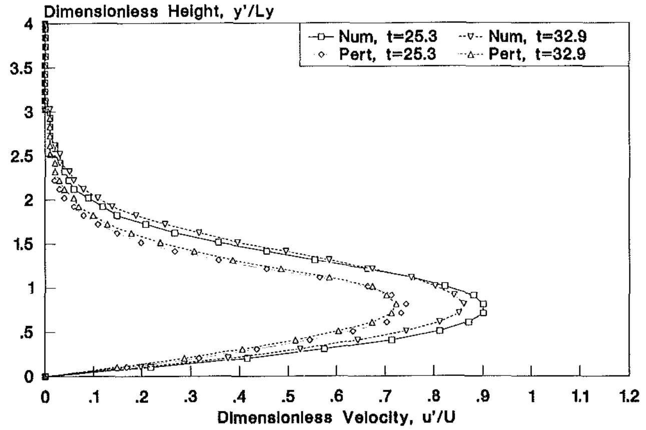

Fig. 6 Horizontal velocity for increasing time numerical and perturbation predictions, $x=5$, Re = 102, Fr = 0.99, Pr = 11.0, $Ly=0.99$ cm, $U=1.56$ cm/s

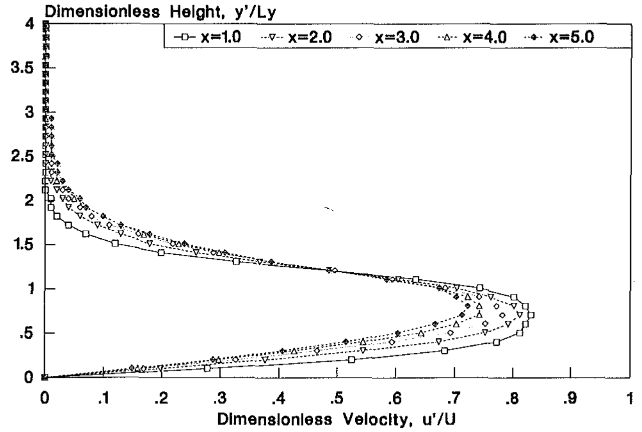

Fig. 8 Horizontal velocity at distances from inlet, perturbation predictions, Re = 102, Fr = 0.99, Pr = 11.0, $t=32.9$, $Ly=0.99$ cm, $U=1.56$ cm/s

velocities are less than those in the numerical solution in Fig. 6, the temperature lags behind as well. The region of highest discrepancy is from about heights 1–2, where the gradient is largest.

Figure 8 shows a plot of predicted velocity profiles from the perturbation formulation at $t = 32.9$, at increasing distances from the inlet. In Fig. 2 it was postulated that the core region shrinks in size with distance from the inlet as the interface and floor regions grow. This behavior can be seen in Fig. 8 where the profiles become more pointed with increasing distance from the inlet, indicating a thinning core region. One might expect that the velocity profile at $x = 1$ would be flatter, because the inlet profile was uniform and $x = 1$ is close to the inlet. A comparison was made (not shown) between the numerical and perturbation formulations at $x = 1$ and $t = 32.9$. The results show the profiles to be almost the same, indicating the profiles develop very fast, and giving some confirmation to the perturbation results.

Direct comparison of the predicted results here with experimental data from Chobotov et al. (1986) is not possible. These data are strictly for the I-B regime, assuming an adiabatic condition at the floor. Chobotov's data is for heat transferring flow, which he shows is constantly decelerating. Nevertheless, qualitatively, the shape of the profiles in Chobotov et al. (1986), are very similar to the temperature profiles presented here. See, for example, Fig. 3.14 in Chobotov et al. (1986).

A useful comparison can be made between the classical, inviscid result in an infinitely deep fluid and the results presented here. In the classical result, the speed of the current is given by the following result (see Benjamin, 1968):

$$u' = (2hg[\Delta\rho/\rho])^{1/2} = (2hg_r)^{1/2} \tag{23}$$

The maximum nondimensional speed in Fig. 5 at $t = 12.6$, which has the lowest viscous effect of the curves shown, is about $u = 1.05$. As time progresses, viscous effects become more pronounced and the speed drops. $u = 1.05$ translates into a dimensional velocity of $u' = 1.05(L_y g_r)^{1/2} \approx 1.05$ $(hg_r)^{1/2}$, which is less than the inviscid solution of $u' = 1.41$ $(hg_r)^{1/2}$. The inviscid result predicts a speed about $(2)^{1/2}/1.05$ $= 1.35$ times faster than the results presented here. This higher speed would be expected, because the results from this work include viscous terms.

Conclusions

1) The analysis shows that a gravity current can, at least qualitatively, be modelled using two formulations in the I-B regime, numerical and perturbation.

2) The current behind the head can be modelled in two or three regions. In the numerical formulation the two regions are the main body and the mixed region above the main body. In the perturbation formulation they are the floor, core and interface regions.

3) Comparisons of experimental and predicted temperature data are good for the numerical formulation. Comparison

between predictions from the numerical and perturbation formulations is fair to good.

Acknowledgment

The author would like to acknowledge the mentorship of Professor M. W. Wildin through many years of association, and his encouragement which helped in the completion of this work.

References

Benjamin, T. B., 1968, "Gravity Currents and Related Phenomena," *Journal of Fluid Mechanics*, Vol. 31, pp. 209-248.

Britter, R. E., and Simpson, J. E., 1978, "Experiments on the Dynamics of a Gravity Current Head," *Journal of Fluid Mechanics*, Vol. 88, Part 2, pp. 223-240.

Chobotov, M. V., Zukowski, E. E., and Kubota, T., 1986, "Gravity Currents with Heat Transfer Effects," NBS publication NBS-GRC-87-522, U.S. Department of Commerce, National Bureau of Standards, Center for Fire Research, Gaithersburg, MD 20899, December.

Didden, N., and Maxworthy, T., 1982, "The Viscous Spreading of Plane and Axisymmetric Gravity Currents," *Journal of Fluid Mechanics*, Vol. 121, pp. 27-42.

Nakos, J. T., 1987, "Prediction of Velocity and Temperature Profiles in Thermally Driven Gravity Currents Applied to Stratified Thermal Storage Tanks," Dissertation, Department of Mechanical Engineering, University of New Mexico, December.

Nakos, J. T., and Wildin, M. W., 1988, "Prediction of Velocity and Temperature Profiles in Thermally Driven Gravity Currents Applied to Stratified Thermal Storage Tanks," Paper #88-3810-CI, AIAA/ASME/SIAM/APS 1st National Fluids Dynamics Congress, Cincinnati, Ohio, July 25-28, pp. 2027-2035.

Roache, P. J., 1982, *Computational Fluid Dynamics*, Hermosa Publishers, Albuquerque, N.M.

Simpson, J. E., and Britter, R. E., 1979, "The Dynamics of the Head of a Gravity Current Advancing over a Horizontal Surface," *Journal of Fluid Mechanics*, Vol. 94, Part 3, pp. 477-495.

Van Dyke, 1975, *Perturbation Methods in Fluid Mechanics*, The Parabolic Press, Stanford, CA.

Yoo, J., Wildin, M. W., and Truman, C. R., 1986, "Initial Formation of a Thermocline in Stratified Thermal Storage Tanks," *ASHRAE Transactions*, Vol. 92, Part 2, pp. 280-292.

Yoo, J., 1986, "An Investigation of Reynolds Number Effects in Thermally-Driven Gravity Currents Applied to Stratified Thermal Storage Tanks," Dissertation, Department of Mechanical Engineering, University of New Mexico, December.

Interpreting Vortex Interactions With a Free Surface

E. P. Rood
Fluid Dynamics Program,
Office of Naval Research,
Arlington, VA 22217

An understanding of the process by which vorticity interacts with a free surface is sought by analytical examination of the free-surface condition for the vorticity flux. A novel mechanism is suggested that permits closed vortex loops to evolve into open loops terminating at the free surface. It is hypothesized that abrupt vortex "disconnection," observed in physical experiments, arises from a smooth diffusion of vorticity through the interface, with a necessary coincident tangential acceleration of the interface attributed to viscous forces.

Introduction

The unsteady flowing water in streams and rivers, the water surface disturbances observed at discharges from hydroelectric plants, and the wakes of boats, are all characterized by vortex interactions with the free surface. A feature common to all of these flows is the presence of swirls or eddies. These surface eddies are manifestations of vorticity aligned normal to the free surface and organized to form coherent vortices with end points at the free surface. In many cases these two-dimensional features are produced by complex three-dimensional vortical flow generated beneath the surface.

The approach of a continuous vortex element, such as a ring, to the free surface presents an interesting situation, because the vortex element is sometimes observed to become discontinuous (within the fluid through which it is moving), with the vortex lines attached nearly normal to the free surface. This dramatic reconfiguration of the vorticity is kinematically permissible although not required. Whereas vortices cannot end on a no-slip surface such as a stationary rigid wall, they are permitted to terminate on a full-slip boundary such as a free surface. The question is what dynamic mechanisms are associated with this abrupt transformation in which there is disappearance of surface-parallel vorticity and coincident appearance of surface-normal vorticity.

Examples of the recent research with wakes are reported by Hirsa et al. (1991) and Sarpkaya (1992). Research with jets and vortex rings is reported by Bernal and Kwon (1989), Anthony, Hirsa, and Willmarth (1991), and Kachman et al. (1991). These recent efforts consistently report observations of the normal attachment of vorticity which was previously not attached to the free surface. All of the accounts of the process for attachment are equally ambiguous, usually requiring conceptual notions of image vortices to invoke attachment, yet using such terms as "broken" vortices to describe the process.

The concept of a free surface results in a boundary condition on the fluid in which the external tangential stresses are negligible and the normal stress is approximately a constant. In other words, the boundary is specified by a constant pressure condition. Such a free surface is observed in practice at the surfaces of rivers and oceans. Under such conditions, the vortex interaction with the boundary, the free surface, depends only on the dynamics in that boundary and not, for example, on the dynamics of a fluid on the other side of the boundary. Furthermore, explanations of the vortex interactions must in general allow for the deformation of the free surface during the interaction. For both of these reasons, vortex image methods which require flow symmetry about the interface are generally not appropriate although they may produce some of the interaction features. Since these methods are not based on physics of the actual flow, they result in erroneous requirements such as existence of a vortex in the air to solve the interface problem. An explanation is needed, based on rational mathematical models, first to describe why the phenomenon of vortex attachment exists and second to provide a basis for scientific investigation of flows that include the process of vortex attachment.

The purpose of this paper is to propose a rigorous explanation for the vortex attachment process. The explanation is based on the fact, shown here, that vorticity coincidentally fluxes into the boundary of a fluid when the boundary experiences an acceleration *in the plane of the boundary*. There is no need to invoke models of vortex reconnection, or models of vortex images, to explain vortex attachment. In fact, there is no requirement concerning the existence of a fluid on the other side of the free surface. Vorticity can flux into the free surface and simply disappear from the flow field with a coincident acceleration of the flow in the plane of the free surface, a fact that has apparently been overlooked by researchers in this field.

The focus here is on the incompressible interaction between vorticity in water and an air-water interface that is a free surface; the viscosity and density of the air are sufficiently small, leading to the zero-tangential stress and constant normal stress conditions on the water at the interface. Although a general approach is mathematically intractable, the essential physics of the interaction can be elucidated by performing a local analysis. Lugt (1987) investigated the two-dimensional interaction for steady flow. The focus of his investigation was on the steady flux of vorticity at a curved surface of fixed shape. Here his approach is adapted in a more general formulation that includes the unsteady case where the evolving vorticity field interacts with the free surface.

Contributed by the Fluids Engineering Division for publication in the JOURNAL OF FLUIDS ENGINEERING. Manuscript received by the Fluids Engineering Division April 1, 1993; revised manuscript received January 7, 1994. Associate Technical Editor: D. P. Telionis.

The Vorticity Flux Equation

A general formulation of the vorticity flux equation (Rood, 1993) for a surface with unit normal $\hat{n}$ is based on the vector identity:

$$\hat{\mathbf{n}} \times \nabla \times \omega = (\nabla \omega) \cdot \hat{n} - \hat{n} \cdot \nabla \omega \tag{1}$$

The two terms on the right-hand side of Eq. (1) are direct products of the normal vector and the gradient vorticity tensor. It is important that the order of the tensor contractions be maintained, and that the effects of spatial gradients of the unit vectors for curvilinear coordinate systems be included. For cases where the curvature of the free surface is important, the curvilinear expression for the gradient vorticity tensor includes cross-terms among the vorticity components.

Under certain conditions these terms can be neglected. These conditions are embodied in two cases. In the first case the criterion is the restriction that free surface be planar, and in the second case the criterion is the less restrictive requirement that the surface-parallel vorticity lines be straight (the free surface may be curved in the direction perpendicular to the vorticity lines).

The first case is exemplified by a flow described in a rectangular coordinate system in which one of the coordinates is normal to the free surface. In this case the first term on the right-hand side of Eq. (1) is simply the gradient of the surface-normal component of vorticity. It is observed by inspection that a surface-parallel gradient of the surface-normal vorticity contributes to the surface-normal flux of surface-parallel vorticity. If there is no surface-normal vorticity, the value of this term is zero. In cases where the free surface is only slightly deformed and the local radius of curvature is very large, the exact curvilinear coordinate system (with coordinate surface coexisting with the free surface) is approximated by a rectangular coordinate system. This is the case for two-dimensional flow in an open channel (with a no-slip bottom and a free surface at the top) in which it is assumed that there is no surface-normal vorticity at the free surface prior to the interaction of the bottom-generated vorticity with the free-surface.

The second case is exemplified by a flow naturally described in a cylindrical coordinate system (the cylindrical coordinate surface approximating the free surface). If the surface parallel vorticity is tangential to a curve with very large radius of curvature (the axial coordinate, in fact) then this term approaches zero as shown in Rood (1993) using expansions of generalized coordinates described in Batchelor (1967). This is the case for the interaction of a vortex ring with the free surface, especially for the flow in the vertical symmetry plane. In this case, there is no pre-existing surface-normal vorticity at the free surface and the first term on the right hand side of Eq. (1) has the value of zero.

An expression for the rate of change of vorticity at the free surface is obtained by integrating Eq. (1) over the free surface to produce the equation:

$$\nu \int \hat{\mathbf{n}} \cdot \nabla \omega ds = \nu \int \nabla \omega \cdot \hat{\mathbf{n}} ds - \nu \int (\hat{\mathbf{n}} \times \nabla \times \omega) ds \tag{2}$$

which is combined with the equation for the momentum:

$$\frac{\partial \mathbf{u}}{\partial t} + \mathbf{u} \cdot \nabla \mathbf{u} + \frac{\nabla p}{\rho} - \mathbf{g} = -\nu(\nabla \times \omega) \tag{3}$$

to produce the equation:

$$\nu \int_{f.-s.} \hat{\mathbf{n}} \cdot \nabla \omega ds = \nu \int_{f.-s.} \nabla \omega \cdot \hat{\mathbf{n}} ds + \int_{f.-s.} \hat{\mathbf{n}} \times \left[\frac{\partial \mathbf{u}}{\partial t} + \mathbf{u} \cdot \nabla \mathbf{u} + \frac{\nabla p}{\rho} - \mathbf{g} \right] ds \tag{4}$$

relating the flux of vorticity at the free surface to the tangential component of the acceleration of the flow in the free surface.

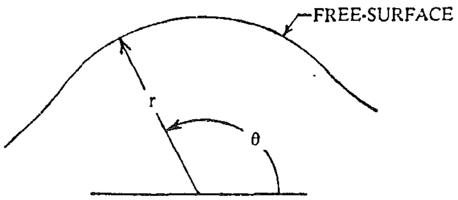

Fig. 1 Circular arc approximation for the free surface

The tangential component of acceleration in the free surface is nonzero if there is a viscous imbalance in the forces acting tangentially on the fluid in the interface. If there are no viscous forces, that term is zero. The present concern is with interactions of tangential components of vorticity exemplified by closed vortex loops interacting with the free surface. Therefore the first term on the right can be neglected. In the second term, the component of the pressure gradient tangential to the free surface is zero and does not contribute to the integral. Under these conditions the equation describing the flux of tangential vorticity at the free surface is written:

$$\nu \hat{\mathbf{n}} \cdot \nabla \omega = \hat{\mathbf{n}} \times \left[\frac{\partial \mathbf{u}}{\partial t} + \mathbf{u} \cdot \nabla \mathbf{u} - \mathbf{g} \right] \tag{5}$$

where the term in brackets is the viscous acceleration expressed as the difference between the local and advective accelerations and the gravitational acceleration.

Application of the Equation

Equation (5) can be evaluated in a local analysis to investigate the vorticity flux. Consider a polar coordinate system with a circular arc approximation for the free surface in the vicinity of the point at which the vorticity flux is being investigated, shown in Fig. 1. In order to permit elucidation of the features of vorticity flux, assume that the free surface maintains its shape during the interaction. For this flow, the following equation describes the flux of surface-parallel vorticity through the free surface:

$$\nu \left(\frac{\partial \omega}{\partial r} \right) = \frac{\partial u_\theta}{\partial t} + \frac{u_\theta}{R} \frac{\partial u_\theta}{\partial \theta} + g \cos(\theta - \theta_0) \tag{6}$$

Equation (6) relates the flux of the surface-parallel, or tangential, component of vorticity at the free surface to the sum of the tangential accelerations of the fluid in the free surface. The physical significance of the equation is that, for viscous fluids, there is a flux of vorticity into the free surface coincident with the acceleration of the boundary. That flux results in a net change in the quantity of vorticity in the fluid as well as a mechanism for vortex filaments to attach to the free surface.

The sign for the flux depends, of course, on the positive direction chosen for the normal vector. Convection dictated by the application of the divergence theorem to a volume of fluid specifies that the unit normal is the outward normal. In this case a negative value for the flux implies a net outward flow of positive vorticity and a coincident deceleration of the flow in the free surface.

Discussion

There is an essential distinction between the physics of the flow for a solid boundary and the physics of the flow for a free surface that permits interpretation of vortex attachment to the free surface. For a fixed rigid body boundary, the flux of vorticity is proportional to the pressure gradient on the no-slip surface. On the other hand, the flux of vorticity for a full slip free surface is proportional to the accelerations of the fluid in the interface. Note, however, that this is carefully drawn distinction. In both cases the flux is produced by viscous forces. The relationship between vorticity flux and surface-parallel acceleration is made apparent in the following problem.

Consider the two-dimensional flow between two horizontal parallel plates, initially at rest but with the lower plate suddenly imparted a constant velocity. The vorticity generated at the instant of acceleration of the moving plate diffuses into the flow interior and the flow approaches a state of constant vorticity (a linear distribution of velocity between the plates). Now consider the response if the experiment is repeated with the nonmoving upper plate replaced with a free surface. The flow again approaches a state of constant vorticity but the value is zero because the entire flow has the velocity of the lower plate. According to the above analysis, the vorticity produced by the accelerated plate diffuses through the flow and fluxes into the free surface with a coincidental change in the tangential component of velocity. The interaction is completely contained in the time derivative of the velocity, since the advective and gravitational accelerations are exactly zero. In this example vorticity has "disappeared" from the flow, but no conservation principle has been violated because mass and momentum are conserved.

This disappearance of the vorticity is unsettling only if vorticity is assumed to have attributes that are conserved in the manner that linear momentum is conserved. The linear momentum equation is a statement of the balance between force and rate of change of momentum (Newton's second law), which when coupled with the statement of action and reaction (Newton's third law) completes the requirement for conservation of momentum (Goldstein, 1950). Vorticity is a kinematic variable governed by an evolution field equation similar to the equation for the evolution of momentum (Morton, 1984). However, there is no equivalent "action-reaction" statement to govern the overall conservation of vorticity. Furthermore, vorticity is not related to the local angular velocity except as a geometrical feature (Tritton, 1982), and hence is not fundamentally related to angular momentum. The conclusion is that the disappearance of vorticity is physically permissible. It is noted, however, that in practice the free surface separates two fluids such that the vorticity flux out of one fluid is a flux into the other fluid.

The usefulness of this explanation for vortex interactions with a free surface is evident in the case of a vortex ring approaching the free surface along an inclined path. It is observed experimentally (Bernal and Kwon, 1989) that the upper arc of the ring "breaks" to form a loop with its ends terminating at the free surface. As the vortex loop approaches the free surface, the core is deformed against the free surface leading to large vorticity diffusion. As stated above, the value of the vorticity at the free surface is determined by the curvature of the free surface and the tangential component of the velocity in the free surface. For low Froude numbers, the surface is almost flat with an imposed condition of a negligible value for the vorticity. The vorticity in the vortex loop rapidly diffuses to the free surface, where it fluxes out of the field with a coincident tangential acceleration (actually a deceleration) of the fluid in the free surface. In this case both the temporal and the spatial accelerations are important to the vorticity flux. During this process the surface-parallel vorticity at the free surface disappears with a coincident attachment of the vortex lines to the free surface. Quite simply, a portion of the closed vortex loop fluxes out of the fluid, leaving the remainder of the loop with ends terminating at the free surface. The terminated ends are made manifest by the appearance of eddies, or surface-normal vorticity, at the free surface. For a deformed free surface the results are modified by the specification of a nonzero value for the tangential component of the vorticity at the free surface, but otherwise the concept is identical.

Note that the deceleration of the fluid as the vorticity fluxes into the free surface counters the acceleration of the fluid that was produced by the inviscid interaction of the vortex with the free surface. In that inviscid interaction, which occurs before the vorticity contacts the free surface, the approximate model of a vortex image correctly indicates that the fluid is accelerated.

There are other dynamic processes that produce changes in the vorticity configuration during the interactions of a vortex ring with the free surface. Based on detailed velocity and vorticity field measurements, Gharib et al. (1992) have recently demonstrated the disappearance of the surface-parallel vorticity in the plane of symmetry. Their detailed analysis of the data concludes that neither cancellation by counter-sign vorticity nor convection by the flow are mechanisms for the disappearance of the surface-parallel vorticity.

The analysis here is also found useful upon re-examination of well-referenced results in the literature. The famous experiments of Barker and Crow (1977) showed apparent rebound of the vortices from the free surface similar to what is observed when vortices interact with a rigid no-slip boundary where secondary boundary layer vorticity induces the primary vorticity away from the wall. A subsequent numerical experiment by Peace and Riley (1983) also showed a rebound of the vortex. In this numerical experiment the center of the diffusing vortex was defined to be the location of maximum vorticity. A new explanation for the rebound is found using the description here of a process by which vorticity fluxes into the free surface. As the primary vortex approaches the free surface and deforms, the vorticity diffuses to the free surface, where it fluxes out of the field. Saffman (1991) analytically shows for these experiments that the location of the centroid of maximum vorticity moves away from the free surface during the interaction. He states that the centroid is not a Lagrangian quantity and hence fluid particles associated with the vortex move toward the free surface and the vortex only seems to rebound. Here it is shown how the vorticity leaves the field.

An interesting consequence arises relevant to experiments in which dye is used to mark the fluid and, by inference, the vorticity near the free surface. It is expected that most of the vorticity will eventually diffuse through the free surface, which must be maintained at zero vorticity if it is flat and shear-free. In this case the resulting flow would be irrotational and would have acquired a velocity in the interface consistent with the flux of vorticity through the interface. However, the dye must diffuse according to a different dispersion relation and may not flux into the free surface. Hence the dye may erroneously be perceived as marking vorticity that is not there.

Acknowledgments

The author is grateful to Prof. M. Gharib for his valuable discussions of the implications of the analysis presented in this paper, and to the Office of Naval Research for providing partial support for the preparation of this paper.

References

Anthony, D. G., Hirsa, A., and Willmarth, W. W., 1991, "On the Interaction of a Submerged Turbulent Jet with a Clean or Contaminated Free Surface," *Physics of Fluids A*, Vol. 3, No. 2, pp. 245-247.

Barker, S. J., and Crow, S. C., 1977, "The Motion of Two-Dimensional Vortex Pairs in a Ground Effect," *Journal of Fluid Mechanics*, Vol. 82, pp. 659-671.

Batchelor, G. K., 1967, *An Introduction to Fluid Dynamics*, Cambridge University Press, Cambridge, pp. 598-603.

Bernal, L. P., and Kwon, J. T., 1989, "Vortex Ring Dynamics at a Free Surface," *Physics of Fluids A*, Vol. 1, No. 3, pp. 449-451.

Gharib, M., Weigand, A., Willert, C., and Liepmann, D., 1992, "Experimental Studies of Vortex Reconnection to a Free Surface: A Physical Flow Model," *Nineteenth Symposium on Naval Hydrodynamics*, National Academy Press.

Goldstein, H., 1950, *Classical Mechanics*, Addison-Wesley Publishing Company, Inc., Atlanta, p. 4.

Hirsa, A., Tryggvason, G., Abdollahi-Alibeik, J., and Willmarth, W. W., 1991, "Measurement and Computaions of Vortex Pair Interaction with a Clean or Contaminated Free Surface," *Eighteenth Symposium on Naval Hydrodynamics*, National Academy Press.

Kachman, N. J., Koshimoto, E., and Bernal, L. P., 1991, "Vortex Ring

Interaction with a Contaminated Surface at Inclined Incidence," *Dynamics of Bubbles and Vortices Near a Free Surface*, ASME AMD-Vol. 119, pp. 45–58.

Lugt, H. J., 1987, "Local Flow Properties at a Viscous Free Surface," Physics of Fluids, Vol. 30, pp. 3647–3652.

Morton, B. R., 1984, "The Generation and Decay of Vorticity," *Geophysical Astrophysical Fluid Dynamics*, Vol. 28, pp. 277–308.

Peace, A. J., and Riley, N., 1983, "A Viscous Vortex Pair in Ground Effect," *Journal of Fluid Mechanics*, Vol. 129, pp. 409–426.

Rood, E. P., 1993, "Free-Surface Vorticity," *Fluid Vortices*, S. Green ed., in review.

Saffman, P. G., "Approach of a Vortex Pair to a Rigid Free Surface in Viscous Fluid," *Physics of Fluids A*, Vol. 3, pp. 984–985.

Sarpkaya, T., 1992, "Three Dimensional Interactions of Vortices with a Free Surface," 30th Aerospace Sciences Meeting, AIAA 92-0059.

Tritton, D. J., 1982, "Discussion of 'Vorticity and Rotation'," *American Journal of Physics*, Vol. 50, No. 5, pp. 421–424.

The Initialization of Vortical Free-Surface Flows

D. G. Dommermuth
Research Scientist,
Naval Hydrodynamics Division,
Science Applications
International Corporation,
10260 Campus Point Drive, MS 34,
San Diego, CA 92121

Numerical simulations of vortical free-surface flows are prone to developing spurious high-frequency dispersive waves unless the flow field is given sufficient time to adjust. At low Froude numbers, the high-frequency waves obscure the true hydrostatic balance of the free-surface elevation with the component of the pressure that is induced by the vortical portion of the flow. The high-frequency waves must be eliminated for remote sensing applications because otherwise the roughening of the free surface and the predicted radar backscatter will be incorrect. A procedure is developed for reducing the initial impulse of the pressure and the subsequent generation of high-frequency waves. Numerical simulations of whirls illustrate the effectiveness of the procedure. The pressure field of the whirls forms dimples on the free surface.

Introduction

Remote sensing simulations of the ocean surface currently use a wave-action equation to model the effects of turbulence, wind, surfactants, and nonlinear wave interactions (Hughes, 1978). The difficulties that are associated with parameterizing all of these physical effects are substantially reduced by performing direct numerical simulations of turbulent free-surface flows. However, as will be shown, the improper initialization of vortical or turbulent free-surface flows will generate high-frequency waves that will adversely affect estimates of the radar backscatter from the ocean surface.

The concept of *initialization* is very familiar to meteorologists, but almost foreign to the naval hydrodynamic community. Meteorologists use initialization procedures to eliminate spurious high-frequency gravity-inertia waves from numerical weather predictions. This process produces a *balanced* model of the atmosphere that is dominated by the low-frequency Rossby modes that are important at planetary length and time scales. Two examples of procedures to initialize weather simulations include the methods of Machenhauer (1977) and Bauer and Tribbia (1977) who separate the governing equations into the slow and fast modes, and then they formulate initial conditions that do not excite the high-frequency gravity-inertia waves.

The generation of high-frequency waves in numerical simulations of vortical and turbulent free-surface flows is similar to the problems that occur in numerical weather prediction. As an analogy, consider the impulsive wave motion that is imparted by a stone hitting the water surface. In this Cauchy-Poisson problem, the high-frequency dispersive waves that radiate away from the impact zone correspond to the undesirable inertia-gravity waves that are present in unbalanced numerical weather predictions. The localized nonpropagating disturbance of the stone, which includes the water displaced by the stone, corresponds to the desirable Rossby modes. Our present objective is to model the slow entry of a stone or more specifically, the interaction of vortical structures with a free surface at low to moderate Froude numbers. Unlike the stone-entry problem, submerged vortical structures do not suddenly appear in nature so numerical simulations require special treatment to ensure that undesirable dispersive waves are not generated.

Our analysis will show that the component of the pressure that is induced by the vortical portion of the flow will generate spurious high-frequency waves unless the free surface is given sufficient time to adjust, even if the initial free-surface elevation is zero. Our procedure is similar to the *adjustment* process that actually occurs in nature, whereby the high-frequency waves radiate away from a disturbance to leave behind the desirable low-frequency response. In nature the physical domain is large enough to permit the radiation of the high-frequency waves, whereas in our numerical simulations we make the time scale of the disturbance so long that no high-frequency waves are generated.

An alternative numerical procedure, that is even more closely related to what actually occurs in nature, is to use open-boundary conditions. However, open-boundary conditions for time-domain problems with nonlinear free-surface boundary conditions have transmission problems (Dommermuth and Yue, 1987). Even if perfect transmission could be attained, it would still take at least one wave period for a disturbance at one end of the computational domain to cross to the opposite end where it could make an exit. This is the same amount of time that our adjustment procedure requires, and our adjustment procedure does not incur any of the overhead costs that are associated with computing open-boundary conditions.

The original initialization procedures of Machenhauer (1977) and Bauer and Tribbia (1977) are difficult to apply to deep water problems because their schemes require changes to the

---

Contributed by the Fluids Engineering Division for publication in the JOURNAL OF FLUIDS ENGINEERING. Manuscript received by the Fluids Engineering Division June 30, 1992; revised manuscript received February 23, 1993. Associate Technical Editor: T. T. Huang.

free-surface elevation that affect every quantity in the governing equations throughout the entire depth. Rather than alter the initial free-surface elevation, the present adjustment procedure circumvents this problem by altering how quickly the initial conditions are applied. This simpler approach has been outlined by Dommermuth (1993) who reduces the initial impulse of the free-surface stresses by applying an atmospheric forcing term. The details and performance of this procedure are provided in this paper.

The adjustment procedure is used to simulate whirls. Sarpkaya and Suthon (1990 and 1991) and Sarpkaya (1992), who use a two-dimensional vortex element method, show that whirls may undergo a reverse energy cascade that leads to the formation of large vortical structures. Our formulation, which allows significant core deformation, extends their results to three-dimensional flows with a free surface.

Comparisons between unadjusted and adjusted solutions show that high-frequency standing waves are generated if the flow is not given sufficient time to adjust. These standing waves obscure the true hydrostatic balance of the free-surface elevation with the component of the pressure that is induced by the whirls. We call this particular component of the pressure the vortical pressure. A precise mathematical definition of the vortical pressure is provided in Dommermuth (1993), and a brief derivation is provided in the next two sections.

The hydrostatic balancing that occurs between the free-surface elevation and the vortical pressure affects interpretations of shadowgraph images of free-surface flows. Sterling et al. (1987) show that the intensity of shadowgraph images is proportional to the curvature of the dimples that are formed by individual whirls. By comparing shadowgraph images to measurements using digital particle image velocimetry, Gharib and Weigand (1992) observe that the dimples are not centered over the whirls. In a private communication, Alex Weigand had suggested that dimples and pressure are related. The numerical simulations confirm that pressure field of the whirls forms dimples on the free surface. At the low Froude numbers that occur in the laboratory, which are also typical for full-scale ship wakes, the depths of the dimples are directly proportional to the pressure. So the intensity of shadowgraph images indicates local variations in the pressure field of the whirls rather than the position of individual whirls.

Field Equations

Consider the unsteady incompressible flow of a Newtonian fluid under a free surface, and let $\mathbf{u}=\mathbf{u}(x, y, z, t)=(u, v, w)$ represent the three-dimensional velocity field as a function of time. Applying Helmholtz's theorem gives

$$\mathbf{u}=\nabla\phi+\mathcal{U}, \tag{1}$$

where $\phi(x, y, z, t)$ is a velocity potential which describes the irrotational flow and $\mathcal{U}=(x, y, z, t)=(U, V, W)$ is a solenoidal field which describes the vortical flow such that

$$\nabla^2\phi=0 \tag{2}$$

$$\nabla\cdot\mathcal{U}=0. \tag{3}$$

Since ϕ satisfies Laplace's equation and the divergence of the rotational field $\mathcal{U}$ is chosen zero, the total velocity field $\mathbf{u}$ conserves mass. Note that $\mathcal{U}$ may contain a portion of the irrotational field depending on how the boundary conditions are defined.

Based on this Helmholtz decomposition of the velocity field, define the total pressure Π in terms of a vortical pressure P and an irrotational pressure as follows:

$$\Pi=P-\frac{\partial\phi}{\partial t}-\frac{1}{2}\nabla\phi\cdot\nabla\phi-\frac{1}{\mathrm{F}_\mathrm{r}^2}z. \tag{4}$$

Here, the pressure terms are normalized by ρu_e^2 where u_e is characteristic velocity of an eddy and ρ is the density. $\mathrm{F}_\mathrm{r}^2=u_e^2/gl_e$ is the Froude number and l_e is the characteristic length of an eddy. The vertical coordinate z is positive upward, and the origin is located at the mean free surface. Substituting these decompositions (1 and 4) into the Navier-Stokes equations gives

$$\frac{\partial\mathcal{U}}{\partial t}+((\mathcal{U}+\nabla\phi)\cdot\nabla)\mathcal{U}+(\mathcal{U}\cdot\nabla)\nabla\phi=-\nabla P+\frac{1}{\mathrm{R_e}}\nabla^2\mathcal{U}. \tag{5}$$

where $\mathrm{R_e}=u_el_e/\nu$ is the Reynolds number and ν is the kinematic viscosity.

The divergence of the momentum Eqs. (5) used in combination with the mass-conservation Eqs. (2) and (3) can be used to derive a Poisson equation for the vortical pressure. This equation expressed in indicial notation ($U_i=(U, V, W)$) is as follows:

$$\nabla^2P=-\frac{\partial U_j}{\partial x_i}\frac{\partial U_i}{\partial x_j}-2\frac{\partial U_j}{\partial x_i}\frac{\partial^2\phi}{\partial x_j\partial x_i}. \tag{6}$$

As shown by Dommermuth (1993), the vortical pressure is also subject to a solvability condition.

Exact Free-Surface Boundary Conditions

The Helmholtz decomposition of the velocity field requires that an additional boundary condition be imposed on the free surface. An expedient boundary condition that can be specified is that the normal component of the rotational velocity is zero on the free surface:

$$\mathcal{U}\cdot\mathbf{n}=\frac{-U\eta_x-V\eta_y+W}{\sqrt{\eta_x^2+\eta_y^2+1}}=0. \tag{7}$$

where $z=\eta(x, y, t)$ is the free-surface elevation and $\mathbf{n}$ is the unit normal on the free surface. The preceding constraint which is imposed on the rotational velocity field means that the evolution of the free-surface elevation is entirely prescribed in terms of the free-surface elevation itself and the velocity potential as follows:

$$\frac{\partial\eta}{\partial t}+\eta_x\phi_x+\eta_y\phi_y-\phi_z=0, \tag{8}$$

where everything is evaluated on the exact position of the free surface, $z=\eta$.

The normal stress on the free surface must balance with the atmospheric pressure and the surface tension:

$$\frac{d\phi}{dt}+\frac{1}{2}(\phi_x^2+\phi_y^2-\phi_z^2)+(\eta_x\phi_x+\eta_y\phi_y)\phi_z+\frac{1}{\mathrm{F}_\mathrm{r}^2}\eta$$
$$=P-P_a-\frac{n_in_j}{\mathrm{R_e}}\left(\frac{\partial u_i}{\partial x_j}+\frac{\partial u_j}{\partial x_i}\right)-\frac{1}{\mathrm{W_e}}\nabla\cdot\mathbf{n}. \tag{9}$$

where P_a is the atmospheric pressure, $\mathrm{W_e}=\rho u_e^2l_e/T$ is the Weber number, and T is the surface tension. $d/dt=\partial/\partial t+\nabla\phi\cdot\nabla$ is a substantial derivative. n_i are the components of the unit normal on the free surface and $u_i=U_i+\partial\phi/\partial x_i$ is the total velocity. In addition to the normal-stress condition, there are also two tangential-stress conditions that are provided in Dommermuth (1993).

One advantage of the Helmholtz formulation relative to a primitive-variable formulation is the separation of the potential portions of the flow from the vortical portions of the flow. Based on this separation, the terms that excite spurious high-frequency waves can be isolated as shown in the next section.

Adjustment Procedure

Recall that l_e and u_e denote the length and velocity of a characteristic eddy, then the time scales of the vortical and wavy motions are respectively $t_v\sim l_e/u_e$ and $t_w\sim\sqrt{l_e/g}$, where g is gravity. The ratio of these two time scales is $t_w/t_v=u_e/\sqrt{gl_e}=\mathrm{F_r}$, where $\mathrm{F_r}$ is the Froude number. At low Froude numbers, when the time scale of the vortical motions is longer than the time scale of the wavy motions, the free-surface elevation (η) balances with the vortical pressure field (P) that is induced by the eddys:

$$\eta = \mathrm{F}_\mathrm{r}^2 P|_{z=0} + O(\mathrm{F}_\mathrm{r}^4), \tag{10}$$

where we have taken the inviscid limit of the normal-stress condition (9) at a low Froude number and assumed that the effects of capillarity are small. The balancing between the gravity and vortical pressure terms is primarily hydrostatic, no dispersive waves are generated to leading order. For initial-value problems, Eq. (10) is only valid for time $t > t_w$, i.e., after the dispersive waves have propagated away (Hall, 1979). Since finite domains do not permit the radiation of waves, standing waves will form if the flow is not given sufficient time to adjust.

The preceding example can be generalized to initial-value problems by including the time-dependent terms in Eqs. (8) and (9). The linearized inviscid free-surface boundary conditions for a single Fourier mode are

$$\frac{\partial \hat{\phi}}{\partial t} + \frac{1}{\mathrm{F}_\mathrm{r}^2}\hat{\eta} = \hat{P} - \hat{P}_a$$

$$\frac{\partial \hat{\eta}}{\partial t} = k\hat{\phi}, \tag{11}$$

where $\hat{\eta}$, $\hat{\phi}$, $\hat{P}$, $\hat{P}_a$ are the normalized Fourier modes of the free-surface elevation, the velocity potential, the vortical pressure on the free surface, and the atmospheric pressure, and k is the wavenumber. These equations are valid at low Froude numbers, when the coupling between potential and vortical portions of the flow is weak. The preceding equations can also be made valid for capillary waves by making a small modification to the hydrostatic term.

Suppose $\hat{\phi}$ and $\hat{\eta}$ are initially zero, $\hat{P}$ is a constant with respect to time, and $\hat{P}_a = 0$, then the unadjusted solution to Eq. (11) is

$$\hat{\eta} = -\mathrm{F}_\mathrm{r}^2 \hat{P}(\cos(\omega t) - 1)$$

$$\hat{\phi} = \frac{\hat{P}}{\omega}\sin(\omega t), \tag{12}$$

where $\omega^2 = k\mathrm{F}_r^{-2}$ is the wave frequency. The oscillatory components represent undesirable standing waves, and the mean component is the desirable hydrostatic response. Since the amplitudes of the standing waves are equal to the mean hydrostatic response, the correlation between the vortical pressure and the free-surface elevation is very poor. We can remedy this situation by applying an atmospheric pressure that reduces the impulse of the vortical pressure as follows:

$$\hat{P}_a = \hat{P}\exp\left(\frac{-t^2}{\delta^2}\right), \tag{13}$$

where δ is the adjustment time. To minimize transients, the adjustment time is chosen greater than the wave period. The adjusted solution to Eq. (11) is

$$\hat{\eta} = \mathrm{F}_\mathrm{r}^2\hat{P}(1 - \exp(-\alpha^2 t^2)) - 2\mathrm{F}_\mathrm{r}^2\hat{P}\frac{\alpha^2}{\omega^2}\exp(-\alpha^2 t^2) + 2\mathrm{F}_\mathrm{r}^2\hat{P}\frac{\alpha^2}{\omega^2}\cos(\omega t) + O(\alpha^4)$$

$$\hat{\phi} = 2\hat{P}\frac{\alpha^2 t}{\omega^2}\exp(-\alpha^2 t^2) - \frac{2\hat{P}}{\omega}\frac{\alpha^2}{\omega^2}\sin(\omega t) + O(\alpha^4), \tag{14}$$

where $\alpha = 1/\delta < \omega/2\pi$. The exponential terms are small after two standing-wave periods ($t > 2\delta$), and the oscillatory terms relative to the mean hydrostatic term are order $2\alpha^2/\omega^2 < 1/2\pi^2$. So for reasonable adjustment periods, we can reduce the amplitude of the standing waves by almost two orders of magnitude.

Based on Eq. (13), a whole family of filters can be defined with the general form:

$$\hat{P}_a = \hat{P}\exp(-(\alpha t)^m) \tag{15}$$

Based on numerical analysis, the optimal exponent $m \approx 2.42$ minimizes the amplitude of the standing wave relative to the mean hydrostatic response when $\alpha = 1/2\pi$ and $\omega = k = 1$. In this case, the relative amplitude of the standing wave ($a \approx 5.01 \times 10^{-2}$) is slightly better than the Gaussian filter with $m = 2$ ($a \approx 6.18 \times 10^{-2}$). The Gaussian filter is used in the present study.

Numerical Simulations

The adjustment procedure is applied to the unsteady and incompressible Navier-Stokes equations with exact free-surface boundary conditions. A Helmholtz decomposition is used to decompose the flow field into wavy and vortical components. The wavy and vortical portions of the flow are modeled using a velocity potential and a solenoidal field (see Eqs. (2) and (3)). The system of equations are discretized using a fourth-order finite-difference formulation. A third-order Runge-Kutta scheme is used to perform the numerical time integration. The details of the numerical algorithm are provided in Dommermuth (1993).

As an illustration of the adjustment procedure, we consider the chaotic interaction of sixteen whirls (4 rows × 4 columns) in a box. The sides and bottom of the box use free-slip boundary conditions, and the top of the box uses exact free-surface boundary conditions. The vertical coordinate z is positive upward, and the origin is located at the mean free surface. The lengths of the box along the x-, y-, and z-axes are respectively denoted L, W, and D. The initial vorticity distribution is

$$\Omega_x = \sum_{i=0}^{3}\sum_{j=0}^{3}\omega_c s_{ij}\exp\left(-\frac{(x-i)^2 + (y-j)^2}{r_c^2}\right) \quad \text{for } -D \le z \le 0, \tag{16}$$

where ω_c is the core vorticity and r_c is the core radius. $s_{ij} = \pm 1$ is a random sign subject to the constraint that the total circulation on the free surface is zero. The free-surface elevation and the velocity potential are initially zero. The flow is initially two-dimensional, but the deformation of the free-surface leads to three-dimensional interactions.

The rows and columns of whirls are evenly spaced based on a characteristic length $l_e = 1$. The characteristic velocity, $u_e = \Gamma/(2\pi l_e) = 1$, is equal to the velocity one whirl induces on its nearest neighbor. $\Gamma = \pi r_c^2 \omega_c$ is the circulation of a single whirl. Based on these scales, the Reynolds number is $\mathrm{R_e} = u_e l_e/\nu = \Gamma/(2\pi\nu)$, the Froude number is $\mathrm{F}_\mathrm{r}^2 = u_e^2/(g l_e) = \Gamma^2/(4\pi^2 g l_e^3)$, and the Weber number is $\mathrm{W_e} = \rho u_e^2 l_e/T = \rho\Gamma^2/(4\pi^2 T l_e)$, where ν is the kinematic viscosity and T is the surface tension.

Unadjusted and adjusted simulations are performed with $\mathrm{R_e} = 100$, $\mathrm{F}_\mathrm{r}^{-2} = 300$, and $\mathrm{W_e} = 1$. The ratio $\mathrm{F}_\mathrm{r}^2/\mathrm{W_e} = T/(\rho g l_e^2) = 1/300$ corresponds to a 5 cm gravity/capillary wave in water. In this parameter regime, the free-surface elevation and the vortical pressure are hydrostatically balanced as in Eq. (10). The adjusted simulation reduces the impulse of the vortical pressure and the normal component of the viscous stress by applying an atmospheric forcing term:

$$P_a = \left(P - \frac{n_i n_j}{\mathrm{R_e}}\left[\frac{\partial u_i}{\partial x_j} + \frac{\partial u_j}{\partial x_i}\right]_{z=\eta}\right)\exp\left(\frac{-t^2}{\delta^2}\right), \tag{17}$$

whre n_i are the components of the unit normal on the free surface and $u_i = U_i + \partial\phi/\partial x_i$ is the total velocity. U_i and ϕ are the solenoidal and potential velocity fields. At low Froude numbers the viscous term relative to the vortical pressure term in the preceding equation is $O(\mathrm{F}_r^2)$. Even though this term is small, the viscous normal stress is also adjusted because it too can generate spurious high-frequency standing waves. The adjustment time (δ) is chosen larger than the wave period of the longest standing wave that is permitted in the computational domain. The details of the numerical simulations are summarized in Table 1.

The following table highlights some important differences between unadjusted and adjusted simulations:

	$\eta_{\min}$	$\eta_{\max}$	$\lvert\eta_x\rvert_{\max}$	$\lvert\eta_{xx}\rvert_{\max}$	$\lvert\eta_y\rvert_{\max}$	$\lvert\eta_{yy}\rvert_{\max}$
Unadjusted	−0.0373	0.0512	0.203	2.19	0.192	1.71
Adjusted	−0.0269	0.0225	0.0406	0.201	0.0454	0.206

We observe that the extreme free-surface amplitudes vary from 25 to 50 percent of the laminar boundary-layer thickness at the free surface ($\mathrm{R}_e^{-1/2} = .10$) depending on the solution procedure. The maximum wave slopes for the unadjusted solution are almost 50 percent of Stokes two-dimensional breaking-wave criterion, but the wave slopes of the adjusted solution are only 10 percent. The radii of curvature are the same order as the core radius for the unadjusted solution, but the curvature of the adjusted solution is an order of magnitude less. The results imply that unadjusted solutions may be prone to unnatural wave breaking at higher Froude numbers.

The balance of energy quantifies other differences between the adjusted and unadjusted solutions. A conservation of energy formula can be derived by taking the vector product of the total velocity with the momentum equations integrated over the fluid volume. The transport theorem in conjunction with divergence theorem may be used to simplify the resulting equations. Upon substitution of the exact free-surface boundary conditions into this energy equation, the following formula may be derived:

$$\frac{d}{dt}\left(\int_V \frac{U_iU_i}{2}+\frac{1}{2}\int_{S_o}\eta_t\phi+\frac{1}{2\mathrm{F}_r^2}\int_{S_o}\eta^2\right)$$
$$= -\int_{S_o}\eta_t P_a-\frac{1}{\mathrm{W}_e}\int_{S_o}\eta_t\nabla\cdot\mathbf{n}$$
$$-\frac{1}{\mathrm{R}_e}\int_V\left(\frac{\partial u_i}{\partial x_j}+\frac{\partial u_j}{\partial x_i}\right)\frac{\partial u_i}{\partial x_j}, \qquad (18)$$

where S_f is the free surface and S_o is the projection of the free surface onto the xy-plane. The first term ($d\mathcal{E}_{UU}/dt$) represents the change in kinetic energy of the vortices integrated over the material volume of the fluid (V), the second and third terms ($d\mathcal{E}_{\phi\phi}/dt$ and $d\mathcal{E}_{\eta\eta}/dt$) represent the changes in the kinetic and potential energies of the waves, the fourth term ($d\mathcal{W}_{pa}/dt$) represents the power generated by atmospheric forcing, the fifth term ($d\mathcal{W}_{st}/dt$) represents the power in capillary waves, and the last term ($d\mathcal{W}_v/dt$) represents the power expended by viscous stresses. Note that the work due to stresses on all other boundaries besides the free surface is assumd to be zero.

Figure 1 shows the two dominant terms in the energy balance of the adjusted solution procedure. For time $t=2$ the kinetic energy is almost half of its initial value due to viscous dissipation. Figure 2(a) shows the potential energy for the adjusted and unadjusted solutions, and the work due to atmospheric forcing in the adjusted solution. Comparing Figs. 1 and 2(a) shows that the potential energies are $O(\mathrm{F}_r^2\mathcal{E}_{UU}/D)$, where $\mathcal{E}_{UU}/D$ is the depth-averaged kinetic energy of the vortices. In Fig. 2(b), the kinetic wave energy for the adjusted solution is $O(\mathrm{F}_r^4\mathcal{E}_{UU}/D)$, which is expected for flows that are dominated by hydrostatics. (The kinetic wave energy is scaled by F_r^{-2} in this figure, and the jaggedness of the curve is due to a lower sampling rate than the other curves.) The potential energy of the unadjusted solution is very oscillatory. The period of the oscillation corresponds to the beating of standing waves, and the period gets longer as time increases because the short standing waves rapidly attenuate. The oscillations in the kinetic wave energy of the adjusted solution are from remnants of standing waves. Figure 2(a) also shows that the amount of work required to prevent the formation of standing waves is the same order as the potential energy. The work due to atmospheric forcing levels off near time $t=1.5$. After this time, the free-surface elevation is fully adjusted.

Table 1 Data for numerical simulations of whirls

Item	Unadjusted	Adjusted
R_{e_2}	100	100
F_r^{-2}	300	300
W_e	1	1
r_c	0.25	0.25
ω_c	32	32
δ	0	1
L	4	4
W	4	4
D	4	4
Δt	0.001	0.001
N_{time}	2501	2501
N_{iter}	2	2
$I_{\max}$	73	73
$J_{\max}$	73	73
$K_{\max}$	73	73
γ	0.125	0.125

Fully nonlinear free-surface boundary conditions are used on the top of the computational domain and free-slip boundary conditions are used on the sides and bottom of the computational domain. The Reynolds, Froude, and Weber numbers are respectively denoted by R_e, F_r, and W_e. The initial core radius and peak vorticity are denoted by r_c and ω_c. δ is the adjustment time. The lengths of the computational domain along the x-, y-, and z-axes are, respectively, L, W, and D. The time step is Δt. The number of time steps is N_{time}, and the number of iterations required to solve the nonlinear elliptic equations is N_{iter}. The number of grid points along the x-, y-, and z-axes are respectively $I_{\max}$, $J_{\max}$, and $K_{\max}$. The parameter γ specifies the grid solution in the free-surface boundary layer. More detailed descriptions of the numerical parameters are provided in Dommermuth (1993). Note, however, that the Reynolds, Froude, and Weber numbers are defined differently in the present paper.

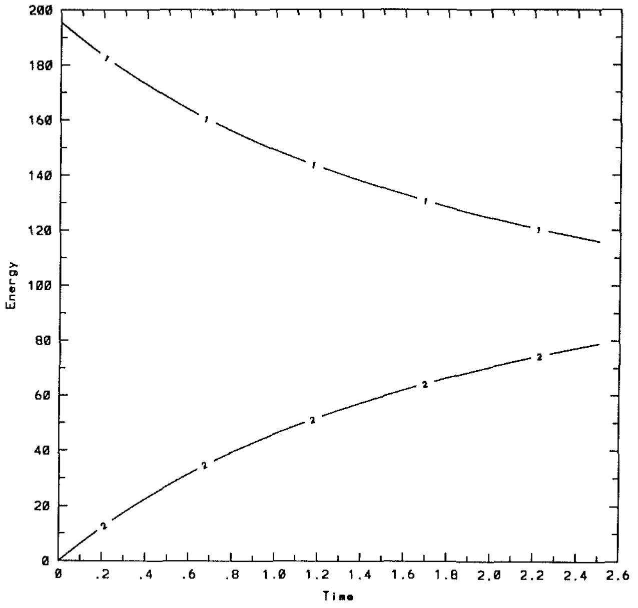

Fig. 1 The energy balance of the adjusted solution. (—1—) and (—2—) denote the kinetic energy ($\mathcal{E}_{UU} + \mathcal{E}_{\phi\phi}$) and the negative of the work due to viscous stresses ($-\mathcal{W}_v$)

Both the unadjusted and adjusted numerical simulations conserve energy to within 0.1 percent relative to the initial kinetic energy. Based on this level of energy conservation and the convergence studies that are reported in Dommermuth

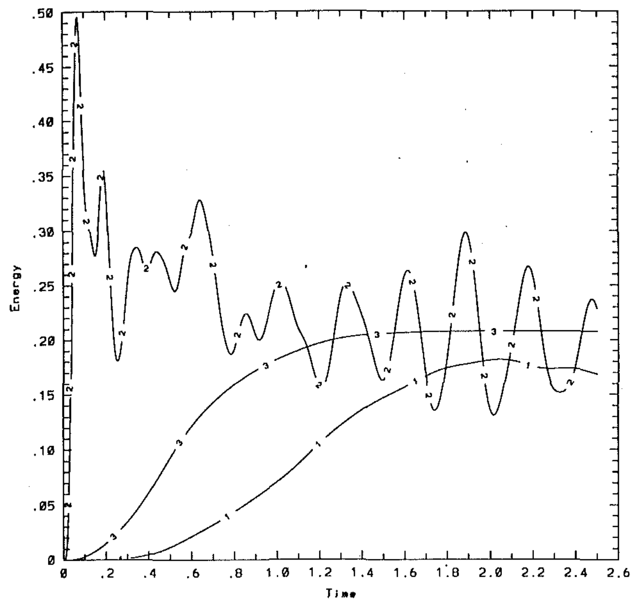

Fig. 2(*a*)

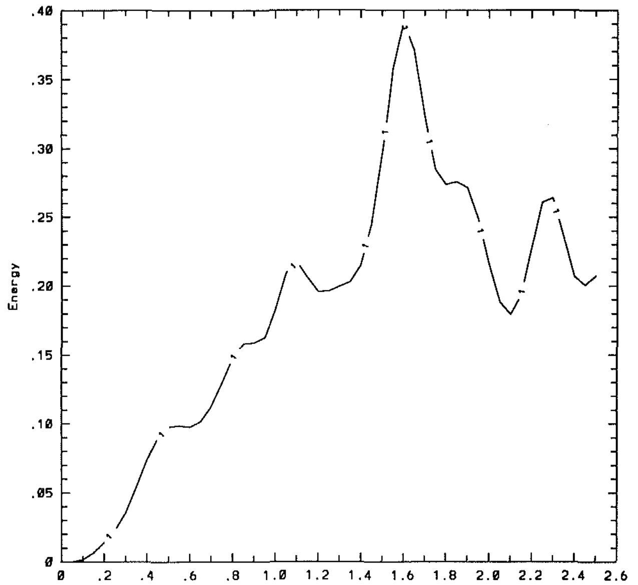

Fig. 2(*b*)

Fig. 2 The potential and kinetic wave energy. In Part (*a*) (—1—) and (—2—) denote the potential energy ($\mathcal{E}_{\eta\eta}$) of the adjusted and unadjusted solutions, and (—3—) denotes the negative of the work required to adjust the solution by atmospheric forcing ($-\mathcal{W}_{pa}$). In Part (*b*) (—1—) denotes the scaled kinetic energy of the waves ($\mathcal{E}_{\phi\phi}/F_r^2$) for the adjusted solution.

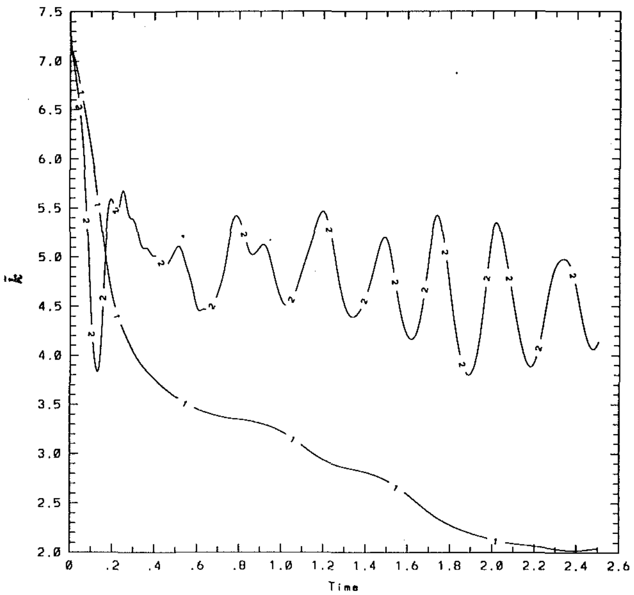

Fig. 3 The characteristic wavenumber. (—1—) and (—2—) denote $\bar{k}$ for the adjusted and unadjusted solutions

(1993), both numerical simulations are estimated to have three significant digits of accuracy.

The energy plots in Fig. 2(*a*) are similar to the surface-pressure plots that Williamson and Temperton (1981) use to illustrate the differences between initialized and uninitialized solutions of a global baroclinic forecast model. They used Machenhauer's (1977) method to eliminate undesirable pressure fluctuations. The comparisons between their uninitialized and initialized simulations clearly demonstrate the effectiveness of the procedure. Similarly, the potential energy plots in Fig. 2(*a*) illustrate the effectiveness of present adjustment procedure as applied to vortical free-surface flows in deep water.

A characteristic wavenumber that measures where most of the work due to surface tension is performed can be defined by $\bar{k}^2 = -W_e \mathcal{W}_{st}/F_r^2 \mathcal{E}_{\eta\eta}$, where $\bar{k}$ is a function of capillary-wave energy relative to gravity-wave energy. This characteristic wavenumber is plotted in Fig. 3. The initial distribution of 16 whirls corresponds to $\bar{k} \approx 2\pi$. This estimate is slightly exceeded in Fig. 3 because of the random signs that are assigned to each whirl. For both the adjusted and unadjusted simulations, $\bar{k}$ gets smaller as time increases. This evidence tends to support Sarpkaya's (1992) observations and calculations of a reverse energy cascade. However, the present simulations are primarily two-dimensional and the Reynolds number is very low. The characteristic wavenumber could merely indicate that high wavenumbers are attenuated more rapidly than low wavenumbers. Full three-dimensional numerical simulations at higher Reynolds numbers need to be performed before making a final conclusion. For time $t \geq 2$, the characteristic wavenumber of the adjusted solution is almost three times lower than it is for the unadjusted solution. This effect is due to the high-frequency standing waves that are present in the unadjusted solution.

Based on the energy plots in Fig. 2(*a*) and the characteristic-wavenumber plots in Fig. 3, we can conclude that a remote sensing simulation that used the unadjusted solution instead of the adjusted solution would predict free-surface elevations that have wave amplitudes with twenty-five percent relative error centered at a wavenumber that is almost three times too high. Based on these large discrepancies, remote sensing simulations should use adjusted solutions to make better predictions of radar backscatter from the ocean surface.

The effects that are measured by $\bar{k}$ are also visible in the contour plots of Figs. 4(*a*–*e*), where various free-surface quantities are plotted near the beginning and the end of the adjusted solution. Figures 4(*a*) and (*b*) plot the initial pressure field of the whirls (the vortical pressure) and the *z*-component of the vorticity at $t = 0$. Recall that the initial free-surface elevation is zero. The initial distribution of whirls (4 rows × 4 columns) is clearly visible in Fig. 4(*b*). Comparing Parts (*a*) and (*b*) shows that the vortical pressure and the whirls are poorly correlated. Figures 4(*c*–*e*) show the free-surface elevation, the vortical pressure, and the whirls at the end of the simulation, when the solution is fully adjusted. As a result of amalgamation, only seven distinct whirls are visible in Fig. 4(*e*). Once again, the correlation between the vortical pressure and the whirls is poor, but vortical pressure and the free-surface elevation are very well correlated. A detailed comparison of Parts (*c*) and (*d*) shows that the dimples on the free surface and the vortical pressure are hydrostatically balanced (see Eq. (10)). Based on this hydrostatic balance, the dark spots that are observed in shadowgraph images of free-surface flows correspond to the dimples that are formed by the vortical-component of the pressure. Since the dimples are not necessarily centered over the whirls, the dark spots are also not centered over the whirls.

The cross-correlation coefficient for the free-surface elevation and the vortical pressure is plotted in Fig. 5 for the adjusted and unadjusted solutions. The definition of this coefficient is provided below:

$$c_o(a,b)=\frac{[a,b]}{([a,a][b,b])^{1/2}},$$

where a and b are two-dimensional functions and $[a,b]$ denotes a surface integral over the xy-plane. Near the ends of the simulations, the correlation for the adjusted solution is almost three orders of magnitude stronger than it is for the unadjusted solution. The correlation is stronger for the adjusted solution because there are no standing waves.

The cross-correlation coefficient for the z-component of vorticity on the free surface and the free-slip bottom is plotted in Fig. 6 for the adjusted solution. The good correlation supports Leighton et al.'s (1992) assumption that a free-slip boundary condition models a clean free surface at low Froude

$P(z=\eta, t=0)$

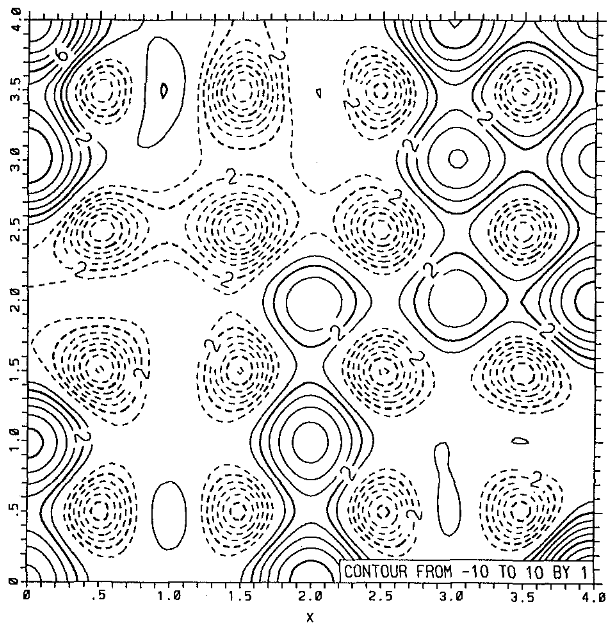

Fig. 4(*a*)

$\eta(t=2.5)$

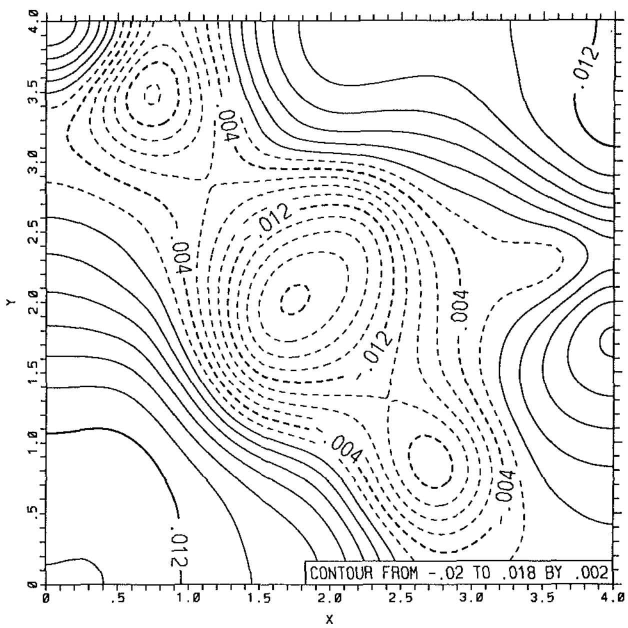

Fig. 4(*c*)

$\Omega_z(z=\eta, t=0)$

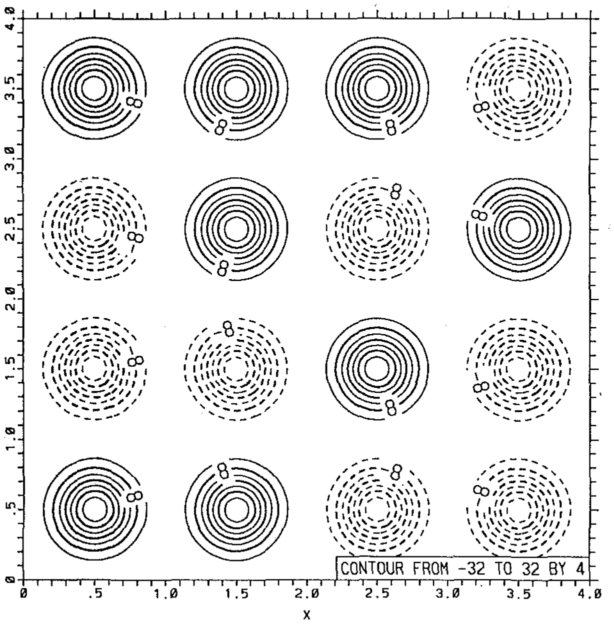

Fig. 4(*b*)

$P(z=\eta, t=2.5)$

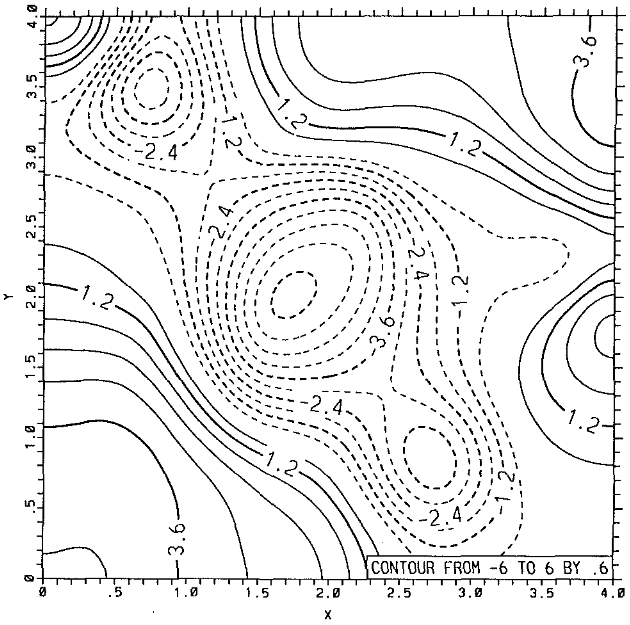

Fig. 4(*d*)

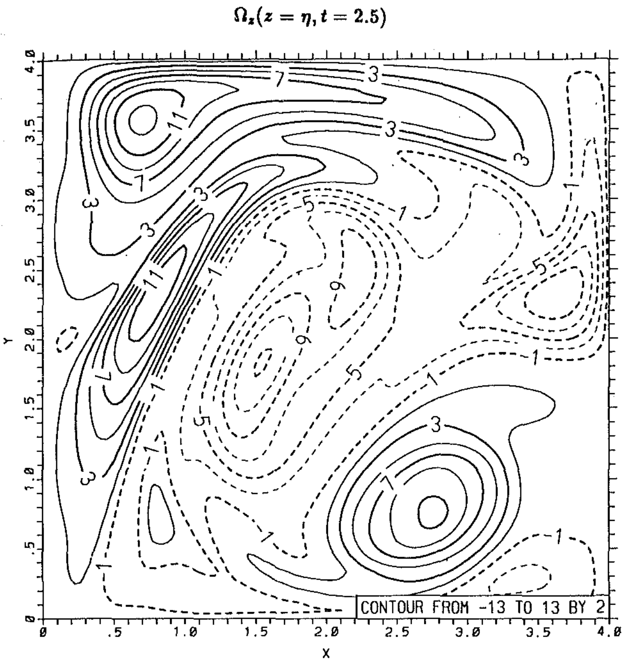

Fig. 4(*e*)

Fig. 4 Contour plots of free-surface quantities. Parts (*a*) and (*b*) correspond to $t = 0$ and parts (*c*-*e*) correspond to $t = 2.5$ for the adjusted solution. The solid and dashed lines respectively denote positive and negative quantities.

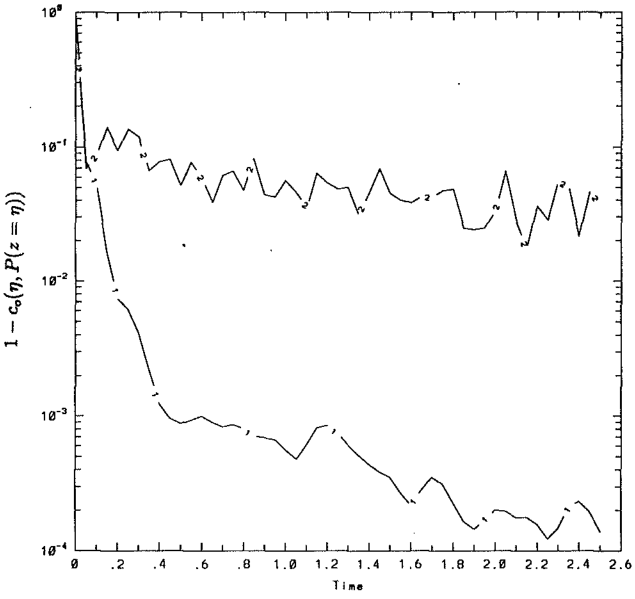

Fig. 5 The cross-correlation coefficient of the free-surface elevation and the vortical pressure. (—1—) and (—2—) denote the adjusted and unadjusted solutions. Zero is perfect correlation.

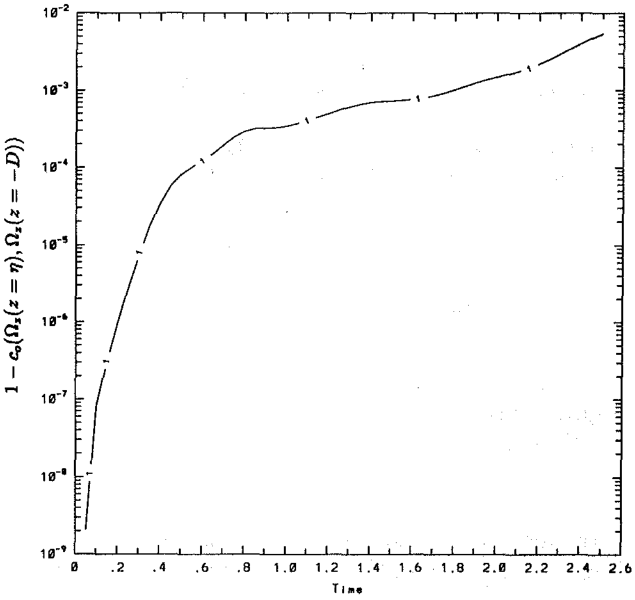

Fig. 6 The cross-correlation coefficient of the free-surface vorticity and the bottom vorticity. The results are plotted for the adjusted solution. Zero is perfect correlation.

numbers. The slight deterioration in the coefficient illustrates that the approximation is valid for times $t \leq O(\mathrm{F}_r^{-2})$. The present calculations show that the free-surface elevation can be calculated from the pressure using free-slip boundary conditions. As is evident in Dommermuth's (1993) simulations of vortex tubes impinging on a free surface, the approximation is valid even at intermediate Froude numbers.

Conclusions

Unadjusted numerical solutions to vortical free-surface flows are prone to developing high-frequency standing waves. These high-frequency standing waves obscure the true hydrostatic balance of the free-surface elevation and the vortical pressure that actually occurs in nature. The generation of high-frequency standing waves is minimized by reducing the impulse of the vortical pressure. Numerical simulations of whirls illustrate the effectiveness of the procedure relative to unadjusted initial conditions. The results of numerical simulations show that dimples are formed on the free surface by the pressure field of whirls. The long-lasting dark spots that are observed in shadowgraph images of free-surface flows are not necessarily the signature of just a single whirl. Similarly, the center of a dark spot may not correspond to the center of a whirl. The results of the numerical simulations confirm that a free-slip wall is an useful approximation of clean free surfaces at low to intermediate Froude numbers. Aside from applications to laboratory measurements, direct numerical simulations of free-surface turbulence, and remote sensing of ship wakes, the adjustment procedure can also be applied to numerical simulations of the nonlinear interactions of waves amongst themselves and vortices with ambient waves (Dommermuth, 1992).

Acknowledgments

This research is financially supported by the Fluid Dynamics Program at the Office of Naval Research. The numerical simulations have been performed on the CRAY Y-MP 8/8128 at the Primary Oceanographic Prediction System (POPS).

References

Baer, F., and Tribbia, J. J., 1977, "On Complete Filtering of Gravity Modes Through Nonlinear Initialization," *Monthly Weather Review*, Vol. 105, pp. 1536–1539.

Dommermuth, D. G., and Yue, D. K. P., 1987, "Numerical Simulations of Nonlinear Axisymmetric Flow With a Free Surface," *Journal of Fluid Mech.*, Vol. 178, pp. 195–219.

Dommermuth, D. G., 1992, "An Efficient Numerical Algorithm for Simulating Short- and Long-Wave Interactions With Applications to Parasitic Capillary Waves," Submitted for publication.

Dommermuth, D. G., 1993, "The Laminar Interactions of a Pair of Vortex Tubes With a Free Surface," *Journal of Fluid Mechanics*, Vol. 246, pp. 91–115.

Gharib, M., and Weigand, A., 1992, To be submitted for publication.

Hall, R. E., 1979, "The Complete Wave Interaction Analysis of the Standard Equations of Geophysical Fluid Dynamics, With Application to the Triple Problem of Adjustment, Nonlinear Evolution, and Weak Radiation," Yale University, Unpublished technical report.

Hughes, B. A., 1978, "The Effect of Internal Waves on Surface Wind Waves. 2. Theoretical Analysis," *Journal of Geophysical Research*, Vol. 83, pp. 455-465.

Leighton, R. I., Swean, T. F., Handler, R. A., and Swearingen, J. D., 1992, "Interaction of Vorticity With a Free Surface in Turbulent Open Channel Flow," *Proceedings of the 29th Aerospace Sciences Meeting & Exhibit*, Reno, Nevada, AIAA 91-0236.

Machenhauer, B., 1977, "On the Dynamics of Gravity Oscillations in a Shallow Water Model With Application to Normal Mode Initialization," *Contributions to Atmospheric Physics*, Vol. 50, pp. 253-271.

Sarpkaya, T., and Suthon, P., 1990, "Scarred and Striated Signature of a Vortex Pair on the Free Surface," *Proceedings of the 18th Symposium on Naval Hydrodynamics*, Ann Arbor, MI, National Academy of Sciences, Washington, D.C., pp. 503-520.

Sarpkaya, T., and Suthon, P., 1991, "Interaction of a Vortex Couple With a Free Surface," *Experiments in Fluids*, Vol. 11, pp. 205-217.

Sarpkaya, T., 1992, "Three-Dimensional Interactions of Vortices With a Free Surface," *Proceedings of the 30th Aerospace Sciences Meeting & Exhibit*, Reno, Nevada, AIAA 92-0059.

Sterling, M. H., Gorman, M., Widmann, P. J., Coffman, S. C., Strozier, J., and Kiehn, R. M., 1987, "Why Are These Disks Dark? The Optics of Rankine Vortices," *Physics of Fluids*, Vol. 30(11), 3624-3626.

Williamson, D., and Temperton, C., 1981, "Normal Model Initialization for a Multilevel Grid-Point Model. Part II: Non-Linear Aspects," *Monthly Weather Review*, Vol. 109, pp. 745-757.

Mass Imbalance Error of Waterhammer Equations and Leak Detection

Chyr Pyng Liou
Associate Professor,
Department of Civil Engineering,
University of Idaho,
Moscow, ID 83843

The waterhammer equations can be used to compute mass inventory changes for pipeline leak detection. In such applications the pipeline is monitored continuously in time and there is no clear demarcation between steady-state and transients. This paper addresses a mass imbalance error of the waterhammer equations. We establish that the net mass influx error for the waterhammer equations at the steady-state with maximum flow-rate bounds the same error during transients. A method to evaluate this bound is presented. Using petroleum products pipelines as an example, we show that the waterhammer equations are not accurate enough for leak detection in some systems.

1 Introduction

Using real-time data from a Supervisory Control and Data Acquisition (SCADA) system as boundary conditions, a real-time transient flow simulator can be an effective tool for monitoring abnormalities in pipelines. Many crude oil and petroleum products pipelines use such an approach for leak detection (API, 1991).

Some transient flow simulations use the waterhammer equations. In these equations, two convective-change terms are neglected. This simplification is well accepted for transients studies where the primary focus is on pressure. However, advances in SCADA technology make it possible to drive the simulators with increasingly accurate data. Consequently, the demand for higher model accuracy has increased as well. The simplification may limit model accuracy. This paper addresses a mass imbalance error associated with the waterhammer equations. A realistic bound for this error, its determination, and its impact on leak detection are discussed.

2 Leak Detection and Transient Simulations

The methods for leak detection vary from intermittent physical inspection to software-based real-time monitoring. Within the software-based category, there are many variations. We only address mass balance methods here.

The state of flow in a pipeline may be steady or transient, and there is no clear demarcation between the two. The simplest approach to leak detection uses the idea that if there is no leak, then the mass fluxes at the pipe ends ought to be equal. When the flow is not at steady-state, a difference in the mass fluxes does not imply leakage. Transient flow simulations account for any mass inventory changes. The transient model simulates steady-state flow as a special case of transients. However, the accuracy of the model may vary for these two flow regimes.

3 Governing Equations

The equations that describe isothermal transient flow are (Wylie and Streeter, 1983)

$$\frac{1}{\rho}\frac{\partial P}{\partial X}+V\frac{\partial V}{\partial X}+\frac{\partial V}{\partial T}+\frac{fV|V|}{2D}+g\sin\alpha=0 \tag{1}$$

$$\frac{1}{\rho a^2}\left(\frac{\partial P}{\partial T}+V\frac{\partial P}{\partial X}\right)+\frac{\partial V}{\partial X}=0 \tag{2}$$

where P = pressure, V = discharge velocity, D = pipe diameter, A = cross-sectional area of the pipe, g = gravitational acceleration, f = Darcy-Weisbach friction factor, ρ = density, a = wave speed, X = distance, T = time, and α = the upward angle between the pipe and the horizontal.

The governing equations are hyperbolic and can be transformed into a pair of compatibility equations

$$\frac{dV}{dT}\pm\frac{1}{\rho a}\frac{dP}{dT}+g\sin\alpha+\frac{fV|V|}{2D}=0 \tag{3}$$

valid along the characteristics

$$\frac{dX}{dT}=V\pm a \tag{4}$$

The wave speed a is expressed as

$$a=\sqrt{\frac{K/\rho}{1+KDc_1/(\mathrm{E}e)}} \tag{5}$$

where E = Young's modulus of elasticity of the pipe material, K = bulk modulus of the fluid, e = pipe wall thickness, and c_1 = a constant that reflects the state of stress in the pipe wall (Wylie and Streeter, 1983).

Note that density appears in the coefficient of dP/dT in Eq. (3). We view density as pressure dependent and wish to eliminate the density to avoid approximation during integration. This is done by replacing the pressure in Eq. (3) with piezometric head H, using the generalized definition

---

Contributed by the Fluids Engineering Division for publication in the JOURNAL OF FLUIDS ENGINEERING. Manuscript received by the Fluids Engineering Division May 8, 1992; revised manuscript received February 22, 1993. Associate Technical Editor: F. T. Dodge.

$$H=\frac{1}{g}\int_0^P \frac{dP}{\rho(P)}+Z \tag{6}$$

where Z is the elevation of the pipe with respect to a datum. Equation (3) becomes

$$\pm\frac{g}{a}\frac{dH}{dT}+\frac{dV}{dT}+\frac{fV|V|}{2D}\mp\frac{g\sin\alpha}{a}V=0 \tag{7}$$

Like Eq. (3), Eq. (7) is valid only along the characteristics defined by Eq. (4).

4 Uncertainties in Fluid Data and Modeling Assumptions

We need to justify the usage of variable density but constant wave speed in solving Eqs. (1) and (2). Liou (1992) summarized the density-pressure relationship (API 1984-a) and the density-temperature relationship (ASTM, 1980) for petroleum products. From these relationships and using the root-sum-squares (RSS) method, the total probable errors (TPEs) for density and for wave speed can be expressed as

$$\frac{\delta\rho}{\rho}=\sqrt{\left(\frac{P}{K-P}\frac{\delta K}{K}\right)^2+\left(\frac{\delta C_T}{C_T}\right)^2} \tag{8}$$

$$\frac{\delta a}{a}=\frac{1}{2}\sqrt{\left(\frac{\delta K}{K}\right)^2+\left(\frac{\delta\rho}{\rho}\right)^2} \tag{9}$$

where C_T is a volume correction factor for temperature. ASTM (1980) states an uncertainty of ± 0.05 percent for C_T. API (1984a) gives an uncertainty of ± 6.5 percent for K. Both uncertainties are associated with a 95 percent confidence level. From Eq. (8), the corresponding TPEs in density are ± 0.05 percent and 0.078 percent at 0 and 7000 KPa. From Eq. (9), the TPE in wave speed is ± 3.25 percent at all pressure levels.

Liou (1992) established the variations of density and wave speed (excluding the influence of pipe wall) of petroleum products for pressures ranging from 0 to 7000 kPa at 15°C. Using the values at 0 kPa as the basis, the variations in a gasoline with a reference density (density at 1 atm and 15°C) of 700 kg/m^3 are 0.90 percent for density and 2.20 percent for wave speed. We see that, over the pressure range considered, the density changes significantly exceed the TPE in the density data. At the same time, the wave speed changes over the pressure range fall within the TPE of the associated data. Therefore, we use variable density but constant wave speed in the governing equations.

5 Steady-State Solution

It can be shown that for steady-state, the two compatibility equations in Eq. (7) yield

$$\frac{dV}{dX}+\frac{1}{2}\frac{fV^3}{D(V^2-a^2)}+\frac{gV\sin\alpha}{V^2-a^2}=0 \tag{10}$$

$$\frac{dH}{dX}-\frac{fV^2a^2}{2gD(V^2-a^2)}-\frac{V^2\sin\alpha}{V^2-a^2}=0 \tag{11}$$

The effect of dropping the convective terms on the steady-state solution for nonhorizontal pipes can be found in Wylie (1984) and in the discussions and closure of Wylie (1984). We limit our scope to horizontal pipes only.

Since the fluid velocity is much smaller than the wave speed, we can approximate V^2-a^2 by $-a^2$ and obtain the steady-state solution for velocity and piezometric head as

$$V=V_i\left(1-\frac{fV_i^2X}{Da^2}\right)^{-0.5} \tag{12}$$

$$H=H_i+\frac{a^2}{2g}\ln\left(1-\frac{fV_i^2X}{Da^2}\right) \tag{13}$$

where V_i and H_i are the velocity and head at the pipe inlet.

6 Changes of Density, Cross-Sectional Area, and Mass Inventory During Transients

Density of liquids is related to pressure through bulk modulus. For water where the bulk modulus can be considered as constant, it can be shown that

$$\rho=\rho_0 e^{P/K} \tag{14}$$

where ρ_0 = density at zero gauge pressure. Equations (6) and (14) yield the common expression $P=\rho gH$. Usually P/K is small and ρ is closely approximated by ρ_0. For petroleum products, we have (Liou, 1992)

$$\rho=\rho_0\frac{K}{K-P} \tag{15}$$

$$P=K\left(1-\sqrt{1-2\rho_0 gH/K}\right) \tag{16}$$

Petroleum products are much more compressible than water and their density changes with pressure may be significant. Similar relationships can be obtained for other fluids with known relationships between bulk modulus, density, and pressure. We will use petroleum products as an example for the remainder of this paper.

For thin-walled pipe undergoing elastic deformation, the pipe cross-sectional area is related to the pressure by

$$A=A_0 e^{\frac{Dc_1P}{Ee}} \tag{17}$$

where A_0 = pipe cross-sectional area at $P=0$.

At any instant and for the entire pipeline, the rate of mass inventory increase S is

$$S=(\rho VA)_{\text{inlet}}-(\rho VA)_{\text{outlet}} \tag{18}$$

7 Net Mass Flux Error in Waterhammer Equations

For many applications it is acceptable to neglect the convective terms $V\partial V/\partial X$ and $V\partial P/\partial X$ in Eqs. (1) and (2). The simplified equations are known as the waterhammer equations (Parmakian, 1963). After the transformation, the compatibility equations are identical in form to Eq. (7) but the differentiations are now carried out along the characteristics

$$\frac{dX}{dT}=\pm a \tag{19}$$

This simplification yields constant slopes of the characteristics. It enables straight forward integration and speedy simulations. Both features are desirable in real-time simulations. However, the simplification causes a mass imbalance. This is apparent at the steady-state. Equation (2) dictates that, with $V\partial P/\partial X$ dropped, $\partial V/\partial X=0$ when $\partial P/\partial T=0$. Thus the simplified equations yield a uniform velocity at steady-state. We known from Eqs. (12), (15), and (17) that the velocity increases in the downstream direction and that density and pipe area at the pipe inlet exceed those at the outlet. Thus the steady-state uniform velocity from the waterhammer equations results in a mass imbalance if local values of ρ and A are used to compute mass fluxes. Consequently, mass imbalance during transients should also exist. This mass imbalance is insignificant for most applications where pressure is the primary concern. However, it is important for applications where high accuracy of mass flux is required.

8 Method of Approach

We compute head, velocity, and mass inventory changes for the full equations and for the waterhammer equations over a range of transients. The differences between the two equation sets are establish and considered to be the errors of the waterhammer equations. The magnitude of the convective terms are then examined. This leads to the formulation of a method to determine a reasonable bound for the mass imbalance error.

Next, we establish the TPEs in petroleum product properties and in volumetric flow-rate measurements. Relative to these uncertainties, we discuss the adequacy of waterhammer equations in pipeline leak detection.

9 System Specification, Boundary Conditions, and Numerical Solution Procedure

Liou (1991) demonstrated that the waterhammer equations can be scaled so that all system parameters can be grouped into a single constant R

$$R=\frac{fL}{2D}\frac{V_i}{a}=\frac{fL}{2D}\mathrm{Ma}_i \qquad (20)$$

where L denotes the length of the pipeline and Ma_i is the Mach number at the inlet. Thus, on a dimensionless basis, diverse systems with a common R behave the same if their scaled initial and boundary conditions are equal. Liou et al. (1992) provided a distribution of R for 209 petroleum products pipeline segments. The R values vary from 0.07 to 34. Of these values, 64 are below 1, 111 are below 2, 134 are below 3, and 186 are below 10. An R value around 2 is common and is used here as an example.

One realization of this R value is a 0.61 m (2 ft) diameter 98.17 km (61 mile) long steel pipe carrying gasoline with a reference density of 700 kg/m^3 and a kinematic viscosity of 4.65×10^{-7} m^2/s (5.0×10^{-6} ft^2/s). A constant inlet head of 500 m (1640 ft) and an initial inlet velocity of 2 m/s (6.56 ft/s) are used. The initial friction factor is 0.0122. The pressures at the pipe inlet and outlet are 3439 kPa (498.8 psi) and 668 kPa (96.9 psi) respectively. Corresponding to an average pressure of 2054 kPa (298 psi) and an ambient temperature of 15°C, the bulk modulus of the gasoline is 760.1 MPa (110,315 psi), and the wave speed of the system is 983 m/s (3225 ft/s).

We create transients starting at 12 L/a seconds by linearly reducing the outlet velocity to 1 m/s (3.28 ft/s) in L/a seconds. We then hold the outlet velocity at 1 m/s for 12 L/a seconds before restoring it back to 2 m/s in L/a seconds. We continue the simulation for another 12 L/a seconds before stopping. This boundary condition allows us to see the density and mass inventory discrepancies during periods of mass storage increase and decrease. In a separate simulation, the ramping periods for the exit velocity are increased to 32 L/a seconds so that we can examine the effects of transient severity. For leak detection purposes, we can regard the L/a case as severe transients while the 32 L/a case is mild (Liou, 1992).

In leak detection practice, a flow regulator is usually used at the outlet of a pipeline. It may seem more appropriate to use a valve as the outlet boundary condition instead of a specified velocity. However, a highly accurate exit flow-rate is always measured and used directly in leak detection software. Obtaining the outlet velocity indirectly through valve modeling is undesirable since the valve's position and its inherent flow characteristic introduce additional uncertainties. The specified velocity at the outlet is the preferred and natural boundary condition to use. Similarly, a specified head is a natural inlet boundary condition since the head is known accurately through direct pressure measurement at the pump discharge. Modeling a pump itself would needlessly involve additional uncertainties.

The method of characteristics with specified time intervals and with a second order approximation to the frictional term was used. The details of this method can be found in Wylie and Streeter (1983). One difference is that for the full equations the velocities at the two ends of the characteristics were used to establish the directions of the characteristics. This was implemented through linear interpolations and iterations. The explicit formula of Swamee and Jain (1976) is used to obtain the friction factor as the Reynolds number changes during transients. The friction factors so obtained deviate no more than 3 percent from the Colebrook-White formula.

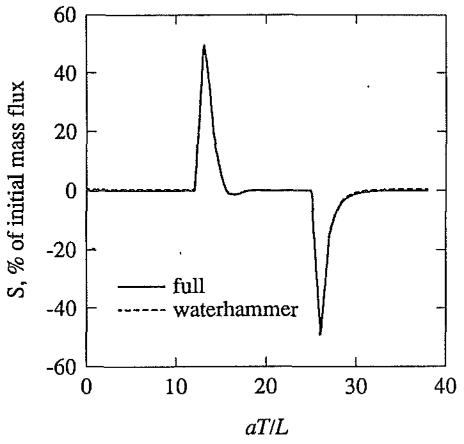

Fig. 1 Net mass influx comparison—severe transients

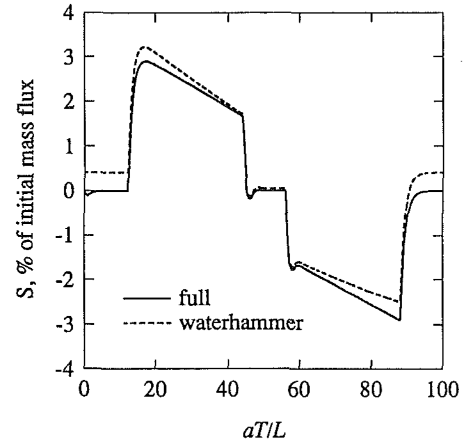

Fig. 2 Net mass influx comparison—mild transients

10 Results

The net mass influxes S for the two modeling approaches are plotted in Fig. 1 for the mild and in Fig. 2 for the severe transients. It is seen that the error is the greatest at the initial steady state for both cases.

The head and velocity comparisons between the two equation sets are shown in Figs. 3 and 4 for the severe transients only. The inlet velocities are identical. At the outlet, the convective acceleration modeled by the full equations yields a slightly higher velocity. The error diminishes during the transition period, and reappears when the original steady-state is restored. The outlet head from the full equations is slightly lower than that from the waterhammer equations because of greater head loss associated with the higher velocity. The discrepancy between the two approaches diminishes during the transition period, and re-appears at the final steady-state. Like the net mass influx, the velocities and the heads between the two approaches differ the most at the initial steady-state. The reason for this and a more complete picture will be offered later.

11 Accuracy of Numerical Solutions

Interpolation errors occur when the method of characteristics is used to solve the full equations. This type of error

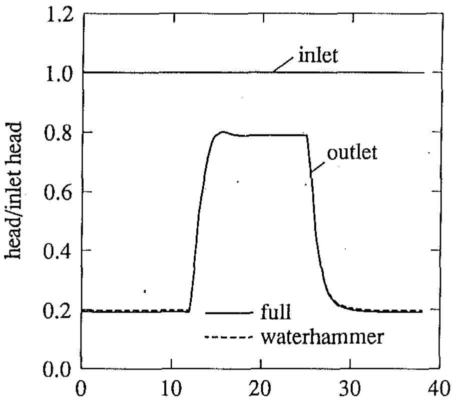

Fig. 3 Comparison of heads—severe transients

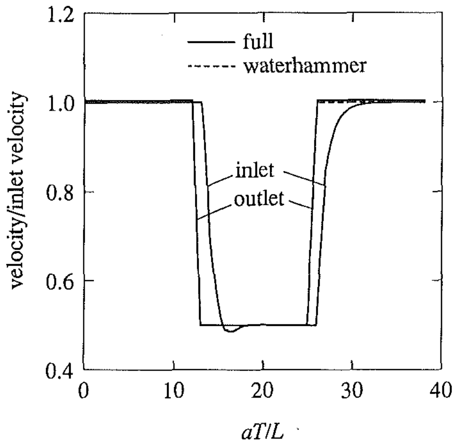

Fig. 4 Comparison of velocities—severe transients

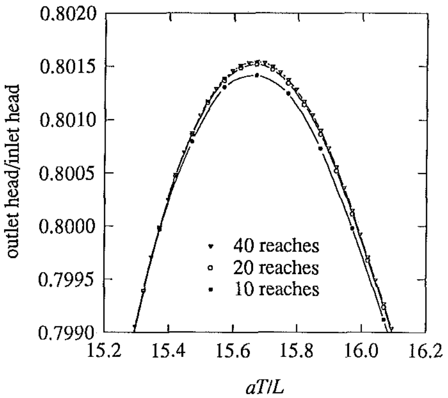

Fig. 5 Convergence of the numerical solutions

arises due to interpolations used in obtaining heads and velocities between grid points. Separately, for both the full equations and the waterhammer equations, discretization errors are introduced when the integral of the friction term over computational reaches is approximated by velocities at grid points. Both errors can be minimized if enough computational reaches are used in the numerical solution. Shown in Fig. 5 is the convergence of the numerical solution for the full equations. The computed outlet head for the severe transients within a time window around the instant of maximum error is shown. The percentage differences are 0.0127 between 10 and 20, and 0.00297 between 20 and 40 reaches. These errors are even smaller for the mild transient case. The errors at 20 reaches are about two orders of magnitude smaller than the differences we are trying to discern (see Eq. (26) and Fig. 10). These numerical errors are negligible and will not be addressed further.

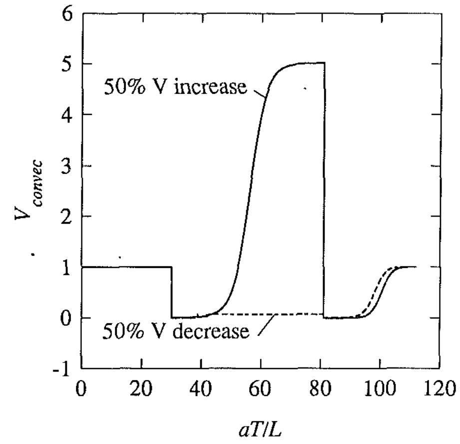

Fig. 6 Convective change of velocity over time

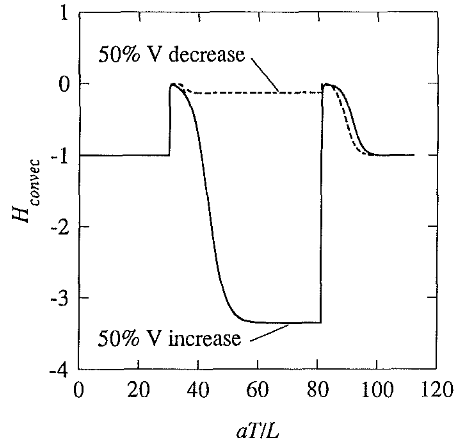

Fig. 7 Convective change of head over time

12 Magnitude of the Convective Terms

The magnitude of $V\partial V/\partial X$ and $V\partial H/\partial X$ can be examined relative to the local changes $\partial V/\partial T$ and $\partial H/\partial T$. Define

$$V_{\text{convec}} = \frac{V\dfrac{\partial V}{\partial X}}{\left|\dfrac{\partial V}{\partial T}\right| + \left|V\dfrac{\partial V}{\partial X}\right|_0} \qquad (21)$$

where the subscript 0 denotes steady-state. The terms on the right-hand side are the average values of the entire pipeline. Similarly, we define

$$H_{\text{convec}} = \frac{V\dfrac{\partial H}{\partial X}}{\left|\dfrac{\partial H}{\partial T}\right| + \left|V\dfrac{\partial H}{\partial X}\right|_0} \qquad (22)$$

Figures 6 and 7 show these two quantities over time for two new transient episodes. The full equations were used to generate these results. Again, a pipeline with an R of 2 was used as an example. The solid line represents a transient where the outlet velocity was increased by 50 percent in L/a seconds, held constant for 50 L/a seconds and then restored to the initial value linearly in another L/a seconds. The dashed lines represent a transient where the outlet velocity was decreased by 50 percent and then restored in the same sequence. The 50 L/a seconds is long enough to allow a new steady-state to develop before we begin to restore the original outlet velocity. We used the full equations with a fixed friction factor of 0.015 in generating these two figures. The V_{convec} and the H_{convec} traces stay at 1 and -1 during the initial steady-state. They drop to nearly zero when $\partial V/\partial T$ and $\partial H/\partial T$ greatly exceed $V\partial V/\partial X$ and $V\partial H/\partial X$ during the first period of transient creation. Afterwards, the flow settles towards a new steady-state with increased (solid line) or decreased (dashed line) velocity. V_{convec} and H_{convec} become negligible again when $\partial V/\partial T$ and $\partial H/\partial T$ are large as the restoration of the original outlet velocity begins. Eventually they approach 1 and -1 as the original steady-state is restored.

The limiting values reached by V_{convec} and H_{convec} during the interceding steady-state depend on the ratio of the interceding steady-state velocity to the original steady-state velocity. From Eqs. (20) and (21), we obtain

$$V\frac{\partial V}{\partial X}=\frac{fV^4}{2Da^2} \tag{23}$$

$$V\frac{\partial H}{\partial X}=-\frac{fV_i^3}{2gD} \tag{24}$$

In establishing Eq. (24) from Eq. (11), we expanded the natural logarithm by a series and only retained the first term since $fV_i^2X/(Da^2)$ is much less than unity. We see that the convective changes in velocity and in head are proportional to the 4th and the 3rd power of velocity. In Fig. 6, the limiting values of V_{convec} for the flow increase (solid line) and flow decrease cases (dashed line) are $1.5^4 = 5.06$ and $0.5^4 = 0.06$. In Fig. 7, the limiting values for H_{convec} for the flow increase and flow decrease cases reach $1.5^3 = 3.38$ and $0.5^3 = 0.13$. These figures show that when the interceding steady-state has a velocity greater than the initial steady-state value, the convective terms can be greatly amplified.

Figures 8 and 9 contrast the effect of the interceding steady-state on the net mass influx error. For flow-reduction transients, the error at the initial steady-state is the greatest since the convective change terms are the greatest. For flow-increase transients, the convective terms become greater as the flow approaches the interceding steady-state. Consequently, the net mass influx error is also greater. In general, it is the net mass influx error of the steady-state with the maximum velocity that bounds the net mass influx error during transients.

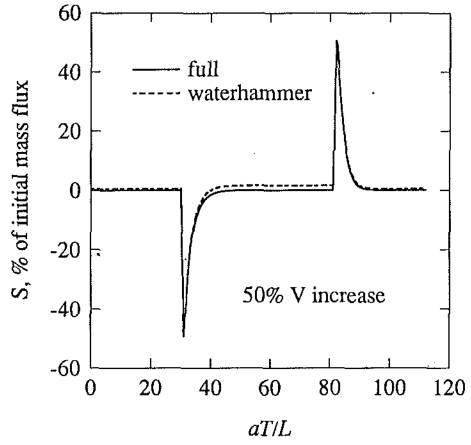

Fig. 8 **Net mass influx comparison—flow increase**

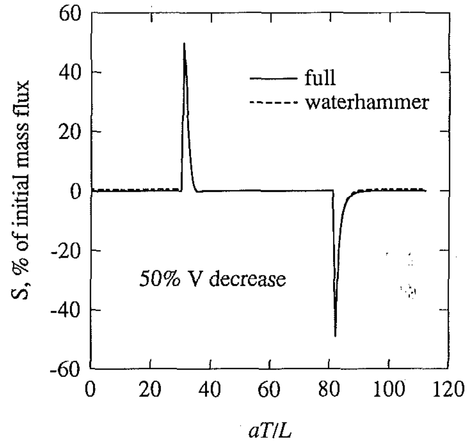

Fig. 9 **Net mass influx comparison—flow decrease**

13 Net Mass Influx Error at Steady-State

We regard all variables at the inlet as correct and examine the scaled net mass flux error U. From Eqs. (15), (17), and (18), we can write

$$\begin{aligned} U&=\frac{\delta S}{(\rho AV)_{\text{inlet}}}=-\frac{\delta(\rho VA)_{\text{outlet}}}{(\rho AV)_{\text{inlet}}} \\ &\approx -\left(\frac{\delta V}{V_{\text{inlet}}}+\frac{Dc_1\delta P}{\text{E}e}+\frac{\delta P}{K-P}\right) \end{aligned} \tag{25}$$

where δ represents an error, defined as the difference between like variables in the two modeling approaches. For example, δV = velocity from the waterhammer equations minus the velocity from the full equations. The three terms on the right-hand side represent fractional errors in outlet velocity, in outlet cross-sectional area, and in outlet density. The latter two result from δP at the outlet. Usually, K is much larger than P and E is much larger than D/e. Consequently, the fractional errors in cross-sectional area and in density are much smaller than the frictional error in outlet velocity. In our example associated with Figs. 1 through 4, these fractional errors are 2.55×10^{-6}, 2.13×10^{-5}, and -4.10×10^{-3} respectively. In general, the error in the outlet velocity dominates. Thus, U can be closely approximated as

$$U\approx -\frac{\delta V}{V_i}=\frac{V_{\text{outlet}}}{V_i}-1=\frac{1}{\sqrt{1-2R\text{Ma}_i}}-1 \tag{26}$$

In arriving at the above equation, we employ the fact the V_{outlet} is the outlet velocity from the full equations and V_i is the inlet as well as the outlet velocity from the waterhammer equations.

The RSS TPE in U as a result of uncertainties in f and a can be expressed as

$$\delta U=\sqrt{\left(\frac{R\text{Ma}_i}{(1-2R\text{Ma}_i)^{1.5}}\,\frac{\delta f}{f}\right)^2+\left(\frac{2R\text{Ma}_i}{(1-2R\text{Ma}_i)^{1.5}}\,\frac{\delta a}{a}\right)^2} \tag{27}$$

U and its uncertainty are plotted in Fig. 10 as a function of Ma_i for several R values. We have used a 3 percent uncertainty in the friction factor f and in the wave speed a to establish the uncertainty bands (areas between dotted lines). It is seen that the fractional net mass influx error is significant even with the presence of uncertainties. Equations (26), (27), and Fig. 10 apply to petroleum products pipelines as well as to pipelines transporting other liquids.

14 Application Example

Consider an initial steady state with $R = 2$, $\text{Ma}_i = 0.002$ and $U = 0.40$ percent (from Fig. 10). Let the velocity be increased to 1.5 times the initial steady-state value. This changes R to 3, Ma_i to 0.003 and U to 0.91 percent. Let the initial steady-state mass flux be 100 units. The initial mass imbalance error of the waterhammer equation is then 0.40 units. The

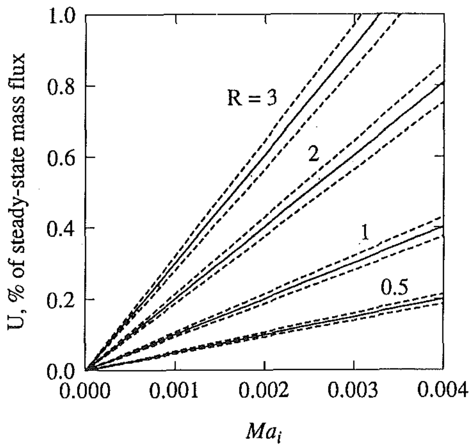

Fig. 10 Net mass influx error of the waterhammer equations

steady-state mass flux associated with the increased velocity is 150 units and the mass imbalance error becomes 0.0091 × 150 = 1.365 units. This error is 341 percent of the initial error! However, when the velocity is reduced to 0.5 times the initial steady-state value, R reduces to 1, Ma_i to 0.001 and U to 0.10 percent. The error is now $0.0010 \times 50 = 0.050$ units, or only 12.5 percent of the initial error.

In estimating the mass imbalance error of the waterhammer equations, one should examine the simulated velocity history and identify the highest "sustained" velocity. The U value associated with this velocity is a reasonable bound for the mass imbalance error. Spiky or "short duration" velocity peaks exceeding the sustained velocity should be discarded since the convective terms are negligible during those moments.

15 Uncertainties in Volumetric Flow Measurement

Turbine meters are common for volumetric flow measurements in leak detection. The flow-rate is inferred by the speed of rotation of turbine blades. A voltage pulse is generated as each blade passes the base of an externally mounted magnetic pickup coil. Each pulse represents a fluid volume to be determined through calibration. Counting the pulses over precise time intervals yields volumetric flow-rate. Because the pulses are discrete signals, turbine meters can be highly accurate.

Manufacturers use nonlinearity and nonrepeatability to characterize turbine meter performance. Typical nonlinearity and nonrepeatibility for turbine meters are ±0.15 percent over a 10:1 flow range and ±0.02 percent of reading respectively (Baker and Kalivoda, 1980). The nonlinearity error is a known bias error, and can be eliminated either by a flow computer or by the SCADA host in modern practice (Nunweiler, 1991). Nonrepeatability is a random error and not removable. In general, nonrepeatability is stated at a 95 percent confidence level (Miller, 1983).

Turbine meters are accurately calibrated at field conditions using a known volume in a meter prover. There are two uncertainties in meter proving. The first is an uncertainty in the least significant bit of meter pulse count. An API standard (API 1984b) recommends that the minimum pulse count during proving should be greater than 10,000. Thus this uncertainty should be less than ±0.005 percent (i.e., ±0.5/10000). The second is uncertainty in prover volume under field flowing conditions. If the API standard is followed, this uncertainty should not exceed ±0.01 percent. Meter proving removes most of the bias error that may have developed since the last prove.

Turbine meters behave as first-order dynamic systems for small flow changes about an operating point. The time constant for turbine meters is between 0.002 and 0.01 seconds at maximum flow and is inversely proprotional to the operating-point flow-rate (Doebelin, 1983). A turbine manufacturer suggested a time constant of about 0.05 seconds for a range of sizes (Laird, 1991). Cross-country pipelines typically have an L/a ratio in minutes or longer. Thus turbine meters should be sufficiently responsive for transient flow measurements.

With the nonlinearity bias removed, the RSS TPE is ±0.02 percent. If the nonlinearity bias is present, then the TPE depends on the flow range. For the maximum 10:1 flow range, the TPE is ±0.15 percent, which is dominated by the nonlinearity. For a more common 3:1 flow range the nonlinearity is reduced to about ±0.03 percent and the TPE becomes ±0.04 percent. As another indication of the high precision of turbine meters, Withers et al. (1972) experimentally verified claimed short term (i.e., bias-free) TPE of less than ±0.05 percent from four turbine meter manufacturers.

Although the above uncertainty estimates are achievable, the TPE may be larger in actual field measurements. With good equipment and good practice, this error can be kept to within ±0.2 percent or ±0.1 percent (Laird, 1991). However, if meter proving is not performed regularly, unknown bias errors set in and the overall uncertainty can be as great as ±1 percent. However, turbine meters used in leak detection are also used in custody-transfer. Consequently, these meters are proven periodically and highly accurate.

16 Adequacy of Waterhammer Equations for Leak Detection

Assuming the flow area is known precisely, the RSS TPE in the "measured" mass flux m is

$$\frac{\delta m}{m} = \sqrt{\left(\frac{\delta \rho}{\rho}\right)^2 + \left(\frac{\delta V}{V}\right)^2} \tag{28}$$

Through linear interpolations using the initial steady-state pressures at the pipe ends (Section 9) and the density data uncertainties (Section 4), we estimate the uncertainties in density to be 0.058 percent at the inlet and 0.052 percent at the outlet. Suppose that turbine meters are used for volumetric flow measurements and that the uncertainty for each measurement is ±0.02 percent. Using Eq. (28), the "measured" mass flux uncertainty is ±0.061 percent at the inlet and ±0.056 percent at the outlet. The resulting RSS TPE for the net mass influx for steady flow based on "measurements" is ±0.083 percent.

The above uncertainty is the least possible value since no bias is included. If biases exist, then the TPE can be much greater. For example, if the turbine meters are not proved in the field, then the RSS TPE can be as large as ±1.4 percent.

In the flow reduction example in section 9, we have $R = 2$ and $\mathrm{Ma}_i = 0.002$. From Fig. 10, $U = 0.4$ percent. For this example, which is typical of cross-country pipelines, there is a 0.317 percent (0.4 percent − 0.083 percent) loss of leak detectability during true steady-state. If the flow measurement uncertainty is kept at the nonrepeatability level through good meter proving practice, then it is the inaccuracy of the waterhammer equations, not the uncertainties in property data and flow measurement, that limits the ability to detect small leaks. On the other hand, when the turbine meters are not proven, then the 0.4 percent inaccuracy of the waterhammer equations becomes insignificant as inaccuracy falls within the ±1.4 percent uncertainty level of volumetric flow measurement.

17 Conclusions

When waterhammer equations are used to monitor mass inventory changes in pipelines, the net mass influx error becomes an issue. We demonstrate that this error is bounded by the mass imbalance error in the steady-state with maximum flow, irrespective of the severity of the transients. A simple method to determine this bound is presented.

With the available accuracy in flow property data and in flow-rate measurements, the waterhammer equations are not accurate enough for systems with high friction and high inlet Mach number. For a specified leak detection limit, Eqs. (26), (27), and Fig. 10 can be used, in conjuction with flow-rate measurement uncertainties, to evaluate the adequacy of the waterhammer equations in such applications.

Acknowledgment

The writer would like to thank the American Petroleum Institute for funding a portion of this study.

References

API, 1991, *Pipeline Leak Dectection: A Literature Review on Software-Based Pipeline Leak Detection*, American Petroleum Institute, Washington, D.C.

API, 1984-a, *Manual of Petroleum Measurement Standards*, Chapter 11.2.1M—Compressibility factors for Hydrocarbons: 638-1074 Kilograms per Cubic Metre Range, pp. 1-4, American Petroleum Institute, Washington, D.C.

API, 1984-b, *Manual of Petroleum Measurement Standards*, Chapter 4, Proving Systems, American Petroleum Institute, Washington, D.C.

ASTM, 1980, *Petroleum Measurement Tables—Volume Correction Factors*, Volume X—Background, Development, and Program Documentation, ASTM D1250, API Standard 2540, and IP 200, pp. x-73 – x-85.

Baker, P. D., and Kalivoda, R. J., 1980, "Turbine Meters for Liquid Measurements," Bulletin TP02001 (Technical Paper 103A), Smith Meter Inc., Erie, PA.

Doebelin, E. O., 1983, *Measurement Systems—Application and Design*, McGraw-Hill, New York.

Laird, C. B., (of Smith Meters Inc., Erie, Pennsylvania) 1991, Personal Communication.

Liou, C. P., 1991, "Maximum Pressure Head Due to Linear Valve Closure," ASME JOURNAL OF FLUIDS ENGINEERING, Vol. 113, No. 4, pp. 643-647.

Liou, C. P., Brockway, C. G., and Miller, R. B., 1992, "Pipeline Variable Uncertainties and Their Effects on Leak Detectability," 1992 API Cybernetics Symposium, American Petroleum Institute, Houston, Texas, pp. 127-149.

Liou, C. P., 1992, "Adequacy of Waterhammer Equations for Leak Detection in Petroleum Products Pipelines," *Unsteady Flow and Fluid Transients*, Bettess & Watts, eds., Balkema, Rotterdam, pp. 355-364.

Miller, R. W., 1983, *Flow Measurement Engineering Handbook*, McGraw-Hill, New York.

Nunweiler, D., 1991, "How to Determine Warning Alarm Levels for Leak Detection Systems," Vol. 1, Pipelines in a Changing Environment: 1991 CPA Pipeline Conference, May 15-16, Calgary, Alberta, Canadian Petroleum Association.

Parmakian, J., 1963, *Waterhammer Analysis*, Dover Publications, New York.

Swamee, P. K., and Jain, A. K., 1976, "Explicit Equations for Pipe Flow Problems," *Journal of the Hydraulics Division*, American Society of Civil Engineers, Vol. 102, No. HY5.

Withers, V. R., Inkley, F. A., and Chesters, D. A., 1972, "Flow Characteristics of Turbine Flowmeters," *Modern Developments in Flow Measurement*, Clayton, ed., Peter Peregrinus Ltd., London, pp. 305-320.

Wylie, E. B., and Streeter, V. L., 1983, *Fluid Transients*, FEB Press, Ann Arbor, Michigan.

Wylie, E. B., 1984, "Fundamental Equations of Waterhammer," *Journal of Hydraulic Engineering*, Vol. 110, No. 4, Apr., pp. 539-542. Five discussions and closure in Vol. 111, No. 8, pp. 1185-1200.

Experimental Results for the Rotordynamic Characteristics of Leakage Flows in Centrifugal Pumps

A. Guinzburg

C. E. Brennen

A. J. Acosta

T. K. Caughey

California Institute of Technology,
Division of Engineering and Applied Science,
Pasadena, CA 91125

In recent years, increasing attention has been given to fluid-structure interaction problems in turbomachines. The present research focuses on just one such fluid-structure interaction problem, namely, the role played by fluid forces in determining the rotordynamic stability and characteristics of a centrifugal pump. The emphasis of this study is to investigate the contributions to the rotordynamic forces from the discharge-to-suction leakage flows between the front shroud of the rotating impeller and the stationary pump casing. An experiment was designed to measure the rotordynamic shroud forces due to simulated leakage flows for different parameters such as flow rate, shroud clearance, face-seal clearance and eccentricity. The data demonstrate substantial rotordynamic effects and a destabilizing tangential force for small positive whirl frequency ratios; this force decreased with increasing flow rate. The rotordynamic forces appear to be inversely proportional to the clearance and change significantly with the flow rate. Two sets of data taken at different eccentricities yielded quite similar nondimensional rotordynamic forces indicating that the experiments lie within the linear regime of eccentricity.

1 Introduction

In turbomachinery, the trend toward higher speeds and higher power densities has led to an increase in the number and variety of fluid-structure interaction problems in pumps, compressors, turbines and other machines. This occurs because the typical fluid forces scale like the square of the speed and thus become increasingly important relative to the structural strength. This becomes particularly acute in rocket engine turbopumps where demands to minimize the turbopump mass may also lead to reductions in the structural strength. Consequently designers and manufacturers are concerned with the fluid-induced rotordynamic forces on impellers in turbomachines. Knowledge of the steady and unsteady forces and the associated rotordynamic coefficients is required to effectively model the rotordynamics of high speed turbomachines.

2 Background

Rotordynamic forces imposed on a centrifugal pump by the fluid flow through it were first measured by Domm and Hergt (1970), Hergt and Krieger (1969–70), Chamieh et al. (1985) and Jery et al. (1985). In the Rotor Force Test Facility (RFTF) at Caltech (Jery et al., 1985; Adkins et al., 1988; Franz et al., 1989) known whirl motions over a full range of frequencies (subsynchronous, supersynchronous as well as reverse whirl) are superimposed on the normal motion of an impeller.

The hydrodynamic force on a rotating shroud or impeller (see Fig. 1) which is whirling can be expressed in the stationary laboratory frame in linear form as:

$$\begin{bmatrix} F_x^*(t) \\ F_y^*(t) \end{bmatrix} = \begin{bmatrix} F_{ox}^* \\ F_{oy}^* \end{bmatrix} + [A^*] \begin{bmatrix} x^*(t) \\ y^*(t) \end{bmatrix} \qquad (1)$$

The first term on the right-hand side represents the radial force in the absence of whirl motion, so that F_{ox}^*, F_{oy}^* are the steady, time-averaged forces in a stationary frame which result from flow asymmetries in the volute or the inlet duct. These

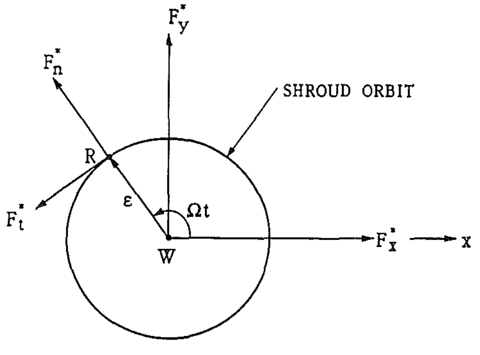

Fig. 1 Schematic of the fluid-induced radial forces acting on an impeller whirling in a circular orbit. F_x^* and F_y^* represent the instantaneous forces in the stationary laboratory frame. F_n^* and F_t^* are the forces normal and tangential to the whirl orbit where Ω is the whirl frequency.

Contributed by the Fluids Engineering Division for publication in the JOURNAL OF FLUIDS ENGINEERING. Manuscript received by the Fluids Engineering Division April 21, 1992; revised manuscript received April 22, 1993. Associate Technical Editor: S. B. Zakem.

steady radial forces are discussed in detail elsewhere (Iverson et al., 1960; Domm and Hergt, 1970; Chamieh, 1983; Chamieh et al., 1985; Adkins, 1986). The matrix $[A^*]$ is the rotordynamic matrix which operates on the instantaneous displacement $[x^*]$ of the rotor center. Note that $[A^*]$ will in general be a function not only of the mean flow conditions and pump geometry but also of the frequency of whirl, Ω. If outside the linear range, it may also be a function of the amplitude of the whirl motion, ϵ. At small, linear amplitudes $[A^*]$ should be independent of ϵ and presented as a function of the whirl frequency ratio, Ω/ω. In the case of a circular whirl orbit $x^*=\epsilon\cos\Omega t$, $y^*=\epsilon\sin\Omega t$. Then the forces normal and tangential to the imposed circular whirl orbit are related to the matrix elements as follows:

$$F_n^*(t)=\frac{1}{2}(A_{xx}^*+A_{yy}^*)\epsilon$$

$$F_t^*(t)=\frac{1}{2}(-A_{xy}^*+A_{yx}^*)\epsilon \qquad (2)$$

The reader is referred to Jery et al. (1985) and Franz et al. (1989) for details. In the analysis which follow, the above equations will be expressed in nondimensional terms. If, in addition, $[A]$ is to be rotationally invariant, then

$$A_{xx}=A_{yy}=F_n$$

$$A_{xy}=-A_{yx}=F_t \qquad (3)$$

The experimental investigation of Jery et al. (1985) and the fluid mechanical model of Adkins et al. (1988) for centrifugal pump impellers demonstrated that there are two sources for these fluid-induced forces. It was recognized that contributions to the rotordynamic forces could arise not only from azimuthally nonuniform pressures in the discharge flow acting on the impeller discharge area but also from similar nonuniform pressures acting on the exterior of the impeller front shroud as a result of the leakage flow passing between this shroud and the pump casing. The tentative conclusion was that the leakage flow contribution to the normal force was about 70 percent of the total and the contribution to the tangential force was about 30 percent of the total. These substantial contributions of the leakage flow to rotordynamic forces motivated this study.

There are several other indications which suggest the importance of leakage flows to the fluid-induced rotordynamic forces. It is striking that the total rotordynamic forces measured by Bolleter et al. (1987) from Sulzer Brothers, Ltd., for a conventional centrifugal pump configuration are about twice the magnitude of those measured by Jery (1986) or Adkins (1986) at Caltech. Both test programs used a radial face seal to minimize the forces which would be developed by the wearring seals. So the measured hydrodynamic forces are due to a combination of the impeller-volute and the impeller-shroud interaction. It now seems sensible to suggest that this difference is due to the fact that the clearance in Bolleter's leakage flow annulus is substantially smaller than that in the experiments of Jery (1986) and Adkins (1986).

Subsequently, Childs (1989) adapted the bulk-flow model which was developed for the analysis of fluid-induced forces in seals to evaluate the rotordynamic forces due to these leakage flows. The magnitude and overall form of the model predictions are consistent with the experimental data. In particular, the model also predicts positive, rotordynamically destabilizing tangential forces over a range of positive whirl ratios. However, Childs' theory yielded some unusual results including peaks in the rotordynamic forces at particular positive whirl ratios. It is clear that a detailed comparison of model predictions with experimental measurement remains to be made and is one of the purposes of the present program.

3 Leakage Flow Test Apparatus

A detailed description of the test facility, can be found in many of the references (Chamieh, 1983; Adkins, 1986; Jery, 1986; Arndt, 1988; Franz, 1989), so only a brief description will be given here. The experiments were conducted in the Rotor Force Test Facility (RFTF), which was constructed to study fluid induced forces on an impeller whirling around the machine axis of rotation. The experimental objective was to impose well-controlled rotational and whirl motions on a very stiff impeller/shaft system and to measure directly the resulting force on the impeller. This is accomplished by an eccentric

Nomenclature

$[A^*]$ = rotordynamic matrix
$[A]$ = rotordynamic matrix normalized by $\rho\pi\omega^2R_2^3L$
C,c = rotordynamic damping coefficients normalized by $\rho\pi\omega R_2^3L$
$F^*(t)$ = hydrodynamic forces
$F(t)$ = hydrodynamic forces normalized by $\rho\pi\omega^2R_2^3L\epsilon/R_2$
$F_x^*(t),F_y^*(t)$ = lateral forces on the rotating shroud in the stationary laboratory frame
$F_x(t),F_y(t)$ = lateral forces on the rotating shroud in the stationary laboratory frame normalized by $\rho\pi\omega^2R_2^3L\epsilon/R_2$
F_{ox}^*,F_{oy}^* = steady hydrodynamic forces
F_{ox},F_{oy} = steady hydrodynamic forces normalized by $\rho\pi\omega^2R_2^3L$
$F_n^*(t),F_t^*(t)$ = unsteady hydrodynamic forces
$F_n(t),F_t(t)$ = unsteady hydrodynamic forces normalized by $\rho\pi\omega^2R_2^3L\epsilon/R_2$
H = shroud clearance between rotor and casing
K,k = rotordynamic stiffness coefficients normalized by $\rho\pi\omega^2R_2^3L$
L = axial length of the shroud
M,m = rotordynamic inertial coefficients normalized by $\rho\pi R_2^3L$
Q = volume flow rate
R = shroud radius
Re_φ = axial flow Reynolds number, $2HU_s/\nu$
Re_ω = Reynolds number based on tip speed, $\omega R_2^2/\nu$
t = time
$x^*(t)$ = instantaneous displacement in the x direction normalized by the leakage inlet radius, R_2
$y^*(t)$ = instantaneous displacement in the y direction normalized by the leakage inlet radius, R_2
δ = offset or distance between the center of the whirl orbit and the center of the stationary casing
ϵ = eccentricity or radius of the whirl motion
ν = dynamic viscosity of the fluid
ρ = density of the fluid
ϕ = flow coefficient, $Q/2\pi R_2^2H\omega$
ω = radian frequency of rotor rotation
Ω = radian frequency of whirl motion

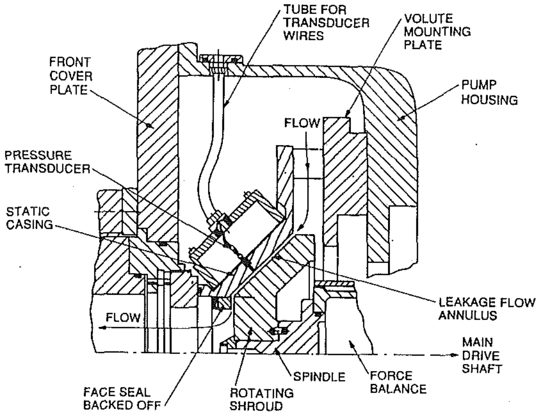

Fig. 2 Layout of the leakage flow test apparatus for installation in the Rotor Force Test Facility (Zhuang, 1989)

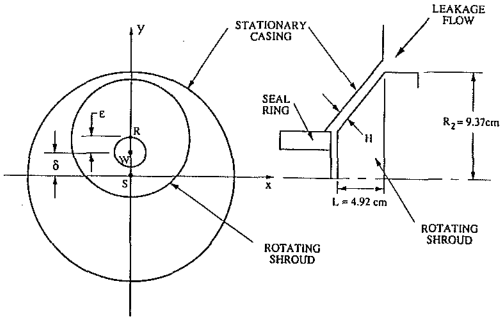

Fig. 3 Schematic of the whirling shroud where *S* is the center of the stationary casing, *R* is the center of the rotating shroud, *W* is the center of the whirl orbit along which *R* travels, $WR=\epsilon$ is the eccentricity and $WS=\delta$ is the offset

drive mechanism which superposes a circular orbit on the basic rotation. The shroud is mounted on a spindle attached to the rotating force balance (Jery et al., 1985; Franz et al., 1989), which measures the forces directly on the shroud. The experimental apparatus sketched in Fig. 2 was designed and constructed to simulate the leakage flow along the shroud from the impeller discharge to the impeller inlet (Zhuang, 1989; Guinzburg et al., 1990). The clearance between the rotating shroud and the stationary casing can be varied by both axial and radial adjustment of the stationary casing. For the present experiment, the initial geometric configuration consists of a straight annular gap inclined at an angle of 45 deg to the axis of rotation. The schematic in Fig. 3 shows the clearance in the centered position when the centers of the shroud and the casing both coincide. In order to model losses in the flow, an adjustable face seal was used (refer to Fig. 2). In the present experiment, the face seal clearance permits the pressure drop to be adjusted separately from the flowrate.

The flow through the leakage path is generated by an auxiliary pump and the selection of the flow rates through the leakage path was based on performance characteristics of a typical centrifugal pump. The shroud can be driven at speeds up to 3500 rpm and a circular whirl motion with a frequency up to 1800 rpm can be superimposed on the basic rotation. The eccentric drive mechanism permits testing with the amplitude of the whirl motion or eccentricity, ϵ adjustable from 0.000 cm to 0.152 cm. The distance from the center of the whirl orbit to the center of the casing, termed the fixed offset, δ is also variable. So concentric and nonconcentric circular whirl orbits could be investigated. However, the present experiments are confined to the case of zero offset. Further details of the experimental equipment can be found in Guinzburg (1992).

The results from these experiments will be presented nondimensionally by dividing the forces by $\rho\pi\omega^2 R_2^3 L\epsilon/R_2$. In most pumps L, the axial length of the leakage path and the impeller discharge width are comparable and hence, the dimensionless data from the leakage flow tests may be qualitatively compared with that from the impeller tests.

4 Experimental Results for Rotordynamic Forces

Typical experimental measurements of the dimensionless normal and tangential forces, F_n and F_t, will be presented in this section. The fluid medium in which the experiments were conducted was water. The rotordynamic results from the force balance measurements were obtained for different rotating speeds of 500, 1000, 2000 rpm, different leakage flow rates (zero to 50 gpm), three different clearances, H, and two eccentricities, ϵ. Another parameter which has an effect on the results is the swirl velocity at the inlet to the leakage flow. The present paper will be confined to a presentation of the results for zero inlet swirl, since the effect of swirl is dealt with in another paper (Guinzburg et al., 1992). The range of rotational Reynolds numbers was 462×10^3–1851×10^3 and the range of axial flow Reynolds numbers was 2136–8546. While the rotational Reynolds numbers for the experimental flows are clearly in the developed turbulent regime, it is possible that the axial flow Reynolds numbers were too small to manifest the kind of resonances predicted by Childs.

The components of the generalized hydrodynamic force matrix that result when the impeller whirls in an eccentric orbit of 0.0254 cm, at 1000 rpm, and a clearance of 0.140 cm are shown in Fig. 4. Note that the general form and magnitude of the data is very similar to that obtained for impellers by Jery (1986) and Adkins (1986) and to that from Childs' model in the absence of the "resonance." One of the most significant features of these results is the range of positive whirl frequency ratios within which the tangential force is positive and therefore potentially destabilizing rotordynamically. Note also that a positive normal force is directed outward and would tend to increase the displacement of the impeller. The parabolic shape of the normal force curve results from the added mass of the fluid.

Since the data of Figs. 4 and 5 were obtained under conditions which were the same except for the magnitude of the eccentricity, ϵ it is reassuring to note the similarity between the two sets of data. Evidently these experiments lie within the linear regime of small eccentricities (note that the assumption of linearity was implicit in Eq. (1)). Other experiments were performed for the same conditions as Figs. 4 and 5 except that the rotor speeds are 500 rpm and 2000 rpm with satisfactory agreement (Guinzburg, 1992). It is somewhat startling to find that the linear regime extends up to and beyond the point where the eccentricity is 60 percent of the clearance.

In Figs. 4 and 5, the effect of flow rate on the normal force is clearer than its effect on the tangential force. Clearly the Bernoulli effect on the normal force increases with increasing flow at both positive and negative whirl frequency ratios. It would also appear that the positive tangential forces at small positive whirl frequency ratios are smallest at the highest flow rate and therefore increasing the flow is marginally stabilizing. From experiments performed with different clearances, the forces are roughly inversely proportional to the clearance (Guinzburg, 1992). For the same eccentricity and two different clearances, the smaller clearance generates larger perturbations in the flow which accentuates the acceleration in the fluid and increases the pressure differences.

It is interesting to compare the magnitudes of the forces with previous results obtained for a real centrifugal impeller in the same facility. The data presented by Franz et al. (1989) for a Byron Jackson centrifugal pump were obtained with an eccentricity of 1.25 mm which is significantly larger than the present

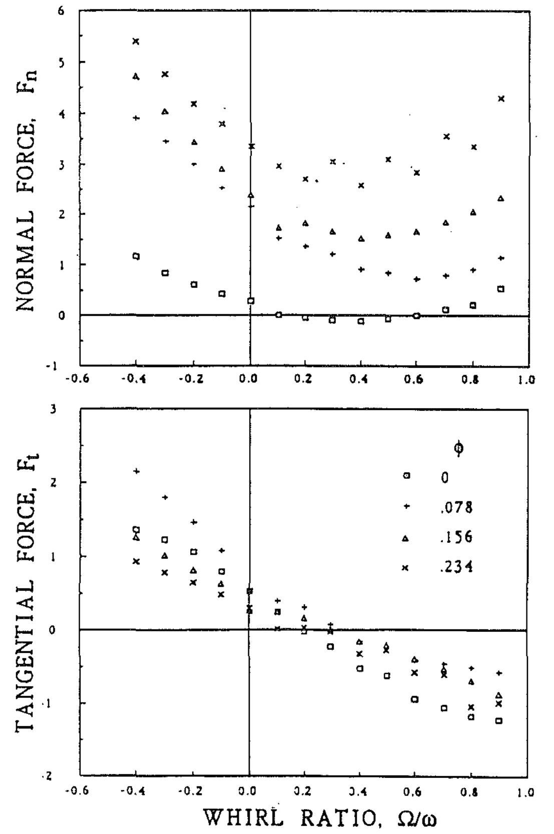

Fig. 4 Dimensionless normal and tangential forces normalized by $\rho\pi\omega^2R_2^3L\epsilon/R_2$ at 1000 rpm, for an eccentricity $\epsilon = 0.0254$ cm, a clearance $H = 0.140$ cm, offset $\delta = 0$ and different flow rates as follows: 0 l/s ($\phi = 0$), 0.631 l/s ($\phi = 0.078$), 1.262 l/s ($\phi = 0.156$), 1.892 l/s ($\phi = 0.234$). Uncertainty expressed as a standard deviation: F_n, $F_t \pm 0.05$.

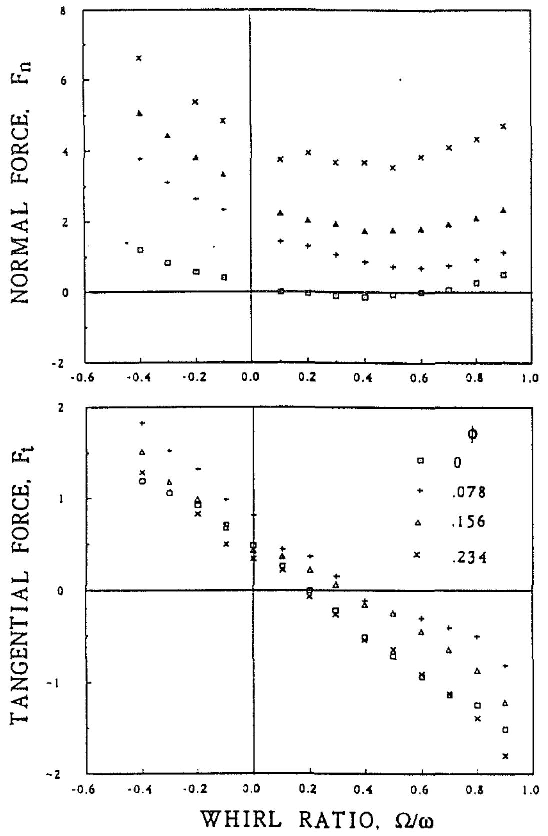

Fig. 5 Dimensionless normal and tangential forces normalized by $\rho\pi\omega^2R_2^3L\epsilon/R_2$ for zero inlet swirl at 1000 rpm, for an eccentricity $\epsilon = 0.0118$ cm, a clearance $H = 0.140$ cm, offset $\delta = 0$ and different flow rates as follows: 0 l/s ($\phi = 0$), 0.631 l/s ($\phi = 0.078$), 1.262 l/s ($\phi = 0.156$), 1.892 l/s ($\phi = 0.234$). Uncertainty expressed as a standard deviation: F_n, $F_t \pm 0.05$.

value of 0.254 mm. Thus, it is appropriate to compare the "stiffnesses" F_n^*/ϵ and F_t^*/ϵ rather than the forces themselves. At zero whirl frequency ratio the present data for a clearance of 1.40 mm (or 4.24 mm), yields values of 2.8 KN/m (or 0.46 KN/m) and 7.6 KN/m (or 1.88 KN/m) respectively compared to 6.8 KN/m and 2.28 KN/m for the data of Franz et al. (1989). Though the geometries of the leakage pathways are quite different this still suggests that the contribution of the shroud leakage flow to the rotordynamic forces is substantial.

The Reynolds number effect is investigated by examining the results of experiments which were identical except that the velocities (rotational, whirl and flowrate) were all increased or decreased by the same factor (Guinzburg, 1992). Hence, for example, the flow coefficients were identical. It was found that the coefficients do not change substantially as Reynolds number $\mathrm{Re}_\omega = \omega R_2^2/\nu$ increases. In the earlier work of Zhuang (1989), the normal and tangential forces were seen to decrease slightly as the Reynolds number increased. Those experiments were performed for no flow conditions. The present finding is consistent with the measurements of Jery (1987) on a centrifugal pump which were not affected by the Reynolds number.

5 Rotordynamic Coefficients

Conventionally, rotordynamics represent the force matrix by subdividing into components which depend on the orbit position (x,y), the orbit velocity $(\dot{x},\dot{y})$ and the orbit acceleration $(\ddot{x},\ddot{y})$. It is convenient for analytical purposes to evaluate these components by fitting quadratics to the experimental data. Though the functional dependence of F_n on the whirl frequency ratio is not necessarily quadratic and that of F_t is not necessarily linear, it is nevertheless of value to the rotordynamicists to fit the data of the figures from the previous section to the following expressions:

$$F_n = M\left(\frac{\Omega}{\omega}\right)^2 - c\left(\frac{\Omega}{\omega}\right) - K$$

$$F_t = +m\left(\frac{\Omega}{\omega}\right)^2 - C\left(\frac{\Omega}{\omega}\right) + k \tag{8}$$

where M, C, c, K, k are the dimensionless direct added mass (M), direct damping (C), cross-coupled damping (c), direct stiffness (K) and cross-coupled stiffness (k). The cross-coupled added mass (m) is omitted for simplicity, since a linear fit for F_t is adequate. From a stability point of view, the tangential force is most interesting; a positive cross-coupled stiffness is destabilizing because it drives the forward orbital motion of the rotor. Positive direct damping and negative cross-coupled stiffness are stabilizing because they oppose orbital motion.

6 Discussion of Results

The dimensionless rotordynamic coefficients, which were obtained by curve fitting the present experimental data, are presented in graphical form in Fig. 6 for a wide range of conditions; the coefficients are plotted against the flow coefficient, ϕ. Various effects such as speed, eccentricity and shroud clearance are shown together in Fig. 6 in order that the global effect on each coefficient with increasing leakage flow can be seen. A large negative stiffness results in a positive normal force which would tend to increase the radius of the orbital motion; increasing the leakage flow increases this force. On the other hand, a positive cross-coupled stiffness would result in the flow being destabilizing because it drives the forward

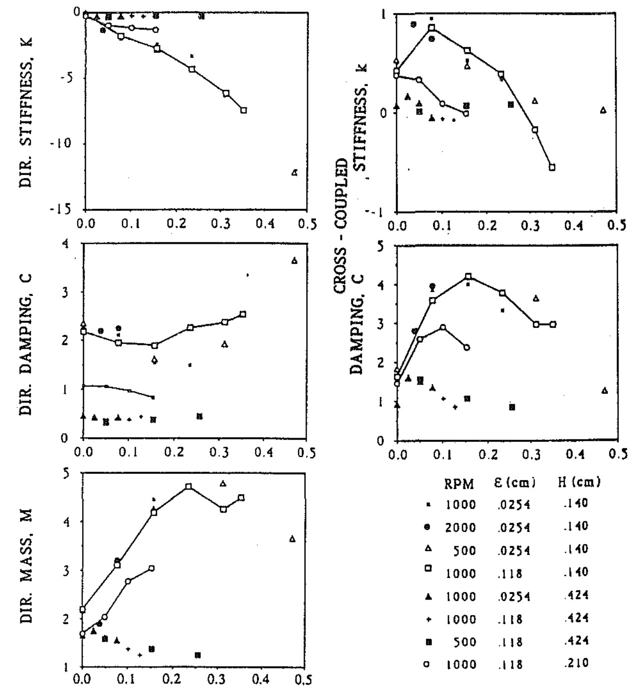

Fig. 6 Rotordynamic coefficients for different experimental conditions as a function of the flow coefficient

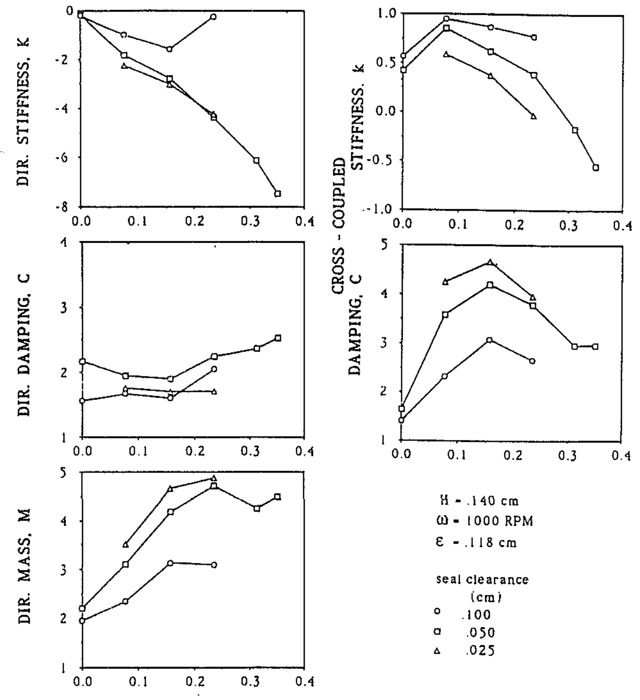

Fig. 7 Rotordynamic coefficients showing the effect of seal clearance as a function of flow coefficient for 1000 rpm and an eccentricity of 0.118 cm

orbital motion of the rotor so as to encourage whirl. The leakage flow is stabilizing in that the tangential force decreases with leakage flow. However, direct damping decreases slightly with flow, so the tangential force increases and the flow would therefore be less stabilizing. Below a flow coefficient of 0.7, direct damping is negative so the flow would encourage whirl. At higher flow rates, direct damping begins to increase and since this decreases the tangential force, the flow is stabilizing. However, these flow rates are much higher than realistic leakage flow rates in centrifugal pumps. The effect of the coefficients relating to the normal force is as follows. As the flow increases, the cross-coupled damping decreases slightly and the added mass term increases, thus contributing to a larger normal force. In other words, inertial motion would discourage orbital motion of the impeller but drive the impeller in the direction of displacement. It is interesting to note that at higher flow rates, the trend of the added mass changes.

In Fig. 6, the results for an eccentricity of 0.0254 cm and a clearance of 0.140 cm (obtained for a range of shaft speeds from 500 rpm to 2000 rpm) are seen to be independent of speed. Similar results were obtained with the same clearance but with a higher eccentricity of 0.118 cm (Guinzburg, 1992). This is simply another demonstration that the nondimensionalization of the forces with respect to speed is appropriate and that the Reynolds number effects are small.

The effect of eccentricity can be seen in Fig. 6 by examining the two sets of data (two different eccentricities) at 1000 rpm and a clearance of 0.140 cm. Even when the shroud clearance is of the same order of magnitude as the eccentricity, the results are still in the linear regime. Thus the magnitude of the eccentricity has no effect on the rotordynamic coefficients provided the latter are properly normalized.

The effect of the clearance between the rotating shroud and the stationary casing on the rotordynamic coefficients will next be presented for a speed of 1000 rpm and three clearances: 0.140, 0.212, and 0.424 cm. As the clearance is decreased, the stiffness and hence the normal force increases, which would drive the motion into a larger orbit. As the cross-coupled stiffness increases so does the tangential force and therefore the flow becomes more destabilizing. However, the direct damping acts in competition with k, because it increases as the clearance decreases. Rotordynamically speaking, the net effect is that a smaller force is generated with a larger clearance. The seal clearance also has an effect on the rotordynamic coefficients and this effect is presented in Fig. 7. In practice such a change could occur as a result of wear. Indeed the adjustable seal ring was used (Fig. 2) to model such effects. Measurements were obtained for face seal clearances of 0.0254 cm, 0.051 cm and 0.1016 cm. The larger seal clearance exhibits a smaller normal force and the tangential force is larger, which therefore decreases the range of destabilization. In other words, the range of positive whirl frequency ratios for which the tangential force is positive is decreased. The direct stiffness and the direct damping change so as to decrease the normal force which is in competition with the effect of the cross-coupled damping. The tangential force increases as a result of the cross-coupled stiffness, but the effect of the direct damping is not clear. So it would seem that wear in the seal is rotordynamically destabilizing.

7 Rotordynamic Stability

A convenient measure of rotordynamic stability is the ratio of cross-coupled stiffness to direct damping k/C, known as the whirl ratio. This provides an estimate of the whirl frequency ratio at which the force would no longer be destabilizing. Indeed, if the tangential force data lay exactly on a straight line, it would be exactly that whirl frequency ratio which corresponded to zero tangential force. Thus, reducing k/C improves the stability of the rotor system. As with the rotordynamic coefficients, the whirl ratios obtained from the present experiments are independent of rpm. Figure 8 also shows that as the clearance is decreased for a given flow rate, the whirl ratio increases. This is similar to the conclusion of Hawkins and Childs (1988) who showed that, in annular seals, decreasing the clearance increases the stability. The effect of increasing the seal clearance, illustrated in Fig. 9, is to decrease the whirl ratio.

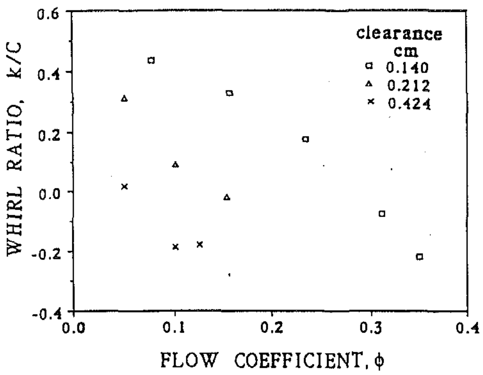

Fig. 8 Whirl ratio for an eccentricity $\epsilon = 0.118$ cm, speed of 1000 rpm, offset $\delta = 0$ and various clearances as a function of flow coefficient

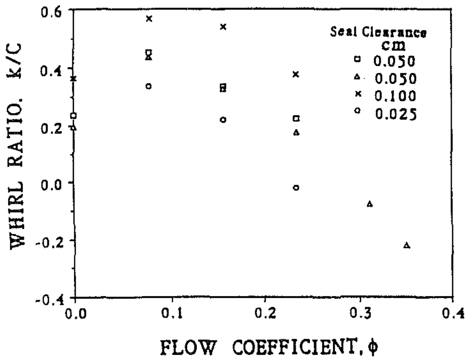

Fig. 9 Whirl ratio for an eccentricity $\epsilon = 0.118$ cm, speed of 1000 rpm, clearance $H = 0.140$ cm, offset $\delta = 0$ and various seal clearances as a function of flow coefficient

The whirl ratio from the results of Bolleter et al. (1989) gives surprisingly different results from the present research. For the total impeller, the whirl ratio is 1.4; for the seal the whirl ratio is 0.85 and for the difference of these contributions, the ratio is 2.26. The range for the results of the present experiments is smaller (−0.12 to 0.45). The discrepancies can be traced to differences in the cross-coupled stiffness and the direct damping, both of which are substantially larger in Bolleter et al. (1989) than in the present experiments.

8 Conclusions

A review of the existing experimental and analytical results shows that the discharge-to-suction leakage flow in a centrifugal pump can contribute substantially to the fluid-induced rotordynamic forces for that turbomachine. This motivated the current experimental study of leakage flows between the shroud and the stationary casing of a centrifugal pump and their rotordynamic effects. Experimental results for simulated leakage flows of rather simple geometry are presented for different whirl frequencies, eccentricities, clearances and flow rates. As with previous results for impellers, the forces scaled with the square of the rotor speed. The functional dependence on whirl frequency to rotating frequency ratio (termed the whirl frequency ratio) is very similar to that measured in experiments and to that predicted in the theoretical work of Childs.

Two sets of results taken at different eccentricities yield quite similar nondimensional rotordynamic forces indicating that the experiments lie within a linear regime. The dimensionless forces are found to be functions not only of the whirl frequency ratio but also of the flow rate and of the clearance. A region of forward whirl for which the average tangential force is destabilizing, was found. This region decreased with the flow coefficient for the leakage flow. While the dependence on the shroud clearance is not simple, it would appear that the dimensionless rotordynamic forces are roughly inversely proportional to the clearance. The change with the discharge resistance was somewhat more complicated. Finally, the tests showed none of the "resonances" predicted by the bulk-flow model proposed by Childs (1989).

Acknowledgments

The assistance provided by F. Zhuang, A. Bhattacharyya, F. Rahman, and Sandor Nagy with the experimental program is greatly appreciated. We would also like to thank NASA George Marshall Space Flight Center for support under NASA grant NAG8-118.

References

Adkins, D. E., 1986, "Analyses of Hydrodynamic Forces on Centrifugal Pump Impellers," Ph.D. thesis, California Institute of Technology, Pasadena, CA.

Adkins, D. R., and Brennen, C. E., 1988, "Analyses of Hydrodynamic Radial Forces on Centrifugal Pump Impellers," ASME JOURNAL OF FLUIDS ENGINEERING, Vol. *110*, No. 1, pp. 20–28.

Bolleter, U., Wyss, A., Welte, I., and Stürchler, R., 1987, "Measurement of Hydrodynamic Interaction Matrices of Boiler Feed Pump Impellers," ASME *Journal of Vibration, Acoustics, Stress, and Reliability in Design*, Vol. 109, pp. 144–151.

Bolleter, U., Leibundgut, E., and Stürchler, R., 1989, "Hydraulic Interaction and Excitation Forces of High Head Pump Impeller," *Pumping Machinery*, Vol. 81, 3rd Joint ASCE/ASME Mechanics Conference, UCSD, July 9–12, pp. 187–193.

Chamieh, D. S., 1983, "Forces on a Whirling Centrifugal Pump-Impeller," Ph.D. thesis, Division of Engineering and Applied Science, California Institute of Technology, Pasadena, CA.

Chamieh, D. S., Acosta, A. J., Brennen, C. E., and Caughey, T. K., 1985, "Experimental Measurements of Hydrodynamic Radial Forces and Stiffness Matrices for a Centrifugal Pump-Impeller," ASME JOURNAL OF FLUIDS ENGINEERING, Vol. 107, No. 3, pp. 307–315.

Childs, D. W., 1989, "Fluid Structure Interaction Forces at Pump-Impeller-Shroud Surfaces for Rotordynamic Calculations," ASME *Journal of Vibration, Acoustics, Stress, and Reliability in Design*, Vol. 111, pp. 216–225.

Domm, U., and Hergt, P., 1970, "Radial Forces on Impeller of Volute Casing Pumps," *Flow Research on Blading*, L. S. Dzung, ed., Elsevier Publ. Co., Netherlands, pp. 305–321.

Franz, R., Acosta, A. J., Brennen, C. E., and Caughey, T. K., 1989, "The Rotordynamic Forces on a Centrifugal Pump Impeller in the Presence of Cavitation," *Proceedings of 3rd Joint ASCE/ASME Mechanics Conference*, UCSD, July, *Pumping Machinery*, Vol. 81, pp. 205–212.

Guinzburg, A., Brennen, C. E., Acosta, A. J., and Caughey, T. K., 1990, "Rotordynamic Forces Generated By Discharge-to-Suction Leakage Flows in Centrifugal Pumps," NASA CP-3092.

Guinzburg, A., Brennen, C. E., Acosta, A. J., and Caughey, T. K., 1990, "Measurements of the Rotordynamic Shroud Forces for Centrifugal Pumps," ASME Turbomachinery Forum, Toronto, Canada, June.

Guinzburg, A., 1992, "Rotordynamic Forces Generated By Discharge-to-Suction Leakage Flows in Centrifugal Pumps," Ph.D. thesis, Division of Engineering and Applied Science, California Institute of Technology, Pasadena, CA.

Guinzburg, A., Brennen, C. E., Acosta, A. J., and Caughey, T. K., 1992, "The Effect of Inlet Swirl on the Rotordynamic Shroud Forces in a Centrifugal Pump," Presented at the ASME Turbo Expo, June.

Hawkins, L., and Childs, D. W., 1988, "Experimental Results for Labyrinth Gas Seals With Honeycomb Stators: Comparisons to Smooth-Stator Seals and Theoretical Predictions," 3rd Conference on Advanced Earth-to-Orbit Propulsion Technology, Huntsville, Alabama, May, pp. 94–111.

Hergt, P., and Krieger, P., 1969–70, "Radial Forces in Centrifugal Pumps With Guide Vanes," *Proceedings Institute of Mechanical Engineers*, Vol. 184, Part 3N, pp. 101–107.

Jery, B., 1986, "Experimental Study of Unsteady Hydrodynamic Force Matrices on Whirling Centrifugal Pump Impellers," Ph.D. thesis, California Institute of Technology.

Jery, B., Acosta, A. J., Brennen, C. E., and Caughey, T. K., 1985, "Forces on Centrifugal Pump Impellers," *Second International Pump Symposium*, Houston, TX, April 29–May 2.

Zhuang, F., 1989, "Experimental Investigation of the Hydrodynamic Forces on the Shroud of a Centrifugal Pump Impeller," E249.9, Division of Engineering and Applied Science, California Institute of Technology.

T. C. Vu
Hydro Business,
GE Canada,
Lachine, Québec, Canada, H8S-2S8

W. Shyy
Department of Aerospace Engineering,
Mechanics and Engineering Science,
University of Florida,
231 Aerospace Bldg.,
Gainesville, FL 32611

Performance Prediction by Viscous Flow Analysis for Francis Turbine Runner

Validation of a three-dimensional computational algorithm for viscous flow analysis has been conducted for two types of Francis turbine runner geometry, one low head and one high head, using experimental measurement. Assessment has been made for both qualitative features of flow behavior, as well as quantitative distribution of blade pressure and head loss. The influence of the grid size on the accuracy of the numerical solution is also discussed. Effort has been made to address some of the design issues, and to demonstrate that the present computational algorithm can make useful contributions to help improve the current design practices.

Introduction

Traditionally, the design and development of hydraulic turbine runners has been based mostly on slight modification of existing components and the performance assessment of the units has relied only on laboratory model testing. Computational methods based on the potential or inviscid flow approximation have been developed and applied to aid the design optimization of hydraulic turbine runners (Holmes and McNabb, 1982; Geoder et al., 1990); however, they cannot represent the complex behavior of truly turbulent viscous flows and cannot predict the associated energy losses.

For the past several years, we have applied the viscous flow analysis to predict flow characteristics and energy losses in different nonrotating hydraulic turbine components and favorable comparison between experimental information and numerical prediction have been obtained (Vu and Shyy, 1988, 1990; Shyy and Vu, 1993). Recently, intensive validation work for Francis turbine runner has been performed and, as will be demonstrated in the following, good correlation with experimental data has been obtained. In the present paper, we report the work for two Francis runner geometries. The first validation work is for a medium-low head Francis runner tested by the Swiss Federal Institute of Technology in Lausanne for the 1989 GAMM-Workshop. The second one is a comparative study of two high head Francis Runners which are designed and tested in our own hydraulic laboratory. Numerical prediction of flow velocity, pressure distributions and head loss will be compared against the experimental data. Also parametric study such as the influence of grid size on the accuracy of the numerical result will be reported. Based on these studies, an assessement can be made regarding our current capability of using computational fluid dynamics (CFD) as an aid for design improvement.

Numerical Algorithm and Boundary Conditions

The viscous flow analysis is based on the Reynolds-averaged three-dimensional Navier–Stokes equations. The equations for the continuity and momentum of the incompressible fluid written relative to a rotating coordinate system are:

$$\nabla \cdot \mathbf{q} = 0$$

$$\mathbf{q} \cdot \nabla \mathbf{q} = -\frac{1}{\rho} \nabla p + \nabla \cdot (\nu_{\text{eff}} \nabla \mathbf{q}) + \mathbf{f}$$

where $\mathbf{q}$ is the velocity vector with three velocity components, ν_{eff} is the effective viscosity, p the pressure and $\mathbf{f}$ the body forces vector including the Coriolis, centrifugal, and gravitational term:

$$\mathbf{f} = -2\boldsymbol{\Omega} \times \mathbf{q} - \boldsymbol{\Omega} \times \boldsymbol{\Omega} \times \mathbf{r} + \mathbf{g}$$

$\boldsymbol{\Omega}$, $\mathbf{r}$, and $\mathbf{g}$ are, respectively, angular velocity of the rotating coordinate, local radius, and gravitational acceleration. With regard to the turbulence closure, the original $k-\epsilon$ two equation turbulence model (Launder and Spalding, 1974) is adopted here. As demonstrated previously (Vu and Shyy, 1988, 1990), this turbulence model can yield satisfactory predictions for several nonrotating turbine components. Here its performance will be further tested for the runner. The computational flow domain of the Francis runner consists of a single inter-blade channel including a corresponding portion of the distributor housing at the inlet and a portion of the draft tube inlet cone at the outlet. A radial projection of the flow domain along with prescribed boundary conditions are illustrated in Fig. 1. Three types of boundary conditions are applied for the solid walls. In the rotating coordinate system, all the solid walls rotating with the runner, BCD,D'C' and BCC'B', are considered as non-rotating solid surfaces. Nonrotating solid walls such as AB, A'B', and C'E', which represent top and bottom of the distributor housing and the draft tube inlet, are considered as rotating solid surfaces. Surface DE, which is an extension of the hub, is considered as a symmetry boundary with slip condition prescribed. The periodic boundary con-

---

Contributed by the Fluids Engineering Division for publication in the JOURNAL OF FLUIDS ENGINEERING. Manuscript received by the Fluids Engineering Division June 23, 1992; revised manuscript received February 3, 1993. Associate Technical Editor: N. A. Cumpsty.

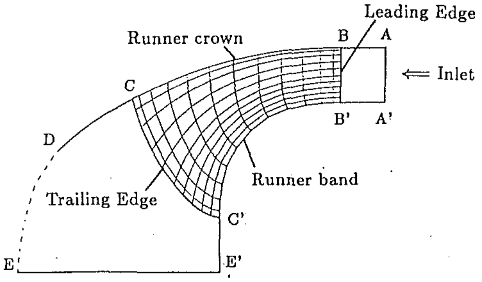

Fig. 1 Computational flow domain of a Francis turbine runner

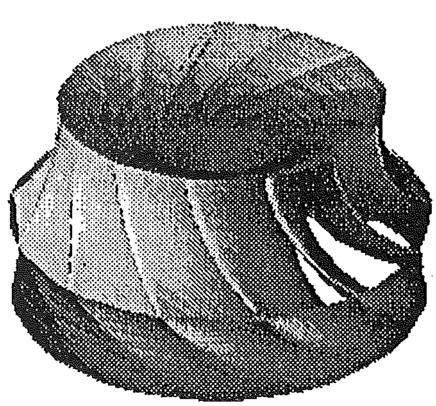

Fig. 2 Geometry of the GAMM Francis runner

Table 1 Effect of grid size on the numerical result accuracy

Grid size	Head Loss (%)	Torque (Nm)	CPU time (hr)	Remarks
7×15×45	2.9	423.0	2	Grid I
7×19×55	1.1	433.5	5	Grid II
9×21×55	0.9	438.7	8	Grid III
11×21×75	0.4	441.5	12	Grid IV
15×21×75	0.3	445.5	20	Grid V

dition is applied to the surfaces ABB'A' and CDEE'C'. At the inlet of the flow domain, surface AA', the velocity profiles, both in term of magnitude and direction, have to be specified. The flow direction is specified by Pitot measurement or by using the outlet flow profile of the previously computed flow field solution of the distributor (at upstream of the runner). The magnitude of the velocity vector at the inlet is calculated according to the specified total flow rate. The the exit, surface EE', zero value of the first order derivatives along the streamwise direction is adopted for all the dependent variables, except for the static pressure. There is no need to specify the static pressure distribution in either inlet or outlet plane due to the merit of the staggered grid system used by our algorithm (Patankar, 1980; Shyy and Vu, 1991). This characteristic comes from the fact that in the present algorithm, the pressure correction is iteratively computed according to the deviation of the mass flux balance within each computational cell. With the staggered grid, the mass flux across the outflow boundary is computed via velocity extrapolation, with a subsequent enforcement of the global mass conservation (Shyy, 1985). This practice allows the pressure field to be computed without resorting to any artificial pressure boundary condition, a practice consistent with the mathematical characteristics of the fluid flow equations. The turbulence quantities at the inlet plane are not available from the measurement; they are specified according to the standard procedure, namely, the local equilibrium condition is utilized between the turbulent kinetic energy and the rate of the turbulent energy dissipation. Besides the inlet, the outlet, and the periodic conditions, the wall function is used in the wall region (Launder and Spalding, 1974). We have used no special treatment for either the leading or the trailing edge of the runner blade. The numerical procedure adopted for the computation is essentially a pressure-correction type of semi-implicit finite volume/finite difference formulation implemented in a general curvilinear coordinate system. The convection terms in the momentum equations are approximated by the second-order upwind scheme (Shyy et al., 1992). The pressure and all the second-order derivative terms are discretized by the second-order central difference schemes. Details of the numerical algorithm and solution procedures are explained in (Braaten and Shyy, 1985; Shyy and Vu, 1991; Shyy, 1994) and are not repeated here.

Application to the Gamm Francis Runner

The Francis runner geometry of the GAMM-Workshop, held in September, 1989 at the Swiss Federal Institute of Technology (EPFL) in Lausanne, is shown in Fig. 2. It is a medium-low head 13 blade runner with a throat diameter of 0.4 m. A total of 28 pressure transducers are flush mounted to the blade surfaces, along three different streamlines. The experimental data, which are provided by the GAMM-Workshop organizer, were taken at the optimum operating conditions of the runner (Avellan et al., 1990). The angular velocity is 52.35 rad/s. The flow rate is 0.372 m^3/s (measured by the Venturi) a 25.5 deg wicket gate opening. The water density is specified at 1000 kg/m^3 and the water viscosity is assumed to be 1.31 Pascal-s. The corresponding Reynolds number, based on the throat diameter, the throat axial velocity and the dynamic viscosity, is equal to 1.3×10^6. The velocity profile at the runner inlet, assumed to be axisymmetrical, is specified by the Pitot measurement. The flow rate, calculated from the runner inlet Pitot measurement, is 6 percent lower than the Venturi's flow rate. But given the low level of precision of Pitot's measurement, we use the Venturi's flow rate for subsequent flow analyses.

Parametric study has been performed for different important geometry and flow parameters, such as grid size, grid concentration, flow rate, flow inlet angle, etc. The grid size greatly influences the accuracy of the numerical result and the CPU time. A comparative study on the effect of the grid size, which varies from Grid I, 7×15×45 nodes, to Grid V, 15×21×75 nodes, is presented in Table 1. The required CPU time varies approximatively from 1 hour for Grid I to 20 hours for Grid V on a Silicon Graphics work station with a computing power of 6 Mflops. Although we observe that even Grid I could predict relatively well the flow behavior and the blade pressure distribution, it overpredicts the runner head loss by a large margin compared to the solution on Grid V. The head loss is calculated by comparing the predicted energy loss of the runner flow passage and the useful energy required for the predicted torque for a given angular velocity and a given flow rate. The predicted runner head loss should always be smaller than the actual head loss, because we assume a perfect axisymmetrical flow condition at the inlet. An uneven flow distribution around the runner due to imperfect casing design and the downstream effect of the wicket gates should contribute more head loss to the runner. The grid size of 75×21×11, Grid V, is found to be a good compromise in term of the accuracy and CPU time requirement. The following numerical results are calculated with this grid size.

Figure 3 represents the distribution of the blade pressure coefficient C_p at three different streamline locations, near the crown (section 2), at the blade centerline (section 9) and near the band (section 15). The multiple symbols at the same location indicate the experimental error observed in the course of measurement. The numerical result agrees quite well with experimental data. The low pressure zone at the blade leading edge, near the runner band (section 15), is well predicted. The

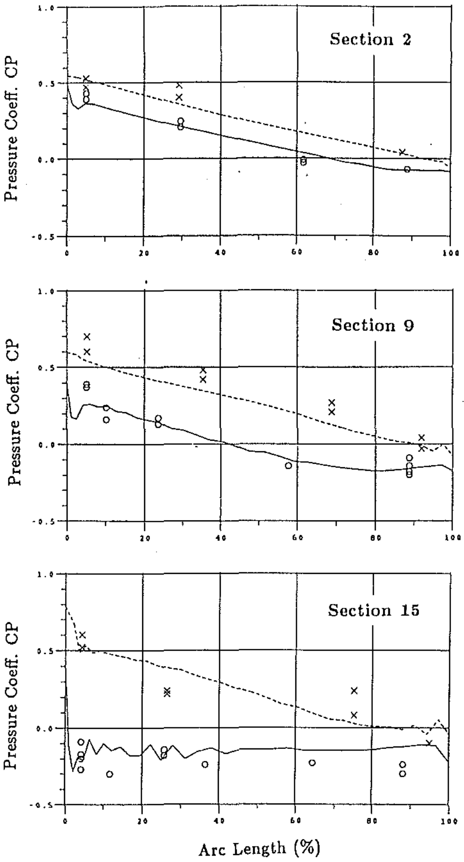

Fig. 3 Blade pressure distribution of the GAMM runner (symbols: measurement; lines: prediction)

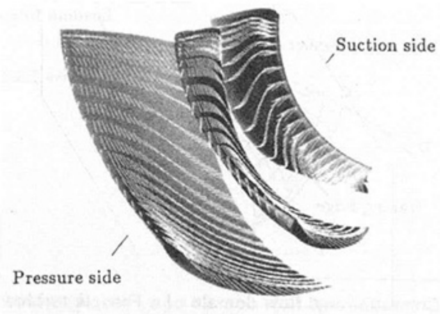

Fig. 4 Velocity field near blade surfaces

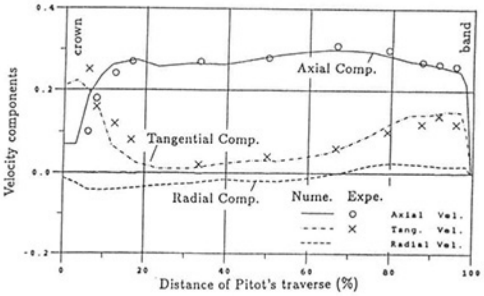

Fig. 5 Velocity profile at runner exit

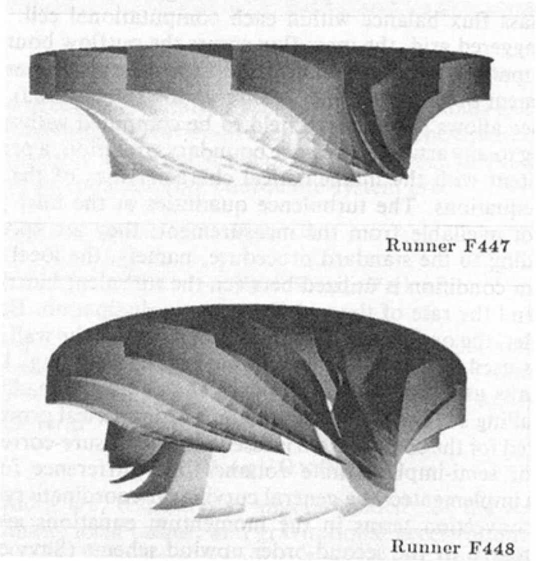

Fig. 6 Geometries of two high head Francis runners

large variation of the static pressure computed at that location is consistent with the measurement. We have observed that this feature is more accentuated with finer grid solution. Figure 4 illustrates a 3-D view of the velocity fields at the pressure and suction sides of the blade. At the pressure side, with the stagnation occurring near the leading edge, the flow is pushed toward the runner band. Whereas at the suction side, the flow is highly accelerated. Figure 5 shows an excellent agreement between prediction and measurement for the velocity profile at the runner exit. Both the axial and tangential components follow precisely all the variation of the experimental measurement. The comparison for the radial component with the experimental data is not possible because this information is not available.

Application to High Head Francis Runners

Figure 6 illustrates two high head Francis runner geometries, F447 and F448. Both runners have 15 blades and have the same throat diameter of 0.3048 m. The two runners have similar geometric characteristics and they were both tested in the laboratory with the same assembly. The uncertainty of measured efficiency of the whole turbine assembly is ±0.25 percent. We do not have the measurement of absolute performance of individual component, but the relative performance between the two runner designs can be assessed by testing them in the same assembly. At the best efficiency operating point, the runner F448 is found to be 0.5 percent more efficient than F447. Flow analyses are performed for the two runners at their optimal operating conditions. For F447, the gate opening is 16 degrees, the flowrate is 0.197 m^3/sec and the angular speed is 878.88 rpm. For F448, the gate opening is 18 degrees, the flow rate is .222 m^3/s and the angular speed is 899.41 rpm. Since their operating conditions are quite similar, except for the wicket gate opening, we can reasonably attribute the difference in efficiency of 0.5 percent between the two runners to the difference in head loss within the flow passage of the two runners.

Three types of grid size, with $13\times 25\times 85$, $11\times 21\times 85$ and $9\times 21\times 75$ nodes, are used to perform the flow analysis. The runner torques are well predicted by all three grid sizes to within 1.5 percent accuracy (see Table 2). The flow characteristics are also found to be similar for both runner geometries. Figure 7(*a*) shows, in radial projection, the typical velocity field at the pressure side of the runner F447, whereas Figs. 7(*b*) and 7(*c*) show the velocity fields, in the blade to blade projection, near the crown and the band of the same runner. A local recirculation zone is observed at the region near the crown at the exit of both runners. This recirculation zone creates high fluctuation and prevents us from performing the

Table 2 Effect of grid size on the calculated torque (Nm)

Grid size	Runner F447	Runner F448
Measurement	721.1	800.6
9×21×75	736.9	812.4
11×21×85	732.1	807.7
13×25×85	727.2	803.7

Table 3 Effect of grid size on the calculated head loss

Grid size	Runner F447	Runner F448	Δ Head loss
Measurement	0.5% higher		0.5%
9×21×75	4.1%	3.8%	0.3%
11×21×85	3.9%	3.6%	0.3%
13×25×85	4.2%	3.7%	0.5%

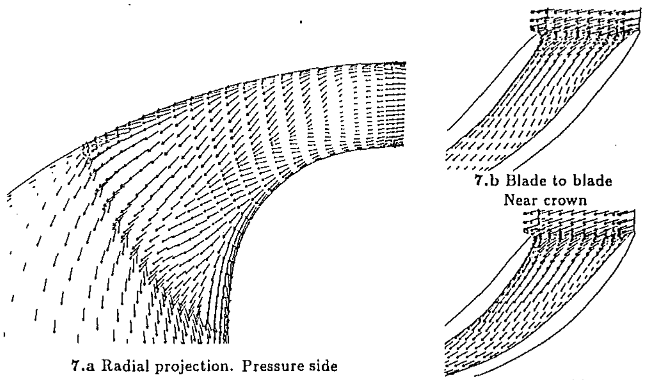
7.a Radial projection. Pressure side

7.b Blade to blade Near crown

7.c Blade to blade Near band

Fig. 7 Velocity distribution of the F447 at the best efficiency point

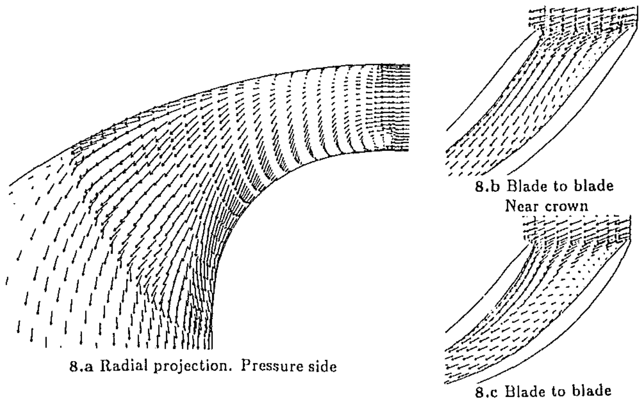
8.a Radial projection. Pressure side

8.b Blade to blade Near crown

8.c Blade to blade Near band

Fig. 8 Velocity distribution of the F447 with 1° higher inlet flow angle from the best efficiency point

Pitot measurement in this region. It is noted that the flow behavior in a high head Francis runner is very sensitive to the flow inlet condition; a small change in the flow inlet angle of 1 degree from the best efficiency point could produce large recirculation zones near the leading edge of the blade as seen in Fig. 8(*a*). Figures 8(*b*)and 8(*c*) represent the blade to blade projection of the velocity fields near the crown and band region of F447 for this particular operating condition. Unlike the best efficiency case of F447 (Fig. 7), a recirculation zone is observed here. Consequently, the runner head loss jumps up to 5.3 percent instead of 4.2 percent at the best efficiency point. Table 3 shows the head losses calculated for the two runners with the three grid sizes. It has been found that the viscous energy loss in a high head Franics (about 4 percent) is much higher, compared to the one of low head Francis (about 0.4 percent). In the present experimental test rig, it is difficult to determine the absolute value of the viscous loss in the runner, only the relative performance between the two designs can be evaluated. It is this relative performance of the two runners that can be validated between prediction and measurement. Based on the result presented, it is concluded that the direction of the design improvement can be well captured by the flow analysis. The runner F448 is found to perform better by all three grid sizes.

Concluding Remarks

We have presented an assessment of a viscous flow computational algorithm for two different runner geometries, a low head and a high head Francis turbine runner. The predicted flow characteristics, blade pressure distribution and runner head loss have all been compared well with the experimental data. It has been demonstrated that the qualitative flow characteristics and the quantitative blade pressure distribution can be predicted correctly, even with a relative small grid size. Similar to the experience gained from the computation of the nonrotating components (Vu and Shyy, 1988, 1990; Shyy and Vu, 1993), the originally proposed $k-\epsilon$ two equation model is capable of yielding satisfactory prediction. What has been attempted here is an engineering assessment of the runner performance, based on a pragmatic turbulence closure model, state-of-the-art numerical algorithm, and compared with actual measurements. In view of the substantial degrees of uncertainties that any engineering turbulence models have right now, unless a direct simulation can be made, which is unpractical, a selective use of CFD is desirable. It is our opinion that depending on the purpose of the computation, there can be a range of approaches and grid sizes that will make useful contribution to the current engineering practices. Although not all the detail of the flow field can be accurately captured by the present grid resolution, the overall comparison between measurement and prediction, including some of the secondary flow features, looks favorable. Furthermore, the key parameters related to the runner performance can be assessed. A concerted effort has been made in this regard to address some of the design issues that have not been adequately covered so far, and to find out what and how a design engineer can improve a given design with reasonable computing resources. In the present work, we have inspected not only the pressure distribution, but also velocity profiles and total pressure losses. The latter aspect can be predicted only by a viscous flow algorithm; the solution of the inviscid flow based on the Euler equations cannot supply the necessary information. Our findings have demonstrated that the present approach is capable of yielding quite useful information of the runner performance. The present approach has been found reliable enough to be used to optimize the actual design of Francis runner geometry.

Acknowledgments

The software for runner grid generation was developed by Mr. B. Ozell, under the CASTOR project of Ecole Polytechnique de Montréal. The 3-D flow animation and visualization software, VISAGE, was developed at GE Corporate Research and Development Center.

References

Avellan, F., Dupont, P., Farhat, M., Gindroz, B., Henry, P., Hussain, M., Parkinson, E., and Santal, O., 1990, "Flow Survey and Blade Pressure Measurements in a Francis Turbine Model," *IAHR Symposium 1990*, Belgrade, Yugoslavia, Vol. 2, paper I5.

Braaten, M. E., and Shyy, W., 1986, "A Study of Recirculating Flow Computation using Body-fitted Coordinates: Consistency Aspects and Skewness," *Numerical Heat Transfer*, Vol. 9, pp. 559–574.

Geoder, E., Guenod, R., Grunder, R., 1990, "An Advanced Flow Simulation Technique for Hydraulic Turbomachinery," *IAHR Symposium 1990*, Belgrade, Yugoslavia, Vol. 1, paper C6.

Holmes, G., and McNabb, J., 1982, "Application of Three Dimensional Finite Element Potential Flow Analysis to Hydraulic Turbines," *IAHR Symposium 1982*, Paris, France.

Launder, B. E., and Spalding, D. B., 1974, "The Numerical Calculation of Turbulence Flows," Computer Methods in Applied Mechanics and Engineering, Vol. 3, pp. 269–289.

Patankar, S. V., 1980, *Numerical Heat Transfer and Fluid Flow*, Hemisphere, Washington, D.C.

Shyy, W., 1985, "Numerical Outflow Boundary Condition for Navier-Stokes Flow Calculations by a Line Iterative Method," *AIAA Journal*, Vol. 23, pp. 1847–1848.

Shyy, W., 1994, *Computational Modeling for Fluid Flow and Interfacial Transport*, Elsevier, Amsterdam, The Netherlands.

Shyy, W., and Vu, T. C., 1991, "On the Adoption of Velocity Variable and Grid System for Fluid Flow Computation in Curvilinear Coordinates," *Journal of Computational Physics*, Vol. 92, pp. 82–105.

Shyy, W., Thakur, S., and Wright, J. A, 1992, "Second-order Upwind and Central Difference Schemes for Recirculating Flow Computation," *AIAA Journal*, Vol. 30, pp. 923–932.

Shyy, W., and Vu, T. C., 1993, "Modeling and Computation of Flow in a Passage with 360° Turning and Multiple Airfoils," ASME JOURNAL OF FLUIDS ENGINEERING, Vol. 115, pp. 103–108.

Vu, T. C., and Shyy, W., 1988, "Navier-Stokes Computation of Radial Inflow Turbine Distributor," ASME JOURNAL OF FLUIDS ENGINEERING, Vol. 110, pp. 29–32.

Vu, T. C., and Shyy, W., 1990, "Viscous Flow Analysis for Hydraulic Turbine Draft Tubes," ASME JOURNAL OF FLUIDS ENGINEERING, Vol. 112, pp. 199–206.

F. Bakhtar
School of Manufacturing and
Mechanical Engineering,
University of Birmingham,
Birmingham B15 2TT, UK

M. Ebrahimi
University of Science & Technology,
Narmak, Tehran, Iran

R. A. Webb
School of Manufacturing and
Mechanical Engineering,
University of Birmingham,
Birmingham B15 2TT, UK

An Investigation of Nucleating Flows of Stream in a Cascade of Turbine Blading—Wake Traverses

During the course of expansion in turbines, steam first supercools and then nucleates to become a two-phase mixture consisting of a very large number of minute droplets suspended in the parent vapor. To reproduce turbine two-phase flow conditions realistically requires a supply of supercooled vapor, which can be achieved under blow-down conditions. This paper is one of a set describing the equipment which has been constructed and the first family of results obtained on a short duration cascade tunnel working on the blow-down principle. The arrangements for traversing downstream of a cascade of nozzle blades and the results obtained are described in the paper.

Introduction

This paper is one of a set describing the equipment and the first set of results obtained on an experimental facility constructed to study the problems associated with the flow of nucleating and wet steam in turbines. Turbine stages operating on nucleating and wet steam have a lower thermodynamic efficiency than those in which the fluid is superheated. The difference is loosely attributed to wetness losses but despite the dominant role played by steam turbines in the generation of electrical power, there is considerable uncertainty in the literature about the detailed mechanisms which give rise to these losses. The reason is partly the difficulty of reproducing turbine two-phase flow conditions in steady state tunnels.

At low and moderate pressures the supercooling associated with the first reversion of steam is substantial. Consequently in studies of condensation in steady state tunnels the zones of rapid condensation occur in the supersonic parts of the flow. This is in contrast to conditions in turbines where because moving blades extract energy from the flow, steam can supercool sufficiently to nucleate without attaining the speed of sound. Thus steady-state tunnels cannot reproduce turbine wet steam conditions realistically. For examples, the release of latent heat associated with condensation produces opposite effects in sub-sonic and supersonic flows.

To produce turbine conditions realistically requires a supply of supercooled steam. Following an examination of potential possibilities it was shown in a feasibility study that such a supply can be produced under blow down conditions (Bakhtar and Heaton, 1986). Short duration tunnels are widely used in aerodynamic studies (Jones et al., 1993) and the technique can be adapted for the investigation of wet steam flows. As the next step in the treatment of the problem a short duration cascade tunnel working on this principle has been constructed. The aim of evaluating the capabilities of the equipment has been combined with the investigation of flow in a cascade of typical nozzle blading. The main features of the equipment, the surface pressure measurements, typical optical observations and droplet measurements have already been described. (Bakhtar et al., 1991, 1992, and 1993). The arrangements for traversing downstream of the cascade and the results obtained are reported in this paper.

Main Features of the Equipment and Principle of Operation

The general features of the equipment are illustrated diagrammatically in Fig. 1. The steam receiver is a tank of 28 m^3 capacity. Valve (1) is a quick acting valve with a typical opening time of 70 ms and releases the flow to the test section. Valve (2) is a butterfly valve used for setting the downstream pressure. The spent steam is discharged to a condenser with a condensing surface area of 60 m^2. The test section is essentially a steel fabrication which holds two cover plates 76 mm apart. The blades forming the cascade are mounted on circular supporting plates which fit into the test section. The opening of the quick-

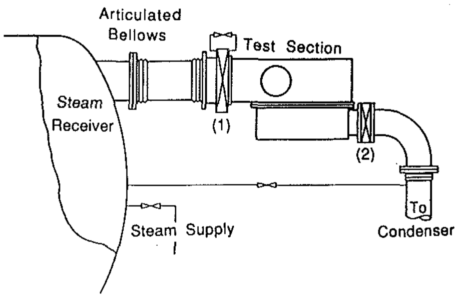

Fig. 1 General arrangement

Contributed by the Fluids Engineering Division for publication in the JOURNAL OF FLUIDS ENGINEERING. Manuscript received by the Fluids Engineering Division June 30, 1992; revised manuscript received April 28, 1993. Associate Technical Editor: O. C. Owens.

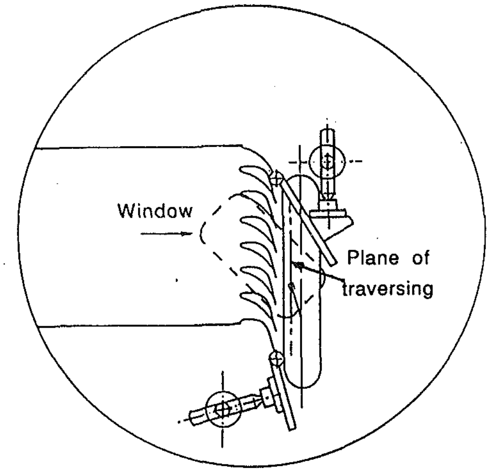

Fig. 2 Flow passage through cascade

acting valve is followed by transients which in the present equipment decay in 700 ms. A quasi-steady flow is then established in the test section which can be studied. The drop in the stagnation pressure was 0.5 percent per second and the run time of the equipment was normally regarded as 0.5 s.

To generate supercooled steam the receiver is first charged with saturated steam and then vented to the condenser. This has the effect of expanding the steam remaining in the tank to predetermined degrees of supercooling without the penalty of giving it kinetic energy.

To take pressure measurements during the short run times each tapping point was connected by a hypodermic tube to a separate pressure transducer. These were piezo-resistive instruments each built integral with its own amplifier. To prevent the formation of vapor bubbles and to protect the transducer elements from exposure to steam, the connecting lines were kept full of oil and purged when necessary. To achieve this the transducers were mounted each in a separate cell in special manifold blocks and the cells fitted with individual purge lines. The use of oil-filled lines had the further advantage of reducing the time response of the transducers to approximately 1 ms. The transducers were calibrated in situ through the data acquisition system and the measurements were accurate to within ±.01 bar.

Recording of data was controlled by a microcomputer. For this purpose the signals from the instruments after individual processing were connected each to a separate sample and hold module. To take a set of readings all the sample and hold units were signalled from the processor simultaneously and subsequently scanned. The analogue signals were converted to digital form and stored in the computer memory. Having completed a set of readings the sample and hold units were signalled once more and the procedure repeated. The time taken to record one signal was 25 μs. Thus with a relatively small number of signals recorded at each position when traversing, a very large number of readings could be taken as the probe was driven across the flow passage.

A diagrammatic view illustrating the flow passage through the cascade is given in Fig. 2. The cascade consisted of six blades and two half profiles machined in the spacer blocks forming seven passages. The central blades were mounted as a separate interchangeable unit. To carry out the LDA measurements, the central unit used was fitted with optical windows.

To traverse the flow downstream of the cascade one of the blade support plates was replaced with one machined with a slot to allow for probe access. The position of the slot and the traversing plane relative to the blades is given in Fig. 2. The probe was mounted in a holder supported by a traversing mechanism and driven across the passage by a pneumatic cylinder. To provide for sealing, the whole assembly was mounted in a steel chamber bolted to the test section cover.

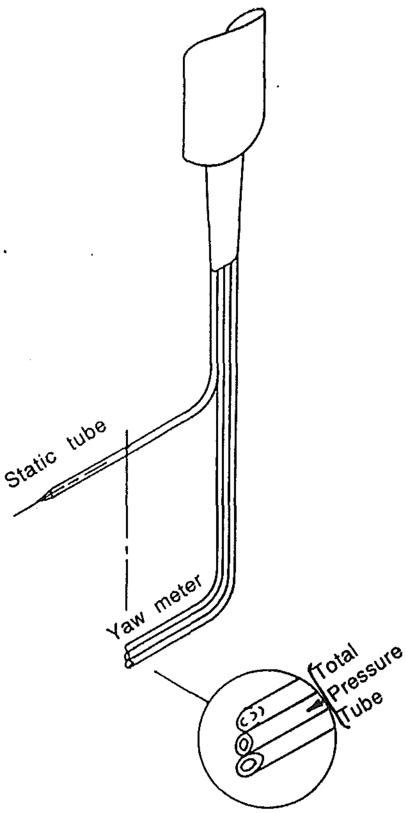

Fig. 3 Probe

Arrangements for Traversing

An important factor in the design of the probe was the need to minimize the blockage of the flow. Based on the experience described by Cox (1980) an isometric view of the arrangement adopted is shown in Fig. 3. This was a three holed yaw type instrument with a separate static tube. To keep the disturbance of the flow to a minimum the outer tubes of the yawmeter which were chamfered at 45 deg in opposite directions, were placed above and below the total pressure tube. Initially the probe was constructed from tubes of 0.255mm bore and without a static tube. Considerable problems were experienced with blockage of the holes. Consequently the tube size was increased to one of 0.51mm bore and 0.75mm outside diameter. With this arrangement the probe width in the flow direction was 0.75mm. In addition the data logging system available had an 8 bit accuracy which proved insufficient to allow the static pressures to be deduced from the readings of the yawmeter satisfactorily. It was, therefore, decided to add a static pressure tube to the probe. This tube had a 20° cone at its tip and was of the same gauge as the yawmeter tubes. To sense the static pressure only one tapping point was drilled into the tube 7.34 mm from its tip and positioned vertically above its axis and in line with the tip of the total pressure tube. With the cascade flow two-dimensional the variations of static pressure in the spanwise direction were negligible and the static tube was taken to indicate the static pressure at probe tip position accurately.

To record the pressures, as already stated each tapping point was connected to its own transducer, mounted in a cell via oil filled capillary tubing. To minimize the disturbance of the joints during the probe travel, the transducers used in conjunction with the probe were mounted in a special manifold, attached to the traversing mechanism carriage via its guidance bar. Thus the whole assembly formed a unit and the transducer

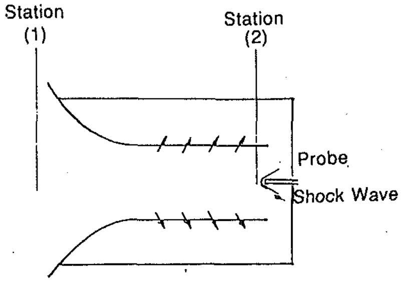

Fig. 4 Calibration nomenclature

manifold moved with the probe. In addition, to provide for increased accuracy and to allow for cross checking of results some differential pressure transducers were also mounted in the manifold and used to measure differences between strategic pressures.

In the absence of any other supply of supercooled steam, to calibrate the probe it was necessary to use the test section. For this purpose a special slotted nozzle fitting in the test section in place of the cascade, was designed and constructed.

With the inclusion of the static tube the calibration of the instrument for the measurement of all flow characteristics in superheated steam and for the measurement of flow angle and static pressure in wet steam was straightforward. The procedure used was essentially that described by Cox (1980). But the measurement of total pressure in wet steam in supersonic flow presented a problem because of the standing shock wave in front of the tube.

The flow configuration illustrating the position of the total pressure tube relative to the slotted nozzle is shown in Fig. 4. The station upstream of the nozzle is designated as (1), the position in the downstream plane of the nozzle and upstream of the probe is designated as (2) while the reading of the total pressure tube is given the suffix TD.

To calibrate the tube it is necessary to establish the relation between the tube reading P_{TD}, the static pressure P_2 and the total pressure at station (2), P_{02}. In the absence of phase change the total pressure at (2) can be taken to be the same as the that at (1) which can be measured. But if the fluid nucleates in the passage, the flow in the core of the nozzle is no longer isentropic. There will be irreversible internal heat transfer and loss of total pressure between stations (1) and (2). Under these circumstances, the determination of the total pressure at station (2) presented a problem. Computer programs predicting paths of nucleating and two phase flows of steam have been available to the authors from earlier studies (Bakhtar and Zidi, 1990 and Bakhtar and So, 1991). The increase of entropy and associate loss of total pressure experienced by the fluid can be obtained directly from the solutions. A series of solutions for typical conditions was carried out. In the notation of Fig. 4 the average of calculated losses of total pressure expressed as a fraction of the upstream total pressure $(P_{01} - P_{02})/P_{01}$ was 3 percent. This was adopted as the loss experienced by the flow between stations (1) and (2).

In all the measurements where the fluid had nucleated upstream of station (2), Po_2 was taken as $0.97\,P_{01}$ and the resulting data is plotted as a calibration curve against $1 - Ps/P_{TD}$ in Fig. 5. As in the case of the superheated tests the measurements at flow angles of + 10, 0, and − 10 degrees relative to the probe fell on the same graph. It will be seen that for values of $1 - Ps/P_{TD}$ less than 0.4 corresponding with subsonic flows, the total pressure tube reads the total pressure P_{02} accurately. But above this range as the flow exceeds the sonic velocity and as shown in Fig. 4, a standing shock wave will develop in front of the probe causing a further loss of total pressure between station (2) and the probe. Thus in supersonic flows the tube reading needs correction.

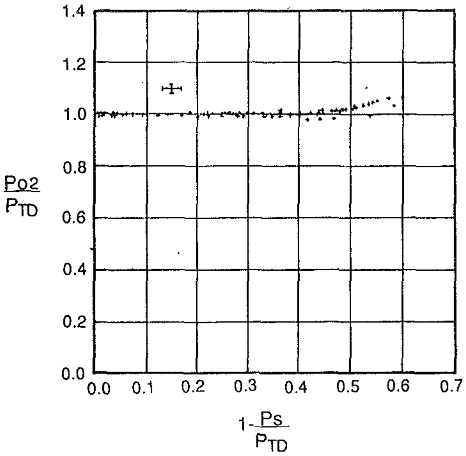

Fig. 5 Calibration curve in nucleating steam (uncertainty in measured pressures ±.01 bar)

A further set of specimen calculations was also carried out to estimate the loss of total pressure experienced by the fluid between station (2) and the total pressure tube. For this purpose it was assumed that when wet steam encounters a standing shock wave, the discontinuity affects only the vapor phase initially and the droplets pass through the front unaffected. There is then a relaxation as the droplets adjust to the new conditions in the vapor surrounding them. The loss of total pressure will include two components: one the loss associated with flow through the shock wave and a further loss resulting from the thermal relaxation. The calculated differences between P_{02} and P_{TD} were lower than those indicated in Fig. 5. It was therefore decided to adopt the calibration graph shown in this figure but to regard it as the upper bound correction for the error. It will be recalled that the probe had also been calibrated in superheated steam. Under these conditions there was no loss of total pressure due to phase change. The total pressures at stations (1) and (2) were equal and in supersonic flow the loss of total pressure between station (2) and the tube was solely due to the standing shock wave and lower than the values indicated in Fig. 5. It was thus argued that if the wet measurements were interpreted by using the superheated calibration curve the error would be underestimated. Thus the superheated calibration curve could be used for estimating the lower bound case of the correction to the readings and both sets of calibration curves have been used in the interpretation of the measurements.

To investigate the feasibility of using LDA in wet steam and at the same time to provide some comparison with velocity traverses two sets of measurements were carried out. These were at the same plane downstream of the cascade as the flow traverses and at corresponding superheated and nucleating flows and were performed without seeding the flow.

The L-D anemometer utilized a 10mW Helium-Neon laser operating in forward scatter. Particle transits through the LDA measurement volume were processed by a Burst Spectrum Analyzer. The characteristics of the instrument permitted measurements to be taken within the short tunnel run times but the observations could be carried out only at one location in each run. To obtain the velocity distribution across the passage, the instrument was repositioned and the measurements repeated.

Experimental Results

To check the time response of the data acquisition system a number of preliminary measurements were carried out in which the probe was fixed in position and the readings were compared with measurements in which the probe was moving

Table 1 Summary of experimental results. (Uncertainty in measured pressures ±.01 bar, in temperatures ±1 K in measured angles ±0.5 degree.)

Test No.	Po_1 bar	To_1 K	Ps_2 bar	$\frac{Po_1}{Ps_2}$	Outlet Angle Degrees	Efficiency %
			Superheated tests			
$1^{\#}$	1.68	417	1.03	1.63	73.4	94.4
$2^{\dagger}$	1.67	416	0.76	2.20	74.3	94.2
$3^{\dagger}$	1.67	416	0.84	1.99	74.5	95.1
$4^{\dagger}$	1.67	414	0.79	2.11	74.5	94.7
			Nucleating tests			
$5^{\#}$	1.73	380	1.02	1.70	71.4	87.4
$6^{\dagger}$	1.69	378	0.84	2.01	72.0	90.8^{*} 89.7^{+}
$7^{\#}$	1.68	379	1.09	1.54	69.8	87.3
$8^{\dagger}$	1.75	381	0.86	2.04	72.8	91^{*} 90.5^{+}
$9^{\dagger}$	1.68	385	0.73	2.30	70.5	91.2^{*} 90.4^{+}
$10^{\dagger}$	1.68	385	0.84	2.00	71.1	92.8^{*} 91.4^{+}

*Method 1.
$^{+}$Method 2.
$^{\#}$Subsonic outlet.
†Supersonic outlet.

and no differences were observed. A further set of comparisons was also carried out between the measurements of the pressures read directly and those inferred by using differential pressure transducers. The resulting readings fell identically on the same graph. Measurements were then carried out for flow conditions listed in Table 1.

Typical measured variations of downstream static and total pressures across the passage for a case of superheated steam flow in the cascade with subsonic outlet are given in Fig. 6(*a*). A sketch showing the traversing plane relative to the blades is given as an inset to the figure. The values of total pressure as measured at a fixed location upstream of the cascade concurrently with the other measurements are also plotted. The difference between the upstream and downstream total pressures represents the losses incurred by the flow. The effect of the wakes on the flow is clearly evident. It can also be seen that in the space between the wakes the total pressure recovers its upstream value indicating that in this part of the flow the expansion has been isentropic. Similar measurements for a typical case of superheated steam flow with supersonic outlet are plotted in Fig. 6(*b*). Between the wakes the downstream total pressure does not recover the inlet value. This is due to the losses resulting from the trailing edge shock waves.

Corresponding typical measurements taken with steam supercooled at inlet for cases with subsonic and supersonic outlets are plotted in Figs. 7(*a*) and 7(*b*), respectively. By comparing the results of superheated and supercooled tests with subsonic outlet given in Figs. 6(*a*) and 7(*a*) it will be seen that the features are similar except for the differences between inlet and downstream total pressures. In the superheated test the core of the flow is isentropic and there is no loss of total pressure suffered by the fluid during the expansion. In contrast when the fluid is supercooled at inlet, it will nucleate in the course of expansion. This process is accompanied by irreversible internal heat transfer which is experienced by the flow as a loss.

The comparison between the results for flows with supersonic outlet given as Figs. 6(*b*) and 7(*b*) is similar except for the presence of trailing edge shock waves. In both tests the downstream traverses indicate a loss of total pressure between the wakes. In the case of the superheated test shown in Fig. 6(*b*), the loss is attributed to the effect of trailing edge shock waves. The measurements plotted in Fig. 7(*b*) show a larger loss in similar positions for the nucleating test. Only part of this loss is due to shock waves, the reminder is the nucleation loss suffered by the flow.

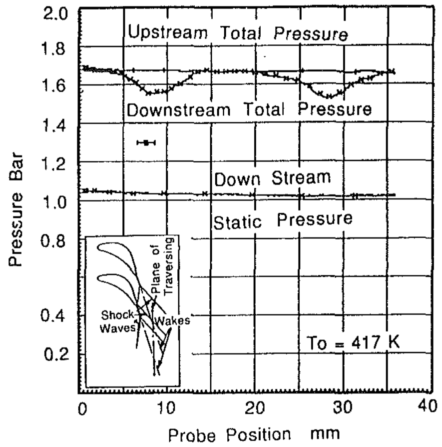

Fig. 6(*a*) Subsonic outlet

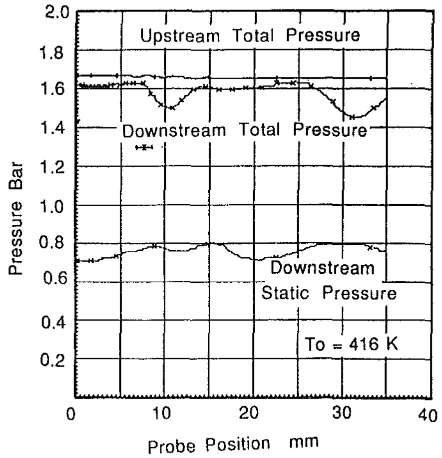

Fig. 6(*b*) Supersonic outlet

Fig. 6 Traverse results in superheated steam (uncertainty in measured distances ±1.0mm, in pressures ±.01 bar)

Analysis of Results

From the recorded observations determination of the downstream total pressure and flow angle was straightforward. The procedure used for the calculation of flow velocity and effi-

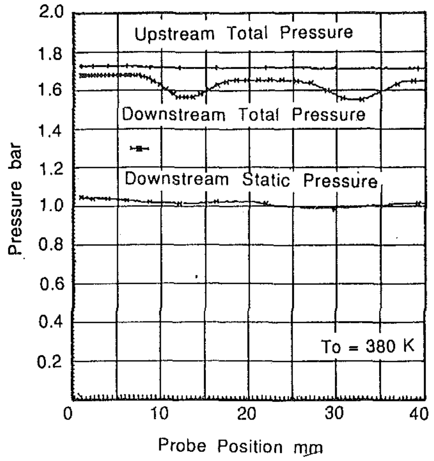

Fig. 7(*a*) Subsonic outlet

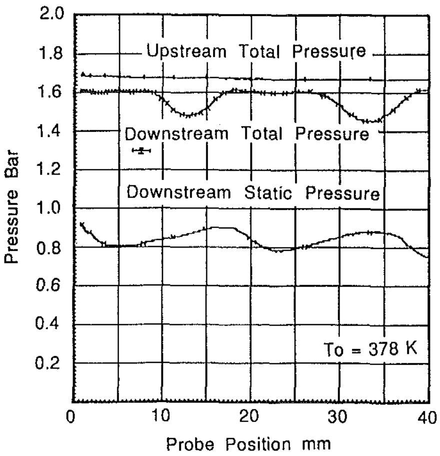

Fig. 7(*b*) Supersonic outlet

Fig. 7 Traverse results in nucleating steam (uncertainty in measured distances ±1.0mm, in pressures ±.01 bar)

ciency is given in the Appendix. The method of analysis was applied to the measurements listed in Table 1. The efficiencies and flow angles quoted are mass mean values calculated over one pitch.

It will be recalled that the determination of total pressure is supersonic wet flows from the probe pressure reading was subject to some uncertainty. For this reason the analysis of nucleating flows with supersonic outlet was carried out using two separate calibration curves. The first was that shown in Fig. 5 in which the thermodynamic losses during calibration were estimated theoretically. The second was the superheated calibration curve. Both sets of results have been presented. In each case the lower of the two efficiencies resulted from the use of superheated calibration curve.

Tests numbers 1-4 are superheated tests in which the pressure ratios P_{01}/Ps_2 range from 2.20 to 1.63. This may be compared with the critical pressure ratio of 1.85 for dry steam. The efficiencies of the expansions are similar for all these cases. It is slightly higher for test 3 but the difference is comparable with the experimental error. It may thus be concluded that the superheated tests have an average efficiency of 94-95 percent.

Tests 5-8 are supercooled tests of which the outlets for tests numbers 6 and 8 are supersonic while those of tests 5 and 7 are subsonic. As already discussed there was some uncertainty in the calculation of efficiencies of the tests with supersonic outlet. The calculations were carried out using the two methods and yielded a gross average of approximately 90-91 percent for the two tests. Thus in these cases the efficiency is approximately 4 percent lower than that of the corresponding superheated tests. In contrast the average of the efficiencies of the subsonic tests is 87.3 percent which is 7 percent less than that of the superheated tests.

Theoretical solutions predict the thermodynamic component of the wetness loss to be about 5 percent which is similar to the difference between the measured efficiencies of supersonic superheated and nucleating tests. Thus the aerodynamic losses in the supersonic supercooled and superheated tests are very similar. In contrast in tests with sub-sonic outlet approximately 3 percent of the additional loss must be attributed to aerodynamic causes.

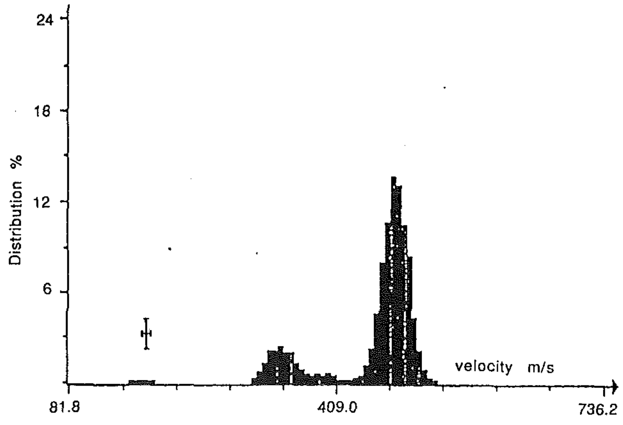

Fig. 8 Typical distribution of velocity counts by LD Anemometer (uncertainty in individual measurements ±1 percent, uncertainty in frequency distribution ±1 percent)

Experimental Accuracy

The distance travelled by the probe was measured by a displacement transducer which had an accuracy of ±1mm. The inlet stagnation temperature of steam has been measured to within ±1K. All the other quantities have been derived from pressure measurements which have been to an accuracy of ±0.01 bar. The estimated uncertainties in the inferred velocities and efficiencies are ±0.5 and ±1 percent, respectively in all the tests except those with supersonic wet steam outlets in which the corresponding uncertainties are ±0.75 and ±1.5 percent, respectively. The deduced flow angles are within ±1 degree. It must however be said that the quoted uncertainties refer to individual data points. As the overall efficiencies quoted are based on the average of a large number of readings they must involve smaller uncertainties. Mutual consistency of the results and comparisons with the results of air tests on similar profiles suggest an uncertainty of ±0.6 percent in the measured efficiencies.

Laser-Doppler Anemometry

A typical example of the data resulting from a measurement in wet stream is shown in Fig. 8. The distributions generally showed two peaks suggesting the presence of two groups of particles in the flow. It was reasoned that the higher velocities could be attributed to the smaller nucleated droplets which moved with the flow. Thus for the purposes of comparison with the traversed data the higher velocities were adopted. It is thought that the second group are droplets formed by condensation on foreign particles present in the steam. In each test an attempt was made to clear the steam of these impurities through a preliminary expansion and a pause for the droplets to settle. But as seen from the results some particles still remain in the vapor. Their presence is a major complicating factor in the measurement of droplet sizes by light scattering or extinction.

It will be recalled that when carrying out LDA the measurements could be taken at only one location in each run. To obtain the velocity distribution across the passage the measurements had to be carried out over a number of runs but it was not possible to repeat the conditions of the tests exactly. To carry out comparisons between these measurements and traversed data, they were normalized. For each set of observations the procedure was carried out in two steps. In the first stage average inlet and overall pressure ratios for the set of LDA results were calculated. The results differing substantially from the average were excluded and the remainder of the results were normalized to the average conditions. A set of velocity traverses corresponding closely to the average of the LDA test was then identified. The second adjustment consisted of normalizing the LDA data to the condition of the velocity traverses.

The comparison between the velocities as measured by the two methods for the nucleating tests is shown in Fig. 9. It can be seen that the agreement between the traversing and LDA measurements for these tests is satisfactory. The agreement obtained between the measurements is superheated tests was poor. This was thought to be due to the absence of seeds in the LDA measurements.

Conclusions

1. Nucleating flow conditions experienced in steam turbine blading can be reproduced for systematic study by the blowdown technique. It has been demonstrated that under the short run times available, the flow can be traversed downstream of the cascade satisfactorily.
2. It has been confirmed that the use of LDA in wet steam during the short run times is possible and the quality of agreement between the LDA and traversed velocities has been satisfactory.
3. For the typical configuration studied, nucleating flows have exhibited lower thermodynamic efficiencies than those obtained in superheated flows.
4. The measured drop in efficiency has been 7.3 percent for the tests with subsonic outlet and 4 percent in those where the outlet has been supersonic. No analysis of the individual factors contributing to the loss have been presented but in parallel theoretical studies the thermodynamic component of the loss has been estimated to be approximately 5 percent. Comparison of this estimate with the measured losses indicates that in the case of the blade geometry investigated the aerodynamic losses experienced by the flow are not significantly affected by condensation when the outlet flow is supersonic. This contrasts with tests with subsonic outlet in which the aerodynamic losses have been greater in nucleating flows.

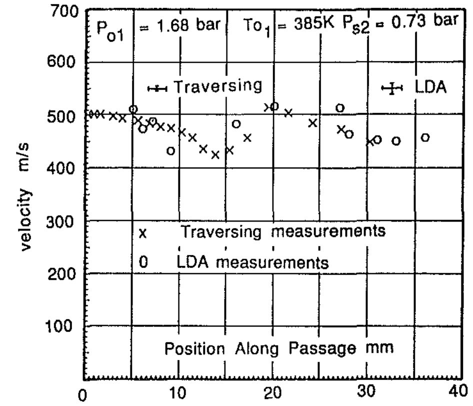

Fig. 9 **Comparison of velocity measurements by LDA and by probe (uncertainty in measured distances ±1.0mm, in deduced traversed velocities ±0.5 percent, in LDA Data + 10 m/s)**

5. In the range of conditions investigated the efficiency of nucleating flows does not appear to vary greatly with the extent of the supercooling of the steam supply.

Acknowledgments

The investigations were carried out in the School of Manufacturing and Mechanical Engineering of University of Birmingham and supported by grant GR/D 65961 from the Science and Engineering Research Council. The generous help of Messrs. NEI Parsons in the provision of some components for the test section is gratefully acknowledged. The authors are also grateful to Messrs. H. J. A. Cox and B. B. Archer, formerly of Messrs. GEC/Alsthom Turbine Generators Ltd. for help with the design of the probe. The LDA measurements were carried out in collaboration with Mr. Peter Jones of Dantec Electronic Ltd.

References

Bakhtar, F., and Heaton, A. V., 1986, "On the Potential of Blow-down Conditions in Studies of Nucleating and Two-Phase Flows of Steam," *Proceedings 8th International Heat Transfer Conference*, San Francisco, pp. 2277–2282.

Bakhtar, F., Siraj, M. A., Bamkole, B. O., Webb, R. A., and Ebrahimi, M., 1992, "A Study of Nucleating and Wet Steam Flows in a Cascade of Turbine Blading—Droplet Measurements," *Proceedings ASME Cavitation and Multiphase Flow Forum*, O. Furuya, ed., FED Vol. 135, pp. 167–170.

Bakhtar, F., and So, K. S., 1991, "A Study of Nucleating Flows of Steam in a Cascade of Supersonic Blading by the Time Marching Method," *International Journal of Heat & Fluid Flow*, Vol. 12, No. 1, pp. 54–62.

Bakhtar, F., Webb, R. A., Shojaee-Fard, M. H., and Siraj, M. A., 1991, "An Experimental Facility for Studies of Nucleating and Wet Steam Flows in Turbine Blading," *Proc. Instn. Mech. Engrs.*, *European Conference on Turbomachinery*, C423/003, Mechanical Engineering Publications, pp. 191–199.

Bakhtar, F., Webb, R. A., Shojaee-Fard, M. H., and Siraj, M. A., 1993, "An Investigation of Nucleating Flows of Steam in a Cascade of Turbine Blading," ASME JOURNAL OF FLUIDS ENGINEERING, Vol. 115, pp. 128–134.

Bakhtar, F., and Zidi, K., 1990, "Nucleation Phenomena in Flowing High Pressure Steam Part 2—Theoretical Analysis," *Proceedings Institution Mechanical Engineers A*, Vol. 204, pp. 233–242.

Cox, H. J. A., 1980, "Experimental Development of Bladings for Large Steam Turbines," Von Karman Institute for Fluid Dynamics Lecture Series," Steam Turbines for Large Power Outputs, 1980-6 Chapter 6.

Jones, T. V., Oldfield, M. L. G., Ainsworth, R. W., and Art, T., 1993, "Transient Cascade Testing," Chapter 5 *Advanced Methods for Cascade Testing* AGARDOGRAPH AG238, Charles Hirsch, ed.

APPENDIX

Calculation of Flow Velocity and Efficiency of Expansion

The state path of a typical flow element is shown on the enthalpy-entropy diagram in Fig. 10. The inlet stagnation conditions are known and are represented by point 01. Point 2 represents the state of the fluid at the traversing plane, point 02 is the corresponding stagnation state and point 2′ represents the downstream conditions resulting if the expansion were isentropic. To estimate the flow velocity from the measured static and total pressures P_2 and P_{02} at this plane it was assumed

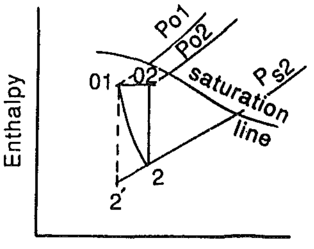

Fig. 10 **Expansion path**

that (*a*) heat transfer between the fluid streams was negligible and (*b*) that in the plane of traversing the fluid was substantially in thermodynamic equilibrium and the interphase slip was negligibly small. This was because it was noted from the earlier observations that the zone of rapid condensation occurred just downstream of the throat. The nucleated droplets were very small in size, possessed considerable amount of surface for interaction with the vapor and the changes in the flow were more gradual in the plane of traversing.

With the assumption of no heat exchange between streams, stagnation enthalpy at the downstream plane h_{02} was taken to be equal to the inlet value h_{01} which together with P_{02} was sufficient to determine the remainder of the properties at point 02. As the fluid is assumed to be at equilibrium at (2), the stagnation properties at 02 are also those of equilibrium states. With the stagnation conditions determined entropy at point 2 can be set equal to that at 02. Thus from known pressure and entropy at point 2 and the assumption (b) above all other properties at the downstream plane can be calculated.

With the fluid states thus determined, the outlet velocity is calculated from the enthalpy drop $h_{01} - h_2$ and the efficiency of the expansion as $(h_{01} - h_2)/(h_{01} - h_{2'})$.

M. Lopez de Bertodano

R. T. Lahey, Jr.

O. C. Jones

Center for Multiphase Research,
Rensselaer Polytechnic Institute,
Troy, NY 12180-3590

Development of a k-ϵ Model for Bubbly Two-Phase Flow

An extension of the k-ε model for bubbly two-phase flow is proposed and tested against experimental data. The basic assumption made is that the shear-induced turbulence and bubble-induced turbulence may be linearly superposed. This assumption results in a model with two time constants that matches both homogeneous two-phase turbulence data (Lance and Bataille, 1991) and pipe data (Serizawa, 1986). The coefficients of the single-phase k-ε model have not been modified and only one additional coefficient is required: the virtual volume coefficient of the bubbles, which may be determined from first principles. This model not only agrees with the data trends, but it also predicts the turbulence suppression which has been measured for high Reynolds number bubbly air/water flows in pipes.

Introduction

The formulation of constitutive relations for the Reynolds stresses in the two-fluid model (Ishii, 1975) is an important step in the development of multidimensional two-phase flow computational fluid dynamics (CFD). One of the earlier works on turbulence modeling for this purpose was performed by Drew and Lahey (1982) who applied mixing length theory to analyze the phase distribution in vertical bubbly pipe flows. Lee et al. (1989) were the first to perform closed-loop CFD predictions of lateral phase distribution in vertical pipes by applying the k-ϵ model to bubbly flows. Lopez de Bertodano et al. (1990) extended this work to the τ-ϵ model to account for the non-isotropy of the turbulence.

The experimental data base available to develop a two-phase turbulence model is small. Lance and Bataille (1991) measured homogeneous two-phase grid generated turbulence with a laser doppler anemometer (LDA). Serizawa et al. (1986) used an X-sensor hot-film probe to measure the shear stress and the normal stresses for bubbly flow in a pipe. Wang (1987) used a single sensor boundary layer hot-film probe and a three-sensor conical hot-film probe for both bubbly up and down flows in a pipe. Both Serizawa and Wang observed two-phase turbulence suppression for superficial liquid velocities greater than 1 m/s (i.e., the liquid phase turbulence decreased when bubbles were added to the flow).

The object of this paper was to investigate the constitutive relations necessary to adapt the k-ϵ model (Launder and Spalding, 1974) to bubbly flows. First the standard single-phase k-ϵ model will be presented, followed by an analytic solution of homogeneous turbulence decay. Then the two-phase turbulent kinetic energy equation (Kataoka and Serizawa, 1991) will be discussed followed by two possible two-phase k-ϵ model variations. The merits of each will be discussed in terms of two simple cases of bubbly flow turbulence: bubbles rising in a still tank of liquid, and homogeneous decay of bubbly flow turbulence. Finally the best model will be used to analyze the effect of phase distribution and turbulence suppression in bubbly pipe flows.

The Transport Equation of Single Phase Turbulence Kinetic Energy. The Reynolds stress conservation equations may be derived by time averaging the dot product of the Navier-Stokes equations and the fluctuating component of the liquid velocity, $\mathbf{u}'$. Taking the trace of these equations yields the conservation equation for the turbulent kinetic energy (Tennekes and Lumley, 1974):

$$\frac{Dk}{Dt} = -\nabla \bullet \overline{\mathbf{u}'\left(k+\frac{p'}{\rho}\right)} - \overline{\mathbf{u}'\mathbf{u}'}:\nabla\overline{\mathbf{u}} - \upsilon\overline{\nabla\mathbf{u}':(\nabla\mathbf{u}')^T} \tag{1}$$

where, the turbulent kinetic energy is given by:

$$k = \frac{1}{2}\overline{u'\bullet u'}, \tag{2}$$

p' is the fluctuating pressure, ρ is the liquid density, and υ is the kinematic viscosity of the liquid. The first term on the right-hand side of Eq. (1) is a diffusion term. The second term is the production of the turbulent kinetic energy, which may be shown to be identical to the loss of kinetic energy of the mean flow. Finally, the last term represents the viscous dissipation, and since it is a squared quantity it is positive definite.

The Single-Phase k-ϵ Model. This model, which was developed by Launder and Spalding (1974), is based on a set of constitutive relations for the right hand side of Eq. (1). The Reynolds stress tensor in the production term is modeled according to the customary relation:

$$\overline{\mathbf{u}'\mathbf{u}'} = -\upsilon_t(\nabla\overline{\mathbf{u}} + \nabla\overline{\mathbf{u}}^T) \tag{3}$$

where υ_t is the turbulent kinematic viscosity.

Similarly, the diffusion term is modeled as:

$$\overline{\mathbf{u}'\left(k+\frac{p'}{\rho}\right)} \cong \overline{\mathbf{u}'k} = -\upsilon_t\nabla k \tag{4}$$

Contributed by the Fluids Engineering Division for publication in the JOURNAL OF FLUIDS ENGINEERING. Manuscript received by the Fluids Engineering Division August 10, 1992; revised manuscript received May 13, 1993. Associate Technical Editor: A. Prosperetti.

The remaining term is the turbulence dissipation rate:

$$\epsilon \underline{\underline{\Delta}} \upsilon \overline{\nabla \mathbf{u}' : (\nabla \mathbf{u}')^T} \tag{5}$$

Thus the turbulence kinetic energy transport equation may be written:

$$\frac{Dk}{Dt} = \nabla \bullet \upsilon_t \nabla k + \upsilon_t (\nabla \overline{\mathbf{u}} + \nabla \overline{\mathbf{u}}^T) : \nabla \overline{\mathbf{u}} - \epsilon \tag{6}$$

Similarly, the turbulence dissipation rate is modeled with another transport equation proposed by Hanjalic and Launder (1972):

$$\frac{D\epsilon}{Dt} = \frac{1}{\sigma_\epsilon} \nabla \bullet \upsilon_t \nabla \epsilon + \frac{1}{k/\epsilon} [c_{\epsilon 1} \upsilon_t (\nabla \overline{\mathbf{u}} + \nabla \overline{\mathbf{u}}^T) : \nabla \overline{\mathbf{u}} - c_{\epsilon 2} \epsilon] \tag{7}$$

where (Launder and Spalding, 1974), $\sigma_\epsilon = 1.3$, $c_{\epsilon 1} = 1.44$, and $c_{\epsilon 2} = 1.92$. This equation possesses production and dissipation terms that are similar to those in the kinetic energy transport equation, Eq. (6), but are divided by the turbulence time constant, $\tau_t = k/\epsilon$.

The correlation for the turbulent viscosity is derived from Prandtl's mixing length theory, assuming that the turbulence time constant is proportional to the time that it takes for a fluid particle to move half way around a large eddy. The resulting equation proposed by Launder and Spalding (1974) is:

$$\upsilon_t = c_\mu \frac{k^2}{\epsilon} \tag{8}$$

with $c_\mu = 0.09$.

Once the total kinetic energy is calculated the Reynolds stresses may be computed using an extension of Eq. (3):

$$\overline{\mathbf{u}'\mathbf{u}'} = -\upsilon_t (\nabla \overline{\mathbf{u}} + \nabla \overline{\mathbf{u}}^T) + \frac{2}{3} \underline{\underline{A}} k \tag{9}$$

where $\underline{\underline{A}}$ is the turbulence anisotropy tensor which may be calculated by one of the various algebraic stress models available (e.g., Naot and Rodi, 1987). Naturally, for the case of isotropic turbulence $\underline{\underline{A}} = \underline{\underline{I}}$.

Single-Phase Homogeneous Turbulence. Let us next consider the homogeneous decay of turbulence, since it is a very simple case. Indeed, there are no turbulence or velocity gradients so there are no diffusion terms and no production terms, only dissipation. Then Eq. (6) becomes:

$$\frac{Dk}{Dt} = -\epsilon \tag{10}$$

Similarly Eq. (7) simplifies to:

$$\frac{D\epsilon}{Dt} = -c_{\epsilon 2} \frac{\epsilon}{k} \epsilon \tag{11}$$

Thus combining Eqs. (10) and (11) and integrating yields:

$$\frac{\epsilon}{\epsilon_0} = \left(\frac{k}{k_o}\right)^{c_{\epsilon 2}} \tag{12}$$

where k_0 and ϵ_0 are the initial conditions. Inserting this into Eq. (10) yields:

$$\frac{D}{Dt}\left(\frac{k}{k_o}\right) = -\frac{\epsilon_o}{k_o}\left(\frac{k}{k_o}\right)^{c_{\epsilon 2}} \tag{13}$$

which has the solution:

$$\frac{k}{k_o} = \left[\frac{1}{1 + (c_{\epsilon 2} - 1)\frac{\epsilon_o}{k_o} t}\right]^{\frac{1}{c_{\epsilon 2} - 1}} \tag{14}$$

We note that $c_{\epsilon 2} = 1.92 \cong 2$, thus Eq. (14) may be simplified to:

$$\frac{k}{k_o} \cong \frac{1}{\left(1 + \frac{\epsilon_0}{k_o} t\right)} \cong e^{-t/(k_o/\epsilon_o)} \tag{15}$$

Therefore the turbulence decays with a time constant, $\tau_{1\phi} = k_o/\epsilon_o$.

The Transport Equation of Two-Phase Turbulence Kinetic Energy. Kataoka and Serizawa (1991) obtained an equation for the two-phase turbulent kinetic energy which is similar to Eq. (1) and was obtained with the two-phase time averaging method (Ishii, 1975):

$$\alpha_l \frac{Dk_l}{Dt} = -\nabla \bullet \alpha_l \overline{\mathbf{u}_l' \left(k_l + \frac{p_l'}{\rho_l}\right)} - \alpha_l \overline{\mathbf{u}_l' \mathbf{u}_l'} : \nabla \overline{\mathbf{u}}_l - \alpha_l \upsilon \overline{\nabla \mathbf{u}_l' : \nabla \mathbf{u}_l'^T} + S_{k_l i} \tag{16}$$

where l is the liquid phase subscript, α_l is the liquid fraction, and $S_{k_l i}$ is the interfacial source of turbulence, which is

$$S_{k_l i} = \mathbf{M}_{li}^D \overline{\mathbf{u}}_R, \tag{17}$$

assuming no interfacial area change, where $\mathbf{M}_{li}^D$ is the interfacial drag force, $\overline{\mathbf{u}}_R = \overline{\mathbf{u}}_g - \overline{\mathbf{u}}_l$, and g is the subscript for the gas phase. This term represents the work done by the gas on the liquid phase which gets transformed into turbulent eddies.

Two-Phase k-ϵ Models. Constituting a kinetic energy equation from Eq. (16) is similar to the single-phase flow case:

$$\alpha_l \frac{Dk_l}{Dt} = \alpha_l \frac{D}{Dt} \nabla \bullet [\alpha_l \upsilon_t \nabla k_l] + \alpha_l [\upsilon_t (\nabla \overline{\mathbf{u}} + \nabla \overline{\mathbf{u}}_l^T) : \nabla \overline{\mathbf{u}} - \epsilon] + S_{ki} \tag{18}$$

The problem is how to constitute the dissipation term, ϵ, for the case of bubbly flows.

Single Time Constant Model. The straightforward way to model the two-phase dissipation equation is to proceed in an analogous way to the single-phase k-ϵ model. Then

$$\alpha_l \frac{D\epsilon}{Dt} = \nabla \bullet \left[\alpha_l \frac{\upsilon_t}{\sigma_\epsilon} \nabla \epsilon\right] + \frac{\alpha_l}{k/\epsilon} [C_{\epsilon 1} \upsilon_t (\nabla \overline{\mathbf{u}}_l + \nabla \overline{\mathbf{u}}_l^T) : \nabla \overline{\mathbf{u}}_l - C_{\epsilon 2} \epsilon] + S_{\epsilon i} \tag{19}$$

and the problem that remains is how to constitute the interfacial source of dissipation term. For the case of bubbles rising in a still-water tank, assuming steady fully developed flow, Eqs. (18) and (19) become (Lee et al., 1988):

$$0 = -\alpha_l \epsilon + S_{ki} \tag{20}$$

$$0 = -\alpha_l C_{\epsilon 2} \frac{\epsilon}{k} \epsilon + S_{\epsilon i} \tag{21}$$

So the interfacial production of dissipation is constrained to be:

$$S_{\epsilon i} = C_{\epsilon 2} \frac{\epsilon}{k} S_{ki} \tag{22}$$

For two-phase homogeneous decay of turbulence Eqs. (18) and (19) become:

$$\alpha_l \frac{Dk_l}{Dt} = S_{ki} - \alpha_l \epsilon \tag{23}$$

and,

$$\alpha_l \frac{D\epsilon}{Dt} = S_{\epsilon i} - \alpha_l \epsilon_\epsilon \tag{24}$$

where for uniform and homogeneous flow, the diffusion and

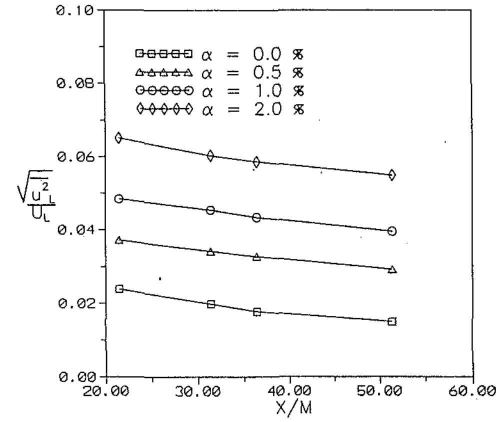

Fig. 1 Decay of grid generated turbulence for bubbly flow (U_l = 0.6 m/s) (Lance and Bataille, 1991)

production terms are negligible. Inserting Eq. (22) into (24) yields:

$$\alpha_l \frac{D\epsilon}{Dt} = c_{\epsilon 2}\frac{\epsilon}{k_l}(S_{ki}-\alpha_l \epsilon) \tag{25}$$

and then, similarly to the single-phase case, Eqs. (23) and (25) may be combined to yield Eq. (12). Inserting this result into Eq. (23) gives:

$$\frac{D}{Dt}\left(\frac{k}{k_o}\right) = \frac{S_{ki}}{\alpha_l k_o} - \frac{\epsilon_o}{k_o}\left(\frac{k}{k_o}\right)^{c_{\epsilon 2}} \tag{26}$$

which may be solved by separation of variables. Defining:

$$a = \left(\frac{S_{ki}}{\alpha_l \epsilon_o}\right)^{1/2}, \text{ and, } \tau_{1\phi} = \frac{k_o}{\epsilon_o}$$

and assuming $C_{\epsilon 2} \cong 2$ the solution to Eq. (26) is:

$$\ln\left|\frac{k_l/k_o - a}{k_l/k_o + a}\right| = -2at/\tau_{1\phi} \tag{27}$$

For $a < 1$ and, $2at/\tau_{1\phi} \gg 1$, Eq. (27) can be rewritten as:

$$\frac{k_l}{k_o} \cong a(1 + 2e^{-2at/\tau_{1\phi}}) \tag{28}$$

thus the asymptotic value of k_l/k_o is 'a' and the time constant for turbulence decay is '$\tau_{1\phi}/2a$'. Since $a = (S_{ki}/\alpha_l \epsilon_o)^{1/2}$, we see that the asymptotic value depends on the initial dissipation rate, ϵ_o, though it should only depend on the bubble-induced turbulence. Moreover, as can be seen in Fig. 1, Lance and Bataille (1991) observed that the time constant for the decay of bubbly flow grid generated turbulence, both with bubbles and without them, is approximately the same (i.e., k_o/ϵ_o). This is true for this model only if $a \cong 1/2$. Therefore the single time-constant model fails to reproduce both the asymptotic value and the time constant of homogeneous decay of bubbly flow turbulence; clearly something is missing.

Two Time-Constant Model. This model was originally formulated in terms of physical arguments so they will be presented first. Then it will be shown that it can be cast in a form consistent with the two-phase averaged equation for turbulence (i.e., Eq. (18)).

The experimental data of Lance and Bataille (1991), Fig. 1, shows that for low void fractions the linear superposition of grid generated shear-induced (SI) turbulence and bubble-induced (BI) turbulence is appropriate:

$$k_l = k_{\mathrm{SI}} + k_{\mathrm{BI}} \tag{29}$$

Theofanous (1982) made the same observation for turbulence on the centerline of a vertical pipe, for up to 10 percent void fraction. The bubble-induced turbulence is primarily composed of the irrotational motion (i.e., pseudo-turbulence due to liquid displacement by the bubbles), for all but Taylor bubbles. However, there is a small rotational contribution due to the wakes.

The approach of linear superposition for an inherently nonlinear process such as turbulence should only be considered to be an approximation. Even for the case of dilute flows (i.e., negligible bubble-to-bubble interactions) Lance et al. (1992) have identified three types of nonlinear couplings. First is the stretching of the shear-induced vortices in the potential flow around the bubbles. Second is the deformation of the bubbles by these vortices which changes the virtual volume coefficient of the bubbles and also the drag force. Similarly, the liquid eddies may be expected to deform also (Kataoka and Serizawa, 1991). Third, is the interaction between the small vortices in the wakes with the shear-induced vortices.

Another type of nonlinear coupling has been identified by Squires and Easton (1989) for particle laden flows. They performed direct numerical simulation analysis of small particles in homogeneous turbulence and found that the drag of the particles on the eddies produced a damping effect on the turbulence field of the continuous phase. This effect was greater for higher particle loadings (i.e., higher volume void fractions) and it was uniform across the whole energy spectrum. For the case of bubbles which are relatively large it would be expected that the low frequency part of the spectrum would be primarily affected. Another nonlinear effect could occur if the bubbles preferentially locate themselves in certain regions of the turbulence field. Anyhow all these important effects are being neglected at this early stage of model development and one of the tasks that remains is to determine at which point the linear superposition approach used is no longer valid.

In order to use the superposition model given by Eq. (29) it is necessary to constitute the bubble-induced turbulence. Arnold (1988) performed cell averaging to obtain the pseudo-turbulence around a group of spheres in potential flow. His result is:

$$(\overline{\mathbf{u}'\mathbf{u}'})_{\mathrm{BI}} = \alpha_g\left[\frac{1}{20}\,\bar{\mathbf{u}}_R\bar{\mathbf{u}}_R + \frac{3}{20}\,|\bar{\mathbf{u}}_R|^2\underline{\underline{\mathrm{I}}}\right] \tag{30}$$

which may be rewritten in matrix form as:

$$(\overline{\mathbf{u}'\mathbf{u}'})_{\mathrm{BI}} = \begin{pmatrix} 4/5 & 0 & 0 \\ 0 & 3/5 & 0 \\ 0 & 0 & 3/5 \end{pmatrix}\alpha_g\,\frac{1}{2}\,C_{vm}|\bar{\mathbf{u}}_R|^2 \tag{31}$$

where for potential flow around a sphere, the virtual volume coefficient is $C_{vm} = 1/2$. The bubble-induced turbulent kinetic energy is obtained by taking the trace of Eq. (31):

$$k_{\mathrm{BI}a} = \alpha_g\,\frac{1}{2}\,C_{vm}|\bar{\mathbf{u}}_R|^2 \tag{32}$$

For completeness of the formulation the effects of inertia and diffusion may be included even though they are normally negligible. A first order relaxation type transport equation for bubble-induced turbulence is thus obtained:

$$\alpha_l\frac{Dk_{\mathrm{BI}}}{Dt} = \nabla\cdot[\alpha_l \nu_t \nabla k_{\mathrm{BI}}] + \frac{1}{\tau_b}(k_{\mathrm{BI}a} - k_{\mathrm{BI}}) \tag{33}$$

where $k_{\mathrm{BI}a}$ is the asymptotic value given in Eq. (32), for the case when u_R reaches its terminal value, and τ_b is the time constant of a bubble. Hence, a second time constant has been introduced.

The shear-induced turbulence of the liquid is modeled with the standard single-phase transport equation, Eq. (6), as modified by the two-phase volumetric fraction terms:

$$\alpha_l\frac{Dk_{\mathrm{SI}}}{Dt} = \nabla\cdot[\alpha_l \nu_t \nabla k_{\mathrm{SI}}] + \alpha_l[P_{\mathrm{SI}} - \epsilon_{\mathrm{SI}}] \tag{34}$$

where P_{SI} and ϵ_{SI} are the production and the dissipation of the shear-induced turbulence. P_{SI} is given by the second term on the right hand side of Eq. (6). ϵ_{SI} is given by the standard ϵ

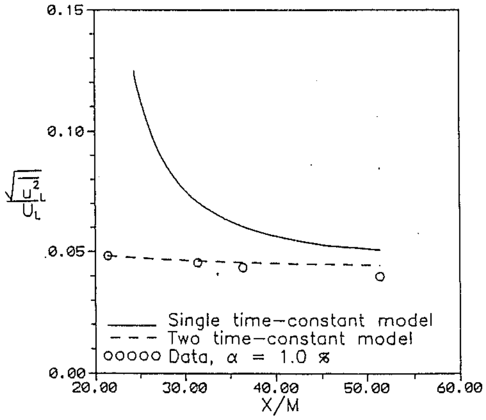

Fig. 2 Comparison of turbulence models with bubbly flow grid generated turbulence data of Lance and Bataille, 1991, (U_l = 0.6 m/s, α = 1%)

equation modified for two-phase flow in an analogous way as Eq. (34). If Eqs. (33) and (34) are added, then:

$$\alpha_l \frac{Dk_l}{Dt} = \nabla \cdot [\alpha_l \nu_t \nabla k_l] + \alpha_l [P_{SI} - \epsilon_{SI}] + \frac{1}{\tau_b}\,(k_{BIa} - k_{BI}) \qquad (35)$$

Now Eqs. (18) and (35) are equivalent if:

$$\alpha_l \epsilon = \alpha_l \epsilon_{SI} + \frac{k_{BI}}{\tau_b} \qquad (36)$$

and,

$$S_{ki} = \frac{k_{BI_a}}{\tau_b} \qquad (37)$$

Equation (36) means that the total dissipation is the linear superposition of the shear-induced and the bubble-induced dissipation, where the latter is given by a first order relaxation model.

Finally, using the well-known expression for interfacial drag:

$$M_{li}^D = \alpha_g \frac{3}{4} \frac{C_D}{D_b} \rho_l u_R^2 \qquad (38)$$

and inserting Eqs. (17) and (32) into Eq. (37) yields the requirement that the relaxation time constant must be:

$$\tau_b = \left(\frac{2}{3} \frac{C_{vm}}{C_D}\right) \frac{D_b}{u_R} \qquad (39)$$

for this model to be consistent with Kataoka's two-phase averaged turbulent kinetic energy equation. This time constant is proportional to the residence time of a bubble, which is an appropriate value for pseudo-turbulence. This time interval is usually very short compared to the time constant of the shear-induced turbulence and may be neglected for most practical cases. Hence, Eq. (33) reduces to:

$$k_{BI} = k_{BI_a} \qquad (40)$$

Applying this model to the problem of bubbles rising in a still water tank yields:

$$k_{SI} = 0, \quad \epsilon_{SI} = 0, \quad k_l = k_{BI} = k_{BI_a} \qquad (41)$$

which is the correct solution.

For the case of homogeneous decay of turbulence,

$$\frac{Dk_{SI}}{Dt} = -\epsilon_{SI}, \quad k_{BI} = k_{BI_a}. \qquad (42)$$

$$\frac{D\epsilon_{SI}}{Dt} = -\frac{C_{\epsilon 2}}{k_{SI}/\epsilon_{SI}}\,\epsilon_{SI} \qquad (43)$$

So the shear-induced turbulence decays as in the case of single-phase flow, Eq. (15). A comparison between the single time constant model, the two time constant model and the data of Lance and Bataille for grid generated bubbly flow turbulence is shown in Fig. 2. It can be seen that the two time constant model yields far superior results.

Bubbly Pipe Flow Turbulence. The two time constant turbulence model together with the multidimensional two-fluid model (Ishii, 1975) were used to perform CFD calculations for bubbly flows in pipes. The computations were done with PHOENICS 1.4, developed by Spalding et al. (1988), on the NCSA CRAY-YMP. PHOENICS is a transport equation solver with two-fluid model capability. It is based on the SIMPLE algorithm developed by Patankar (1980). The transport of mass and momentum equations for the liquid and the gas and the equations for liquid turbulent kinetic energy and dissipation were solved. A more detailed description of the two-phase constitutive models used in the momentum equations has been given by Lance and Lopez de Bertodano (1992). Significantly, the turbulence model presented in this paper is a key component of these constitutive models.

In order to solve the phasic momentum equations it was necessary to define closure laws for the two-phase Reynolds stresses and the turbulent viscosity. As with the turbulent kinetic energy, the Reynolds stresses were constituted using linear superposition:

$$\overline{\mathbf{u}'\mathbf{u}'} = (\overline{\mathbf{u}'\mathbf{u}'})_{SI} + (\overline{\mathbf{u}'\mathbf{u}'})_{BI} \qquad (44)$$

where the shear-induced (SI) component is given by Eq. (9) and the bubble-induced component is given by Eq. (31). The principle of superposition was also used for the two-phase turbulent viscosity. That is, Sato (1981) proposed that,

$$\nu_t = \nu_{t_{SI}} + \nu_{t_{BI}} \qquad (45)$$

where,

$$\nu_{t_{BI}} = 1.2 \frac{D_b}{2} \alpha_g |\bar{\mathbf{u}}_R| \qquad (46)$$

This model for the bubble-induced enhancement in viscosity is based on the concept of mixing length, where the bubble radius is taken to be the bubble-induced turbulence length scale. The shear-induced turbulent viscosity was calculated according to the standard k-ϵ model:

$$\nu_{t_{SI}} = 0.09 \frac{k_{SI}^2}{\epsilon_{SI}} \qquad (47)$$

The boundary conditions are now discussed. First, the time-averaged steady-state gas continuity equation is a first order hyperbolic equation that, given the velocity field, may be solved along its characteristics for the void fraction. Hence the value of the void fraction at the channel inlet is the only required boundary condition.

The rest of the equations were made parabolic (i.e., axial diffusion was neglected), with axial distance as the time-like variable. This approximation is legitimate in cases where axial convection is dominant, as occurs after the flow becomes fully developed. Therefore the velocities, the turbulent kinetic energy and the dissipation were specified at the channel inlet and at the walls but not at the channel outlet. There was one exception that occurred with the gas velocity. For bubbly flow it is customary to neglect all the diffusion terms in the gas momentum equation so the only constraint applicable at impervious walls is that the normal velocity must be zero. For the liquid velocity the no slip condition was replaced with the logarithmic law of the wall at an appropriate point in the inertial sublayer. The boundary conditions for the k-ϵ model are the conventional ones given by Launder and Spalding (1974).

To obtain computational convergence the under-relaxation false time-step parameter used by PHOENICS was adjusted. The optimum false time-step was given by the Courant criterion

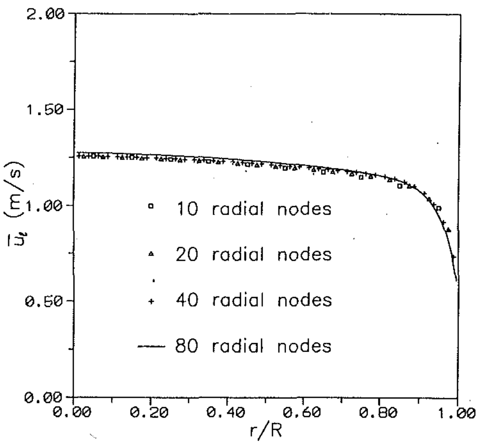

Fig. 3 Effect of radial mesh refinement on the velocity

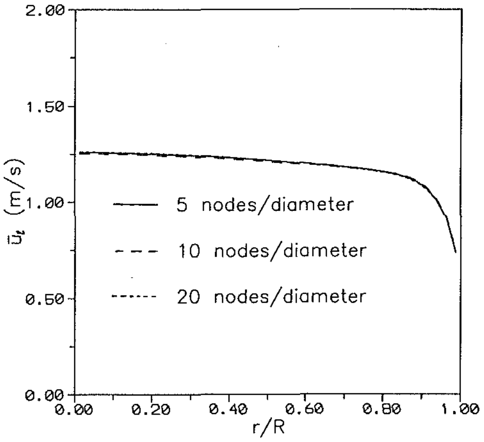

Fig. 4 Effect of axial mesh refinement on the velocity

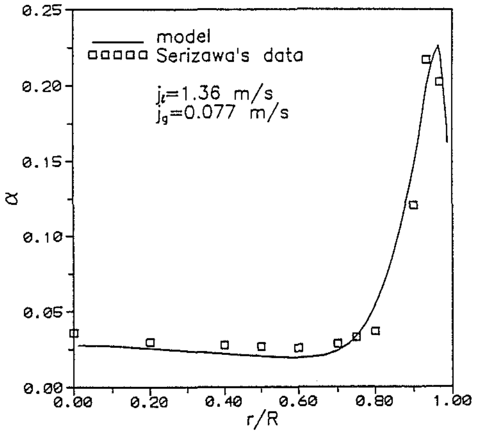

Fig. 5 Pipe: Comparison with Serizawa's data: void fraction (j_l = 1.36 m/s; j_g = 0.077 m/s; D_b = 3 mm)

$$j\,\frac{\Delta t_{\text{false}}}{\Delta x}=1, \tag{48}$$

where j is the volumetric flux of the mixture and Δx is the axial node size. Figures 3 and 4 show a nodal convergence test for the mesh size used in the computations (i.e., 40 radial nodes and five nodes per diameter in the axial direction).

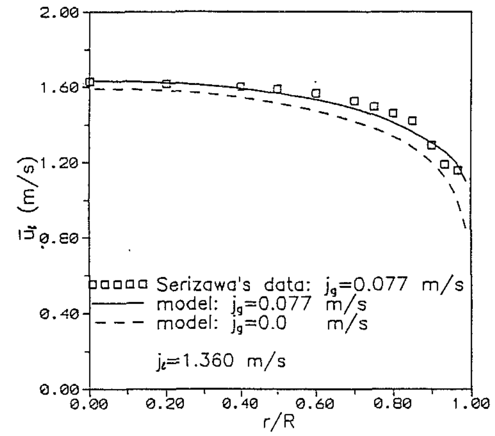

Fig. 6 Pipe: Comparison with Serizawa's data: velocity (j_l = 1.36 m/s; j_g = 0.077 m/s; D_b = 3 mm)

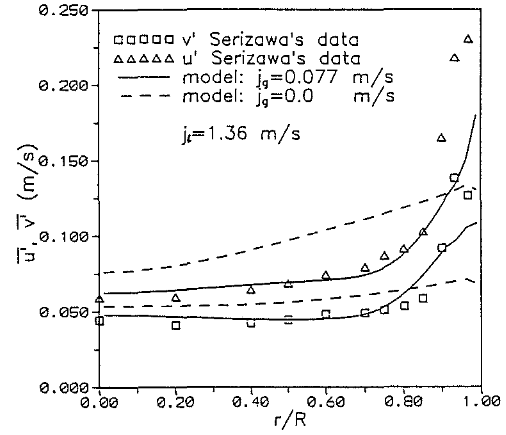

Fig. 7 Pipe: Comparison with Serizawa's data: normal stress (j_l = 1.36 m/s; j_g = 0.077 m/s; D_b = 3 mm)

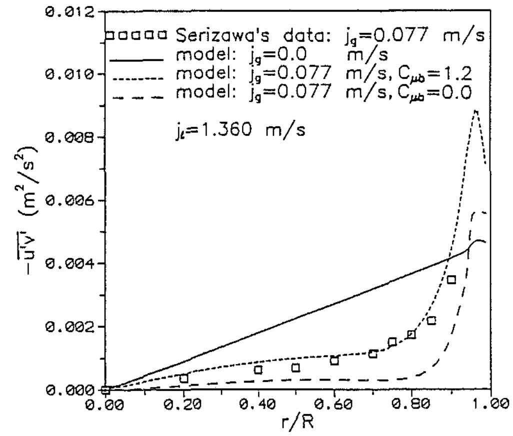

Fig. 8 Pipe: Comparison with Serizawa's data: shear stress (j_l = 1.36 m/s; j_g = 0.077 m/s; D_b = 3 mm)

A comparison with one set of data by Serizawa et al. (1986) for bubbly upflow in a pipe is shown in Figs. 5 to 8. Interestingly, Fig. 5 shows that for j_l = 1.36 m/s the liquid phase turbulence levels for bubbly flow are lower than for single-phase flow. This may be explained in terms of Figs. 6 and 8; for two-phase flow the velocity profile is flatter and the Reynolds shear stress is lower, except near the wall, so, as can be seen in Fig. 9, the production of shear-induced turbulence:

$$P_{\text{SI}}=-\overline{u'v'}\,\frac{\partial u}{\partial r} \tag{49}$$

is significantly reduced and the contribution from bubble-induced turbulence cannot make up the difference. Therefore the turbulence suppression is not caused by additional bubble-induced dissipation but by a reduction of shear-induced production.

In Fig. 7 the bubble-induced turbulence, which was the dom-

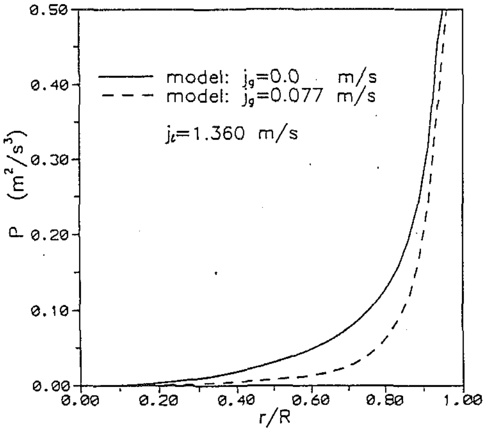

Fig. 9 Turbulence production for single-phase and two-phase flows (j_l = 1.36 m/s; j_g = 0.077 m/s)

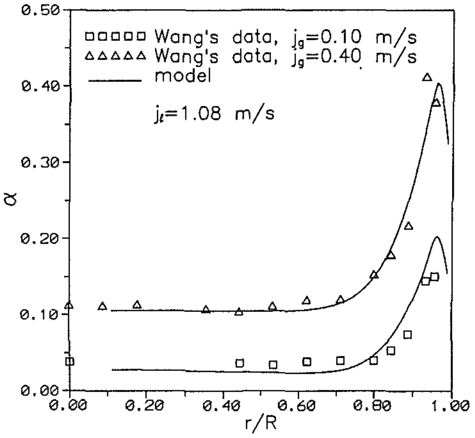

Fig. 10 Comparison with Wang's data: void fraction

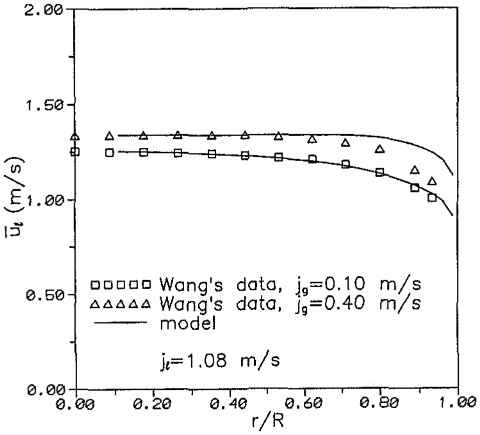

Fig. 11 Comparison with Wang's data: velocity

inant component of the turbulence at the centerline of the pipe, was calculated using $C_{vm} = 2$. This value, which is much higher than for spheres moving in a straight line, is appropriate for oblate bubbles moving in helical paths. Lance and Bataille (1991) developed an equation for the kinetic energy of the flow around such bubbles starting with the potential flow equations of Saffman (1956). Then they proceeded to measure the shape and trajectory of 5 mm bubbles rising in a tank of still water. From their equations and measurements, $1.2 < C_{vm} < 3.4$, thus the value chosen for the pipe computations is reasonable.

The results of the shear stress (i.e., $\overline{u'v'} = \nu_t \partial u/\partial r$) computations with ($C_{\mu b} = 1.2$) and without ($C_{\mu b} = 0.0$) bubble-induced turbulent viscosity are shown in Fig. 8. It can be seen that, as expected, Sato's model gives better results.

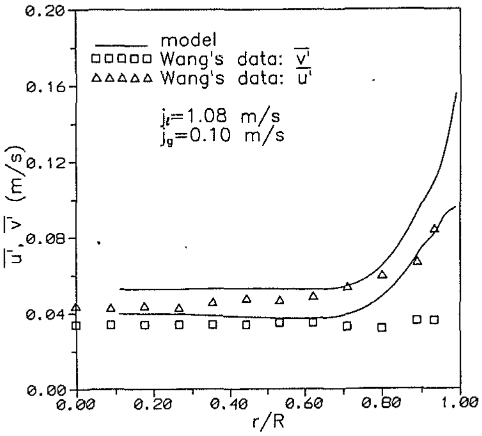

Fig. 12 Comparison with Wang's data: velocity fluctuations (j_l = 1.08 m/s, j_g = 0.10 m/s)

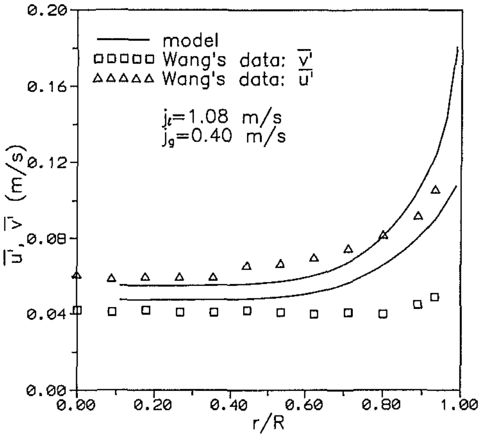

Fig. 13 Comparison with Wang's data: velocity fluctuations (j_l = 1.08 m/s; j_g = 0.4 m/s)

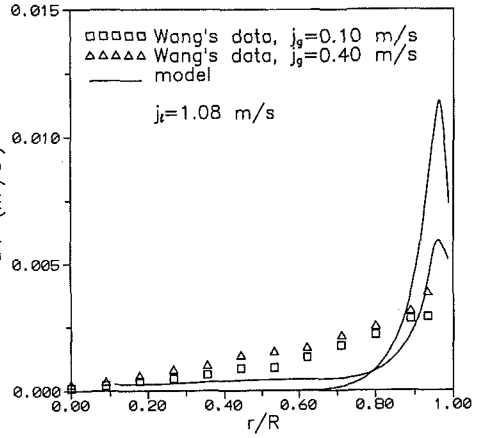

Fig. 14 Comparison with Wang's data: shear stress

Figures 10 to 14 show a comparison with Wang's data (1987). The agreement between model and data is quite good except for the shear stresses (Fig. 14). It is hard to reproduce the shear stresses measured by Wang because the velocity profile is practically flat. Since the data was obtained with a conical three-sensor probe, and not an X-sensor probe, the discrepancy may be due in part to the data and not the model. Unfortunately, there are very few sets of bubbly flow shear stress data. The only other available set is Serizawa's which shows better agreement. In any event, the comparisons with Wang's data are very useful in other respects. Figure 11 shows that the model reproduces the low void fraction velocity data better than the high void fraction data. The problem may be attributed to the two-phase viscosity model. The value calculated for the viscosity at high void fractions is too high. Therefore the calculated velocity profile is too flat. For the same reason the calculated shear stresses near the wall, where the void peaks are located, appears to be too high. This is true for the comparisons with Wang's data and Serizawa's data. Hence the linear superposition assumption appears to fail at high values of the local void fraction. A more systematic analysis is needed in order to quantify the range of validity of this assumption, but the limited amount of data presently available precludes this.

The comparison of the normal turbulent stresses shown in Fig. 12 is another example of "bubble-induced dissipation" which is explained by the absence of shear in the flow. Figure 13 is a similar comparison for higher void fraction. In this case the model seems to predict the magnitude of the turbulence but not the anisotropy. In general, the agreement is better away from the wall. Interestingly, in order to match the data a lower virtual mass coefficient (cf. Eq. (31)) can be used for the high void fraction case (i.e., $C_{vm} = 1.2$ instead of 2.0). While $C_{vm} = 2.0$ seems appropriate for the ellipsoidal bubbles observed in the experiments, the lower virtual volume apparently reflects nonlinear bubble-bubble interactions that appear at high void fractions.

Conclusions

The development of a two-phase turbulence model is a necessary prerequisite to perform accurate two-phase CFD analysis. A model for dilute bubbly flows has been proposed based on the assumption that the coupling between shear-induced and bubble-induced fluctuations is weak. This model is based on experimental and analytical information about flow around a bubble. It works well in reproducing experimental air/water data for homogeneous decay of turbulence and turbulent flow in a pipe.

Further research is needed to determine the limitations of the model when nonlinear coupling effects are significant, to understand what these effects are and how to modify the model to take them into account.

Acknowledgment

The authors wish to gratefully acknowledge the financial support given this research by the NSF and the USDOE-BES. In addition, the stimulating discussions with Dr. Michel Lance (Ecole Centrale de Lyon) were helpful and appreciated.

References

Arnold, G. S., Drew, D. A., and Lahey, R. T., Jr., 1988, "Derivation of Constitutive Equations for Interfacial Force and Reynolds Stress for a Suspension of Spheres Using Ensemble Averaging," *Journal of Chemical Engineering Communications*, Vol. 86, pp. 43-54.

Drew, D., and Lahey, R. T., 1982, "Phase Distribution Mechanisms in Turbulent Two-Phase Flow in a Circular Pipe," *Journal of Fluid Mechanics*, Vol. 117, pp. 91-106.

Hanjalic, K., and Launder, B. E., 1972, "A Reynolds Stress Model of Turbulence and Its Application to Thin Shear Flows," *Journal of Fluid Mechanics*, Vol. 52, Part 4, pp. 609-638.

Ishii, M., 1975, *Thermofluid Dynamic Theory of Two-Phase Flow*, Eyrolles, France.

Lance, M., and Bataille, J., 1991, "Turbulence in the Liquid Phase of a Uniform Bubbly Air-Water Flow," *Journal of Fluid Mechanics*, Vol. 22, pp. 95-118.

Lance, M., and Lopez de Bertodano, M., 1992, "Phase Distribution Phenomena and Wall Effects in Bubbly Two-Phase Flows," paper presented at the Third International Workshop on Two-Phase Flow Fundamentals, Imperial College, London, June 15-19.

Launder, B. E., and Spalding, D. B., 1974, "The Numerical Computation of Turbulent Flows," *Computer Methods in Applied Mechanics and Engineering*, Vol. 3, pp. 269-289.

Lee, S. J., Lahey, R. T., and Jones, O. C., 1989, "The Prediction of Two-Phase Turbulence and Phase Distribution Using a k-ϵ Model," *Japanese Journal of Multiphase Flow*, Vol. 3, No. 4, pp. 335-368.

Lopez de Bertodano, M., Lee, S. J., Lahey, R. T., Jr., and Drew, D. A., 1990, "The Prediction of Two-Phase Turbulence and Phase Distribution Phenomena Using a Reynolds Stress Model," ASME JOURNAL OF FLUIDS ENGINEERING, Vol. 112, pp. 107-113.

Lopez de Bertodano, M., 1992, "Turbulent Bubbly Two-Phase Flow in a Triangular Duct," Ph.D. thesis, Rensselaer Polytechnic Institute, Troy, NY 12180.

Naot, D., and Rodi, W., 1982, "Calculation of Secondary Currents in Channel Flow," *Proceedings of the American Society of Civil Engineers*, Vol. 108, No. HY8, pp. 948-968.

Patankar, S., 1980, *Numerical Heat Transfer and Fluid Flow*, Hemisphere Publishing Corporation, New York.

Saffman, P. G., 1956, "On the Rise of Small Air Bubbles in Water," *Journal of Fluid Mechanics*, Vol. 23, pp. 249-275.

Sato, Y., Sadatomi, M., and Sekoguchi, K., 1981, "Momentum and Heat Transfer in Two-Phase Bubbly Flow—I," *International Journal of Multiphase Flow*, Vol. 7, pp. 167-177.

Serizawa, A., Kataoka, I., and Michiyoshi, I., 1986, "Phase Distribution in Bubbly Flow," Data Set No. 24, *Proceedings of the Second International Workshop on Two-Phase Flow Fundamentals.*

Serizawa, A., and Kataoka, I., 1990, "Turbulence Suppression in Bubbly Two-Phase Flow," to be published, *Nuclear Engineering & Design.*

Squires, K. D., and Eaton, J. K., 1989, "Study of the Effects of Particle Loading on Homogeneous Turbulence Using Direct Numerical Simulation," ASME, Fluids Engineering Division, FED Vol. 80, pp. 37-44.

Sun, T. Y., and Faeth, G. M., 1986, "Structure of Turbulent Bubbly Jets—II, Phase Property Profiles," *International Journal of Multiphase Flow*, Vol. 12, No. 1, pp. 115-126.

Tennekes, H., and Lumley, J. L., *A First Course in Turbulence*, MIT Press, 1972.

Theofanous, T. G., and Sullivan, J., 1982, "Turbulence in Two-Phase Dispersed Flows," *Journal of Fluid Mechanics*, Vol. 116, pp. 343-362.

Wang, S. K., Lee, S. J., Jones, O. C., Jr., and Lahey, R. T., Jr., 1987, "3-D Turbulence Structure and Phase Distribution Measurements in Bubbly Two-Phase Flows," *International Journal of Multiphase Flow*, Vol. 13, No. 3.

Analysis of Linear Encroachment in Two-Immiscible Fluid Systems in a Porous Medium

Vijayaraghavan Srinivasan[1]
Mem. ASME

Kambiz Vafai
Professor.
Fellow ASME

Department of Mechanical Engineering,
The Ohio State University,
Columbus, OH 43210

The flow of two immiscible fluids in a porous medium was analyzed accounting for boundary and inertia effects. This problem was first solved by Muskat using Darcy's equation for fluid flow in a saturated porous medium. In the present analysis the boundary and inertia effects have been included to predict the movement of the interfacial front that is formed as one fluid displaces the other. In the present work a theoretical study that accounts for the boundary and inertia effects in predicting the movement of the interface for linear encroachment in two immiscible fluid system in a porous material is presented for the first time. The results of the present study when compared with the Muskat's model show that consideration of the boundary and inertia effects becomes important for low values of mobility ratio ($\epsilon < 1.0$) *and higher values of permeability* ($K > 1.0 \times 10^{-10}$ m^2).

1 Introduction

Linear encroachment or displacement of immiscible fluid is an important problem in various applications such as the oil industry and some manufacturing processes. For example, in the oil industry, the simultaneous flow of oil, water, and gas in porous rock strata occurs with the production of oil from oil fields. For this application, the porous strata which is saturated with oil is contiguous to the water bearing sands and when an oil pool is tapped the oil in it begins to move toward the wells and neighboring waters begin to encroach upon the oil pool. In some situations, the encroaching fluid drives the second fluid and the second fluid flow is entirely due to the hydrostatic head of the encroaching fluid column. The general features of linear encroachment were discussed by Muskat (1937). His work corresponds to a case where the two fluids are moving in a "narrow" channel where the cross sectional area is small compared to its length. The problem was treated as a one dimensional flow through a porous medium by Muskat and the Darcy's law was used as the basis for analysis. In this work a theoretical study that accounts for the boundary and inertia effects in predicting the movement of the interface for linear encroachment in two immiscible fluid system in a porous material is presented for the first time.

2 Analysis

A schematic diagram of the problem considered in the present study is shown in Fig. 1. It should be noted that the results obtained here are applicable to any two immiscible fluids. The porous strata is initially saturated with fluid "1" at uniform pressure. It is subjected to a flow of fluid "2" from a reservoir that has a higher pressure than those initially prevailing in the porous strata. Thus, the problem becomes one of studying the progress of the "interfacial front" as fluid "2" displaces fluid "1" and eventually saturates the porous media. The model developed for the analysis of the problem employs the following assumptions and simplifications:

1 Fluid "1" and fluid "2" are incompressible.
2 The porous strata has uniform porosity and is isotropic.
3 Variable porosity effects are neglected in the momentum equation.
4 No mixing of the fluids occur at the interface.

2.1 Governing Equations.

It is customary to use the "local volume averaging" technique to develop a rigorous set of governing equations for the transport processes in porous strata. The local volume average velocity (Vafai and Tien, 1982) is used to derive the governing momentum equation.

With the assumptions previously stated, taken into account, the volume-averaged governing balance equations (separately for regions saturated with fluid "1" and "2") are established as (Vafai and Thiyagaraja, 1987):

Continuity:

$$\nabla \cdot \langle \mathbf{V}_i \rangle = 0 \tag{1}$$

$i = 1, 2$ (for regions 1 and 2, respectively).

and *Momentum:*

$$-\nabla \langle P_i \rangle + \mu_{\mathrm{eff},i} \nabla^2 \langle \mathbf{V}_i \rangle - \frac{\mu_i}{K_i} \langle \mathbf{V}_i \rangle - \frac{F_i \delta}{\sqrt{K_i}} \rho \langle | V_i | \rangle \langle \mathbf{V}_i \rangle = 0 \tag{2}$$

$i = 1, 2$

In the present case Eq. (2) reduces to (Vafai, 1984 and Vafai, 1986):

---

[1] Currently, Process and Systems R&D, Praxair, Inc., Tonawanda, NY 14150.

Contributed by the Fluids Engineering Division for publication in the JOURNAL OF FLUIDS ENGINEERING. Manuscript received by the Fluids Engineering Division September 15, 1992; revised manuscript received April 28, 1993. Associate Technical Editor: O. C. Jones.

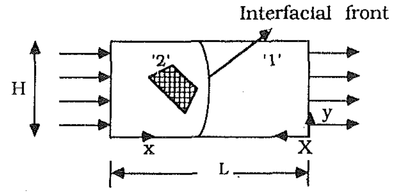

Fig. 1 Schematic diagram of the problem

$$-\frac{d\langle P_i\rangle}{dx}+\mu_i\frac{\partial^2\langle u_i\rangle}{\partial y^2}-\frac{\mu_i}{K_i}\langle u_i\rangle-\frac{F_i\delta}{\sqrt{K_i}}\rho\langle u_i^2\rangle=0 \qquad (3)$$

$$i=1,\,2$$

In Eq. (3), μ is the fluid viscosity, ρ the fluid density, K the permeability of the porous medium, δ the porosity, $\mathbf{V}$ the velocity vector, μ_{eff} effective viscosity of the porous/fluid system, $\langle P\rangle$ the average pressure read off a pressure gage, and $i=1$, 2 refers to regions 1 and 2, respectively. It should be noted that F is an empirical function that depends on the Reynolds number and the microstructure of the porous medium. The experimental procedure for determining the value of F and K are described in Vafai and Tien (1982). Typical values of K and the given functional dependence of F can be deduced from a number of empirical results such as those of Muskat (1937), Beavers and Sparrow (1969), and Koh et al. (1977). In the above formulation, the pressure gradient in the y-direction is negligible. This has rigorously been shown to be the case in Vafai (1984) and Vafai and Thiyagaraja (1987). Therefore, the flow is driven primarily by the pressure gradient in the x-direction.

The following boundary and interface conditions are applicable for the present problem

$$\langle u_i\rangle=0 \text{ at } y=0$$

$$\langle P\rangle=P_{in} \text{ at } x=L \text{ and } \langle P\rangle=P_e \text{ at } x=0$$

$$\langle u_1\rangle=\langle u_2\rangle \text{ at the interface } x-x_o(t)=0$$

$$\frac{\partial\langle u_i\rangle}{\partial y}=0 \text{ at } y=\frac{H}{2}$$

and location of the interface $x_o(t)$, using the Darcy's law, is given by

$$x_o(t)=\int_o^t u_p dt \qquad (4)$$

where u_p is the pore velocity. In terms of $\langle u_i\rangle$, that is using the generalized model Eq. (3), the location of the interface is given by

$$x_o(t,y)=\int_o^t\langle u_i\rangle dt+c(y) \quad i=1 \text{ or } 2 \qquad (5)$$

3 Analysis

To analyze the problem, the velocity field is nondimensionalized on the basis of the characteristic Darcian-convective velocity u_{ci} as $\langle u\rangle_i/u_{ci}$ where $\langle u\rangle_i$ is the velocity in the ith region and u_{ci}, the Darcian velocity in the ith region is obtained using the result obtained by Muskat (1937). The expression for u_{ci} is given by:

$$u_{ci}=-(K_i/\mu_i)\frac{d\langle P_i\rangle}{dx} \qquad (6)$$

where the subscript "i" refers to the ith region in the porous media ($i=1$ represents the region saturated by the resident fluid and $i=2$ represents the region saturated by the penetrating fluid).

Thus Eq. (3) after nondimensionalizing with the Darcian velocity reduces to

$$\left(\frac{K}{\delta}\right)\frac{d^2u_i}{dy^2}-u_i-\beta_i\delta u_i^2+1=0 \qquad (7)$$

where

$$u_i=\langle u\rangle_i/u_{ci}$$

and, β_i is given by:

$$\beta_i=F\text{Re}_i \qquad (8)$$

and

$$\text{Re}_i=\frac{\rho\sqrt{K}u_{ci}}{\mu_i} \qquad (9)$$

Equation (7) is solved using the singular perturbation analysis for obtaining velocity profiles in the boundary layer and the core region (Vafai and Thiyagaraja, 1987). The two velocity profiles, one originating from the boundary layer and the other from the core are matched at their interface. This matching process is done as outlined in Vafai (1984, 1986).

The porosity of the matrix is selected as the perturbation

Nomenclature

F = an empirical function that depends on the Reynolds number and the micro-structure of the porous medium
H = width of the channel [m]
J = unit vector aligned along the pore velocity, $u_p/|u_p|$
K = permeability of the porous structure [m^2]
L = horizontal extent of the channel [m]
P = pressure [Nm^{-2}]
P_{in} = pressure at inlet [Nm^{-2}]
P_e = pressure at exit [Nm^{-2}]
Re = Reynolds number defined by Eq. (9)
u = the dimensionless velocity field in the x-direction, $u=\langle u\rangle/u_c$
u^b = the dimensionless velocity field in the boundary layer region
u^* = the dimensionless velocity field in the core region
$\langle u\rangle$ = the dimensional velocity field in the x-direction [ms^{-1}]
u_c = modified Darcian convective velocity [ms^{-1}]
u_D = Darcian convective velocity [ms^{-1}]
u_p = pore velocity [ms^{-1}]
$\mathbf{V}$ = vector velocity [ms^{-1}]
x = coordinate along the horizontal length of the channel from left to right as shown in Fig. 1 [m]
X = coordinate along the horizontal length of the channel from right to left as shown in Fig. 1 [m]
X_o = location of the interface using the generalized model, Eq. (2), [m]
X_o^M = location of the interface using the Muskat's model [m]
y = coordinate along the vertical length of the channel
ρ = fluid density [kg m^{-3}]
δ = porosity of the medium
μ = fluid viscosity [kg m^{-1} s^{-1}]
μ_{eff} = effective viscosity of the porous/fluid system [kg m^{-1} s^{-1}]
ϵ = mobility ratio defined by Eq. (22)
$\langle\ \rangle$ = 'local volume average' of a quantity

Subscripts

i = refers to regions 1 or 2 defined in section 2.0

parameter. Thus the velocity in the boundary layer region is expanded in terms of powers of the porosity δ as:

$$u_i^b = u_b^0 + \delta u_b^1 + \delta^2 u_b^2 + \ldots \tag{10}$$

and similarly the velocity in the core region as:

$$u_i^* = u_*^0 + \delta u_*^1 + \delta^2 u_*^2 + \ldots \tag{11}$$

where $i=1$ or 2 for regions 1 (oil) or 2 (water) and u^b is the dimensionless velocity field in the boundary layer region and u^* is the dimensionless velocity field in the core region. It should be noted that Vafai and Thiyagaraja (1987) have shown that the obtained singular perturbation solutions are valid even for porosities as high as 0.98.

Substituting the assumed profiles in Eq. (7) we get the solutions for the velocity in the boundary layer region and core region separately as follows:

$$u_b^0 = 1 - e^{-\eta} \tag{12}$$

$$u_b^1 = \beta\left[-1 + \left(\frac{2}{3} + \eta\right)e^{-\eta} + \frac{1}{3}e^{-2\eta}\right] \tag{13}$$

$$u_b^2 = \beta^2\left[2 + \left\{-\frac{\eta^2}{2} - \frac{13}{6}\eta - \frac{29}{36}\right\}e^{-\eta} + \left\{-\frac{2}{3}\eta - \frac{10}{9}\right\}e^{-2\eta} - \frac{1}{12}e^{-3\eta}\right] \tag{14}$$

where

$$\eta = \frac{y}{\sqrt{K/\delta}} \tag{15}$$

In the core region, the velocity profile is obtained as:

$$u_i^* = 1 - \beta\delta + 2\beta^2\delta^2 - 5\beta^3\delta^3 \tag{16}$$

The velocity in the boundary layer region u_i^b and in the core region u_i^* were both nondimensionalized based on the Darcian velocity u_{ci}. Next, the progression of the interfacial front for immiscible displacement is traced using Darcy's law. In what follows Darcy's model is used to predict the Darcian velocity as a function of the position of interface.

According to Darcy's law, the velocities in region "1" and "2" are given by:

$$u_{c1} = \frac{K}{\mu_1}\frac{dP_1}{dx} \tag{17}$$

and

$$u_{c2} = -\frac{K}{\mu_2}\frac{dP_2}{dx} \tag{18}$$

where "1" and "2" represents the two fluid regions separated by the interface. Also

$$\left.\begin{array}{ll} \text{at } x=L & P=P_{in} \\ \text{at } x=0 & P=P_e \end{array}\right\} \tag{19}$$

$$\left.\begin{array}{ll} \text{and at the interface } (x=x_o), & u_{c1}=u_{c2} \\ \text{and} & P_1=P_2 \end{array}\right\} \tag{20}$$

Solving Eqs. (17) and (18) and substituting the boundary and interface conditions given by Eqs. (19) and (20), the Darcian velocity u_D at the interface is obtained as:

$$u_D = \frac{K}{\mu_1}\frac{\{P_{in} - P_e\}}{\{\epsilon L + X_o^M(1-\epsilon)\}} \tag{21}$$

where ϵ is the mobility ratio defined as:

$$\epsilon = \left(\frac{K}{\mu_1}\right)\Bigg/\left(\frac{K}{\mu_2}\right) \text{ or } \frac{\mu_2}{\mu_1} \tag{22}$$

Table 1 Input parameters for the analysis

Porosity, δ	0.45
Length, L	100.0 cm
Half width, H	20.0 cm
Pressure difference, N/m^2	2.2545×10^7
Viscosity, resident fluid, kg/m-s	0.01002

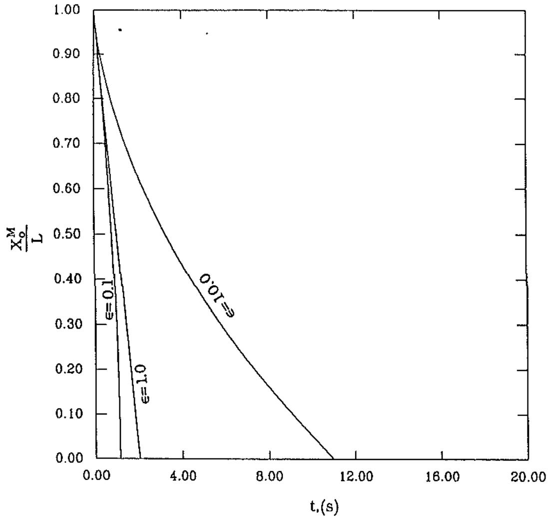

Fig. 2 Prediction of the location of interface using Darcy's model

and the equation for X_o^M is obtained as:

$$\left(\frac{X_o^M}{L} - 1\right)\left(\frac{X_o^M}{L}(1-\epsilon) + (1+\epsilon)\right) + \frac{2K}{\mu_1\delta}\frac{(P_{in} - P_e)}{L^2}t = 0 \tag{23}$$

Equation (23) is quadratic in X_o^M/L and the solution is obtained as:

$$\frac{X_o^M}{L} = \frac{-2\epsilon + \sqrt{4\epsilon^2 - 4(1-\epsilon)\left\{\frac{2K}{\mu_1\delta}\left(\frac{P_{in} - P_e}{L^2}\right)t - (1+\epsilon)\right\}}}{2(1-\epsilon)} \tag{24}$$

Thus, we have arrived at an analytical solution for the time-dependent velocity profile defined by Eqs. (11) through (16) along with Eqs. (21) and (24). The solution from these equations is substituted into Eq. (5) and the following expressions are obtained for X_o separately for the boundary layer and the core region as a function of time.

$$\epsilon\left(\frac{X_o}{L}\right) + \left(\frac{X_o}{L}\right)^2\left(\frac{1-\epsilon}{2}\right) + \frac{K}{\mu_1\delta}\frac{(P_{in} - P_e)}{L^2}t(u_b^0 + \delta u_b^1 + \delta^2 u_b^2 + \ldots) = 0 \tag{25}$$

$$\epsilon\left(\frac{X_o}{L}\right) + \left(\frac{X_o}{L}\right)^2\left(\frac{1-\epsilon}{2}\right) + \frac{K}{\mu_1\delta}\frac{(P_{in} - P_e)}{L^2}t(1 - \beta\delta + 2\beta^2\delta^2 - 5\beta^3\delta^3) = 0 \tag{26}$$

Equation (25) is used to predict the movement of the interface in the boundary layer region and Eq. (26) for the core region. The details of the encroachment is thus obtained by studying the progress of X_o with respect to t.

4 Results and Discussions

4.1 Encroachment Using Darcy's Model. Equation (24) gives the location of the interface with time using the Darcy model. Setting the values of the parameters as per Table 1, the values of X_o^M/L is plotted against t for different values of mobility ratio ϵ as shown in Fig. 2. The corresponding values

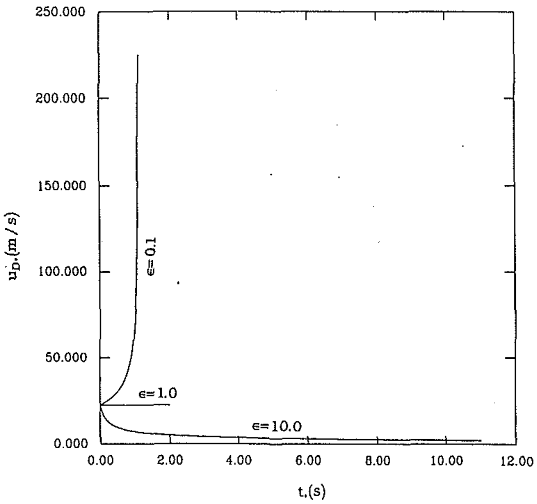

Fig. 3 Prediction of the Darcian velocity using Darcy's model

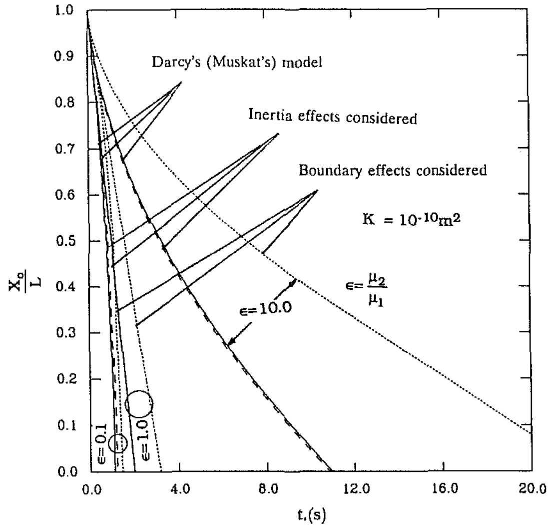

Fig. 4 Progress of the interfacial front at $y=\sqrt{K/\delta}$ using different models

of the Darcian velocity is plotted in Fig. 3. These figures illustrate that, if the encroaching fluid has lower viscosity ($\epsilon<1$), then the interface is accelerated as it advances or u_D increases with time. For ($\epsilon>1$), which implies that the encroaching fluid has higher viscosity, the progress of the interface is retarded. For the case where $\epsilon=1$, the Darcian velocity u_D remains constant with time. These results are obtained, however, without considering the boundary and inertial effects.

4.2 Encroachment With Boundary and Inertia Effects. The generalized equation for the velocity profile that takes into account the boundary and inertia effects was given by Eq. (7). The solution for Eq. (7) was obtained using the singular perturbation analysis. The solution consisted of two parts—the velocity in the boundary layer region u_i^b given by Eq. (10) and the velocity in the core region u_i^* given by Eq. (16). The boundary layer extends until the value of u_i^b asymptotically reaches the value of u_i^*. Assuming that at $t=0.0$, the interfacial front is at $X_o/L=1.0$, the progress of the front was obtained as a function of time using Eqs. (25) and (26). The location of the interface $X_o(t)$ was used to determine the Darcian velocity, u_D (or u_{ci}) using Eq. (21) where X_o^M is replaced by $X_o(t)$. The value of Darcian velocity u_{ci} was in turn used to evaluate β_i [Eq. (8)] and the values of u_i^b and u_i^*. Thus the progress of

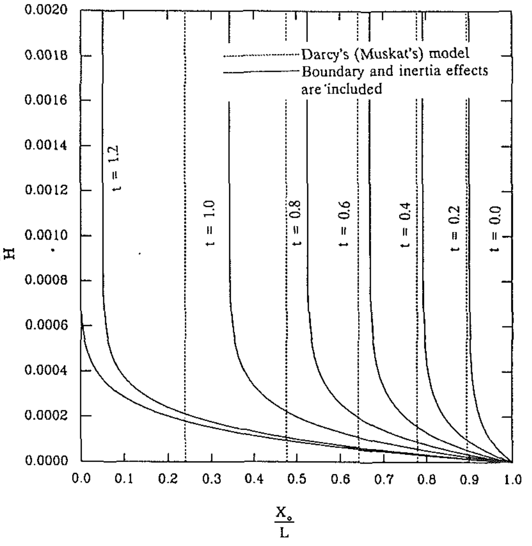

Fig. 5 Progress of the interfacial front ($\epsilon=0.1$, $K=1.0\times10^{-10}$ m^2)

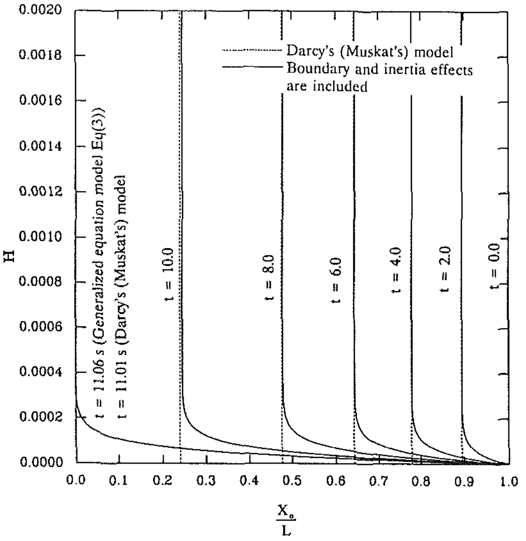

Fig. 6 Progress of the interfacial front ($\epsilon=0.1$, $K=1.0\times10^{-11}$ m^2)

the interfacial front was sequentially obtained for the boundary layer region and the core region separately using the generalized equation model [Eq. (7)]. The expressions given by Eqs. (25) and (26) were used to study the time taken for the interfacial front to progress from $X_o/L=1.0$ to $X_o/L=0.0$. These results are compared in Fig. 4 along with the predictions of Muskat's (or Darcy's) model [Eq. (24)]. The predictions were made for a permeability of $K=1.0\times10^{-10}$ m^2 and for three different values of ϵ viz. 0.1, 1.0, 10.0. It is clear from the figure that both the boundary and inertia effects reduce the velocity and therefore slow down the progress of the front. At $y=\sqrt{K/\delta}$, the boundary effects are significant. The divergence between the Darcy's model and the model that takes into account the boundary and inertia effects, becomes more pronounced at higher values of ϵ (see Fig. 4). In Fig. 5 through Fig. 7, the effect of varying the permeability on the progress of the interfacial front is illustrated. As expected, it is noted that as permeability is decreased to very low values the boundary layer becomes negligibly small. Also at a permeability of 1.0×10^{-12} m^2, the solution predicted by the generalized equation model collapses to that of Muskat's model (Darcian model). This is illustrated in Fig. 7.

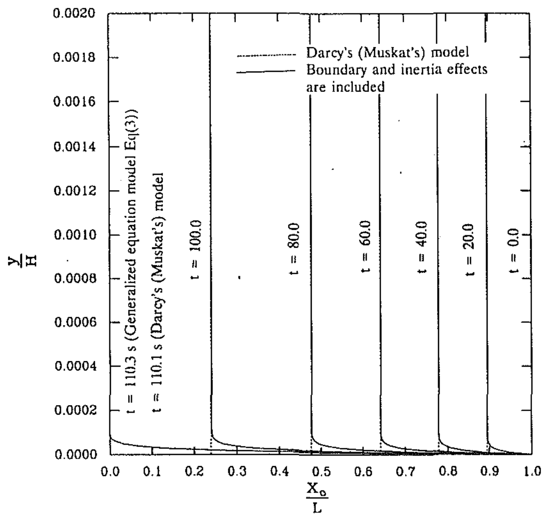

Fig. 7 Progress of the interfacial front ($\epsilon = 0.1$, $K = 1.0 \times 10^{-12}$ m^2)

5 Conclusions

In this work a theoretical analysis that accounts for the boundary and inertia effects in predicting the movement of the interface for linear encroachment in two immiscible fluid system in a porous material is presented. This model is required in the neighborhood of solid boundaries and/or faster moving flows. The main results given in this work shed some light on the importance of the boundary and inertia effects on encroachment of two immiscible fluid systems. It is shown that for higher permeabilities of the porous strata ($K > 1.0 \times 10^{-10}$ m^2) Muskat's model can significantly underpredict the time taken for the porous media to be completely displaced by the encroaching fluid.

References

Beavers, G. S., and Sparrow, E. M., 1969, "Non-Darcy Flow Through Fibrous Porous Media," ASME *Journal of Applied Mechanics*, Vol. 36, pp. 711-714.

Koh, J. C., Dutton, J. C., Benson, B. A., and Fortini, A., 1977, "Friction Factor For Isothermal and Non-Isothermal Flow Through Fibrous Porous Media," ASME *Journal of Heat Transfer*, Vol. 99C, pp. 367-373.

Muskat, M., 1937, *The Flow of Homogeneous Fluids Through Porous Media*, 1st edition, Edwards, Ann Arbor, MI.

Vafai, K., and Tien, C. L., 1981, "Boundary and Inertia Effects on Flow and Heat Transfer in Porous Media," *International Journal of Heat and Mass Transfer*, Vol. 24, No. 7, pp. 195-203.

Vafai, K., and Tien, C. L., 1982, "Boundary and Inertia Effects on Convective Mass Transfer in Porous Media," *International Journal of Heat and Mass Transfer*, Vol. 25, No. 8, pp. 1183-1190.

Vafai, K., 1984, "Convective Flow and Heat Transfer in Variable-Porosity Media," *Journal of Fluid Mechanics*, Vol. 147, pp. 233-259.

Vafai, K., 1986, "Analysis of the Channeling Effect in Variable Porosity Media," *Journal of Energy Resources Technology*, Vol. 108, pp. 131-139.

Vafai, K., and Thiyagaraja, R., 1987, "Analysis of Flow and Heat Transfer at the Interface Region of a Porous Medium," *International Journal of Heat and Mass Transfer*, Vol. 30, No. 7, pp. 1391-1405.

Determination and Characteristics of the Transition to Two-Phase Slug Flow in Small Horizontal Channels[1]

M. W. Wambsganss

J. A. Jendrzejczyk

Materials and Components
Technology Division,
Argonne National Laboratory,
Argonne, IL 60439

D. M. France

University of Illinois at Chicago,
Department of Mechanical Engineering,
Chicago, IL 60680

Two-phase pressure drop and fluctuating static pressures were measured in a small horizontal rectangular channel (hydraulic diameter = 5.44 mm). The two-phase fluid was an air/water mixture at atmospheric pressure tested over a mass flux range of 50 to 2000 kg/m^2*·s. Two-phase flow patterns were identified and an objective method was found for determining the flow pattern transition from bubble or plug flow to slug flow. The method is based on an RMS static pressure measurement. In particular, it is shown that the transition is accompanied by a clear and abrupt increase in the RMS pressure when plotted as a function of mass quality. Use of the RMS pressure as a two-phase flow pattern transition indicator is shown to have advantages over pressure-versus-time trace evaluations reported in the literature. The transition is substantiated by a clear local change in slope in the curve of two-phase pressure drop plotted as a function of either Martinelli parameter or mass quality. For high mass fluxes, the change in slope is distinguished by a local peak. Some degree of substantiation was found in previous work for both of the results (the RMS static pressure change and the local pressure drop change) at the transition to slug flow.*

Introduction

It is well known that in two-phase channel flow, a change in pressure drop is often associated with a change in flow pattern. Vince and Lahey (1982) reported that Govier and coworkers, in their study of flow patterns, void fraction, and pressure drop in two-phase vertical pipe flow, found as early as 1957 (Govier et al., 1957, 1958) that a change in pressure drop accompanies a change of flow pattern. Govier and coworkers analyzed their results on the premise that the flow pattern transitions occur at inflection points of the void-fraction curves and at minimums in the pressure-drop curves. Vince and Lahey further suggested that the work of Hubbard and Dukler (1966), which categorized power spectral density (PSD) plots obtained from measured wall-pressure fluctuations, represents the first attempt at objective classification of flow patterns. As a result of their study, Hubbard and Dukler concluded that such an analysis of pressure-drop fluctuations represents a viable means of studying flow pattern transitions.

Jones and Zuber (1975) and, more recently, Vince and Lahey (1982), used a photon attenuation technique employing a dual-beam X-ray system to measure chordal-average void fraction. Each set of investigators computed the probability density function (PDF) and PSD function from their data. Jones and Zuber identified characteristics in the PDF that can be related to the various flow patterns. Vince and Lahey generated the first four statistical moments (mean, variance, skewness, and kurtosis) associated with the distributions and attempted to use the resulting information to develop an objective flow pattern indicator. They recommend using the variance of the PDF, because that moment responded to the observed changes in flow pattern and was found to be independent of liquid superficial velocity. The PSD function and its moments were not recommended for use as an objective flow pattern indicator. While the technique put forth by Vince and Lahey is promising, it is also difficult and expensive to employ because it requires knowledge of the void fraction fluctuations, which in this case were determined with an X-ray system.

Kelessidis and Dukler (1989) used PDF analysis of the voltage/time traces obtained from conductance probes to identify flow patterns associated with upward two-phase flow in vertical concentric and eccentric annuli. Their approach is similar to that of Jones and Zuber (1975), in that they associate distinct characteristics of the PDF plots with particular flow patterns. However, Kelessidis and Dukler carried their work one step further, analyzing the PDF data with the objective of obtaining a quantitative basis for determining the various transition boundaries. Toward this end, they identified characteristics in

---

[1] Work supported by the U.S. Department of Energy, Office of Conservation and Renewable Energy, under Contract W-31-109-Eng-38.

Contributed by the Fluids Engineering Division for publication in the JOURNAL OF FLUIDS ENGINEERING. Manuscript received by the Fluids Engineering Division June 26, 1992; revised manuscript received March 30, 1993. Associate Technical Editor: E. E. Michaelides.

the PDF plots that occur when the transitions are taking place. They then used the information to derive mathematical models describing the transitions.

Several investigators have attempted to use two-phase pressure data, either from pressure-drop or static measurements, in attempts to develop objective criteria for identifying flow pattern transition boundaries. Pressure data has the distinct advantage of being more easily obtained than void fraction data. In particular, Nishikawa et al. (1969), Weisman et al. (1979), Lin and Hanratty (1987), and Damianides and Westwater (1988) used the characteristics of the pressure/time signals to identify selected flow pattern transitions.

Nishikawa et al. (1969) reported the statistical characteristics (PDF, RMS value, characteristic length as determined from correlation coefficients, and PSD) of two-phase pressure oscillations as they varied with flow rate and flow pattern. Air-water mixtures were introduced into a transparent, vertically-oriented test section, with 26.0 mm inner diameter and 5.2 m long. Series of static pressure measurements were made using pressure taps distributed along the length of the test section. The various statistical measures of the pressure oscillations were correlated with observed flow patterns. Relative to the RMS pressure data, they observed that the RMS values of pressure are small in the bubble and annular flow regions and large in the slug and froth flow regions.

Weisman et al. (1979) studied differential-pressure-versus-time traces obtained under different conditions of two-phase flow in horizontal pipes 12 to 50 mm in diameter and concluded that distinctive features in the time signals can be associated with the various flow patterns and thereby used as the basis for objective prediction of flow patterns. They used a combination of information, including amplitude, frequency, and overall shape of the time signal, to establish their criteria. Their results can be summarized as follows:

- *Slug flow* has the most distinctive trace: regularly spaced peaks occur with the time duration of the quiescent periods between peaks at least twice as long as the time duration of the peaks. This distinctive pattern is used to definitively establish the location of the *slug-to-annular* transition.
- *Stratified* flow shows virtually no fluctuations and can be distinguished from readily observed fluctuations of *wave* flow; the frequency of the fluctuations associated with wavy flow increases with increasing gas flow but the amplitudes remain low.
- The observation of *annular* flow is accompanied by an increase in fluctuation amplitude over that for stratified or wave flow. The transition from *wave* to *annular* flow is determined by this increase in amplitude.
- Within the annular region, as liquid flow is increased the fluctuation amplitude increases somewhat. However, a large amplitude increase occurs when the dispersed (bubble) flow region is reached.
- The amplitude of the fluctuations associated with *dispersed* flow decreases with decreasing gas flow rate. However, the frequency of the oscillations remains high. As a consequence, frequency provides the basis for distinguishing between *dispersed* flow and *plug* flow.
- Pressure-drop fluctuations produced by wave and plug flow are similar and are characterized by low-amplitude, low-frequency oscillations.

Weisman et al. (1979) presented their criteria in tabular form and used the criteria in establishing flow pattern maps for various two-phase flow situations.

Ruder and Hanratty (1990) used a relatively large-diameter horizontal pipe (95.3 mm diameter) to study the plug-to-slug flow transition. They considered the fluctuation amplitude of pressure-versus-time traces similarly to that of Weisman et al. (1979). The results for the large-diameter pipe did not conform to earlier work in smaller pipes. The particular transition studied was found to generally occur at a superficial gas velocity of approximately 0.6 m/s and was independent of superficial liquid velocity.

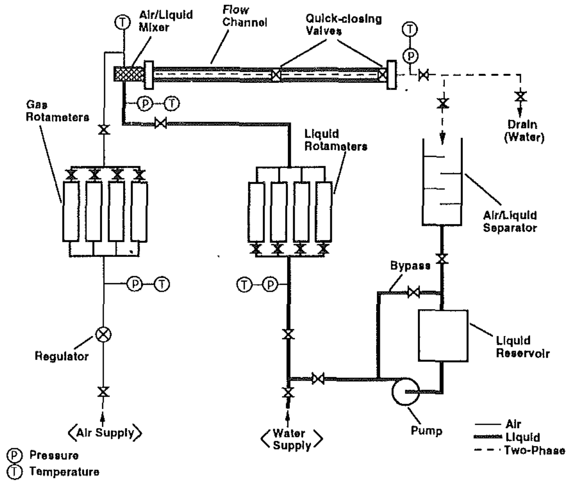

Fig. 1 Schematic diagram of adiabatic two-phase flow apparatus

Fukano et al. (1989) studied two-phase flow patterns in small-diameter (1, 2.4, and 4.9 mm) horizontal tubes. Pressure-drop fluctuation amplitudes and visual observations were used to define flow patterns. In addition, the RMS pressure was calculated and an increase in the amplitude was seen, predominantly with plug and slug flow patterns.

In the present work, the transition from bubble or plug flow to slug flow was studied experimentally in a small horizontal rectangular channel (5.44 mm hydraulic diameter); supplemental data were also obtained for a small diameter (6.35 mm) tube. This transition can be particularly important because it was found to be associated with a local increase in pressure drop, and an objective method, based on RMS static pressure, was used to clearly identify it. This method goes a step beyond the pressure/time traces of Weisman et al. (1979) and Ruder and Hanratty (1990). It also utilizes more fully the RMS pressure considered by Fukano et al. (1989). The small rectangular channel of this study has direct application to compact heat exchangers for two-phase flow applications.

Experiment

The flow apparatus (illustrated schematically in Fig. 1) is designed to allow adiabatic flow experiments with air/liquid mixtures in channels of small cross-sectional area. Air is supplied from a compressed air storage tank and flows through a pressure regulator and preselected rotameter to an air/liquid mixer. Laboratory water was used as the liquid in the current experiments. The water flows through a control valve and preselected rotameter to the mixer, where air is injected into the liquid stream through a porous medium in opposing walls of the flow channel. The two-phase mixture then flows through the transparent channel. The mixture exiting from the channel flows through an expansion to a drain. A vane-type dry gas meter was utilized to calibrate the gas rotameters, and a weighing-technique-with-stop-watch was used to calibrate the liquid rotameters. The estimated uncertainty in flow rate measurement is ±3 percent. The flow channel is rectangular, 1.14 m in length, with cross-sectional dimensions of 19.05×3.18 mm (aspect ratio of 6). (The aspect ratio is defined as the ratio of the height of the vertical side of the channel to the width of the horizontal side.)

The measured dependent variable is pressure. Pressure taps are spaced at intervals of 114 mm along the entire length of the channel and are located at the center of the long (vertical) side. Both differential pressure, over a specified channel length, and static pressures, at two locations, are measured using cal-

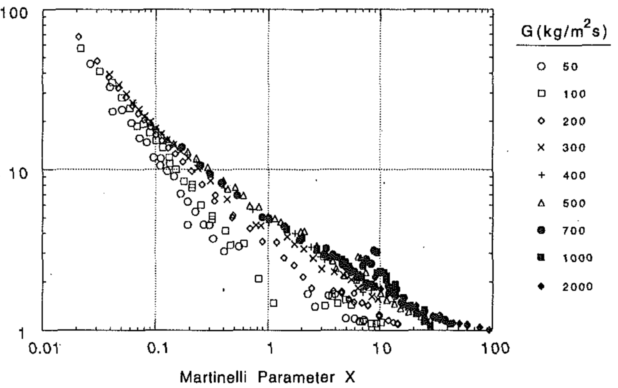

Fig. 2 Two-phase frictional pressure gradient as a function of Martinelli parameter

ibrated electrical transducers. Relative to the exit of the mixer, the pressure taps used with the static-pressure-measuring transducers, P_1 and P_2, are located at L/D_h equal to 79 to 142, respectively. The channel length over which the differential pressure measurement is made corresponds to an L/D_h ratio of 132. The estimated uncertainty in pressure measurements is ±5 percent.

The test procedure consisted of establishing total mass flux G and a mass quality x in the test section. At steady state, visual and photographic observations were made and pressures were measured. Multiple photographs were taken and pressure measurements were recorded and averaged on a computer-controlled data acquisition system. Real-time pressure measurements were made at a sampling rate of 2048 samples/s, and RMS calculations were made from 2048 samples taken over a period of 10.24 s. RMS values reported are the average of 10 such RMS calculations for a single test. As overall test channel pressure drop allowed, tests were performed over a range of quality (typically 10^{-4} to 1) for each mass flux used (50 to 2000 kg/m^2·s).

Results

As discussed above, it is expected that flow pattern will influence the frictional pressure gradient and, consequently, that the transition from one flow pattern to another will be evident in the frictional pressure gradient data. Previously, Wambsganss et al. (1992) presented frictional pressure gradient data in the form of two-phase frictional multipliers plotted as a function of both mass quality x and Martinelli parameter X. Presentation of the data as a function of Martinelli parameter is given in Fig. 2, while presentation as a function of mass quality is represented by a typical result ($G=500$ kg/m^{2}s) in Fig. 3. A study of these representations of the data leads to the identification of a distinguishing feature in the results, viz., a local change in slope or peak in the curves at a Martinelli parameter of approximately 10 (see Fig. 2) and a mass quality of approximately 0.002 (see Fig. 3). The flow pattern transition boundaries shown in Fig. 3 were determined from the flow pattern map (Wambsganss et al., 1991) given in Fig. 4. The flow pattern map was generated from a combination of visual observation, photographs, and pressure fluctuation information. A detailed definition of the various flow pattern descriptors is given by Wambsganss et al. (1991).

The results shown in Fig. 3 lead one to conclude that the *transition to slug flow is evident in the two-phase frictional pressure gradient data, while the slug-to-annular transition (also slug-to-wave and wave-to-annular for the low values of mass flux) is not evident.* The transition from plug/bubble-to-slug flow is abrupt and readily identified by visual observation of the flow patterns. This result was also readily apparent from a series of photographs of the flow patterns.

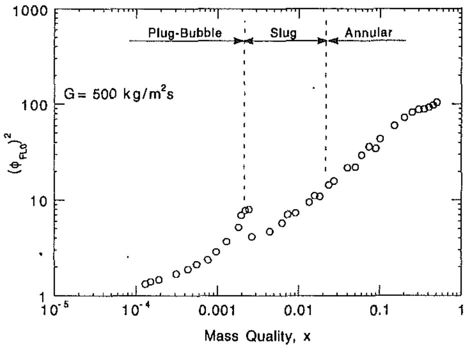

Fig. 3 Typical two-phase frictional pressure gradient as a function of mass quality with flow pattern transitions; $G=500$ kg/m^{2}s

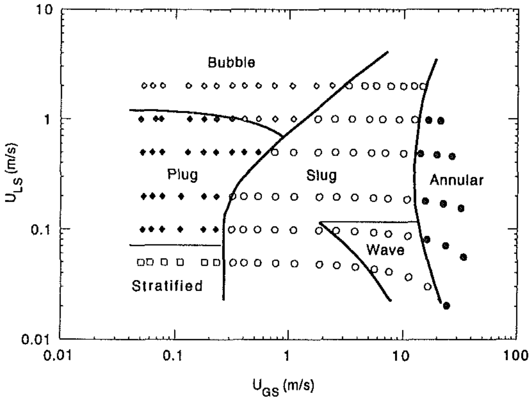

Fig. 4 Flow pattern map: horizontal air/water flow in 19.05 × 3.18 mm rectangular channel

Conversely, the slug-to-annular transition is more gradual and is difficult to distinguish from visual observations. This plug/bubble-to-slug flow transition result is especially significant because it is accompanied by a local pressure-drop change.

Typical pressure/time traces from the present study are shown in Fig. 5; they exhibit different characteristics corresponding to the different flow patterns. This is the basis for the methodology put forth by Weisman et al. (1979) as discussed previously. While the results given in Fig. 5 are from a static pressure measurement (rather than a pressure-drop measurement), there is nevertheless general agreement with the criteria proposed by Weisman et al. (1979). In particular, plug flow is characterized by low-frequency, low-amplitude fluctuations, and annular flow is characterized by a higher-frequency, but also low-amplitude, oscillation. The slug flow pattern trace shows a higher-amplitude fluctuation, which clearly distinguishes that flow pattern from the plug and annular patterns. However, the slug flow pattern trace does not exhibit the regularly spaced peaks observed by Weisman et al. (1979); this might be a consequence of the small channel used in the present study.

Following the direction of this pressure/time trace approach used in earlier work, RMS pressures in the present study were considered as a possible indicator of flow pattern transition. RMS pressures from the static pressure/time signals from transducer P_1 are plotted as a function of mass quality x in a composite plot in Fig. 6; a typical individual curve is given in Fig. 7 for a mass flux of 500 kg/m^{2}s. In Fig. 7, the flow pattern transition boundaries, obtained from visual observation, are also indicated.

The curves of Figs. 6 and 7 exhibit well-defined breakpoints in the narrow mass quality range of approximately 0.002 to 0.008. A breakpoint here is defined as a relatively abrupt increase in slope of the curve from near zero. This increase in the RMS value of the static pressure can be correlated with

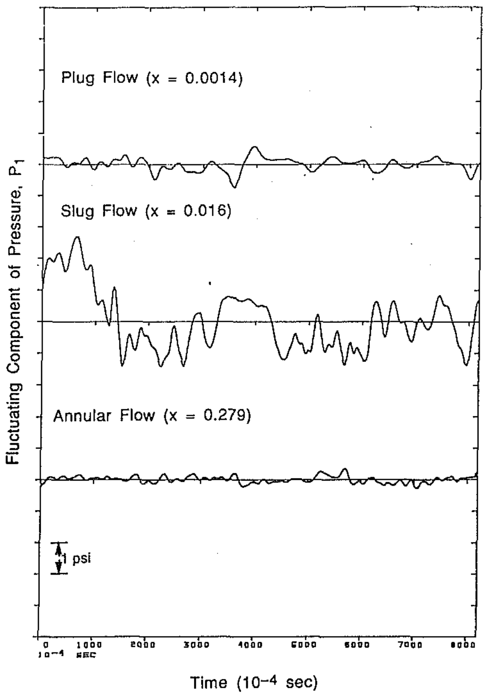

Fig. 5 Typical pressure/time traces from pressure transducer P_1; $G = 100$ kg/m^{2}s

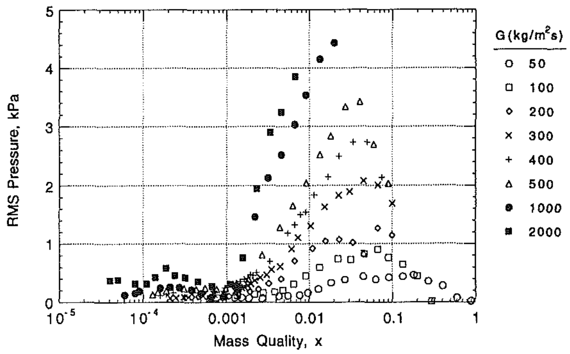

Fig. 6 RMS pressure (P_1) as a function of mass quality for small rectangular channel oriented with long side vertical

the change in slope and/or local peak in the curves of two-phase friction multiplier given in Figs. 2 and 3 and, in turn, with the transition to slug flow pattern. In particular, the pressure gradient results of Fig. 3 indicate transition to slug flow at a mass quality of approximately 0.002 and this value was constant for the higher mass fluxes tested, $G \geq 500$ kg/m^{2}s. This is substantiated by the RMS pressure plot of Fig. 6. At the lower mass fluxes, below 500 kg/m^{2}s, most information is derived from the RMS pressure results. These results show a change in transition quality that is inversely proportional to mass flux. The range of transition quality of the data is $0.002 \leq x \leq 0.008$.

Another characteristic observed in the data of Figs. 6 and 7 is a well-defined peak that is a function of total mass flux. The qualities at which the peaks occur decrease with increasing mass flux and correlate, approximately, with the slug-to-annular flow transitions defined from visual observations. This last result is significant because the slug-to-annular flow pattern transition is difficult to identify visually and is not apparent in the pressure-drop data as given, for example, by the two-phase friction multiplier representation in Fig. 3. However, because the transition to annular flow is rather gradual, it is difficult to conclusively attribute the peaks in Figs. 6 and 7 to this transition.

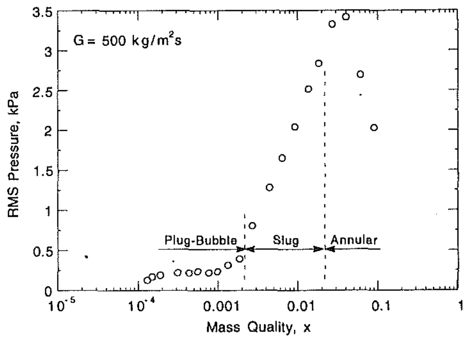

Fig. 7 Typical correlation between RMS pressure and observed flow pattern transitions; $G = 500$ kg/m^{2}s

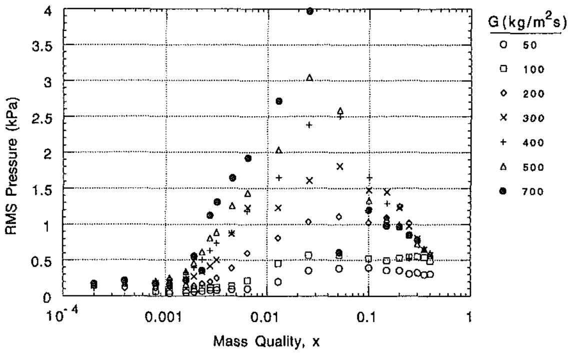

Fig. 8 RMS pressure (P_1) as a function of mass quality x and mass flux G for small rectangular channel oriented with long side horizontal (Wambsganss et al., 1990)

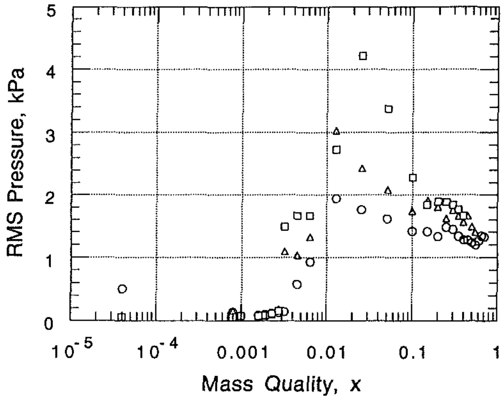

Fig. 9 RMS pressure as a function of mass quality for 6.3-mm circular tube; ○ $G = 300$ kg/m^{2}s, △ $G = 500$ kg/m^{2}s, □ $G = 700$ kg/m^{2}s

While the results presented in this paper are focused on the horizontal rectangular channel oriented with the long side vertical, experiments were also performed with the channel oriented to have the long side horizontal (Wambsganss et al., 1990). Similar results were obtained as shown in Fig. 8.

To gain insight into possible geometry dependence of the phenomenon, a limited number of tests were performed with a small-diameter (6.35 mm) tube. Three values of mass flux were tested, with the results given in Fig. 9. A comparison with the results from the small rectangular channel (see Fig. 6) reveals that the general behavior is the same for the two channels with different geometry, viz., with increasing mass quality, a well-defined breakpoint, followed by an increase in the amplitude of the RMS static pressure fluctuations that peaks and falls off. Besides the good qualitative agreement of the results, quantitatively the magnitude of the RMS fluctuations, as well as the value of the mass quality at the breakpoint (interpreted herein as the transition to slug flow), is also in good agreement.

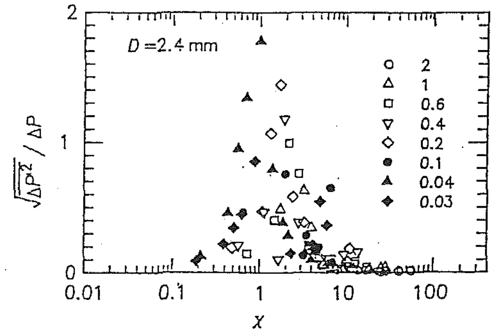

Fig. 10 Normalized RMS pressure drop as a function of Martinelli parameter; $d = 2.4$ mm (Fukano et al., 1989). Reproduced by permission of the American Nuclear Society.

For these tests, the test channel was metal and there was no provision for visual observation of the flow patterns.

Discussion

Some substantiation of the characteristics of the static pressure fluctuations measured in this study and shown in Fig. 6 can be obtained from the data presented by Fukano et al. (1989). Fukano et al. measured the fluctuating component of a differential pressure signal from two-phase air/water flow in a capillary tube (2.4 mm diameter). A coefficient was computed as the standard deviation divided by the time-averaged value and presented as a function of Martinelli parameter, as shown in Fig. 10. With increasing air flow rate and a constant superficial liquid mass velocity, the coefficient calculated by Fukano et al. increases, peaks in the Martinelli-parameter range of 0.5-5, and then decreases; this behavior is similar to that exhibited in Fig. 6. Fukano et al. noted that the maximum values occur in the intermittent flow pattern region. However, they did not attempt to correlate the unique behavior of the data with specific flow pattern transitions. The breakpoints in the data of Fukano et al. (1989) occur in a Martinelli-parameter range of approximately 3-10; this is in good agreement with the range of values of Martinelli parameter obtained in this study for transition to slug flow.

Nishikawa et al. (1969) presented their RMS pressure data as plots of RMS pressure as a function of superficial mean velocity for constant values of superficial liquid velocity. As such, their data can not be directly compared with the data of this study. Nevertheless, the authors indicate the flow patterns on selected plots and two observations can be made. First, it is of interest to note that no distinct break in the RMS pressure curve is exhibited at the transition to slug or froth flow. This is in contrast to the results of the small horizontal channel study in which a well-defined break is observed at this transition. This suggests that this transition phenomenon may be a small channel phenomenon, not exhibited in large channels. Second, as discussed above, Nishikawa et al. observed that the RMS values of pressure are small in the bubble and annular flow regions and large in the slug and froth flow regions. This observation is in qualitative agreement with the results of the small horizontal channel study.

An examination of the photographs of the flow patterns (typical results for a mass flux of 1000 kg/m^{2}s are given in Fig. 11) suggested that the physical mechanism leading to the increase in two-phase frictional pressure gradient as the bubble-to-slug transition is approached is directly related to an increase in bubble packing density. This is easily envisioned by studying the flow patterns of Fig. 11, in sequence, viz., Figs. 11(*a*)–11(*f*). As mass quality is increased, bubble size decreases and the number of bubbles increases to eventually fill the channel (Figs. 11(*a*)-11(*d*)). When the channel is "full," the bubbles effectively collapse/coalesce, resulting in a slug flow pattern (Figs. 11(*e*) and 11(*f*)).

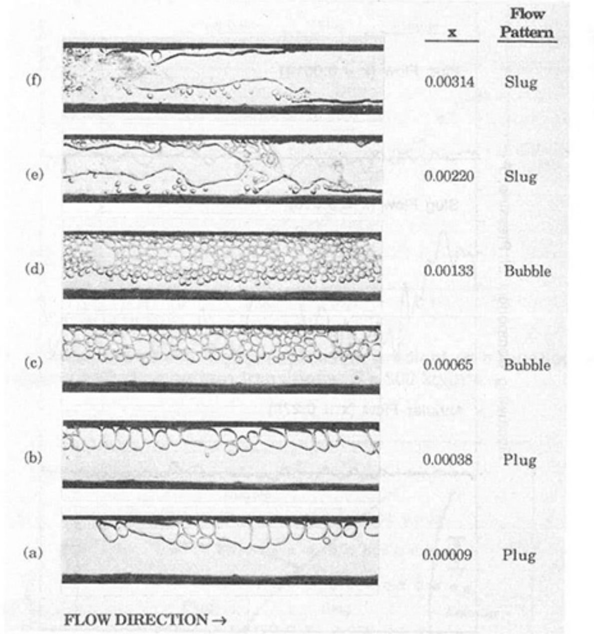

Fig. 11 Typical flow patterns illustrating "bubble packing" and the transition to slug flow; $G = 1000$ kg/m^{2}s

The physical situation giving rise to the distinct characteristics of the pressure-drop curve at the higher mass fluxes tested ($G \geq 500$ kg/m^{2}s), viz., a local peaking at the bubble-to-slug flow transition, was considered as follows: where well-defined bubbles exist, it is speculated that the increase in number of bubbles, as mass quality increases, contributes to an increased "flow resistance," and thereby an increased mean pressure, thus accounting for the local peak in the pressure-drop curve. Because it can be safely conjectured that bubble flow cannot exist at a packing density greater than some maximum, when the maximum packing density is reached, a further increase in gas flow rate causes the bubbles to break down (collapse/coalesce), forming slug flow. In so doing, the "pseudo flow restriction" is effectively relieved, allowing the mean pressure drop to suddenly decrease, thus accounting for the decrease in pressure drop following the local peaking (see Figs. 2 and 3). At the same time, the magnitude of the fluctuating component increases (Figs. 6 and 7) as a result of the emergence of large vapor slugs compared to the smaller and more random vapor bubbles preceding the transition.

Well-defined bubbles do not exist at the low values of mass flux tested ($G \leq 400$ kg/m^{2}s). Nevertheless, it is suggested that a related phenomenon is involved. This is because the RMS pressure data of Figs. 6 and 7 exhibit the same characteristics, and the monotonic increase in friction multiplier curves with increasing mass quality (which is interrupted at the bubble-to-slug flow transition) is similarly interrupted at the plug-to-slug flow transition, as illustrated in Figs. 2 and 3.

Bubble packing density is directly related to void fraction. In turn, mass quality x and void fraction α are related as

$$x = S\alpha v_L / [(1-\alpha) v_G + S\alpha v_L] \tag{1}$$

where v_L and v_G are specific volumes of the liquid and vapor phases, respectively, and S is the slip ratio (ratio of gas to liquid phase velocities). For horizontal flow, it is reasonable to assume that when plugs or bubbles are present they travel at the liquid velocity; that is, $S = 1$. As discussed previously, from Figs. 2 and 3 it can be observed that the peak (for $G > 500$ kg/m^{2}s) in the two-phase friction multiplier curves occurs at a mass quality of approximately 0.002. With Eq. (1), and $S = 1$, a mass quality of 0.002 corresponds to a void fraction of 0.6. This value for a maximum packing density is judged reasonable when compared with theoretical maximum packing densities

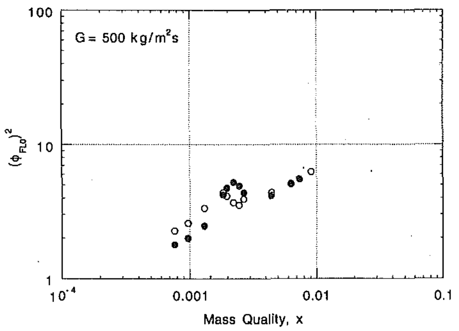

Fig. 12 Hysteresis effect associated with mass quality (○ increasing mass quality, ● decreasing mass quality)

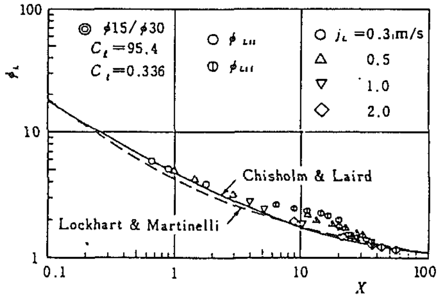

Fig. 13 Two-phase frictional pressure gradient in an annulus (Sadatomi et al., 1982). Reproduced by permission of Pergamon Press PLC.

of $\alpha = 0.52$ for spherical bubbles and $\alpha = 0.78$ for pancake (flat) bubbles on square-oriented packing configurations.

Taitel et al. (1980) also considered packing density in developing a relationship for predicting the bubble-to-slug flow pattern transition for vertical two-phase flow in large pipes. However, it should be noted that in an earlier study (Taitel and Dukler, 1976), Taitel and coworkers did not consider this phenomenon in their development of prediction methods for transitions in large, horizontal pipes. For vertical two-phase flow, Taitel et al. (1980) in developing their transition criteria assumed that the transition from bubble to slug flow occurs when the void fraction reaches 0.25. The rationale behind selection of this value is that in vertical flow the upward motion of the bubbles is in a zig-zag path with considerable randomness, and that prior to agglomeration or coalescence there must be sufficient spacing between bubbles to allow the bubbles to move; Taitel et al. assumed this critical spacing to be half the bubble radius, which leads to a void fraction of 0.25.

This value of void fraction is considerably less than that of 0.6 obtained in this study, using Eq. (1), an experimentally determined transition mass quality of 0.002, and assuming a slip of 1, which is reasonable for horizontal flow. In the case of vertical flow, the slip will not be 1 because of the buoyancy effects of the bubbles. If the same transition mass quality of 0.002 is assumed for the vertical flow case, together with a void fraction of 0.25 (as specified by Taitel et al., 1980), and Eq. (1) is solved to obtain the slip required to satisfy those conditions, one obtains a slip value of approximately 3. This value does not seem unreasonable, and the exercise serves to alleviate concern over what might be perceived as a discrepancy between the results of the two studies. Further, from the photographs of bubble flow given in Fig. 11, it is readily observed that at least for horizontal two-phase flow in small channels, the bubble packing is indeed very tight, i.e., the spacing is considerably less than half a bubble radius. Thus, the transition void fraction of the present study would be larger than that of Taitel et al. (1980), supporting a void fraction of 0.6 rather than 0.25.

Hysteresis in the present data was investigated by performing a special test. The pressure gradient for $G = 500$ kg^{2}s was measured for increasing and decreasing mass quality; results are shown in Fig. 12. As can be observed, a weak hysteresis effect is indicated.

The local pressure-drop increase at the transition to slug flow occurs at very low qualities and low pressure drops. Experiments in these parameter ranges require particular attention to instrumentation and calibration. The result discussed here of the local increase in pressure drop at this flow transition has not generally been reported in the engineering literature. However, the results of Sadatomi et al. (1982) show an indication of the peak.

Sadatomi et al. (1982) presented their data for circular, triangular, and annular channels in the form of the two-phase friction multiplier ϕ_{FL} versus Martinelli parameter X. Of particular interest is the "scatter," occurring at a value of about 10 for the Martinelli parameter, in the data corresponding to two-phase flow in the annulus (Fig. 13). Sadatomi et al. suggest that the scatter may be due to measurement error. However, a comparison with the results of this study for mass fluxes greater than 500 kg/m^{2}s (see Fig. 2) reveals a remarkable similarity in the two independent sets of data. Consequently, it appears that what Sadatomi interpreted as data scatter due to measurement error is, in fact, the transition to slug flow seen in this study. In this regard, Sadatomi's data support the current measurements. The "scatter" was not seen in the data for the circular and triangular flow channels. However, the characteristic dimension of the circular channel (diameter of 25 mm) and of the triangular channel (height of 55 mm) was larger than that of the annulus (width of 7.5 mm), and, as such, it may be inappropriate to classify those channels as "small." Sadatomi also reported (with no graphic representation) that the data from his rectangular channels were quite similar to those from his triangular and circular channels, which did not show the "scatter." However, it must be remembered that Sadatomi's interpretation of the data and measurements was different from that in the current work, which used a rectangular channel.

A second distinguishing feature in the RMS pressure-versus-mass quality curve is the peak that occurs, for the small channel of this study, in the mass quality range of 0.01 to 0.1 (see Figs. 6 and 7). With increasing mass flux, the amplitude of the peak RMS pressure montonically increases, while the mass quality at which the peak occurs appears to monotonically decrease. Wambsganss et al. (1991) noted that this peak correlated approximately with the slug-to-annular transition as determined from visual observations and photographs of the flow patterns. However, more data and additional study will be required to substantiate this result.

Conclusions

Based on the approaches used by previous investigators of two-phase flow phenomena, statistics relating to the fluctuating component of the measured pressure signals were analyzed with the objective of relating such results to flow pattern transition boundaries. In particular, RMS pressures were generated. When plotted as a function of mass quality, the curves exhibited distinct features (see Figs. 6 and 7), at least one of which can be directly related to a flow pattern transition. That feature is a well-defined increase in RMS pressure that occurs as mass quality is increased. For the different mass fluxes tested, the abrupt increase occurs in a mass quality range of approximately 0.002 to 0.008 and can be directly correlated with the plug/bubble-to-slug flow transition. This increase was supported by the work of Fukano et al. (1989).

The criterion presented for the objective determination of the transition to slug flow is very simple and straightforward. Unlike methods that require expensive X-ray equipment or a gamma densitometer, the method is easy to implement, as it requires only a pressure port, a pressure transducer, and RMS measurement. Further, it is effectively nonintrusive and can be readily applied in conjunction with phase-change heat transfer experiments. These features combine to make the methodology especially attractive. While other researchers (e.g., Fukano et al., 1989) have computed RMS pressure in small channel two-phase flows, it seems that the characteristic break in the curve had not previously been identified with the transition to slug flow.

The local peak in pressure drop at the bubble/plug-to-slug flow pattern transition is itself not a well-documented phenomenon. The work of Sadatomi et al. (1982) came close to showing this feature for two-phase flow in a narrow annulus.

The data used in this study are from experiments with air/water mixtures in a small horizontal rectangular channel, oriented with the long side vertical as well as horizontal, and in a small-diameter tube. Supporting data are provided from the studies of Fukano et al. (1989), for small diameter tubes. It remains to be shown whether RMS pressure measurements made with similar flows in larger horizontal channels and in both small and large vertical channels, exhibit the same characteristics that can be correlated with the transition to slug flow pattern.

Acknowledgments

The authors thank Mr. R. K. Smith and Ms. J. A. Stephens for their important contributions to this effort. This work was supported by the U.S. Department of Energy, Office of Conservation and Renewable Energy, Division of Advanced Industrial Concepts, and represents a U.S. contribution to the International Energy Agency (IEA) program on Research and Development in Heat Transfer and Heat Exchangers.

References

Damianides, C., and Westwater, J. W., 1988, "Two-Phase Flow Patterns in a Compact Heat Exchanger and in Small Tubes," *Proceedings of the 2nd United Kingdom National Conference on Heat Transfer*, Glasgow, Scotland, Vol. II, pp. 1257–1268.

Fukano, T., Kariyasaki, A., and Kagawa, M., 1989, "Flow Patterns and Pressure Drop in Isothermal Gas-Liquid Concurrent Flow in a Horizontal Capillary Tube," *American Nuclear Society Proceedings 1989 National Heat Transfer Conference*, Vol. 4, pp. 153–161.

Govier, G. W., Radford, B. A., and Dunn, J. S. C., 1957, "The Upwards Vertical Flow of Air-Water Mixtures," *Canadian Journal of Chemical Engineering*, pp. 58–70.

Govier, G. W., and Short, W. L., 1958, "The Upward Vertical Flow of Air-Water Mixtures," *Canadian Journal of Chemical Engineering*, pp. 195–202.

Hubbard, M. G., and Dukler, A. E., 1966, "The Characterization of Flow Regimes for Horizontal Two-Phase Flow," *Proceedings of 1966 Heat Transfer and Fluid Mechanics Institute*, Stanford University Press, pp. 100–121.

Jones, O. C., and Zuber, N., 1975, "The Interrelation Between Void Fraction Fluctuations and Flow Patterns in Two-Phase Flow," *International Journal of Multiphase Flow*, Vol. 2, pp. 273–306.

Kelessidis, V. C., and Dukler, A. E., 1989, "Modeling Flow Pattern Transitions for Upward Gas-Liquid Flow in Vertical Concentric and Eccentric Annuli," *International Journal of Multiphase Flow*, Vol. 15(2), pp. 173–191.

Lin, P. Y., and Hanratty, T. J., 1987, "Detection of Slug Flow From Pressure Measurements," *International Journal of Multiphase Flow*, Vol. 13, pp. 13–21.

Nishikawa, K., Sekoguchi, K., and Fukano, T., 1969, "On the Pulsation Phenomena in Gas-Liquid Two-Phase Flow," *Bulletin of the Japanese Society of Mechanical Engineers*, Vol. 12(54), pp. 1410–1416.

Ruder, Z., and Hanratty, T. J., 1990, "A Definition of Gas-Liquid Plug Flow in Horizontal Pipes," *International Journal of Multiphase Flow*, Vol. 16(2), pp. 233–242.

Sadatomi, M., Sato, Y., and Saruwatari, S., 1982, "Two Phase Flow in Vertical Noncircular Channels," *International Journal of Multiphase Flow*, Vol. 6, pp. 641–655.

Taitel, Y., and Dukler, A. E., 1976, "A Model for Predicting Flow Regime Transitions in Horizontal and Near Horizontal Gas-Liquid Flow," *American Institute of Chemical Engineers Journal*, Vol. 22(1), pp. 47–55.

Taitel, Y., Bornea, D., and Dukler, A. E., 1980, "Modelling Flow Pattern Transitions for Steady Upward Gas-Liquid Flow in Vertical Tubes," *American Institute of Chemical Engineers Journal*, Vol. 26(3), pp. 345–354.

Vince, M. A., and Lahey, R. T., Jr., 1982, "On the Development of an Objective Flow Regime Indicator," *International Journal of Multiphase Flow*, Vol. 8(2), pp. 93–124.

Wambsganss, M. W., Jendrzejczyk, J. A., France, D. M., and Obot, N. T., 1990, "Two-Phase Flow Patterns and Frictional Pressure Gradients in a Small Rectangular Channel: A Comparison Between Two Horizontal Orientations," Argonne National Laboratory Report, ANL-90/46.

Wambsganss, M. W., Jendrzejczyk, J. A., France, D. M., 1991, "Two-Phase Flow Patterns and Transitions in a Small, Horizontal, Rectangular Channel," *International Journal of Multiphase Flow*, Vol. 17(3), pp. 327–342.

Wambsganss, M. W., Jendrzejczyk, J. A., France, D. M., and Obot, N. T., 1992, "Frictional Pressure Gradients in Two-Phase Flow in a Small Horizontal Rectangular Channel," *Experimental Thermal and Fluid Science*, Vol. 5, pp. 40–56.

Weisman, J., Duncan, O., Gibson, J., and Crawford, T., 1979, "Effects of Fluid Properties and Pipe Diameter in Two-Phase Flow Patterns in Horizontal Lines," *International Journal of Multiphase Flow*, Vol. 5, pp. 437–462.

A. J. Chamkha
Assistant Professor,
Department of Mechanical Engineering,
Kuwait University,
Safat 13060 Kuwait
Mem. ASME

J. Peddieson, Jr.
Professor,
Department of Mechanical Engineering,
Tennessee Technological University,
Cookeville, TN 38505

Boundary Layer Theory for a Particulate Suspension

Order of magnitude considerations are employed to develop boundary layer equations for two phase particle/fluid suspension flows. It is demonstrated that a variety of possibilities exist and three of these are examined in detail. Two are applied to the problem of flow past a semi-infinite flat plate.

Introduction

This paper is concerned with boundary layer theory for a particulate suspension. Given the importance of boundary layers in applications, this topic has received surprisingly little attention. There is a history of work on the problem of the steady laminar boundary layer on a semi-infinite flat plate with recent contributions by Osiptsov (1980), Prabha and Jain (1980), and Wang and Glass (1988). References to earlier work can be found in these papers. In contrast to investigations of the flat plate and a few other specific geometries, there appears to have been little effort devoted to determining the general form of boundary layer equations. The present paper deals with this topic.

A boundary layer order of magnitude analysis is carried out using a typical set of two fluid equations representative of the current literature. It is found that a variety of outcomes are possible depending on the order of magnitude assumptions selected. Three of the most interesting cases are singled out for explicit presentation. Some specific numerical results are then given for the problem of steady laminar boundary layer flow past a semi-infinite flat plate. It is shown that the boundary layer model employed greatly influences predictions.

Governing Equations

The boundary layer analysis to be described in the present work is based on the following typical set of two phase flow equations.

$$\partial_t\phi-\nabla\cdot((1-\phi)\mathbf{v}_c)=0,\quad \partial_t\phi+\nabla\cdot(\phi\mathbf{v}_d)=0 \qquad (1)$$

represent respective balances of mass for the fluid and particulate phases (with the true densities of both phases assumed constant). In Eqs. (1) ∇ is the gradient operator, t is time, ϕ is the particulate volume fraction, $\mathbf{v}_c$ is the fluid phase velocity vector, and $\mathbf{v}_d$ is the particulate phase velocity vector.

$$\rho_c(1-\phi)(\partial_t\mathbf{v}_c+\mathbf{v}_c\cdot\nabla\mathbf{v}_c)=\nabla\cdot\underline{\underline{\sigma}}_c-\mathbf{f}$$

$$\rho_d\phi(\partial_t\mathbf{v}_d+\mathbf{v}_d\cdot\nabla\mathbf{v}_d)=\nabla\cdot\underline{\underline{\sigma}}_d+\mathbf{f} \qquad (2)$$

represent respective balances of linear momentum for the fluid and particulate phases (with external body forces neglected). In Eqs. (2) ρ_c is the fluid true density, ρ_d is the particulate true density, $\underline{\underline{\sigma}}_c$ is the fluid phase stress tensor, $\underline{\underline{\sigma}}_d$ is the particulate phase stress tensor, and $\mathbf{f}$ is the interphase force per unit volume acting on the particulate phase. The balance laws discussed above will be supplemented by the constitutive equations

$$\underline{\underline{\sigma}}_c=-(1-\lambda\phi)p\underline{\underline{I}}+2\mu_c(1-\phi)\underline{\underline{D}}_c;\quad \underline{\underline{D}}_c=(\nabla\mathbf{v}_c+\nabla\mathbf{v}_c^T)/2$$

$$\underline{\underline{\sigma}}_d=-(\lambda\phi p+q)\underline{\underline{I}}+2\mu_d\phi\underline{\underline{D}}_d;\quad \underline{\underline{D}}_d=(\nabla\mathbf{v}_d+\nabla\mathbf{v}_d^T)/2$$

$$\mathbf{f}=\rho_d\phi\mathbf{v}_r/\tau+\lambda p\nabla\phi;\quad \mathbf{v}_r=\mathbf{v}_d-\mathbf{v}_c \qquad (3)$$

where p is the indeterminate pressure, q is the particulate phase dynamic pressure, λ is a coefficient which determines the apportionment of the indeterminate pressure gradient between the phases (see below), μ_c and μ_d are dynamic viscosity coefficients, τ is the interphase relaxation time, $\underline{\underline{I}}$ is the unit tensor, and a superposed T indicates the transpose of a second order tensor. In general q, λ, μ_c, μ_d, and τ are functions of such quantities as ϕ, v_r, and the invariants of $\underline{\underline{D}}_c$ and $\underline{\underline{D}}_d$.

The following brief comments about Eqs. (3) are in order. The forms of Eqs. (3*b*,*c*) should be such that Eq. (2*b*) will reduce to the Eulerian form of the equation of motion for a single particle when the volume fraction is sufficiently small. Angular momentum considerations do not require that $\underline{\underline{\sigma}}_c$ and $\underline{\underline{\sigma}}_d$ be individually symmetric but do require that the combination $\underline{\underline{\sigma}}_c+\underline{\underline{\sigma}}_d$ be symmetric (in the absence of body moments). Several particle phase stress mechanisms have been proposed. These include direct contact between particles, wall effects, local particle deformations, and the consequences of the averaging required to model a system containing discrete particles as a continuum. The precise forms of λ, μ_c, μ_d, and q are model dependent. In the present work it is not necessary to restrict attention to a specific model and this has not been done.

The focus of the present paper is on laminar flow. The inclusion of $\underline{\underline{D}}_c$ and $\underline{\underline{D}}_d$ in the list of arguments given above formally allows Eqs. (3) to include algebraic turbulence models. It is highly doubtful, however, that such models are sufficiently inclusive to simulate two phase turbulence under any but the simplest conditions.

Contributed by the Fluids Engineering Division for publication in the JOURNAL OF FLUIDS ENGINEERING. Manuscript received by the Fluids Engineering Division May 7, 1992; revised manuscript received March 18, 1993. Associate Technical Editor: M. W. Reeks.

Equations (2) and (3) are representative of several models which have appeared in the literature such as those discussed by Marble (1970), Ungarish and Greenspan (1983), Gidaspow (1986), Ungarish (1988), Foscolo et al. (1989), Tsuo and Gidaspow (1990), Ham et al. (1990), Ganser and Lightbourne (1991), Foscolo et al. (1991), and McCarthy (1991). These equations are, however, by no means meant to be all inclusive. In fact, several important phenomena (lift, added mass, and gravity, for example) have been purposely omitted in order to create a model containing only the most fundamental two phase flow effects. It is felt that a good understanding of this case is essential to establish a baseline for future studies of more complicated models. The omission of a given physical effect should not be interpreted as a statement that this effect is always negligible in boundary layer situations.

The primary purpose of the present work is to illustrate the variety of boundary layer equations that can be produced by different order of magnitude assumptions. For this reason, attention will be confined herein to a relatively simple case. It will be assumed that the boundary layer exists on a flat wall and can be characterized by free stream velocity v_∞, pressure p_∞, and volume fraction ϕ_∞ and a characteristic length L. It will further be assumed that q, μ_c, μ_d, and τ are functions only of ϕ and that λ is constant (either zero or unity). Finally, attention will be confined to steady flow. Extension to more complicated cases is straightforward.

Let x and y be respective coordinates tangent and normal to the surface and $\nu_c=\mu_c/\rho_c$ and $\nu_d=\mu_d/\rho_d$ be kinematic viscosities. The Reynolds number is defined to be

$$N_1=Lv_\infty/\nu_c(\phi_\infty)=1/\epsilon^2 \tag{4}$$

Let

$$x=Ls,\ y=\epsilon Ln,\ p=\rho_c v_\infty^2 H(s,n),\ q=\rho_c v_\infty^2 J(\phi),\ \phi=\phi_\infty Q(s,n)$$
$$\mathbf{v}_c=v_\infty(\mathbf{e}_x U_c(s,n)+\mathbf{e}_y\epsilon V_c(s,n))$$
$$\mathbf{v}_d=v_\infty(\mathbf{e}_x U_d(s,n)+\mathbf{e}_y\epsilon V_d(s,n)) \tag{5}$$

with $\mathbf{e}$ denoting a unit vector. Substituting Eqs. (5) into Eqs. (1-3), combining the results, and rearranging leads to the equations

$$\partial_s((1-\phi_\infty Q)U_c)+\partial_n((1-\phi_\infty Q)V_c)=0$$
$$\begin{aligned}&(1-\phi_\infty Q)(U_c\partial_s U_c+V_c\partial_n U_c)+(1-\lambda\phi_\infty Q)\partial_s H\\&\quad+N_2\phi_\infty QC_2(U_c-U_d)-(\epsilon^2\partial_s((1-\phi_\infty Q)C_1(2\partial_s U_c+\partial_n V_c))\\&\quad\quad+\partial_n((1-\phi_\infty Q)C_1\partial_n U_c))=0\end{aligned}$$
$$\begin{aligned}&\epsilon^2(1-\phi_\infty Q)(U_c\partial_s V_c+V_c\partial_n V_c)+(1-\lambda\phi_\infty Q)\partial_n H\\&\quad+\epsilon^2 N_2\phi_\infty QC_2(V_c-V_d)-\epsilon^2(\epsilon^2\partial_s((1-\phi_\infty Q)C_1\partial_s V_c)\\&\quad\quad+\partial_n((1-\phi_\infty Q)C_1(\partial_s U_c+2\partial_n V_c)))=0\end{aligned} \tag{6}$$

for the fluid phase and

$$\partial_s(QU_d)+\partial_n(QV_d)=0$$
$$\begin{aligned}&Q(U_d\partial_s U_d+V_d\partial_n U_d)+(\lambda Q\partial_s H+C_3\partial_s Q)/N_2\\&\quad+QC_2(U_d-U_c)-(\epsilon^2\partial_s(QC_4 2\partial_s U_d+\partial_n V_d))\\&\quad\quad+\partial_n(QC_4\partial_n U_d))=0\end{aligned}$$
$$\begin{aligned}&\epsilon^2 Q(U_d\partial_s V_d+V_d\partial_n V_d)+(\lambda Q\partial_n H+C_3\partial_n Q)/N_2\\&\quad+\epsilon^2 QC_2(V_d-V_c)-\epsilon^2(\epsilon^2\partial_s(QC_4\partial_s+V_d)\\&\quad\quad+\partial_n(QC_4(\partial_s U_d+2\partial_n V_d)))=0\end{aligned} \tag{7}$$

for the particle phase. In Eqs. (6) and (7)

$$\begin{aligned}&C_1(Q)=\nu_c(\phi_\infty Q)/\nu_c(\phi_\infty),\ C_2(Q)=L/(v_\infty\tau(\phi_\infty Q))\\&\quad C_3(Q)=J'(\phi_\infty Q),\ C_4(Q)=\nu_d(\phi_\infty Q)/\nu_c(\phi_\infty)\end{aligned} \tag{8}$$

are functions of the normalized volume fraction Q and

$$N_2=\rho_d/\rho_c \tag{9}$$

is the true density ratio. A prime denotes the derivative of a function of one variable with respect to its argument. It can be seen from Eqs. (6) and (7) that if $\lambda=0$ the entire indeterminate pressure gradient is assigned to the fluid phase while if $\lambda=1$ it is shared between the two phases in proportion to their volume fractions. Both of these formulations have appeared in the literature. Equations (6) and (7) form the basis for the order of magnitude analysis to be carried out in the next section.

Most of the dimensionless quantities appearing in this paper do not have well established names at present. A consistent notation has, therefore, been adopted in which all dimensionless functions are denoted by C's and all dimensionless numbers are denoted by N's. It is hoped that the reader will not find this notation confusing. The function C_1 is a measure of the variation of fluid phase viscosity with volume fraction. The function C_2 is a measure of the variation of relaxation effects with volume fraction. It can be viewed as the ratio of the characteristic time L/v_∞ to the relaxation time of a homogeneous particle phase released with speed v_∞ in a fluid held at rest. Microscopic models indicate that C_2 is proportional to the ratio of L to a characteristic particle dimension. While this ratio is large, the coefficient of proportionality can realistically take on any magnitude (depending on flow geometry and flow conditions). Thus, C_2 is not necessarily large. The function C_3 plays the role of a bulk modulus of compressibility for the particle phase. The function C_4 is a measure of the variation of particle phase viscosity with volume fraction. In some models (see, for instance, Soo (1967)) an identification is made between the particle phase kinematic viscosity and the particle phase diffusion coefficient (see below). If this is done, C_4 becomes the local inverse Schmidt number.

Order of Magnitude Analysis

Boundary layer equations are found by taking the limits of Eqs. (6) and (7) as $\epsilon\to 0$. This will be done herein assuming that $C_1=O(1)$ and $C_4=O(1)$ (thus omitting, for the sake of concreteness, many interesting possibilities at the outset) but leaving the magnitudes of C_2 and C_3 arbitrary. Then the mass balances (6*a*) and (7*a*) remain

$$\partial_s((1-\phi_\infty Q)U_c)+\partial_n((1-\phi_\infty Q)V_c)=0$$
$$\partial_s(QU_d)+\partial_n(QV_d)=0; \tag{10}$$

Eqs. (6*b*) and (7*b*) yield the tangential linear momentum balances

$$\begin{aligned}&(1-\phi_\infty Q)(U_c\partial_s U_c+V_c\partial_n U_c)\\&\quad+(1-\lambda\phi_\infty Q)\partial_s H+N_2\phi_\infty QC_2(U_c-U_d)\\&\quad\quad-\partial_n((1-\phi_\infty Q)C_1\partial_n U_c)=0\end{aligned}$$
$$\begin{aligned}&Q(U_d\partial_s U_d+V_d\partial_n U_d)+(\lambda Q\partial_s H+C_3\partial_s Q)/N_2+QC_2(U_d-U_c)\\&\quad-\partial_n(QC_4\partial_n U_d)=0;\end{aligned} \tag{11}$$

and Eqs. (6*c*) and (7*c*) yield the normal linear momentum balances

$$\partial_n H+\epsilon^2 N_2\phi_\infty QC_2(V_c-V_d)/(1-\lambda\phi_\infty Q)=0$$
$$\begin{aligned}&C_3\partial_n Q+\epsilon^2 N_2(Q(U_d\partial_s V_d+V_d\partial_n V_d+C_2(V_d-V_c)/(1-\lambda\phi_\infty Q))\\&\quad-\partial_n(QC_4(\partial_s U_d+2\partial_n V_d)))=0\end{aligned} \tag{12}$$

The terms multiplied by ϵ^2 in Eqs. (12) have been retained to allow for a variety of orders of magnitude of C_2 and C_3. Three interesting cases will be discussed below.

The first situation to be considered is

$$C_2=O(1),\ C_3=O(1) \tag{13}$$

Then taking the limit of Eqs. (12) as $\epsilon\to 0$ and solving the resulting equations yields

$$H=H_\infty(s),\ Q=Q_\infty(s) \tag{14}$$

where H_∞ and Q_∞ are, respectively, the values of H and Q at the edge of the boundary layer (as determined from an inviscid analysis). Now Eqs. (10) and the results of substituting Eqs. (14) into Eqs. (11) constitute four equations in which H, Q, C_1, C_2, C_3, and C_4 are known functions of s and the dependent variables are U_c, V_c, U_d, and V_d. The equations for each phase closely resemble the boundary layer equations for single phase flow. That is the primary reason for selecting order of magnitude assumptions (13) for attention.

A second situation of interest is that of

$$C_2 = \mathrm{O}(1),\ C_3 = \mathrm{O}(\epsilon^2) \qquad (15)$$

Then the limit of Eq. (12*a*) can be taken as $\epsilon \rightarrow 0$ to yield Eq. (14*a*). This, in turn, renders determinate the terms in Eqs. (11) involving H. For convenience, let

$$C_3 = \epsilon^2 C_5/N_2;\ C_5 = C_5(Q) = \mathrm{O}(1) \qquad (16)$$

Substituting Eq. (16) into Eqs. (11*b*) and (12*b*), dividing the latter by ϵ^2, and taking the limits as $\epsilon \rightarrow 0$ produces, respectively,

$$Q(U_d\partial_s U_d + V_d\partial_n U_d) + QC_2(U_d - U_c) - \partial_n(QC_4\partial_n U_d) = 0$$
$$Q(U_d\partial_s V_d + V_d\partial_n V_d) + C_5\partial_n Q + QC_2(V_d - V_c)/(1 - \lambda\phi_\infty Q) - \partial_n(QC_4(\partial_s U_d + 2\partial_n V_d)) = 0 \qquad (17)$$

Now Eqs. (10), (11*a*), and (17) are a set of five equations in which H is a known function of s and the dependent variables are U_c, V_c, U_d, V_d, and Q. It should be pointed out that the particle phase normal momentum balance appears as one of the equations to be solved. This phenomenon (somewhat unusual in boundary layer formulations) is also a feature of the dusty gas model discussed by Marble (1970) (and often employed when the volume fraction of particulate material is expected to be small). The boundary layer theory associated with order of magnitude assumptions (15) can, therefore, be thought of as a generalization of dusty gas boundary layer theory to account for finite volume fractions. This is the primary reason for interest in these order of magnitude assumptions.

The third situation to be discussed herein is that of

$$C_2 = \mathrm{O}(1/\epsilon^2),\ C_3 = \mathrm{O}(1) \qquad (18)$$

To avoid obtaining a singular limit under these circumstances one must add Eq. (11*a*) to $\phi_\infty N_2 \times$ Eq. (11*b*), add Eq. (12*a*) to $\phi_\infty N_2 \times$ Eq. (12*b*), then take the limit of the results as $\epsilon \rightarrow 0$ to get, respectively,

$$(1 - \phi_\infty Q)(U_c\partial_s U_c + V_c\partial_n U_c) + \phi_\infty N_2 Q(U_d\partial_s U_d + V_d\partial_n U_d) + \partial_s(H + J) - \partial_n((1 - \phi_\infty Q)C_1\partial_n U_c + \phi_\infty N_2 QC_4\partial_n U_d) = 0$$
$$\partial_n(H + J) = 0 \qquad (19)$$

where Eq. (8*c*) has been used. Equation (19*b*) can be solved to yield

$$H + J = H_\infty(s) + J(\phi_\infty Q_\infty(s)) \qquad (20)$$

Making the substitution

$$C_2 = (1 - \lambda\phi_\infty Q)C_3/(\epsilon^2 N_2 C_6);\ C_6 = C_6(Q) = \mathrm{O}(1) \qquad (21)$$

in Eqs. (11*b*) and (12*b*) and taking the limits of the results as $\epsilon \rightarrow 0$ yields, respectively,

$$U_d = U_c,\ V_d = V_c - C_6\partial_n(\ln Q) \qquad (22)$$

Substituting Eqs. (22) into Eq. (10*b*) and the combination of Eqs. (19*a*) and (20) produces the respective results

$$\partial_s(QU_c) + \partial_n(QV_c) - \partial_n(C_6\partial_n Q) = 0$$
$$(1 - \phi_\infty Q + N_2\phi_\infty Q)(U_c\partial_s U_c + V_c\partial_n U_c) + H_\infty{}'(s) + \phi_\infty C_3(\phi_\infty\partial_\infty(s))Q_\infty{}'(s) - (\partial_n(((1 - \phi_\infty Q)C_1 + \phi_\infty N_2 QC_4)\partial_n U_c) + \phi_\infty N_2 C_6\partial_n Q\partial_n U_c) = 0 \qquad (23)$$

Equations (10*a*) and (23) are a set of three equations with dependent variables U_c, V_c, and Q. Once these equations have been solved, U_d and V_d can be determined from Eqs. (22).

The boundary layer equations consistent with order of magnitude assumptions (18) represent a generalization of the usual convection/diffusion model of particle transport to account for a finite volume fraction. It is this feature that makes order of magnitude assumptions (18) of interest. Equations (22) are equivalent to the boundary layer forms of Fick's law of diffusion with a dimensionless diffusion coefficient C_6. In particular, if ν_c becomes constant as its argument becomes small, assuming $\phi_\infty << 1$ makes $C_1 = 1$ (from Eq. (8*a*)). Then Eqs. (10*a*) and (23) reduce to

$$\partial_s U_c + \partial_n V_c = 0,\ U_c\partial_s U_c + V_c\partial_n U_c + H_\infty{}'(s) - \partial_{nn} U_c = 0$$
$$U_c\partial_s Q + V_c\partial_n Q - \partial_n(C_6\partial_n Q) = 0 \qquad (24)$$

where Eq. (24*a*) has been used in Eq. (23*a*) to obtain Eq. (24*c*). Equations (24*a*,*b*) are the usual single phase boundary layer equations and Eq. (24*c*) is the usual convection/diffusion equation for a passive scalar.

It should be mentioned that the three special cases discussed above by no means exhaust all physically plausible possibilities. They were chosen both to illustrate the variety of possible formulations and because each has interesting features. It should also be recognized that the magnitude of some or all of the C's may vary significantly due to relatively modest changes in Q (see, for example, Gidaspow (1986) and Foscolo et al. (1991)). Under these circumstances there may be no single set of order of magnitude assumptions which is appropriate throughout the entire flow field. Then extreme care would be necessary in applying the concepts of boundary layer theory.

Flat Plate Boundary Layer

To illustrate the application of some of the equations developed in the previous section, attention will be directed to the flow past a semi-infinite flat plate subjected to zero pressure gradient with its leading edge at $(s,n) = (0,0)$. This problem is of both theoretical and practical interest in itself and, in addition, serves as a first approximation for many flow situations involving ducts and wings. In this case the inviscid flow is simply a uniform stream characterized by

$$U_{c,\infty} = U_{d,\infty} = 1,\ V_{c,\infty} = v_{d,\infty} = 0,\ H_\infty = 1,\ Q_\infty = 1 \qquad (25)$$

Since the convection/diffusion problem associated with flow past a flat plate is well known, attention will be confined herein to the first two boundary layer formulations discussed in the previous section.

First, consider a solution based on order of magnitude assumptions (13). Equations (14) will now read

$$H = Q = 1 \qquad (26)$$

Substituting Eq. (26*b*) into Eqs. (8) yields

$$C_1 = 1,\ C_2 = 1,\ C_3 = 0,\ C_4 = \nu_d/\nu_c = N_3 \qquad (27)$$

where the choice $L = v_\infty\tau$ has been used to get Eq. (27*b*) (since there is no natural characteristic length associated with flow past a semi-infinite flat plate). Equation (27*b*) illustrates the point made earlier that C_2 need not be large.

Substituting Eqs. (26) and (27) and the modified Blasius transformations

$$s = \xi/(1 - \xi),\ n = (2\xi/(1 - \xi))^{1/2}\eta$$
$$U_c = F_c(\xi,\eta),\ V_c = ((1 - \xi)/(2\xi))^{1/2}(G_c(\xi,\eta) + \eta F_c(\xi,\eta))$$
$$U_d = F_d(\xi,\eta),\ V_d = ((1 - \xi)/(2\xi))^{1/2}(G_d(\xi,\eta) + \eta F_d(\xi,\eta)) \qquad (28)$$

into Eqs. (10) and (11) yields

$$\partial_\eta G_c + F_c + 2\xi(1 - \xi)\partial_\xi F_c = 0$$
$$\partial_\eta G_d + F_d + 2\xi(1 - \xi)\partial_\xi F_d = 0$$
$$\partial_{\eta\eta} F_c - G_c\partial_\eta F_c - 2\xi(1 - \xi)F_c\partial_\xi F_c + 2N_4\xi(F_d - F_c)/(1 - \xi) = 0$$
$$N_3\partial_{\eta\eta} F_d - G_d\partial_\eta F_d - 2\xi(1 - \xi)F_d\partial_\xi F_d + 2\xi(F_c - F_d)/(1 - \xi) = 0 \qquad (29)$$

where

$$N_4 = N_1\phi_\infty/(1-\phi_\infty) = \rho_d\phi_\infty/(\rho_c(1-\phi_\infty)) \tag{30}$$

is the particle loading. The boundary and matching conditions employed to solve Eqs. (29) were

$$F_c(\xi,0)=0,\ G_c(\xi,0)=0$$

$$F_d(\xi,0)=N_5((1-\xi)/(2\xi))^{1/2}\partial_\eta F_d(\xi,0),\ G_d(\xi,0)=0$$

$$F_c(\xi,\eta)\rightarrow 1,\ F_d(\xi,\eta)\rightarrow 1 \text{ as } \eta\rightarrow\infty \tag{31}$$

where N_5 is a particle phase wall slip parameter. Equation (31*c*) allows for particle phase wall slip in a manner similar to that used in rarefied gas dynamics. In reality the particle phase wall slip velocity is controlled by a variety of physical effects such as sliding friction, rolling friction, the nature of particle/surface collisions, particle shapes, etc. It is not possible to model such effects with precision at present, but by adjusting the slip parameter N_5 it is at least possible to produce a wide variety of wall slip profiles. Equations (31*c*,*d*) should be dropped if particle phase viscosity is omitted from the model.

For the subsequent presentation of numerical results it is convenient to define the respective skin friction coefficients of the fluid and particulate phases as

$$C_c(\xi)=\partial_\eta F_c(\xi,0),\ C_d(\xi)=N_3\partial_\eta F_d(\xi,0) \tag{32}$$

and the respective displacement thickness coefficients of the fluid and particulate phases as

$$\Delta_c(\xi)=\int_0^\infty (1-F_c(\xi,\eta))d\eta,\ \Delta_d(\xi)=\int_0^\infty (1-F_d(\xi,\eta))d\eta \tag{33}$$

These parameters were selected (from many available) to illustrate parametric trends.

Numerical solutions of Eqs. (29) subject to Eqs. (31) were computed using an extension of the methodology described by Blottner (1970) to two phase flow. Some typical results are presented in Figs. 1-6. For these calculations N_5 was taken to be zero, thus eliminating particle phase wall slip.

Figures 1 and 2 show representative tangential velocity profiles. They illustrate the transition from frozen to equilibrium behavior which is a characteristic of two phase flows. Near $\xi=0$ the effect of interphase drag is negligible and each phase moves independently of the other (frozen flow). Near $\xi = 1$ the effect of interphase drag dominates and both phases move with the same speed (equilibrium flow). This type of transition is not confined to boundary layer flows but appears, in one form or another, in a variety of two phase flow situations.

Figures 3-6 present typical distributions of the displacement thickness and skin friction coefficients. To allow a transition from fluid/fluid behavior at small volume fractions to fluid/solid behavior at volume fractions close to maximum packing requires a particle phase viscosity function which increases rapidly with volume fraction. According to this interpretation, the results corresponding to the larger values of N_3 can be thought of as representing finite volume fraction situations.

It was possible to obtain numerical solutions to Eqs. (29) without difficulty for all parametric combinations attempted. The results presented in Figs. 1-6 are representative of these computations.

Second, consider a solution based on the order of magnitude assumptions (15) and the further assumptions $\phi \ll 1$, $\rho_d/\rho_c \gg 1$, and $\lambda=0$ (inherent in the dusty gas model discussed by Marble (1970)). Then making the normal assumptions that $\nu_c(\phi)$, $\nu_d(\phi)$, $\tau(\phi)$ and $J'(\phi)$ approach constants as their arguments approach zero (in Eqs. (8) and (16)) leads to Eqs. (27*a*,*b*,*d*) and

$$C_5 = J'/\epsilon^2 = N_6 \tag{34}$$

Using the assumptions mentioned at the beginning of this paragraph and substituting Eqs. (26*a*), (27*a*,*b*,*d*), (28), and (34) into Eqs. (10), (11*a*), and (17) yields

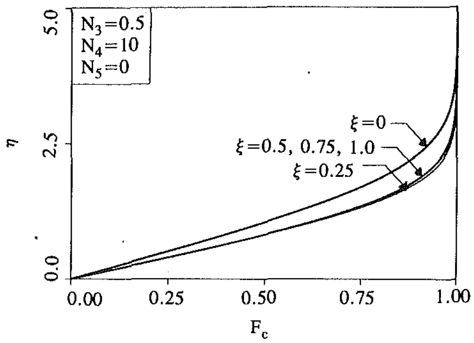

Fig. 1 Fluid phase tangential velocity profiles

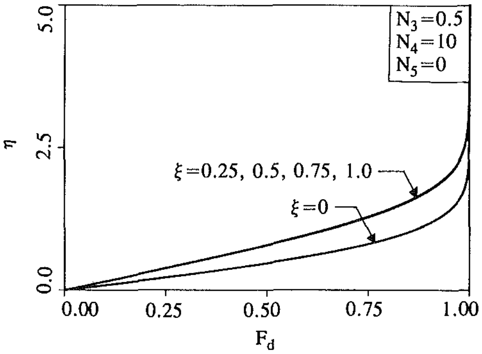

Fig. 2 Particle phase tangential velocity profiles

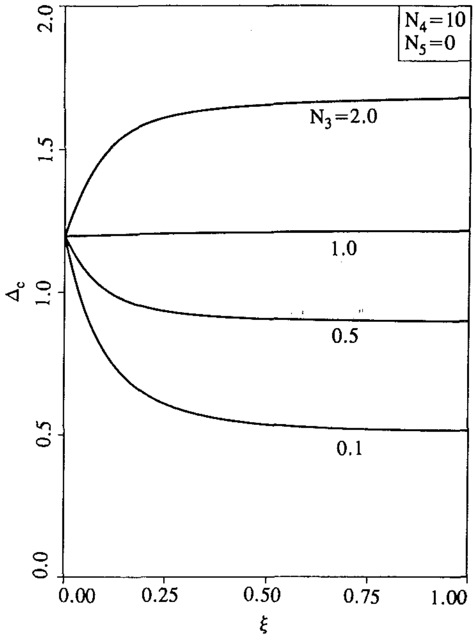

Fig. 3 Fluid phase displacement thickness coefficient versus position

$$\partial_\eta G_c + F_c + 2\xi(1-\xi)\partial_\xi F_c = 0$$

$$(\partial_\eta G_d + F_d + 2\xi(1-\xi)\partial_\xi F_d)Q + G_d\partial_\eta Q + 2\xi(1-\xi)F_d\partial_\xi Q = 0$$

$$\partial_{\eta\eta}F_c - G_c\partial_\eta F_c - 2\xi(1-\xi)F_c\partial_\xi F_c + 2N_4\xi Q(F_d - F_c)/(1-\xi) = 0$$

$$N_3(\partial_{\eta\eta}F_d + \partial_\eta(\ln\ Q)\partial_n F_d) - G_d\partial_\eta F_d - 2\xi(1-\xi)F_d\partial_\xi F_d + 2\xi(F_c - F_d)/(1-\xi) = 0$$

$$N_3(2(\partial_{\eta\eta}G_d + \partial_\eta(\ln Q)\partial_\eta G_d) + 3\partial_\eta F_d + \partial_\eta(\ln \mathrm{Q})F_d + 2\xi(1-\xi)(\partial_{\xi\eta}F_d + \partial_\xi(\ln\ Q)\partial_\eta F_d)) - G_d\partial_\eta G_d - 2\xi(1-\xi)F_d\partial_\xi G_d + \eta F_d^2 + 2\xi(G_c - G_d - N_6\partial_\eta(\ln Q))/(1-\xi) = 0 \tag{35}$$

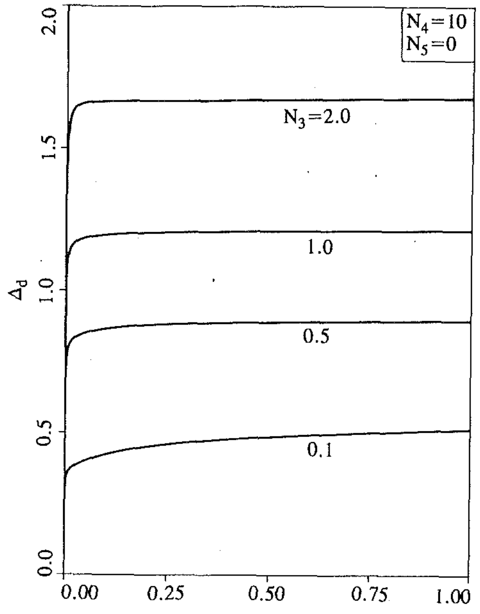

Fig. 4 Particle phase displacement thickness coefficient versus position

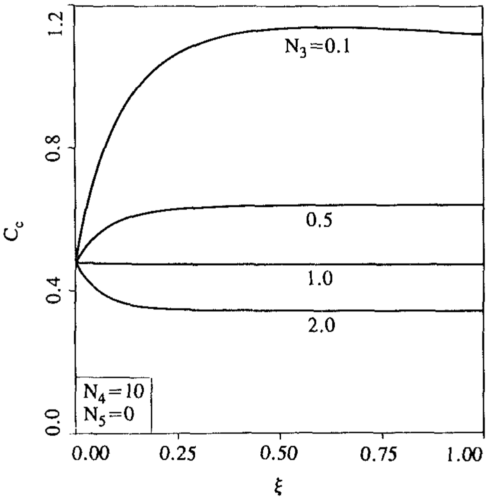

Fig. 5 Fluid phase skin friction coefficient versus position

where Eq. (30) for the particle loading now assumes the small volume fraction form $N_4 = \phi_\infty N_1 = 0(1)$. Equations (35) are to be solved subject to boundary and matching conditions (31) supplemented by

$$G_d(\xi,\eta)\rightarrow G_c(\xi,\eta),\ Q(\xi,\eta)\rightarrow 1 \text{ as } \eta\rightarrow\infty \qquad (36)$$

The dusty gas equations follow from Eqs. (35) by equating N_3 and N_6 to zero. Thus, Eqs. (35) generalize the dusty gas equations to allow for particulate phase stresses while retaining the small volume fraction assumption.

In contrast to the well-behaved nature of Eqs. (29), no combination of the parameters N_3, N_4, N_5, and N_6 was found for which a numerical solution to Eqs. (35) exhibited a positive bounded Q throughout the flow field. This phenomenon has already been observed by Osiptsov (1980), Prabha and Jain (1980), and Wang and Glass (1988) in their work using the dusty gas equations ($N_3 = N_6 = 0$) where Q always became infinite in the vicinity of $\xi = 0.5$. For all solutions attempted in the present work it was found that Q would either become extremely large or become negative somewhere in the range $0 < \xi < 1$. Many parametric combinations were tried without success.

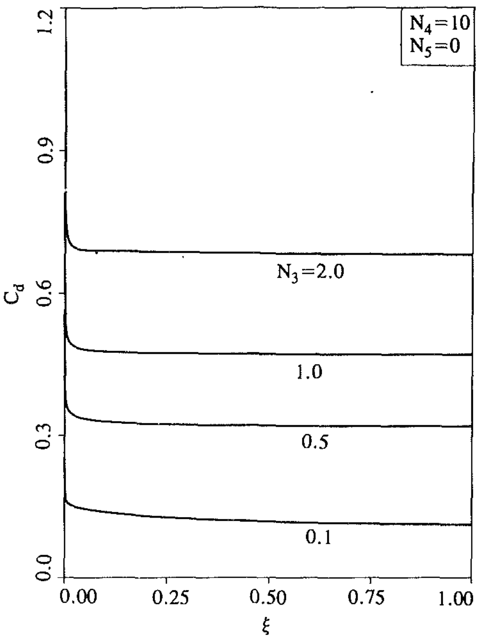

Fig. 6 Particle phase skin friction coefficient versus position

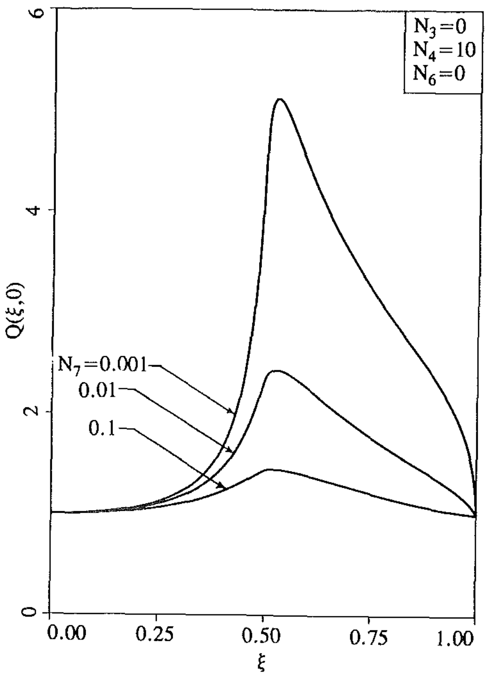

Fig. 7 Particle phase normalized wall volume fraction versus position

The addition of a fictitious diffusion term $N_7\partial_{\eta\eta}Q$ to the right-hand side of Eq. (35*b*) (and the imposition of an associated boundary condition $\partial_\eta Q(\xi,0) = 0$) was found to control the behavior of Q (as previously reported in a different context by Ungarish and Greenspan, 1983). This device was employed to obtain numerical solutions which could be used to illustrate the behavior observed. Some typical results are reported in Figs. 7-10.

Figures 7 and 8 present computations based on the dusty gas model. Figure 7 shows the approach of the wall volume fraction to singular behavior in the vicinity of $\xi = 0.5$ as the fictitious diffusion coefficient N_7 is reduced. For $N_7 = 0$ a continuous solution could not be found. Figure 8 exhibited corresponding values of the fluid phase skin friction coefficient. It can be seen that this quantity is only weakly influenced

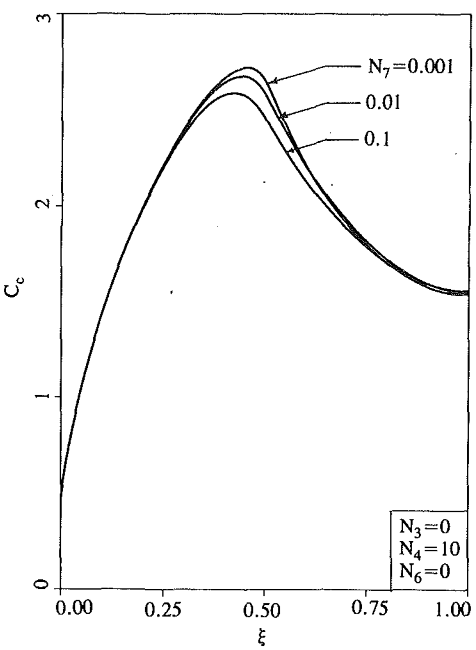

Fig. 8 Fluid phase skin friction coefficient versus position

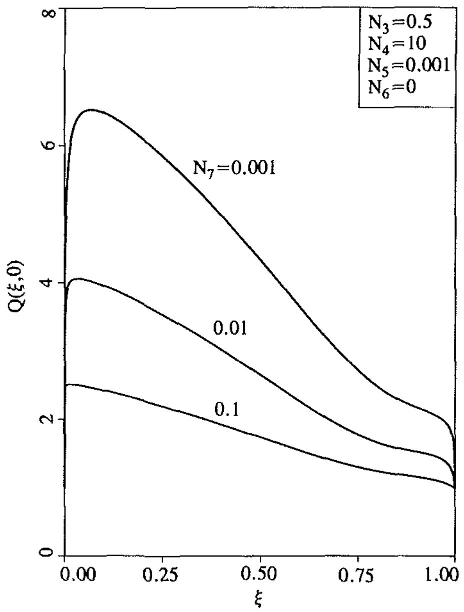

Fig. 9 Particle phase normalized wall volume fraction versus position

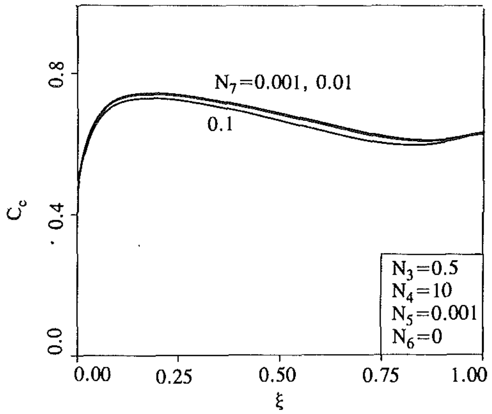

Fig. 10 Fluid phase skin friction coefficient versus position

by the value of N_7. This is typical of the behavior of all quantities other than Q.

Figures 9 and 10 show results which illustrate the influence of particle phase stresses. For these calculations a small value of N_5 was used, thus eliminating particle phase wall slip except in the immediate vicinity of the plate's leading edge. Figure 9 indicates the formation of a singularity in the wall volume fraction near the leading edge as N_7 reduced. For $N_7 = 0$ no solution was found. As in the situation discussed in the previous paragraph, the volume fraction was the only quantity found to be strongly affected by the value of N_7. This is illustrated by Fig. 10 in which the fluid phase skin friction coefficient is chosen as representative.

As mentioned previously, many important physical effects have been omitted from the model employed herein. Some of these may have an effect on the signular behavior reported above. This matter deserves to be pursued but was felt to be beyond the scope of the present work which was to discuss the structure of two phase boundary layer equations rather than give exhaustive results for a specific problem. (It should be mentioned that a few preliminary calculations indicated that the inclusion lift forces did not affect the existence of singularities.)

The singular behavior observed is probably indicative of the formation of a packed bed of particles (see, for instance, Soo, 1967) or a particle free zone (see, for instance, Young and Hanratty, 1991) near the plate surface. To predict either of these phenomena would require a model capable of dealing with the entire range of volume fractions. Since Eqs. (35) are based on the assumption that the volume fraction is small, it would appear better to base boundary layer calculations on a set of equations which allows for a finite volume fraction and to investigate effects omitted from the present model in that context. All that can be said with certainty at this point is that Eqs. (35) do not appear to admit self consistent solutions for the flat plate problem.

In the present work the term multiplied by N_7 was treated as a purely mathematical device employed to achieve the computational goal discussed above. It is referred to, therefore, as a fictitious diffusion term. It is interesting, however, to speculate on potential physical interpretations of this term. Some discussion of this matter is contained in the next two paragraphs.

It is possible that Figs. 7 and 9 are indicative of the strongly discontinuous behavior which can be exhibited by a medium devoid of pressure (see, for example, Kraiko, 1979, 1982). If so, fictitious diffusion could be interpreted as a device to smooth these discontinuities. This issue, while beyond the scope of the present work, is an interesting one which deserves to be pursued.

The effect of fictitious diffusion is to interest for two additional reasons. First, many numerical methods employ artificial diffusion either directly or indirectly (by upwind differencing, for example). It is possible, therefore, that such numerical methods could produce a bounded continuous solution to the problem of steady flow past a flat plate when, in fact, none should exist. Second, many two phase turbulence models (see, for example, Pourahmadi and Humphrey, 1983; Elghobashi et al., 1984; Chen and Wood, 1986; and Rizk and Elghobashi, 1989) contain diffusion terms in the particle phase mass balance. It is possible that the presence of such terms is critical to the existence of solutions in these models.

The results presented in this section show that physically plausible changes in fluid/particle suspension models can lead to significant qualitative (not just quantitative) changes in predictions. This makes clear the need for pertinent experimental data which can be used for model verification. The present authors were unable to locate any experimental work in the literature dealing with laminar flow of a particulate suspension past a flat plate. Such information, when it becomes available, will be quite useful in deciding the most fruitful directions for extension of the work reported herein.

Conclusion

In this paper the issue of developing boundary layer equations for fluid/particle two phase flows was addressed. It was shown that a variety of possibilities exist. This is, of course, a manifestation of the fact that the number of dimensionless parameters required to characterize the behavior of a two phase system is considerably greater than that required to characterize a single phase system. Three specific examples of boundary layer equations were given and related to previous work. Numerical solutions to the problem of flow past a semi-infinite flat plate subjected to zero pressure gradient were given based on two of the boundary layer formulations developed. It was shown that the predictions associated with the two formulations were quite different.

The present work was confined to plane steady flow past a flat surface. It is believed, however, that the basic findings reported herein are also relevant to flows involving such phenomena as unsteadiness, three dimensionality, and surface curvature. In addition, the results of this investigation should be directly applicable to other thin layer flows such as those occurring in ducts, jets, and wakes.

References

Blottner, F. G., 1970, "Finite Difference Methods of Solution of the Boundary-Layer Equations," *AIAA Journal*, Vol. 8, pp. 193-205.

Chen, C. P., and Wood, P. E., 1986, "Turbulence Closure Modeling of the Dilute Gas-Particle Axisymmetric Jet," *AIChE Journal*, Vol. 32, pp. 163-166.

Elghobashi, T., Abou-Arab, Rizk, M., and Mostafa, A., 1984, "Prediction of the Particle-Laden Jet with a Two-Equation Turbulence Model," *International Journal of Multiphase Flow*, Vol. 10, pp. 697-710.

Foscolo, P. U., Di Felice, R., and Gibilaro, L. G., 1989, "The Pressure Field in an Unsteady-State Fluidized Bed," *AIChE Journal*, Vol. 35, pp. 1921-1926.

Foscolo, P. U., Gibilaro, L. G., and Di Felice, R., 1991, "Hydrodynamic Scaling Relationships for Fluidization," *Applied Scientific Research*, Vol. 48, pp. 315-328.

Ganser, G. H., and Lightbourne, J. H., 1991, "Oscillatory Traveling Waves in a Hyperbolic Model of a Fluidized Bed," *Chemical Engineering Science*, Vol. 46, pp. 1339-1347.

Gidaspow, D., 1986, "Hydrodynamics of Fluidization and Heat Transfer: Supercomputer Modeling," *Applied Mechanics Reviews*, Vol. 39, pp. 1-23.

Ham, J. M., Thomas, S., Gauzzelli, E., Homsey, G. M., and Anselmet, M.-C., 1990, "An Experimental Study of the Stability of Liquid-Fluidized Beds," *International Journal of Multiphase Flow*, Vol. 16, pp. 171-185.

Kraiko, A. N., 1979, "On Discontinuity Surfaces in a Medium Devoid of Proper pressure'," *PMM*, Vol. 43, pp. 539-549.

Kraiko, A. N., 1982, "The Two-Fluid Model of Gas with Particles Dispersed in It," *PMM*, Vol. 46, pp. 75-82.

Marble, F. E., 1970, "Dynamics of Dusty Gases," *Annual Review of Fluid Mechanics*, Vol. 2, pp. 397-446.

Mc Carthy, M. F., 1991, "Shock Waves in a Particulate Suspsension," *Archive of Rational Mechanics and Analysis*, Vol. 115, pp. 167-178.

Osiptsov, A. N., 1980, "Structure of the Laminar Boundary Layer of a Disperse Medium on a Flat Plate," *Fluid Dynamics*, Vol. 15, pp. 512-517.

Pourahmadi, F., and Humphrey, J. A. C., 1983, "Modeling Solid-Fluid Turbulent Flows with Application to Predicting Erosive Wear," *Physico Chemical Hydrodynamics*, Vol. 4, pp. 191-219.

Prabha, S., and Jain, A. C., 1980, "On the Use of Compatibility Conditions in the Solution of Gas Particulate Boundary Layer Equations," *Applied Scientific Research*, Vol. 36, pp. 81-91.

Rizk, M. A., and Elghobashi, S. E., 1989, "A Two-Equation Turbulence Model for Dispersed Dilute Confined Two-Phase Flows," *International Journal of Multiphase Flow*, Vol. 15, pp. 119-133.

Soo, S. L., 1967, *Fluid Dynamics of Multiphase Systems*, Blaisdell Publishing Co., Waltham, Mass.

Tsuo, Y. P., and Gidaspow, D., 1990, "Computation of Flow Patterns in Circulating Fluidized Beds," *AIChE Journal*, Vol. 36, pp. 885-896.

Ungarish, M., and Greenspan, H. P., 1983, "On Two-Phase Flow in a Rotating Boundary Layer," *Studies in Applied Mathematics*, Vol. 69, pp. 145-175.

Ungarish, M., 1988, "Numerical Investigation of Two-Phase Rotating Flow," *International Journal of Multiphase Flow*, Vol. 14, pp. 729-747.

Wang, B. Y., and Glass, I. I., 1988, "Compressible Laminar Boundary-Layer Flows of a Dusty Gas Over a Semi-Infinite Flat Plate," *Jounral of Fluid Mechanics*, Vol. 186, pp. 223-241.

Young, J. B., and Hanratty, T. J., 1991, "Trapping of Solid Particles at a Wall in a Turbulent Flow," *AIChE Journal*, Vol. 37, pp. 1529-1536.

Numerical Simulation of Heavy Particle Dispersion—Scale Ratio and Flow Decay Considerations

Lian-Ping Wang[1]

David E. Stock

Department of Mechanical &
Materials Engineering,
Washington State University,
Pullman, WA 99164-2920

Lagrangian statistical quantities related to the dispersion of heavy particles were studied numerically by following particle trajectories in a random flow generated by Fourier modes. An experimental fluid velocity correlation was incorporated into the flow. Numerical simulation was performed with the use of nonlinear drag. The simulation results for glass beads in a nondecaying turbulent air showed a difference between the horizontal dispersion coefficient and vertical dispersion coefficient. This difference was related to the differences of both the velocity scale and the time scale between the two direction. It was shown that for relatively small particle sizes the particle time scale ratio dominates the value of the diffusivity ratio. For large particles, the velocity scale ratio reaches a value of $1/\sqrt{2}$ *and thus fully determines the diffusivity ratio. Qualitative explanation was provided to support the numerical findings. The dispersion data for heavy particles in grid-generated turbulences were successfully predicted by the simulation when flow decay was considered. As a result of the reduction in effective inertia and the increase in effective drift caused by the flow decay, the particle dispersion coefficient in decaying flow decreases with downstream location. The particle rms fluctuation velocity has a slower decay rate than the fluid rms velocity if the drift parameter is large. It was also found that the drift may substantially reduce the particle rms velocity.*

1 Introduction

Heavy particles are any small passive particles in the flow with a density much larger than the density of the fluid. Heavy particles have a free fall velocity that is of the order of the fluid rms velocity. We are interested in the dispersion process of heavy particles when suspended in and driven by turbulent flows. A knowledge of heavy particle dispersion is beneficial for improving energy conversion and reducing pollution. Lagrangian statistical quantities, calculated by following the random motion of a solid particle, are needed to understand the dispersion process, but they are difficult to obtain experimentally. However, numerical simulation can provide this information by tracking particles through a simulated turbulent flow. Since numerical simulation has a different set of limitations than a theoretical analysis, it can sometimes be used to test the applicability of analytical results. In this paper, we report on the results of a simulation of particle dispersion. Particular attention is paid to ratio of horizontal to vertical scales and effect of flow decay.

We consider the dispersion of heavy particles by turbulence, assuming the particulate phase mass loading is low and, therefore, the particles do not alter the flow. Earlier analytical approaches (Yudine, 1959; Csanady, 1963; Meek and Jones, 1973) have shown that the drift velocity of a particle due to an external body force greatly reduces the particle dispersion. The drift is also found to cause nonisotropic dispersion. Particles disperse more in the direction parallel to the drift velocity (the vertical direction) than in the directions normal to the drift (the horizontal directions). This is known as the continuity effect (Csanady, 1963). Reeks (1977), Pismen and Nir (1978), Nir and Pismen (1979) have simultaneously considered the effect of the particle inertia and the drift on the dispersion. However, their work has been limited to small particles for which Stokes' drag force applies, and to homogeneous, isotropic turbulence.

Particle dispersion in grid-generated turbulence has been experimentally measured by Snyder and Lumley (1971), Wells and Stock (1983), and Ferguson (1986). The experimental work qualitatively confirms the theoretical predictions. The grid-generated turbulence, while being the simplest experimental turbulent flow, is not homogeneous in the mean flow direction, since the turbulence decays due to viscous dissipation. Approximate quantitative comparison between the experimental data and the analytical predictions is possible by making a quasi-stationarity assumption (Nir and Pismen, 1979). Particle dispersion can also be predicted by direct numerical simulation (Riley and Paterson, 1974; Ueda et al., 1983, and Squires and Eaton, 1990), but this method is prohibitively time consuming and is limited to flows of low Reynolds numbers.

Kraichnan's method (1970) for simulating turbulence using Fourier modes is physically sound and computationally efficient. It is especially useful for particle dispersion studies since a large number of particle trajectories have to be computed.

---

[1] Current Address: Department of Mechanical Engineering, Pennsylvania State University, University Park, PA 16802.

Contributed by the Fluids Engineering Division for publication in the JOURNAL OF FLUIDS ENGINEERING. Manuscript received by the Fluids Engineering Division February 7, 1992; revised manuscript received March 18, 1993. Associate Technical Editor: M. W. Reeks.

This turbulence-simulation method has been used to test the analytical results of particle dispersion obtained by Eulerian direct interaction (Reeks, 1980) and to study the effect of Basset history force on particle dispersion (Reeks and McKee, 1984). The same model was used by Ferguson (1986) to simulate the effect of fluid continuity on heavy particle dispersion and by Maxey (1987) to calculate the average settling velocity of particles in a turbulent flow. Turfus and Hunt (1986) extended the model to inhomogeneous turbulence by adding an irrotational velocity field. The model has the potential to include the advection of small eddies by large eddies (Fung et al., 1992). Recently, Ounis and Ahmadi (1989) employed Kraichnan's model to study the relative importance of various forces acting on a solid particle and to find Lagrangian velocity moments. Wang and Stock (1992) studied the effect of nonlinear drag on the particle dispersion using the same numerical simulation techniques. They found that the nonlinear drag must be considered when calculating particle dispersion if the ratio of the drift velocity to the fluid rms fluctuating velocity is greater than two. They also compared the results of numerical simulations to those of an analytical calculation based on the second order iteration technique (Reeks, 1977). Among these studies, only Ounis and Ahmadi (1989) tried to compare the simulation results with experimental data.

The purpose of this study was to use numerical simulations based on Kraichnan's method to help us understand experimental data for heavy particle dispersion in the grid-generated turbulent flow (i.e., the data of Snyder and Lumley, 1971; Wells and Stock, 1983; and Ferguson, 1986). Particular attention was paid to the following two questions: 1) How does the diffusivity ratio (the ratio of particle dispersion coefficient in the horizontal direction to that in the vertical direction) change with particle size for glass beads in typical wind tunnel turbulence and how is the diffusivity ratio related to the velocity scale ratio and the integral time scale ratio? 2) What is the effect of the flow decay on the dispersion of heavy particles? The answer to the first question will help clarify the results of Ferguson (1986). The answer to the second question will allow us to compare the simulation results with the experimental data.

The paper is organized as follows. First, Kraichnan's model of turbulence generation is extended to allow various fluid velocity correlations to be used. Some programming techniques necessary for large drift velocity are then discussed. The results of numerical simulation for long-time dispersion statistics for glass beads in nondecaying turbulence are reported in Section 4. In Section 5, flow decay is considered and comparisons are made between the simulation results and the experimental data (Synder and Lumley, 1971; and Wells and Stock, 1983).

2 Structure of Simulated Turbulence

The flow field was represented by the following equation which is a linear superposition of a large number of Fourier modes with random amplitudes and phases (Kraichnan, 1970)

$$u_i(x_i,t)/u_0=\sum_{n=1}^{N}\{b_i^{(n)}\cos(k^{(n)}\cdot x+\omega^{(n)}t)+c_i^{(n)}\sin(k^{(n)}\cdot x+\omega^{(n)}t)\}. \quad (1)$$

Here N is the number of Fourier modes and u_0 is the rms fluctuation velocity. The mean velocity is zero, and the velocity field is understood to represent the velocity field in a frame of reference moving with the mean velocity of the flow (moving Eulerian frame or mE). For each n, values of $k_1^{(n)}$, $k_2^{(n)}$, $k_3^{(n)}$, and $\omega^{(n)}$ are chosen independently with probability density functions (pdf) $P_{11}(k_1)$, $P_{12}(k_2)$, $P_{13}(k_3)$ and $P_2(\omega)$, respectively. Real coefficients $b_i^{(n)}$ and $c_i^{(n)}$ are independent Gaussian random variables which have been filtered such that $b^{(n)}\cdot k^{(n)}$ and $c^{(n)}\cdot k^{(n)}$ vanish, to make the overall flow field incompressible. The ensemble averaged two-point correlation for this random flow field is (Maxey, 1987)

$$R_{ij}(r,\tau)/u_0^2=N\int_{-\infty}^{\infty}d^3k\int_{-\infty}^{\infty}d\omega \times P_{11}(k_1)P_{12}(k_2)P_{13}(k_3)P_2(\omega)\Gamma^2(k_1,\ k_2,\ k_3,\ \omega) \times\left[\delta_{ij}-\frac{k_ik_j}{k^2}\right]\cos(k\cdot r+\omega\tau). \quad (2)$$

where $\Gamma(k_1,\ k_2,\ k_3,\ \omega)$ is the scaling function.

Nomenclature

b_i, c_i = random coefficients
d_p = diameter of particle
$D(\tau)$ = one-point fluid velocity correlation in the moving Eulerian frame
$E(k)$ = scalar energy spectrum function
f = ratio of drag coefficient to Stokes drag
$f(r)$ = fluid longitudinal spatial velocity correlations
$g(r)$ = fluid transverse spatial velocity correlation
$F(\omega)$ = frequency spectrum
q = external body force acting on particle
k = wave number
k_0 = characteristic wave number
L_f = integral length scale of $f(r)$
M = grid spacing
N = number of Fourier modes
$P_{1i}(k_i)$ = probability density function of k_i
$P_2(\omega)$ = probability density function of ω
r = space separation
$R_{ij}(r,\tau)$ = fluid velocity correlation
Re_p = particle Reynolds number
St = Stokes number
t = time
T = integral time scale
u = flow velocity
u_0 = fluid rms fluctuation velocity
U = mean flow velocity
v = particle velocity
v_{i0} = particle rms fluctuation velocity
v_d = particle Stokes velocity = $\tau_a q$
v_{d0} = particle drift velocity in still fluid
x = Eulerian coordinate
x_0 = virtual origin of the grid-generated turbulence
y = particle's location
$\alpha(k_i)$ = see Eq. (4)
$\beta(\omega)$ = see Eq. (5)
δ_{ij} = Kronecker delta
ϵ_{ij}^p = particle dispersion coefficient tensor
γ = v_d/u_0
Γ = scaling function
μ = fluid viscosity
ρ = fluid density
ρ_p = particle density
τ = time delay
τ_a = particle aerodynamic response time
ω = frequency
ω_0 = characteristic frequency

Superscripts

(j) = jth mode

Subscripts

1 or 11 = horizontal direction
3 or 33 = vertical direction
fE = fixed Eulerian
i = ith component
L = Lagrangian
mE = moving Eulerian

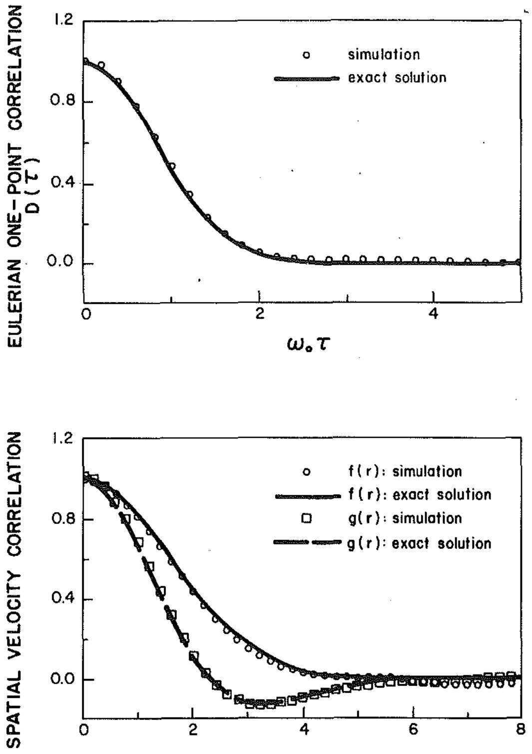

Fig. 1 Velocity correlations computed from the simulated turbulence with finite-modes ($N=80$), compared to the exact forms in Case I. 1800 realizations are used.

For homogeneous isotropic turbulence, the flow structure can be represented by the two functions, $D(\tau)$ and $E(k)$, (Wang and Stock, 1988). $D(\tau)$ is the one point velocity correlation and $E(k)$ is the scalar energy spectrum. For the sake of simplicity, the scaling function is assumed to have the following form,

$$N\Gamma^2(k_i,\omega)=\alpha(k_i)\beta(\omega). \qquad (3)$$

Further, the product of $\alpha(k_i)P_{11}(k_1)P_{12}(k_2)P_{13}(k_3)$ is chosen (this can always be done) to be a function of k only, where $k=\sqrt{(k_1^2+k_2^2+k_3^2)}$. Then the spatial energy spectrum is determined by $\alpha(k_i)$ and pdf's of wave number $k_i^{(n)}$ as

$$E(k)=4\pi u_0^2k^2P_{11}(k_1)P_{12}(k_2)P_{13}(k_3)\alpha(k_i). \qquad (4)$$

The frequency spectrum (the Fourier transform of $D(\tau)$) is related to $\beta(\omega)$ and the pdf of $\omega^{(n)}$ by

$$F(\omega)\equiv\frac{1}{\pi}\int_0^\infty D(\tau)\cos(\omega\tau)d\tau=\beta(\omega)P_2(\omega). \qquad (5)$$

The flow structure is prescribed by giving $E(k)$ and $D(\tau)$ and the scaling function Γ is specified as

$$\Gamma^2(k_i,\omega)=\frac{1}{N}\frac{E(k)}{4\pi u_0^2k^2P_{11}(k_1)P_{12}(k_2)P_{13}(k_3)}\frac{F(\omega)}{P_2(\omega)}. \qquad (6)$$

In other words, the scaling function Γ can be adjusted, according to the probability density functions of random numbers, to produce the proper Eulerian flow statistics. The choice for the pdf functions is not unique but is made to ensure a rapid convergence of fluid velocity correlations (or spectrum functions) for the simulated turbulence.

In all the previous papers (Maxey, 1987; Ferguson, 1986; Ounis and Ahmadi, Wang and Stock, 1992), the pdf functions are assumed to be Gaussian distributions with the scaling function Γ of the form

$$\Gamma(k_1,k_2,k_3,\omega)=\frac{k}{\sqrt{2N}k_0}. \qquad (7)$$

It follows that the spectrum function and the correlation function are

$$E(k)=\frac{u_0^2}{\sqrt{2\pi}}\frac{k^4}{k_0^5}\exp\left(-\frac{k^2}{2k_0^2}\right). \qquad (8)$$

$$D(\tau)=\exp(-\omega_0^2\tau^2/2). \qquad (9)$$

The random velocity field with this structure will be referred to as Case I turbulence. The longitudinal and transverse fluid spatial velocity correlations, $f(r)$ and $g(r)$, can be derived from (8) and are

$$f(r)=\exp(-k_0^2r^2/2), \qquad (10a)$$

$$g(r)=(1-k_0^2r^2/2)\exp(-k_0^2r^2/2). \qquad (10b)$$

In the simulation, a finite number of Fourier modes, N, was used for one realization of the flow. A separate flow realization was used to calculate each particle trajectory.

The fluid velocity correlations can be accurately reproduced by the simulated turbulence. Figure 1 shows the velocity correlations calculated from the simulated flow by averaging over 1800 flow realizations with $N=80$ for each realization. They all compare well to their exact forms.

The structure of many real turbulent flows is not described by Eqs. (8) and (9). Theoretically, the above simulation method can be used to generate flow fields with any turbulence structure functions by choosing proper pdf functions for the random numbers and proper scaling function. To show this and test how the shape of the correlation curves may affect particle dispersion, we introduce the following forms for the energy spectrum and the one-point Eulerian velocity correlation,

$$E(k)=\frac{3u_0^2}{2\pi}\frac{k^4}{k_0^5[1+k^2/(4k_0^2)]^4}, \qquad (11)$$

$$D(\tau)=\cos(\omega_0\tau)\exp(-\omega_0\tau) \qquad (12)$$

We will refer to the random velocity field with such a spectrum and correlation function as Case II turbulence. Consequently, the spatial velocity correlations are

$$f(r)=(1+2k_0r)\exp(-2k_0r), \qquad (13a)$$

$$g(r)=(1+2k_0r-2k_0^2r^2)\exp(-2k_0r). \qquad (13b)$$

The above forms of the temporal and the spatial velocity correlations have appeared in the literature (Townsend, 1976; Calabrese and Middleman, 1979; and Gouesbet et al., 1984).

To generate Case II turbulence, we need to select the proper pdf functions, $P_{1i}(k_i)$ and $P_2(\omega)$. When Gaussian distributions were used, the velocity correlations of the simulated flow were found to converge very slowly to the prescribed forms. The convergence was slow because the resulting scaling function was extremely large for large wave numbers (or frequencies), thus, the large wave numbers can not be quickly realized in the simulation. To avoid this, we used the Cauchy distributions,

$$P_{1i}(k_i)=\frac{1}{\pi k_0\left[1+\frac{k_i^2}{k_0^2}\right]} \qquad (14a)$$

$$P_2(\omega)=\frac{1}{\pi\omega_0\left[1+\frac{\omega^2}{\omega_0^2}\right]}. \qquad (14b)$$

Figure 2 shows the comparison between the velocity correlations obtained directly from the simulated flow and the exact forms. The comparison is satisfactory when 1800 realizations of 80 Fourier modes were used.

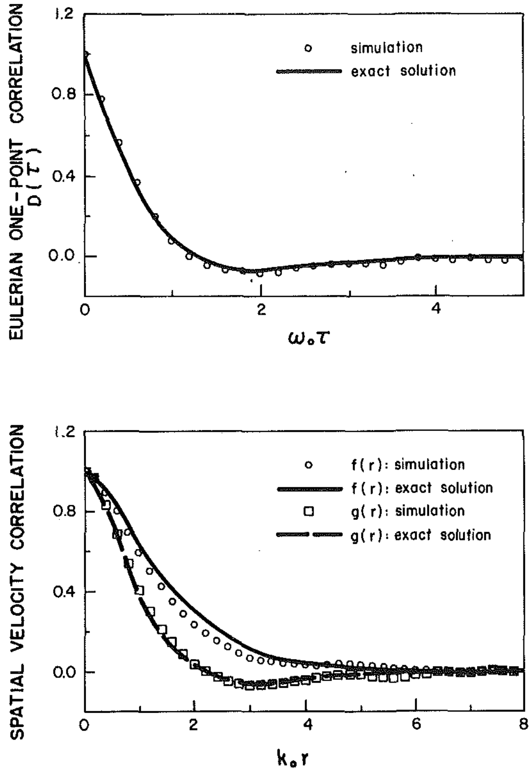

Fig. 2 Velocity correlations computed from the simulated turbulence with finite-modes ($N=80$), compared to the exact forms in Case II. 1800 *realizations are used.*

Comparing Case I turbulence and Case II turbulence, we find both spectrum functions, (8) and (11), achieve their maximum values at $k=2k_0$, but (11) has a relatively larger fraction of turbulence energy in the higher wave number portion. The integral length scales for $f(r)$ are: $L_f=1.2533/k_0$ for Case I, $L_f=1/k_0$ for Case II. The one-point velocity correlations, (9) and (12), have very different curvatures at $\tau=0$. (12) has negative loops for large decay time while (9) gives positive correlation for all τ. The integral time scale for $D(\tau)$ are: $T_{\mathrm{mE}}=1.2533/\omega_0$ for I, $T_{\mathrm{mE}}=0.5/\omega_0$ for II. The integral scales, T_{mE} and L_f, were set to the same value for the two cases so that results based on the two turbulences could be compared.

The simulated flow is governed by three parameters, i.e., u_0, T_{mE} (or ω_0), and L_f (or k_0). They are constant for a stationary (nondecaying) flow. If flow decays, they will change with time.

3 Programming Techniques

Some programming techniques used to ensure a successful simulation of the motion of heavy particles are discussed in this section. In our earlier paper (Wang and Stock, 1992), the equations of motion of a heavy particle

$$\frac{dv_i}{dt}=\frac{(u_i(y,t)-v_i)f}{\tau_a}+q\delta_{i3}, \tag{15}$$

$$\frac{dy_i}{dt}=v_i, \tag{16}$$

were numerically integrated by Hamming method, and the particle velocity, $v_i(t)$, and location, $y_i(t)$, were used to calculate the velocity correlations and mean square dispersions. Here q is the body force per unit mass, τ_a is the aerodynamic response time based on the Stokes drag. The factor f is the ratio of nonlinear drag coefficient to Stokes drag and is well represented for Reynolds number up to 1000 by the empirical relation (Rowe, 1961)

$$f=1+0.15\,\mathrm{Re}_p^{0.687}, \tag{17}$$

where Re_p is the particle Reynolds number. f/τ_a can be viewed as the drag force per unit mass per slip velocity acting on a moving particle.

When the drift parameter $\gamma=q\tau_a/u_0$ is large, the mean velocity of the particle in the vertical direction is much larger than the fluctuating velocity of the particle. Since the mean velocity was not known a priori, the computation of particle velocity correlations involved subtracting two large numbers, the mean square of particle velocity and the square of the mean velocity. The same situation is found when the mean square dispersion in the vertical direction is calculated. Therefore, for accurate results a very small time step size must be used.

To circumvent this difficulty, we can solve for the particle velocity relative to its drift velocity in still fluid v_{d0},

$$v_i'(t)=v_i(t)-\delta_{i3}v_{d0}. \tag{18}$$

v_{d0} is determined a priori from,

$$\frac{v_{d0}}{u_0}\left\{1+0.15\left[\frac{\rho d_p v_{d0}}{\mu}\right]^{0.687}\right\}=\gamma. \tag{19}$$

The drift velocity of a particle in the simulated turbulent flow is slightly larger than v_{d0} (Maxey, 1987), but the difference between the true drift and v_{d0} can be safely neglected (Wang and Stock, 1992). Therefore, the mean of $v_i'(t)$ should be close to zero. From (15) and (18), $v_i'(t)$ satisfies the following equation,

$$\frac{dv_i'(t)}{dt}=\frac{\{u_i(v_{d0}\delta_{i3}t+y_i'(t),t)-v_i'\}}{\tau_a}f(|u-v_{d0}\delta_{i3}-v'|)$$
$$-\{v_{d0}f(|u-v_{d0}\delta_{i3}-v'|)+\gamma u_0\}\delta_{i3}/\tau_a. \tag{20}$$

The last term of (20) is very small due to Eq. (19). $y_i'(t)$ is the particle displacement relative to the mean location of particle in still fluid,

$$y_i'(t)=y_i(t)-\delta_{i3}v_{d0}t. \tag{21}$$

The relative displacement is given by

$$\frac{dy_i'(t)}{dt}=v_i'(t) \tag{22}$$

Now Eqs. (20) and (22) are solved simultaneously instead of (15) and (16). the Lagrangian velocity correlations and mean square dispersion are calculated from the relative velocity and relative displacement. This change avoids subtracting two large numbers and improves the accuracy of the results. Using the new set of equations, we found that, in the case of large particle drift velocity, the strict requirements for time-step size noted in the earlier paper (Wang and Stock, 1992) can be substantially relaxed.

A second improvement in the program was to numerically integrate Eqs. (20) and (22) for a sufficiently long time so that about 10 realizations of particle Lagrangian velocity correlations were obtained from each realization of the flow field. This technique can only be used for nondecaying flow and was found to reduce the effect of initial conditions on the results. Most of the results for nondecaying flow were obtained using 500 realizations of the random flow field with each realization providing 10 independent trajectories.

4 Scale Ratios in a Nondecaying Flow

4.1 The Continuity Effect. Particle dispersion coefficient *is not isotropic due to the continuity effect, even if the carrying* flow is isotropic and homogeneous. The particle dispersion coefficient in the horizontal direction (normal to the drift) is less than the particle dispersion coefficient in the vertical direction (parallel to the drift). For a large drift velocity, the ratio of the horizontal dispersion coefficient to the vertical dispersion coefficient approaches one half (Csanady, 1963). The particle rms fluctuation velocity (the velocity scale) and

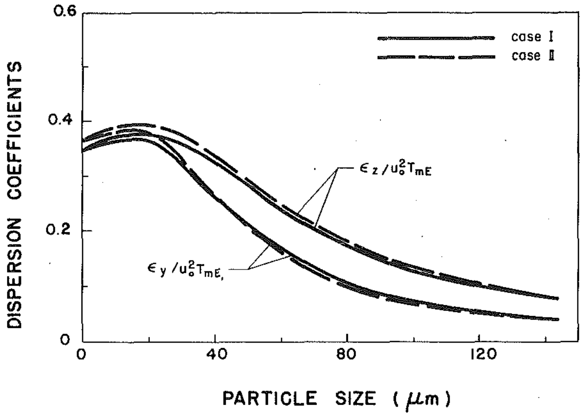

Fig. 3 Dispersion coefficients normalized by $\epsilon_0 = T_{\mathrm{mE}} u_0^2$ as a function of particle size. ϵ_z is the dispersion coefficient in the vertical direction, and ϵ_y is the dispersion coefficient in the horizontal direction.

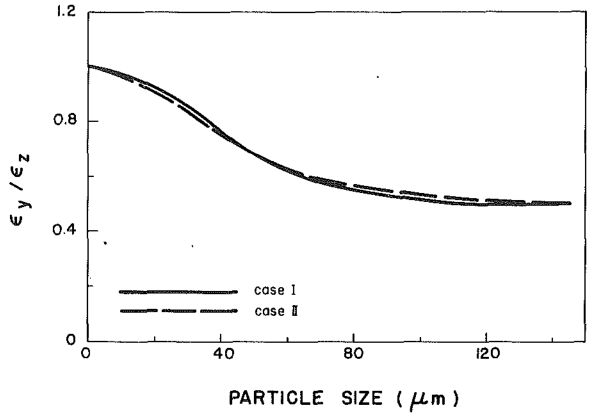

Fig. 4 Ratio of horizontal dispersion to vertical dispersion

the particle velocity-correlation time (the time scale) in the horizontal direction are also less than their respective values in the vertical direction (Reeks, 1977). Since the long-time dispersion coefficient is equal to the product of the velocity scale squared and the time scale, the diffusivity ratio, $\epsilon_{11}^p(\infty)/\epsilon_{33}^p(\infty)$, is related to the velocity scale ratio, v_{10}/v_{30}, and the time scale ratio, T_{11}/T_{33}, by

$$\frac{\epsilon_{11}^p(\infty)}{\epsilon_{33}^p(\infty)} = \left(\frac{v_{10}}{v_{30}}\right)^2 \times \frac{T_{11}}{T_{33}}, \tag{23}$$

where the subscript 1 (or 11) refers to the horizontal direction, and the subscript 3 (or 33) refers to the vertical direction.

Recently, Ferguson (1986) studied the continuity effect, using both numerical simulation and experimental measurements. His main consideration was the diffusivity ratio. His measurements showed the diffusivity ratio was close to one for 29 μm glass beads and the diffusivity ratio was close to a half for 62 μm glass beads. The experiment was not complete in the sense that the velocity scale ratio and time scale ratio were not considered. His simulation results verified the continuity effect on the diffusivity ratio and also showed that both the velocity scale ratio and time scale ratio were less than one. However, no comparison was made between his simulation and his measurements.

We can use numerical simulation to determine how the diffusivity ratio, the velocity scale ratio, and time scale ratio change with particle size for glass beads in grid-generated turbulence. In a real grid-generated turbulence, the flow scales change with time, so do the particle velocity scale and time scale. We postulate, however, that flow decay does not play a significant role in the scale ratios and diffusivity ratio. Based on this postulation, the scale ratios were simulated using a stationary (nondecaying) flow. Not considering flow decay in this section also facilitates the interpretation of results. To make possible a comparison between simulation results and Ferguson's experimental data, we used in the simulation the flow scales from the center of the test section in Ferguson's (1986) grid-generated turbulence. The flow scales were (see Appendix): $u_0 = 11.2$ cm/s, $T_{\mathrm{mE}} = 0.225$ s, $L_f = 1.75$ cm. Both Case I turbulence and Case II turbulence were considered in this simulation.

4.2 Simulation Results. We consider the dispersion of glass beads ($\rho_p = 2600$ kg/m^3) in turbulent air under the normal gravity. The fluid viscosity is 1.8×10^{-5} kg/m·s and the fluid density is 1.14 kg/m^3. With the above flow scales, the Stokes number, drift parameter, and particle Reynolds number are given as a function of particle size in micrometers by,

$$\mathrm{St} = \tau_a / T_{\mathrm{mE}} = 3.56 \times 10^{-5} d_p^2, \tag{24}$$

$$\gamma = \tau_a q / u_0 = 7.04 \times 10^{-4} d_p^2, \tag{25}$$

$$\mathrm{Re}_p = 7.1 \times 10^{-3} \left| \frac{u - v}{u_0} \right| d_p. \tag{26}$$

Figure 3 shows the simulation results for particle diffusivities, normalized by $T_{\mathrm{mE}} u_0^2$, as a function of particle size. The long-time particle diffusivity was calculated from the mean square dispersion curves. When the particle size approaches zero, the heavy particles reduce to fluid elements and the normalized particle diffusivities are the same in both vertical and horizontal directions and equal to T_L/T_{mE}. T_L is the fluid Lagrangian correlation time. From Fig. 3, T_L/T_{mE} is 0.35 for Case I turbulence and 0.37 for Case II turbulence. The slight difference in T_L/T_{mE} between the two turbulences is due to the different shapes of fluid velocity correlations. The effect of the shape of fluid correlations on the particle dispersion coefficient tends to disappear as the particle size increases. The ratio T_L/T_{mE} for Case I turbulence is about the same as the value predicted by the second-order-iteration approximation (Wang and Stock, 1992).

Interestingly, the dispersion coefficients increase slightly with particle size when particle size is small. Since $T_{\mathrm{mE}} > T_L$ in our simulation, the particle dispersion coefficient should increase with the inertia parameter in the absence of the drift (Reeks, 1977). On the other hand, the increase of the drift tends to reduce the particle dispersion coefficient due to the crossing trajectory effect. Because both the inertia and the drift increase with particle size, we have here the competing effects of inertia and drift on the particle dispersion coefficient. Our results imply that the inertia dominates the particle dispersion coefficient for the small size region. The dispersion coefficients reach maximum values at $d_p = 20$ μm, this is where the crossing trajectory effect offsets the inertia effect. Further increase in particle size causes rapid decrease in the particle diffusivities since the crossing trajectory effect controls the particle dispersion.

The diffusivity ratio is shown in Fig. 4. It decreases with particle size and approaches one half. The ratio is larger in Case I turbulence than in Case II for small particle size, but the opposite is true for large particle size. Nevertheless, the difference is very small. At $d_p = 62$ μm, our simulation predicts a ratio of 0.61 ± 0.03, which is in rough agreement with the measured value of 0.48 ± 0.11 (Ferguson, 1986).

The results for the time scale ratio and velocity scale ratio are more interesting (Fig. 5). The velocity scale ratio is very close to one for particle size up to 30 μm, which implies that particles respond to flow oscillations equally well in the horizontal direction as compared to the vertical direction for small particles. But as particle size goes beyond 40 μm, the velocity scale ratio drops very quickly with increasing particle size and reaches $1/\sqrt{2}$ for large particles. The time scale ratio decreases with particle diameter for small particles and has a minimum value at $d_p = 60$ μm. However, it increases with particle diameter for $d_p > 60$ μm and eventually returns to one.

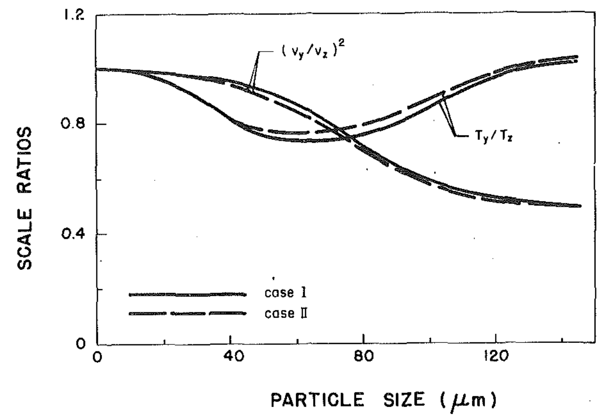

Fig. 5 Velocity scale ratio and time scale ratio

The two scale ratios, v_{10}^2/v_{30}^2 and T_{11}/T_{33}, determine the diffusivity ratio, according to Eq. (23). For small particle size, Fig. 5 shows that the time scale ratio governs the diffusivity ratio. Both the velocity scale ratio and the time scale ratio can affect the diffusivity ratio for intermediate particle size. As the particle size becomes large the reduction of the horizontal dispersion coefficient over the vertical dispersion coefficient is totally related to the difference in particle velocity scales in the two directions.

4.3 Discussions The motion of a heavy particle is governed by two time scales, the particle response time τ_a, which increases with the particle size, and the fluid correlation time in the neighborhood of the particle. The second scale can be direction-dependent. In the vertical direction it is related to the longitudinal fluid correlation and is roughly equal to L_f/v_d. L_f is the length scale of longitudinal spatial velocity correlation of fluid flow. However in the horizontal direction it is one half L_f/v_d, since the length scale for the transverse fluid correlation is one half L_f for a homogeneous and isotropic turbulence (Hinze, 1975).

Small particles ($\tau_a \ll L_f/v_d$) can respond quickly to fluid velocity fluctuations. The flow fluctuations have the same intensity in both direction because the flow is isotropic and homogeneous. Therefore, the particle velocity scale in the horizontal direction should be the same as that in the vertical direction. But, since the second time scale (fluid velocity time scale along the particle path) is direction-dependent, the particle time scale will be direction-dependent as well, as shown in Fig. 5. In summary, when particle size is small, the time scale ratio determines the diffusivity ratio.

For very large particles, we have $\tau_a \gg L_f/v_d$. The fluid velocity correlation time near the particle is very small compared to the particle response time. In this case, the particle motion resembles Brownian motion. The time scale of the particle is simply τ_a in all directions, i.e., the time scale ratio is one. Since the fluid velocity correlation time seen by the particle, the second time scale, in the horizontal direction is one half that in the vertical direction, the mean "frequency" of the random force acting on the particle due to the neighboring fluid in the horizontal direction is about twice the mean "frequency" in the vertical direction. Since the inertia is large, the particle can not respond to the fluid motion in the horizontal direction as to the same extent as in the vertical direction. Therefore, the particle velocity scale in the vertical direction is larger than that in the horizontal direction. More precisely, for very large particles

$$v_{10}^2 = u_0^2 \frac{L_f}{2 v_d \tau_a}, \; v_{30}^2 = u_0^2 \frac{L_f}{v_d \tau_a}, \; \frac{v_{10}}{v_{30}} = \frac{1}{\sqrt{2}}. \tag{27}$$

This is also shown in Fig. 5.

It is of interest to find the particle size for which the two scales, τ_a and L_f/v_d, are equal. The equality of the two time scales gives $\mathrm{St} \times \gamma = L_f/(u_0 T_{\mathrm{mE}})$. For the particular flow used in this simulation, $u_0 = 11.2$ cm/s, $T_{\mathrm{mE}} = 0.225$ s, and $L_f = 1.75$ cm, therefore, $\mathrm{St} \times \gamma = 0.694$. Using Eqs. (24) and (25), we find $d_p = 72$ μm. Therefore, if $d_p < 72$ μm, the time scale ratio mainly contributes to the diffusivity ratio; if $d_p > 72$ μm, the velocity scale ratio determines the diffusivity ratio. This same result can be seen in Fig. 5.

5 Comparisons With Experimental Data

5.1 The Grid-Generated Turbulence. Detailed experimental measurements of heavy particle dispersion in grid turbulence were made by Snyder and Lumley (SL 1971) and Wells and Stock (WS 1982). Both experiments used a grid with a mesh of spacing 2.54 cm. SL aligned their tunnel test section vertically; therefore, their measurements of dispersion in the plane perpendicular to the mean flow direction represent dispersion normal to the direction of the external force (horizontal dispersion). Their particles were released at $x/M = 20$, and they measured dispersion in the region from $x/M = 68.4$ to $x/M = 168$ where the flow decay rate is small. Here x is the distance from the grid and M is grid spacing. On the other hand, WS used a horizontal tunnel as a test section and they measured the dispersion of particles in the vertical direction. Their data represent particle dispersion in the direction of the drift velocity (vertical dispersion). The particles in WS's experiment were released at the grid, and they measured dispersion from $x/M = 20$ to $x/M = 70$ where the decay rate is large. They used charged particles and applied an electric field to control the particle drift velocity.

Grid-generated turbulence decays as (WS)

$$u'^2 \propto (x - x_0)^{-1}, \tag{28}$$

and the time scale grows as

$$T_{\mathrm{mE}} \propto (x - x_0), \tag{29}$$

where x is the distance from the grid and x_0 is the virtual origin. The dispersion coefficient of fluid elements is almost independent of x since it is roughly proportional to $u_0^2 \times T_{\mathrm{mE}}$. Because of this mutual balance of the turbulence energy and the time scale, the diffusion of fluid elements or small particles can be reasonably simulated with a stationary flow of scales matching at one point in the tunnel. However, the dispersion of heavy particles may be different from that of fluid elements. Using a direct numerical simulation, Ueda et al. (1983) found that the dispersion coefficient of heavy particles in decaying turbulence is not constant but rather decreases with time. The purpose of this section is to study the effect of the flow decay on the particle dispersion.

In what follows, the simulation results are compared with SL's and WS's data. Only the Case II turbulence is used for the following simulations because there is little effect of the shape of fluid velocity correlations on the particle dispersion.

5.2 Simulation Results Without Flow Decay. In this section the experiments of SL and WS are simulated using only one-point information for the flow scales and ignoring the flow decay. In simulating the particle dispersion of SL's experiment, the velocity scale and the spatial length scale were estimated based on Table 2 of SL's paper at $x/M = 73$: $u_0 = 13.1$ cm/s, $L_f = 3.1$ cm. Location $x/M = 73$ is about the center of the test section where the mean square dispersion was measured. No information on the integral time scale in the moving Eulerian frame, T_{mE}, was available. By matching the mean square dispersion curve for hollow glass beads from the simulation to the measured data, we obtained $T_{\mathrm{mE}} = 410$ ms. This value of T_{mE} was then used to predict the dispersion and velocity correlation for other particles in the experiment.

Figure 6 shows the simulation results and experimental data for the mean square dispersion. The relative uncertainty for the mean square dispersion in the simulations was estimated

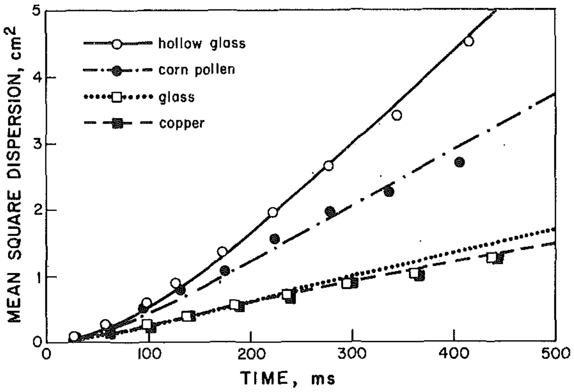

Fig. 6 Experimental and predicted mean square dispersions for the experiment of Snyder and Lumley. Flow decay is neglected in the simulation.

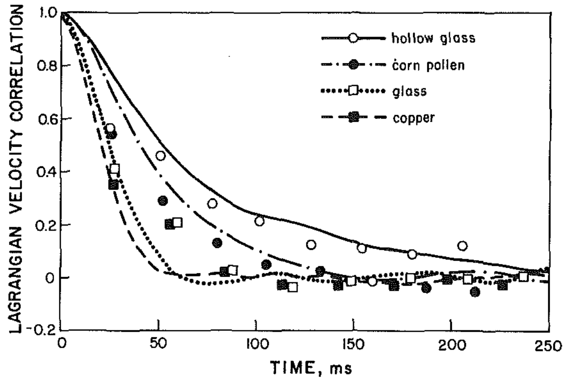

Fig. 7 Experimental and predicted Lagrangian velocity correlations for the experiment of Snyder and Lumley. Flow decay is neglected in the simulation.

to be 4 percent at a 95 percent confidence level. The simulated dispersion is in good agreement with the measured data. In particular, the slope for the mean square dispersion curve which is proportional to the dispersion coefficient is reasonably predicted. We note that for the glass and copper particles, the simulated dispersion coefficient is 10 ~ 20 percent larger. This may be partly due to the effect of flow decay, as discussed in the next section. The computed Lagrangian velocity correlation of the particle is compared to measured data in Fig. 7. The predicted shape of the correlations is fair but it is an improvement over the results of Ounis and Ahmadi (1989). The improvement is a result of using Case II turbulence.

The flow scales used to simulate WS's experiment were: $u_0 = 19.1$ cm/s, $T_{\mathrm{mE}} = 122$ ms, and $L_f = 1.264$ cm. They were estimated using the flow details at $x/M = 30$ and matching the mean square dispersion for 5 μm particles with zero drift.

The simulated mean square dispersion for 5 μm particles with different falling velocities are shown in Fig. 8 along with the experimental data. The agreement between the simulated curves and the measured data is considered to be good. However, the agreement is not satisfactory for 57 μm particles (Fig. 9), particularly when the drift velocity is large. The predicted dispersion coefficient for 57 μm particles with 54.4 cm/s drift velocity is about 40 percent larger than the dispersion coefficient obtained from the mean slope of the measured dispersion data.

5.3 Inclusion of Flow Decay. In the last section, the numerically generated flow used in the simulation was stationary and the flow scales were constant. The flow decay in the streamwise direction of a grid-generated turbulence transforms into nonstationary of the flow in the moving Eulerian frame. The flow decay can be incorporated into the simulation by making the flow scales time-dependent. We shall only consider Wells and Stock's (1983) experiment where the flow decay has a significant effect on the particle dispersion.

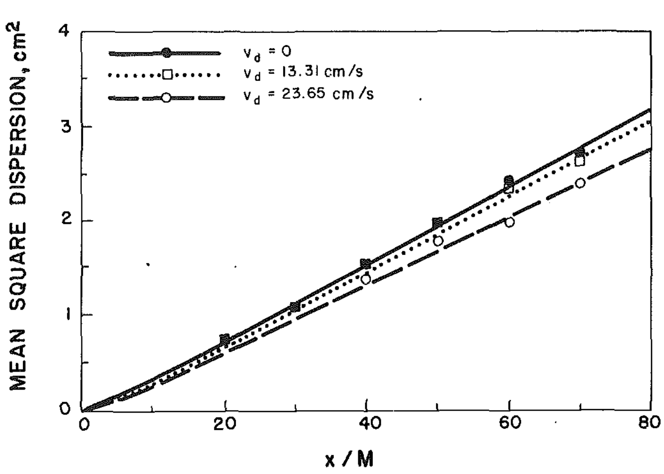

Fig. 8 Experimental and predicted mean square dispersions of 5 μm particles for the experiment of Wells and Stock. Flow decay is neglected in the simulation.

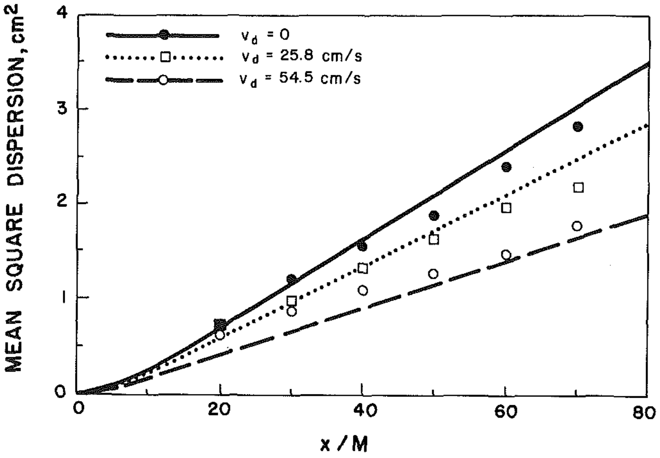

Fig. 9 Experimental and predicted mean square dispersions of 57 μm particles for the experiment of Wells and Stock. Flow decay is neglected in the simulation.

To include flow decay in the simulation, we need to know how the flow velocity scale and the flow time scale change with x/M. Using the flow scales at $x/M = 30$ and Eqs. (28) and (29) for WS's flow, we find

$$u_0 = 89.6\left(\frac{x}{M} - 7.987\right)^{-1/2} \text{ cm/s}, \qquad (30)$$

$$T_{\mathrm{mE}} = 1.39\left(\frac{x}{M} - 7.987\right) \text{ ms}. \qquad (31)$$

The length scale is given by $L_f = T_{\mathrm{mE}} u_0$, i.e.,

$$L_f = 0.125\left(\frac{x}{M} - 7.987\right)^{0.5} \text{ cm}. \qquad (32)$$

The first point where the measurements of mean square dispersion were taken was $x/M = 20$. Before this point, the flow was very irregular. For convenience, we start the simulation at this location. Then the time in the simulation is related to the location in the tunnel by

$$t = \left(\frac{x}{M} - 20\right)\frac{M}{U}, \qquad (33)$$

where the mean flow velocity U is 655 cm/s and the grid spacing M is 2.54 cm. Substituting (33) into (30)-(31), we obtain the flow scales required for the flow simulation,

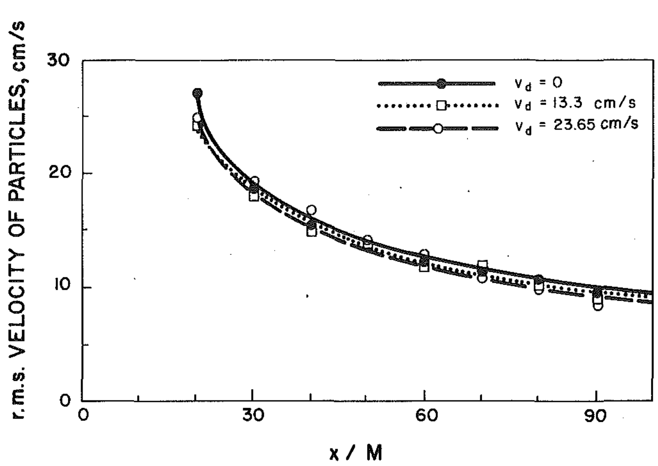

Fig. 10 Experimental and predicted RMS fluctuating particle velocities of 5 μm particles for the experiment of Wells and Stock. Flow decay is included in the simulation.

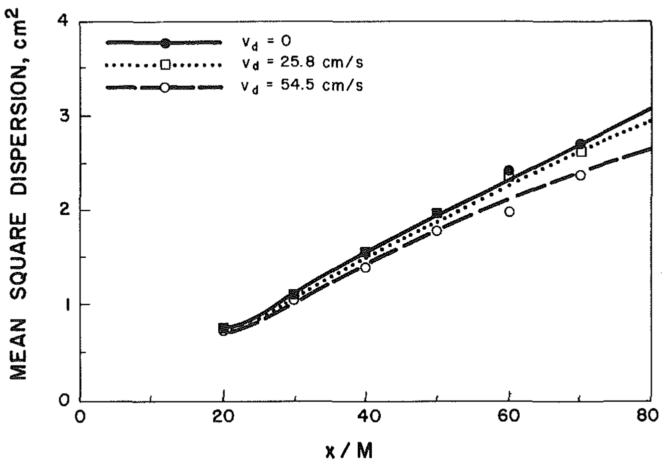

Fig. 11 Experimental and predicted mean square dispersions of 5 μm particles for the experiment of Wells and Stock. Flow decay is included in the simulation.

$$u_0(t)=23.1(t+46.6)^{-1/2}\ \text{cm/s}, \tag{34}$$

$$T_{\mathrm{mE}}(t)=0.358(t+46.6)\ \text{ms}, \tag{35}$$

$$L_f(t)=0.0635(t+46.6)^{0.5}\ \text{cm}, \tag{36}$$

with t in ms. The flow was again simulated by Fourier modes as described in Section 2, using the modifications to the time-dependent scales given above.

The initial conditions for the particle were assumed to match the data at the first location, i.e., the initial location and the initial velocity were taken randomly with normal distributions of variances equal to the measured mean square dispersion and particle rms fluctuation velocity, respectively, at $x/M=20$. The simulation results for $t>0$ can then be compared to the measured mean square dispersion and rms velocity beyond $x/M=20$. 3000 realizations of particle trajectories were used for the following results.

5.4 Simulation Results With Flow Decay. Figure 10 compares the predicted particle rms velocities with the measured data for 5 μm particles. The relative uncertainty for the simulated value of rms velocity is 3 percent at a 95 percent confidence level. For all three drift velocities, a good agreement is observed. As a result of the flow decay, the particles rms velocity decreases with the downstream location. The increase in the particle drift velocity tends to slightly reduce the particle rms velocity. The predicted mean square dispersions for 5 μm particles are shown in Fig. 11. They are in good agreement with the measured data. In addition, a small downward curvature for the largest drift case can be seen, indicating the local dispersion coefficient slowly decreases with distance down the tunnel.

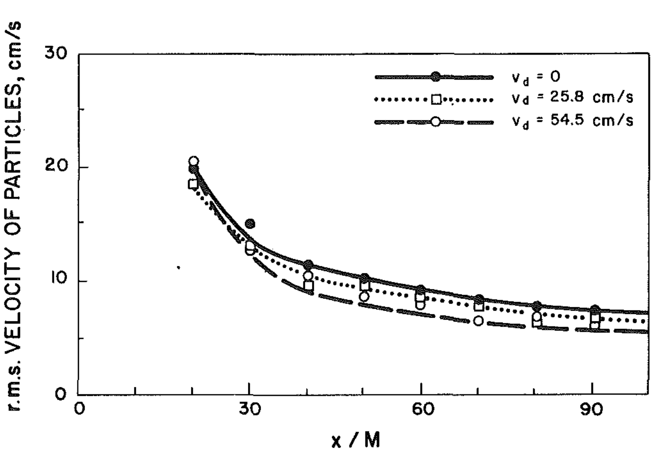

Fig. 12 Experimental and predicted RMS fluctuating particle velocities of 57 μm particles for the experiment of Wells and Stock. Flow decay is included in the simulation.

The predicted particle rms velocities for 57 μm particles are shown in Fig. 12. The predicted particle rms fluctuation velocities are very close to the measured data. The dependence of the particle rms velocity on the drift velocity is clearly shown by the simulation. The particle velocity scale decreases with the drift, even though the inertia is kept the same. This decrease is caused by the fluid velocity correlation time in the neighborhood of the particle decreasing with the drift due to the effect of crossing trajectories, i.e., the "frequency" of the driving force is increased by the drift. In Fig. 12 we find a maximum of 25 percent difference in the rms fluctuation velocities between the largest drift particle and the zero-drift particle. Comparing Fig. 12 and Fig. 10, we see the rms velocity of 57 μm particles of zero drifts is about 25 percent less than that of 5 μm particles of zero drift. The 5 μm glass beads with zero drift follow closely the motion of fluid elements. Therefore, the reduction of the rms velocity for 57 μm particles with largest drift over that of fluid elements is half due to the particle inertia and half due to the particle drift. The effect of the drift on the particle velocity scale is substantially enhanced in this experimental work because of the artificial increase of the drift by an electric field.

The effect of flow decay on particle dispersion can be seen more obviously when the mean square dispersions of 57 μm particles are considered. Figure 13 shows the predicted curves and the measured data. For the largest drift case, the predicted curve of the mean square dispersion has an obvious downward curvature, i.e., the slope decreases with the downstream location. This indicates that particle dispersion coefficient decreases with time, as a result of the flow decay. WS (1983) simply calculated the dispersion coefficient based on the averaged slope of the measured dispersion data. The measurement of local dispersion coefficient is required in this case. The method used by Arnason and Stock (1984) might be used to make these measurements.

5.5 Explanation and Discussions. In general, particle dispersion coefficient in a given flow is controlled by the Stokes number (St) and the drift parameter (γ). St is a measure of the inertia and is defined as τ_a/T_{mE}. In grid-generated turbulence, St is related to x/M by

$$\mathrm{St}=\frac{\tau_a}{1.39}\,(x/M-7.987)^{-1}. \tag{37}$$

The effective particle inertia is reduced because of the increase of the flow time scale. For 57 μm particles ($\tau_a=24.4$ ms), St

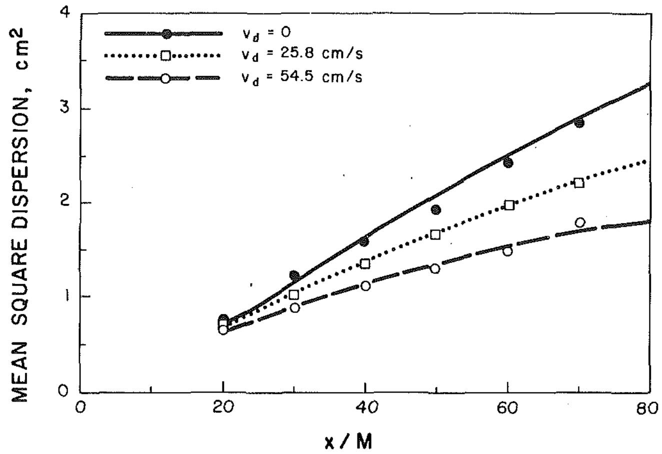

Fig. 13 Experimental and predicted mean square dispersions of 57 μm particles for the experiment of Wells and Stock. Flow decay is included in the simulation.

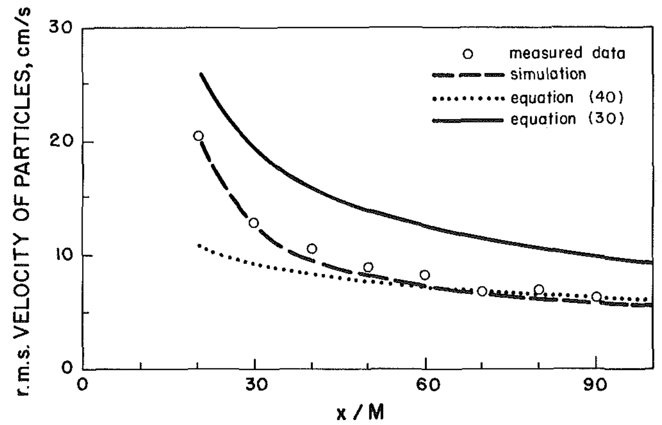

Fig. 14 The decay of the rms velocity for 57 μm particle of a drift velocity $v_d = 54.5$ cm/s, as compared to the asymptotic relation, Eq. (40), and the fluid rms velocity decay, Eq. (30)

is 1.46 at $x/M = 20$ but reduces to 0.28 at $x/M = 70$. On the other hand, the drift parameter defined as v_d/u_0 increases with the downstream location. Using Eq. (30), we have

$$\gamma=\frac{v_d}{89.6}\,(x/M-7.987)^{0.5}. \qquad (38)$$

For the 57 μm particles with $v_d = 54.5$ cm/s, γ is 2.1 at $x/M = 20$ and increases to 4.79 at $x/M = 70$. The drift parameter is much larger than the inertia parameter and the difference between γ and St grows quickly with x/M. As a result, particle dispersion is governed by the crossing trajectory effect and the local particle dispersion coefficient decreases with x/M, as shown by Fig. 13.

In the limit of large drift, the vertical particle dispersion coefficient is approximated by $u_0^2 L_f/v_d$ (Yudine, 1959). Using Eqs. (30) and (32), we have

$$\epsilon_{33}^{p}\propto\left(\frac{x}{M}-7.987\right)^{-0.5}. \qquad (39)$$

This approximation indicates that the local particle dispersion coefficient for particles of large drift decreases with distance at a -0.5 power in grid turbulence. Using Eqs. (27), (30), and (32), the vertical velocity scale for the 57 μm particles with a 54.5 cm/s drift is approximately equal to

$$v_{30}\approx 19.4\left(\frac{x}{M}-7.987\right)^{-0.25}, \qquad (40)$$

which implies that the particle velocity scale decreases with distance from the virtual origin by a power of -0.25. This power is one half the power for the decay of fluid velocity scale (see Eq. (30)). Figure 14 compares the simulated particle rms velocity and the measured data to Eq. (30) and Eq. (40). Both the simulation and the measurements show better agreement with Eq. (40) for $x/M > 50$. This suggests that the particle velocity scale has a slower decay rate than the fluid velocity scale, although the magnitude of the former is less due to particle inertia.

6 Summary and Conclusions

The aim of this study was to understand heavy particle dispersion by turbulence through a numerical simulation of particle motion in random velocity field generated by Fourier modes. We first extended the method for generating the flow to allow exponential fluid velocity correlations. Detailed numerical simulations were performed to study: 1) the anisotropic ratios of particle dispersion coefficient and scales; 2) the particle dispersion statistics in decaying grid-generated turbulences. Comparisons with the previous experimental data were made.

We found the time scale ratio decreases with particle size when the particle response time is less than the fluid velocity time scale in the neighborhood of the particle. It increases with particle size and returns to one when the particle size is large. The particle velocity scale ratio decreases monotonically with size and asymptotically reaches a value of $1/\sqrt{2}$. Therefore, for small particles, the particle time scale ratio determines the diffusivity ratio; but for large particles, the difference between the horizontal dispersion coefficient and the vertical dispersion coefficient is related to the difference between the particle velocity scale in the two directions. This result is embedded in the analysis of Reeks (1977) and partially shown in the simulation of Ferguson (1986). We expect the same scale-ratio behavior might be observed experimentally in isotropic wind tunnel flows.

Comparison of the simulation with the experimental measurements gives the following conclusions: 1) the simulation without flow decay can predict reasonable well the dispersion of heavy particles in a flow with slow decay (such as Snyder and Lumley, 1971); 2) for particle dispersion in faster decaying turbulence (such as Wells and Stock, 1983), the flow decay must be included in the simulation to predict the measured dispersion data; 3) the particle drift can reduce the particle rms velocity; 4) in a decaying flow, the local particle dispersion coefficient decreases with downstream location and the particle rms velocity decays slower than the fluid rms velocity.

The simulation indicates that the shape of fluid velocity correlations affects the shape of Lagrangian velocity correlation of the particle, but has little effect on the mean square dispersions, particle time scale and velocity scale.

This work was supported in part by funds of Summer Graduate Research Assistantship provided by Washington State University. The simulations were done on the University Computer Center's IBM 3090/300.

References

Arnason, G., and Stock, D. E., 1984, "Dispersion of Particles in Turbulent Pipe Flow," *Gas-Solid Flows*, J. T. Jurewicz, ed., FED-Vol. 10, pp. 25-29.

Csanady, G. T., 1963, "Turbulent Diffusion of Heavy Particles in the Atmosphere," *Journal of Atmospheric Science*, Vol. 20, pp. 201-208.

Calabrese, R. V., and Middleman, S., 1979, "The Dispersion of Discrete Particles in a Turbulent Fluid Flow," *American Institute of Chemical Engineers Journal*, Vol. 25, No. 6, pp. 1025-1035.

Ferguson, J. R., 1986, "The Effects of Fluid Continuity on the Turbulent Dispersion of Particles," Ph.D. dissertation, Washington State University.

Fung, J. C. H., Hunt, J. C. R., Malik, N. A., and Perkins, R. J., 1992, "Kinematic Simulation of Homogeneous Turbulence by Unsteady Random Fourier Modes," *Journal of Fluid Mechanics*, Vol. 236, pp. 281-318.

Gouesbet, G., Berlemont, A., and Picart, A., 1984, "Dispersion of Discrete Particles by Continuous Turbulent Motion. Extensive Discussion of the Tchen's Theory, Using a Two-Parameter Family of Lagrangian Correlation Functions," *Physics of Fluids*, Vol. 27, pp. 827-837.

Hinze, J. O., 1975, *Turbulence*, McGraw-Hill Book Co., New York.

Kraichman, R. H., 1970, "Diffusion by Random Velocity Fields," *Physics of Fluids*, Vol. 12, pp. 22-31.

Maxey, M. R., 1987, "The Gravitational Settling of Aerosol Particles in Homogeneous Turbulence and Random Flow Fields," *Journal of Fluid Mechanics*, Vol. 174, pp. 441-465.

Meek, C. C., and Jones, B. G., 1973, "Studies of the Behavior of Heavy Particles in a Turbulent Fluid Flow," *Journal of Atmospheric Science*, Vol. 30, pp. 239-244.

Mel, R., Adrain, R. J., and Hanratty, T. J., 1992, "Particle Dispersion in Isotropic Turbulence Under Stokes Drag and Basset Force with Gravitational Settling," *Journal of Fluid Mechanics*, Vol. 225, pp. 481-495.

Nir, A., and Pismen, L. M., 1979, "The Effect of a Steady Drift on the Dispersion of a Particle in Turbulent Fluid," *Journal of Fluid Mechanics*, Vol. 94, pp. 369-381.

Ounis, H., and Ahmadi, G., 1989, "Motions of Small Rigid Spheres in Simulated Random Velocity Field," *American Society of Civil Engineering Journal of Engineering Mechanics*, Vol. 115, pp. 2107-2121.

Pismen, L. M., and Nir, A., 1978, "On the Motion of Suspended Particles in Stationary Homogeneous Turbulence," *Journal of Fluid Mechanics*, Vol. 84, pp. 193-206.

Reeks, M. W., 1977, "On the Dispersion of Small Particles Suspended in an Isotropic Turbulent Field," *Journal of Fluid Mechanics*, Vol. 83, pp. 529-546.

Reeks, M. W., 1980, "Eulerian Direct Interaction Applied to the Statistical Motion of Particles in a Turbulent Fluid," *Journal of Fluid Mechanics*, Vol. 97, pp. 569-590.

Reeks, M. W., and McKee, S., 1984, "The Dispersive Effects of Basset History Forces on Particle Motion in a Turbulent Flow," *Physics of Fluids*, Vol. 27, pp. 1573-1582.

Riley, J. J., and Paterson, G. S., 1974, "Diffusion Experiments with Numerically Integrated Isotropic Turbulence," *Physics of Fluids*, Vol. 17, pp. 292-287.

Rowe, P. N., 1961, "The Drag Coefficient of a Sphere," *Transactions of Institute of Chemical Engineering*, Vol. 39, pp. 175-181.

Snyder, W. H., and Lumley, J. L., 1971, "Some Measurements of Particle Velocity Autocorrelation Functions in a Turbulent Flow," *Journal of Fluid Mechanics*, Vol. 48, pp. 41-71.

Squires, K. D., and Eaton, J. K., 1990, "Particle Response and Turbulence Modification in Isotropic Turbulence," *Physics of Fluids*, Vol. 2, pp. 1191-1203.

Townsend, A. A., 1976, *The Structure of Turbulent Shear Flow*, Cambridge University Press.

Turfus, C., and Hunt, J. C. R., 1979, "A Stochastic Analysis of the Displacements of Fluid Elements in Inhomogeneous Turbulence Using Kraichnan's Method of Random Modes," *Proceedings European Turbulence Conference*, Lyon.

Ueda, T., Jinno, K., Momii, K., and Maehama, K., 1983, "Numerical Study on the Diffusivity of Settling Particles in Homogeneous Isotropic Turbulence," *Transactions JSCE*, Vol. 15, pp. 293-296.

Wang, L. P., and Stock, D. E., 1988, "Theoretical Method for Obtaining Lagrangian Statistics from Measurable Eulerian Statistics for Homogeneous Turbulence," *Proceedings 11th Symposium on Turbulence*, Rolla, Missouri, B14.1-B14.12.

Wang, L. P., and Stock, D. E., 1992, "Numerical Simulation of Heavy Particle Dispersion-Time Step and Nonlinear Drag Considerations," ASME JOURNAL OF FLUIDS ENGINEERING, Vol. 114, pp. 100-106.

Wells, M. R., and Stock, D. E., 1983, "The Effects of Crossing Trajectories on the Dispersion of Particles in a Turbulent Flow," *Journal of Fluid Mechanics*, Vol. 136, pp. 31-62.

Yudine, M. I., 1959, "Physical Considerations on Heavy-Particle Dispersion," *Advances in Geophysics*, Vol. 6, pp. 185-191.

APPENDIX

Scale Estimation Based on the Flow of Ferguson (1986)

We report here how the parameters, u_0, T_{mE}, and L_f, were obtained from the information given in Ferguson (1986). They were estimated based on the flow of a mean velocity 4.5 m/s in Ferguson's experiment at $x/M=60$. The rms fluctuation velocity, u_0, was calculated from Eq. (4.7) of his dissertation, namely,

$$u_0 = 11.2 \text{ cm/s}. \tag{A.1}$$

The integral time scale, T_{mE}, was directly taken from Table 4.4 of his work,

$$T_{mE} = 0.225 \text{ s}. \tag{A.2}$$

T_{mE} was obtained based on the approximated relation, $T_{\mathrm{mE}} = T_{\mathrm{fE}} U/u_0$, where U is the mean flow velocity and T_{fE} is the Eulerian integral time measured at a fixed point $x/M=60$.

Since no direct information on the spatial length scale L_f was reported, we estimated it by examining Ferguson's data on thermal wake experiment. He found the dispersion coefficient of a thermal wake was about 15.5 cm^2/s with a different mean flow velocity of 6.7 m/s. In this flow, the velocity scale at $x/M=60$ was 16.8 cm/s (Eq. (4.8) of his dissertation) and $T_{\mathrm{mE}}=0.182$ s. Then the Lagrangian scale $T_L = 15.5/(16.8)^2 = 0.055$ s. It follows that $T_L/T_{\mathrm{mE}}=0.30$. According to Wang and Stock (1988), we have $2k_0 T_{\mathrm{mE}} u_0 = 4.2$ (Case I turbulence). This gives an estimated value for the wave number, $k_0 = 4.2/(2\times 0.182 \times 16.08) = 0.718 \text{ cm}^{-1}$. The spatial length scale associated with this k_0 is

$$L_f = 1.2533/k_0 = 1.75 \text{ cm}. \tag{A.3}$$

We assumed the length scale of the flow field with a mean velocity of 4.5 m/s at the same location was the same. This is a reasonable assumption since both flows were generated with the same grid (thus the same initial length scale) and in the same tunnel.

Flow Through Porous Media of Packed Spheres Saturated With Water

Ifiyenia Kececioglu
Assistant Professor.

Yuxiang Jiang
Graduate Research Assistant.

Department of Mechanical Engineering,
The University of Illinois at Chicago,
Chicago, IL 60680

The existing literature on the flow of fluids through porous packed beds gives very limited quantitative information on the criteria employed in marking the applicability of the different flow regimes. It is the objective of this paper to provide experimental evidence for determining the demarcation criteria during the flow of water through a bed of randomly packed spherical beads. Two different sizes of glass beads, 3 mm and 6 mm, were employed as the porous matrix through which water flowed at rates varying from 5.07×10^{-6} *m*^{3}*/s to* 4920×10^{-6} *m*^{3}*/s. Our dimensionless pressure drop data showed less variation when the characteristic length of the porous medium was taken to be proportional to the square root of the permeability over the porosity and not the bead diameter. Curves of properly nondimensionalized pressure drop* ($P'K/\mu v$) *plotted against the actual flow Reynolds number based on the porous medium permeability* ($\hat{R}e_K$) *provided the following information. It was found that Darcy's law has very limited applicability and is valid for a small range of Reynolds numbers* ($0.06<\hat{R}e_K<0.12$)*. This leads to a pre-Darcy flow that is valid for a much broader range of Reynolds numbers than expected* ($\hat{R}e_K<0.06$)*. Alternatively, the range of validity of the post-Darcy laminar Forchheimer flow is also found to be of much more limited applicability* ($0.34<\hat{R}e_K<2.30$) *than previous studies (Fand et al., 1987) have indicated* ($0.57<\hat{R}e_{K\ \mathrm{Fand\ et\ al.}}<9.00$)*. Transition to turbulence takes place earlier than expected and turbulent flow prevails from then on* ($\hat{R}e_k>3.40$)*. The dimensionless pressure drop in both the Forchheimer and turbulent flow regimes can be modeled by an appropriately nondimensionalized Ergun's equation (Carman, 1937), i.e., a first-order inertia term correction is sufficient in both flow regimes. However, the magnitude of the correction coefficients in the Forchheimer regime differs significantly from that in the turbulent flow regime* ($\hat{A}_F=1.00$, $\hat{B}_F=0.70$, $\hat{A}_T=1.90$, $\hat{B}_T=0.22$)*. Again, this differs from previous findings (Fand et al., 1987). The effect of the angle of inclination of the porous medium with respect to the horizontal on the transition mechanisms was also experimentally investigated. No changes other than the correction in the pressure drop due to the static liquid column height were observed.*

1 Introduction

A large number of papers in the literature has been written on the subject of theoretical modeling and experimental verification of flow through porous media. As a result, the experimentally verified Darcy's law constituted a goal in itself for theorists to interpret. One such paper, written recently by Fand et al. (1987), concentrates on the resistance to the flow of fluids through simple and complex porous media whose matrices are composed of randomly packed spheres. According to this paper, the four different regimes of flow through porous media were identified as pre-Darcy, Darcy, Forchheimer, and turbulent. Although these flow regimes had been identified before, the transition criteria had not been explicitly verified. In Fand et al. (1987), the demarcation parameter for the different flow regimes is considered to be the particle Reynolds number $\mathrm{Re}=vd\rho/\mu$, where v is the superficial flow velocity defined as the interstitial or actual fluid flow velocity v^f times the porosity ϕ, d is the characteristic diameter of the particles that constitute the porous matrix, and ρ and μ are the fluid density and dynamic viscosity, respectively. In this study, pre-Darcy flow occurred for $\mathrm{Re}<10^{-5}$, Darcy flow for $10^{-5}<\mathrm{Re}<2.3$, Forchheimer flow for $5<\mathrm{Re}<80$, and turbulent flow for $\mathrm{Re}>120$. Quantitatively our experimental results are different, although they agree qualitatively with these findings.

In the middle 1800's, Henry Darcy observed that under certain conditions the volume rate of flow of water through a pipe packed with sand was proportional to the negative of the

---

Contributed by the Fluids Engineering Division for publication in the JOURNAL OF FLUIDS ENGINEERING. Manuscript received by the Fluids Engineering Division July 20, 1992; revised manuscript received by the Fluids Engineering Division February 23, 1993. Associate Technical Editor: J. A. C. Humphrey.

pressure gradient. This relationship, known as Darcy's law, after being modified to include the fluid viscosity, can be stated as follows:

$$\frac{dp}{dx} = -\frac{\mu v}{K}, \tag{1}$$

where K is a constant of proportionality called the permeability, and dp/dx represents the pressure gradient in the direction of flow. A large amount of effort has been expended on determining K for various porous media. The following semiempirical expression has been found to accurately represent many experimental data. It is

$$K = \frac{\phi^3}{s_v^2 \kappa (1-\phi)^2} = \frac{d^2 \phi^3}{36\kappa (1-\phi)^2}, \tag{2a,b}$$

where s_v is the surface area per unit volume of the particles, and κ is an experimentally determined constant known as the Kozeny-Carman constant and is a measure of the tortuosity of the fluid path through the pores (Carman, 1937, and Wyllie and Gregory, 1955). When the porous media consist of spherical particles $s_v = 6/d$ and Eq. (2b) results.

Darcy flow is an expression of the dominance of viscous forces applied by the solid porous matrix on the interstitial fluid and is of limited applicability. Post-Darcy flow is effected by inertia forces and turbulence. Forchheimer (1901) is generally credited as first suggesting a nonlinear relationship between the pressure gradient and the fluid velocity. In 1952, Ergun (1952) examined this phenomenon for gas flow through crushed porous solids based on its dependence upon the flow rate and properties of the fluid, the fractional void volume or porosity, and orientation, size, and shape of the porous matrix. Generalizing Forchheimer's equation

$$-\frac{dp}{dx} = av + bv^2, \tag{3}$$

where a and b are empirical constants, Ergun (1952) obtained the following equation:

$$-\frac{dp}{dx} = A\,\frac{(1-\phi)^2}{\phi^3}\,\frac{\mu v}{d^2} + B\,\frac{(1-\phi)}{\phi^3}\,\frac{\rho v^2}{d}, \tag{4}$$

where A and B are dimensionless constants. The degree to which the above equation may be applied to various porous media is dependent on the constants A and B. Ergun (1952) concluded that a large quantity of experimental data could be represented by $A = 150$ and $B = 1.75$. Subsequent experimental data have shown that these values are not definitive. For media consisting of smooth particles, Macdonald et al. (1979) recommended that for engineering applications $A = 180$ and $B = 1.8$ should be used. In other words, their results indicated that for smooth spherical particles, such as, for example, most glass beads, for which the Kozeny-Carman constant κ is related to A by $A = 36\kappa$ exactly, κ is equal to 5. Other investigators have disputed the functional dependence of the pressure drop on the porosity of the medium. Rumpf and Gupte (1971) recommended the following expression:

$$-\frac{dp}{dx} = A\phi^{-5.5}\,\frac{\mu v}{d^2} + B\,\frac{(1-\phi)}{\phi^3}\,\frac{\rho v^2}{d}. \tag{5}$$

2 Dimensionless Expressions

If one is to determine the flow demarcation criteria that determine transition from pre-Darcy to Darcy, Forchheimer, and turbulent flows, one has to identify the appropriate dimensionless parameters that would affect the magnitude of an appropriately nondimensionalized pressure drop.

Ergun's expression for resistance to flow through packed columns (Eq. (4)) can be recast in dimensionless form through rearrangement of terms as follows:

$$-\frac{dp}{dx}\,\frac{d^2}{\mu v} = A\,\frac{(1-\phi)^2}{\phi^3} + B\,\frac{(1-\phi)}{\phi^3}\,\mathrm{Re}, \tag{6a}$$

or

$$-\frac{dp}{dx}\,\frac{d^2}{\mu v} = \frac{d^2}{K} + B\,\frac{(1-\phi)}{\phi^3}\,\mathrm{Re}. \tag{6b}$$

Alternatively, Ergun's equation can also be nondimensionalized using the square root of the permeability as a measure of the characteristic dimension of the porous medium. Then,

$$-\frac{dp}{dx}\,\frac{K}{\mu v} = 1 + \frac{B}{\sqrt{A}\,\phi^{3/2}}\,\frac{\rho v\sqrt{K}}{\mu} = 1 + \frac{B}{\sqrt{A}\,\phi^{3/2}}\,\mathrm{Re}_K, \tag{7a}$$

or

Nomenclature

a = first Forchheimer constant
A = first Ergun constant
$\hat{A}$ = first constant in Eq. (17)
b = second Forchheimer constant
B = second Ergun constant
$\hat{B}$ = second constant in Eq. (17)
$\mathbf{B}$ = post-Darcy second-order tensorial coupling coefficient Eq. (15)
$\mathbf{C}$ = pre-Darcy second-order tensorial coupling coefficient Eq. (15)
d = diameter of sphere
$\mathbf{g}$ = gravitational acceleration vector
$\mathbf{I}$ = second-order unit tensor
K = permeability of isotropic, homogeneous porous medium
$\mathbf{K}$ = permeability tensor
$\mathbf{m}^{+f}$ = interaction body force exerted by fluid phase on solid phase
p = pressure
P' = $-dp/dx$ for horizontal flow; $-d(p+\rho g z)/dx$ for inclined flow
Re = Darcian Reynolds number based on particle diameter $= \rho v d/\mu$
Re_K = Darcian Reynolds number based on porous medium permeability $= \rho v\sqrt{K}/\mu$
$\hat{Re}_K$ = actual flow Reynolds number based on pore permeability and interstitial fluid velocity $= \rho v^f\sqrt{K/\phi}/\mu$
s_v = surface area per unit volume of particles making up porous matrix
t = time
$\mathbf{t}^f$ = fluid stress tensor
v = superficial flow velocity $= \phi v^f$
v^f, $\mathbf{v}^f$ = interstitial flow velocity magnitude and vector
$\mathbf{v}^s$ = solid porous matrix velocity vector
x = coordinate in direction of flow
z = coordinate opposite to direction of gravity
κ = Kozeny-Carman constant
μ = dynamic viscosity of fluid
ρ = fluid density
ϕ = porosity

Superscripts

f = fluid phase property
s = solid phase property

Subscripts

F = Forchheimer flow
T = turbulent flow

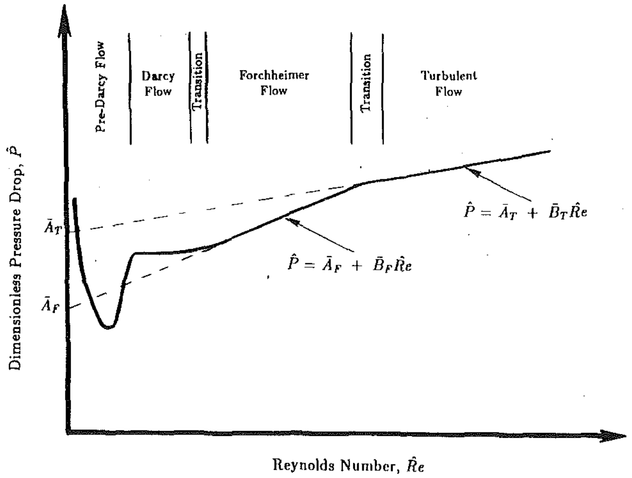

Fig. 1 Flow regimes for fluid flow through porous media

$$-\frac{dp}{dx}\frac{K}{\mu v}=1+\frac{B}{\sqrt{A}}\frac{v}{\phi}\frac{\rho\sqrt{\dfrac{K}{\phi}}}{\mu}=1+\frac{B}{\sqrt{A}}\,\hat{\mathrm{R}}\mathrm{e}_K. \tag{7b}$$

As observed from the above equations, the relevant nondimensional group that governs the resistance to flow of fluids through packed columns of porous aggregates is either the Darcian Reynolds number based on particle diameter, Re, or the Darcian Reynolds number based on the square root of the permeability of the medium, Re_K, or the actual flow Reynolds number, $\hat{\mathrm{R}}\mathrm{e}_K$, based on the interstitial fluid velocity $v^f = v/\phi$ and a characteristic length equal to the square root of the permeability over the porosity. These authors prefer the latter formulation to the first two because of the weaker dependence of the equation on the porosity of the medium ϕ which is an experimental variable. As then indicated by the above equations, the dimensionless pressure drop as a function of Reynolds number, for the different flow regimes, can be depicted by the plot of Fig. 1. Accordingly, both Forchheimer and turbulent flows should have the same functional dependence on the Reynolds number but the slope of the curve should differ. Equations (6) and (7) above can then be viewed as the constitutive relations or laws that describe the resistance to flow through a bed of porous aggregates. It is the intention of this investigation to show the limited validity of Darcy's law and to point out the pronounced differences between Forchheimer and turbulent flows.

3 Interpretation of the Constitutive Expressions

We next turn to interpreting the constitutive expressions given by Eqs. (6) or (7) by specializing the momentum equation, obtained from a continuum point of view of the fluid-solid phase mixture, to the physical system of interest.

The equation of conservation of linear momentum of the fluid phase in the mixture of fluid and solid porous matrix is given by the expression previously derived by Kececioglu and Rubinsky (1989). Accordingly,

$$\frac{\partial}{\partial t}(\phi\rho\mathbf{v}^f)+\nabla\cdot(\phi\rho\mathbf{v}^f\mathbf{v}^f)=\nabla(\phi\mathbf{t}^f)+\mathbf{m}^{+f}+\phi\rho\mathbf{g}, \tag{8}$$

where $\mathbf{t}^f$ is the stress tensor in the fluid phase, $\mathbf{m}^{+f}$ is the interaction body force exerted on the fluid phase by the solid phase, and $\mathbf{g}$ is the gravitational acceleration vector.

To completely specify the momentum equation for the interstitial fluid velocity $\mathbf{v}^f$ one has to specify the constitutive forms of the fluid phase stress tensor $\mathbf{t}^f$ and the momentum interaction $\mathbf{m}^{+f}$ between the fluid phase and the rest of the porous medium mixtures. One first assumes that the fluid phase stress is adequately represented by an isotropic fluid pressure p so that

$$\mathbf{t}^f = -p\mathbf{I}, \tag{9}$$

where $\mathbf{I}$ is the second-order unit tensor. A more comprehensive constitutive representation of the fluid stress $\mathbf{t}^f$ would have allowed for a nonisotropic viscous contribution that would have incorporated a fluid-velocity gradient dependence. However, as demonstrated by the experiments of Taylor (1971) and Beavers and Joseph (1967), the effects of fluid-velocity gradients decay rapidly within a few pore diameters, the length scale of the continuum approximation of the pore structure, and, therefore, they can be neglected in the constitutive relation for the fluid stress tensor. Instead, the viscous drag between the fluid phase and the solid phase should be taken into account through the body force type momentum interaction force vector $\mathbf{m}^{+f}$. $\mathbf{m}^{+f}$ can then be taken as the sum of an equilibrium component given by the fluid pressure exerted on the increase in void area in the flow direction per unit bulk volume and a nonequilibrium component due to viscous drag of the fluid on the solid matrix and an added mass inertia term due to the acceleration of the fluid as it moves around the solid particles in the porous matrix. Then,

$$\mathbf{m}^{+f}=p\nabla\phi-\mathbf{K}^{-1}\mu\phi^2(\mathbf{v}^f-\mathbf{v}^s)-\rho\phi^3(\mathbf{v}^f-\mathbf{v}^s)|\mathbf{v}^f-\mathbf{v}^s|\mathbf{B} \tag{10}$$

In the above equation, $\mathbf{B}$ is a second-order tensorial coupling coefficient similar to the second-order inverse permeability tensor $\mathbf{K}^{-1}$. If we substitute Eqs. (9) and (10) into Eq. (8), and assuming steady flow of a constant density fluid, i.e., $\partial/\partial t = 0$, $\nabla\cdot\mathbf{v}^f = 0$, and a fully developed flow, i.e., $(\mathbf{v}^f\cdot\nabla)\mathbf{v}^f = 0$, then, we obtain,

$$\nabla p-\rho\mathbf{g}=-\mathbf{K}^{-1}\mu\phi(\mathbf{v}^f-\mathbf{v}^s)-\rho\phi^2(\mathbf{v}^f-\mathbf{v}^s)|\mathbf{v}^f-\mathbf{v}^s|\mathbf{B}. \tag{11}$$

We then recognize Eq. (11) above to be the modified form of the familiar Ergun's equation for high Reynolds number fluid seepage through a deforming porous medium. If we neglect the inertia terms associated with the coupling coefficient $\mathbf{B}$ we recover the vectorial form of Darcy's law

$$\phi(\mathbf{v}^f-\mathbf{v}^s)=-\frac{\mathbf{K}}{\mu}\{\nabla p-\rho\mathbf{g}\}. \tag{12}$$

If we assume that the solid phase is at rest and does not deform, the momentum equation for the solid phase is replaced by the trivial expression $\mathbf{v}^s = 0$, and, furthermore, if the porous medium is isotropic and homogeneous, then the permeability tensor is replaced by a constant times the second-order unity tensor and we recover Eq. (1) from Eq. (12). Similarly, if we include the inertia terms, and consider a nondeforming solid porous matrix which is isotropic and homogeneous, we recover Ergun's equation provided

$$\mathbf{B}=\frac{(1-\phi)}{\phi^3 d}B\mathbf{I}, \tag{13}$$

and

$$\mathbf{K}^{-1}=\frac{(1-\phi)^2}{\phi^3 d^2}A\mathbf{I}. \tag{14}$$

The magnitudes of the constants A and B above should vary depending on whether the inertia dominated flow regime is Forchheimer or turbulent. As the above equations indicate, the dimensionless pressure drop is independent of Reynolds number in the Darcy flow regime, and proportional to Reynolds number in the Forchheimer or nonlinear laminar flow and turbulent flow regimes when the inertia terms become important. In the pre-Darcy flow regime, as suggested by our experimental results, the pressure drop seems to be inversely proportional to the Reynolds number. This, then, implies a momentum interaction body force term of the form:

$$\mathbf{m}^{+f} = p\nabla\phi - \mathbf{K}^{-1}\mu\phi^2(\mathbf{v}^f - \mathbf{v}^s) - \rho\phi^3(\mathbf{v}^f - \mathbf{v}^s)|\mathbf{v}^f - \mathbf{v}^s|\mathbf{B} - \frac{\mu^2\phi}{\rho}\frac{(\mathbf{v}^f - \mathbf{v}^s)}{|\mathbf{v}^f - \mathbf{v}^s|}\mathbf{C}. \quad (15)$$

In the equation above, the second term on the right-hand side leads to Darcy's law, the third term leads to post-Darcy inertia dominated flows, and the fourth term is descriptive of the pre-Darcy flow regime.

4 Experimental Apparatus and Procedure

A schematic diagram of the experimental apparatus is given in Fig. 2. The primary portion of the apparatus consisted of a clear Plexiglas cylindrical tube 92 cm long whose inside diameter is 5.715 cm and outside diameter 6.400 cm. The tube was filled with either 3 mm or 6 mm uniformly sized randomly packed glass beads; they served as the solid porous matrix through which water flowed. The glass beads were held in place by means of two circular pieces of wire mesh located at the two ends of the tube. Water was either pumped with a variable speed drive or gravity fed through the packed beads via a loop instrumented with flowmeters to measure the flow rates. During the experiments the flow rate varied from 5.07×10^{-6} m^3/s to 4920×10^{-6} m^3/s. Gravity feed from a constant head tank was used to create low flow rates (less than 300×10^{-6} m^3/s) and the variable speed pump was used for higher flow rates. The thermal and fluid properties of the flowing water were determined at the temperature measured by two thermocouples placed at each end of the tube.

The pressure drop was measured across two pressure ports located 76 cm apart along the tube. Each one of these ports was located 8 cm from the left- and right-hand side ends of the tube, respectively. This ensured that the pressure measurements were made across a portion of the tube where the flow had been fully developed. For small pressure differences (less than 1.37 kPa), the measurements were made with a Validyne Differential Pressure Transducer. For large pressure differences (from 1.40 kPa to 10.40 kPa), manometers were employed. Each time the experiments were initiated at the largest flow rates; the objective was to produce a stable packing of the beads and to prevent the effects of changing porosity on pressure drop as the flow rate was varied.

The angle of inclination of the main apparatus with respect to the horizontal was also varied and was either maintained at 0 or at 20 deg. This was done to check the effect of inclination on flow transition and to verify Darcy's law when the porous medium is inclined. At all times, special caution was taken to ensure the flow loop was free of air bubbles.

5 Experimental Results and Discussion

Experimental data of pressure drop versus flow rate, acquired for two particle diameters ($d = 3$ mm, and $d = 6$ mm) and two angles of inclination (0 and 20 deg) with respect to the horizontal, were plotted employing the dimensionless coordinates suggested by Eqs. (6) and (7). These were plots of $-(dp/dx)(d^2/\mu v)$ versus Re, of $-(dp/dx)(K/\mu v)$ versus Re_K, and of $-(dp/dx)(K/\mu v)$ versus $\hat{\mathrm{Re}}_K$. Plots of $-(dp/dx)(d^2/\mu v)$ versus Re and of $-(dp/dx)(K/\mu v)$ versus $\hat{\mathrm{Re}}_K$ for the 6 mm particles and 0 deg inclination are shown piecemeal in Figs. 3 to 8. For the data acquired when the packed bed was inclined, $-dp/dx$ was replaced by $-d(p + \rho g z)/dx$, where z is the cartesian spatial coordinate increasing in the direction opposite to that of the gravitational acceleration vector, and x is still the spatial coordinate in the direction of flow. As discussed earlier, for constant porosity media, such as ours were, (i.e., $\nabla\phi = 0$), these derivatives are properties of the porous medium and are proportional to the resistance to flow brought up by the presence of the porous medium. From now on either one of these derivatives will be denoted by P'.

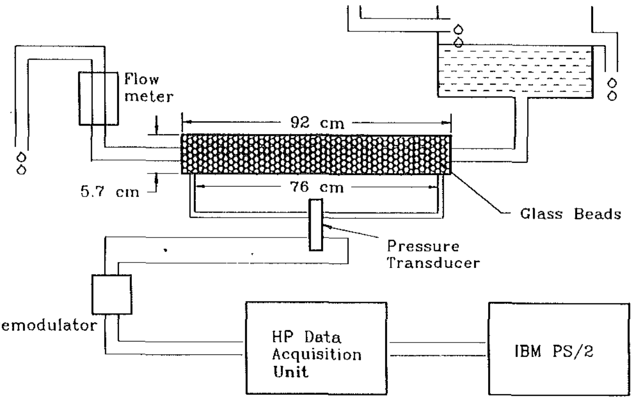

Fig. 2 Schematic diagram of the experimental apparatus

The dimensionless plots covered a broad range of Reynolds numbers and corresponding flow resistances. The plots of $P'd^2/\mu v$ versus particle Reynolds numbers Re varied with particle size but not with inclination. The range of particle Reynolds numbers represented by the experimental data extended from $\mathrm{Re} = 0.1$ to $\mathrm{Re} = 90$, for the 3 mm particles, and from $\mathrm{Re} = 0.2$ to $\mathrm{Re} = 180$ for the 6 mm particles. $P'd^2/\mu v$ for both particles varied from about 100 to 5000 for both inclinations provided the gravitational correction was made in the P′ term. The variation in the experimental curves with particle diameter, however, was eliminated when the third form of nondimensionalization was selected. For an $\hat{\mathrm{Re}}_K$ variation from about 0.04 to 24.00, $P'K/\mu v$ varied from about 0.6 to 7.5 for both sets of particles and both inclinations.

The changes in the slopes in both sets of curves (Figs. 3 to 5 and 6 to 8) indicated the prevalence of the same four flow regimes: a pre-Darcy regime, a Darcy regime over a range of Reynolds numbers for which $P'd^2/\mu v$ is equal to a constant given by d^2/K provided the particle Reynolds number Re is of order one or less (this is the section of the curves from which the porous medium permeability K is determined), and two linear post-Darcy regions, the first considered to be the Forchheimer regime, and the second one the turbulent flow regime. As shown by the experimental curves, the differences in the slopes of the Forchheimer and turbulent flows are pronounced.

The flow regime demarcation sites varied with particle diameter when the particle Reynolds number Re was used as the demarcation criterion; by contrast, when the permeability based actual flow Reynolds number was used as the demarcation criterion, for both particle sizes, each one of the four flow regimes was identified by the same corresponding $\hat{\mathrm{Re}}_K$ range. Specifically, for the 3 mm beads, Darcy's flow was observed for $0.3 < \mathrm{Re} < 0.7$, Forchheimer flow for $1.6 < \mathrm{Re} < 10.0$, and turbulent flow for $13.0 < \mathrm{Re} < 90.0$. For the 6 mm beads, Darcy's flow was established for $0.6 < \mathrm{Re} < 1.0$, Forchheimer flow for $3.0 < \mathrm{Re} < 21.0$, and turbulent flow for $25.0 < \mathrm{Re} < 180.0$. As already pointed out, the corresponding $\hat{\mathrm{Re}}_K$ ranges for both sets of particles were the same; they were: Darcy flow for $0.06 < \hat{\mathrm{Re}}_K < 0.12$, Forchheimer flow for $0.34 < \hat{\mathrm{Re}}_K < 2.30$, and turbulent flow for $\hat{\mathrm{Re}}_K > 3.4$. The variation of the apparatus inclination had no effect on the flow regime demarcation points. These results with uncertainty estimates are summarized in Table 1. On this table, we also list the findings of Fand et al. (1987) for comparison. It can be seen, that, although the disparity between their results and ours is pronounced when the particle Reynolds number is used as the flow regime demarcation criterion, the differences become compressed when we recalculate their findings using $\hat{\mathrm{Re}}_K$ instead. Their results indicate that Darcy's flow prevails for $\hat{\mathrm{Re}}_K < 0.26$, Forchheimer flow for $0.57 < \hat{\mathrm{Re}}_K < 9.00$, and turbulent flow for $\hat{\mathrm{Re}}_K > 13.5$. Fand et al.'s recalculated experimental results extend the upper limit of turbulent flow to 50.0.

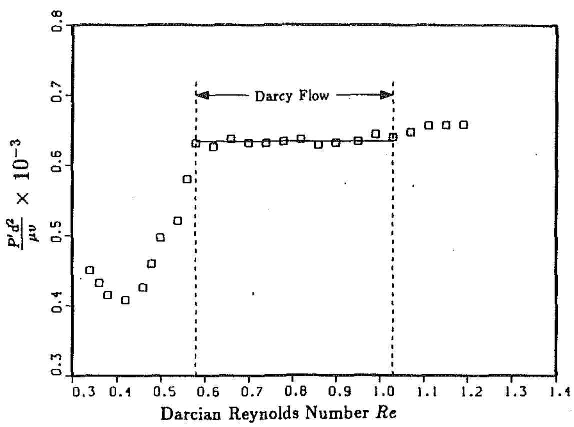

Fig. 3 Plot of dimensionless pressure drop $P'd^2/\mu v$ versus Darcian Reynolds number Re for Darcy flow through 6 mm beads. (Uncertainty in $P'd^2/\mu v$ is ±0.03 $P'd^2/\mu v$ and uncertainty in Re is ±0.03 Re at 95 percent confidence level.) (Apparatus maintained horizontal.)

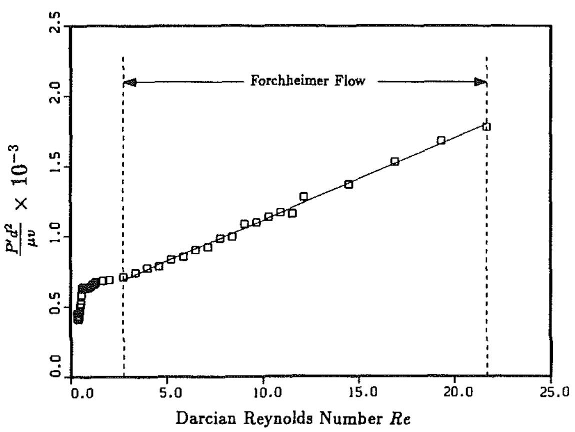

Fig. 4 Plot of dimensionless pressure drop $P'd^2/\mu v$ versus Darcian Reynolds number Re for Forchheimer flow through 6 mm beads. (Uncertainty in $P'd^2/\mu v$ is ±0.06 $P'd^2/\mu v$ and uncertainty in Re is ±0.03 Re at 95 percent confidence level.) (Apparatus maintained horizontal.)

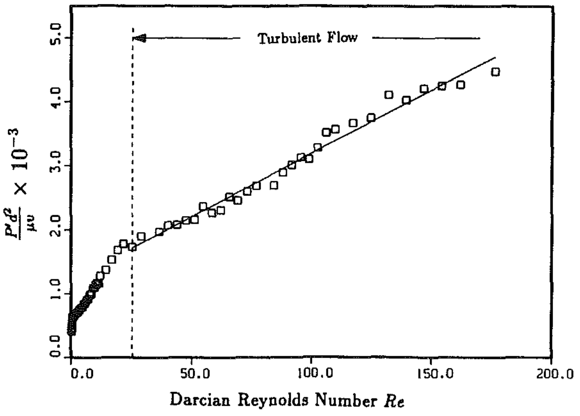

Fig. 5 Plot of dimensionless pressure drop $P'd^2/\mu v$ versus Darcian Reynolds number Re for turbulent flow through 6 mm beads. (Uncertainty in $P'd^2/\mu v$ is ±0.06 $P'd^2/\mu v$ and uncertainty in Re is ±0.03 Re at 95 percent confidence level.) (Apparatus maintained horizontal.)

When all the data (for both particle sizes and both inclinations) were plotted together, they suggested three piecewise continuous curves for the Darcy and post Darcy variation in dimensionless pressure drop with Reynolds number. The three least squares straight lines at 95 percent confidence level are:

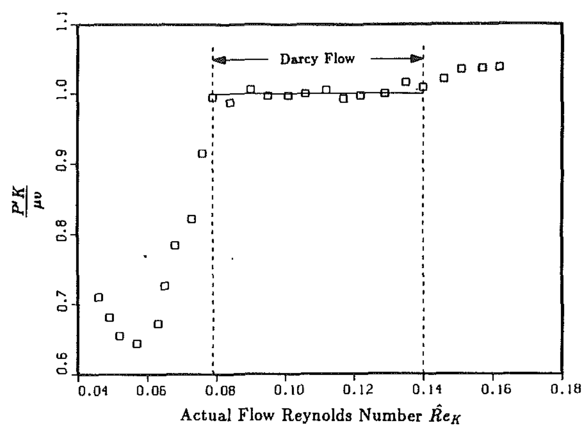

Fig. 6 Plot of dimensionless pressure drop $P'K/\mu v$ versus actual flow Reynolds number $\hat{R}e_K$ for Darcy flow through 6 mm beads. (Uncertainty in $P'K/\mu v$ is ±0.10 $P'K/\mu v$ and uncertainty in $\hat{R}e_K$ is ±0.06 $\hat{R}e_K$ at 95 percent confidence level.) (Apparatus maintained horizontal.)

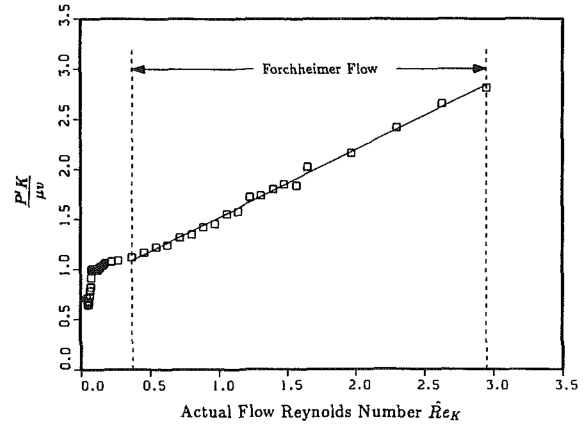

Fig. 7 Plot of dimensionless pressure drop $P'K/\mu v$ versus actual flow Reynolds number $\hat{R}e_K$ for Forchheimer flow through 6 mm beads. (Uncertainty in $P'K/\mu v$ is ±0.10 $P'K/\mu v$ and uncertainty in $\hat{R}e_K$ is ±0.06 $\hat{R}e_K$ at 95 percent confidence level.) (Apparatus maintained horizontal.)

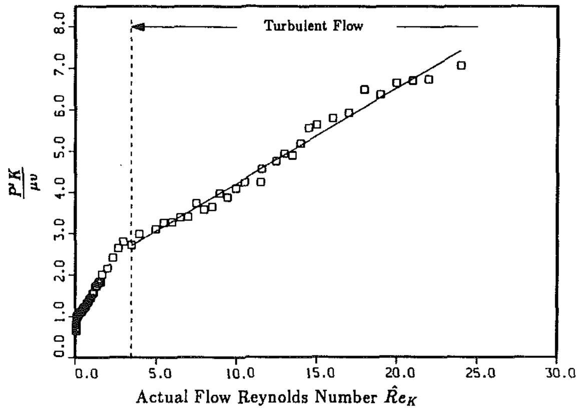

Fig. 8 Plot of dimensionless pressure drop $P'K/\mu v$ versus actual flow Reynolds number $\hat{R}e_K$ for turbulent flow through 6 mm beads. (Uncertainty in $P'K/\mu v$ is ±0.10 $P'K/\mu v$ and uncertainty in $\hat{R}e_K$ is ±0.06 $\hat{R}e_K$ at 95 percent confidence level.) (Apparatus maintained horizontal.)

$$\frac{P'K}{\mu v}=1,\ 0.062(\pm 0.015)<\hat{R}e_K<0.120(\pm 0.020), \qquad (16a)$$

$$\frac{P'K}{\mu v}=1.00(\pm 0.15)+0.70(\pm 0.15)\hat{R}e_K,$$

$$0.34(\pm 0.06)<\hat{R}e_K<2.30(\pm 0.70), \qquad (16b)$$

Table 1 Flow regime demarcation criteria for flow through porous media

	3 mm beads (this study)	6 mm beads (this study)	Fand et al. (1987)
Darcy flow	$0.30(\pm 0.02) < \mathrm{Re} < 0.70(\pm 0.05)$ $0.062(\pm 0.015) < \hat{\mathrm{Re}}_K < 0.120(\pm 0.020)$	$0.60(\pm 0.02) < \mathrm{Re} < 1.00(\pm 0.03)$ $0.062(\pm 0.015) < \hat{\mathrm{Re}}_K < 0.120(\pm 0.020)$	$\mathrm{Re} < 2.3(\pm 0.1)$ $\hat{\mathrm{Re}}_K < 0.26(\pm 0.01)$
Forchheimer flow	$1.6(\pm 0.3) < \mathrm{Re} < 10.0(\pm 0.5)$ $0.34(\pm 0.06) < \hat{\mathrm{Re}}_K < 2.30(\pm 0.70)$	$3.0(\pm 0.3) \leq \mathrm{Re} < 21(\pm 1)$ $0.34(\pm 0.06) < \hat{\mathrm{Re}}_K < 2.30(\pm 0.70)$	$5.0(\pm 0.5) \leq \mathrm{Re} < 80(\pm 5)$ $0.57(\pm 0.06) < \hat{\mathrm{Re}}_K < 9.00(\pm 0.60)$
Turbulent flow	$\mathrm{Re} > 13(\pm 1)$ $\hat{\mathrm{Re}}_K > 3.4(\pm 0.6)$	$\mathrm{Re} > 25(\pm 1)$ $\hat{\mathrm{Re}}_K > 3.4(\pm 0.6)$	$\mathrm{Re} > 120$ $\hat{\mathrm{Re}}_K > 13.5$

Table 2 Correlations for dimensionless pressure drop versus Reynolds number for flow through porous media

	Forchheimer flow	Turbulent flow
This study	$\frac{P'K}{\mu v} = 1.00(\pm 0.15) + 0.70(\pm 0.15)\hat{\mathrm{Re}}_K$; $0.34(\pm 0.06) < \hat{\mathrm{Re}}_K < 2.30(\pm 0.70)$	$\frac{P'K}{\mu v} = 1.90(\pm 0.10) + 0.22(\pm 0.04)\hat{\mathrm{Re}}_K$; $\hat{\mathrm{Re}}_K > 3.40(\pm 0.60)$
Fand et al. (1987)	$\frac{P'K}{\mu v} = 0.93 + 0.14\hat{\mathrm{Re}}_K$; $0.57(\pm 0.06) < \hat{\mathrm{Re}}_K < 9.00(\pm 0.60)$	$\frac{P'K}{\mu v} = 1.14 + 0.12\hat{\mathrm{Re}}_K$; $\hat{\mathrm{Re}}_K > 13.5$
Macdonald et al. (1979)	$\frac{P'K}{\mu v} = 1.00 + 0.19\hat{\mathrm{Re}}_K$; $0.003 < \hat{\mathrm{Re}}_K < 32.7$	
Ergun et al. (1952)	$\frac{P'K}{\mu v} = 0.83 + 0.19\hat{\mathrm{Re}}_K$; $0.08 < \hat{\mathrm{Re}}_K < 196$	

$$\frac{P'K}{\mu v} = 1.90(\pm 0.10) + 0.22(\pm 0.04)\hat{\mathrm{Re}}_K,$$

$$\hat{\mathrm{Re}}_K > 3.40(\pm 0.60). \quad (16c)$$

In other words, both post-Darcy flow regimes, i.e., laminar Forchheimer and turbulent, can be adequately modeled with only a first order inertia term correction of the form

$$\frac{P'K}{\mu v} = \hat{A} + \hat{B}\hat{\mathrm{Re}}_K. \quad (17)$$

These results are summarized in Table 2. In this table the recalculated correlations of Fand et al. (1987), Macdonald et al. (1979), and Ergun (1952) are also cited for comparison. To recast Ergun's and Macdonald's correlations in the required dimensionless form of Eq. (17), an average porosity of 0.4 was assumed for all the represented data. The information in Table 2 indicates that all correlations (represented now in terms of the new dimensionless groups $P'K/\mu v$ and $\hat{\mathrm{Re}}_K$) are of the same order of magnitude. By contrast to the piecewise continuous representations of the results of this investigation and that of Fand et al., both works of Macdonald et al. and Ergun provide a unified correlation for all their data that span Darcy, Forchheimer and turbulent flow regimes. Ergun's data are the most comprehensive and extend the upper limit of the turbulent flow regime to $\hat{\mathrm{Re}}_K = 196$. The primary difference between our results and other data in the literature lies in that our data suggest more pronounced differences in the coefficients between the Forchheimer flow regime and the turbulent flow regime.

6 Conclusions

The existing literature on the flow of fluids through porous packed beds provides very limited quantitative information on the criteria employed in marking the applicability of the different flow regimes. In this paper we provided experimental evidence for determining the flow regime demarcation criteria during the flow of water through a bed of randomly packed spherical beads. Two different sizes of glass beads, 3 mm and 6 mm, were employed as the porous matrix through which water flowed at rates varying from 5.07×10^{-6} m^3/s to 4920×10^{-6} m^3/s. Dimensionless pressure drop data as a function of Reynolds number revealed the following:

1 Our dimensionless pressure drop data showed less variation when the characteristic length of the porous medium was taken to be proportional to the square root of the permeability over the porosity and not the bead diameter. Accordingly, curves of properly nondimensionalized pressure drop ($P'K/\mu v$) plotted against the actual flow Reynolds number based on the porous medium permeability ($\hat{\mathrm{Re}}_K$) were viewed as the more physically meaningful way of data presentation.

2 The changes in the slope of the experimental curves indicated four flow regimes: a considerable pre-Darcy flow regime, rather limited Darcy flow and Forchheimer flow regimes, and a turbulent flow regime. It was found that Darcy's Law has very limited applicability and is valid for a small range of Reynolds numbers ($0.06 < \hat{\mathrm{Re}}_K < 0.12$). This leads to a pre-Darcy flow that is valid for a much broader range of Reynolds numbers than expected ($\hat{\mathrm{Re}}_K < 0.06$). Alternatively, the range of validity of the post-Darcy laminar Forchheimer flow is also found to be of limited applicability ($0.34 < \hat{\mathrm{Re}}_K < 2.30$). Transition to turbulence takes place at $\hat{\mathrm{Re}}_K = 3.4$ and turbulent flow prevails from then on ($\hat{\mathrm{Re}}_K > 3.4$).

3 The dimensionless pressure drop in both the Forchheimer and turbulent flow regimes can be modeled by an appropriately nondimensionalized Ergun's equation (1952), i.e., a first-order inertia term correction is sufficient in both flow regimes. However, the magnitude of the correction coefficients in the Forchheimer regime differs significantly from that in the turbulent flow regime ($\hat{A}_F = 1.00$, $\hat{B}_F = 0.70$; $\hat{A}_T = 1.90$, $\hat{B}_T = 0.22$).

4 The effect of the angle of inclination of the porous medium with respect to the horizontal on the transition mechanisms was also experimentally investigated. No changes other than the correction in the pressure drop due to the static liquid column height were observed.

5 The experimental data (for both particle sizes and both inclinations) were correlated in terms of three piecewise continuous curves for the Darcy and post Darcy variation in dimensionless pressure drop with Reynolds number given at 95 percent confidence level by equation 16. Correlations of our results and of recalculated results of other investigators are summarized in Table 2.

Acknowledgments

The authors gratefully acknowledge the support provided by the National Science Foundation under grant numbers CTS-8908376 and BSR-9008178. The are also grateful for the support of the University of Illinois, Chicago, Campus Research Board.

References

Beavers, G. S., and Joseph, D. D., 1967, "Boundary Conditions at a Naturally Permeable Wall," *Journal of Fluid Mechanics*, Vol. 30, pp. 197-207.

Carman, P. C., 1937, *Transactions of the Institution of Chemical Engineers*, London, Vol. 15, p. 150.

Ergun, S., 1952, "Fluid Flow Through Packed Columns," *Chemical Engineering Progress*, Vol. 48, No. 2, pp. 89-94.

Fand, R. M., Kim, B. Y. K., Lam, A. C. C., and Phan, R. T., 1987, "Resistance to Flow of Fluids through Simple and Complex Porous Media whose Matrices Are Composed of Randomly Packed Spheres," *Journal of Fluids Engineering*, Vol. 109, pp. 268-274.

Forchheimer, P., 1901, "Wasserbeweguing durch Boden," *Zeischrift. Verein Deutscher Ingenieure*, Vol. 45, pp. 1782-1788.

Kececioglu, I., and Rubinsky, 1989, "A Continuum Model for the Propagation of Discrete Phase-Change Fronts in Porous Media in the Presence of Coupled Heat Flow, Fluid Flow and Species Transport Processes," *International Journal of Heat and Mass Transfer*, Vol. 32, No. 6, pp. 1111-1130.

Macdonald, I. F., El-Sayed, M. S., Mow, K., Dullien, F. A. L., 1979, "Flow Through Porous Media—the Ergun's Equation Revisited," *Industrial & Engineering Chemistry Fundamentals*, Vol. 18, No. 3, pp. 199-208.

Rumpf, H., and Gupte, A. R., 1971, "Einflusse der Porositat und KorngroBenverteilung im Widerstandsgesetz der Porenstromung," *Chemie Ingenieur Technik*, Vol. 43, pp. 367-375.

Taylor, G. I., 1971, "A Model for a Boundary Condition of a Porous Material, Parts I and II," *Journal of Fluid Mechanics*, Vol. 49, pp. 319-326.

Wyllie, M. R. J., and Gregory, A. R., 1955, "Fluid Flow through Unconsolidated Porous Aggregates: Effect of Porosity and Particle Shape on Kozeny-Carman Constants," *Industrial and Engineering Chemistry*, Vol. 47, pp. 1379-1388.

Journal of Fluids Engineering
Technical Briefs

Asymptotic Wake Behavior of Swept, Blunt Trailing-Edge Airfoils

G. V. Selby[1] and F. H. Miandoab[1]

The effect of base sweep and the addition of passive flow-control devices at constant base sweep angle (30 deg) on the asymptotic behavior of turbulent wakes produced by flatplate airfoils was experimentally examined. It was determined that values of the nondimensional streamwise velocity defect and wake thickness parameters for the grooved model with 30 deg swept base at fourteen base thicknesses downstream of the base at mid-span were closer to asymptotic values from empirical plane wake predictions than values for the 0, 30, and 45 deg swept baseline models and the 30 deg swept model with Wishbone vortex generators. The grooves apparently inhibited the three-dimensionality of the resulting wake flow.

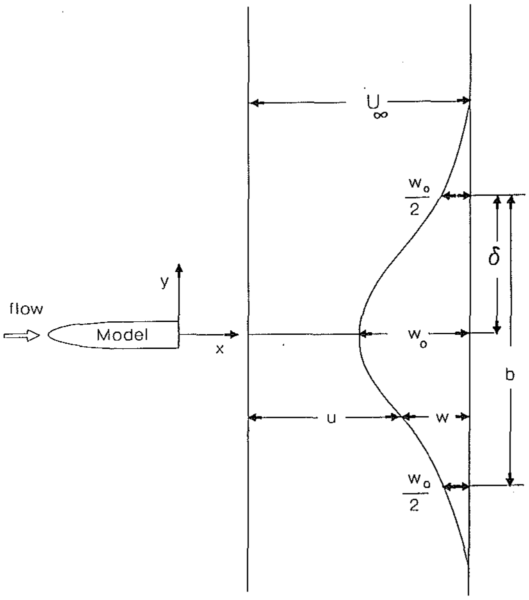

Fig. 1 Definition of wake parameters

Introduction

Blunt trailing-edge airfoils have a significant structural advantage over sharp trailing-edge airfoils. However, a major disadvantage is the increased base drag associated with blunt trailing-edge airfoils. Previous studies conducted by the present authors have examined the effect of various passive devices on the base pressures of blunt trailing-edge airfoils with unswept and swept bases (Selby and Miandoab, 1990; Selby et al., 1990).

The effect of base sweep angle and the addition of flow-control devices (longitudinal V-grooves and "Wishbone" vortex generators (Wheeler, 1989)) on the asymptotic behavior of turbulent wakes generated by blunt trailing-edge airfoils of varying base sweep angle (β) has been studied. It has been previously demonstrated that these modifications decrease the base drag of two-dimensional and swept blunt trailing-edge airfoils by increasing the base pressure (Selby and Miandoab, 1990; Selby et al., 1990). For the unswept airfoil, the resulting base pressure distribution became more uniform (two-dimensional) upon the introduction of three-dimensional longitudinal (vortical) structures into the wake (Selby and Miandoab, 1990). These results suggested that the present three-dimensional base flows might be similarly affected and thus provided the motivation for the present study of three-dimensional wakes and wake flow control. That is, the modified 3-D wake flow might asymptote toward a plane turbulent wake state closer to the base (in terms of the mean streamwise flow), than would the unmodified 3-D wake flow.

Plane turbulent wakes generated by models of different shapes are noted to approach a unique self-preserving state (Sreenivasan, 1981). A self-preserving state is attained when the mean velocity profile normalized by the appropriate velocity and length scales is independent of streamwise position. A two-dimensional self-preserving turbulent wake in the asymptotic limit of vanishing velocity defect (w) is characterized by constant values of two parameters (Narasimha and Prabhu, 1972),

$$W = \left(\frac{w_o}{U_\infty}\right)\left(\frac{x}{\theta}\right)^{1/2} \text{ and } \Delta = \delta(x\theta)^{-1/2}$$

where w_o is the maximum velocity defect and δ is the half-wake thickness measured from the maximum velocity defect to where $w = w_o/2$ in the transverse direction (see Fig. 1). Momentum thickness, θ, is defined as

$$\theta = \int_{-\infty}^{\infty}\left(\frac{w}{U_\infty}\right)\left(1-\frac{w}{U_\infty}\right)dy$$

Uniqueness of the asymptotic self-preserving state requires that the parameters W and Δ assume universal values W^* ($=1.63 \pm 0.02$) and Δ^*($=0.30 \pm 0.005$), respectively (Sreeni-

---

[1] Associate Professor, and Research Assistant Professor, respectively, Department of Mechanical Engineering, Old Dominion University, Norfolk, VA 23529. Professor Selby is a Mem. ASME.

Contributed by the Fluids Engineering Division of THE AMERICAN SOCIETY OF MECHANICAL ENGINEERS. Manuscript received by the Fluids Engineering Division March 30, 1992; revised manuscript received May 18, 1993. Associate Technical Editor: Ho, Chih-Ming.

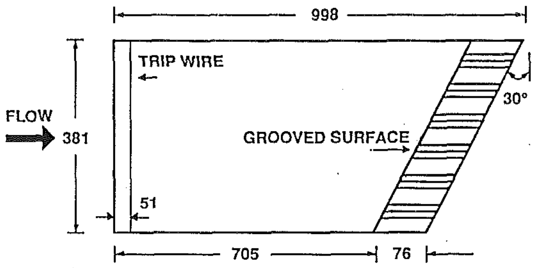

Fig. 2(*a*) 30 deg swept trailing edge flat plate with V-groove modification

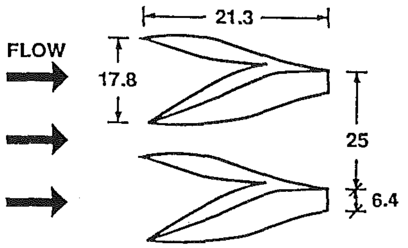

Fig. 2(*b*) Wishbone vortex generators

Fig. 2 30 deg swept-base model with V-groove and Wishbone modifications

vasan and Narasimha, 1982). Additional parameters, I_1 and I_2, estimated from the normalized wake defect profile and defined as

$$I_n = \int_{-\infty}^{+\infty} \left(\frac{w}{w_o}\right)^n d\eta, \quad n = 1, 2 \text{ and } \eta = \frac{y}{\delta}$$

are also pertinent to the analysis (Sreenivasan and Narasimha, 1982). Integral parameters I_1 and I_2 are expected to have constant values independent of streamwise position for self-preserving profiles. Sreenivasan and Narasimha's (1982) average measured values were reported to be $I_1 = 2.06 \pm 0.01$ and $I_2 = 1.51 \pm 0.02$. An attempt is made herein to characterize asymptotic wake behavior in this study in terms of the parameters discussed.

Experimental Apparatus

All tests were conducted in the 91 cm × 122 cm test section of the Old Dominion University low-speed closed-circuit wind tunnel. Three flat-plate airfoil models with an elliptical leading edge, maximum thickness (h) of 2.54 cm, span of 38 cm, and base sweep angles of 0, 30, and 45 deg were tested. All three models had a chord length of 31 cm at midspan. The airfoil models were attached to the middle of 76 cm high side walls which extended 1.3 m in the freestream direction, beginning at the leading edge of the models. In order to eliminate the effect on the flow of protuberances located on the test section ceiling and to provide uniform flow over the model, horizontal plates were attached to the top and bottom end of the side walls. These horizontal plates, as well as the airfoil model, were installed parallel to the floor of the test section. To attain fully developed turbulent flow at the base of the models, flow on both the upper and lower surfaces was tripped by a wire (diameter = 1.02 mm) located 5 cm downstream of the leading edge. A 2 cm thick turbulent boundary layer existed 2.5 cm upstream of the base of the wind tunnel models ($\mathrm{Re} = 2.6 \times 10^6$ at a free-stream speed of 43 m/s, based on distance to base at midspan). Only the 30 deg swept-base model was tested with Wishbone and V-groove modifications (see Fig. 2). Longitudinal V-grooves (7.6 cm long, 100 deg total included angle) spaced 2.54 cm apart were used on the upper and lower surfaces of the model near the base. The tips of the Wishbone vortex generators were placed at the trailing edge of the model with similar spanwise spacing. These generators consisted of a single row of triangular, ramp-like devices shaped like individual downstream-facing arrowheads. All tests were conducted at a free-stream speed of 43 m/s. A pitot-static probe was used to survey the wake to define mean velocity profiles. For each model tested, surveys were conducted at three spanwise positions (25, 50, and 75 percent span or $z/s = 0.25$, 0.50, and 0.75) in three streamwise planes.

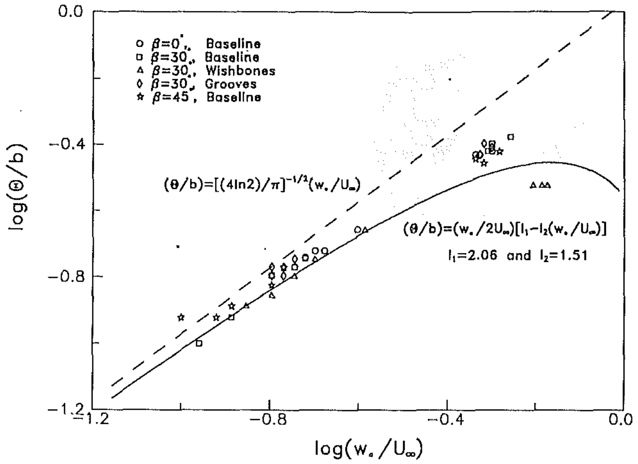

Fig. 3 Relationship between defect ratio and wake width

Discussion of Results

Sharma (1987) used normalized graphs of θ, as a function of w_o, to examine wake velocity profiles for self-preservation by comparing them to theoretical curves obtained from the definition of momentum thickness and integral parameters (solid line, Fig. 3) and from the asymptotic wake relations (dashed line, Fig. 3) (Patel and Scheuerer, 1982). Similar data for the present study are also shown in Fig. 3. There is close agreement between the experimental data and the theoretical curves for all cases tested. A survey of the wake generated by the 30 deg swept-base model modified by Wishbones placed in the vicinity of the trailing edge resulted in measurements which noticeably departed from the other experimental data at the two upstream measurement stations. The Wishbones apparently introduced highly three-dimensional flow into the wake near the trailing edge of the model. Lin et al. (1991) have shown that in the nominal orientation, these generators shed horseshoe vortices. However, the effect of the vortices generated by the Wishbones seemed to rapidly diminish in the downstream direction, as evidenced by the fact that the Wishbone data became in closer agreement with the other experimental data at the measurement station farthest downstream ($x/h = 14$).

Figures 4–6 show a comparison between the asymptotic profile $[w/w_o = \exp(-\eta^2 \ln 2)]$ and measured wake velocity defect profiles at three spanwise positions for $x/h = 14$. There is good agreement between the asymptotic profile and the measured profiles. However, observed deviations between the asymptotic and measured profiles (especially in Figs. 5 and 6) are partially due to increased cross-stream mixing produced by the longitudinal vortices introduced into the wake (model with Wishbones). In addition, near the upstream corner of the base, the 45 deg swept-base data significantly deviated from the asymptotic profile due to three-dimensional end effects. However, as Figs. 5 and 6 indicate, in this latter case, the asymptotic profile is approached at midspan. The data then deviated again from the asymptotic profile as the downstream corner of the base was approached. However, as Fig. 6 shows, end effects are not as pronounced at $z/s = 0.75$ as at $z/s = 0.25$. In general,

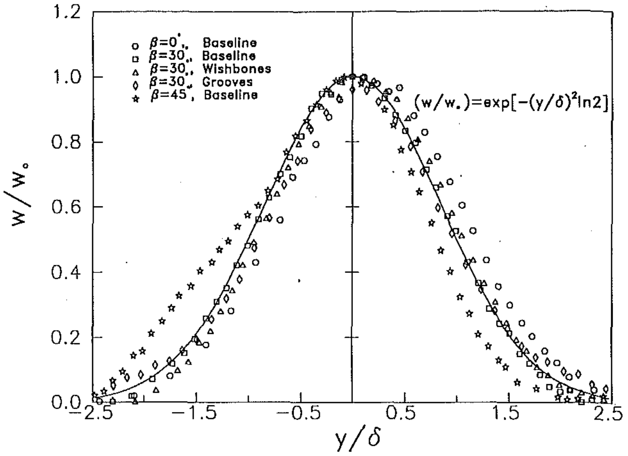

Fig. 4 Velocity profiles in the self-similar form at $z/s=0.25$ and $x/h=14$ (uncertainty in: $y/\delta < \pm 0.7$ percent, $W/W_o < \pm 0.5$ percent)

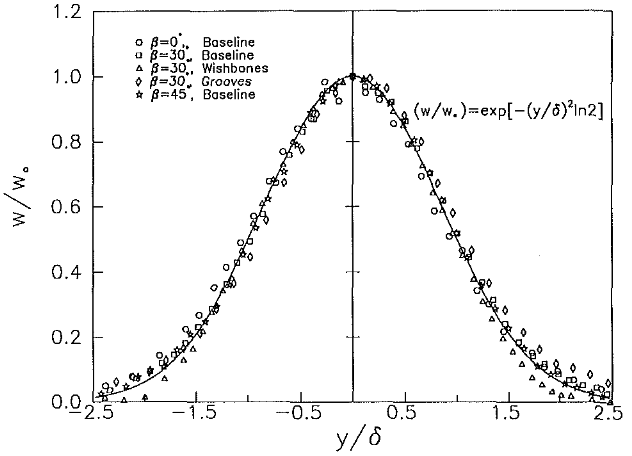

Fig. 5 Velocity profiles in the self-similar form at $z/s=0.50$ and $x/h=14$

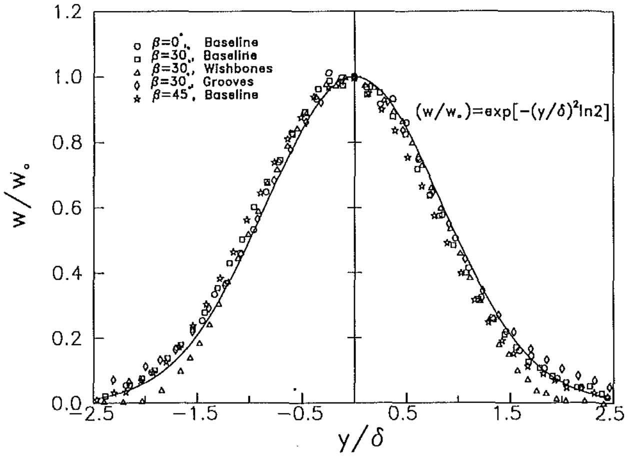

Fig. 6 Velocity profiles in the self-similar form at $z/s=0.75$ and $x/h=14$

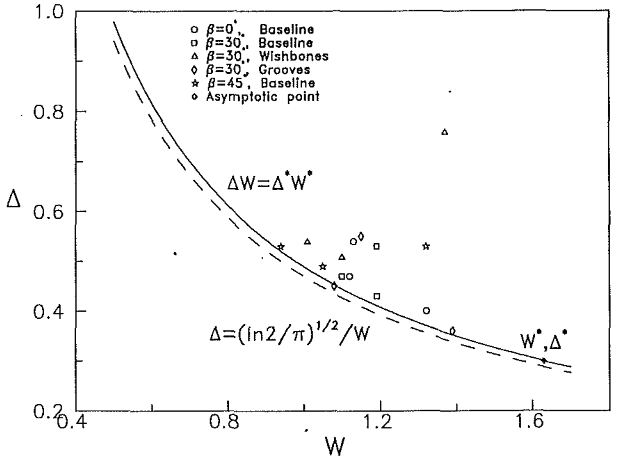

Fig. 7 Correlation of wake parameters Δ and W

Table 1 Measured wake parameters, I_1 and I_2

Model	I_1	I_2
$\beta=0$ deg, Baseline	2.20 ± 0.09	1.51 ± 0.03
$\beta=30$ deg, Baseline	2.20 ± 0.10	1.50 ± 0.01
$\beta=30$ deg, Wishbones	2.04 ± 0.03	1.57 ± 0.11
$\beta=30$ deg, Grooves	2.26 ± 0.08	1.50 ± 0.01
$\beta=45$ deg, Baseline	2.22 ± 0.15	1.53 ± 0.12
Sreenivasan and Narasimha (1982)	2.06 ± 0.01	1.51 ± 0.02

the agreement between the asymptotic profile and measured data appeared best at midspan, as expected, based on the first author's experience with 3-D separated flows associated with swept, rearward-facing steps (Selby, 1989).

Sreenivasan (1981), in his study of plane turbulent wakes, observed the convergence of wake parameters Δ and W to asymptotic values Δ^* and W^*. Following the approach of Sharma (1987), Δ as a function of W for the present study for surveys conducted at midspan are calculated and plotted in Fig. 7 against Sreenivasan's (1981) curve ($\Delta W = \Delta^* W^*$) and a theoretical curve for two-dimensional asymptotic wakes (Patel and Scheuerer, 1982). All data points appear to asymptotically approach the point (W^*, Δ^*). The wake of the grooved 30 deg swept-base model appears to be closer to the asymptotic state at the farthest downstream measurement location than the other configurations, while the baseline 45 deg swept-base model and 30 deg swept-base model with Wishbones are farthest from the asymptotic self-preserving state at this same measurement location ($x/h=14$). An additional mechanism behind the effectiveness of the grooved models might be the attenuation of the Karman vortex street in the base flow. Commenting on the fast approach to the equilibrium state demonstrated by the wake of their twin-plate model, Sreenivasan and Narasimha (1982) report that "the mean strain field immediately behind the twin-plate generator promotes the disintegration of energetic large eddies, resulting in a simpler behavior further downstream."

Average values of I_1 and I_2 for the present models and values from Sreenivasan and Narasimha (1982) are presented in Table 1. I_1 and I_2 represent nondimensional wake momentum and kinetic energy deficits, respectively. The data compare resonably well, considering that the present measurements were made within $x/h<20$.

Conclusions

In general, the turbulent wakes of flat plates with swept bases exhibited behavior similar to plane wakes, in terms of the identified mean streamwise parameters, even as close to the base as $x/h=14$. However, as the swept base was approached, three-dimensional wake behavior deviated considerably from the behavior of plane wakes, as expected. This deviation also increased with sweep angle and with the addition of three-dimensional vortical structures to the wakes. However, attached flow in the surface grooves upstream of the 30 deg swept base apparently inhibited the three-dimensionality of the resulting wake flow, resulting in values of the nondimensional streamwise velocity defect and wake thickness parameters at $x/h=14$ that were closer to asymptotic values from empirical plane wake predictions compared to values for the baseline 30 deg swept-base model with and without Wishbone vortex generators.

Acknowledgment

The work presented herein was largely accomplished under National Science Foundation grant no. CTS-8519116.

References

Lin, J. C., Selby, G. V., and Howard, F. G., 1991, "Exploratory Study of Vortex-Generating Devices for Turbulent Flow Separation Control," AIAA Paper No. 91-0042, AIAA 29th Aerospace Sciences Meeting.

Narasimha, R., and Prabhu, A., 1972, "Equilibrium and Relaxation in Turbulent Wakes," *Journal of Fluid Mechanics*, Vol. 54, pp. 1-17.

Patel, V. C., and Scheuerer, G., 1982, "Calculation of Two-Dimensional Near and Far Wakes," *AIAA Journal*, Vol. 20, No. 7, pp. 900-907.

Selby, G. V., 1989, "Passive Control of Three-Dimensional Separated Vortical Flow Associated with Swept Rearward-Facing Steps," ASME JOURNAL OF FLUIDS ENGINEERING, Vol. 11, No. 1, pp. 99-101.

Selby, G. V., and Miandoab, F. H., 1990, "Effect of Surface Grooves on Base Pressure for a Blunt Trailing-Edge Airfoil," *AIAA Journal*, Vol. 28, No. 6, pp. 1133-1135.

Selby, G. V., Miandoab, F. H., and Lin, J. C., 1990, "Effect of Passive Devices on Low-Speed Wake Flow for Unswept and Swept Blunt Trailing-Edge Airfoil Models," *Proceedings: 111th ASME Winter Annual Meeting—Forum on Unsteady Flow*, FED-Vol. 102, Dallas, TX, pp. 57-59.

Sharma, S. D., 1987, "Development of Pseudo-two-dimensional Turbulent Wakes," *Physics of Fluids*, Vol. 30, pp. 357-363.

Sreenivasan, K. R., 1981, "Approach to Self-Preservation in Plane Turbulent Wakes," *AIAA Journal*, Vol. 19, pp. 1365-1367.

Sreenivasan, K. R., and Narasimha, R., 1982, "Equilibrium Parameters for Two-Dimensional Turbulent Wakes," ASME JOURNAL OF FLUIDS ENGINEERING, Vol. 104, pp. 167-170.

Wheeler, G. O., 1989, Proprietary to Mr. Gary Wheeler, U. S. Patent pending.

Weak Thermal Vortex Rings

R. Ganapathy[1]

A simple mathematical model is proposed and a similarity solution is obtained to study the behavior of very weak thermal vortex rings induced by a horizontal line source of thermal energy in an unbounded fluid. The temperature distribution is assumed to be unaffected by the fluid motion, and the Stokes flow approximation is invoked. Streamlines are computed to demonstrate the evolution of the flow field.

1 Introduction

Determination of the flow field induced by a heat-generating body in the fluid surrounding the body is essential to the solution of many engineering problems such as the hydrodynamics of weak thermal explosions, cooling of the components of electrical and electronic equipment, and the management of nuclear waste materials. Providing the rate of heat generation is small, the flow may be modeled as Stokes flow. One may then neglect the convective terms in comparison to the local acceleration term in the momentum equations, and adopt the Boussinesq approximation to express the buoyancy force field in terms of the temperature field.

Although the importance of buoyancy driven flows due to the presence of horizontal line sources has been well established in the literature (for instance, Serruk, 1958; Crane, 1959; Spalding and Cruddace, 1961; Brodowicz and Kierkus, 1966; Forstrom and Sparrow, 1967; Vest and Lawson, 1972; Fuji et al., 1973; and Jaluria and Gebhart, 1977), time-dependent Stokes flows have remained largely untreated. But such flows have the important utility that flow fields due to the presence of solid boundaries can be synthesized from these flows using the method of images or some well-known reflection techniques. It is thus worthwhile to provide the solution to this problem and to study the behavior of the ensuing very weak thermal vortex rings.

We assume that the temperature field is unaffected by the fluid motion. By a dimensional analysis, it can be shown that this assumption does not lead to significant errors when the Prandtl number is small, which is a reasonable assumption here since the heat-generating rate is assumed to be small so that the induced flow is slow.

2 Problem Statement

Consider a horizontal line source of thermal energy embedded in an unbounded fluid of density ρ and kinematic viscosity ν. The fluid is Boussinesq incompressible with the density-temperature relation

$$\rho = \rho_0[1-\beta(T-T_0)], \tag{1}$$

where T is the temperature, β the volumetric coefficient of thermal expansion, and the subscript 0 denoting a reference state. Initially, the temperature is uniform everywhere in the system. At time $t=0$, the heat source starts liberating heat at a rate Q (watts per unit length of a rod). A cylindrical polar coordinate system (r, ϕ, z) is chosen with the $\phi=0$ plane horizontal and the z-axis along the line heat source. As the flow field is uniform on all planes normal to the z-axis, neither z nor the z-component of velocity appears in the analysis.

Taking advantage of the continuity equation

$$\nabla \cdot \mathbf{q} = 0 \tag{2}$$

where $\mathbf{q}=(u, v, w)$ is the fluid velocity, we define a stream function Ψ such that

$$u = r^{-1}\partial\Psi/\partial\phi, \quad v = -\partial\Psi/\partial r. \tag{3}$$

We introduce a set of nondimensional quantities

$$R = r/d, \quad t_* = \alpha t/d^2, \quad \Psi_* = \Psi/\nu, \quad T_* = (T-T_0)k/Q, \tag{4}$$

where d is a reference scale for length, k is the thermal conductivity and other symbols have their usual meanings. The energy equation in this nondimensional form reads (after dropping the asterisk):

$$\frac{\partial T}{\partial t} + \frac{\Pr}{R}\left(\frac{\partial \Psi}{\partial \phi}\frac{\partial T}{\partial R} - \frac{\partial \Psi}{\partial R}\frac{\partial T}{\partial \phi}\right) = \left(\frac{\partial^2}{\partial R^2} + \frac{1}{R}\frac{\partial}{\partial R} + \frac{1}{R^2}\frac{\partial^2}{\partial \phi^2}\right)T, \tag{5}$$

where $\Pr = \nu/\alpha$ is the Prandtl number. When the Prandtl number is small ($\Pr \leq 1$), the second term on the left side of Eq. (5) may be neglected in preference to the local derivative term, which is indeed in accordance with Stokes flow approximation. Thus, eliminating the pressure terms in the momentum equations through cross-differentiation and invoking Stokes flow approximation, we obtain for the conservation of momentum and energy in the nondimensional form in the limit of small Prandtl number (after dropping the asterisk):

$$D^2\left[D^2 - \frac{1}{\Pr}\frac{\partial}{\partial r}\right]\Psi = \frac{\mathrm{Ra}}{\Pr}\left[\cos\phi\,\frac{\partial T}{\partial R} - \frac{\sin\phi}{R}\frac{\partial T}{\partial \phi}\right], \tag{6}$$

$$\partial T/\partial t = D^2 T, \tag{7}$$

where

---

[1] Department of Mathematics, National College, Tiruchirapalli—620 001, India.

Contributed by the Fluids Engineering Division of THE AMERICAN SOCIETY OF MECHANICAL ENGINEERS. Manuscript received by the Fluids Engineering Division June 26, 1992; revised manuscript received February 23, 1993. Associate Technical Editor: F. T. Dodge.

from empirical plane wake predictions compared to values for the baseline 30 deg swept-base model with and without Wishbone vortex generators.

Acknowledgment

The work presented herein was largely accomplished under National Science Foundation grant no. CTS-8519116.

References

Lin, J. C., Selby, G. V., and Howard, F. G., 1991, "Exploratory Study of Vortex-Generating Devices for Turbulent Flow Separation Control," AIAA Paper No. 91-0042, AIAA 29th Aerospace Sciences Meeting.

Narasimha, R., and Prabhu, A., 1972, "Equilibrium and Relaxation in Turbulent Wakes," *Journal of Fluid Mechanics*, Vol. 54, pp. 1-17.

Patel, V. C., and Scheuerer, G., 1982, "Calculation of Two-Dimensional Near and Far Wakes," *AIAA Journal*, Vol. 20, No. 7, pp. 900-907.

Selby, G. V., 1989, "Passive Control of Three-Dimensional Separated Vortical Flow Associated with Swept Rearward-Facing Steps," ASME JOURNAL OF FLUIDS ENGINEERING, Vol. 11, No. 1, pp. 99-101.

Selby, G. V., and Miandoab, F. H., 1990, "Effect of Surface Grooves on Base Pressure for a Blunt Trailing-Edge Airfoil," *AIAA Journal*, Vol. 28, No. 6, pp. 1133-1135.

Selby, G. V., Miandoab, F. H., and Lin, J. C., 1990, "Effect of Passive Devices on Low-Speed Wake Flow for Unswept and Swept Blunt Trailing-Edge Airfoil Models," *Proceedings: 111th ASME Winter Annual Meeting—Forum on Unsteady Flow*, FED-Vol. 102, Dallas, TX, pp. 57-59.

Sharma, S. D., 1987, "Development of Pseudo-two-dimensional Turbulent Wakes," *Physics of Fluids*, Vol. 30, pp. 357-363.

Sreenivasan, K. R., 1981, "Approach to Self-Preservation in Plane Turbulent Wakes," *AIAA Journal*, Vol. 19, pp. 1365-1367.

Sreenivasan, K. R., and Narasimha, R., 1982, "Equilibrium Parameters for Two-Dimensional Turbulent Wakes," ASME JOURNAL OF FLUIDS ENGINEERING, Vol. 104, pp. 167-170.

Wheeler, G. O., 1989, Proprietary to Mr. Gary Wheeler, U. S. Patent pending.

Weak Thermal Vortex Rings

R. Ganapathy[1]

A simple mathematical model is proposed and a similarity solution is obtained to study the behavior of very weak thermal vortex rings induced by a horizontal line source of thermal energy in an unbounded fluid. The temperature distribution is assumed to be unaffected by the fluid motion, and the Stokes flow approximation is invoked. Streamlines are computed to demonstrate the evolution of the flow field.

1 Introduction

Determination of the flow field induced by a heat-generating body in the fluid surrounding the body is essential to the solution of many engineering problems such as the hydrodynamics of weak thermal explosions, cooling of the components of electrical and electronic equipment, and the management of nuclear waste materials. Providing the rate of heat generation is small, the flow may be modeled as Stokes flow. One may then neglect the convective terms in comparison to the local acceleration term in the momentum equations, and adopt the Boussinesq approximation to express the buoyancy force field in terms of the temperature field.

Although the importance of buoyancy driven flows due to the presence of horizontal line sources has been well established in the literature (for instance, Serruk, 1958; Crane, 1959; Spalding and Cruddace, 1961; Brodowicz and Kierkus, 1966; Forstrom and Sparrow, 1967; Vest and Lawson, 1972; Fuji et al., 1973; and Jaluria and Gebhart, 1977), time-dependent Stokes flows have remained largely untreated. But such flows have the important utility that flow fields due to the presence of solid boundaries can be synthesized from these flows using the method of images or some well-known reflection techniques. It is thus worthwhile to provide the solution to this problem and to study the behavior of the ensuing very weak thermal vortex rings.

We assume that the temperature field is unaffected by the fluid motion. By a dimensional analysis, it can be shown that this assumption does not lead to significant errors when the Prandtl number is small, which is a reasonable assumption here since the heat-generating rate is assumed to be small so that the induced flow is slow.

2 Problem Statement

Consider a horizontal line source of thermal energy embedded in an unbounded fluid of density ρ and kinematic viscosity ν. The fluid is Boussinesq incompressible with the density-temperature relation

$$\rho = \rho_0[1 - \beta(T - T_0)], \tag{1}$$

where T is the temperature, β the volumetric coefficient of thermal expansion, and the subscript 0 denoting a reference state. Initially, the temperature is uniform everywhere in the system. At time $t = 0$, the heat source starts liberating heat at a rate Q (watts per unit length of a rod). A cylindrical polar coordinate system (r, ϕ, z) is chosen with the $\phi = 0$ plane horizontal and the z-axis along the line heat source. As the flow field is uniform on all planes normal to the z-axis, neither z nor the z-component of velocity appears in the analysis.

Taking advantage of the continuity equation

$$\nabla \cdot \mathbf{q} = 0 \tag{2}$$

where $\mathbf{q} = (u, v, w)$ is the fluid velocity, we define a stream function Ψ such that

$$u = r^{-1}\partial\Psi/\partial\phi, \quad v = -\partial\Psi/\partial r. \tag{3}$$

We introduce a set of nondimensional quantities

$$R = r/d, \quad t_* = \alpha t/d^2, \quad \Psi_* = \Psi/\nu, \quad T_* = (T - T_0)k/Q, \tag{4}$$

where d is a reference scale for length, k is the thermal conductivity and other symbols have their usual meanings. The energy equation in this nondimensional form reads (after dropping the asterisk):

$$\frac{\partial T}{\partial t} + \frac{\Pr}{R}\left(\frac{\partial\Psi}{\partial\phi}\frac{\partial T}{\partial R} - \frac{\partial\Psi}{\partial R}\frac{\partial T}{\partial\phi}\right) = \left(\frac{\partial^2}{\partial R^2} + \frac{1}{R}\frac{\partial}{\partial R} + \frac{1}{R^2}\frac{\partial^2}{\partial\phi^2}\right)T, \tag{5}$$

where $\Pr = \nu/\alpha$ is the Prandtl number. When the Prandtl number is small ($\Pr \leq 1$), the second term on the left side of Eq. (5) may be neglected in preference to the local derivative term, which is indeed in accordance with Stokes flow approximation. Thus, eliminating the pressure terms in the momentum equations through cross-differentiation and invoking Stokes flow approximation, we obtain for the conservation of momentum and energy in the nondimensional form in the limit of small Prandtl number (after dropping the asterisk):

$$D^2\left[D^2 - \frac{1}{\Pr}\frac{\partial}{\partial r}\right]\Psi = \frac{\mathrm{Ra}}{\Pr}\left[\cos\phi\,\frac{\partial T}{\partial R} - \frac{\sin\phi}{R}\frac{\partial T}{\partial\phi}\right], \tag{6}$$

$$\partial T/\partial t = D^2 T, \tag{7}$$

where

---

[1] Department of Mathematics, National College, Tiruchirapalli—620 001, India.

Contributed by the Fluids Engineering Division of THE AMERICAN SOCIETY OF MECHANICAL ENGINEERS. Manuscript received by the Fluids Engineering Division June 26, 1992; revised manuscript received February 23, 1993. Associate Technical Editor: F. T. Dodge.

$$\mathrm{Ra}=(\beta g d^3/\alpha \nu k)Q \quad \text{(thermal Rayleigh number)},$$

$$D^2=\partial^2/\partial R^2+(1/R)\partial/\partial R+(1/R^2)\partial^2/\partial\phi^2. \tag{8}$$

These equations are solved subject to the initial and boundary conditions:

$$U=0, \quad V=0, \quad T=0 \text{ at } t=0,$$

$$U\rightarrow 0, \quad V\rightarrow 0, \quad T\rightarrow 0 \text{ as } R\rightarrow\infty,$$

$$V=\partial U/\partial\phi=\partial T/\partial\phi=0 \text{ at } \phi=\pm\pi/2, \tag{9}$$

where, $(U,V)=(d/\nu)\,(u,\,v)$ are the nondimensional form of the velocity components. Further, the conservation of heat flux requires that

$$\lim_{R\rightarrow 0}\,[-2\pi R\partial T/\partial R]=1. \tag{10}$$

With the help of (9) and (5) we conclude that

$$T=\mathrm{O}\,(\log R), \quad U=\mathrm{O}\,(R^{-1}\log R),$$

$$V=\mathrm{O}\,(R^{-1}) \text{ as } R\rightarrow 0. \tag{11}$$

3 Results and Discussion

From Carslaw and Jaeger (1959), the solution of Eq. (7) that satisfies the initial and boundary conditions is:

$$T=-(4\pi)^{-1}Ei(-R^2/4t), \tag{12}$$

where Ei is the exponential integral given by

$$Ei(-x)=-\int_x^{\infty}\exp(-u)/u\,du. \tag{13}$$

The function Ψ is now found from the solution of Eq. (6) in which the variables are separated by setting

$$\left[D^2-\frac{1}{\mathrm{Pr}}\frac{\partial}{\partial t}\right]\Psi=(\mathrm{Ra}/\mathrm{Pr})\,(4\pi)^{-1}\cos\phi f(R,\,t), \tag{14}$$

where $f(R,\,t)$ is the function to be determined.

Substituting (12) and (14) into (6), we obtain after taking the Laplace transform,

$$\bar{f}''+(1/R)\bar{f}'-(1/R^2)\bar{f}=K_1(R\sqrt{s})/\sqrt{s}, \tag{15}$$

where

$$\bar{f}=\int_0^{\infty}\exp(-st)\cdot f(R,\,t)dt, \tag{16}$$

is the Laplace transform of f and the primes denote differentiation with respect to R, K_1 being the modified Bessel function of the second kind of order 1. The general solution of (15) is

$$\bar{f}=a_1(s)/R+a_2(s)R^2+K_1(pR)/p^3, \tag{17}$$

where a_1 and a_2 are the constants of integration and $p=\sqrt{s}$. Finally, setting

$$\Psi=(\mathrm{Ra}/\mathrm{Pr})(4\pi)^{-1}\cos\phi\cdot F(R,\,t), \tag{18}$$

we obtain from (14) after taking the Laplace transform

$$\bar{F}''+(1/R)\bar{F}'-(W^2+1/R^2)\bar{F}=\bar{f}, \tag{19}$$

where $W^2=s/\mathrm{Pr}$ and all other symbols have their usual meaning. The complete solution of (19) is

$$\bar{F}=a_3(s)\cdot I_1(WR)+a_4(s)\cdot K_1(WR)$$

$$+\int G(R,\,x)\cdot\bar{f}(x)dx, \tag{20}$$

where a_3 and a_4 are the constants of integration and

$$G(R,\,x)=-K_1(WR)\cdot I_1(Wx), \quad (x\leq R)$$

$$=-K_1(Wx)\cdot I_1(WR). \quad (x>R) \tag{21}$$

The boundary conditions ensure that

$$a_1=W^3/[p^4(W^2-p^2)], \quad a_2=0, \quad a_3=0,$$

$$a_4=W/[2p^4(W+p)]. \tag{22}$$

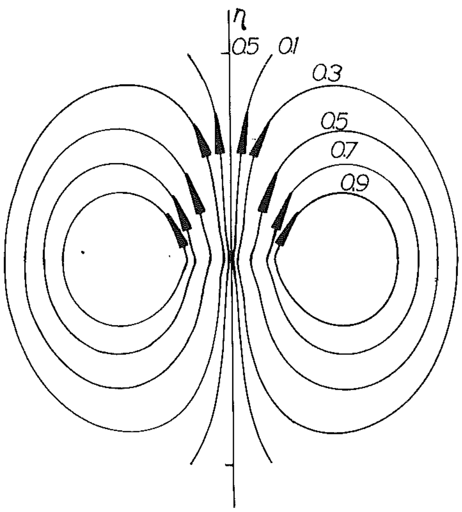

Fig. 1 Transient natural convection flow around a horizontal line heat source. Curves represent $[At^{3/2}]^{-1}\Psi=\text{const}$.

We now obtain from (17)

$$\bar{f}=[-1/R+pK_1(pR)]/[p^4(W^2-p^2)]. \tag{23}$$

Using the table of Laplace transform due to Campbell and Foster (1961), we have after inverting (23),

$$\Psi=t^{3/2}A[-1/\eta+(1/\eta+\eta)\exp(-\eta^2)$$

$$+\eta(2+\eta^2)Ei(-\eta^2)]\cos\phi, \tag{24}$$

where,

$$\eta=R/2\sqrt{t} \text{ and } A=(4\pi)^{-1}[\mathrm{Ra}/(1-\mathrm{Pr})].$$

The streamlines $[At^{3/2}]^{-1}\Psi=\text{const}$ as computed from Eq. (24) are shown in Fig. 1. The transient flow pattern for small values of η in the region close to the source consists of an expanding vortex whose radius increases with time as $t^{3/2}$, the whole process being dominated by viscous and thermal diffusion. This is physically meaningful since the rapid release of the quantity of heat from the source into the large region of fluid at rest sets in motion a small volume of heated fluid and as it rises, this buoyant fluid grows in volume through conduction of heat and viscous diffusion of momentum outwards. Since the heated fluid is displaced upwards by the ambient fluid from approximately its own level and in turn displaces the ambient fluid from its path, the flow has the general pattern of a vortex ring but unlike the case of a point heat source where we witness ciruclar vortices (see Morton, 1960) here the vortices are toroidal in shape. Near the origin the streamlines come close together illustrating the fact that the velocity is infinite at the source and as t increases, the flow pattern present near the source is likely to spread outwards filling the entire space. Nevertheless, as the solution for Ψ (Eq. (24)) contains $\cos\phi$, the symmetry of the streamlines about the $\phi=0$ plane is preserved at all times. The slight bulging of the streamlines near the origin indicates the impulsive effect of the source on the fluid particles in its vicinity and is created by the fluid particles driven upward under the action of buoyancy. There is no accumulation of heat into the vortex ring and the flow in and around the vortex rings remains laminar, which is similar to the buoyant plumes that rise from steady sources of heat or other sources of positive buoyancy. Further, as the heat-generating rate is small, the vortex ring will be thermally weak and the pattern differs only slightly from that of an ordinary vortex ring without buoyancy (see Lamb, 1931); in particular, there is a larger core to the ring, which is a consequence of the inherently stable nature of such a light core under forces produced by rotation about its axis.

In order to exemplify the results, numerical values of the

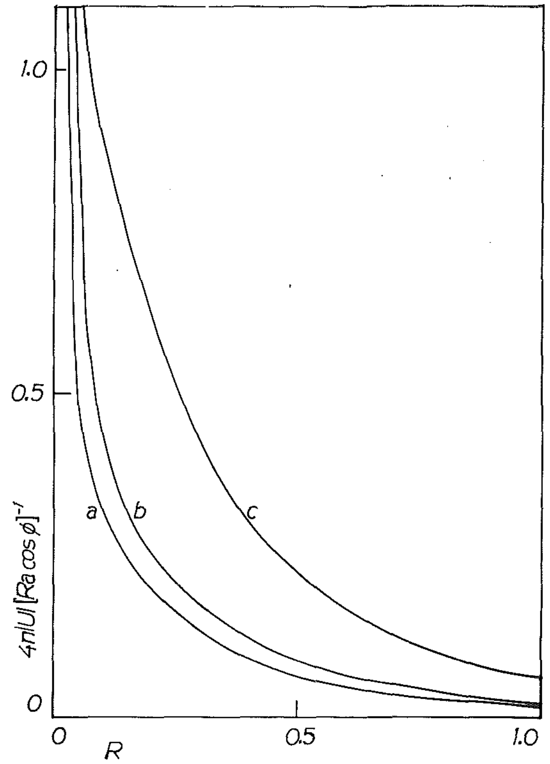

Fig. 2 Radial velocity profiles ($t = 0.1$) (*a*) Pr = 0.025, (*b*) Pr = 0.25, (*c*) Pr = 0.7

magnitudes of the radial velocity were computed for different values of Pr and for different spacial positions at time $t = 0.1$. These results are plotted in Fig. 2 from which it is deducible that the magnitudes of the velocity diminish with distance, but increase with Prandtl number. This then tacitly implies and confirms that our solution is valid for small Prandtl numbers only.

4 Conclusion

The similarity solution we have obtained for the stream function is indeed the Green's function for this class of problems and is valid in the limit of small Prandtl number only ($\mathrm{Pr} \leq 1$). From this solution, solutions to problems where the heat-generating rate is a general but known function of space and time, in bounded and unbounded domains can be synthesized using known techniques. As the flow field is thermally weak, the solution is expected to give a reasonably good picture of the free convection motion induced by the line heat source and in the absence of stability effects, the behavior is unlikely to change radically for moderate values of the Prandtl number also. In the case of large Pr ($> > 1$), some simplification in the analysis may be achieved by treating the velocity field as a quasistatic Stokes flow (see for instance, Krenk, 1981). Under this circumstance, it would, however, not be justifiable to ignore the interaction between velocity and temperature fields.

It is worth noting that for large t, the fluid velocity is given by

$$(u,\ v) \propto \log \eta (\sin \phi, \quad \cos \phi). \tag{25}$$

Since $\eta = R/2\sqrt{t}$, the magnitude of this velocity grows without bounds in the limit $t \rightarrow \infty$, which is expected for such problems of line heat sources and which only mirrors the well-known results for conduction problems. Consequently, our solution is valid for small and moderate values of t only. Even if we consider higher-order corrections to the velocity and temperature fields, this peculiarity of unboundedness of the fluid velocity will persist whenever $t \rightarrow \infty$. Since the thermal field is very weak and the induced flow is slow, the unboundedness or otherwise of the velocity field for large time is not of great significance. Since the temperature distribution is not influenced by the fluid motion, we have not presented the results in terms of a Nusselt number.

Though explicity not shown, the method adopted in this work is analogous to a regular perturbation involving series expansions for the dependent variables in terms of Pr. Hence the result we have obtained for T represents the zeroth-order solution for the thermal field, whereas the solution for Ψ [Eq. (24)] is the first-order convective correction to the velocity field and consequently it represents the solution for conduction aided free convective flow. Such is always the case whenever a heat-generating body is suddenly embedded in a fluid which is otherwise at rest. In fact, the flow may be realized when an electric current is passed through a horizontal wire, which is submerged in an unbounded medium.

Acknowledgment

The author is thankful to the referees for their useful suggestions which led to a definite improvement of the paper.

References

Brodowicz, K., and Kierkus, W. T., 1966, "Experimental Investigation of Laminar Free Convection Flow in Air Above a Horizontal Wire With Constant Heat Flux," *International Journal of Heat Mass Transfer*, Vol. 9, pp. 81–94.

Campbell, G. A., and Foster, R. M., 1961, *Fourier Integrals for Practical Applications*, Van Nostrand.

Carslaw, H. S., and Jaeger, J. C., 1959, *Conduction of Heat in Solids*, Oxford University Press, pp. 261–262.

Crane, L. J., 1959, "Thermal Convection From a Horizontal Wire," Z. Angew Mathematics Physics, Vol. 10, pp. 453–460.

Forstrom, R. J., and Sparrow, E. M., 1967, "Experiments on the Buoyant Plume Above a Heated Horizontal Wire," *International Journal of Heat Mass Transfer*, Vol. 10, pp. 321–331.

Fuji, T., Marioka, I., and Uhera, H., 1973, "Buoyant Plume Above a Horizontal Line Heat Source," *International Journal of Heat Mass Transfer*, Vol. 16, pp. 755–768.

Jaluria, Y., and Gebhart, B., 1977, "Buoyancy-Induced Flow Arising From a Horizontal Thermal Source on an Adiabatic Vertical Surface," *International Journal of Heat Mass Transfer*, Vol. 10, pp. 153–157.

Krenk, S., 1981, "Creeping Viscous Flow Around a Heat-Generating Solid Sphere," ASME *Journal of Applied Mechanics*, Vol. 48, No. 2, pp. 239–242.

Lamb, H., 1931, *Hydrodynamics*, Cambridge University Press.

Morton, B. R., 1960, "Weak Thermal Vortex Rings," *Journal of Fluid Mechanics*, Vol. 9, pp. 107–118.

Serruk, L. G., 1958, "Laminar Convection Over a Heated Wire," *Journal of Applied Mathematics Mechanics*, Vol. 22, pp. 807–812.

Spalding, D. B., and Cruddace, R. G., 1961, "Theory of Steady Laminar Flow Above a Line Heat Source in a Fluid of Large Pr and Temperature-Dependent viscosity," *International Journal of Heat Mass Transfer*, Vol. 3, pp. 55–59.

Vest, C. M., and Lawson, M. L., 1972, "Onset of Convection Near a Suddently Heated Horizontal Wire," *International Journal of Heat Mass Transfer*, Vol. 15, pp. 1281–1283.